

*Thermodynamical Properties of Nuclear Matter
from a Self-Consistent Green's Function Approach*

Memòria presentada per
Arnau Rios Huguet
per optar al títol de
Doctor en Ciències Físiques.
Barcelona, 23 febrer de 2007.

Programa de doctorat
Física Avançada
Bienni 2002-2004,
del Departament d'Estructura
i Constituents de la Matèria,
Universitat de Barcelona.

Directors de tesi

Artur Polls Martí
Àngels Ramos Gómez

*Als meus pares,
pel seu suport incondicional.*

*A la Rosa,
per l'amor.*

In a way, he realized, I'm part of the form-destroying process of entropy.

Do androids dream of electric sheep?
Philip K. Dick

Contents

List of figures	v
Agraïments	ix
Chapters	1
1 The Nuclear Many-Body Problem	1
1.1 Nucleon-nucleon interaction	2
1.2 Nuclear matter	8
1.3 Correlations in nuclear physics	10
1.4 Many-body physics at finite temperature	16
1.5 Program of the Thesis	18
2 Many-Body Green's Functions at Finite Temperature	21
2.1 Quantum statistical mechanics	21
2.2 Green's functions at finite temperature	24
2.3 Free case	42
2.4 Self-energy	44
2.5 Quasi-particle approximation	47
2.6 Diagrammatic expansion of the propagator	51
2.7 Self-consistent renormalization	55
3 Luttinger-Ward Formalism	59
3.1 Linked cluster expansion	59
3.2 Coupling constant method	61
3.3 Luttinger-Ward partition function	66
3.4 Free partition function	77
3.5 Partition function of a correlated system of fermions	79
3.6 Entropy of a correlated system of fermions	84
4 Hartree-Fock Approximation	93
4.1 Formulation in terms of Σ	93

CONTENTS

4.2	Self-Consistent Hartree-Fock	95
4.3	Formulation in terms of \mathcal{G}_{II}	97
4.4	Partial wave expansion	101
4.5	Microscopic results	106
4.6	Macroscopic results	113
5	Ladder Approximation	123
5.1	Two-body propagator	123
5.2	In-medium interaction	127
5.3	Lippman-Schwinger equation	132
5.4	Ladder self-energy	135
5.5	Self-Consistent Green's Functions scheme	139
5.6	Connection to other approaches	142
5.7	Microscopic results	146
5.8	Beyond the ladder approximation	167
6	Thermodynamical properties of nuclear matter	171
6.1	Microscopic results	171
6.2	Comparison among different approximations	176
6.3	Thermodynamical consistency	187
6.4	Macroscopic results	190
6.5	Future perspectives	203
	Summary and conclusions	207
	Appendices	215
A	Perturbation Expansion of the Green's Function	215
B	Feynman rules and diagrams	225
C	Sums over Matsubara frequencies	229
C.1	Functions with a single pole	229
C.2	Functions with double poles	231
C.3	Functions with cuts in the real axis	232
D	Degenerate and classical limits	235
D.1	Degenerate limit	235
D.2	Classical limit	242
E	Numerical implementation of the SCGF scheme	245

Resum en català	253
El problema nuclear de molts cossos	253
Funcions de Green de molts cossos a temperatura finita	257
Formalisme de Luttinger-Ward	260
L'aproximació de Hartree-Fock	263
L'aproximació d'escala	268
Propietats termodinàmiques de la matèria nuclear	275
Resum i conclusions	282
Bibliography	285
List of publications	299

CONTENTS

List of Figures

1.1	NN interaction phase shifts	4
1.2	CDBONN potential matrix elements in momentum space	6
2.1	Convergence regions for $\mathcal{G}^>$ and $\mathcal{G}^<$	27
2.2	Quasi-particle and background contributions to the spectral function	49
2.3	First order diagrams that contribute to the Green's function	51
2.4	Second order diagrams that contribute to the Green's function	52
2.5	Diagrammatic expression of the reducible self-energy	53
2.6	Reducible self-energy as an iterated series of irreducible self-energy pieces	54
2.7	Diagrammatic representation of Dyson's equation	54
2.8	Self-energy in terms of the free and the dressed propagator	55
2.9	Self-consistent renormalization on a fermion line of a second order diagram	56
2.10	Self-consistent renormalization of a whole second order diagram	57
3.1	Some first and second order contributions to $e^{-\beta(\Omega-\Omega_0)}$	60
3.2	Examples of Φ functionals	70
3.3	Ambiguous self-energy insertions in closed diagrams	71
3.4	Different contributions to $\Xi(k, \omega)$: results	87
3.5	Energy dependence of $\lambda(k, \omega)$	88
4.1	Hartree-Fock self-energy	94
4.2	Complete single-particle propagator in the Hartree-Fock approxi- mation	95
4.3	Self-Consistent Hartree-Fock self-energy	96
4.4	Iterations in the Self-Consistent Hartree-Fock approximation	98
4.5	Diagrammatic representation of the two-body propagator	99
4.6	Diagrammatic representation of the decoupling in the Hartree-Fock approximation	100
4.7	Diagrammatic representation of the decoupling in the Self-Consistent Hartree-Fock approximation	101
4.8	HF and SCHF self-energies: results	108

LIST OF FIGURES

4.9	HF and SCHF momentum distributions: results	109
4.10	SCHF effective mass at the Fermi surface	112
4.11	SCHF energy per particle: results	114
4.12	Φ -functional for the SCHF approach	115
4.13	Density and temperature dependence of the entropy per particle within the SCHF approach	117
4.14	Free energy per particle and chemical potential within the SCHF approach	119
4.15	Pressure within the SCHF approach	120
5.1	Diagrammatic expansion of the two-body propagator in the ladder approximation	124
5.2	Diagrammatic representation of the two-body propagator in the lad- der approximation	125
5.3	Diagrammatic representation of the two-body propagator from the decoupling of the three-body propagator	126
5.4	Diagrammatic expression of the T -matrix	127
5.5	Diagrammatic expansion of the T -matrix	128
5.6	Diagrammatic representation of \mathcal{G}_{II}^0	131
5.7	Ladder self-energy	136
5.8	Diagrammatic representation of the generalized Hartree-Fock con- tribution to the ladder self-energy	137
5.9	Density plots of the in-medium interaction	147
5.10	Temperature dependence of the imaginary part of the T -matrix	148
5.11	Temperature dependence of the real part of the T -matrix	149
5.12	Momentum and energy dependence of the self-energy	150
5.13	High energy tails of $\text{Im } \Sigma(k=0, \omega)$	151
5.14	Density and temperature dependence of $\text{Im } \Sigma(k, \omega)$	153
5.15	Self-consistent spectrum: graphical solution	154
5.16	SCHF, BHF and SCGF single-particle spectra	155
5.17	Density and temperature dependence of the \mathcal{A} spectral function	158
5.18	Low temperature momentum distribution	161
5.19	Density and temperature dependence of the SCGF momentum dis- tribution	162
5.20	Convolution of $\mathcal{A}(k, \omega)$ and $f(\omega)$ at different temperatures	164
5.21	Depletion: density and temperature dependence	165
5.22	Diagrams appearing and lacking in the ladder approximation	168
6.1	\mathcal{A} and \mathcal{B} spectral functions: comparison	173
6.2	Density and temperature dependence of the \mathcal{B} spectral function	174
6.3	Momentum dependence of the ζ function for different densities	178
6.4	Momentum dependence of the ζ function for the different approxi- mations	180

6.5	Different approximations to the entropy as a function of the density	182
6.6	Different approximations to the entropy as a function of the temperature	184
6.7	Fulfillment of thermodynamical consistency	189
6.8	SCGF energy per particle: results	190
6.9	Contribution of the momentum distribution to the kinetic energy .	191
6.10	Ratio of correlated to mean-field kinetic and potential energies . . .	193
6.11	Density and temperature dependence of the entropy per particle within the SCGF approach	195
6.12	Ratio of correlated to mean field entropies	196
6.13	Theoretical and experimental values of the entropy per particle: comparison	197
6.14	Free energy per particle and chemical potential within the SCGF approach	198
6.15	Pressure within the SCGF approach	201
6.16	The Maxwell construction and the liquid-gas phase transition . . .	202
B.1	Prescription for the in- and out-going fermion lines in the interaction vertices	226
B.2	Application of the Feynman rules to some one-body propagator Feynman diagrams	227
C.1	Integration contours C and C' in the complex plane for a function with a single pole	230
C.2	Integration contours C and C' in the complex plane for a function with two poles	231
C.3	Integration contours C and C' in the complex plane for a function with a cut in the real axis	233
D.1	$f'(x)$ and $\sigma(x)$ as functions of x	238
1	Representació diagramàtica de l'equació de Dyson	259
2	Autoenergia Hartree-Fock	264
3	Autoenergia en les aproximacions de HF i SCHF	265
4	Dependència en densitat i temperatura de l'entropia per partícula en l'aproximació de SCHF	266
5	Expansió diagramàtica del propagador a dos cossos en l'aproximació d'escala	268
6	Expansió diagramàtica de la matriu T	269
7	Autoenergia en l'aproximació d'escala	270
8	Dependència en temperatura i densitat de la funció espectral	272
9	Espectres mono-particulars en les aproximacions de SCHF, BHF i SCGF	273

LIST OF FIGURES

10	Distribució de moments en l'aproximació de SCGF: dependència en densitat i temperatura	274
11	Dependència en temperatura i densitat de la funció espectral \mathcal{B} . . .	276
12	Dependència en densitat i temperatura de l'entropia per partícula en l'aproximació de SCGF	277
13	Energia per partícula en l'aproximació de SCGF: resultats	279
14	Consistència termodinàmica en l'aproximació de SCGF	280
15	Construcció de Maxwell i transició de fase líquid-gas	281

Agraïments

Una tesi doctoral, en contra d'allò que us puguin dir, és més un esforç col·lectiu que un projecte personal. En el seu desenvolupament, en la seva redacció i en la seva defensa hi participen tota una colla de persones, el nom de les quals queda sovint soterrat en l'oblit. I això que, en el pitjor dels sentits, el doctorand no és més que un simple lladre, que s'emporta el bo i millor de cada casa i ho acaba emprant pel seu propi bé personal! Aquests agraïments intenten, d'alguna manera, esmenar aquesta injustícia...

És ben clar que, en el procés de manlleu constant que suposa una tesi (si em deixeu continuar amb la metàfora), els que en surten pitjor parats són els directors. L'estudiant els roba les idees, els comentaris, les propostes i, a vegades, fins i tot, els gestos i les manies. Aquest ha estat, em temo, el meu cas i he assimilat tant la personalitat de l'Artur que més d'un cop m'han dit que "aquest comentari és molt del teu jefe" o "no siguis tan pessimista, que ja sembles l'Artur!". En tot cas, jo no crec que aquesta assimilació tingui res de nociu, sinó més aviat al contrari i haig de dir que, ara per ara, el considero el meu pare científic i un molt bon amic. Amb l'Àngels potser aquest procés ha estat menys tangible, però tant de bo que hagi pogut robar-li una mica de la seva capacitat d'anàlisi, d'una profunditat extraordinària, o un xic de la seva personalitat càlida, que m'ha permès superar, més d'una i de dues vegades, els daltabaixos que tota tesi comporta. Gràcies, A&A, per tenir sempre la vostra porta oberta a totes les meves preocupacions!

D'altra banda, el doctorand no és només un lladre casolà. És també un espia industrial a escala internacional, que visita diferents laboratoris i n'importa les idees més fonamentals. Curiosament, el lloc on menys temps he passat és on s'han gestat la major part de les idees exposades en aquesta tesi! Let me thus thank Prof. Herbert Müther for his kind hospitality during my visits to Tübingen. I am also extremely grateful to that extraordinary physicist, Tobias Frick, whose work laid the basis for this thesis and whose collaboration was fundamental in its development. I also have to thank Prof. Bengt Friman, for allowing me to stay for a couple of months in the theoretical division of GSI: an amazing place where one seems to be learning physics endlessly. ¿Hubiera yo sobrevivido en Alemania sin Isaac? Hubo entonces momentos (y sobre todo comidas!) difíciles de olvidar: muchas gracias por tus enseñanzas y por tu amistad, que todavía perduran! Un abrazo también para todos los que hicisteis que mi estancia en el GSI fuese de bien

a mucho mejor: Alberto, Noelia, Gonzalo, Barbara y frau Rinnert, por supuesto!

A més a més, tot criminal que es preciï ha de passar algun cop per París, la ciutat del lladre de “guant blanc”, la cuna d’Arsène Lupin. Je dois donc remercier à Jérôme de m’avoir accueilli pendant un stage qui a tout à fait changé ma vie. Ton hospitalité, la volonté que tu as mis à me montrer la physique (et Paris!) et les sages conseils que tu m’as donné pendant et après mon séjour à Orsay sont de choses que je n’oublierais jamais. Des salutations au group de physique théorique de l’IPN, qui a été une très agréable compagnie pendant mon séjour: Giaï, Elias, Marcella, Nicole, Marie-Thérèse. Et des salutations aussi à Camille, pour les croissants d’un certain matin... I què puc dir de la colla d’amics que van fer que la meva estada a París fos inoblidable? Què dir de Montorgueil, del Fèlix, de la seva paciència, els seus sopars, la seva inquietud cultural? No he tingut mai una vida tan (positivament) agitada com la que vaig tenir a París (començant per la Nuit Blanche i acabant per les sessions de Pirdidos) i és sens dubte gràcies al que fou, durant dos mesos, el meu pianista particular. Gràcies també al Xavi, per creuar sol el Sena innombrables vegades i fer-nos aquelles visites interminables, assegut dins el forat del nostre sofà... Tant de bo no s’hagués acabat mai!

En un bon “cop” criminal, és molt important disposar d’una bona colla de professionals. El meu *rat pack* particular el formen dos bons amics: el Jordi i el Chumi. Si l’Artur i l’Àngels han estat els meu pares científics, crec que el Jordi vindria a ser el meu germà gran. M’ha ensenyat tot el que es necessita per sobreviure en aquest món i hem fet un munt de coses junts (els Encontres en són només un exemple) que perduraran més enllà d’una amistat que espero que no acabi mai! El Chumi, en canvi, és com un germà bessó: aquell en qui et fixes i en qui et veus sempre reflexat. També hem passat per un munt de coses plegats (des de Granada a Gràcia) i sempre recordaré la seva comprensió, la seva inquietud sense fronteres i el fet que sigui el culpable d’un vici que no tenia abans de trepitjar el departament: la cervesa! Tota banda criminal necessita, a més, una component femenina, que aporti el seu toc de glamour i de sentit comú. No puc deixar d’esmentar, doncs, les tres noies que, amb la seva companyia, han aconseguit que el nostre despatx no es convertís en un pou de masculinitat sense fons: la Laura (la germana pròdiga), la Glòria (no per ser la més efímera ets la menys important) i l’Estela (ánimos con esas tres letras malditas: la Q, la C y la D).

Un bon lladre ha saber viure entre les dues fronteres, la justícia i la criminalitat, i per fer-ho li cal tenir una bona xarxa d’informadors. En el meu cas, crec que puc considerar el grup de Física Atòmica i Nuclear com el meu grup d’assistents particulars, sempre amb savis consells que m’han ajudat a moure’m a través d’aquesta jungla d’asfalt que és la recerca. A la Muntsa haig d’agrair-li que s’hagi preocupat per mi i m’hagi aconsellat per on tirar, sense esperar mai res a canvi. Com l’Assum, de qui admiro el seu contrapunt realista, molt necessari en la nostra professió. Don Bruno, el torbellino que ha revolucionado nuestro grupo

para bien: gracias a tí y a Charlotte por cuidar de Rosa y de mí! Ay, ay, ay: my dearest Tapas, wherever you and Jaya are, I can positively say that you changed the way I look into the world: thanks for a friendship without borders! I also want to thank Tetsuro Mizutane, for the advices on Paris. Last but not least, thanks to Bolodya and Erik for making our lunches much more tasty! I records a un parell de FANs petitets: la Mariona, de moment l'única en la línia successòria de l'Artur (no deixis que cap espinor et faci baixar el cap!) i el Xavi Roca (som la demostració viva que la física nuclear no està morta!).

Més enllà de FAN, hi ha membres d'altres màfies criminals d'ECM que m'han ajudat a perpetrar aquest acte criminal que teniu a les mans. L'Oliver m'ha acompanyat en les classes del Curs 0, en molts berenars (al despatx interior i al Dunkin de Palau Reial) i en els incansables brainstormings dels Encontres. Amb el Jorge he compartit moltes passejades després del Goethe, que han estat la meva principal motivació per a continuar estudiant alemany. Al David, que no per ser el més jove és el més inexpert, vull desitjar-li sort (tot i que no la necessita!) i agrair-li la seva incessant activitat durant la nostra col·laboració. Vull agrair també l'Ernest i el Jaume per haver compartit amb mi un Curs 0 cadascun i haver-me ajudat a portar-ho molt millor. Una salutació als companys de paret, el Carlos (i les seves sempre benvingudes visites), el Xavi Garcia, el Roman i la Míriam. Finalment, vull agrair als PAS d'ECM per l'ajuda inestimable en tràmits burocràtics, informàtics i logístics diversos: sense el vostre guiatge no sé on hauria arribat!

Les primeres escomeses de tot criminal, però, s'han de fer sota la supervisió d'experts en la matèria. En aquest cas, la meva primera incursió en el tema de la recerca van ser dos treballs de DEA i voldria aprofitar per agrair als dos tutors corresponents, el Mario Centelles i el Joan Soto, per la seva ajuda. También quiero agradecer a Cristina Manuel por haber confiado en mí para lo que fue una corta pero intensa colaboración. Deixeu-me donar les gràcies també al Josep Maria Pons, per tenir sempre oberta la porta als Encontres amb el Tercer Cicle. A ell i al Josep Perelló voldria agrair-los l'oportunitat d'haver pogut participar en un acte tan extraordinari com fou el sopar de cloenda de l'Any Mundial de la Física.

La perpetuació de l'espècie és una regla fonamental també en el món criminal, i jo he intentat seguir-la tan bé com he pogut. Des d'aquí voldria agrair els meus alumnes del Curs 0 pel seu esforç i, sobretot, per les seves preguntes, que més d'un cop m'han posat en un compromís... També voldria agrair la predisposició dels participants als Encontres al Tercer Cicle (conferenciants i públic), perquè han convertit aquesta activitat en un referent de la divulgació en la nostra Facultat. A la nova comissió organitzadora (Francesc, Sònia, Miguel...) els desitjo moltíssima sort!

En aquests anys de doctorat, he tingut l'oportunitat de formar part d'algun càrtel nacional i internacional. El primero de ellos fue con Manolo Valverde, en unos días más que agradables en Granada (con visita al Amador incluida) y en

Polonia. Greetings to the Oromana gang, a rare example with a large survival rate: Lorenzo, Giulia and, especially, Rolf, for keeping it alive after four years and for your nice visits to Barcelona! I also hope that the Like-a-River community will persist for a long time: thanks for those amazing days at Erice and Favignana to Audrey, Beatriz, Simone, Raul, Tudi and the others! Thanks to Arthur Ankowski in Wroclaw, I might have not survived without your help. I also want to send my best regards to Hutaurok Parada, for the days spent together in Trieste.

Tant robar i robar pot comportar dures seqüeles psicològiques, que podrien fer-se persistents sense una bona vàlvula d'escapament. En el meu cas, els amics, tots aquells que m'heu aguantat aquests anys, m'heu ajudat a no perdre el nord. Y mi Norte, claro está, siempre apunta a Nacho: por ser buen compañero de viajes y por haberme dado la oportunidad de conocer a gente maravillosa (Rosa, claro, pero también Juan, Flor, Galicia entera). Y por ser, sobre todo, el mejor de los amigos, de Barcelona a Estocolmo, de Lugo a Wisconsin y al fin del mundo, que son diez mil. Mención aparte merecen los integrantes del equipo de Jesús 18, que han convivido conmigo y han aguantado muchas malas caras y malos humores: gracias a María por los dos años maravillosos en que convivimos como los mejores *friends*, a Kepa por ser tan comprensivo i a la Carme per cuidar-nos tan i tan bé! No me olvido, claro, de mi amor platónico, Yago, que siempre ha estado ahí para “amarme en secreto”. Els sopars de francés han estat un desfogament, una alenada d'aire fresc cada dimarts a la nit: gràcies a la Laia i la Mireia per ser, senzillament, com són. L'Ermengol, per mèrits propis, també entra en la llista pels (quants, vint?) anys d'amistat, de rialles, de vida plegats, que hem compartit amb la colla de sempre (Pau, Fer, Xavi i companyia): encara ens queden molts anys per compartir! Unos cuantos años nos unen también a Manelé y a mí: muchas gracias por esforzarte en no perderme de vista! Y, por muy lejos que estén, no me olvido nunca de esas tordisimas, que, desde el primer día, me dejaron ser “una más”. También quiero mandar un abrazo muy fuerte a la familia Sanchis-Guarner Herrero, porque os habeis convertido en mi segundo hogar (y no lo digo sólo por la comida!).

La facultat té part de culpa en el meu procés de caiguda al costat obscur. Víctimes primerenques de les meves primeres aventures amb la física han estat els companys que, en un moment o altre, han passat per aquí. Al Jose li haig d'agrair la seva comprensió, el seu bon humor i la seva capacitat per crear frases que fan història: contigo todo mola más de lo que parece! Aprovecho para saludar también a la Isa, que no por ser economista (o de l'Hospitalet) es menos importante, y darle muchos ánimos: ya verás como en un plis esto está hecho! Amb el Manèlix ens uneixen moltes hores de problemes i de teoria, de xerrades metafísiques i mundanes, i ja no ens les pot treure ningú! El Raimon és una font d'activitats imparabile, mentre que el Pep ha estat l'únic capaç de trobar un treball de veritat: gràcies als dos per aguantar les meves interminables històries! Al Joan Rojo i a mi ens guia una espècie de trajectòria comú, des de primer fins fa uns mesos, tot i que tu

sovint prens la branca més valenta: una abraçada per la Sònia i el Jaume! Durant la carrera, vaig coincidir amb molta gent a qui vull saludar des d'aquí: l'Ignasi (el barri ha donat bona gent), el Ramon (per fer-me descobrir Laszlo Biro i moltíssimes coses més), el Josep de la Puente, el Xavi Illa, el Marc Manera (sempre coincidim!), el Tòbal, el Gonçal, l'Anna Cabré... Massa tard vaig descobrir que tenia una vena artística, i voldria agrair als festivaleros per fer-m'ho veure: Cumi, Mau, Isaac, Rubén (sempre et recordarem) i companyia. D'altra banda, ser pessebrista és una experiència que va molt més enllà d'un simple bar, és més un estil de vida que conjuga tota una constel·lació de personatges: en Jordi Garra (gràcies per les xocolatines), el Sandro, el jaijondo... De Majo, me gusta haber descubierto que tenemos mucha geografía en común: de Valencia a Michigan pasando por Londres!

Mirant encara una mica més enrera, potser la meva inspiració criminal deuria forjar-se a la Pegaso i al Príncep de Viana, una escola i un institut de què guardo sobretot bons records. Vull agrair l'ajuda d'alguns professors que van guiar els meus passos en aquells temps. Molt especialment, l'Albert Violant i el Conrad Noguer, un matemàtic i un físic, que em van convèncer per escollir aquesta carrera i són, per tant, responsables de la meva felicitat posterior. Y Cari, gracias por aquel viaje a Madrid y por comprender, a tu manera, que yo no era un chico de letras!

Bé, això ja s'acaba: he repassat tot el meu historial del·lictiu, des dels primers dies fins al "gran golpe". I, amb tot, encara no us he parlat de la meva còmplice més íntima i especial: una persona que em complementa, m'entén i em millora; que em cuida, m'ajuda i m'estima; que em fa tenir els peus a terra i em fa mirar endavant. Amb ella, les coses més petites (una cançó, les nostres bicicletes, Rigus i Rigustina) es converteixen en grans meravelles. Fa una llarga temporada que viatgem junts i segur que ho continuarem fent molt de temps, independentment de la distància que ens separi. Al capdavant, si m'has aguantat durant els darrers mesos en què aquesta tesi s'ha convertit en una obsessió, pots aguantar-ho tot! Rosa, gràcies per la teva comprensió i pel teu amor sense límits: són, molt de llarg, el millor que m'ha passat mai.

Deixeu que m'aparti ja definitivament de la metàfora criminal per referir-me a la meva família. Als meus pares els dec tot el que sóc. D'ells em ve aquest afany de coneixement i d'ells he après a sentir passió per allò que faig. Heu guiat la meva vida i m'heu entès millor ningú. També voldria que la resta de Rios, Huguets, Duràs i Serranos us sentíssiu part d'aquesta tesi, que no hauria estat possible sense vosaltres. Deixeu-me destacar la comprensió i el recolzament de la meva àvia Rosita, que han estat fonamentals des que vaig néixer fins avui mateix. També, després de molts estius a Llançà, sóc qui sóc gràcies als meus "tatos" i a l'Alba. Ja ho veus, tato: tants anys d'ensenyances científiques han acabat donant el seu fruit! A més, Accent Idiomes és una part fonamental de la meva vida: els pocs rudiments d'anglès que sé i que m'han permès escriure el "totxo" que hi ha a continuació els dec a el Fabricio, la Karen i la resta de professors que, amb la seva

AGRAÏMENTS

paciència, van anar moldejant l'Arnauet i el van fer tornar una mica Arnold. Un abrazo muy fuerte también a todos los Huguet que siempre estais allí: tío Amadeo, Enrique, Ana...

Finalment, vull acabar aquests agraïments amb un petit record per tots aquells que hi eren abans i que han desaparegut al llarg d'aquests quatre anys i mig. Molt especialment, voldria recordar el meu tío Pepito que, durant la seva llarga enfermetat, em va servir d'exemple. És d'ell que he après la lliçó més important d'aquests anys: la vida és un regal preciós que hem d'expressar al màxim i que hem de gaudir intensament, per sobre de totes les desgràcies i fins l'últim dels seus instants.

Chapter 1

The Nuclear Many-Body Problem

The essential aim of quantum many-body physics is the description of the observable properties emerging from the underlying quantum behavior of systems formed by a large number of particles. The tools that many-body physics provides are general enough as to describe a large variety of these systems. From large astrophysical objects composed by degenerate gases of hadrons, to the innermost structure of the nucleon, along with the description of ultracold gases, the atom and its shells or the electronic structure of molecules, many-body physics is a discipline that englobes a vast amount of different problems in a common framework. This global view of the physics of very distinct systems is precisely what makes many-body theory very appealing. Among the problems that this discipline has faced, the *nuclear many-body problem* is of special relevance because of its long history. Although first proposed in the fifties, the nuclear many-body problem is still a source of all kind of theoretical challenges for physicists. As a matter of fact, it requires a lot of effort to get acquainted with the large number of different techniques that have been used in the treatment of this problem. This wide variety of approaches has been a major source of developments in many-body physics and it is perhaps the reason why nuclear physics is still one of the more relevant fields of research within many-body quantum mechanics.

And, yet, the definition of this problem is extremely simple. In the first place, one chooses the suitable degrees of freedom which, for standard nuclear physics, are the neutron and the proton, *i.e.* the nucleons. Secondly, the interaction among these constituent degrees of freedom has to be introduced. In contrast to other physical systems, where the interaction is given *a priori* (the Coulomb interaction in electronic systems, for instance), the nucleon-nucleon (NN) interaction is not completely known. A lot of its properties, however, can be derived from the analysis of NN scattering experiments and from the phenomenology of nuclear physics, and several parameterizations which describe accurately the properties of two- and three-body nuclear systems are presently available. These are the so-called *microscopic interactions*, which will be briefly described in the following section.

Once the constituents and their interactions are chosen, one should in principle solve the Schrödinger equation. In the nuclear many-body problem, one usually assumes a non-relativistic treatment because of the relatively low energies involved in conventional nuclear physics. Moreover, and to simplify the problem, one usually considers an infinite system of nucleons with the same fraction of protons and neutrons. This corresponds to symmetric nuclear matter, a fictitious homogeneous system in which the electromagnetic interaction among the protons is disregarded. In a sense, nuclear matter can be thought as a very large nucleus and, even though nuclear matter itself is not present in the universe, one expects it to describe qualitatively the interior of heavy nuclei and neutron stars. Indeed, there are some “experimental” properties of nuclear matter which are well-known from the nuclear physics phenomenology. These will be discussed in Section 1.2.

In spite of the apparent simplicity of the problem, the complicated structure of the bare NN interaction complicates the treatment of nuclear matter quite a lot. Actually, a sophisticated many-body machinery is needed to treat the problem in a sensible way and, even after decades of theoretical effort, one finds that the most simple properties of nuclear matter are only roughly described in terms of its basic constituents. In contrast to these *ab initio* approaches, in which one tries to find the properties of nuclear systems from its fundamental building blocks, some *phenomenological* approaches have also been devised. These are usually simpler treatments, which fit empirical properties of nuclear systems in a given region of isospin and density and then wisely extrapolate the results to different conditions. In Section 1.3, a general overview of the available many-body techniques which are presently used as well as some of its respective advantages and disadvantages will be given.

Finally, once the theoretical framework is settled, one has to study the properties of nuclear matter as a function of some external conditions, like its density or, eventually, its temperature. Many-body physics is studied at finite temperature for a bunch of systems in which thermal effects are unavoidably important. These include electron systems, quantum liquids (such as ^3He) or ultracold gases (which, despite their name, show important thermal effects). The thermal component in the nuclear many-body problem, however, is usually disregarded because nuclear systems are assumed to be cold, *i.e.* the relevant energy scales of nuclear systems correspond to extremely large temperatures which are difficult to achieve experimentally. Nevertheless, there are a few physical situations in which finite temperature effects need to be taken into account. The interest of these “hot” nuclear matter calculations will be discussed in the closing section of this chapter.

1.1 Nucleon-nucleon interaction

In the nuclear many-body problem, one chooses the neutron and the proton as the fundamental constituents (or degrees of freedom) of the problem. These are the two

baryons with lowest masses, $m_p = 938.27$ MeV and $m_n = 939.56$ MeV respectively [Yao06]. Note that these masses are very close to each other. The neutron and the proton differ in their total charge (0 and +1 respectively) as well as in the combination of their constituent quarks (uud for the proton, udd for the neutron). Besides these differences, however, they are quite similar. Up to the point that, if one neglects the electromagnetic interaction among protons, one can treat the neutron and the proton as two degenerate states of the same particle, the nucleon. This fact introduces a new symmetry in the system, the so-called isospin symmetry, which states that the strength of the interaction between any pair of nucleons is the same, independently of whether they are protons or neutrons. Isospin symmetry is quite well fulfilled in nature, and it is translated in the charge independence of NN scattering as well as in the spectroscopic properties of light mirror nuclei, like ${}^3\text{He}$ and ${}^3\text{H}$ [Rin80]. In addition, any microscopic interaction should fulfill some other general properties [Eis72]. The force should respect the conditions imposed by basic quantum mechanics (hermiticity, invariance under coordinate exchange) as well as the invariances imposed by the non-relativistic treatment of a bare force in the vacuum (translational, Galilean, time reversal, rotational invariances).

Most of the information available on two-nucleon systems is obtained from NN collisions in a certain range of nucleon kinetic energies, which goes roughly from 0 to 300 MeV in the laboratory frame. A complete compilation of the available experimental data for these processes is given, for instance, in the websites [nnoa; nnob]. The analysis in terms of phase shifts of this information, together with the previous symmetry requirements, constrains the physical properties of the different microscopic NN interactions in free space. As a consequence, all the realistic potentials share some common properties. NN forces must be of a short-range nature, as seen by the fact that nuclei are very compact objects, a few fermis ($1 \text{ fm} = 10^{-15} \text{ m}$) wide, and by the fact that the binding energies of finite nuclei tend to saturate [Rin80]. Moreover, if finite nuclei have to be bound, the NN interaction has to be attractive in a certain range of distances. Furthermore, the central density of heavy nuclei is fairly constant due to the strongly repulsive short-range core of the NN force, which prevents one nucleon to penetrate the hard core created by another nucleon. A sketch of these ideas can be found in Fig. 1.1, where the phase shifts of the NN interaction obtained from the compilation of [nnoa] are shown. On the one hand, S -wave phase shifts are positive for low ($E_{lab} < 250$ MeV) energies, which is an indication of an overall attractive potential for large distances [Eis72]. On the other hand, most partial waves yield negative results for large energies, which indicates the presence of a repulsive core. Note however that the details of this short-range hard core cannot be resolved from the phase shift analysis due to the lack of data above 350 MeV.

A very important property of two-nucleon phenomenology is the existence of a proton-neutron bound state with a binding energy of -2.22 MeV. This bound state, the deuteron, is an important source of information on the NN interaction.

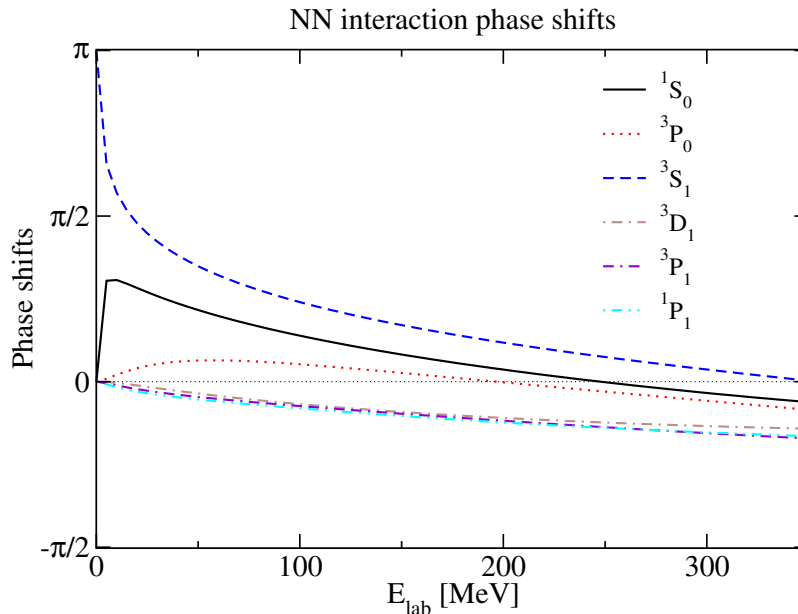


Figure 1.1: *NN interaction phase shifts as a function of the nucleon kinetic energy in the laboratory system. The partial wave analysis has been performed by the Nijmegen group [nnoa].*

Its strength is mostly concentrated in the 3S_1 partial wave, as seen by the fact that the phase shift of this partial wave approaches π for very low energies. Still, the deuteron has a certain quadrupole moment, which cannot be caused by a spherically symmetric S -wave wave function. Instead, the wave function is an admixture of a S - and a D -wave states, with the deuteron staying about 4% of the time in the second state. One can explain this mixture from a theoretical point of view by including a *tensor* component in the NN interaction that admixes partial waves with different angular momenta. Indeed, this is one of the main sources of correlations in the nuclear many-body wave function, because it determines to a large extent the off-shell structure of the in-medium interaction [Müt00]. Among the several outstanding properties of finite nuclei, there is one which is especially relevant for the underlying NN interactions. To reproduce the observed nuclear magic numbers, a spin-orbit component in the mean-field is needed. In contrast to the remaining terms of the force, however, the spin-orbit NN interaction is of a non-local nature. The degree of non-locality of each potential has also an important influence on the structure of the nuclear wave function.

The large amount of existing NN scattering data, together with the restrictions imposed by symmetries, allow for the construction of accurate microscopic NN interactions. There are however several ways in which one can build phase-shift equivalent potentials. One can, for instance, expand the NN potential in terms of all the operators which, in configuration as well as in spin-isospin spaces, respect

the underlying symmetries of the NN force. Each operator is usually assumed to have a certain spatial dependence, with some free parameters which can be fitted to NN scattering data. A large amount of microscopic NN potentials are based on this philosophy, but probably the Argonne “family” are the most accurate of them. The Argonne V18 interaction, for instance, contains 18 of these operatorial structures in spin-isospin space and can be used as a starting point for realistic many-body calculations [Wir95].

This kind of empirically restricted interactions are extremely accurate, despite the fact that they do not try to describe the underlying physics phenomena that generate the NN force. The description of the strong interaction should be carried out in terms of quantum chromodynamics (QCD), which governs the properties of the particles forming the nucleons, *i.e.* the quarks. The strong non-perturbative character of QCD at low energies makes the problem almost intractable, and since the very old days of nuclear physics the interaction between nucleons has been described in terms of some other effective degrees of freedom, the mesons. The first to propose such a model was Yukawa, who supposed that the NN interaction was mediated by pions [Yuk35]. These are the lightest mesons in nature and would be responsible for the long-range behavior of the force. One can however extend the number of mesons which is incorporated to this boson exchange potential and take profit of the different properties of these mesons (their scalar, pseudoscalar or vector nature) to reproduce the various terms of the NN force. The one-pion exchange potential, for instance, includes a term of a tensorial nature which can account for the tensor component of the NN interaction. It is important to note that the mesons included in this kind of potentials should be taken as effective degrees of freedom and thus their properties might not coincide with those of the existing mesons. This is the case of the well-known σ meson, which is supposed to mimic the effects of two correlated pions. In addition, the scalar-isoscalar η , the vector-isovector ρ and the isoscalar-vector ω mesons are usually incorporated in these potentials. Each of them accounts for some characteristics of the NN force (the ω is responsible for the short-range core, etc.). Since the coupling constants (as well as some other properties) of these mesons are not well-known, the existent amount of NN scattering data is used to fit these parameters. Choosing a correct set of degrees of freedom and of mesonic couplings, these fits can achieve a high degree of accuracy. The calculations of this Thesis have been performed with the CDBONN potential [Mac96; Mac01], a boson exchange potential with a particularly strong non-local nature. The matrix elements in momentum space for different partial waves of this interaction are shown in Fig. 1.2. The strong dominance of the 1S_0 partial wave at low momenta is clearly observed, as well as the attractive regions of the 3P_0 and the $^3S_1 - ^3S_1$ waves.

Recently, a new kind of NN potentials have achieved the same degree of accuracy in the fitting procedure of NN scattering data [Ent03]. The Idaho-Salamanca potential is based on chiral perturbation theory, an effective field theory which

1.1. NUCLEON-NUCLEON INTERACTION

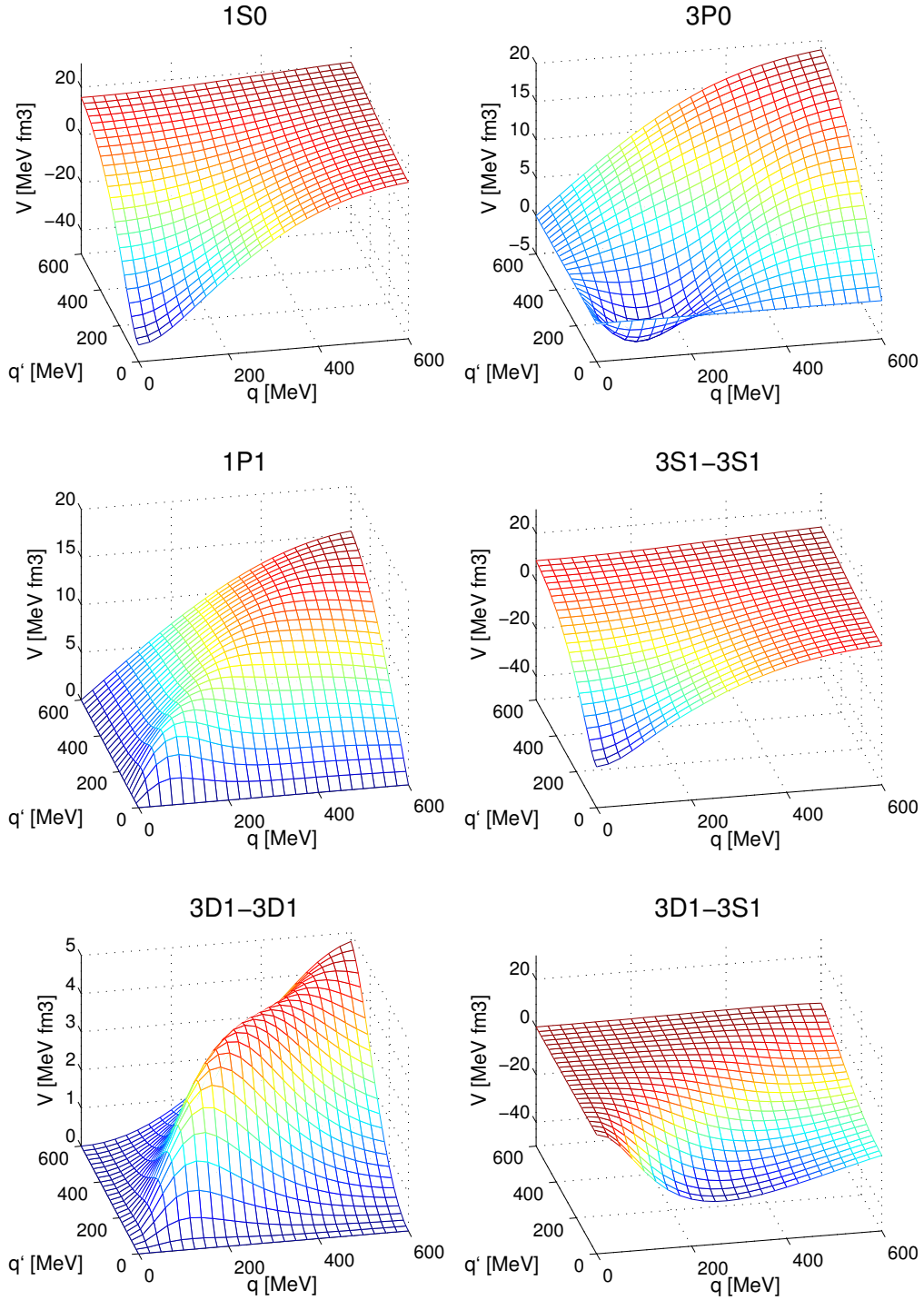


Figure 1.2: *CDBONN* potential in different partial waves as a function of the relative momenta q and q' .

uses the fact that the chiral symmetry is only slightly broken in the QCD Lagrangian. The Goldstone bosons associated to this symmetry breaking are the low-lying nonet of mesons. The interactions among these mesons as well as their interactions with the octet of baryons are strongly restricted by the underlying chiral symmetry. As a result, the Lagrangian can be expanded in a power series in terms of the momentum of the particles. When this series is expanded to $N^3\text{LO}$ and its free parameters are fitted to data, the interaction that is obtained reproduces the NN phase shifts with an accuracy comparable to any other realistic NN interaction. This effective field theory approach to the NN interaction includes aspects of the previous approaches, in the sense that it is formulated in terms of effective degrees of freedom (pions and nucleons) with an interaction that is strongly restricted by symmetry requirements. Furthermore, an interesting outcome of this chiral perturbation theory approach are the three- and four-nucleon forces which arise naturally as counterterms in the chiral expansion.

The need of three-body interactions in nuclear physics is a well-known feature. The effects of three-body forces in nuclear physics are important, either for the correct description of very light systems, like the ground and excited states of light nuclei [Pie01], or for an accurate treatment of the many-body nuclear problem [Day81]. Unfortunately, the introduction of three-body forces in many-body formalisms is usually very complicated. This is precisely the case for the Green's function approach presented in this Thesis and in the following no three-body forces will be considered.

The NN forces that have been mentioned so far are supposed to describe NN interactions in free space, *i.e.* they are fitted to the data of two-body scattering processes. In order to describe the in-medium properties of nucleons in an effective way, one can build phenomenological forces which include density dependences to mimic the effects of many-body correlations. This kind of interactions are essentially devoted to describe dense systems as well as finite nuclei and, instead of reproducing the data of NN scattering, they are fitted to the empirical saturation properties of nuclear matter as well as to some properties of medium and heavy spherical nuclei. The success of these forces is explained by their simple functional and operatorial structure as well as by the fact that they are conceived to work within a mean-field quasi-particle approach. They are thus easy to handle and they can predict the properties of most nuclei close to the stability valley with a good degree of accuracy. Note, however, that their spirit is different to that of the many-body nuclear problem for, even if they are more practical, they do not predict the properties of nuclei from their very basic building blocks. Among these phenomenological in-medium NN interactions, the Skyrme force [Vau72] is probably the more popular one: it is a zero-range force with a simple spin-isospin structure. Nowadays, there are more than a hundred parameterizations of this force [Sto03], most of them devoted to study a particular region of the nuclear chart. Another widespread NN many-body phenomenological interaction is the

Gogny force [Dec80], which mimics the short and long-range effects of the NN interactions by means of gaussians. Although there are less parameterizations of this interaction [Far99], the results obtained with it can be considered to be more realistic. The fact that these phenomenological forces fit the properties of matter in a certain region of density and isospin asymmetries limits their applicability to other regions of the density-isospin parameter space [Rio05b; LV06].

1.2 Nuclear matter

Nuclear matter is an ideal system. Therefore, one might very reasonably wonder why it has so much interest for nuclear many-body theorists. There are several answers to this question. To begin with, nuclear matter is an infinite system and thus it is translationally invariant. As a consequence, the single-particle states are well-known: they are given by simple plane waves. Note that this does not happen in finite systems, where the choice of an appropriate single-particle basis can already be problematic. This supposes a great advantage for theoreticians, which can use nuclear matter as a test bench for their many-body approximations before applying them to treat the more involved finite systems.

In the studies of nuclear matter, one tries to reproduce the empirical information which is known for this system. It is actually quite surprising that one can have access to the empirical properties of an ideal system. These properties are extracted from the extrapolation of the experimental knowledge of finite nuclei to infinite matter. Consider, for instance, the binding energy per particle, $B(Z, N)/A$, of finite nuclei. For sufficiently large nuclei (with more than, say, 15 nucleons) this is a fairly constant magnitude, which is around 8.5 MeV/nucleon [Rin80]. This constant energy per particle can be explained in terms of the saturation mechanism of nuclear forces. The short-range nature of the NN interaction modifies the total energy per particle of the A -particle system in such a way that, instead of it being proportional to $A(A - 1)$ (as it should be for a two-body interaction), it is approximately proportional to A . Actually, the binding energy per particle has a certain soft dependence on A for finite nuclei. For low- A systems, the energy per particle increases with A due to the fact that the nucleons inside the nuclear core get more bound. Above $A = 56$ (*i.e.* above the iron mass number), the number of protons is large enough for the Coulomb interaction among them to become relevant and the repulsive effect is such that, for heavy nuclei, B/A decreases with A . One can fit this behavior by means of the semi-empirical (or Bethe-Wieszäcker) mass formula [Rin80]:

$$B(N, Z) = a_V A + a_S A^{2/3} + a_C \frac{Z^2}{A^{1/3}} + a_I \frac{(N - Z)^2}{A} - \delta(A). \quad (1.1)$$

Each term of this formula represents a different physical effect which is important for finite nuclei. The first contribution corresponds to the volume term and

accounts for the binding in the interior of the nucleus. The second contribution is associated to surface effects, while the Coulomb repulsion among nucleons is taken into account by means of the third term. The fourth term corrects the mass formula to consider the loss of binding in isospin asymmetric systems. The last term, $\delta(A)$, is associated to pairing effects and varies according to the even or odd character of the number of nucleons.

Traditionally, electron scattering experiments have been an essential tool to obtain information on the interior of nuclei. These experiments provide us with the charge distribution of heavy nuclei, which is basically proportional to the total density inside the nucleus. It is a well-known experimental evidence that the charge density inside medium and heavy nuclei is fairly constant. Correcting for the difference in the number of neutron and protons, one can derive a corresponding total central density for nuclei with different A . When these data are extrapolated to very large A , one finds that the central density converges to the value $\rho_0 \sim 0.16 \text{ fm}^{-3}$. This is the so-called *empirical saturation density* of nuclear matter and coincides with the density at which it would be stable. From the semi-empirical mass formula, one can find the corresponding binding energy per particle:

$$\lim_{A \rightarrow \infty} \frac{B}{A} = a_V \sim 16 \text{ MeV}. \quad (1.2)$$

Note that the only contribution considered here is the volume term, because the remaining contributions are not active in infinite isospin symmetric matter. Any *ab initio* many-body calculation of nuclear matter which tries to be realistic should reproduce the empirical *saturation point* of nuclear matter, *i.e.* it should have a minimum of energy $E/A = -16 \text{ MeV}$ at the density $\rho_0 = 0.16 \text{ fm}^{-3}$.

The semi-empirical mass formula supplies more information on nuclear matter. For an isospin asymmetric system (with a different number of neutrons and protons), characterized by the isospin asymmetry parameter $\alpha = (N - Z)/A$, one finds that the extrapolation of the mass formula, once Coulomb effects are disregarded ($a_C = 0$), yields:

$$\lim_{A \rightarrow \infty} \frac{B}{A} = a_V + a_I \alpha^2. \quad (1.3)$$

The quadratic dependence on α is explained both in terms of Pauli blocking effects and of the charge symmetry of the nuclear interactions. Most fits yield values of a_I around -24 MeV . This is usually called the symmetry energy and its negative sign accounts for the loss of binding energy when a proton is exchanged by a neutron in the system (or viceversa). The extrapolation of this fitted parameter to infinite matter is somehow controversial [Ste05]. However, if a many-body approach can give the energy per particle in terms of the total density and the asymmetry parameter, one customarily computes the symmetry energy from the formula:

$$a_s = \frac{1}{2} \frac{\partial^2}{\partial \alpha^2} \frac{E(\rho, \alpha)}{A} \Big|_{\rho_0}. \quad (1.4)$$

This quantity is usually around 30 MeV for realistic many-body approaches and it is especially relevant for very asymmetric systems, like neutron stars, where it determines the composition in the interior of the star. The symmetry energy also sets to a large extent the neutron skin thickness of heavy nuclei and, from the experimental point of view, its density dependence close to saturation can be explored with the help of intermediate heavy-ion collisions [Ste05]. Another empirical property of nuclear matter which should be reproduced by *ab initio* calculations is the so-called compressibility modulus of nuclear matter. This is normally defined as:

$$K = 9\rho_0^2 \frac{\partial^2}{\partial^2 \rho} \frac{E(\rho, \alpha)}{A} \Big|_{\rho=\rho_0, \alpha=0}, \quad (1.5)$$

and it is proportional to the second derivative of the energy per particle of symmetric matter with respect to the density close to the saturation density. In a way, it characterizes the density dependence of the energy per particle of nuclear matter close to saturation. The values accepted for this quantity are in the range $K \sim 200 - 250$ MeV and they are mainly determined from the energy of monopolar resonances in the nuclear spectra [Bla95]. The lack of three-body forces in the treatments of this Thesis as well as the restriction to symmetric nuclear matter will prevent us to give explicit values for these two quantities.

1.3 Correlations in nuclear physics

The word “correlations” is used in several fields of physics with a lot of different meanings. Even within the many-body community, one uses it in many contexts and, as a matter of fact, in some fields the adjective “correlated” is given to approximations which, in other fields, might not be considered as such. The correlation effects of main concern in this Thesis are those which go beyond the mean-field and the quasi-particle pictures. These effects are related to the energy dependence of the self-energy and induce a non-vanishing imaginary part for this quantity. Let us now briefly review the different kind of many-body approaches in order to pin down more specifically which are the correlations that our approach tries to describe.

Mean-field approaches are based on the Hartree-Fock approximation. A common idea underlying these approaches is the concept of quasi-particle. In a mean-field scheme, a nucleon in nuclear matter is described in terms of its single-particle energy:

$$\varepsilon(k) = \frac{k^2}{2m} + U(k), \quad (1.6)$$

which is formed by a kinetic term plus a single-particle potential, $U(k)$, which accounts for its interaction with the remaining nucleons of the system. In the

Hartree-Fock approximation, the single-particle potential is given by the sum of the interaction of a nucleon with momentum k with the remaining nucleons in the system in terms of the bare interaction. This is generally known as the “mean-field” and defines a one-to-one correspondence between a momentum state k and a unique quasi-particle energy $\varepsilon(k)$. As matter of fact, the mean-field approximation gives very bad results for the saturation properties of nuclear matter (see Chapter 4) when it is computed from realistic NN interactions. This is caused by the fact that, in the Hartree-Fock approximation, the strongly repulsive short-range interactions are overestimated, leading generally to unbound systems. Therefore, one needs to use phenomenological parameterizations of many-body interactions, like the Skyrme or the Gogny interactions, which describe in an effective way the many-body effects that influence the mean-field. These parameterizations usually have a simple functional form and do not include tensor components. Strictly speaking, these are not *ab initio* calculations, but they are among the few which can reproduce fairly well the properties of finite nuclei among the whole nuclear chart. In addition, simple mean-field theories can be recast easily as functionals for the energy that can be used in a Kohn-Sham density functional scheme which, in principle, can be improved in a systematic way [Ben03].

Realistic NN interactions, however, do have a strong short-range repulsion and present tensor components, which induce important changes in the many-body wave function of the system. These are not taken into account in a pure mean-field approach, where the single-particle potential is computed assuming that the system can be described in terms of a simple Slater determinant. One can proceed in different ways to introduce these short-range and tensor correlations in the nuclear many-body problem. One might, for instance, try to account for the correlations directly in the wave function, by means of a Jastrow-type trial wave function:

$$\Phi(1, \dots, A) = \prod_{i>j=1}^A f(r_{ij}) \Phi_0(1, \dots, A). \quad (1.7)$$

The Jastrow factors $f(r_{ij})$ act on the free many-body wave function, Φ_0 , and give the correlated wave function of the system, Φ . They suppress the short-range components of the wave function and their operatorial structure, which includes tensor components, accounts for the complicated spin-isospin dependence of the wave function. Moreover, they need to be properly normalized according to the fermionic nature of the many-body wave function. The functional dependence of the Jastrow factors in the inter-particle distance r_{ij} is free to some extent, and it can be adjusted with the help of a variational minimization of the ground state energy of the system. One can use different techniques to compute this energy from the Jastrow trial wave functions. In the *Fermi Hypernetted-Chain* approximation, the correlations induced to the energy can be studied in terms of graphs and lead to a set of coupled integral equations that need to be solved

within certain approximations (like the Single Operator Chain) [Fan75; Cla79]. One can also compute the ground state energy in an exact way by means of a *Variational Monte Carlo* calculation, which however needs of an efficient sampling in the spin-isospin configuration space in order to obtain sensible results. The strong spin-isospin structure of the nuclear wave function complicates a lot this kind of calculations. Alternatively, one might try to guess directly the many-body wave function and improve it systematically by minimizing the ground state energy. If the correlated basis is close enough to the exact basis, one can compute the energy from perturbation theory, which improves the results with respect to the naive Jastrow approach. This leads to the *Correlated Basis Functions* method [Cla66; Fan97], which has been successfully applied to liquid ^3He as well as to nuclear matter [Ben92].

The *Coupled Cluster* (or $\exp(S)$) method is similar in spirit to the Jastrow trial wave function, in the sense that the correlations of the full many-body wave function are generated by applying an $\exp(S)$ operator on a Slater determinant of model states. The S operator is formed by sets of n creation-destruction operators that produce excitations of n particles and holes on top of the non-correlated Fermi sea [Müt00]. The exponential form of the operator guarantees that the excitations at different orders are not overcounted. The application of the coupled cluster method to the nuclear many-body problem seems to have a promising future, especially in the domain of finite nuclei where it allows for a quantitative description of the shell structure [Bis91]. Somewhat similar to this approach, the *Unitary Correlated Operator Method* renormalizes the short-range and tensor correlations of the many-body wave function by means of a unitary transformation with an exponential structure. This transformation is cut at the second order in the n -body irreducible operator expansion, in such a way that only two-body correlations are taken into account [Fel98; Nef02]. So far, this method has been applied to the calculation of the shell structure of finite nuclei as well as to the spectroscopic properties of heavier systems. One can also determine very accurately the structure in shells of light nuclei by means of the *Green's Function Monte Carlo* method, a technique which has been mainly pushed forward in nuclear systems by the Urbana group and which yields the more exact *ab initio* results available in the nuclear field [Pud97].

In the last five years, new many-body techniques have been derived to treat the nuclear many-body problem. These have been inspired by different formalisms which so far had been used in other fields of physics. Renormalization group techniques, for instance, have recently been applied to realistic NN potentials [Bog03]. Starting from these potentials at a very high cutoff, one can build a scattering amplitude which is evolved to lower cutoff values requiring that the observables (such as the phase shifts) are preserved up to the cutoff external momenta. In this way, one obtains an interaction, the so-called *low momentum interaction* or V_{lowk} , which is the same independently of the initial NN potential. The differ-

ences in the original NN potentials at the numerical level are essentially due to the different way in which they treat the non experimentally observable short-range components and the V_{lowk} potential has integrated out this high energy modes in a consistent way. Thanks to the fact that the short-range components have been “extracted” from the interaction, the V_{lowk} potential is less correlated in a way and thus it can be used as the starting point of perturbative calculations for nuclear matter [Bog05].

Effective field theory techniques have also been applied to the nuclear many-body problem [Lut00; Kai02]. In these approaches, a chiral perturbation theory interaction is used to describe the NN interaction, although finite density effects involve a different power counting than the one used in free space. Note, moreover, that since the Fermi momentum at saturation density ($k_F \sim 260$ MeV) is comparable to the pion mass, pions need to be explicitly taken into account in the calculations. Within this finite density chiral effective field theory, one can obtain the energy per particle in an expansion of k_F/m_N (or k_F/Λ , with Λ a large cut off). The results thus obtained turn out to be quite reasonable, even though some of the unknown constants in the approach have to be fitted to reproduce the empirical saturation point.

There is a common assumption in all the previous treatments, namely that nuclear matter is a non-relativistic system. Such an assumption seems sensible, since the energies involved in nuclear matter (of the order of some MeVs) involve Fermi velocities of the order of $v_F/c \sim k_F/M_n \sim 0.3$, much smaller than the speed of light, c . Still, in a Lagrangian picture the one boson exchange model is much more easy to treat and one can indeed try to reproduce the properties of nuclear matter directly from it. In the *Relativistic Mean Field* approach (also known as Quantum Hadrodynamics or Walecka model), one approximates the expectation values of the mesonic degrees of freedom by means of mean classical values [Ser86]. The couplings of the phenomenological mesons are then adjusted to reproduce the empirical saturation point. An attractive feature of this approach is the fact that it predicts the experimental spin-orbit splitting observed in nuclear single-particle levels in a straightforward fashion. In addition, and even though it is a phenomenological model, the Relativistic Mean Field approach can be derived in an effective field theory spirit from the chiral properties of the underlying QCD lagrangian [Fur97]. Furthermore, it is also possible to understand it in terms of a density functional which includes relativistic effects [lal04].

None of the previous approaches has enjoyed the same success or has been studied in such detail as the *Brueckner-Hartree-Fock* (BHF) approach to the nuclear many-body problem [Bru54; Day67]. This is based on the Goldstone expansion for the total energy of a many-body system at zero temperature and its diagrammatic interpretation [Gol57]. Actually, in contrast to the previous approaches, the BHF approximation is entirely based on a diagrammatic expansion for the energy per particle. In the BHF case, the diagrams which are considered are dictated by the

hole-line expansion. An infinite series of these diagrams can be summed in terms of an in-medium interaction (or G -matrix) which includes the correlations induced by the original bare NN force as well as the Pauli blocking effects in the intermediate propagation of particles. Note that in this approach, one renormalizes the in-medium interaction and not its wave function, although it can be obtained from the renormalized interaction [Müt00]. In principle, the BHF approach can be improved by including higher order terms in the hole-line expansion. So far, only the three hole-line contribution has been computed [Son98], and the convergence of the series seems to be at least qualitatively proven. Note also that there exists a relativistic version of the BHF approach, in which the relativistic scattering amplitude is corrected by medium effects [Bro90; vD04]. Since these studies are unavoidably carried out with the help of Dirac spinors, the approach is called *Dirac-Brueckner-Hartree-Fock*. Starting from realistic boson exchange potentials that describe the phase shifts of the free space interaction, one obtains good saturation properties of nuclear matter, although some doubts exist on the exact formulation of the approach (especially in what concerns the Lorentz structure of the self-energy).

In terms of correlations, the non-relativistic BHF accounts, in its renormalization process, for the simultaneous particle-particle propagation of in-medium nucleons. Still, in a certain sense, the BHF is a quasi-particle approach, since each single-particle momentum has an associated quasi-particle energy, given by an expression equivalent to Eq. (1.6). In this case, however, the single-particle potential $U(k)$ is computed from the renormalized interaction, whose energy dependence is restricted to the quasi-particle energies. One says that the particle is on its mass shell (on-shell). The BHF approximation is however not completely on-shell, because the in-medium interaction has a certain energy dependence associated to the off-shell behavior of the self-energy. To distinguish this approach from the usual mean-field or Hartree-Fock approximation (which is also on-shell), any approach in which there is a one-to-one correspondence between a single momentum and a single energy will be referred to as a quasi-particle approach in the following. Yet, experimental information coming from proton ($e, e'p$) knockout reactions contradicts this assertion [Kel96; Dic04]. One finds that there is a certain probability to find knocked out protons of a certain momentum within an extended range of energies [Roh04]. This so-called fragmentation of the quasi-particle strength is described in terms of the spectral function, which gives the probability of finding a nucleon with momentum k and energy ω in the many-body nuclear system. This cannot be directly computed from the BHF approximation, but it is an outcome of other approaches, like the Fermi Hypernetted Chain or the Correlated Basis Function approximations [Fan84; Ben89].

The fully correlated one and two-body Green's function have an infinite diagrammatic expansion in terms of non-interacting one-body propagators and two-body potentials. In the ladder approximation, one sums an infinite subset of the

diagrams for the two-body propagator. In doing so, an in-medium interaction (the so-called T -matrix) has to be introduced. In contrast to the G -matrix of the BHF approach, this interaction accounts consistently for the correlations induced by the in-medium propagation of pairs of particles and pairs of holes. The final result is expressed in terms of a self-energy and a spectral function which are fully momentum and energy dependent. The process of finding the Green's function for such a many-body system is unavoidably self-consistent, since the propagation of a nucleon is affected by the interactions with the surrounding nucleons, which in turn are also described in terms of the Green's function. When the procedure is iterated in a self-consistent way (in the sense that, at each iteration, the spectral function of the previous iteration is used), the diagrammatic expansion is modified by the inclusion of self-energy insertions that dress the one-body propagator. This allows for an extension of the approach to higher densities. Moreover, the self-consistency of the approach is essential for the fulfillment of the Hugenholtz-van Hove theorem and the sum rules for the spectral function, which are known to hold from basic principles and which are not well reproduced in other many-body approximations.

The set of equations which defines the *Self-Consistent Green's Function* (SCGF) scheme can be written down in a more or less straightforward way. A full numerical treatment with all the off-shell dependence of this approximation is however quite involved in the nuclear case, due to the short-range components of the force, which induce non-negligible strengths to the region of high and low energies. At the same time, one has to deal with very abrupt structures close to the quasi-particle energy as well as with delta-like peaks close to the Fermi surface. All in all, the numerical treatment of the problem is quite difficult and only a few groups have achieved a partial solution of the problem. Very soon after the Green's function theory for many-body systems was formulated [Mar59], Puff and collaborators carried out the first schematic attempts to study nuclear matter from a Green's function point of view with the very simple potentials available at the time [Puf61; Rey63]. In the eighties, with the new computational tools available, Green's function theory and its application to nuclear matter were pushed forward [Web85], mostly with simple separable potentials within the quasi-particle approximation. The first attempts to solve the problem with more realistic potentials were carried out in a quasi-particle approximation of the formalism, in which the self-consistency is demanded at the on-shell level, by the Barcelona and the Saint Louis groups [Ram88; Ram89; Von93]. Within their approach, the off-shell dependence can be computed at the end of the procedure and a non-trivial spectral function is found. An improved approach can be obtained by parameterizing the off-shell dependence of the spectral function by means of a set of Gaussian functions [Dic99]. The Gent group achieved similar results by approximating the off-shell dependence by a small discrete number of Dirac peaks [Dew02; Dew03]. Complete off-shell results have been obtained for simple separable NN interactions by Bozek

[Boz99; Boz01; Boz02], who has also solved the problem at zero temperature for a separable version of realistic NN potentials [Boz03b]. A full solution of the SCGF scheme with realistic microscopic potentials is however difficult to obtain at zero temperature, and the extension of the formalism to the finite temperature case simplifies the treatment to a large extent [Fri03].

1.4 Many-body physics at finite temperature

Many of the systems studied with quantum many-body techniques are influenced by thermal effects. The properties of electronic systems, for instance, have a strong temperature dependence, and probably the phenomenon of superconductivity is the most spectacular of them. This is also the reason why the electron gas has been used in several textbooks as the starting point for the description of many-body physics at finite temperature [Abr65; Fet71; Mah90]. In ultracold atomic gases, the phenomenon of Bose-Einstein condensation as well as the so-called BEC-BSC crossover have recently renewed the interest on the study of strongly interacting quantum many-body systems at finite temperature.

This is however not a new subject. Finite temperature many-body physics has a long tradition. Among the problems treated with this theory, maybe correlated Fermi liquids and, in particular, ^3He are the most interesting from the theoretical point of view. Due to the strong dynamical correlations induced by the two-body interaction, the thermodynamical properties (and, in particular, the entropy) of ^3He deviates strongly from the free Fermi gas behavior. As a matter of fact, the study of the entropy in correlated Fermi liquids was triggered by the experimental and theoretical studies of ^3He [Ber66; Don66; Ami68a; Ami68b; Bre67; Pet73; Car75]. The specific heat of this system is known to have a non-trivial empirical temperature dependence of the type $T^3 \ln T$ [Gre83]. Such a non-analytical behavior can be seen to arise, within Fermi liquid theory, from the coupling between quasi-particles and quasi-holes in the triplet state, which gives rise to non-analytical energy dependences in the self-energy [Chu06]. These non-analyticities are in fact a general feature of all normal Fermi liquids and their existence is not related to the particular details of ^3He systems, although the strong spin-dependent correlations of this system enhance this behavior.

Traditionally, nuclear matter has been considered as a cold system, *i.e.* it has been studied with the tools provided by zero temperature quantum many-body physics. There is a good reason for this. The energy scales of nuclear systems are of the order of some MeV. This corresponds to temperatures of the order of $T = 1 \text{ MeV} \sim 1.2 \cdot 10^{10} \text{ K}$, which are of course much higher than the room temperatures at which nuclear physics experiments are carried out. In other words, temperature does not play any role in nuclear structure for earthly systems. Still, in some situations, temperatures of the order of tenths of MeV are reached in nature. These are somewhat small temperatures if compared with the typical

energy scales of nuclear matter (the free Fermi energy at empirical saturation density is about $\epsilon_F \sim 40$ MeV, thus $T/\epsilon_F \sim 0.5$ for $T = 20$ MeV, the highest temperatures considered here), but one expects that a finite temperature approach to nuclear matter can fairly describe the properties of the hot environments that exist either inside the cores of supernovae at the latest stage of their evolution [Bet90] or in the collisions of heavy nuclei at intermediate energies [Cho04]. The thermodynamical properties of this high density matter and, in particular, the entropy are important quantities for the understanding of astrophysical and heavy ion physics phenomena. In core-collapse supernovae, for instance, the evolution and dynamics occur at a fixed entropy per baryon [Pra97]. On the other hand, the entropy production in multi-fragmentation events in heavy ion collisions is considered to be a crucial quantity to determine the mass fragment distribution [Cse86].

Traditionally, hot nuclear matter has been studied in a mean-field (Hartree-Fock) approximation with effective phenomenological NN forces, such as the non-relativistic Skyrme or Gogny interactions [Sil04; Hey88] or the Relativistic Mean Field approximation [Mül95]. Other many-body approaches that have been used in the study of this system include lattice models [Mül00] or three-loop calculations within chiral perturbation theory at finite temperature [Fri02]. However, when dealing with realistic NN potentials, more sophisticated many-body techniques are needed. Once again, the strong short-range repulsion and the tensor components of these potentials modify substantially the many-body density matrix, which is not anymore well described in terms of a free Fermi gas density matrix. The BHF approximation arises from a well-defined expansion for the energy of a fermionic system at zero temperature, the so-called Brueckner-Bethe-Goldstone expansion [Day67]. At finite temperature, a similar summation can be achieved in the so-called Bloch-de Dominicis approach [Blo58a; Blo58b; Blo59a; Blo59b]. However, this approach is not devised to reproduce the energy of the system. Instead, it aims to compute the grand-potential and, from it, all the thermodynamical properties of the system. Traditionally, however, the BHF approach has been extended to finite temperatures in a more naive way: the energy of the system is computed from a simple generalization of the $T = 0$ formalism to finite temperature and the entropy of the system is computed from a mean-field expression [Lej86; Bom94]. Finally, let us also note that relativistic Dirac-Brueckner-Hartree-Fock calculations at finite temperature can also be found in the literature [tH86; Hub98].

A consistent treatment of correlations in quantum many-body systems requires the inclusion of particle-particle and hole-hole scattering terms. A major well-known problem of the SCGF approach is related to the so-called pairing instability that appears in the zero temperature formalism when the propagation of holes is considered [Von93; Alm96; Boz99; Dew03]. One of the great advantages of working at finite temperature is the fact that the pairing instability is washed out already at low temperatures. This feature has triggered the theoretical research

on finite temperature many-body propagators and a few modern calculations exist of hot nuclear matter within the Green's function approach. The Rostock group, for instance, have carried out quasi-particle Green's function calculations with separable potentials [Alm93; Alm96; Sch96]. Also the Krakow group has computed the full off-shell spectral function for simple separable [Boz03a] or fully microscopic potentials [Som06]. As a matter of fact, the treatment at non-zero temperature has been the keystone for obtaining a complete numerical solution from a realistic NN potential, as achieved by the Tübingen group [Fri03; Fri04a; Fri05; Rio06b].

Once the self-consistent propagator is found in this method, one can easily obtain information on the microscopic properties (such as the momentum distributions, self-energies or spectral functions of the nucleon) as well as on the bulk properties of the system (the energy per particle via Koltun's sum rule, for instance [Fet71; Kad62]). For a complete thermodynamical description of the system, however, one should compute the relevant thermodynamical potential of a statistical quantum mechanical system, *i.e.* the free energy. A suitable calculation of the entropy is thus required if this formalism is to be used in any practical description of hot nuclear matter. In this Thesis, the Luttinger-Ward approach [Lut60; Car75], in which the grand-potential is computed from the full single-particle propagator, will be discussed and used in the computation of the entropy of the system. An analysis of the properties of nuclear matter within this formalism has been recently published by Soma *et al.* [Som06]. In the following, it shall be shown that one does not need to compute thermodynamical quantities within a full Luttinger-Ward approach as done in [Som06], provided that some approximations for the entropy are valid. Finally, let us notice that the Luttinger-Ward formalism has been widely used in other fields of many-body finite temperature physics, ranging from many-body systems of mesons at finite density [Rap96], to relativistic plasmas [Van98] or to resonances in heavy ion collisions [Wei98b].

1.5 Program of the Thesis

Once the many-body nuclear problem has been introduced and after the Green's function description of nuclear matter has been motivated, a brief summary of the remaining chapters of this Thesis will be given here. In the following chapter, the many-body Green's function formalism at finite temperature will be described. The derivations will try to be as detailed as possible, because the techniques underlying finite temperature physics are quite involved and they are often not very well explained in the literature. Most of the ideas have been taken from the book of Kadanoff and Baym [Kad62], although the books by Mahan [Mah90] and Kraeft *et al.* [Kra86] are also very useful in this context. The self-consistent renormalization procedure will be introduced in the final part of the chapter, following an example by Mattuck [Mat92].

In Chapter 3, the Luttinger-Ward formalism to study the thermodynamical

properties of fermionic systems will be introduced. Within this scheme, the partition function of an interacting system can be computed from the one-body Green's function. Although a full derivation of this formalism goes beyond the scope of this Thesis, the Luttinger-Ward expression for the partition function will be seen to be equivalent to that arising from the more widespread coupling constant method. Following Carneiro and Pethick [Car75], several expressions for the partition function and the entropy per particle of a correlated system of fermions will be derived. The influence of the width induced by dynamical correlations on both quantities will also be briefly discussed.

The first numerical calculations concerning nuclear matter will be presented in Chapter 4, where the Hartree-Fock approximation at finite temperature is studied in detail. Although it is well-known that the results for nuclear matter starting from microscopic NN potentials are not realistic (in the sense that they do not reproduce the empirical saturation point and that might even give rise to unbound systems), the Hartree-Fock approximation is a good benchmark where one can study in detail the self-consistent renormalization procedure. Moreover, the Luttinger-Ward formalism can be used to obtain the well-known expressions for the thermodynamical properties of nuclear matter with a mean-field approximation.

The ladder approximation is discussed in Chapter 5. Its numerical solution by means of the SCGF scheme is also sketched in this chapter, where the first microscopic results are given. These concern the density and temperature dependences of the in-medium interaction, the self-energy, the spectral function and the momentum distribution. These dependences give us a hint on the importance of dynamical correlations in the different temperature and density regimes.

Finally, in Chapter 6 the thermodynamical properties of nuclear matter will be studied within the Luttinger-Ward formalism, starting from the Green's function obtained in the SCGF scheme. The importance of dynamical correlations on the entropy will be studied by comparing different many-body approximations to this quantity. The thermodynamical consistency of the approach will also be discussed in terms of the Hugenholtz-van Hove theorem at the saturation point and compared with the non-consistent BHF approach. The density and temperature dependences of the total energy, the free energy and the pressure will also be given. These results will often be compared with those of the mean-field approach of Chapter 4, which can help us in determining the importance of dynamical correlations on the thermodynamics of the system. A brief summary of some of the future perspectives that this formalism offers is presented at the end of the chapter.

The foundations of the Green's function approach to the nuclear many-body problem are very formal. The same can be said of the Luttinger-Ward formalism. Yet, for the sake of clarity most of the derivations have been kept in the main body of this Thesis. Some of the formal developments which are not essential in the treatment of the problem are given in the Appendices. The first Appendix is concerned with the derivation of the perturbation expansion of the Green's

function at finite temperature, which is the starting point for the diagrammatic approach extensively used in the other sections of this Thesis. The Feynman rules which relate each term in the expansion with a Feynman diagram are given in Appendix B. Appendix C is devoted to the sums of Matsubara frequencies, which rely on different tools of complex analysis. The expansion of some thermodynamical properties of Fermi liquids in two different density and temperature regimes (the degenerate and the classic limit) are studied in Appendix D. These are useful in the interpretation of the density and temperature dependences of both the non-correlated approach of Chapter 4 and the fully correlated one of Chapter 6. Finally, in Appendix E the details of the numerical calculations involved in the SCGF scheme are presented.

Chapter 2

Many-Body Green's Functions at Finite Temperature

The Green's function formalism is a widespread technique in theoretical quantum many-body physics [Mar59; Kad62; Mat92]. It provides a wealth of very interesting results already at the one-particle level [Fey65], and it allows for even more outstanding results when a many-body system is considered. The computation of one-body as well as some of the many-body properties of the system can be achieved from the one-body propagator and thus several approaches have been devised in order to compute this quantity in dense correlated systems. In the following, the general properties of the Green's function will be presented within a finite temperature framework. Starting from the usual aspects of quantum statistical mechanics, the propagator will be defined and a (hopefully) comprehensive review of the imaginary time formalism will be presented. In addition, some analytical results that will be used throughout the rest of this Thesis will be carefully deduced. The properties of the two-body propagator, which shall be useful in the discussion of the ladder approximation, will also be outlined here. In the context of interacting systems, the self-energy will be introduced both from the equation of motion approach and from the diagrammatic point of view. Among the properties of the single-particle propagator in interacting systems, the self-consistency renormalization procedure will be discussed here in order to clarify its importance in the treatment of many-body approaches as well as its fundamental role in the developments of the following chapters.

2.1 Quantum statistical mechanics

The properties of a quantum system composed by many identical particles can be studied conveniently in the framework of the second quantization formalism. The basic cornerstones of this formalism are the creation and annihilation operators in the Heisenberg representation. When a creation operator $\hat{a}^\dagger(\mathbf{r}t)$ acts to the

right on a state of the system, it adds a particle at position \mathbf{r} at time t (for simplicity, in this chapter the presence of any other quantum number such as spin or isospin will be neglected). When its adjoint, the annihilation operator $\hat{a}(\mathbf{r}t)$, acts to the right it destroys a particle at position \mathbf{r} and time t . Most of the micro- and macroscopic operators of physical relevance can be expressed in terms of products of these two operators. In addition, for fermionic systems the second quantization formalism implements in a very convenient way the antisymmetry of the many-body wave function. This is automatically contained in the equal time anticommutation relations:

$$\{\hat{a}(\mathbf{r}t), \hat{a}(\mathbf{r}'t)\} = 0, \quad (2.1)$$

$$\{\hat{a}^\dagger(\mathbf{r}t), \hat{a}^\dagger(\mathbf{r}'t)\} = 0, \quad (2.2)$$

$$\{\hat{a}^\dagger(\mathbf{r}t), \hat{a}(\mathbf{r}'t)\} = \delta(\mathbf{r} - \mathbf{r}'). \quad (2.3)$$

Indeed, with the help of these relations, it is easy to see that $[\hat{a}^\dagger(\mathbf{r}t)]^2 = 0$. This is nothing but the Pauli exclusion principle, which states that two identical fermions cannot be created at the same point of space and time. Notice that here, and in the following, $\hbar = 1$.

Consider any operator \hat{X}_S in the (time-independent) Schrödinger picture. The time evolution of this operator in the Heisenberg representation, $\hat{X}_H = \hat{X}(t)$, is set by the following equation of motion (also known as the von Neumann equation):

$$i \frac{\partial \hat{X}(t)}{\partial t} = [\hat{X}(t), \hat{H}], \quad (2.4)$$

where \hat{H} is the Hamiltonian of the system in the Schrödinger representation. In the case of a system of fermions interacting via a two-body potential $V(\mathbf{r}, \mathbf{r}')$, the Hamiltonian is the sum of a kinetic plus a potential term:

$$\hat{H}(t) = \int d^3r \hat{a}^\dagger(\mathbf{r}t) T(\mathbf{r}) \hat{a}(\mathbf{r}t) + \frac{1}{2} \int d^3r \int d^3r' \hat{a}^\dagger(\mathbf{r}t) \hat{a}^\dagger(\mathbf{r}'t) V(\mathbf{r}, \mathbf{r}') \hat{a}(\mathbf{r}'t) \hat{a}(\mathbf{r}t), \quad (2.5)$$

where $T = -\nabla^2/2m$ is the kinetic energy operator in position space. In fact, the time independence of the Hamiltonian, $\hat{H}(t) = \hat{H}$, allows for the following integration of the von Neumann equation:

$$\hat{X}(t) = e^{i\hat{H}t} \hat{X}(0) e^{-i\hat{H}t}. \quad (2.6)$$

This solution provides the operator \hat{X} at any time t in terms of an initial condition, $\hat{X}(0)$. Let us also note that the Hamiltonian does not change the number of particles $\hat{N}(t)$, $[\hat{H}(t), \hat{N}(t)] = 0$, and thus \hat{N} is also a time independent operator.

Up to this point only the microscopic properties of a quantum many-body system have been considered. Quantum statistical mechanics is the bridge that links the macroscopic thermodynamical observables of a system with its fundamental microscopic properties. In the grand-canonical ensemble, the thermodynamical state of the system is described by the chemical potential μ and the inverse temperature $\beta = 1/T$. Here and in the following the Boltzmann constant will be taken equal to unity, $k_B = 1$. The partition function Z is then defined as the sum over all possible energy and particle number eigenstates of the system (weighted with the corresponding Boltzmann factor):

$$Z = \sum_n e^{-\beta(E_n - \mu N_n)}, \quad (2.7)$$

where E_n and N_n denote the energy and number of particles eigenstates of the many-body system. If one introduces the full many-body states $|n\rangle$, which are exact normalized eigenvectors of the system with energies E_n :

$$\hat{H}|n\rangle = E_n|n\rangle, \quad (2.8)$$

and number of particles N_n :

$$\hat{N}|n\rangle = N_n|n\rangle, \quad (2.9)$$

the partition function can be rewritten in the following compact form:

$$Z = \sum_n \langle n | e^{-\beta(\hat{H} - \mu \hat{N})} | n \rangle = \text{Tr} e^{-\beta(\hat{H} - \mu \hat{N})}, \quad (2.10)$$

where the trace has to be taken as a sum over all the energy and particle number eigenstates of the system. Note that these are eigenvalues and eigenvectors of the Hamiltonian and the number of particles operators and, formally, they have to be computed at zero temperature. From the partition function, one can compute the thermodynamical grand-potential Ω by means of the relation:

$$\Omega(\mu, T) = -T \ln Z. \quad (2.11)$$

In quantum statistical mechanics, the expected value of any operator \hat{X} is computed by using the grand-canonical average:

$$\langle \hat{X} \rangle = \frac{\sum_n e^{-\beta(E_n - \mu N_n)} \langle n | \hat{X} | n \rangle}{\sum_n e^{-\beta(E_n - \mu N_n)}} = \frac{\text{Tr} \left\{ e^{-\beta(\hat{H} - \mu \hat{N})} \hat{X} \right\}}{\text{Tr} \left\{ e^{-\beta(\hat{H} - \mu \hat{N})} \right\}}. \quad (2.12)$$

This expression can be further simplified if one introduces the finite-temperature density matrix operator,

$$\hat{\rho} = \frac{1}{Z} e^{-\beta(\hat{H} - \mu \hat{N})}, \quad (2.13)$$

and one finds:

$$\langle \hat{X} \rangle = \text{Tr} \left\{ \hat{\rho} \hat{X} \right\}. \quad (2.14)$$

This equation relates the microscopic properties of the operator \hat{X} with its mean value in an statistical ensemble. If the operator is an observable, the physical quantity that one might be able to measure would be equal to the left-hand side value, $\langle \hat{X} \rangle$. The thermal average is thus a major source of information in the study of quantum systems at finite temperature.

2.2 Green's functions at finite temperature

2.2.1 Definitions

The one-body propagator (or Green's function) will be the main tool in our discussion of the properties of many-body systems. This function is of capital importance in quantum systems since one can easily prove that, once it is known, all the one-body (and even some two-body) properties of the system can be computed (see Section 2.2.5) [Fet71]. Hence, in the Green's function approach to the many-body problem, one aims at computing the propagator which, in the grand-canonical ensemble, is defined by the following statistical average of creation and annihilation operators:

$$i\mathcal{G}(\mathbf{r}t, \mathbf{r}'t') = \text{Tr} \left\{ \hat{\rho} \mathcal{T} [\hat{a}(\mathbf{r}t)\hat{a}^\dagger(\mathbf{r}'t')] \right\}, \quad (2.15)$$

where \mathcal{T} is the usual Wick time-ordering operator that arranges the operators in a chronological order so that the earliest times appear in the right side. In addition, this operator yields a factor $+1$ (-1) depending on whether the chronological product is an even (odd) permutation of the original one. Writing explicitly the two possibilities, one finds:

$$\mathcal{T} [\hat{a}(\mathbf{r}t)\hat{a}^\dagger(\mathbf{r}'t')] = \begin{cases} \hat{a}(\mathbf{r}t)\hat{a}^\dagger(\mathbf{r}'t'), t > t' \\ -\hat{a}^\dagger(\mathbf{r}'t')\hat{a}(\mathbf{r}t), t' > t. \end{cases} \quad (2.16)$$

The one-body propagator, Eq. (2.15), describes the in-medium propagation of "disturbances" in which one particle is added or removed from the many-body system at thermal equilibrium. When $t > t'$, for instance, an excitation is produced in the system by creating a particle at the position \mathbf{r}' at time t' , that subsequently propagates until the time t , when it is destroyed at \mathbf{r} leaving the system in its original equilibrium state. In the inverse situation, when $t < t'$, the disturbance is produced by the destruction of a particle at position \mathbf{r} and it does not end up until

time t' , where a particle is created at \mathbf{r}' . One can define the so-called correlation functions:

$$i\mathcal{G}^>(\mathbf{r}t, \mathbf{r}'t') = \text{Tr} \left\{ \hat{\rho} \hat{a}(\mathbf{r}t) \hat{a}^\dagger(\mathbf{r}'t') \right\} \quad (2.17)$$

$$i\mathcal{G}^<(\mathbf{r}t, \mathbf{r}'t') = -\text{Tr} \left\{ \hat{\rho} \hat{a}^\dagger(\mathbf{r}'t') \hat{a}(\mathbf{r}t) \right\}, \quad (2.18)$$

which, for each of the two time domains, reduce to the single-particle propagator. Actually, the notation $>$ and $<$ should be taken as a reminder that, for times $t > t'$, the correlation function $\mathcal{G}^>$ equals the propagator \mathcal{G} , while for $t < t'$, $\mathcal{G} = \mathcal{G}^<$. Note, however, that the correlation functions are not limited by any time ordering and thus span to the entire time domain.

In addition to the single-particle Green's functions, it is also customary to define the retarded propagator:

$$i\mathcal{G}^R(\mathbf{r}t, \mathbf{r}'t') = \Theta(t - t') \text{Tr} \left\{ \hat{\rho} \left\{ \hat{a}(\mathbf{r}t), \hat{a}^\dagger(\mathbf{r}'t') \right\} \right\}, \quad (2.19)$$

which can be rewritten in terms of the correlation functions:

$$\mathcal{G}^R(\mathbf{r}t, \mathbf{r}'t') = \Theta(t - t') [\mathcal{G}^>(\mathbf{r}t, \mathbf{r}'t') - \mathcal{G}^<(\mathbf{r}t, \mathbf{r}'t')]. \quad (2.20)$$

In physical terms, the retarded Green's function describes the propagation of a perturbation (caused either by the creation or the destruction of a particle) forward in time. It is thus associated to the causal propagation of events in the system.

Consider an infinite system of fermions, such as nuclear matter. It will be invariant under translations and rotations in space. In addition, if the system is in equilibrium, it will be invariant under time translations. As a consequence, the propagator can only depend on the relative distances in space and time:

$$\mathcal{G}(\mathbf{r}t, \mathbf{r}'t') = \mathcal{G}(x = |\mathbf{r} - \mathbf{r}'|, \tau = t - t'). \quad (2.21)$$

This translational invariance for both space and time can be suitably treated in the momentum-frequency space by means of a Fourier transform. As a first step, one can transform the space dependence of the propagator:

$$\mathcal{G}(k, \tau) = \int d^3x e^{-i\mathbf{k}\cdot\mathbf{x}} \mathcal{G}(x, \tau). \quad (2.22)$$

The inverse Fourier transform (which goes from the momentum-space Green's function to the real space one) is then defined as:

$$\mathcal{G}(x, \tau) = \int \frac{d^3k}{(2\pi)^3} e^{i\mathbf{k}\cdot\mathbf{x}} \mathcal{G}(k, \tau). \quad (2.23)$$

To take profit of the time invariance of the system, one should also Fourier transform the relative time variable to energy space. In the following, however, it will be more convenient to consider an extension of the time variable to the complex plane in order to treat the problem at finite temperatures. This allows for the extraction of some fundamental properties of the Green's function for a system in thermal equilibrium.

2.2.2 Imaginary time formalism

The reader might already have noticed the strong resemblance between the time evolution operator $e^{-i\hat{H}t}$ of Eq. (2.6) and the statistical weighting factor $e^{-\beta\hat{H}}$ of Eq. (2.10). In fact, this resemblance can be exploited to obtain useful relations for the Green's function of a system in thermal equilibrium. As it has already been pointed out, the time evolution of any operator is given by Eq. (2.6). More specifically, the time evolution of a creation (or annihilation) operator in the Heisenberg picture is given by:

$$\hat{a}(\mathbf{r}t) = e^{i\hat{H}t}\hat{a}(\mathbf{r}0)e^{-i\hat{H}t}. \quad (2.24)$$

Suppose now that t is a complex argument. In principle, one can safely use the previous equation to define a complex time evolution for $\hat{a}(\mathbf{r}t)$. Besides, one can write the following expression for the correlation function $\mathcal{G}^<$:

$$\mathcal{G}^<(\mathbf{r}t, \mathbf{r}'t') = -\frac{1}{i} \frac{\text{Tr} \left\{ e^{-\beta(\hat{H}-\mu\hat{N})} e^{i\hat{H}t'} \hat{a}^\dagger(\mathbf{r}'0) e^{-i\hat{H}t'} e^{i\hat{H}t} \hat{a}(\mathbf{r}0) e^{-i\hat{H}t} \right\}}{\text{Tr} \left\{ e^{-\beta(\hat{H}-\mu\hat{N})} \right\}}, \quad (2.25)$$

and use the cyclic invariance of the trace, as well as the fact that \hat{H} and \hat{N} commute, to rewrite the numerator of the previous expression in the following form:

$$\text{Tr} \left\{ e^{-(i\tau+\beta)\hat{H}-\beta\mu\hat{N}} \hat{a}^\dagger(\mathbf{r}'0) e^{i\tau\hat{H}} \hat{a}(\mathbf{r}0) \right\}. \quad (2.26)$$

For real τ 's, one assumes that this trace converges thanks to the presence of the statistical weighting factor $e^{-\beta(\hat{H}-\mu\hat{N})}$. Provided that this holds for real values of τ , the previous definitions for the correlation functions can be generalized to complex relative times. Yet, from Eq. (2.26) one can see that the trace only converges for complex τ 's in the interval $0 < \text{Im} \tau < \beta$. Similarly, one can show that for $\mathcal{G}^>$ the trace only converges in the region $-\beta < \text{Im} \tau < 0$. These two regions of convergence are shown in Fig. 2.1. In addition, from the previous considerations it is easy to prove that the two correlation functions are analytic and bound in their respective open regions of convergence of the complex relative time variable.

Consider now the $\mathcal{G}^<$ correlation function at $t = 0$:

$$\mathcal{G}^<(\mathbf{r}, t=0; \mathbf{r}', t') = -\frac{1}{i} \frac{\text{Tr} \left\{ e^{-\beta(\hat{H}-\mu\hat{N})} \hat{a}^\dagger(\mathbf{r}'t') \hat{a}(\mathbf{r}0) \right\}}{\text{Tr} \left\{ e^{-\beta(\hat{H}-\mu\hat{N})} \right\}}, \quad (2.27)$$

and use again the cyclic invariance of the trace to get:

$$\mathcal{G}^<(\mathbf{r}, 0; \mathbf{r}', t') = -\frac{1}{i} \frac{\text{Tr} \left\{ e^{-\beta(\hat{H}-\mu\hat{N})} \left[e^{\beta(\hat{H}-\mu\hat{N})} \hat{a}(\mathbf{r}0) e^{-\beta(\hat{H}-\mu\hat{N})} \right] \hat{a}^\dagger(\mathbf{r}'t') \right\}}{\text{Tr} \left\{ e^{-\beta(\hat{H}-\mu\hat{N})} \right\}}. \quad (2.28)$$

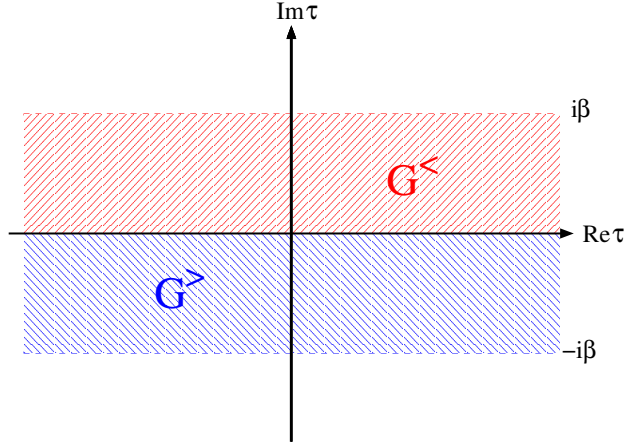


Figure 2.1: Regions in the complex τ plane where $\mathcal{G}^<$ (red) and $\mathcal{G}^>$ (blue) converge.

The sandwich of statistical operators $e^{\beta\hat{H}}$ provides the time evolution of $\hat{a}(\mathbf{r}0)$ to a complex time $t = -i\beta$. In addition, using the relation $\hat{a}(\mathbf{r}t)e^{\beta\mu\hat{N}} = e^{\beta\mu(\hat{N}+1)}\hat{a}(\mathbf{r}t)$, the following useful link between $\mathcal{G}^<$ and $\mathcal{G}^>$ can be established:

$$\begin{aligned} \mathcal{G}^<(\mathbf{r}, t = 0; \mathbf{r}', t') &= -\frac{1}{i} e^{\beta\mu} \frac{\text{Tr} \left\{ e^{-\beta(\hat{H} - \mu\hat{N})} \hat{a}(\mathbf{r}, -i\beta) \hat{a}^\dagger(\mathbf{r}'t') \right\}}{\text{Tr} \left\{ e^{-\beta(\hat{H} - \mu\hat{N})} \right\}} \\ &= -e^{\beta\mu} \mathcal{G}^>(\mathbf{r}, t = -i\beta; \mathbf{r}', t'). \end{aligned} \quad (2.29)$$

This is the so-called Kubo-Martin-Schwinger (KMS) relation. It relates one correlation function at one boundary of its convergence region ($t = 0$) with the opposite correlation function in the corresponding opposite boundary ($t = -i\beta$) in complex times. It is interesting to point out that this is a very general property of the Green's function for any system in thermal equilibrium [Kad62].

As a consequence of the introduction of the complex time evolution of operators, the KMS relation, which links the correlation functions at different complex times, has been obtained. Yet, one would like to know whether a similar relation exists for the propagator. To this end, a certain time ordering in the complex time plane should be defined to link the propagator in a complex time with a certain correlation function. For real times, for instance, this relation is given by Eq. (2.16). In the complex time plane, a natural prescription is to take \mathcal{G} equal to $\mathcal{G}^>$ in the lower half plane of relative complex times (where this function converges,

see Fig. 2.1). The complex time ordering is therefore implemented as follows:

$$\mathcal{G}(\mathbf{r}t, \mathbf{r}'t') = \begin{cases} \mathcal{G}^>(\mathbf{r}t, \mathbf{r}'t'), & \text{for } -\beta < \text{Im } \tau < 0 \\ & \text{or } \text{Re } \tau > 0 \text{ for } \text{Im } \tau = 0 \\ \mathcal{G}^<(\mathbf{r}t, \mathbf{r}'t'), & \text{for } 0 < \text{Im } \tau < \beta \\ & \text{or } \text{Re } \tau < 0 \text{ for } \text{Im } \tau = 0. \end{cases} \quad (2.30)$$

This is a quite general choice that allows one to relate the one-body propagator \mathcal{G} with the correlation functions $\mathcal{G}^<$ and $\mathcal{G}^>$ both in real and complex times.

In practice, however, only two concrete regions of the complex time plane will be of major interest: namely, the real axis (corresponding to *physical times*) and the imaginary axis (corresponding to what will be called *imaginary times*). The time ordering for physical times is clear, and the ordering for imaginary times arises naturally in accordance with Eq. (2.30): one defines t earlier than t' if $\text{Im } t > \text{Im } t'$. In other words, the further down the imaginary axis, the later an imaginary time is. In order to ensure that the correlation functions stay within the region where they are convergent, $-\beta < \text{Im } \tau < \beta$, one can restrict the two imaginary time variables t and t' to the interval:

$$-\beta < \text{Im } t < 0. \quad (2.31)$$

Note that this can also be written as $0 < it < \beta$. The KMS relation guarantees that one does not lose any information by constraining the imaginary times to this interval. Yet, thanks to this constraint, the earliest time will always be $t = 0$ and the latest one $t = -i\beta$. This provides a useful link between the single-particle propagator and the correlation functions. For $t = 0$, for instance, the Green's function equals $\mathcal{G}^<$:

$$\mathcal{G}(\mathbf{r}, t = 0; \mathbf{r}', t') = \mathcal{G}^<(\mathbf{r}, 0; \mathbf{r}', t'), \quad (2.32)$$

while for the largest time, $t = -i\beta$, it is equal to $\mathcal{G}^>$:

$$\mathcal{G}(\mathbf{r}, t = -i\beta; \mathbf{r}', t') = \mathcal{G}^>(\mathbf{r}, t = -i\beta; \mathbf{r}', t'). \quad (2.33)$$

Now, applying the KMS relation, it is clear that the one-body propagator fulfills the following KMS equality:

$$\mathcal{G}(\mathbf{r}, 0; \mathbf{r}', t') = -e^{\beta\mu} \mathcal{G}(\mathbf{r}, -i\beta; \mathbf{r}', t'), \quad (2.34)$$

which connects the Green's functions at a boundary (say $t = 0$) with its value at the other imaginary time boundary ($t = -i\beta$).

The usefulness of this relation can be clearly seen if one considers the Fourier coefficients of Eq. (2.22). The KMS relation, rewritten for relative times, states that:

$$\mathcal{G}(k, \tau) = -e^{\beta\mu} \mathcal{G}(k, \tau - i\beta), \quad (2.35)$$

which is a quasi-periodicity condition for the propagator in the imaginary time variable. This suggests a discrete Fourier representation of the type:

$$\mathcal{G}(k, \tau) = \frac{1}{-i\beta} \sum_{\nu} e^{-iz_{\nu}\tau} \mathcal{G}(k, z_{\nu}), \quad (2.36)$$

where $z_{\nu} = \frac{\nu\pi}{-i\beta} + \mu$ are the so-called Matsubara frequencies. The ν indices in the previous expression have to be odd for the quasi-periodicity condition of Eq. (2.35) to hold with the minus sign in front of the exponential¹. The Fourier coefficients corresponding to the Fourier representation can be obtained from the inverse transform:

$$\mathcal{G}(k, z_{\nu}) = \int_0^{-i\beta} d\tau e^{iz_{\nu}\tau} \mathcal{G}(k, \tau). \quad (2.37)$$

Note that the coefficients $\mathcal{G}(k, z_{\nu})$ are evaluated at a set of infinite frequencies in the complex plane. Still, the physical propagator should be evaluated for real frequencies (corresponding to real times). Further on, the analytical continuation of \mathcal{G} from this set of complex values to the region close to the real axis will be discussed.

2.2.3 Lehmann representation

Before exploiting the properties of the propagator in the complex time and frequency domain, it is useful to understand the properties of the Green's function in physical times and frequencies. Among these, the Lehmann representation and the spectral decomposition are of capital importance. They allow for a physical interpretation of the correlation functions and they are a useful tool in the understanding of the analytical properties of the Green's functions.

Let us go back to the equations that define the $\mathcal{G}^<$ and the $\mathcal{G}^>$ correlation functions, Eq. (2.17) and Eq. (2.18). Consider the time evolution of Eq. (2.6) and introduce a complete set of eigenstates:

$$1 = \sum_n |n\rangle\langle n| \quad (2.38)$$

to obtain the following expressions:

$$\mathcal{G}^>(\mathbf{r}t, \mathbf{r}'t') = \frac{1}{i} \sum_{n,m} \frac{e^{-\beta(E_n - \mu N_n)}}{Z} \langle n | \hat{a}(\mathbf{r}0) | m \rangle \langle m | \hat{a}^{\dagger}(\mathbf{r}'0) | n \rangle e^{i(E_n - E_m)(t - t')}, \quad (2.39)$$

and

$$\mathcal{G}^<(\mathbf{r}t, \mathbf{r}'t') = -\frac{1}{i} \sum_{n,m} \frac{e^{-\beta(E_n - \mu N_n)}}{Z} \langle n | \hat{a}^{\dagger}(\mathbf{r}'0) | m \rangle \langle m | \hat{a}(\mathbf{r}0) | n \rangle e^{i(E_m - E_n)(t - t')}. \quad (2.40)$$

¹ For bosons, this condition does not present a minus sign and the ν indices are even.

Now take the Fourier transforms of the relative space and time variables for the previous expressions:

$$\mathcal{G}^>(k, \omega) = i \int d^3x \int_{-\infty}^{\infty} d\tau e^{-i\mathbf{k}\cdot\mathbf{x} + i\omega\tau} \mathcal{G}^>(\mathbf{x} = \mathbf{r} - \mathbf{r}', \tau = t - t'), \quad (2.41)$$

$$\mathcal{G}^<(k, \omega) = -i \int d^3x \int_{-\infty}^{\infty} d\tau e^{-i\mathbf{k}\cdot\mathbf{x} + i\omega\tau} \mathcal{G}^<(\mathbf{x} = \mathbf{r} - \mathbf{r}', \tau = t - t'). \quad (2.42)$$

The i factors have been conveniently chosen so that both $\mathcal{G}^>$ and $\mathcal{G}^<$ become real and positive functions. In order to obtain a sensible result, one shall in addition consider the relation between real- and momentum-space creation and destruction operators:

$$\hat{a}^\dagger(\mathbf{r}0) = \int \frac{d^3k}{(2\pi)^3} e^{-i\mathbf{k}\cdot\mathbf{r}} \hat{a}_{\mathbf{k}}^\dagger \quad \text{and} \quad \hat{a}(\mathbf{r}0) = \int \frac{d^3k}{(2\pi)^3} e^{i\mathbf{k}\cdot\mathbf{r}} \hat{a}_{\mathbf{k}}. \quad (2.43)$$

Plugging these into the previous equations and taking into account that both correlation functions are diagonal in momentum (*i.e.* they depend on a single k), one finds the following Fourier transform of the correlation functions:

$$\mathcal{G}^>(k, \omega) = 2\pi \sum_{n,m} \frac{e^{-\beta(E_n - \mu N_n)}}{Z} |\langle m | \hat{a}_{\mathbf{k}}^\dagger | n \rangle|^2 \delta[\omega - (E_m - E_n)] \quad (2.44)$$

and

$$\mathcal{G}^<(k, \omega) = 2\pi \sum_{n,m} \frac{e^{-\beta(E_n - \mu N_n)}}{Z} |\langle m | \hat{a}_{\mathbf{k}} | n \rangle|^2 \delta[\omega - (E_n - E_m)]. \quad (2.45)$$

These equations correspond to the Lehmann representation of the correlation functions. A major advantage of this representation is that it can be restated in terms of physical probabilities. Take a closer look at Eq. (2.44), for instance. It includes the square of an amplitude, $\langle m | \hat{a}_{\mathbf{k}}^\dagger | n \rangle$, which gives the probability of adding a particle with momentum \mathbf{k} to an initial thermal state n and bringing it to a final state m . The delta function for the energies ensures that this process only includes a real transition from an initial energy eigenstate E_n to a final eigenstate E_m . Furthermore, one sums over all the possible n and m states. Since the initial state belongs to the thermal bath, one should weight it with the corresponding $e^{-\beta(E_n - \mu N_n)}/Z$ factor. The sum over final m states is an average over the possible final configurations. All in all, $\mathcal{G}^>(k, \omega)d\omega/2\pi$ is a real and positive quantity that gives the probability of exciting the system with an energy between ω and $\omega + d\omega$ when a particle of momentum k is added to the thermal average. Conversely, $\mathcal{G}^<(k, \omega)d\omega/2\pi$ is the probability of exciting the system with an energy between ω and $\omega + d\omega$ when a particle of momentum k is removed from its thermal average.

Consider now the quantity that arises from summing up both correlation functions:

$$\mathcal{A}(k, \omega) = \mathcal{G}^>(k, \omega) + \mathcal{G}^<(k, \omega). \quad (2.46)$$

This is the so-called single-particle *spectral function*. Using the Lehmann representation for $\mathcal{G}^>$ and $\mathcal{G}^<$, Eqs. (2.44) and (2.45), the Lehmann representation of the spectral function is found:

$$\mathcal{A}(k, \omega) = 2\pi \sum_{n,m} \frac{e^{-\beta(E_n - \mu N_n)} + e^{-\beta(E_m - \mu N_m)}}{Z} |\langle m | \hat{a}_{\mathbf{k}}^\dagger | n \rangle|^2 \delta[\omega - (E_m - E_n)]. \quad (2.47)$$

From the positive character of all the quantities inside the previous expression, it becomes clear that the spectral function is a positive definite function, $\mathcal{A}(k, \omega) \geq 0$. In physical terms, the spectral function can be regarded as the probability of adding or removing a particle with momentum k with a change in excitation energy between ω and $\omega + d\omega$.

An important property of the spectral function is the fulfillment of the sum rule:

$$\int_{-\infty}^{\infty} \frac{d\omega}{2\pi} \mathcal{A}(k, \omega) = 1, \quad (2.48)$$

which is intimately related to the Pauli principle, as can be seen from the derivation:

$$\begin{aligned} \int_{-\infty}^{\infty} \frac{d\omega}{2\pi} \mathcal{A}(k, \omega) &= \sum_{n,m} \frac{e^{-\beta(E_n - \mu N_n)}}{Z} \langle n | \hat{a}_{\mathbf{k}}^\dagger | m \rangle \langle m | \hat{a}_{\mathbf{k}} | n \rangle \\ &+ \sum_{n,m} \frac{e^{-\beta(E_n - \mu N_n)}}{Z} \langle n | \hat{a}_{\mathbf{k}} | m \rangle \langle m | \hat{a}_{\mathbf{k}}^\dagger | n \rangle = \\ &= \langle \hat{a}_{\mathbf{k}}^\dagger \hat{a}_{\mathbf{k}} + \hat{a}_{\mathbf{k}} \hat{a}_{\mathbf{k}}^\dagger \rangle = 1. \end{aligned} \quad (2.49)$$

This property can also be understood in terms of probabilities and, in a way, the sum rule sets the normalization of the probability to unity. In other words, the sum rule guarantees that the probability of adding or removing a particle with a given momentum at any accessible energy equals unity.

It is instructive to compare the previous finite temperature definitions with their zero temperature counterparts. Consider, for instance, the hole spectral function at $T = 0$:

$$\mathcal{G}^h(k, \omega) = 2\pi \sum_m |\langle m^{A-1} | \hat{a}_{\mathbf{k}} | 0^A \rangle|^2 \delta[\omega - (E_0^A - E_m^{A-1})]. \quad (2.50)$$

Here, the notation $|0^A\rangle$ is meant to denote the ground-state of an A -body system, while $|m^{A-1}\rangle$ corresponds to the m^{th} excited eigenstate of the $(A-1)$ -body system.

Note that in the context of $T = 0$ Green's function theory the hole spectral function is also denoted by S^h or \mathcal{A}^h . This hole spectral function represents the probability of removing a particle from the ground state of the A -body system, such that the residual system is left with an excitation energy $E_m^{A-1} = E_0^A - \omega$. In terms of energy, this hole spectral function is bound by above: the lowest excited state of the $A - 1$ system is obviously its ground state. Thus, if \mathcal{G}^h has to be non-zero, $\omega < E_0^A - E_0^{A-1} = \mu$. The particle spectral function is defined in similar terms, and it gives the probability of adding one particle on top of the A -body ground state. In that case, one needs to consider the excited states of the $A + 1$ system. A similar reasoning leads to the conclusion that the particle spectral function, \mathcal{G}^p , is only different from zero for $\omega > \mu$. This is quite a reasonable result, since it is easy to convince oneself that the minimum amount of energy that one has to give to the system in order to create a particle is precisely the chemical potential, μ . Nevertheless, at finite temperature there is not such a clean separation of both the particle and the hole contributions to the total spectral function. Since thermally excited states are always included in the correlation functions, one can in principle remove a particle from a thermally excited state and put it in a state close to the ground state of the final system. This leads to a non-vanishing contribution of $\mathcal{G}^<$ for $\omega > \mu$, in contrast to its $T = 0$ counterpart.

2.2.4 Analytical continuation of the propagator

At this point, one can exploit the results of the imaginary time formalism to see that both the correlation functions and the one-body propagator can be found once the spectral function is determined. Let us start by making use of Eqs. (2.44) and (2.45). After some manipulations, one can find the KMS relation in momentum and frequency space:

$$\mathcal{G}^<(k, \omega) = e^{-\beta(\omega - \mu)} \mathcal{G}^>(k, \omega). \quad (2.51)$$

This is actually a detailed balance relation between the two correlation functions, and it is also a basic equation for systems in thermal equilibrium [Kad62]. One can now introduce the definition of the spectral function, Eq. (2.46), to express the correlation functions in terms of it:

$$\mathcal{G}^<(k, \omega) = f(\omega) \mathcal{A}(k, \omega) \quad (2.52)$$

and

$$\mathcal{G}^>(k, \omega) = [1 - f(\omega)] \mathcal{A}(k, \omega), \quad (2.53)$$

with the help of the well-known Fermi-Dirac distribution function:

$$f(\omega) = \frac{1}{e^{\beta[\omega - \mu]} + 1}. \quad (2.54)$$

Equations (2.52) and (2.53) make it possible to obtain the correlation functions once \mathcal{A} is known.

A similar procedure can be applied for the single-particle propagator. Consider its Fourier coefficients, given by Eq. (2.37). These are computed in an interval where $\text{Im } \tau < 0$, which thus corresponds to $\mathcal{G}(k, \tau) = \mathcal{G}^>(k, \tau)$. Introducing now the inverse Fourier transform for the time variable [see Eq. (2.41)]:

$$\mathcal{G}^>(k, \tau) = -i \int_{-\infty}^{\infty} \frac{d\omega}{2\pi} e^{-i\omega\tau} \mathcal{G}^>(k, \omega), \quad (2.55)$$

the Green's function becomes:

$$\begin{aligned} \mathcal{G}(k, z_\nu) &= -i \int_0^{-i\beta} d\tau \int_{-\infty}^{\infty} \frac{d\omega}{2\pi} e^{i(z_\nu - \omega)\tau} [1 - f(\omega)] \mathcal{A}(k, \omega) = \\ &= \int_{-\infty}^{\infty} \frac{d\omega}{2\pi} \frac{\mathcal{A}(k, \omega)}{z_\nu - \omega}. \end{aligned} \quad (2.56)$$

As it has already been mentioned, this Green's function is computed only at a given (infinite) set of Matsubara frequencies. Yet, this is a somewhat limited region of the whole complex plane. One would like to generalize this expression to the full complex plane, in particular to the real axis, which corresponds to physical frequencies. This generalization can be dangerous and must be done with extreme care. In the first place, let us consider the following function of a continuous complex variable:

$$\mathcal{G}(k, z) = \int_{-\infty}^{\infty} \frac{d\omega}{2\pi} \frac{\mathcal{A}(k, \omega)}{z - \omega}. \quad (2.57)$$

It is clear that, when computed at the Matsubara frequencies $z = z_\nu$, this function yields the same result as Eq. (2.56). In this sense, it is a good candidate to become an analytic continuation of $\mathcal{G}(k, z_\nu)$ to the full complex plane. Still, such a continuation is not necessarily unique. One can find other functions of complex frequencies that reproduce the values of the propagator at the Matsubara frequencies. Fortunately, the candidate of Eq. (2.57) satisfies two extra conditions which indeed fix this "uniqueness problem". Namely, $\mathcal{G}(k, z)$ is analytic off the real axis and goes to zero as z approaches to infinity along any straight line in the upper and lower half-planes. One can actually show that, due to these two extra properties, $\mathcal{G}(k, z)$ is the unique analytical continuation of $\mathcal{G}(k, z_\nu)$ and thus determines completely the single-particle propagator in the whole complex plane. The details of this proof can be found in Ref. [Bay61]. Eq. (2.57), which relates the Green's function in the complex plane with the spectral function, is called the *spectral decomposition* of the single-particle propagator.

Up to here, the expressions that have been obtained relate the correlation functions and the single-particle propagator with the spectral function. One can

try to find similar relations for the retarded propagator of Eq. (2.20). Using the representation of the step function in frequency space,

$$\Theta(\tau) = \int_{-\infty}^{\infty} \frac{d\omega}{2\pi i} \frac{e^{i\omega\tau}}{\omega_-}, \quad (2.58)$$

one can take the Fourier transform for real times of the retarded propagator to get:

$$\mathcal{G}^R(k, \omega) = \int_{-\infty}^{\infty} \frac{d\omega'}{2\pi} \frac{\mathcal{A}(k, \omega')}{\omega_+ - \omega'} \quad (2.59)$$

(hereafter the notation $\omega_{\pm} = \omega \pm i\eta$ will be used). This is of course the same quantity that would be obtained by computing the single-particle propagator slightly above the real axis,

$$\mathcal{G}^R(k, \omega) = \mathcal{G}(k, \omega_+). \quad (2.60)$$

The importance of this result arises when it is carefully restated. By means of the spectral decomposition, one finds a unique Green's function, $\mathcal{G}(k, z)$, which coincides both with the Matsubara propagator at the Matsubara frequencies, $z = z_{\nu}$, and with the retarded propagator when it is computed slightly above the real axis, $z = \omega + i\eta$. The knowledge of this function, which is indeed fully determined by the spectral function via Eq. (2.57), is enough for building the one-body propagators (retarded, advanced, etc.) of the system. This result will be important in the following, especially in the computation of Matsubara sums. When performing these sums (see Appendix C), one shall make the assumption that there exists a function $\mathcal{G}(k, z)$, analytical except for the real axis, which can be integrated by means of a Cauchy theorem. The main thing to notice is that this function carries the same information as the coefficients $\mathcal{G}(k, z_{\nu})$, but it can be analytically continued to a region close to the real axis, where it becomes a physical propagator.

In addition, the spectral decomposition of the retarded propagator, Eq. (2.59), is especially useful because, by means of the Plemelj identity:

$$\frac{1}{\omega_{\pm}} = \frac{\mathcal{P}}{\omega} \mp i\pi\delta(\omega), \quad (2.61)$$

one can easily obtain the real and imaginary parts of \mathcal{G}^R . Using the delta function one can compute the imaginary part and check that, indeed, it coincides (up to a factor) with the spectral function:

$$\mathcal{A}(k, \omega) = -2 \text{Im } \mathcal{G}(k, \omega_+). \quad (2.62)$$

In addition, because of the reality of everything except for z inside Eq. (2.57), the following interesting equality holds:

$$\mathcal{G}(k, z^*) = [\mathcal{G}(k, z)]^*, \quad (2.63)$$

which relates the complex conjugate of the Green's function to the Green's function with a complex conjugate argument. With the help of this result, one sees that the spectral function is related to the discontinuity of the propagator at its cut in the real axis:

$$\mathcal{A}(k, \omega) = i \{ \mathcal{G}(k, \omega_+) - \mathcal{G}(k, \omega_-) \} . \quad (2.64)$$

In addition, for future purposes, it will be useful to consider the following decomposition of the propagator. Consider a given complex energy, $z = x + iy$. The propagator can be easily split into two terms:

$$\mathcal{G}(k, x + iy) = \int_{-\infty}^{\infty} \frac{d\omega}{2\pi} \frac{\mathcal{A}(k, \omega)(x - \omega)}{(x - \omega)^2 + y^2} - iy \int_{-\infty}^{\infty} \frac{d\omega}{2\pi} \frac{\mathcal{A}(k, \omega)}{(x - \omega)^2 + y^2} , \quad (2.65)$$

corresponding to its real part,

$$\text{Re } \mathcal{G}(k, x + iy) = \int_{-\infty}^{\infty} \frac{d\omega}{2\pi} \frac{\mathcal{A}(k, \omega)(x - \omega)}{(x - \omega)^2 + y^2} , \quad (2.66)$$

and its imaginary part,

$$\text{Im } \mathcal{G}(k, x + iy) = -y \int_{-\infty}^{\infty} \frac{d\omega}{2\pi} \frac{\mathcal{A}(k, \omega)}{(x - \omega)^2 + y^2} . \quad (2.67)$$

This imaginary part is a negative (positive) quantity for $y > 0$ ($y < 0$). This property is extremely important: it indicates that the imaginary part of the single-particle propagator never vanishes, except for the real axis. That is to say that the single-particle propagator does not have complex zeros [Lut61]. This result is relevant for the inverse propagator and implies that it cannot have complex poles.

2.2.5 One-body properties of a many-body system

In this subsection, it shall be shown that the knowledge of the one-body propagator is enough to compute the thermal averages of any one-body operator. Consider the second quantized version of a generic one-body operator \hat{F} :

$$\hat{F} = \sum_{ij} \langle i|f|j \rangle \hat{a}_i^\dagger \hat{a}_j = \int d^3r \sum_{ij} \phi_i^*(\mathbf{r}) f(\mathbf{r}) \phi_j(\mathbf{r}) \hat{a}_i^\dagger \hat{a}_j = \int d^3r \hat{a}^\dagger(\mathbf{r}) f(\mathbf{r}) \hat{a}(\mathbf{r}) , \quad (2.68)$$

where the matrix elements $\langle i|f|j \rangle$ are given by the one-body matrix elements of two single-particle states, ϕ_i , on the first-quantized (local) operator $f(\mathbf{r})^2$. The

²Sometimes (see, for instance, [Fet71]) the \hat{a}_i operators (which appear in the first equality of Eq. (2.68) and which depend only on the single-particle state i and not on any space variable) are called *creation* and *annihilation* operators, while, in contrast, the \hat{a} operators (which appear in the last equality and do not depend on the state but on the point in space) are called *field operators*. This nomenclature is not used in this Thesis, and the creation and destruction operators employed here have a space-time dependence and no state indices.

thermal average of \hat{F} is given by Eq. (2.14):

$$\begin{aligned} \langle \hat{F} \rangle &= \text{Tr} \left\{ \hat{\rho} \hat{F} \right\} = \int d^3r \lim_{\mathbf{r}' \rightarrow \mathbf{r}} f(\mathbf{r}) \text{Tr} \left\{ \hat{\rho} \hat{a}^\dagger(\mathbf{r}) \hat{a}(\mathbf{r}') \right\} \\ &= -i \int d^3r \lim_{\substack{\mathbf{r}' \rightarrow \mathbf{r} \\ t' \rightarrow t^+}} f(\mathbf{r}) \mathcal{G}(\mathbf{r}t, \mathbf{r}'t'). \end{aligned} \quad (2.69)$$

Note that in this expression the operator f must operate on the Green's function before taking the limit $\mathbf{r}' \rightarrow \mathbf{r}$. Note also that the limit $t' \rightarrow t^+$ is taken to guarantee that the ordering of the operators in the Green's function is the same as in the definition of the operator, Eq. (2.68). Finally, let us also mention that, if any other quantum number such as spin was present, a trace over this quantum number should be taken in order to ensure that the thermal average is a scalar.

A one-body quantity of special interest is the momentum distribution, *i.e.* the number of fermions in a momentum state k :

$$n(k) = \langle \hat{a}_{\mathbf{k}}^\dagger \hat{a}_{\mathbf{k}} \rangle = \frac{1}{Z} \text{Tr} \left\{ e^{-\beta(\hat{H} - \mu \hat{N})} \hat{a}_{\mathbf{k}}^\dagger \hat{a}_{\mathbf{k}} \right\}. \quad (2.70)$$

One can derive a useful expression for this quantity without using the techniques described above. Instead, let us rewrite its definition in the following way:

$$n(k) = \sum_{n,m} \frac{e^{-\beta(E_m - \mu N_m)}}{Z} |\langle m | \hat{a}_{\mathbf{k}}^\dagger | n \rangle|^2. \quad (2.71)$$

The terms inside the previous sum are very close to those in the spectral function of Eq. (2.47):

$$\begin{aligned} (2\pi) \left(e^{-\beta(E_n - \mu N_n)} + e^{-\beta(E_m - \mu N_m)} \right) \delta(\omega + E_n - E_m) = \\ (2\pi) e^{-\beta(E_m - \mu N_m)} \left(1 + e^{\beta(\omega - \mu)} \right) \delta(\omega + E_n - E_m). \end{aligned}$$

The momentum distribution is thus given by the integral:

$$n(k) = \int_{-\infty}^{\infty} \frac{d\omega}{2\pi} A(k, \omega) f(\omega), \quad (2.72)$$

which is a very reasonable expression. The number of fermions in a momentum state k is given by the sum over all energies of the spectral function (the probability of finding a fermion of momentum k in a state of given energy) times the thermal occupation of each energy state, $f(\omega)$.

2.2.6 Two-body propagator

The single-particle propagator describes the excitations of a one-body nature inside the system. Yet, a many-body system presents excitations that affect simultaneously more particles of the system, the so-called collective excitations. Of a capital

importance are the two-body excitations because, as it shall be shown soon, they are unavoidably coupled to the one-body excitations. As a matter of fact, a complete description of the system at the one-body level goes necessarily through a treatment of the two-body correlations. It is thus useful to define the two-particle propagator:

$$i^2 \mathcal{G}_{II}(\mathbf{r}_1 t_1, \mathbf{r}_2 t_2; \mathbf{r}'_1 t'_1, \mathbf{r}'_2 t'_2) = \langle \mathcal{T} [\hat{a}(\mathbf{r}_1 t_1) \hat{a}(\mathbf{r}_2 t_2) \hat{a}^\dagger(\mathbf{r}'_2 t'_2) \hat{a}^\dagger(\mathbf{r}'_1 t'_1)] \rangle, \quad (2.73)$$

which describes excitations produced by the creation or destruction of two particles. For instance, when $t_1 > t'_1$ and $t_2 > t'_2$, the two-body Green's function is related to the propagation of two particles and their subsequent annihilation at latter times. In analogy to the one-body case, one can define $4! = 24$ different correlation functions, according to the different time orderings of the four times, t_1, \dots, t'_2 . Furthermore, one can define the N -body propagator:

$$i^N \mathcal{G}_N(\mathbf{r}_1 t_1, \dots, \mathbf{r}_N t_N; \mathbf{r}'_1 t'_1, \dots, \mathbf{r}'_N t'_N) = \langle \mathcal{T} [\hat{a}(\mathbf{r}_1 t_1) \dots \hat{a}(\mathbf{r}_N t_N) \hat{a}^\dagger(\mathbf{r}'_N t'_N) \dots \hat{a}^\dagger(\mathbf{r}'_1 t'_1)] \rangle, \quad (2.74)$$

related to the excitations produced by the creation and destruction of N particles of the system. These are usually complicated quantities (at least much more difficult to treat than the single-particle propagator), for they involve several (in general, $(2N)!$) time orderings which make their analysis quite difficult.

Still, at the two-body level one can try to handle the Green's function with some chances of success. In the first place, let us notice that the two-body propagator fulfills a KMS condition. The equality holds for any of the t_j time variables and reads:

$$\mathcal{G}_{II}|_{t_j=0} = -e^{\beta\mu} \mathcal{G}_{II}|_{t_j=-i\beta}. \quad (2.75)$$

In analogy to the single-particle propagator, one can profit from the quasi-periodicity in the time variables to expand the two-body propagator in a Fourier series. Taking profit of the homogeneity in time, one can write (the space variables are omitted for brevity):

$$\mathcal{G}_{II}(t_1, t_2; t_3, t_4) = \frac{1}{(-i\beta)^3} \sum_{\nu_1, \nu_2, \nu_3} \mathcal{G}_{II}(z_{\nu_1}, z_{\nu_2}, z_{\nu_3}) e^{-iz_{\nu_1}(t_1-t_4)} e^{-iz_{\nu_2}(t_2-t_4)} e^{-iz_{\nu_3}(t_3-t_4)}, \quad (2.76)$$

where z_{ν_i} are three odd Matsubara frequencies associated to the three possible time differences. Fortunately, in some cases this expressions can be simplified. Imagine, for instance, that two of the time arguments were identical. The two-body Green's function could then be obtained from only two frequencies:

$$\mathcal{G}_{II}(t_1 = t, t_2 = t; t_3, t_4) = \frac{1}{(-i\beta)^2} \sum_{\nu_{12}, \nu_3} \mathcal{G}_{II}(Z_{\nu_{12}}, z_{\nu_3}) e^{-iZ_{\nu_{12}}(t-t_4)} e^{-iz_{\nu_3}(t_3-t_4)}, \quad (2.77)$$

where the two-frequency function $\mathcal{G}_{II}(Z_{\nu_{12}}, z_{\nu_3})$ would then be related to the three-frequency one by the summation:

$$\mathcal{G}_{II}(Z_{\nu_{12}}, z_{\nu_3}) = \frac{1}{-i\beta} \sum_{\nu_2} \mathcal{G}_{II}(Z_{\nu_{12}} - z_{\nu_2}, z_{\nu_2}, z_{\nu_3}). \quad (2.78)$$

The Matsubara frequency $Z_{\nu_{12}}$ is of a bosonic nature, since the index ν_{12} is even. This comes from the summation of two odd integers, ν_1 and ν_2 :

$$Z_{\nu_{12}} = z_{\nu_1} + z_{\nu_2} = \frac{\pi}{-i\beta}(\nu_1 + \nu_2) + \mu_1 + \mu_2. \quad (2.79)$$

Moreover, this results is physically intuitive. The two-body Green's function describes the propagation of a pair of fermions. Whenever one does not resolve this couple of fermions, they will behave as a single boson and thus it is logical that \mathcal{G}_{II} behaves somehow as a bosonic propagator. Following the previous steps, the two-body Green's function of two independent times can be obtained by taking $t_3 = t_4 = t'$. A single Matsubara frequency is then needed:

$$\mathcal{G}_{II}(t_1 = t, t_2 = t; t_3 = t', t_4 = t') = \frac{1}{-i\beta} \sum_{\nu_{12}} \mathcal{G}_{II}(Z_{\nu_{12}}) e^{-iZ_{\nu_{12}}(t-t')}, \quad (2.80)$$

and once again the one-frequency coefficient $\mathcal{G}_{II}(Z_{\nu_{12}})$ is related to the two-frequency one by the sum:

$$\mathcal{G}_{II}(Z_{\nu_{12}}) = \frac{1}{-i\beta} \sum_{\nu_3} \mathcal{G}_{II}(Z_{\nu_{12}}, z_{\nu_3}). \quad (2.81)$$

Note that $Z_{\nu_{12}}$ keeps its bosonic nature. Indeed, $\mathcal{G}(Z_{\nu_{12}})$ describes the ‘‘simultaneous’’ propagation of two particles in an interacting many-body system and thus can be used to determine the two-body properties of the system.

The two-time two-body Green's function can be decomposed in terms of two correlation functions:

$$\mathcal{G}_{II}(t_1 = t, t_2 = t; t_3 = t', t_4 = t') = \Theta(t - t') \mathcal{G}_{II}^<(t - t') + \Theta(t' - t) \mathcal{G}_{II}^>(t - t'), \quad (2.82)$$

given by:

$$i^2 \mathcal{G}_{II}^>(t - t') = \langle \hat{a}(\mathbf{r}_1 t) \hat{a}(\mathbf{r}_2 t) \hat{a}^\dagger(\mathbf{r}_2 t') \hat{a}^\dagger(\mathbf{r}_1 t') \rangle, \quad (2.83)$$

$$i^2 \mathcal{G}_{II}^<(t - t') = \langle \hat{a}^\dagger(\mathbf{r}_1 t') \hat{a}^\dagger(\mathbf{r}_2 t') \hat{a}(\mathbf{r}_2 t) \hat{a}(\mathbf{r}_1 t) \rangle. \quad (2.84)$$

The Lehmann representation of these two expressions is obtained by following the

same steps described above for the one-particle Green's function and yields:

$$\mathcal{G}_{II}^>(t-t') = - \sum_{n,m} \frac{e^{-\beta(E_n - \mu N_n)}}{Z} \langle n | \hat{a}(\mathbf{r}_1) \hat{a}(\mathbf{r}_2) | m \rangle \langle m | \hat{a}^\dagger(\mathbf{r}'_2) \hat{a}^\dagger(\mathbf{r}'_1) | n \rangle e^{i(E_n - E_m)(t-t')}, \quad (2.85)$$

$$\mathcal{G}_{II}^<(t-t') = - \sum_{n,m} \frac{e^{-\beta(E_n - \mu N_n)}}{Z} \langle n | \hat{a}^\dagger(\mathbf{r}'_2) \hat{a}^\dagger(\mathbf{r}'_1) | m \rangle \langle m | \hat{a}(\mathbf{r}_1) \hat{a}(\mathbf{r}_2) | n \rangle e^{-i(E_n - E_m)(t-t')}. \quad (2.86)$$

A Fourier transform of the relative time variable yields the frequency space correlation functions, which can be seen to fulfill the following detailed balance relation:

$$\mathcal{G}_{II}^>(\Omega) = e^{\beta(\Omega - 2\mu)} \mathcal{G}_{II}^<(\Omega). \quad (2.87)$$

A two-body spectral function can then be defined in a similar way as it was done for the one-particle case. In this case, however, it is given by a difference of correlation functions:

$$\mathcal{A}_{II}(\Omega) = \mathcal{G}_{II}^>(\Omega) - \mathcal{G}_{II}^<(\Omega), \quad (2.88)$$

and therefore the following expressions hold:

$$\mathcal{G}_{II}^<(\Omega) = b(\Omega) \mathcal{A}_{II}(\Omega), \quad (2.89)$$

$$\mathcal{G}_{II}^>(\Omega) = [1 + b(\Omega)] \mathcal{A}_{II}(\Omega), \quad (2.90)$$

where the Bose-Einstein distribution function:

$$b(\Omega) = \frac{1}{e^{\beta(\Omega - 2\mu)} - 1}, \quad (2.91)$$

has been introduced. Note that in this expression there is a factor of 2 in front of the chemical potential, in agreement with the fact that \mathcal{G}_{II} describes the propagation of a pair of fermions. This decomposition will be of great help in the treatment of the ladder approximation, where an approximation for \mathcal{G}_{II} which fulfills these analytical properties is carried out.

2.2.7 Equation of motion for the propagator

The time evolution of any operator is dictated in quantum mechanics by Von Neumann's equation, Eq. (2.4). The creation and annihilation operators are not an exception. Taking into account the value of the following commutators:

$$\left[\hat{a}(\mathbf{r}t), \hat{H} \right] = -\frac{\nabla^2}{2m} \hat{a}(\mathbf{r}t) + \int d^3r' V(|\mathbf{r} - \mathbf{r}'|) \hat{a}^\dagger(\mathbf{r}'t) \hat{a}(\mathbf{r}'t) \hat{a}(\mathbf{r}t) \quad (2.92)$$

$$\left[\hat{a}^\dagger(\mathbf{r}t), \hat{H} \right] = \frac{\nabla^2}{2m} \hat{a}^\dagger(\mathbf{r}t) - \hat{a}^\dagger(\mathbf{r}t) \int d^3r' V(|\mathbf{r} - \mathbf{r}'|) \hat{a}^\dagger(\mathbf{r}'t) \hat{a}(\mathbf{r}'t), \quad (2.93)$$

it is easy to write down the equations of motion for the creation and destruction operators:

$$\left\{ i \frac{\partial}{\partial t} + \frac{\nabla^2}{2m} \right\} \hat{a}(\mathbf{r}t) = \int d^3 r' V(|\mathbf{r} - \mathbf{r}'|) \hat{a}^\dagger(\mathbf{r}'t) \hat{a}(\mathbf{r}'t) \hat{a}(\mathbf{r}t) \quad (2.94)$$

$$\left\{ -i \frac{\partial}{\partial t} + \frac{\nabla^2}{2m} \right\} \hat{a}^\dagger(\mathbf{r}t) = \hat{a}^\dagger(\mathbf{r}t) \int d^3 r' V(|\mathbf{r} - \mathbf{r}'|) \hat{a}^\dagger(\mathbf{r}'t) \hat{a}(\mathbf{r}'t). \quad (2.95)$$

These equations are important because they form the starting point for the computation of the equation of motion for the physical propagators of the system. Consider the following expression for the one-body propagator:

$$i\mathcal{G}(\mathbf{r}_1 t_1, \mathbf{r}'_1 t'_1) = \Theta(t_1 - t'_1) \langle \hat{a}(\mathbf{r}_1 t_1) \hat{a}^\dagger(\mathbf{r}'_1 t'_1) \rangle - \Theta(t'_1 - t_1) \langle \hat{a}^\dagger(\mathbf{r}'_1 t'_1) \hat{a}(\mathbf{r}_1 t_1) \rangle, \quad (2.96)$$

and take a time derivative to get:

$$i \frac{\partial}{\partial t_1} \mathcal{G}(\mathbf{r}_1 t_1, \mathbf{r}'_1 t'_1) = \delta(t_1 - t'_1) \delta(\mathbf{r}_1 - \mathbf{r}'_1) + \left\langle \mathcal{T} \left[\frac{\partial}{\partial t_1} \hat{a}(\mathbf{r}_1 t_1) \hat{a}^\dagger(\mathbf{r}'_1 t'_1) \right] \right\rangle. \quad (2.97)$$

Using the equation of motion for the destruction operator, Eq. (2.94), and the definition of the two-body propagator, Eq. (2.73), one obtains the equation of motion for the one-particle propagator:

$$\left\{ i \frac{\partial}{\partial t_1} + \frac{\nabla_1^2}{2m} \right\} \mathcal{G}(\mathbf{r}_1 t_1, \mathbf{r}'_1 t'_1) = \delta(t_1 - t'_1) \delta(\mathbf{r}_1 - \mathbf{r}'_1) - i \int d^3 r_1 V(|\mathbf{r}_1 - \mathbf{r}_1|) \mathcal{G}_{II}(\mathbf{r}_1 t_1, \mathbf{r}_1 t_1; \mathbf{r}'_1 t'_1, \mathbf{r}_1 t_1^+). \quad (2.98)$$

Introducing the notation, $\mathbf{r}_1 t_1 \rightarrow \mathbf{1}$ and $V(|\mathbf{r}_1 - \mathbf{r}_2|) \delta(t_1 - t_2) \rightarrow V(\mathbf{1} - \mathbf{2})$, the previous expression can be rewritten in an easier form:

$$\left\{ i \frac{\partial}{\partial t_1} + \frac{\nabla_1^2}{2m} \right\} \mathcal{G}(\mathbf{1}, \mathbf{1}') = \delta(\mathbf{1} - \mathbf{1}') - i \int d\bar{\mathbf{1}} V(\mathbf{1} - \bar{\mathbf{1}}) \mathcal{G}_{II}(\mathbf{1}\bar{\mathbf{1}}; \mathbf{1}'\bar{\mathbf{1}}^+). \quad (2.99)$$

The one-particle propagator fulfills another similar equation of motion for the primed variables which can be obtained in the same fashion. Note also that the zero temperature one-body propagator fulfills the same equations of motion. Anyway, what becomes clear from inspecting Eq. (2.98) is that, to solve the equation exactly, one should previously know the two-body propagator, \mathcal{G}_{II} . Using the same techniques sketched above, one can obtain an equation of motion for \mathcal{G}_{II} which can be seen to depend on both the one- and the three-body propagator. Indeed, this represents a general result: the equation of motion of the N -body Green's

function is coupled to the $N - 1$ and to the $N + 1$ propagators [Mar59]:

$$\begin{aligned} & \left\{ i \frac{\partial}{\partial t_j} + \frac{\nabla_j^2}{2m} \right\} \mathcal{G}_N(\mathbf{1} \cdots \mathbf{N}; \mathbf{1}' \cdots \mathbf{N}') = \\ & \sum_{l=1}^N (-1)^{j+l} \delta(\mathbf{j} - \mathbf{l}) \mathcal{G}_{N-1}(\mathbf{1} \cdots \mathbf{j} - \mathbf{1}, \mathbf{j} + \mathbf{1} \cdots \mathbf{N}; \mathbf{1}' \cdots \mathbf{l} - \mathbf{1}, \mathbf{l} + \mathbf{1} \cdots \mathbf{N}') \\ & - i \int d\bar{\mathbf{l}} V(\mathbf{j} - \bar{\mathbf{l}}) \mathcal{G}_{N+1}(\bar{\mathbf{l}} \mathbf{1} \cdots \mathbf{j} \cdots \mathbf{N}; \bar{\mathbf{l}}^+ \mathbf{1}' \cdots \mathbf{N}'). \end{aligned} \quad (2.100)$$

This introduces the so-called *hierarchy of the equations of motion*, which needs to be solved by a suitable truncation. Needless to say, this truncation should be sensible if one wants to find realistic results and it will thus depend on the physical problem under study. In the following, some of these truncations for the equations of motion will be sketched. In addition, a special effort will be made in order to outline the relation of these truncation with the diagrammatic approaches (see [Mat71] for more details on the relations of truncations of the equations of motion and diagrammatic approaches).

Before doing so, however, it is important to outline a consequence of Eq. (2.94). Multiply this equation by a destruction operator at a time \mathbf{r}'', t'' ; take the limits $\mathbf{r}'' \rightarrow \mathbf{r}$ and $t'' \rightarrow t$; integrate over the \mathbf{r} space variables and take the thermal average. The following equality concerning the potential energy of the system holds:

$$\begin{aligned} \langle V \rangle &= \left\langle \frac{1}{2} \int d^3 r \int d^3 r' \hat{a}^\dagger(\mathbf{r}t) \hat{a}^\dagger(\mathbf{r}'t) V(\mathbf{r}, \mathbf{r}') \hat{a}(\mathbf{r}'t) \hat{a}(\mathbf{r}t) \right\rangle = \\ &= \frac{1}{2} \int d^3 r \lim_{\substack{\mathbf{r}'' \rightarrow \mathbf{r} \\ t'' \rightarrow t}} \left\{ i \frac{\partial}{\partial t} + \frac{\nabla^2}{2m} \right\} \langle \hat{a}^\dagger(\mathbf{r}''t'') \hat{a}(\mathbf{r}t) \rangle. \end{aligned} \quad (2.101)$$

The term with the gradient on the previous equation is simply minus half of the kinetic energy of the system, which allows one to obtain the total energy of the system by taking into account that the average $\langle a^\dagger a \rangle$ corresponds to $\mathcal{G}^<$:

$$\begin{aligned} \langle H \rangle &= \frac{-i}{2} \int d^3 r \lim_{\substack{\mathbf{r}'' \rightarrow \mathbf{r} \\ t'' \rightarrow t}} \left\{ i \frac{\partial}{\partial t} + \frac{\nabla^2}{2m} \right\} \mathcal{G}^<(\mathbf{r}t, \mathbf{r}''t'') = \\ &= \frac{\mathcal{V}}{2} \int \frac{d^3 k}{(2\pi)^3} \int_{-\infty}^{\infty} \frac{d\omega}{2\pi} \left\{ \frac{k^2}{2m} + \omega \right\} \mathcal{G}^<(k, \omega), \end{aligned} \quad (2.102)$$

where \mathcal{V} denotes the total volume of the system. One should note the importance of this results, which relates a two-body property of the system (the total energy) with a one-body property (the propagator). This is usually called the Galitski-Migdal-Koltun (GMK) sum rule [Gal58b; Kol74]. In the following, it will be extensively used, especially in the form:

$$\frac{E}{\mathcal{V}} = \int \frac{d^3 k}{(2\pi)^3} \int_{-\infty}^{\infty} \frac{d\omega}{2\pi} \frac{1}{2} \left\{ \frac{k^2}{2m} + \omega \right\} f(\omega) \mathcal{A}(k, \omega), \quad (2.103)$$

which gives the total energy per unit volume (or energy density) of the system in terms of the spectral function $\mathcal{A}(k, \omega)$. It is important to note that the GMK sum rule is only valid for a system with two-body interactions. This can be a strong handicap for *ab initio* many-body calculations, where three-body forces are needed to reproduce, for instance, the saturation properties of nuclear matter.

2.3 Free case

In this section, the case of a free Fermi sea of neutrons and protons will be studied with the techniques sketched above. The properties of an infinite system of non-interacting fermions will be thus described in terms of the single-particle propagator. A series of useful results, that will be used later on in our description of interacting nuclear matter, will be derived. Let us start with the equation of motion for the free Green's function, \mathcal{G}_0 :

$$\left\{ i \frac{\partial}{\partial t} + \frac{\nabla^2}{2m} \right\} \mathcal{G}_0(\mathbf{r}t; \mathbf{r}'t') = \delta(t - t') \delta(\mathbf{r} - \mathbf{r}'). \quad (2.104)$$

Multiplying both sides of the previous equation by the factor $e^{-i\mathbf{k}\cdot\mathbf{x} + iz_\nu\tau}$, integrating over the space and time variables, \mathbf{x} and τ , and using the Fourier transform of the propagator, Eq. (2.36), the following equation is obtained:

$$\mathcal{G}_0(k, z_\nu) = \frac{1}{z_\nu - \frac{k^2}{2m}}. \quad (2.105)$$

This is the frequency-momentum representation of the Green's function of an infinite system of non-interacting fermions. As explained previously, this expression, which is only valid for $z = z_\nu$, can be analytically extended to all the complex plane in a non-ambiguous way. The propagator has single poles at the real frequencies $z = k^2/2m$, corresponding to the kinetic energies of the quasi-particles of the system. The retarded propagator is obtained by letting $z \rightarrow \omega_+$. Fourier transforming the real frequency variable in this propagator, one can then see that in the free system this is given by an undamped plane wave:

$$\mathcal{G}_0^R(k, \tau) = -i\Theta(\tau)e^{-i\frac{k^2}{2m}\tau}, \quad (2.106)$$

with frequencies corresponding to the kinetic quasi-particle energies. This expression is interesting, for it clarifies the physical meaning of the retarded one-body propagator. In a non-interacting system, it corresponds to the probability amplitude of propagating through the system a quasi-particle excitation of momentum k and energy $k^2/2m$ during a given time, $\tau > 0$.

With the help of Eq. (2.64), the spectral function for the non-interacting case can be obtained:

$$\mathcal{A}(k, \omega) = i \{ \mathcal{G}(k, \omega_+) - \mathcal{G}(k, \omega_-) \} = (2\pi) \delta \left(\omega - \frac{k^2}{2m} \right). \quad (2.107)$$

This is simply a delta function at the quasi-particle energy. A delta-like form of the spectral function is a generic feature of both the free and the mean-field approaches. The following expressions for the correlation functions are obtained from Eqs. (2.53) and (2.52):

$$\mathcal{G}^<(k, \omega) = (2\pi) f(\omega) \delta\left(\omega - \frac{k^2}{2m}\right) \quad (2.108)$$

$$\mathcal{G}^>(k, \omega) = (2\pi) [1 - f(\omega)] \delta\left(\omega - \frac{k^2}{2m}\right). \quad (2.109)$$

These are delta-like functions with variable strength. At low temperatures, one expects the chemical potential to be close to the zero temperature Fermi energy, $\mu \sim k_F^2/2m > 0$. Therefore, at low temperatures one finds that, for $k^2/2m \ll \mu$, $\mathcal{G}^>$ is negligible in front of $\mathcal{G}^<$, while for $k^2/2m \gg \mu$, the situation is the opposite one. This is in accordance with the fact that, in the zero temperature limit, $\mathcal{G}^<$ becomes a hole spectral function (a hole being a quasi-particle with energy below the Fermi energy μ), while $\mathcal{G}^>$ is associated to the particle spectral function. The momentum distribution can also be easily computed from Eq. (2.72):

$$n(k) = \int_{-\infty}^{\infty} \frac{d\omega}{2\pi} f(\omega) (2\pi) \delta\left(\omega - \frac{k^2}{2m}\right) = f\left[\frac{k^2}{2m}\right]. \quad (2.110)$$

For the non-interacting case, the momentum distribution is given by the Fermi-Dirac distribution computed at the quasi-particle kinetic energies. The usefulness of Koltun's sum rule can now be tested, since the knowledge of the spectral function for the free system allows one to compute the total energy density:

$$\frac{E}{\mathcal{V}} = \int \frac{d^3k}{(2\pi)^3} \frac{k^2}{2m} n(k), \quad (2.111)$$

which is just the sum of all the quasi-particle kinetic energies, $k^2/2m$, weighted by the population of each quasi-particle states, $n(k)$.

Finally, a formal expression for the free one-body propagator can be obtained from the equation of motion. Rewriting this equation with the help of the notation $\mathbf{r}_1 t_1 \rightarrow \mathbf{1}$, one obtains:

$$\left\{ i \frac{\partial}{\partial t_1} + \frac{\nabla_{\mathbf{1}}^2}{2m} \right\} \mathcal{G}_0(\mathbf{1}, \mathbf{1}') = \delta(\mathbf{1} - \mathbf{1}'). \quad (2.112)$$

$\mathcal{G}_0(\mathbf{1}, \mathbf{1}')$ can be considered as an operator linking $\mathbf{1}$ and $\mathbf{1}'$. It is then natural to define the inverse operator of \mathcal{G}_0 , $[\mathcal{G}_0]^{-1}$, as the one fulfilling the following equation:

$$\int d\bar{\mathbf{1}} [\mathcal{G}_0]^{-1}(\mathbf{1}, \bar{\mathbf{1}}) \mathcal{G}_0(\bar{\mathbf{1}}, \mathbf{1}') = \delta(\mathbf{1} - \mathbf{1}'). \quad (2.113)$$

Now, using the equation of motion of the single-particle propagator, one sees that this inverse operator is given by the formal operatorial expression:

$$[\mathcal{G}_0]^{-1}(\mathbf{1}, \mathbf{1}') = \left\{ i \frac{\partial}{\partial t_1} + \frac{\nabla_1^2}{2m} \right\} \delta(\mathbf{1} - \mathbf{1}'). \quad (2.114)$$

This result, which gives a formal expression for the free one-body propagator, is particularly useful in the derivation of the integral equation of motion for the propagator.

2.4 Self-energy

Let us now abandon the somewhat naive free case and enter the much more involved interacting case. For a system interacting with a two-body interaction, the one-body propagator is coupled to the two-body propagator by means of its equation of motion, Eq. (2.99). Yet, formally one can obtain a closed equation of motion by removing the two-body Green's function from the equation. This can be done by means of a new operator, the so-called self-energy $\Sigma(\mathbf{r}t; \mathbf{r}'t')$, which satisfies the equation:

$$\int d\bar{\mathbf{1}} \Sigma(\mathbf{1}, \bar{\mathbf{1}}) \mathcal{G}(\bar{\mathbf{1}}, \mathbf{1}') = -i \int d\bar{\mathbf{1}} V(\mathbf{1} - \bar{\mathbf{1}}) \mathcal{G}_{II}(\mathbf{1}\bar{\mathbf{1}}; \mathbf{1}'\bar{\mathbf{1}}^+). \quad (2.115)$$

The inclusion of the self-energy, of course, does not really solve the problem. There is still a relation between the two-body propagator and the self-energy that has to be worked out. Nevertheless, the self-energy turns out to have interesting properties that are fundamental in several many-body studies. In particular, the approximations in quantum many-body theory are usually defined in terms of the self-energy operator. It is clear that, once introduced into Eq. (2.115), any approximation to the self-energy can be recast into an approximation for the two-body propagator. This might also shed a light on the nature of the approximations under study. Finally, let us also notice that, as it will be seen shortly, the self-energy has a clear diagrammatic interpretation. This is extremely helpful for a proper understanding of the many-body approximations at use.

The “closed” equation of motion for the propagator is easily obtained by replacing the second term of the equation of motion for the one-body propagator, Eq. (2.99), with the left hand side of Eq. (2.115):

$$\left\{ i \frac{\partial}{\partial t_1} + \frac{\nabla_1^2}{2m} \right\} \mathcal{G}(\mathbf{1}, \mathbf{1}') = \delta(\mathbf{1} - \mathbf{1}') + \int d\bar{\mathbf{1}} \Sigma(\mathbf{1}, \bar{\mathbf{1}}) \mathcal{G}(\bar{\mathbf{1}}, \mathbf{1}'). \quad (2.116)$$

This is the so-called *Dyson's equation* in its differential form. For future convenience, it is interesting to obtain an equivalent integral equation. Consider the left hand-side of the previous equation. Let us formally introduce a unit factor

(formed by an integral and a delta function) in between the differential operators and the Green's function and use Eq. (2.114) to get:

$$\int d\mathbf{2} \left\{ i \frac{\partial}{\partial t_1} + \frac{\nabla_{\mathbf{1}}^2}{2m} \right\} \delta(\mathbf{1} - \mathbf{2}) \mathcal{G}(\mathbf{2}, \mathbf{1}') = \int d\mathbf{2} [\mathcal{G}_0]^{-1}(\mathbf{1}, \mathbf{2}) \mathcal{G}(\mathbf{2}, \mathbf{1}') = \delta(\mathbf{1} - \mathbf{1}'). \quad (2.117)$$

One can now multiply the previous result by $\mathcal{G}_0(\mathbf{3}, \mathbf{1})$ and integrate over the variable $\mathbf{1}$:

$$\int d\mathbf{1} \mathcal{G}_0(\mathbf{3}, \mathbf{1}) \delta(\mathbf{1} - \mathbf{1}') = \mathcal{G}(\mathbf{3}, \mathbf{1}'). \quad (2.118)$$

After this integration, one obtains, on the left hand side of Eq. (2.116), the one-body propagator between $\mathbf{1}'$ and $\mathbf{3}$. The same product and integral can be carried out easily for the right hand side of the equation. After taking $\mathbf{3} \rightarrow \mathbf{1}$, the integral form of Dyson's equation is obtained:

$$\mathcal{G}(\mathbf{1}, \mathbf{1}') = \mathcal{G}_0(\mathbf{1}, \mathbf{1}') + \int d\mathbf{2} \int d\bar{\mathbf{2}} \mathcal{G}_0(\mathbf{1}, \mathbf{2}) \Sigma(\mathbf{2}, \bar{\mathbf{2}}) \mathcal{G}(\bar{\mathbf{2}}, \mathbf{1}'). \quad (2.119)$$

The full one-body propagator is given by the sum of a free contribution, \mathcal{G}_0 , plus an integral term. This can be interpreted in the following form: a perturbation propagates freely from $\mathbf{1}'$ to $\bar{\mathbf{2}}$, where it is scattered by the self-energy operator (this also includes multi-scattering processes) to the point $\mathbf{2}$. Finally, the particle propagates from $\mathbf{2}$ to $\mathbf{1}$. Since the propagator gives a probability amplitude, one should integrate over the points $\mathbf{2}$ and $\bar{\mathbf{2}}$ (that can be anywhere in space and time) to obtain the final result.

Still, the discussion is not complete. Dyson's equation, as any differential equation, needs of some boundary condition to be completely solved. For real times, it can be hard to find boundaries in which one exactly knows the value for the propagator or the self-energy. In imaginary time, however, one can use the KMS relation as a boundary condition for Dyson's equation. This establishes the value of the one-body propagator at a given time in terms of the value at another time. Formally, Dyson's equation in imaginary times is the same as for real times (the time variable t simply becomes complex), but in the imaginary axis the only region of physical interest is the $(0, -i\beta)$ line. Thus, one may take into account the equation in the imaginary axis and consider that the time integrals run from 0 to $-i\beta$:

$$\mathcal{G}(\mathbf{1}, \mathbf{1}') = \mathcal{G}_0(\mathbf{1}, \mathbf{1}') + \int_0^{-i\beta} d\mathbf{2} \int_0^{-i\beta} d\bar{\mathbf{2}} \mathcal{G}_0(\mathbf{1}, \mathbf{2}) \Sigma(\mathbf{2}, \bar{\mathbf{2}}) \mathcal{G}(\bar{\mathbf{2}}, \mathbf{1}'). \quad (2.120)$$

If one is able to obtain an expression for the self-energy in a given approximation, the solution of Dyson's equation gives access to the full single-particle propagator of the system.

In addition, from Dyson's equation one can find the analytic structure of the self-energy. This is most easily done by considering the differential form of Dyson's equation in the momentum-frequency representation. Let us first Fourier transform the position variable of Dyson's equation:

$$\left\{ i \frac{\partial}{\partial t_1} - \varepsilon_0(k) \right\} \mathcal{G}(k, t_1 - t'_1) - \int_0^{-i\beta} dt_{\bar{1}} \Sigma(k, t_1 - t_{\bar{1}}) \mathcal{G}(k, t_{\bar{1}} - t_1) = \delta(t_1 - t'_1), \quad (2.121)$$

where $\varepsilon_0(k) = \frac{k^2}{2m}$ is the kinetic energy of a quasi-particle in the system. One can now take the Fourier transform of the relative complex time. Since the propagator in imaginary times is involved in this transform, the transformation involves the Matsubara frequencies:

$$[z_\nu - \varepsilon_0(k) - \Sigma(k, z_\nu)] \mathcal{G}(k, z_\nu) = 1. \quad (2.122)$$

One sees now the utility of Fourier transforming Dyson's equation. From a complicated integral equation in real space, Dyson's equation has been simplified to an algebraic equation in momentum-frequency space. This has an easy solution that, after the usual analytical continuation to continuous complex values, reads:

$$\mathcal{G}(k, z) = \frac{1}{z - \varepsilon_0(k) - \Sigma(k, z)}. \quad (2.123)$$

It is this equality that can be exploited to extract the analytical properties of the self-energy [Lut61]. Consider the following expression for the self-energy:

$$\Sigma(k, z) = z - \varepsilon_0(k) - \mathcal{G}^{-1}(k, z). \quad (2.124)$$

First of all, it is clear, from Eq. (2.63), that:

$$\Sigma(k, z^*) = [\Sigma(k, z)]^*. \quad (2.125)$$

Since the propagator has no complex zeros [see Eq. (2.67)], the quantity \mathcal{G}^{-1} can have no complex poles and thus the self-energy is analytical everywhere in the complex plane (except possibly in the real axis). For the sake of convenience, let us decompose the self-energy on an instantaneous (energy-independent) part, Σ_{HF} , and a non-instantaneous (energy-dependent) term, Σ_C :

$$\Sigma(k, z) = \Sigma_{HF}(k) + \Sigma_C(k, z). \quad (2.126)$$

The quantity Σ_C , indeed, is analytic in the upper and lower-half planes [Lut61]. One can see that this contribution to the self-energy has a spectral representation:

$$\Sigma_C(k, z) = \int_{-\infty}^{\infty} \frac{d\omega}{2\pi} \frac{\Gamma(k, \omega)}{z - \omega}. \quad (2.127)$$

This equation defines the width $\Gamma(k, \omega)$ for the self-energy, in analogy with the spectral function for the propagator. Furthermore, one can define the retarded self-energy by taking $z = w_+$. It is then easy to check that the width can be obtained from the imaginary part of the retarded self-energy:

$$\Gamma(k, \omega) = -2 \operatorname{Im} \Sigma^R(k, \omega). \quad (2.128)$$

Finally, the width is positive definite, as shown by the following equalities:

$$\begin{aligned} \Gamma(k, \omega) &= -2 \operatorname{Im} \Sigma(k, \omega_+) = 2 \operatorname{Im} \mathcal{G}^{-1}(k, \omega_+) = \\ &= \frac{\mathcal{A}(k, \omega_+)}{[\operatorname{Re} \mathcal{G}(k, \omega_+)]^2 + [\operatorname{Im} \mathcal{G}(k, \omega_+)]^2} \geq 0. \end{aligned} \quad (2.129)$$

The function $\Gamma(k, \omega)$ is called the width because it is somehow related to the mean life-time of the particles in the system (and thus to a width in frequency space). An easy way to clarify this concept can be obtained by using Eqs. (2.62) and (2.123) to find the spectral function in terms of the self-energy:

$$\mathcal{A}(k, \omega) = \frac{\Gamma(k, \omega)}{[\omega - \frac{k^2}{2m} - \operatorname{Re} \Sigma(k, \omega)]^2 + [\frac{\Gamma(k, \omega)}{2}]^2}. \quad (2.130)$$

A vanishing width would result in a delta-like spectral function, similar to the one of the free case, Eq. (2.107). A finite width, on the other hand, involves single-particle states that are spread in a band of energy values for each momentum. This is not surprising: a scattered fermion, when propagating across the system, will have a given life-time and mean-free path. This will yield uncertainties on its momentum and its energy, and thus both k and ω have to be treated as independent variables. This image is in contrast with the one arising from the free and the mean-field pictures, where a single energy state (the quasi-particle energy) is associated to each given momentum.

Finally, it is important to know that the real and the imaginary parts of the self-energy are not independent. Instead, they are related by a dispersion relation, which can be obtained by using the Plemelj identity, Eq. (2.61), on Eqs. (2.126) and (2.127):

$$\operatorname{Re} \Sigma(k, \omega) = \Sigma_{HF}(k) + \mathcal{P} \int_{-\infty}^{\infty} \frac{d\omega'}{2\pi} \frac{\Gamma(k, \omega')}{\omega - \omega'}. \quad (2.131)$$

In the following, this relation will be very important. The imaginary part of the self-energy will be computed within the ladder approximation. The previous dispersion relation will allow us to obtain the real part

2.5 Quasi-particle approximation

At this point, an approximation that has been used in several applications and that might be helpful in understanding the behavior of fermionic systems will be

introduced. Consider Eq. (2.130) for the spectral function. For a given momentum and for relatively small widths, the spectral function will have a peak at the so-called quasi-particle energy, given by the solution of the following equation:

$$\varepsilon_{qp}(k) = \frac{k^2}{2m} + \text{Re} \Sigma(k, \varepsilon_{qp}(k)) \quad (2.132)$$

(note that the width is positive definite and thus the spectral function cannot be singular at this point). In the so-called *quasi-particle approximation*, Eq. (2.132) establishes the link between a momentum k and a unique quasi-particle energy, $\varepsilon_{qp}(k)$. Close to this energy, one might expand the energy dependence of the real part of the self-energy to first order:

$$\text{Re} \Sigma(k, \omega) \sim U(k) + \left. \frac{\partial \text{Re} \Sigma(k, \omega)}{\partial \omega} \right|_{\omega=\varepsilon_{qp}(k)} (\omega - \varepsilon_{qp}(k)), \quad (2.133)$$

where the single-particle potential $U(k) = \text{Re} \Sigma(k, \varepsilon_{qp}(k))$ has been introduced. Note that the introduction of this approximation simplifies the energy dependence of the real part of the self-energy. The imaginary part of the self-energy is, on the other hand, also smooth close to the quasi-particle energy, and thus its energy dependence might be neglected:

$$\text{Im} \Sigma(k, \omega) \sim \text{Im} \Sigma(k, \varepsilon_{qp}(k)) = W(k). \quad (2.134)$$

With these approximations, the single-particle Green's function reads:

$$\mathcal{G}_{qp}(k, \omega) = \frac{\mathcal{Z}(k)}{\omega - \varepsilon_{qp}(k) - i\mathcal{Z}(k)W(k)}, \quad (2.135)$$

where $\mathcal{Z}(k)$ is the so-called *renormalization factor* (or simply *Z-factor*) of the quasi-particle pole:

$$\mathcal{Z}(k) = \left[1 - \left. \frac{\partial \text{Re} \Sigma(k, \omega)}{\partial \omega} \right|_{\omega=\varepsilon_{qp}(k)} \right]^{-1}. \quad (2.136)$$

Within this approximation, the simplified energy dependence of the propagator is reflected in the spectral function, which becomes a Breit-Wigner (also called Lorentzian) distribution:

$$\mathcal{A}_{qp}(k, \omega) = \frac{2\mathcal{Z}^2(k)|W(k)|}{[\omega - \varepsilon_{qp}(k)]^2 + [\mathcal{Z}(k)W(k)]^2}, \quad (2.137)$$

centered at the quasi-particle energy, $\varepsilon_{qp}(k)$. The width at half maximum of this distribution, $\Gamma_{qp} = 2\mathcal{Z}(k)|W(k)|$, is directly proportional to W and therefore the imaginary part of the self-energy sets the spread in energies of the quasi-particle states.

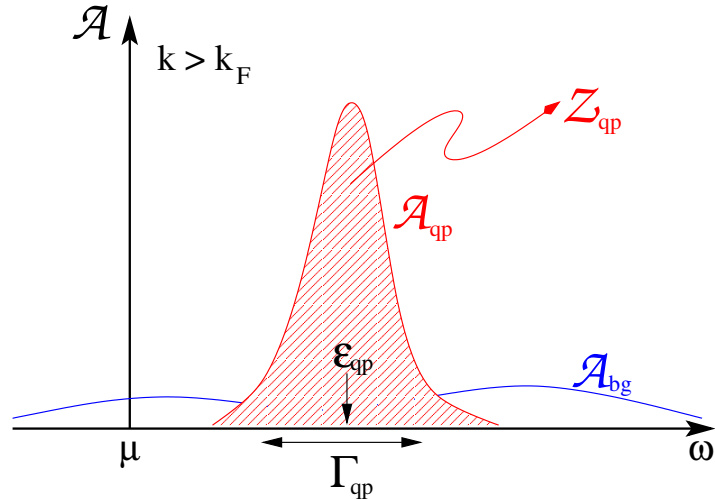


Figure 2.2: *Schematic illustration of the energy dependence of the spectral function in the quasi-particle approximation for a momentum above the Fermi surface. The quasi-particle contribution to the spectral function is given by a strong symmetric peak centered around the quasi-particle energy. The area that this peak covers in energies is given by the \mathcal{Z} -factor. The soft background contribution is also shown.*

At zero temperature, one can show that:

$$\Gamma(k = k_F, \varepsilon_{qp}(k_F)) = 0, \quad (2.138)$$

due to phase space restrictions [Lut61]. In these conditions, *i.e.* at the Fermi surface, the spectral function becomes a delta peak at the quasi-particle energy of Eq. (2.132). The previous definition of the \mathcal{Z} -factor, Eq. (2.136), accounts then for the factor in front of the quasi-particle delta function of the $T = 0$ propagator when computed at the Fermi surface. At finite temperature, the quasi-particle propagator does not have a delta peak for real ω 's and the \mathcal{Z} -factor cannot be interpreted anymore as such a factor. However, within this quasi-particle approximation the sum rule of the spectral function can be computed analytically:

$$\int_{-\infty}^{\infty} \frac{d\omega}{2\pi} \mathcal{A}_{qp}(k, \omega) = \mathcal{Z}(k), \quad (2.139)$$

and therefore one finds that the \mathcal{Z} -factor corresponds to the fraction of single-particle states contained in the quasi-particle peak. This result is valid both at zero and at finite temperatures. In a way, one can say that the \mathcal{Z} -factor measures the strength of the correlations that go beyond the mean-field approximation because, within a mean-field approximation, $\mathcal{Z}(k) = 1$ and therefore the eigenstates of the

system are of a single-particle nature. Whenever correlations beyond the quasi-particle picture are included in the formalism, single-particle states are fragmented in a wide range of energies and the single-particle nature of the energy eigenstates is lost. In those cases, the further away the \mathcal{Z} -factor from unity, the more fragmented the states are. As a consequence, large \mathcal{Z} 's are associated to large fragmentations or, in other words, to important correlations.

It is clear that the Lorentzian-like expression for the spectral function violates the sum rule of Eq. (2.48). To recover the correct normalization, one customarily defines the *background* contribution of the single-particle propagator as the difference:

$$\mathcal{G}_{bg}(k, \omega) = \mathcal{G}(k, \omega) - \mathcal{G}_{qp}(k, \omega). \quad (2.140)$$

For the global sum rule to yield unity, the spectral function associated to this propagator, \mathcal{A}_{bg} , must satisfy the sum rule:

$$\int_{-\infty}^{\infty} \frac{d\omega}{2\pi} \mathcal{A}_{bg}(k, \omega) = 1 - \mathcal{Z}(k). \quad (2.141)$$

The background contribution to the the spectral function is originated by excitations in the system which do not have a single-particle nature. Instead, it is caused by multi-particle or collective excitations in the system, which are usually much more involved to compute. The background contribution to the spectral function is normally considered to be a smooth function of energy and momentum. A sketch of the spectral function within this quasi-particle approximation is given in Fig. 2.2. Note that around the quasi-particle peak, a symmetric Breit-Wigner distribution arises and the area below the peak is given by the \mathcal{Z} -factor. For energies which are far away from the quasi-particle peak, only the small and soft background contribution is found.

Finally, one should also be aware of the fact that, in the literature, the quasi-particle approximation often implies an additional assumption. Namely, that quasi-particles have an infinite life-time and thus their spectral function is given by the limit:

$$\lim_{\frac{\Gamma_{qp}}{2} \rightarrow 0} \mathcal{A}_{qp}(k, \omega) = (2\pi) \mathcal{Z}(k) \delta[\omega - \varepsilon_{qp}(k)], \quad (2.142)$$

which is simply a delta function at the quasi-particle peak. The strength of the peak is given by the \mathcal{Z} -factor, and it will be lower than 1 whenever energy-dependent correlations are taken into account. In this Thesis, this type of approximations will be called *no-width* approximations (in order to differentiate them from the usual Lorentzian quasi-particle approximation of Eq. (2.137)). This type of approaches are very convenient for numerical reasons, because they automatically eliminate the explicit energy integrations of the Green's function. In other words,

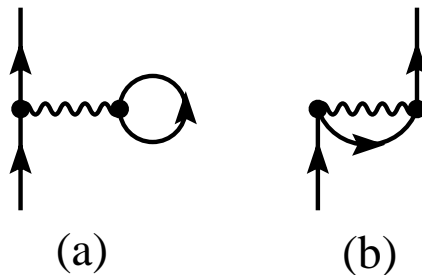


Figure 2.3: *First order diagrams that contribute to the Green's function.*

the off-shell components of the propagator are not taken into account. Note, however, that they do not neglect completely the energy dependence of the self-energy, because this is still included in the calculation of the \mathcal{Z} -factor. In highly correlated systems, where the width of the quasi-particles cannot be taken to be small, a no-width approximation is clearly too simplistic and thus leads to unrealistic results.

2.6 Diagrammatic expansion of the propagator

As explained in detail in Appendix A, the single-particle propagator can be expanded in terms of free single-particle propagators and two-body interactions. At any order n in the number of interaction lines, this expansion is most suitably carried out by using diagrammatic techniques. In Appendix B the rules to construct the diagrams that correspond to any order in the perturbative expansion of the propagator are given. These rules also specify the corresponding value of each diagram. The explicit expressions for the two first-order diagrams of Fig. 2.3 are worked out in detail Appendix B. In Fig. 2.4, all the diagrams that contribute to the one-body Green's function at second order in the interaction are shown.

Let us focus on the structure of these diagrams. In general grounds, all of them share a common structure: an incoming fermion line with momentum k and frequency z_ν enters the diagram, scatters a given number of times, depending on the sophistication of the diagram, and finally becomes an outgoing line with the same initial momentum and frequency. Schematically, one can express this idea in terms of the diagram in Fig. 2.5. The full propagator (represented by a double fermion line) equals the free propagator plus a non-interacting fermion line that enters a “complicated structure” and then goes out of it. For reasons that will become clearer later on, this “structure” is called the *reducible self-energy*. This is formed by all the crooked diagrams that compose the single-particle propagator when one amputates the ingoing and outgoing fermion lines. In itself, it is still an

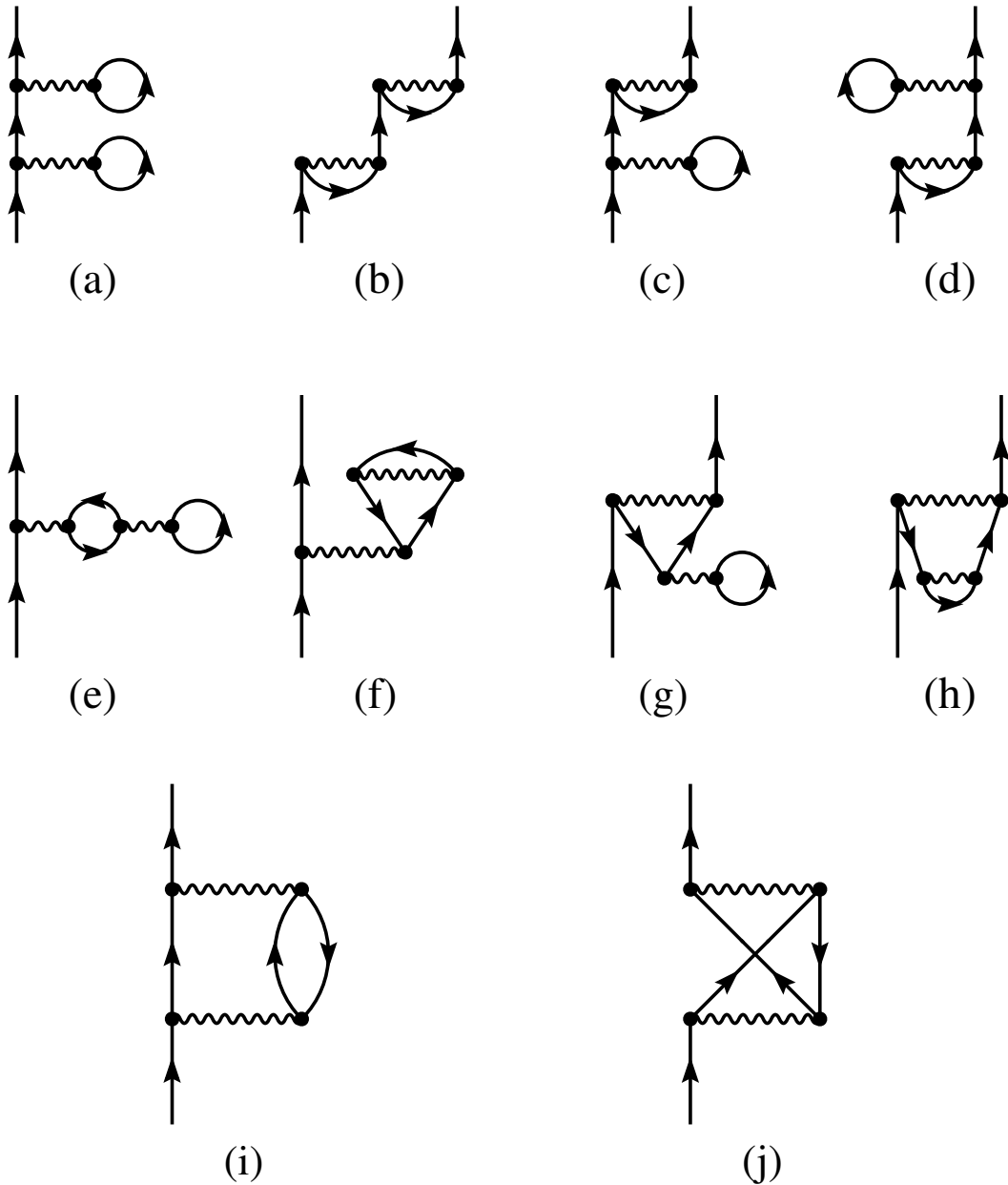


Figure 2.4: All second order diagrams that contribute to the Green's function. The first row [diagrams (a)-(d)] is composed by reducible diagrams, i.e. sequential repetitions of first order diagrams. The second row [diagrams (e)-(h)] is formed by nested diagrams, i.e. a repetition of two first order diagrams in which a one diagram is inserted in an intermediate line of another. The third row [diagrams (i)-(j)] is formed by the second order diagrams which are entirely new.

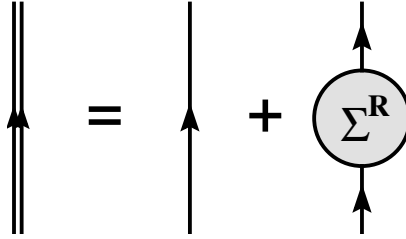


Figure 2.5: *Diagrammatic expression of the reducible self-energy.*

infinite sum of diagrams which needs to be evaluated either perturbatively, *i.e.* as a sum of a finite number of terms obtained from truncating the expansion at some order, or non-perturbatively, *i.e.* by means of an infinite summation of physically suitable diagrams.

One can however simplify these sums by considering in more depth the structure of the diagrams forming the single-particle propagator. Take, for instance, diagrams (a) to (d) of Fig. 2.4. They are second-order diagrams that have been obtained by iterating the first-order diagrams of Fig. 2.3. In other words, if one cuts the intermediate fermion line in diagram (a), one recovers two first-order diagrams (a) of Fig. 2.3. In the jargon of many-body physics, this is called a 1 Particle Reducible (1PR) diagram, because by cutting one of its fermion (particle) lines, it reduces to a lower-order diagram. In contrast, 1 Particle Irreducible (1PI) diagrams, like (i) and (j) of Fig. 2.4, cannot be cut at any fermion line to yield two separate pieces of lower order. Since reducible diagrams are obtained from the iteration of irreducible diagrams, it is quite clear that one only needs 1PI diagrams to compute the full single-particle propagator. If a suitable iterative process is then applied, the 1PR diagrams will be automatically generated. The sum of all the 1PI self-energy diagrams is the so-called *irreducible self-energy*. Diagrammatically, these ideas are depicted in Fig. 2.6, where the expansion of the self-energy in terms of iterated irreducible self-energies is shown.

These ideas can also be cast in terms of mathematical expressions. The full single-particle propagator, for instance, is given by the reducible self-energy Σ^R by means of the equation:

$$\mathcal{G} = \mathcal{G}_0 + \mathcal{G}_0 \Sigma^R \mathcal{G}_0. \quad (2.143)$$

Yet, as it has been explained above, the reducible self-energy is formed by the iteration of irreducible self-energy pieces. Once this irreducible self-energy is introduced, the propagator is given by the infinite series:

$$\mathcal{G} = \mathcal{G}_0 + \mathcal{G}_0 \Sigma^I \mathcal{G}_0 + \mathcal{G}_0 \Sigma^I \mathcal{G}_0 \Sigma^I \mathcal{G}_0 + \dots \quad (2.144)$$

Consider, however, the following trick, in which one factors out a irreducible self-

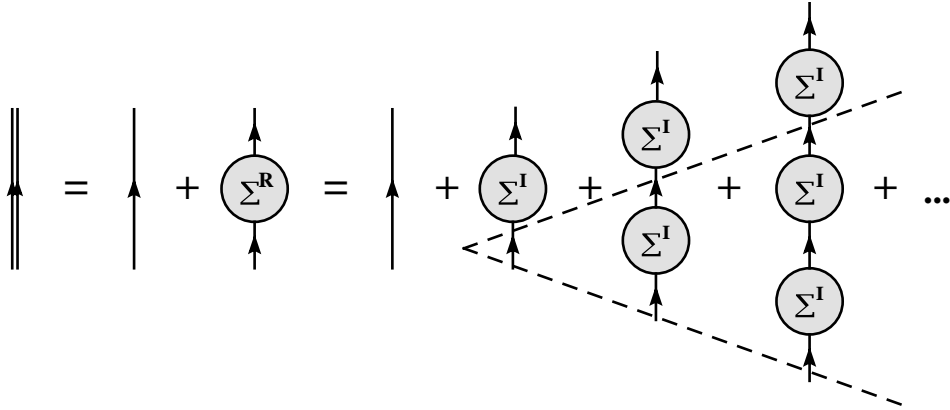


Figure 2.6: *Reducible self-energy as an iterated series of irreducible self-energy pieces.*

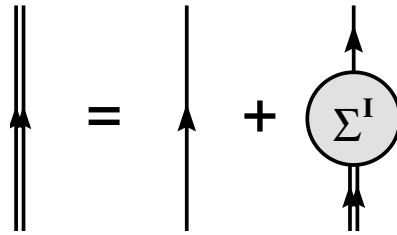


Figure 2.7: *Diagrammatic representation of Dyson's equation.*

energy from the total result:

$$\mathcal{G} = \mathcal{G}_0 + \mathcal{G}_0 \underbrace{\Sigma^I \{ \mathcal{G}_0 + \mathcal{G}_0 \Sigma^I \mathcal{G}_0 + \dots \}}_G. \quad (2.145)$$

The term that factors out is actually the full propagator. This factorization can be cast in terms of diagrams, as in Fig. 2.6, where dashed lines have been used to separate the factored-out part from the full propagator. The final result turns out to be the integral form of Dyson's equation:

$$\mathcal{G}(k, \omega) = \mathcal{G}_0(k, \omega) + \mathcal{G}_0(k, \omega) \Sigma^I(k, \omega) \mathcal{G}(k, \omega), \quad (2.146)$$

which, in contrast to the formal derivation of Eq. (2.123), has been obtained from diagrammatic considerations. Since Dyson's equation can be obtained either from the equation of motion or from a diagrammatic approach, the approximations to the self-energy can be cast in both terms. In the following, when considering approximations to the self-energy and the propagator, it will be very useful to

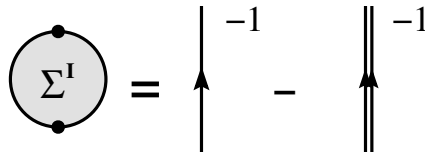


Figure 2.8: Diagrammatic representation of the self-energy in terms of the free and the fully dressed one-body propagators.

have an insight on both methods, each of them providing a different physical point of view on the approximations which are being made. Finally, let us note that the diagrammatic representation of Dyson's equation is shown in Fig. 2.7. In the rest of this Thesis, and unless differently stated, the word "self-energy" will refer to the irreducible self-energy.

2.7 Self-consistent renormalization

In the previous section, the Dyson's equation for the self-energy and the propagator have been introduced. It has been shown that, with the help of this equation, one sums an infinite series of diagrams by means of an iteration of 1PI diagrams. This is already true at lowest order. Take, for instance, diagrams (a) and (b) of Fig. 2.3 and compute the corresponding irreducible self-energy. Inserting this into Dyson's equation (see Fig. 2.6), one obtains a propagator which already includes an infinite sum of iterated irreducible self-energy diagrams. This corresponds to the Hartree-Fock approximation that will be studied in Chapter 4. Yet, one can do a better job even at this first-order level and sum a larger subset of diagrams by means of a (somewhat simple) procedure known as *self-consistent renormalization*. The main idea underlying this method is to self-consistently iterate Dyson's equation for the propagator, given by Fig. 2.7, and the equation defining the self-energy, given by Fig. 2.8. Treating both equations in the same footing and iterating them, one sums extra sets of diagrams with peculiar properties which shall be important for the following discussions.

To put an example of this method, consider the second-order diagram (a) of Fig. 2.9. This diagram, even though of second order, allows for a very graphical discussion on self-consistent renormalization [Mat92]. Take, then, the direct diagram (a), as well as the remaining diagrams, (b)-(g) of Fig. 2.9. Diagrams (b) and (c) are generated by inserting the first order (direct and exchange) self-energy diagrams in the left propagator line of diagram (a). Diagrams (d) and (e) include second order renormalizations to this line, while diagrams (f) and (g) include more complicated third order terms. Yet, all of these diagrams share a common structure: self-energy diagrams are inserted on top of the left fermion line of the (a) diagram,

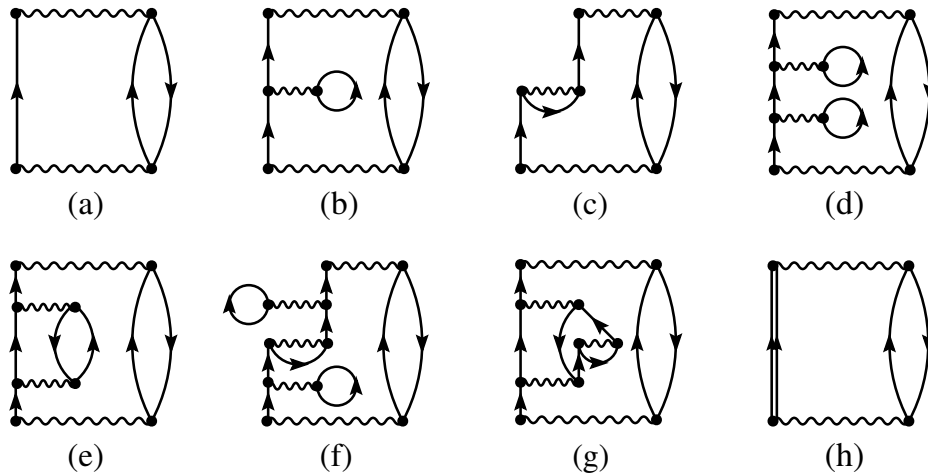


Figure 2.9: *Self-consistent renormalization on a fermion line of a second order diagram.*

leaving the rest of the diagram untouched. In the diagrammatic language, a self-energy diagram inserted on top of a fermion line is called a *self-energy insertion* and one usually says that the fermion line has been *dressed* by these insertions. In the ideal case where one could include all the self-energy insertions on the left fermion line of the (a) diagram, this line would eventually become a full propagator and the lowest order second-order diagram would become diagram (h). Note that this diagram is much richer than the initial one, for it sums automatically an infinite series of diagrams for the left leg. This is of course very satisfying from the diagrammatic point of view, because it allows one to write an infinite series of diagrams... in a single diagram! One can, for instance, dress the remaining fermion lines of the (a) diagram, thus obtaining diagram (f) of Fig. 2.10. In this case, a much more complicated series, including diagrams (a)-(e) of Fig. 2.10, is automatically summed up.

Yet, such a procedure must be done with care. When dressing all the fermion lines on a diagram, one should know which diagrams are being included and which are not. Take, for instance, diagram (g) of Fig. 2.10. This is formed by a second-order self-energy insertion on top of the left leg of diagram (f). However, the dressing of this leg already contains contributions of diagrams with the same structure as (g). Thus, these diagrams are already included in diagram (f) and should not be considered as independent contributions to the irreducible self-energy. To distinguish this redundant contribution, a new type of diagrams is defined. A diagram such as a diagram (f) of Fig. 2.10, which does not include any explicit self-energy insertion, is called a *skeleton diagram*. It is then clear that all the diagrams for the

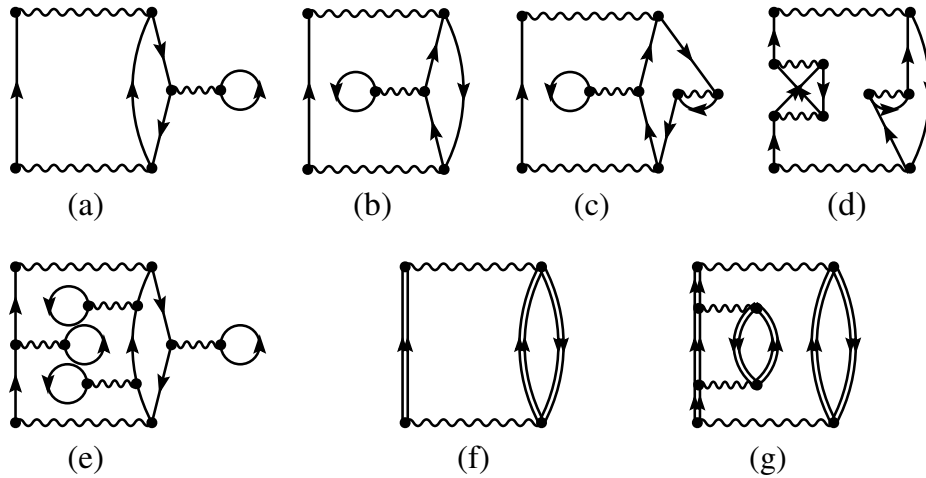


Figure 2.10: *Self-consistent renormalization of a whole second order diagram.*

self-energy can be obtained by drawing all the skeleton diagrams and then dressing its fermion lines with all the possible self-energy insertions. This can be expressed in the following way:

$$\Sigma^I = \sum_n \{ \text{skeleton diagrams with } \mathcal{G}_0 \text{ replaced by } \mathcal{G} \},$$

where n is the order (number of interaction lines) in the expansion of the propagator. Note that this is indeed an implicit equation for Σ^I , because \mathcal{G} contains Σ^I via Dyson's equation.

One should of course find how to dress all the lines of skeleton diagrams in a more or less simple way. This is indeed done by means of the self-consistent renormalization procedure. From a numerical point of view, this procedure is of course not as easy as a simple substitution of a single line for a double one. Instead, a procedure for dressing fermion lines in a consistent way can be derived by considering subsequent iterations of Dyson's equation and the self-energy, defined via Fig. 2.8, in a given approximation. First of all, one uses an approximation to the self-energy which must be both 1PI and of the skeleton type. Next, this self-energy is inserted into Dyson's equation to obtain a first iteration of the dressed propagator. From this propagator, one builds a new self-energy which is richer in diagrammatic content via Fig. 2.8. This can then be included into Dyson's equation, and a new propagator will be obtained. The iteration of this procedure indeed sums a larger set of diagrams than the one included in the initial (1PI, skeleton-type) self-energy and includes, in particular, all the self-energy insertions

2.7. SELF-CONSISTENT RENORMALIZATION

with the same structure as the initial self-energy as well as new nested diagrams. A particular example of this procedure and its diagrammatic content is studied in Chapter 4.

Chapter 3

Luttinger-Ward Formalism

From a statistical mechanics point of view, the macroscopic information of the system is fully contained in the partition function. If this function is known, its derivatives with respect to different quantities give access to all the thermodynamical properties of the system. On the other hand, it has already been argued that, from a microscopic point of view, it is the one-body propagator which provides all the one-body properties of the system. Now one may ask if there is a connection between both functions and, in particular, if the one-body propagator is enough for building the partition function. The answer, given by Luttinger and Ward [Lut60] more than forty years ago, is positive. The Luttinger-Ward expression for the partition function turns out to have some interesting properties that were later on exploited by Baym [Bay62] in his discussion of the thermodynamical consistency of many-body approaches. In the following, the Luttinger-Ward formalism for the computation of the partition function will be described. It will be applied to the free case and to a general interacting case where the width effects of quasi-particles are not disregarded. The explicit numerical results obtained with this formalism for the thermodynamical properties of nuclear matter within different many-body approaches will be discussed in the following chapters.

3.1 Linked cluster expansion

The partition function of a system at finite temperature can be expressed in terms of Feynman diagrams, like the Green's functions. The expansion in terms of diagrams for the grand-potential is, in fact, very close to that of the energy of a zero temperature system and it is well established [Mat92]. Its starting point is Eq. (A.13), which can be rewritten as:

$$e^{-\beta(\Omega-\Omega_0)} = \sum_{n=0}^{\infty} \frac{(-i)^n}{n!} \int_0^{-i\beta} dt_1 \cdots \int_0^{-i\beta} dt_n \text{Tr} \left\{ \hat{\rho}_0 \mathbb{T} \left[\hat{H}_1(t_1) \cdots \hat{H}_1(t_n) \right] \right\}, \quad (3.1)$$

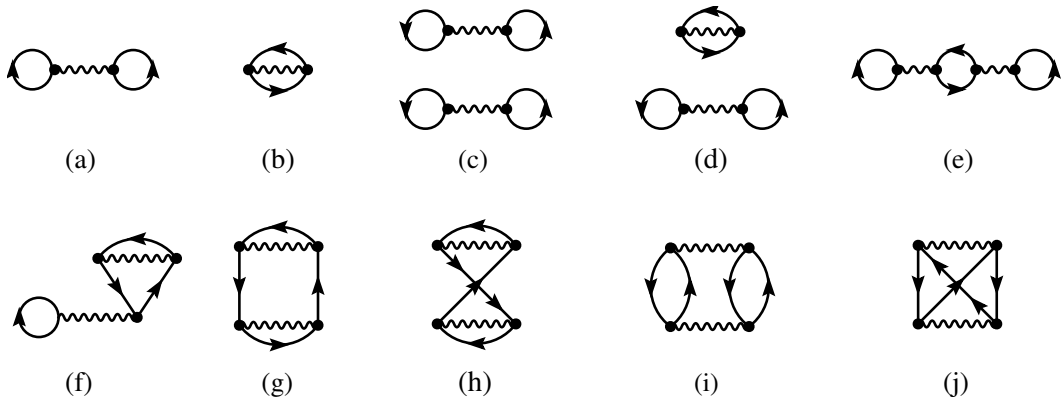


Figure 3.1: All of the first order and some of the second order Feynman diagrams that contribute to $e^{-\beta(\Omega-\Omega_0)}$.

where Ω_0 represents the grand-potential of a free system of fermions evaluated at the chemical potential μ of the interacting system. By using the Wick theorem in the previous expression, one obtains a well-defined expansion of the grand-potential in terms of interactions and free single-particle propagators. The expansion can indeed be treated order by order in the number of interacting lines and can be expressed in terms of diagrams by applying a given set of Feynman rules. Yet, there is a fundamental difference between the diagrams of the one-body Green's function and those of the grand-potential. While the one-body propagator depends on two external points, $\mathbf{r}_1 t_1$ and $\mathbf{r}'_1 t'_1$, the expression in Eq. (3.1) has no external dependence. In terms of diagrams, this is translated into the fact that all the diagrams in the expansion of Ω are made of closed loops.

In Fig. 3.1, the first order, as well as some of the second order diagrams in the expansion of $e^{-\beta(\Omega-\Omega_0)}$, are shown. Interestingly enough, one finds that there are two different kinds of diagrams contributing to $e^{-\beta(\Omega-\Omega_0)}$. The first type is formed by closed connected loops, like diagrams (a), (b) or (e) of Fig. 3.1. The second type is formed by separate pieces, like diagrams (c) and (d). These are the disconnected diagrams. Needless to say, this supposes a great disadvantage. The number of diagrams which are required at each order can become very large if one has to study all the different combinations of connected diagrams that form all the disconnected diagrams at that given order. Fortunately, the *linked cluster theorem* comes to our help in this case. Loosely speaking (see [Abr65; Bla86; Neg88] or [Mah90] for a more complete discussion), the linked cluster theorem states that the diagrammatic expansion of the quantity $\ln e^{-\beta(\Omega-\Omega_0)} = -\beta(\Omega - \Omega_0)$ is only formed by connected diagrams. Or, expressed differently:

$$e^{\text{all connected diagrams}} = \text{all connected} + \text{all disconnected diagrams}.$$

This important theorem leads to the following result:

$$\Omega - \Omega_0 = \sum_n \{ \text{connected diagrams} \}.$$

This is of course a very satisfying expression, because it reduces enormously the number of diagrams needed at each order in the expansion of Ω . One should now relate each diagram to a contribution in the perturbation expansion of Ω by means of a suitable set of Feynman rules. To this end, one should follow a similar path as the one discussed for the one-body propagator in Appendix A. Unfortunately, an extra difficulty arises when dealing with closed diagrams. When the Feynman rules for the one-body Green's function were introduced in Appendix A, one could argue that a factor $\frac{1}{n!2^n}$ in front of each term in the expansion of the propagator was canceled. On the one hand, a factor 2^n came out from the permutations of the variables inside the potentials, which left the value of a diagram unchanged. On the other hand, one could perform $n!$ permutations in the integration variables that lead to the same result for a given diagram. This result is, however, specific for the one-body propagator and it is not anymore valid for closed diagrams. While for one of these diagrams, the 2^n permutations of the variables in the interaction are still possible, there are only $(n-1)!$ permutations which leave an n -th order term invariant. This happens because, with one of the \hat{H}_1 fixed, one can only choose among the $n-1$ remaining operators to perform the change of variables. For the Green's function, in contrast, since the external lines are already fixed, one obtains a $n!$ factor. As a consequence, each topologically non-equivalent diagram in the expansion of Ω carries a factor $1/n$ in front of its value when the Feynman rules are defined. This factor complicates substantially any infinite partial sum of diagrams in the grand-potential and thus sophisticated diagrammatic approaches cannot be directly applied to compute this quantity. This is probably the reason why the diagrammatic approach for the thermodynamical potential of interacting systems has only been used a few times [Mah90].

3.2 Coupling constant method

In this subsection, a more widely used method to compute the partition function will be discussed. The coupling constant approach is particularly suited for its simple mathematical structure and it is discussed in length, for instance, in Ref. [Fet71]. This method relies on the integration of a coupling variable which is related to the strength of the interaction potential. A great advantage of this approach is that it yields exact results once the propagator is computed. Its great disadvantage, as it will be seen in the following, is the coupling constant integration, which requires the computation of the propagator for several different values of the coupling.

Consider a system with a Hamiltonian given by:

$$\hat{H}(\lambda) = \hat{H}_0 + \lambda\hat{H}_1, \quad (3.2)$$

where λ is the so-called coupling constant. The Hamiltonian $\hat{H}(\lambda)$ at $\lambda = 1$ describes the full physical system, while at $\lambda = 0$ it describes a simpler system (not necessarily the free one), which one is able to handle easily. One can also define the operators:

$$\hat{K}_0 = \hat{H}_0 - \mu\hat{N} \quad (3.3)$$

and

$$\hat{K}(\lambda) = \hat{K}_0 + \lambda\hat{H}_1. \quad (3.4)$$

The partition function is then defined by:

$$Z_\lambda = e^{-\beta\Omega_\lambda} = \text{Tr} e^{-\beta\hat{K}(\lambda)}. \quad (3.5)$$

Note that this partition function as well as the associated grand-potential,

$$\Omega_\lambda = -T \ln Z_\lambda, \quad (3.6)$$

are functions of the coupling constant λ . One can obtain a generic expression for Z_λ by expanding the exponential operator on the right hand side of Eq. (3.5):

$$Z_\lambda = \sum_{n=0}^{\infty} \frac{1}{n!} (-\beta)^n \text{Tr} \left\{ \left[\hat{K}_0 + \lambda\hat{H}_1 \right]^n \right\}. \quad (3.7)$$

Let us now compute the derivative of Z_λ with respect to λ . With the help of the previous expression this yields:

$$\frac{\partial Z_\lambda}{\partial \lambda} = \sum_{n=1}^{\infty} \frac{1}{n!} (-\beta)^n \frac{\partial}{\partial \lambda} \text{Tr} \left\{ \left[\hat{K}_0 + \lambda\hat{H}_1 \right]^n \right\}. \quad (3.8)$$

The derivative inside the sum is applied to the n terms in the trace, yielding a factor \hat{H}_1 in all the possible positions in between the $n - 1$ remaining $\left[\hat{K}_0 + \lambda\hat{H}_1 \right]$ operators. Using the cyclic property of the trace, these n terms can be seen to give the same result. The derivative can thus be rewritten as:

$$\begin{aligned} \frac{\partial Z_\lambda}{\partial \lambda} &= \sum_{n=1}^{\infty} \frac{1}{n!} (-\beta)^n n \text{Tr} \left\{ \left[\hat{K}_0 + \lambda\hat{H}_1 \right]^{n-1} \hat{H}_1 \right\} \\ &= -\beta \sum_{n=1}^{\infty} \frac{1}{(n-1)!} (-\beta)^{(n-1)} \text{Tr} \left\{ \left[\hat{K}_0 + \lambda\hat{H}_1 \right]^{n-1} \hat{H}_1 \right\} \\ &= -\beta \text{Tr} \left\{ e^{-\beta\hat{K}(\lambda)} \hat{H}_1 \right\}, \end{aligned} \quad (3.9)$$

where the Taylor expansion of the exponential of the $-\beta\hat{K}(\lambda)$ operator has been used. The previous trace looks very much like a thermal ensemble average of \hat{H}_1 . One can indeed rewrite this in terms of a thermal average by multiplying and dividing by a factor $e^{-\beta\Omega_\lambda}$:

$$\frac{\partial Z_\lambda}{\partial \lambda} = -\frac{\beta}{\lambda} e^{-\beta\Omega_\lambda} \langle \lambda \hat{H}_1 \rangle_\lambda. \quad (3.10)$$

Note that the average $\langle \dots \rangle_\lambda$ denotes the thermal ensemble average with the λ -dependent operator $\hat{K}(\lambda)$. It is also interesting to stress that the average for $\lambda = 0$ is done with the \hat{K}_0 operator and thus requires the knowledge of the real chemical potential of the interacting system, μ . By using the relation that links the grand-canonical potential and the partition function, Eq. (3.6), one finds that the derivative of the grand-canonical potential with respect to λ is given by:

$$\frac{\partial \Omega_\lambda}{\partial \lambda} = \frac{1}{\lambda} \langle \lambda \hat{H}_1 \rangle_\lambda. \quad (3.11)$$

Integrating the previous expression from $\lambda = 0$ to $\lambda = 1$, one gets the fully interacting partition function in terms of the easy-to-compute $\Omega_{\lambda=0}$ and an integral over the coupling constant:

$$\Omega = \Omega_0 + \int_0^1 \frac{d\lambda}{\lambda} \langle \lambda \hat{H}_1 \rangle_\lambda. \quad (3.12)$$

The integrand of this coupling constant integrations can be related to the interaction energy of a system with a coupling constant λ . Indeed, if one chooses \hat{H}_0 as the kinetic energy operator, then $\langle \lambda \hat{H}_1 \rangle_\lambda$ immediately becomes the interaction energy with a damped interaction. In principle, it is not necessary to make this choice but, as it will be seen in the following, this turns out to be very convenient.

Up to this point, the equations have been quite generic and unrelated to the Green's function approach discussed in the previous chapter. It would thus be useful to obtain an expression of Ω in terms of the Green's function. This is also achieved by taking $\hat{H}_1 = \hat{V}$. Consider the equation of motion of the one-body propagator, Eq. (2.98). The last term of that equation (the one involving the interaction potential) can be brought to a more familiar form by taking the limits $t'_1 \rightarrow t_1^+$ and $\mathbf{r}'_1 \rightarrow \mathbf{r}_1$ and integrating over \mathbf{r}_1 . After these operations, this term becomes basically the mean potential energy of the system:

$$2\langle V \rangle = \int d^3 r_1 \lim_{\substack{\mathbf{r}'_1 \rightarrow \mathbf{r}_1 \\ t'_1 \rightarrow t_1^+}} \int d^3 r_{\bar{1}} V(|\mathbf{r}_1 - \mathbf{r}'_1|) \langle \mathcal{T} \{ \hat{a}(\mathbf{r}_1 t_1) \hat{a}(\mathbf{r}_{\bar{1}} t_1) \hat{a}^\dagger(\mathbf{r}_{\bar{1}} t_1^+) \hat{a}^\dagger(\mathbf{r}'_1 t'_1) \} \rangle. \quad (3.13)$$

The same limits and integral can be applied to the remaining terms in the equation of motion. The time derivative, for instance, can be computed using the Fourier

transform of the propagator:

$$\begin{aligned} \int d^3 r_1 \lim_{\substack{r'_1 \rightarrow r_1 \\ t'_1 \rightarrow t_1^+}} i \frac{\partial}{\partial t_1} \mathcal{G}(\mathbf{r}_1 t_1, \mathbf{r}'_1 t'_1) &= \int d^3 r_1 \lim_{\substack{r'_1 \rightarrow r_1 \\ t'_1 \rightarrow t_1^+}} i \frac{\partial}{\partial t_1} \frac{1}{-i\beta} \sum_{k,\nu} e^{i\mathbf{k} \cdot (\mathbf{r}_1 - \mathbf{r}'_1) - iz_\nu(t_1 - t'_1)} \frac{\mathcal{G}(k, z_\nu)}{\mathcal{V}} \\ &= \frac{i}{\beta} \sum_{k,\nu} e^{iz_\nu \eta} z_\nu \mathcal{G}(k, z_\nu). \end{aligned} \quad (3.14)$$

Note that the derivative operator is applied before taking the limits. In addition, an infinitesimal η , such that $t_1 - t_1^+ = -\eta$ and such that $\lim_{\text{Re } z \rightarrow \infty} \eta \text{Re } z = \infty$, has been introduced. This condition is also necessary if the contributions of the arches in the Cauchy integrals appearing in the Matsubara summations have to vanish (see Appendix C). Applying the same procedure to the kinetic term, one finds:

$$\int d^3 r \lim_{\substack{r'_1 \rightarrow r_1 \\ t'_1 \rightarrow t_1^+}} \frac{\nabla^2}{2m} \mathcal{G}(\mathbf{r}_1 t_1, \mathbf{r}'_1 t'_1) = \frac{-i}{\beta} \sum_{k,\nu} e^{iz_\nu \eta} \frac{k^2}{2m} \mathcal{G}(k, z_\nu). \quad (3.15)$$

The term with the two delta functions can be easily rewritten using the Fourier representation of the delta functions in the momentum and Matsubara frequency space:

$$\int d^3 r \lim_{\substack{r'_1 \rightarrow r_1 \\ t'_1 \rightarrow t_1^+}} \delta(t_1 - t'_1) \delta(\mathbf{r}_1 - \mathbf{r}'_1) = \frac{-i}{\beta} \sum_{k,\nu} e^{iz_\nu \eta}. \quad (3.16)$$

Collecting everything together, one obtains the following identity between the potential energy of the system and the one-body propagator:

$$2\langle V \rangle = \frac{1}{\beta} \sum_{k,\nu} e^{iz_\nu \eta} \left[\left\{ z_\nu - \frac{k^2}{2m} \right\} \mathcal{G}(k, z_\nu) - 1 \right]. \quad (3.17)$$

This can be cast in a nicer form by using Dyson's equation in Fourier space, Eq. (2.122), to yield:

$$\langle V \rangle = \frac{1}{2\beta} \sum_{k,\nu} e^{iz_\nu \eta} \Sigma(k, z_\nu) \mathcal{G}(k, z_\nu). \quad (3.18)$$

The previous expression gives directly the mean potential energy of the system in terms of the self-energy and the one-body propagator. In a system with $\lambda H_1 = \lambda V$, this expression will be naturally translated into:

$$\langle \lambda V \rangle_\lambda = \frac{1}{2\beta} \sum_{k,\nu} e^{iz_\nu \eta} \Sigma_\lambda(k, z_\nu) \mathcal{G}_\lambda(k, z_\nu), \quad (3.19)$$

where the subscript λ denotes that the self-energy and the one-body propagator of the system are computed with an interaction potential λV and that the thermal

averages are taken with respect to $\lambda\hat{K}$. Finally, introducing this expression in Eq. (3.12), one finds the following expression for the grand-potential of the fully interacting system:

$$\Omega = \Omega_0 + \frac{1}{2\beta} \int_0^1 \frac{d\lambda}{\lambda} \widetilde{\text{Tr}} \Sigma_\lambda \mathcal{G}_\lambda, \quad (3.20)$$

where Ω_0 now denotes the grand-partition function of the free system (computed at the interacting chemical potential μ) and where the dependence on momentum and Matsubara frequency of the self-energy and the propagator have been simplified using the notation:

$$\sum_{k,\nu} e^{iz_\nu \eta} \rightarrow \widetilde{\text{Tr}}, \quad (3.21)$$

with $\eta = 0^+$ small and positive and such that $\lim_{\text{Re } z \rightarrow \infty} \eta \text{Re } z = \infty$. This shall not be confused with the trace introduced in Chapter 2, which denotes a diagonal sum over all the (energy and particle number) eigenstates of the system. Note that an additional sum over the internal spin-isospin quantum number should be included in $\widetilde{\text{Tr}}$ whenever these quantum numbers are taken into account.

One can work with the previous expressions to write them in terms of the spectral function. This can be done in two different but equivalent means. On the one hand, one can consider the fact that the potential energy of the system is already contained in the GMK sum rule. It can be obtained by extracting the kinetic energy,

$$\mathcal{K} = \sum_k \int_{-\infty}^{\infty} \frac{d\omega}{2\pi} \frac{k^2}{2m} f(\omega) \mathcal{A}(k, \omega), \quad (3.22)$$

from the total energy of the system, Eq. (2.103). This yields the following expression for the potential energy:

$$\mathcal{U} = \langle V \rangle = \sum_k \int_{-\infty}^{\infty} \frac{d\omega}{2\pi} \frac{1}{2} \left\{ \omega - \frac{k^2}{2m} \right\} f(\omega) \mathcal{A}(k, \omega). \quad (3.23)$$

Introducing this into Eq. (3.12), one finds that the grand-partition function is given by the triple integral:

$$\Omega = \Omega_0 + \sum_k \int_0^1 \frac{d\lambda}{\lambda} \int_{-\infty}^{\infty} \frac{d\omega}{2\pi} \frac{1}{2} \left\{ \omega - \frac{k^2}{2m} \right\} f_\lambda(\omega) \mathcal{A}_\lambda(k, \omega). \quad (3.24)$$

Note that, for a given chemical potential μ and inverse temperature β , the coupling constant method involves the calculation of several spectral functions \mathcal{A}_λ in order to compute the integral on the coupling constant. On the other hand, one can compute the previous expression in a complete equivalent way by performing the

implicit Matsubara sum in Eq. (3.20). The result of this sum is easily obtained from the general formula Eq. (C.15), yielding:

$$\langle V \rangle = \frac{1}{2} \sum_k \int_{-\infty}^{\infty} \frac{d\omega}{2\pi} f(\omega) [\Gamma(k, \omega) \text{Re } \mathcal{G}(k, \omega) + \mathcal{A}(k, \omega) \text{Re } \Sigma(k, \omega)] . \quad (3.25)$$

This gives an alternative expression for the grand-partition function. Nevertheless, it is easy to prove that Eq. (3.23) and Eq. (3.25) give the same result, because:

$$\underbrace{\left\{ \omega - \frac{k^2}{2m} - \text{Re } \Sigma(k, \omega) \right\}}_{\text{Re } \mathcal{G}^{-1}(k, \omega)} \mathcal{A}(k, \omega) = \Gamma(k, \omega) \text{Re } \mathcal{G}(k, \omega) , \quad (3.26)$$

which is easily deduced from the identity $\text{Im} \{ \mathcal{G}(k, \omega) \mathcal{G}^{-1}(k, \omega) \} = 0$.

The coupling constant method presented here is essentially exact. In other words, if one is able to compute the propagator and the self-energy within a certain many-body approximation, a grand-partition function containing all the correlations associated to that many-body approach is given by Eq. (3.20). Yet, this method has a clear disadvantage, namely that it requires a coupling constant integration. This means that, for a single chemical potential and temperature, the results have to be generated for several different coupling constants in order to compute accurately the integral over λ . Moreover, the coupling constant integration has to be performed for a fixed external chemical potential μ . This is a problem whenever one tries to work at a constant density, which can be preferable if one wants to deal with more intuitive results. In that case, the implementation of the coupling constant approach requires calculations for a certain number of chemical potentials in order to match the external density. And for each chemical potential one has to use a certain number of coupling constant integrations. Such a proliferation of results makes this method unsuited for sophisticated or time-demanding many-body approaches. It is clear that a closed equation in which the partition function could be expressed directly in terms of the one-body propagator would be much more convenient. One could then skip the coupling constant integration and work at constant density without further inconveniences.

3.3 Luttinger-Ward partition function

3.3.1 Introduction

An explicit formula of the grand-potential in terms of the one-body Green's function is in fact what the Luttinger-Ward formalism achieves and it is the main reason why this approach has been chosen for this Thesis. The Luttinger-Ward expression for the partition function of an interacting system of fermions was first introduced in [Lut60]. This is the second reference of a series in which Luttinger

and his collaborators studied carefully the zero temperature limit of finite temperature many-body approaches. In the first article [Koh60], special attention is paid to the different limiting procedures ($T \rightarrow 0, \mathcal{V} \rightarrow \infty$ or its inverse, $\mathcal{V} \rightarrow \infty, T \rightarrow 0$) in which one can obtain the zero temperature BHF approximation from its finite temperature extension. This involved a study of the so-called “anomalous” diagrams (such as diagrams (g) and (h) of Fig. 3.1) which only appear within a $T \neq 0$ formalism. In the second reference of the series, the same problem was addressed by introducing the self-consistent renormalization procedure for the single-particle potential (see Section 2.7). From this self-consistently renormalized Green’s function, the authors build a functional (the Luttinger-Ward functional) which reproduces the partition function of the system. Note that such an expression is very different from the one that can be obtained from any diagrammatic expansion. While with diagrams one would express the partition function in terms of partial sums of terms including free propagators, the Luttinger-Ward partition function includes somehow an infinite summation of diagrams by means of the self-consistent propagator. Finally, in this reference Luttinger and Ward also discussed the interesting variational properties of this functional.

Some of these properties were soon exploited in more involved studies of many-body systems. Among them, it is probably the pioneering work of Baym [Bay62] which deserves most attention. This is also the second paper of a series (the first one being [Bay61]) in which the fulfillment of the microscopic and macroscopic conservation laws of momentum, angular momentum and energy in quantum transport theories were thoroughly studied. In their first article, Kadanoff and Baym were able to find some conditions that any quantum many-body approximation should accomplish if these conservation laws had to be obeyed at a microscopic level. Among the approximations that do conserve momentum, energy, etc., one finds the Hartree-Fock, the ladder or the RPA approximations. These are also called *conserving* approximations. The second reference, [Bay62], includes a refinement of these results. Baym was actually able to establish a more general condition for the different procedures to be of a conserving type. When applying these ideas to the equilibrium case, Baym showed that any conserving approximation is, at the same time, thermodynamically consistent, which essentially means that a quantity, computed either from microscopic grounds or from a thermodynamical (macroscopic) basis, yields the same result. The fulfillment of thermodynamical consistency, trivial as it might look like, is not intuitive at all. If one uses an approximation to describe the microphysics, for instance, it is by no means evident that the procedures involved in the method should also correctly describe the macrophysics.

Another interesting set of two articles is the couple of references [dD64a] and [dD64b]. In these articles, de Dominicis and Martin show how one can derive the Luttinger-Ward functional from basic principles, within either an algebraic [dD64a] or a diagrammatic approach [dD64b]. In the first case, the Luttinger-Ward func-

tional is derived from a Legendre transform of the partition function. In general, the partition function is a functional of the one- and two-body interactions. By means of an integral transform, however, the explicit functional dependence on the interaction can be replaced by a functional dependence on the Green's functions. Once the many-body approximation has been renormalized self-consistently, this leads exactly to the Luttinger-Ward expression. On the other hand, the formalism can also be derived diagrammatically. In that case, each term of the Luttinger-Ward functional can be seen to have a counterpart in terms of infinite sums of diagrams. These sums can be performed by distinguishing some particular elements of the diagrammatic expansion of the partition function. In this way, one can overcome the problem related to the $1/n$ factor and obtain explicit analytical expressions for each infinite sum of diagrams. It is also interesting to mention that this approach can be pushed beyond the single-particle Green's function and one can also obtain expressions of the partition function in terms of the two-body propagator [dD64b; Bla86].

In the following, the Luttinger-Ward expression for the partition function will be introduced. By means of some simple arguments (that follow [Bay62]), the expression of the grand-potential will be seen to be equivalent to that obtained within the coupling constant method. This shows that the partition function is exact (up to the approximations introduced by the many-body approach within which one computes the one-body propagator) and thus validates the application of this expression. The usefulness of the Luttinger-Ward approach relies on the fact that it is deduced from a self-consistently renormalized theory or, in other words, instead of using free \mathcal{G}_0 propagators, as it is done in the perturbative expansion, it is expressed in terms of dressed Green's functions, \mathcal{G} . In this sense, one can say that the Luttinger-Ward method is a non-perturbative approach. In addition, within the Luttinger-Ward formalism all the microscopic quantities are considered functionals of the dressed propagator. The expression for the partition function (that in this section will be denoted $W = \ln Z$) is given by:

$$W\{\mathcal{G}\} = \widetilde{\text{Tr}} \ln [-\mathcal{G}^{-1}] + \widetilde{\text{Tr}} \Sigma\{\mathcal{G}\} \mathcal{G} - \Phi\{\mathcal{G}\}. \quad (3.27)$$

Here, the notation $X\{\mathcal{G}\}$ denotes that a quantity X that has to be considered a functional of the full propagator. The trace $\widetilde{\text{Tr}}$ defined in Eq. (3.21) is also used, and thus a sum over momenta and Matsubara frequencies is included in the previous formula. Note that the self-energy is given in terms of the propagator via the following equation:

$$\Sigma\{\mathcal{G}\} = \mathcal{G}_0^{-1} - \mathcal{G}^{-1}, \quad (3.28)$$

which is just a manipulation of Dyson's equation, Eq. (2.122), to obtain the self-energy in terms of the free and interacting one-body propagators.

It seems natural to demand that the partition function of a system in equilibrium is stationary under variations of the one-particle propagator. This guarantees

that the Green's function which is used in the formalism minimizes the thermodynamical potential. Mathematically, this can be cast in the following equation:

$$\left. \frac{\delta W\{\mathcal{G}\}}{\delta \mathcal{G}} \right|_{\mathcal{G}_0} = 0, \quad (3.29)$$

where the variation with respect to \mathcal{G} is taken at constant \mathcal{G}_0 , because the free propagator of the theory is supposed to be already known and thus can be taken as a parameter. The variation of W with respect to \mathcal{G} yields:

$$\delta W = -\widetilde{\text{Tr}} \mathcal{G}^{-1} \delta \mathcal{G} + \widetilde{\text{Tr}} \delta \Sigma \mathcal{G} + \widetilde{\text{Tr}} \Sigma \delta \mathcal{G} - \delta \Phi. \quad (3.30)$$

Noting that $\delta \Sigma = \mathcal{G}^{-2} \delta \mathcal{G}$, it is clear that, if Eq. (3.29) must hold, then $\delta \Phi = \widetilde{\text{Tr}} \Sigma \delta \mathcal{G}$ must also hold. This can be restated formally by saying that the functional derivative of the Φ functional with respect to the one-body propagator,

$$\left. \frac{\delta \Phi\{\mathcal{G}\}}{\delta \mathcal{G}} \right|_{\mathcal{G}_0} = \Sigma\{\mathcal{G}\}, \quad (3.31)$$

is the self-energy. This equation sets the functional dependence of the Φ -functional in the one-body Green's function. The properties of this functional will now be briefly discussed.

3.3.2 The Φ functional

The definition of the functional dependence of Φ on \mathcal{G} is given by Eq. (3.31). This has to be taken as a definition in the same sense that Eq. (3.28) is taken as the definition of the self-energy in the Luttinger-Ward approach. Indeed, Dyson's equation together with Eq. (3.31) form a self-consistent set of equations. Within a many-body approach, for instance, one shall define a given approximation to the Φ functional (the way to do this will be discussed below) and derive the corresponding self-energy from it. This self-energy, once iterated via Dyson's equation, defines a propagator with which one can compute the functional again. This self-consistent iterative process can be shown to preserve the symmetries of the system and, in particular, the conservation laws of transport theories out of equilibrium [Bay62]. Actually, the generalization of this procedure to relativistic many-body systems with the help of quantum field theoretical tools has enjoyed a certain success [Cor74; Nor75; Lee75]. It has been applied to study dense interacting systems of pions [Rap96], the transport properties of resonances [Wei98b; Iva99] or the thermodynamics of quark gluon plasma [Bla04]. Moreover, the application of this procedure in the field of non-equilibrium quantum theories is of special relevance [Iva00; Ber04]. In those cases, the feature that makes this formalism especially attractive is the instantaneous sum of diagrams achieved by the use of a self-consistently renormalized propagator as well as the automatic preservation of the

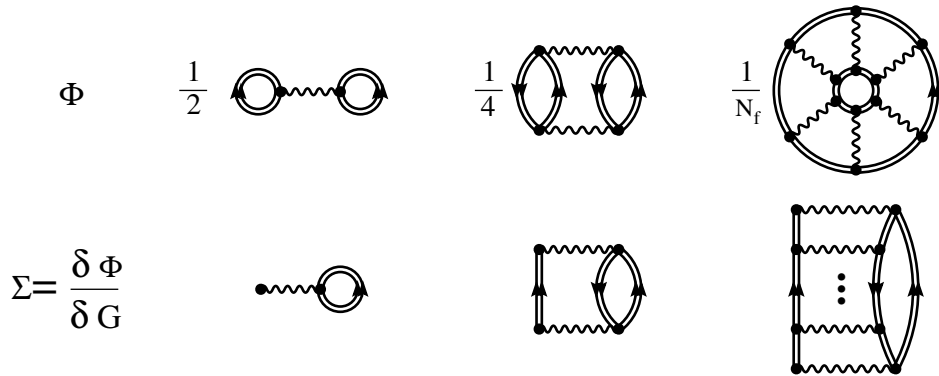


Figure 3.2: *First, second and n -th order diagrams for the Φ functional within the ladder approximation. The corresponding self-energy at each order is shown below. Note that only direct terms have been considered.*

conservation laws. Furthermore, it has been recently shown that the Φ -functional is invariant under renormalization group transformation and thus it is, in a certain sense, “universal” [Bla04; Dup05]. This might open a new interesting field of applications of the formalism to condensed matter systems in a non-perturbative approach [Pot06].

The Φ functional, like \mathcal{G} and Ω , has a diagrammatic interpretation [Bay62; dD64b; Bla86]. Take, for instance, any given closed diagram like those shown in the first row of Fig. 3.2. The functional derivative of one of these diagrams with respect to the propagator is achieved by cutting any fermion line in the diagram and assigning to the remaining extremes the space-time variables of the propagator with respect to which one is taking the derivative. Now, the Φ -functional is such that, whenever it is functionally derived, it should give the self-energy of the system. It is clear that it must then have the form of the closed diagrams of the first row of Fig. 3.2, with a factor $1/N_f$ in front of each diagram denoting the inverse of the number of equivalent fermion lines. In the Hartree case of Fig. 3.2, for instance, a factor $1/2$ in front of the expression is needed to cancel the two propagators that one cuts. Note in addition that, since the self-energy is formed by a sum of 1PI diagrams, the Φ -functional is necessarily formed by 2PI irreducible diagrams. Otherwise, it might have some term of the form $\tilde{A}\mathcal{G}\mathcal{G}\tilde{B}$, where $\mathcal{G}\mathcal{G}$ denote two propagator lines connecting two irreducible parts of a diagram, \tilde{A} and \tilde{B} . After taking a functional derivative with respect to \mathcal{G} , the corresponding self-energy would have a term of the type $\tilde{A}\mathcal{G}\tilde{B}$, which is 1PR and thus should not occur in the self-energy. This allows for a precise definition of the Φ functional in terms of diagrams: it corresponds to the (infinite) sum of all closed 2PI skeleton diagrams in which the free propagators are dressed with self-consistent propagators.

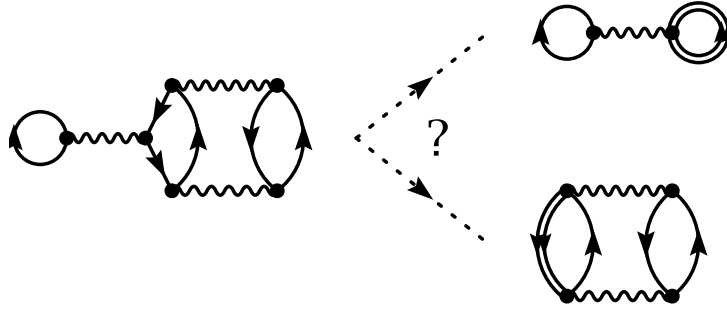


Figure 3.3: *Example of an ambiguous self-energy insertion in a closed Feynman diagram for the grand-potential.*

It is in fact very important to note that, in all the diagrams contributing to the Φ -functional, a double fermion line meaning the dressed one-body propagator is used. It has already been mentioned that in the Luttinger-Ward formalism one always works with self-consistently renormalized propagators. This is essential for the theory to be thermodynamically consistent. Unfortunately, this introduces ambiguities in the case of closed diagrams. As explained in Section 2.7, the self-energy can be formally obtained by first summing all the 1PI skeleton diagrams and then dressing all the free fermion lines with self-energy insertions. For closed diagrams, however, a similar procedure is not possible because the reduction to skeleton diagrams is not unique. To see this, take a look at Fig. 3.3. It is easy to convince oneself that, in a closed diagram, one cannot easily distinguish which part of the diagram is a self-energy insertion of another part. In other words, the full thermodynamical potential cannot be naively computed by means of an expansion of closed skeleton diagrams which are subsequently dressed. This procedure could lead to a double-counting of diagrams. One can instead consider the sum of all 2PI skeleton diagrams. Dressing the free propagators in this diagrammatic sum, one would obtain the Φ -functional. The other terms in Eq. (3.27) (*i.e.* the trace of the logarithm and of the product of the self-energy and the propagator) generate the remaining 2PR diagrams that contribute to Ω , with the appropriate factors to avoid any possible double-counting [dD64b; Bla86].

One cannot, however, compute the full exact Φ -functional in the same way that one cannot calculate the exact self-energy of a many-body system. Instead, one has to use approximate Φ -functionals (and their corresponding self-energies) which should describe correctly the essential correlations of the many-body system under study. Some simple examples of these approximations are given in Fig. 3.2. The first diagram in the second row corresponds, for instance, to the Hartree self-energy and thus this defines the Hartree approximation (see the next chapter for

details on this approximation). A typical diagram of a ladder self-energy is given by the last diagram of the second row. An n -th order contribution of this self-energy includes the repeated scattering of a particle with another particle of the system. By closing this diagram in its free vertices with a dressed propagator, one obtains the corresponding n -th order contribution to the Φ -functional, which is the top right diagram of Fig. 3.2. Note that the value of the N_f factor equals $2n$ in this case, because there are $2n$ possible places where one can cut each propagator to obtain the self-energy contribution at n -th order. Moreover, since the ladder self-energy is given by the sum to all orders of these diagrams, its corresponding Φ functional is also an infinite sum of diagrams.

As already explained, the equation for the Φ -functional, Eq. (3.31), and Dyson's equation, Eq. (3.28), define a self-consistent set of equations if one is able to find a good approximate Φ -functional. Nevertheless, one can proceed in a somewhat different way and profit from the Luttinger-Ward formalism to directly compute the partition function in a self-consistent many-body approach. Suppose, for instance, that one is able to compute a self-consistent Green's function in a given approximation. Through Dyson's equation, one immediately has access to the self-energy and to the Φ -functional if Eq. (3.31) can be inverted. Using these quantities, one will be able to compute the corresponding partition function of the interacting system using the Luttinger-Ward expression. This philosophy is the one that will be followed in this Thesis. The Green's function will be computed within a self-consistent ladder approximation and will then be used to calculate the entropy, from which one can derive most of the thermodynamical properties of the system. Fortunately, the Luttinger-Ward approach can be implemented in a very direct manner in the calculation of the entropy and, in particular, one can compute this quantity without explicitly computing the Φ -functional.

3.3.3 Relation to the coupling constant method

Up to here the variational properties of the Luttinger-Ward formula have been discussed. Yet there has been no justification based on first principles of the Luttinger-Ward expression. In fact, one can obtain this expression from basic principles by using algebraic as well as diagrammatic approaches [dD64a; dD64b]. Nevertheless, these justifications involve rather cumbersome procedures and will not be used here. Instead, the Luttinger-Ward formula will be shown to yield the same results than the coupling constant method for the partition function. Since this second method is essentially exact, one can indeed take this equivalence as a proof that Eq. (3.27) yields the correct expression for the partition function.

To build the bridge between both approaches, one shall start by letting the interaction potential V become λV , where λ once again is a coupling constant. The Luttinger-Ward expression then becomes:

$$W\{\mathcal{G}_\lambda\} = \widetilde{\text{Tr}} \ln \left[-\mathcal{G}_\lambda^{-1} \right] + \widetilde{\text{Tr}} \Sigma\{\mathcal{G}_\lambda\} \mathcal{G}_\lambda - \Phi\{\mathcal{G}_\lambda\} . \quad (3.32)$$

Let us now differentiate this equation with respect to λ . For the logarithmic term, one obtains:

$$\frac{d}{d\lambda} \widetilde{\text{Tr}} \ln [-\mathcal{G}_\lambda^{-1}] = -\widetilde{\text{Tr}} \mathcal{G}_\lambda^{-1} \frac{d\mathcal{G}_\lambda}{d\lambda}. \quad (3.33)$$

The second term yields the following derivative:

$$\frac{d}{d\lambda} \widetilde{\text{Tr}} \Sigma_\lambda \mathcal{G}_\lambda = \widetilde{\text{Tr}} \mathcal{G}_\lambda^{-1} \frac{d\mathcal{G}_\lambda}{d\lambda} + \widetilde{\text{Tr}} \Sigma_\lambda \frac{d\mathcal{G}_\lambda}{d\lambda}. \quad (3.34)$$

Note that the first term of the previous equation cancels the derivative of the logarithmic term, Eq. (3.33). Finally, in order to compute the derivative of the Φ functional, one should take into account that Φ depends on λ both through its explicit dependence on V and its dependence on \mathcal{G} :

$$\frac{d\Phi_\lambda}{d\lambda} = \left. \frac{\partial \Phi_\lambda}{\partial \lambda} \right|_{\mathcal{G}_\lambda} + \widetilde{\text{Tr}} \Sigma_\lambda \frac{d\mathcal{G}_\lambda}{d\lambda}. \quad (3.35)$$

The second term in the previous equation cancels the last term of Eq. (3.34). The total derivative of the partition function with respect to the coupling constant is therefore given by the partial derivative of the Φ -functional with respect to λ ,

$$\frac{dW_\lambda}{d\lambda} = - \left. \frac{\partial \Phi_\lambda}{\partial \lambda} \right|_{\mathcal{G}_\lambda}. \quad (3.36)$$

This partial derivative at constant \mathcal{G}_λ can be computed in a very nice way by considering an invariance of the Φ -functional. Let each explicit interaction V in Φ become αV and let each single-particle propagator \mathcal{G} become $\alpha^{-1/2} \mathcal{G}$. Taking into account that each \mathcal{G} in Φ connects two interaction vertices and that each potential line connects four \mathcal{G} 's, it is easy to see that this α -transformation leaves the Φ -functional invariant, so that:

$$\begin{aligned} \frac{d\Phi_\lambda}{d\alpha} &= \left. \frac{\partial \Phi_\lambda}{\partial \alpha} \right|_{\mathcal{G}_\lambda} + \widetilde{\text{Tr}} \frac{\delta \Phi_\lambda}{\delta \mathcal{G}_\lambda} \frac{d}{d\alpha} [\alpha^{-1/2} \mathcal{G}_\lambda] \\ &= \lambda \left. \frac{\partial \Phi_\lambda}{\partial \alpha \lambda} \right|_{\mathcal{G}_\lambda} - \frac{1}{2} \alpha^{-3/2} \widetilde{\text{Tr}} \Sigma_\lambda \mathcal{G}_\lambda = 0. \end{aligned} \quad (3.37)$$

Taking the previous equality at $\alpha = 1$, one finds the derivative of the Φ -functional with respect to λ :

$$\left. \frac{\partial \Phi_\lambda}{\partial \lambda} \right|_{\mathcal{G}_\lambda} = \frac{1}{2\lambda} \widetilde{\text{Tr}} \Sigma_\lambda \mathcal{G}_\lambda. \quad (3.38)$$

Using Eq. (3.36), this immediately gives the derivative of the partition function with respect to the coupling constant. By using the thermodynamical relation Eq. (3.6), one finds:

$$\frac{\partial \Omega_\lambda}{\partial \lambda} = \frac{1}{2\lambda\beta} \widetilde{\text{Tr}} \Sigma_\lambda \mathcal{G}_\lambda. \quad (3.39)$$

Note that this is the result that one obtains within the coupling constant method when combining Eqs. (3.11) and (3.19). By taking the integral from $\lambda = 0$ to $\lambda = 1$, this gives the coupling constant integration of Eq. (3.20), which yields the exact thermodynamical potential.

The grand-potential of the coupling constant method has thus been obtained from the Luttinger-Ward functional for the partition function. This proves that the Luttinger-Ward formalism yields exact results, within the error of the many-body approximation for the Green's function. In addition to that, the Luttinger-Ward approach has some more useful properties. Among them, the preservation of thermodynamical consistency which will be discussed in the following subsection.

3.3.4 Thermodynamical consistency

One of the main conclusions of Ref. [Bay62] is that, if the microscopic conservation laws of non-equilibrium systems have to be respected within a many-body approximation, a Φ -functional for the approximation must exist. This can be proved from a vanishing curl relation for the self-energy and is indeed the basis for defining Φ as in Eq. (3.31). Furthermore, one can check that this condition involves that thermodynamical consistency is automatically fulfilled. In the following, a simple example of thermodynamical consistency, concerning the total number of particles of a many-body system, will be considered. Other examples involving the energy or the pressure are studied in more detail in Ref. [Bay62].

Let us consider the evaluation of the total number of particles of a system as a function of β and μ . This is equivalent to the computation of its density. From the partition function, the number of particles can be evaluated through the derivative:

$$\langle N \rangle = - \left. \frac{\partial \Omega}{\partial \mu} \right|_{\beta} = \frac{1}{\beta} \left. \frac{\partial \ln Z}{\partial \mu} \right|_{\beta}. \quad (3.40)$$

From a Green's function point of view, on the other hand, the mean number of particles is obtained by summing the momentum distribution over all momentum states:

$$\langle N \rangle = \sum_k n(k). \quad (3.41)$$

To see that both expressions coincide within the Luttinger-Ward formalism, let us consider Eq. (3.27) and take its derivative with respect to the chemical potential:

$$\frac{\partial W}{\partial \mu} = -\widetilde{\text{Tr}} \mathcal{G}^{-1} \frac{\partial \mathcal{G}}{\partial \mu} + \widetilde{\text{Tr}} \frac{\partial \Sigma}{\partial \mu} \mathcal{G} + \widetilde{\text{Tr}} \Sigma \frac{\partial \mathcal{G}}{\partial \mu} - \frac{\delta \Phi}{\delta G} \frac{\partial \mathcal{G}}{\partial \mu}. \quad (3.42)$$

Using the definition of the Φ -functional, Eq. (3.31), this reduces to:

$$\frac{\partial W}{\partial \mu} = \widetilde{\text{Tr}} \frac{\partial \Sigma}{\partial \mu} \mathcal{G} - \widetilde{\text{Tr}} \mathcal{G}^{-1} \frac{\partial \mathcal{G}}{\partial \mu}. \quad (3.43)$$

To compute the derivative of the self-energy, one must consider its definition in terms of \mathcal{G} , Eq. (3.28), which gives:

$$\frac{\partial \Sigma}{\partial \mu} = \frac{\partial \mathcal{G}_0^{-1}}{\partial \mu} - \frac{\partial \mathcal{G}^{-1}}{\partial \mu} = 1 + \mathcal{G}^{-2} \frac{\partial \mathcal{G}}{\partial \mu}, \quad (3.44)$$

where the fact that the inverse of the free propagator depends linearly on the chemical potential (note that this is hidden inside the Matsubara frequencies) has been used. Plugging this into Eq. (3.43), one finds:

$$\frac{\partial W}{\partial \mu} = \widetilde{\text{Tr}} \mathcal{G} = \sum_{k,\nu} e^{z\nu\eta} \mathcal{G}(k, z_\nu) = \beta \sum_k \int_{-\infty}^{\infty} \frac{d\omega}{2\pi} f(\omega) \mathcal{A}(k, \omega), \quad (3.45)$$

where the Matsubara summation has been performed according to the techniques described in Appendix C. Using the thermodynamical relation between $\ln Z$ and Ω , Eq. (2.11), as well as the definition of the momentum distribution, Eq. (2.72), one obtains the result:

$$\frac{\partial \Omega}{\partial \mu} = - \sum_k n(k). \quad (3.46)$$

This equation might seem trivial at first sight, because it arises from the combination of Eqs. (3.40) and (3.41). Yet, one should notice that each side of the equation has a very different origin. While on the left hand side one finds information related to the macroscopic properties of the system through the grand-canonical potential Ω , the right hand side contains information on the microscopic properties of the system through the Green's function and the momentum distribution arising from it. The connection between both sides is possible thanks to the Luttinger-Ward formalism.

In practice, all our calculations will be done at fixed density (or, equivalently, at a fixed total number of particles). In that case, the counterparts to Eqs. (3.40) and (3.41) are inverted to yield the chemical potential of the system. Doing this in each equation, one obtains two different chemical potentials. The microscopic chemical potential, $\tilde{\mu}$, is obtained from the inversion of the following equation:

$$\rho = \sum_k \int_{-\infty}^{\infty} \frac{d\omega}{2\pi} \mathcal{A}(k, \omega, \tilde{\mu}) f(\omega, \tilde{\mu}), \quad (3.47)$$

which comes directly from Green's function theory and where the dependence of both the spectral function and the Fermi-Dirac distribution on $\tilde{\mu}$ have been considered explicitly. On the other hand, the macroscopic chemical potential, μ , comes from the thermodynamical expression:

$$\mu(\rho, T) = \left. \frac{\partial F(\rho, T)}{\partial \rho} \right|_T, \quad (3.48)$$

where F is the free-energy and T is the temperature of the system. Note that the free energy can be obtained from the total energy, E , and the entropy, S , using the relation:

$$F(\rho, T) = E(\rho, T) - TS(\rho, T). \quad (3.49)$$

In the following, the Luttinger-Ward formalism will be used to compute the entropy of the system, while the total energy will be obtained using the GMK sum rule. The derivative as a function of the density of the free energy, obtained from this means, μ , should yield the same result as the microscopic $\tilde{\mu}$ in any conserving approach. Yet, some approximations (like the BHF approach) do not fulfill this condition and large differences between μ and $\tilde{\mu}$ can appear due to the lack of consistency between the microscopic and the macroscopic approaches.

In the context of nuclear matter, the issue of thermodynamical consistency is often discussed in terms of the Hugenholtz-van Hove theorem [Hug58]. This is a local condition for thermodynamical consistency, which is restricted to the surroundings of the saturation density at $T = 0$. Consider the derivative of the energy per unit volume rewritten in terms of the energy per particle, E/A :

$$\mu = \frac{\partial E}{\partial \rho} \frac{1}{\mathcal{V}} = \frac{\partial}{\partial \rho} \rho \frac{E}{A} = e + \rho \frac{\partial E}{\partial \rho} \frac{1}{A}. \quad (3.50)$$

Since the saturation density, ρ_0 , is the point where the energy per particle has a minimum, the previous equation states that:

$$\mu(\rho = \rho_0) = \frac{E(\rho = \rho_0)}{A}. \quad (3.51)$$

From a microscopic point of view, the chemical potential at zero temperature is given by the Fermi energy:

$$\tilde{\mu}(\rho) = \varepsilon_F, \quad (3.52)$$

which is usually defined as the quasi-particle energy at the Fermi surface:

$$\varepsilon_F = \varepsilon_{qp}(k = k_F), \quad (3.53)$$

with $k_F = \left(\frac{6\pi^2\rho}{\nu}\right)^{1/3}$, the Fermi momentum and ν the degeneracy of the system. The Hugenholtz-van Hove theorem then states that the microscopic chemical potential should equal the energy per particle at saturation:

$$\tilde{\mu}(\rho_0) = \frac{E(\rho_0)}{A}. \quad (3.54)$$

This theorem is, for instance, violated by several MeVs within the BHF approach, although the inclusion of higher order correlations within the Goldstone expansion might lead to more consistent results [Bal90; Cze02].

The reason for the lack of thermodynamical consistency of the BHF approach lies in the so-called *rearrangement terms*. These appear when one takes the derivative of Eq. (3.50) on the expression of the total energy of the system given by BHF approach. This yields two terms corresponding to the Fermi energy of Eq. (3.53), plus a derivative of the in-medium interaction (the so-called G -matrix) with respect to the density, which takes into account the effect that a change in the density has in the in-medium interaction. A rigorous calculation of this rearrangement terms is quite complicated [Bru60]. However, it is necessary if one wants to understand the relation between the BHF approach and the Landau theory of Fermi liquids [Bro71].

3.4 Free partition function

As a first application of the Luttinger-Ward formalism, the partition function of a non-interacting non-relativistic fermionic system will be computed. This is useful because it helps in setting all the sign conventions as well as in revising the contour integral techniques that shall be needed in the following chapters. For a non-interacting system, both Σ and Φ vanish and thus the partition function is given by:

$$\ln Z_0 = \widetilde{\text{Tr}} \ln [-\mathcal{G}_0^{-1}] . \quad (3.55)$$

Using the expression for the single-particle propagator in momentum and Matsubara frequency space, Eq. (2.105), and writing explicitly the trace, this becomes:

$$\ln Z_0 = \sum_{k,\nu} e^{z_\nu \eta} \ln [\varepsilon_0(k) - z_\nu] , \quad (3.56)$$

where the free quasi-particle energy is given by $\varepsilon_0(k) = \frac{k^2}{2m}$. This sum over Matsubara frequencies is explicitly computed in Appendix C [see Eq. (C.13)]. Note that it is especially delicate because of the cut of the logarithm function in the real axis. Once this is taken into account, one obtains:

$$\ln Z_0 = -\beta \sum_k \int_{-\infty}^{\infty} \frac{d\omega}{2\pi} 2 \text{Im} \left\{ \ln [\varepsilon_0(k) - \omega_+] \right\} . \quad (3.57)$$

Now one faces the problem of computing the imaginary part of the logarithm. Yet, this imaginary part is essentially the phase of the complex number inside the logarithm. The imaginary part of the logarithm depends only on the sign of the real part of its argument and gives¹:

$$\text{Im} \left\{ \ln [\varepsilon_0(k) - \omega_+] \right\} = \begin{cases} 0, & \varepsilon_0(k) - \omega > 0 \\ -\pi, & \varepsilon_0(k) - \omega < 0 . \end{cases} \quad (3.58)$$

¹To obtain this result one has to work in the Riemann sheet where the logarithm has a cut along the negative axis and it is such that $\ln 1 = 0$.

3.4. FREE PARTITION FUNCTION

This is due to the fact that, when taking the limit of $\eta \rightarrow 0$ and whenever the real part of the argument is negative, one approaches the cut in the real axis from below, giving a phase of $-\pi$. On the other hand, when the real part inside the logarithm is positive, the associated phase is simply zero. The previous expression for the imaginary part sets a restriction in the integration limits of Eq. (3.57). This is now rewritten as:

$$\ln Z_0 = \beta \sum_k \int_{\varepsilon_0(k)}^{\infty} d\omega f(\omega) = \sum_k \ln [1 + e^{-\beta[\varepsilon_0(k)-\mu]}] . \quad (3.59)$$

The last step in the previous equation is obtained by integrating explicitly the Fermi-Dirac distribution with respect to the energy. Finally, one finds the following expression for the grand-canonical potential:

$$\Omega_0 = -\frac{1}{\beta} \sum_k \ln [1 + e^{-\beta[\varepsilon_0(k)-\mu]}] . \quad (3.60)$$

From this expression, the remaining thermodynamical observables of a free fermion system at finite temperature can be obtained. The total number of particles is for instance given by:

$$N_0 = \langle N \rangle_0 = -\frac{\partial \Omega_0}{\partial \mu} = \sum_k \frac{1}{1 + e^{\beta[\varepsilon_0(k)-\mu]}} = \sum_k f[\varepsilon_0(k)] . \quad (3.61)$$

This is the same quantity that one would get from Green's function theory and thus the results are thermodynamically consistent. One can also easily compute the entropy of a free system of fermions:

$$\begin{aligned} S &= -\frac{\partial \Omega_0}{\partial T} = -\sum_k \left\{ f[\varepsilon_0(k)] \ln [f[\varepsilon_0(k)]] + [1 - f[\varepsilon_0(k)]] \ln [1 - f[\varepsilon_0(k)]] \right\} \\ &= \sum_k \sigma[\varepsilon_0(k)] . \end{aligned} \quad (3.62)$$

In the last line, the statistical weighting function:

$$\sigma(\omega) = -\left\{ f(\omega) \ln [f(\omega)] + [1 - f(\omega)] \ln [1 - f(\omega)] \right\} , \quad (3.63)$$

has been introduced for further convenience. Finally, let us notice that the total energy of a non-interacting system of fermions can also be obtained by means of the thermodynamical relation:

$$E - \mu N_0 = \frac{\partial \beta \Omega_0}{\partial \beta} = \sum_k \frac{k^2}{2m} f[\varepsilon_0(k)] - \mu \sum_k f[\varepsilon_0(k)] . \quad (3.64)$$

Note that the first term in the previous expression corresponds to Eq. (2.111), which was obtained directly from the microscopic GMK sum rule.

Eq. (3.60) corresponds to the grand-canonical potential of a non-interacting system of fermions. It can, of course, be obtained by other means not involving the Luttinger-Ward formalism. In [Neg88], for instance, it is obtained from a path integral formulation of quantum statistical mechanics, while in [Mat92] it is computed from a sum over all the allowed thermal averaged states of the system. All of these methods have their corresponding expressions for interacting systems, but they lack a property that makes the Luttinger-Ward particularly attractive, *i.e.* its direct connection to the Green's function. In the following section, this advantage will be exploited to obtain expressions for the partition function of a correlated system of fermions in terms of the single-particle propagator.

3.5 Partition function of a correlated system of fermions

For conceptual as well as for computational purposes, it is interesting to express the Luttinger-Ward functional in terms of magnitudes that can be computed from the Green's function approach such as, for instance, the spectral function $\mathcal{A}(k, \omega)$. This will be done in this section, where the expressions will be kept as generic as possible so that they can be easily reduced to the non-interacting or the quasi-particle cases. Let us start with the Luttinger-Ward functional for the partition function:

$$W = \widetilde{\text{Tr}} \ln [-\mathcal{G}^{-1}] + \widetilde{\text{Tr}} \Sigma \mathcal{G} - \Phi. \quad (3.65)$$

Each trace corresponds to a Matsubara summation that has to be explicitly computed. Let us start with the first term:

$$W_1 = \sum_{k, \nu} e^{z_\nu \eta} \ln [-\mathcal{G}^{-1}(k, z_\nu)]. \quad (3.66)$$

As it has been previously explained, the logarithm function has a cut in the real axis of its arguments, which needs to be taken care of when performing the sum. Yet, both the logarithm and the one-body Green's function fulfill the condition of Eq. (C.14) and thus the general formula of Eq. (C.15) can be used to perform the sum:

$$W_1 = -\beta \sum_k \int_{-\infty}^{\infty} \frac{d\omega}{2\pi} f(\omega) 2 \text{Im} \left\{ \ln [-\mathcal{G}^{-1}(k, \omega_+)] \right\}, \quad (3.67)$$

where now the inverse propagator is computed slightly above the real axis. Note that, in order to carry out the sum, one has to take into account that the inverse propagator does not have any complex pole for complex z , as shown in Section 2.2.4. The imaginary part of the logarithm is related to the phase of its argument.

In the correlated case, when the inverse propagator has a non-zero imaginary part, this can be rewritten as follows:

$$\begin{aligned}
 \operatorname{Im} \left\{ \ln [-\mathcal{G}^{-1}(k, \omega_+)] \right\} &= \operatorname{Im} \left\{ \ln [-\operatorname{Re} \mathcal{G}^{-1}(k, \omega) - i\operatorname{Im} \mathcal{G}^{-1}(k, \omega_+)] \right\} = \\
 &= \operatorname{Im} \left\{ \ln [-\operatorname{Re} \mathcal{G}^{-1}(k, \omega) + i\operatorname{Im} \Sigma(k, \omega_+)] \right\} = \\
 &= \arg \left[-\operatorname{Re} \mathcal{G}^{-1}(k, \omega) - i\frac{1}{2}\Gamma(k, \omega) \right]. \quad (3.68)
 \end{aligned}$$

The width Γ has been introduced according to Eq. (2.128). The function $\arg[z]$ gives the phase of the complex number z (also called its *argument*, which should not be confused with the argument of the logarithm!). The computation of this phase is a little tricky and needs to be performed with care. First of all, note that since $\Gamma(k, \omega)$ is positive definite [see Eq. (2.129)], the complex number $z = -\operatorname{Re} \mathcal{G}^{-1}(k, \omega) - i\frac{1}{2}\Gamma(k, \omega)$, whose argument one is trying to find, lies always in the quadrants III and IV of the complex plane. More precisely, for $\operatorname{Re} \mathcal{G}^{-1} < 0$, z is in quadrant IV. The argument of z is thus simply given by the arctangent function according to:

$$\arg \left[-\operatorname{Re} \mathcal{G}^{-1} - i\frac{1}{2}\Gamma \right] = \arctan \left(\frac{\Gamma}{2\operatorname{Re} \mathcal{G}^{-1}} \right), \quad \text{for } \operatorname{Re} \mathcal{G}^{-1} < 0. \quad (3.69)$$

The situation is somewhat different for $\operatorname{Re} \mathcal{G}^{-1} > 0$. In that case, z is a complex quantity in quadrant III. This corresponds to phases in the interval $(-\frac{\pi}{2}, -\pi)$. Yet, since the $\arctan(z)$ function yields values in the interval $(-\frac{\pi}{2}, \frac{\pi}{2})$, it cannot reproduce the angles in this quadrant. It is easy to check that, in this case, an extra factor of π is needed so that the argument and the value given by the arctangent match:

$$\arg \left[-\operatorname{Re} \mathcal{G}^{-1} - i\frac{1}{2}\Gamma \right] = \arctan \left(\frac{\Gamma}{2\operatorname{Re} \mathcal{G}^{-1}} \right) - \pi, \quad \text{for } \operatorname{Re} \mathcal{G}^{-1} > 0. \quad (3.70)$$

Eqs. (3.69) and (3.70) can be collected together in the following compact expression:

$$\operatorname{Im} \left\{ \ln [-\mathcal{G}^{-1}(k, \omega_+)] \right\} = \arctan [\lambda(k, \omega)] - \pi\Theta[\operatorname{Re} \mathcal{G}^{-1}(k, \omega)], \quad (3.71)$$

where the function λ is defined as:

$$\lambda(k, \omega) = \frac{\Gamma(k, \omega)}{2\operatorname{Re} \mathcal{G}^{-1}(k, \omega)}, \quad (3.72)$$

and corresponds to the ratio between the imaginary and the real parts of the inverse propagator. Considering this final expression for the imaginary part of the logarithm and inserting it into Eq. (3.67), one gets:

$$W_1 = \beta \sum_k \int_{-\infty}^{\infty} \frac{d\omega}{2\pi} f(\omega) \left\{ 2\pi\Theta[\operatorname{Re} \mathcal{G}^{-1}(k, \omega)] - 2\arctan [\lambda(k, \omega)] \right\}. \quad (3.73)$$

Let us now pay attention to the second term of Eq. (3.27). This is again given by a trace, which can be rewritten as:

$$W_2 = \sum_{k,\nu} e^{z\nu\eta} \Sigma(k, z_\nu) \mathcal{G}(k, z_\nu). \quad (3.74)$$

From Eqs. (2.63) and (2.125), it is clear that the object that is being summed in the previous equation fulfills Eq. (C.14). Thus, the general formula Eq. (C.15) can be applied once again to give:

$$W_2 = -\beta \sum_k \int_{-\infty}^{\infty} \frac{d\omega}{2\pi} f(\omega) 2 \operatorname{Im} \left\{ \Sigma(k, \omega_+) \mathcal{G}(k, \omega_+) \right\}. \quad (3.75)$$

This imaginary part can be rewritten in terms of the spectral function and the width:

$$\begin{aligned} \operatorname{Im} \left\{ \Sigma(k, \omega_+) \mathcal{G}(k, \omega_+) \right\} &= \operatorname{Re} \Sigma(k, \omega_+) \operatorname{Im} \mathcal{G}(k, \omega_+) + \operatorname{Im} \Sigma(k, \omega_+) \operatorname{Re} \mathcal{G}(k, \omega_+) \\ &= -\frac{1}{2} \operatorname{Re} \Sigma(k, \omega) \mathcal{A}(k, \omega) - \frac{1}{2} \Gamma(k, \omega) \operatorname{Re} \mathcal{G}(k, \omega), \end{aligned} \quad (3.76)$$

so that the second contribution to the partition function can be rewritten as:

$$W_2 = \beta \sum_k \int_{-\infty}^{\infty} \frac{d\omega}{2\pi} f(\omega) \left[\mathcal{A}(k, \omega) \operatorname{Re} \Sigma(k, \omega) + \Gamma(k, \omega) \operatorname{Re} \mathcal{G}(k, \omega) \right]. \quad (3.77)$$

With W_1 and W_2 one obtains the following closed expression for the total partition function of the system:

$$\begin{aligned} \ln Z &= \beta \sum_k \int_{-\infty}^{\infty} \frac{d\omega}{2\pi} f(\omega) \left[2\pi \Theta [\operatorname{Re} \mathcal{G}^{-1}(k, \omega)] - 2 \arctan [\lambda(k, \omega)] \right. \\ &\quad \left. + \mathcal{A}(k, \omega) \operatorname{Re} \Sigma(k, \omega) + \Gamma(k, \omega) \operatorname{Re} \mathcal{G}(k, \omega) \right] - \Phi. \end{aligned} \quad (3.78)$$

This equation gives directly the thermodynamical observables of the system as a function of the one-body Green's function (note that all the quantities inside the brackets can be derived from it). If one were able to compute exactly this Green's function as well as its corresponding Φ -functional, then the partition function would be automatically given by the previous expression.

Eq. (3.78) has an extra nice feature, *i.e.* one can easily decouple the contribution of (zero width) quasi-particles from the remaining terms. This is useful if one is interested on the effects that correlations induce to the partition function, because it allows to separate the contributions of the quasi-particle pole from the rest of correlations. Take the first term in Eq. (3.78). For a fixed momentum, the function:

$$\operatorname{Re} \mathcal{G}^{-1}(k, \omega) = \omega - \frac{k^2}{2m} - \operatorname{Re} \Sigma(k, \omega) \quad (3.79)$$

is, in nuclear matter, a monotonously increasing function of ω due to the soft energy dependence of $\text{Re } \Sigma$. In this case, there is only one value in which $\text{Re } \mathcal{G}^{-1}$ becomes zero, given by the condition:

$$\varepsilon_{qp}(k) = \frac{k^2}{2m} + \text{Re } \Sigma(k, \varepsilon_{qp}(k)). \quad (3.80)$$

Note that this coincides with the quasi-particle energy of Eq. (2.132). One can thus rewrite the step function as:

$$\Theta [\text{Re } \mathcal{G}^{-1}(k, \omega)] = \Theta \left[\omega - \frac{k^2}{2m} - \text{Re } \Sigma(k, \omega) \right] = \Theta [\omega - \varepsilon_{qp}(k)]. \quad (3.81)$$

One thus finds the following expression for the first term in $\ln Z$:

$$W^{QP} \equiv \beta \sum_k \int_{-\infty}^{\infty} d\omega f(\omega) \Theta [\omega - \varepsilon_{qp}(k)] = \sum_k \ln [1 + e^{-\beta[\varepsilon_{qp}(k) - \mu]}], \quad (3.82)$$

which is very close to the partition function of the free case, but with the free quasi-particle energies, $\varepsilon_0(k)$, replaced by the full interacting quasi-particle energies, $\varepsilon_{qp}(k)$. The previous expression amounts for the following contribution to the grand-canonical potential:

$$\Omega^{QP} = -\frac{1}{\beta} \sum_k \ln [1 + e^{-\beta[\varepsilon_{qp}(k) - \mu]}]. \quad (3.83)$$

This is one of the contributions to the total grand-canonical potential of a gas of undamped (*i.e.* infinitely long-lived) quasi-particles. In a no-width approximation (such as the Hartree-Fock approximation), however, this is not the only term in the total partition function. Indeed, from Eq. (3.78) it is easy to see that, in the limit where $\Gamma \rightarrow 0$, both the $\mathcal{A}\text{Re } \Sigma$ term as well as the Φ -functional do yield a non-vanishing contribution. As it will be seen in the following chapter, these give sizeable and similar contributions in a mean-field approach.

One can obtain an alternative expression for the grand-canonical potential within the Luttinger-Ward formalism by going back to Eqs. (3.67) and (3.75) and using the following identity:

$$\beta f(\omega) = -\frac{\partial}{\partial \omega} \ln [1 + e^{-\beta(\omega - \mu)}]. \quad (3.84)$$

Integrating by parts, one easily obtains:

$$\ln Z = \sum_k \int_{-\infty}^{\infty} \frac{d\omega}{2\pi} \ln [1 + e^{-\beta(\omega - \mu)}] B(k, \omega) - \Phi, \quad (3.85)$$

where the following B function has been introduced:

$$B(k, \omega) = -\frac{\partial}{\partial \omega} 2\text{Im} \left\{ \ln \left[-\mathcal{G}^{-1}(k, \omega_+) \right] + \Sigma(k, \omega_+) \mathcal{G}(k, \omega_+) \right\}. \quad (3.86)$$

Different expressions for B can be obtained depending on whether the derivative or the imaginary part is taken first. In this section, the derivative shall be taken prior to the imaginary part. For the first term, the following result is obtained:

$$\begin{aligned}
B_1(k, \omega) &= -2\text{Im} \left\{ \frac{\partial}{\partial \omega} \ln \left[-\mathcal{G}^{-1}(k, \omega_+) \right] \right\} \\
&= -2\text{Im} \left\{ \mathcal{G}(k, \omega_+) \left[1 - \frac{\partial \Sigma(k, \omega_+)}{\partial \omega} \right] \right\} = \\
&= \mathcal{A}(k, \omega) \left[1 - \frac{\partial \text{Re} \Sigma(k, \omega)}{\partial \omega} \right] - \text{Re} \mathcal{G}(k, \omega) \frac{\partial \Gamma(k, \omega)}{\partial \omega}. \quad (3.87)
\end{aligned}$$

The derivative of the second term is easily computed and can be split in two parts:

$$B_2(k, \omega) = \frac{\partial \text{Re} \mathcal{G}(k, \omega)}{\partial \omega} \Gamma(k, \omega) + \text{Re} \mathcal{G}(k, \omega) \frac{\partial \Gamma(k, \omega)}{\partial \omega}, \quad (3.88)$$

and

$$B_3(k, \omega) = \frac{\partial \text{Re} \Sigma(k, \omega)}{\partial \omega} \mathcal{A}(k, \omega) + \text{Re} \Sigma(k, \omega) \frac{\partial \mathcal{A}(k, \omega)}{\partial \omega}. \quad (3.89)$$

Now one can write a compact expression for the B function:

$$B(k, \omega) = \mathcal{A}(k, \omega) + \frac{\partial \mathcal{A}(k, \omega)}{\partial \omega} \text{Re} \Sigma(k, \omega) + \frac{\partial \text{Re} \mathcal{G}(k, \omega)}{\partial \omega} \Gamma(k, \omega). \quad (3.90)$$

Note that this result arises from the cancellation of the last two terms in Eq. (3.87) with the two first terms of both Eqs. (3.88) and (3.89). This result was previously obtained in Refs. [Wei98a; Wei98b].

The expression for the partition function of Eq. (3.85) has some interesting properties. On the one hand, it has a very intuitive form. Its first term is a convolution in energies of the factor $\ln \{1 + e^{-\beta[\omega - \mu]}\}$, which is basically the thermal factor appearing in the free partition function, times the B function. This is the same kind of generalization that one obtains, for instance, when going from the free momentum distribution, Eq. (2.110), to the correlated one, Eq. (2.72). In that case, the convolution is between the Fermi-Dirac distribution, $[1 + e^{\beta[\omega - \mu]}]^{-1}$, and the \mathcal{A} spectral function. In the same way that $\mathcal{A}(k, \omega)$ accounts for the effect of correlations in the momentum distribution, one can say that the function $B(k, \omega)$ incorporates the effects of the interaction to the partition function. Among these effects, one finds the finite width of the quasi-particles in the medium as well as the rest of correlations induced by the interaction. Note, however, that this is not the only contribution to the partition function: the Φ -functional also plays an important role in the thermodynamical properties of the system! It is also interesting to note that, in contrast to Eq. (3.78), Eq. (3.85) cannot be easily split in terms of the contributions of quasi-particles plus other correlation effects. It is

only when one takes a no-width approximation for $B(k, \omega)$ that a part of Eq. (3.85) becomes the quasi-particle contribution of Eq. (3.83). In this sense, this is different to Eq. (3.78), where this contribution comes out automatically (with the only restriction that the real part of the inverse propagator has a single zero).

3.6 Entropy of a correlated system of fermions

Once the partition function is known, one can readily compute the grand-canonical potential Ω . The entropy of the system then follows from the thermodynamical relation:

$$S = - \left. \frac{\partial \Omega}{\partial T} \right|_{\mu}. \quad (3.91)$$

Using the expressions that have been obtained for $\ln Z$, Eqs. (3.67) and (3.75), different results for the entropy can be found. In the following, these results will be discussed.

Consider first Eq. (3.78). The stationarity of Ω with respect to changes in \mathcal{G} is very useful, because it implies that, when taking the temperature derivative, only the explicit dependence of the Fermi functions is needed. This stationarity is a very attractive feature of the Luttinger-Ward approach, because it allows to skip the (usually involved) thermal dependences of the dynamical quantities and therefore defines a way to compute analytical expressions that relate the thermodynamical observables to the microscopic properties. In the case of the correlated entropy, this yields:

$$S = \sum_k \int_{-\infty}^{\infty} \frac{d\omega}{2\pi} \frac{\partial f(\omega)}{\partial T} \left\{ 2\pi \Theta[\operatorname{Re} \mathcal{G}^{-1}(k, \omega)] - 2 \arctan [\lambda(k, \omega)] \right. \\ \left. + \mathcal{A}(k, \omega) \operatorname{Re} \Sigma(k, \omega) + \Gamma(k, \omega) \operatorname{Re} \mathcal{G}(k, \omega) \right\} - \frac{\partial T \Phi}{\partial T}. \quad (3.92)$$

This expression gives the entropy of a correlated system of fermions as a function of \mathcal{G} , Σ and Φ and it is the fundamental equation from which most of our results will be derived. The usefulness and applications of this formula in the context of Fermi-liquids were extensively discussed in the pioneering work of Carneiro and Pethick [Car75]. Most of what is discussed below can be found in this reference, which has been the main guideline in our discussions of the many-body approximations to the entropy.

One can divide the expression of Eq. (3.92) in two terms:

$$S = S^{DQ} + S', \quad (3.93)$$

given by:

$$S^{DQ} = \sum_k \int_{-\infty}^{\infty} \frac{d\omega}{2\pi} \frac{\partial f(\omega)}{\partial T} \Xi(k, \omega) \quad (3.94)$$

and

$$S' = -\frac{\partial}{\partial T} T\Phi[G] + \sum_k \int_{-\infty}^{\infty} \frac{d\omega}{2\pi} \frac{\partial f(\omega)}{\partial T} \mathcal{A}(k, \omega) \text{Re} \Sigma(k, \omega), \quad (3.95)$$

where the function $\Xi(k, \omega)$:

$$\Xi(k, \omega) = 2\pi\Theta[\text{Re} \mathcal{G}^{-1}(k, \omega)] - 2 \arctan \lambda(k, \omega) + \Gamma(k, \omega) \text{Re} \mathcal{G}(k, \omega) \quad (3.96)$$

has been introduced. Notice that this gathers together the term yielding the quasi-particle approximation to the partition function and two terms which depend on the width of the quasi-particle. In this sense, S^{DQ} is a dynamical quasi-particle entropy which partially takes into account the correlations of the dressed particles in the medium, including the finite width effects, as seen by the fact that it is computed with a non-zero Γ . The dynamical quasi-particle entropy can be rewritten in a more intuitive way by using the following useful relation:

$$\frac{\partial f(\omega)}{\partial T} = -\frac{\partial \sigma(\omega)}{\partial \omega}, \quad (3.97)$$

between the Fermi-Dirac distribution and the statistical weighting function of Eq. (3.63). After a partial integration, one finds that the following expression for the dynamical quasi-particle entropy holds:

$$S^{DQ} = \sum_k \int_{-\infty}^{\infty} \frac{d\omega}{2\pi} \sigma(\omega) \mathcal{B}(k, \omega), \quad (3.98)$$

provided that the \mathcal{B} spectral function is defined as:

$$\mathcal{B}(k, \omega) = \frac{\partial \Xi(k, \omega)}{\partial \omega}. \quad (3.99)$$

The expression Eq. (3.98) has several interesting properties. In the first place, it includes correlations in a very intuitive form, by means of the convolution of the \mathcal{B} spectral function, which takes into account the finite-width (or energy-dependent) effects induced by correlations, and a weighting factor, $\sigma(\omega)$, which carries the thermodynamical information of the system. In addition, in the free and the Hartree-Fock cases the \mathcal{B} function reduces to a delta peak and S^{DQ} becomes the expected expression for the entropy of a system of interacting quasi-particles. This does not mean, however, that in more complete approximations S^{DQ} neglects the finite width of quasi-particles, as has already been discussed. Furthermore, $\mathcal{B}(k, \omega)$

shares some properties with the usual spectral function, $\mathcal{A}(k, \omega)$. Their relationship will be explored in Chapter 6. Before that, however, it will be interesting to study the properties of the Ξ function and its dependence in energy. This will allow for a better understanding on the microscopic effects into the dynamical quasi-particle entropy.

Let us thus analyze the properties of the function $\Xi(k, \omega)$. The first term of Ξ in Eq. (3.96) is a step function with the argument $\text{Re } \mathcal{G}^{-1}$. For a fixed momentum, Ξ_1 equals zero at energies below the quasi-particle energy and 2π for larger values. Using Eq. (3.97), one can see that the contribution of Ξ_1 to the entropy is given by:

$$\begin{aligned} S_1^{DQ} &= \sum_k \int_{-\infty}^{\infty} \frac{d\omega}{2\pi} \frac{\partial \sigma(\omega)}{\partial \omega} 2\pi \Theta[\omega - \varepsilon_{qp}(k)] = \sum_k \int_{-\infty}^{\varepsilon_{qp}(k)} d\omega \frac{\partial \sigma(\omega)}{\partial \omega} = \\ &= \sum_k \sigma[\varepsilon_{qp}(k)] \equiv S^{QP}. \end{aligned} \quad (3.100)$$

This expression could have been obtained alternatively by taking the temperature derivative of Eq. (3.83). It corresponds to the entropy of a system of undamped quasi-particles with real quasi-particle energies given by Eq. (3.80). Whenever quasi-particles have long life-times, this should be a good approximation to the entropy. Indeed, for any many-body approximation where the quasi-particle energies are real (such as the Hartree-Fock case, for instance) the full dynamical quasi-particle entropy is simply given by Eq. (3.100).

The remaining terms in Ξ can be rewritten as a function of $\lambda(k, \omega)$:

$$\Xi_2(k, \omega) = -2 \arctan [\lambda(k, \omega)], \quad (3.101)$$

for the second term and:

$$\Xi_3(k, \omega) = \frac{2\lambda(k, \omega)}{1 + \lambda^2(k, \omega)}, \quad (3.102)$$

for the third one. Their total contribution to the entropy is therefore given by:

$$S_2^{DQ} = \sum_k \int_{-\infty}^{\infty} \frac{d\omega}{2\pi} \frac{\partial f(\omega)}{\partial T} \left\{ \frac{2\lambda(k, \omega)}{1 + \lambda^2(k, \omega)} - 2 \arctan [\lambda(k, \omega)] \right\}. \quad (3.103)$$

This expression involves a non-vanishing width Γ and it can thus be thought as a life-time correction to the dynamical quasi-particle entropy. It is clear that for infinitely long lived quasi-particles ($\Gamma=0$), this contribution will be zero, but for large widths it can have a non-negligible effect on the total entropy.

In order to understand qualitatively the behavior of $\Xi(k, \omega)$ as a function of the energy, in Fig. 3.4 the different contributions Ξ_1 , Ξ_2 and Ξ_3 as well as the total Ξ are shown for a fixed momentum, $k = k_F$. These have been obtained

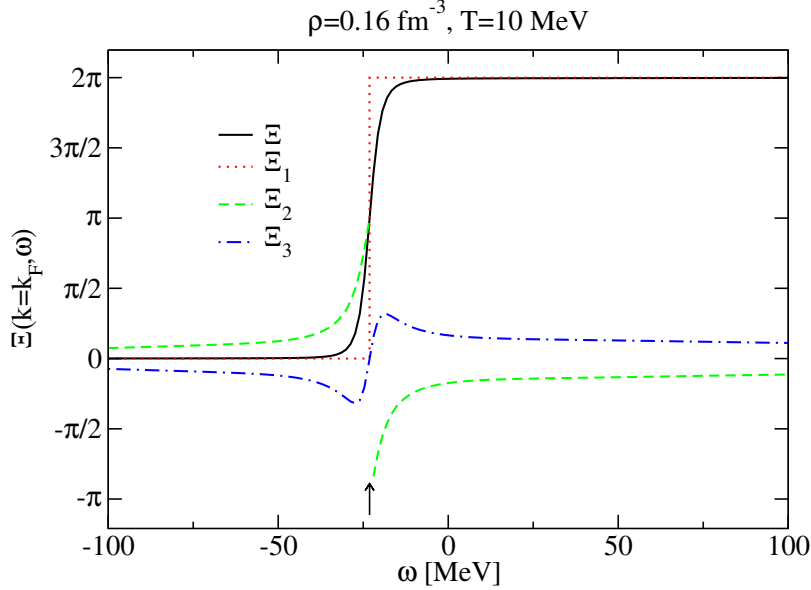


Figure 3.4: Ξ_1 (dotted line), Ξ_2 (dashed line) and Ξ_3 (dot-dashed line) contributions to the total Ξ function (full line) as a function of the energy for a fixed momentum $k = k_F$. This has been computed at ρ_0 for $T = 10$ MeV. The arrow signals the position of the quasi-particle energy at this momentum, $\varepsilon_{qp}(k = k_F) = -23.2$ MeV.

for nuclear matter at the experimental saturation density, $\rho_0 = 0.16 \text{ fm}^{-3}$, and a temperature of $T = 10$ MeV within the SCGF approach that will be discussed in Chapter 5. The quasi-particle contribution Ξ_1 is shown in a dotted line. For a fixed momentum, this is just a step function which goes from 0 to 2π once the energy ω is above the corresponding quasi-particle energy (in this case, $\varepsilon_{qp}(k_F) = -23.2$ MeV). Note that for quasi-particles without width, this step function is the only contribution to S^{DQ} .

The remaining contributions, Ξ_2 (dashed lines) and Ξ_3 (dot-dashed lines), modulate the step-like behavior of Ξ around the quasi-particle energy and soften its energy dependence. This effect is however subtle and has to be studied with care. Consider first the λ variable around the quasi-particle energy, which is shown in Fig. 3.5 for the same conditions as in Fig. 3.4. There is a pronounced structure around the quasi-particle energy which denotes a singularity of λ . Its appearance is related to the fact that the denominator of Eq. (3.72) goes to zero close to $\varepsilon_{qp}(k)$, while the width Γ is a positive definite quantity and cannot cancel the singularity. Moreover, the value of λ close to $\varepsilon_{qp}(k)$ has a different sign according to the direction in which the limit $\omega \rightarrow \varepsilon_{qp}(k)$ is taken:

$$\lim_{\omega \rightarrow \varepsilon_{qp}(k)^\pm} \lambda(k, \omega) = \lim_{\omega \rightarrow \varepsilon_{qp}(k)^\pm} \frac{\Gamma(k, \omega)}{2[\omega - \varepsilon_{qp}(k)]} \sim \frac{\Gamma(k, \varepsilon_{qp}(k))}{0^\pm} = \pm\infty. \quad (3.104)$$

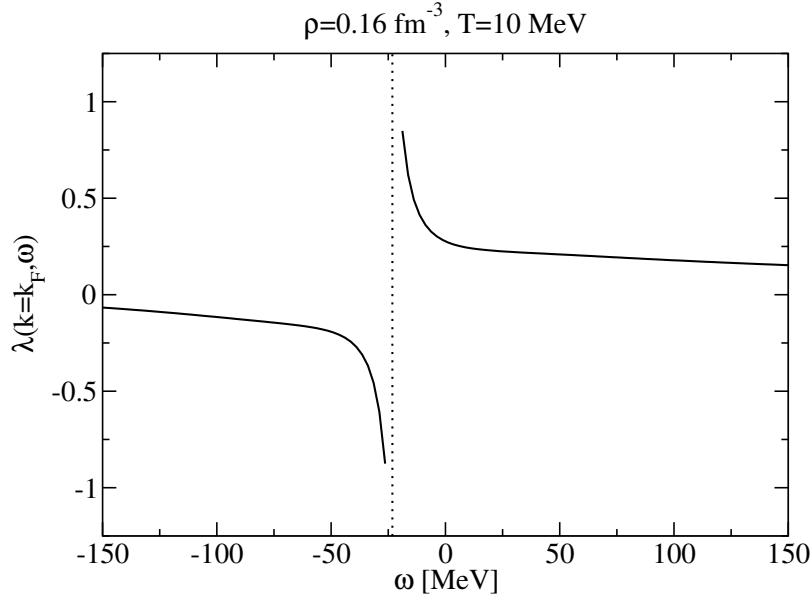


Figure 3.5: $\lambda(k, \omega)$ at the Fermi surface $k = k_F$ as a function of the energy. The conditions are the same as in the previous figure.

Thus λ becomes minus (plus) infinity if one takes the limit to the quasi-particle energy from the left (right). As a consequence of this behavior, the Ξ_2 contribution is discontinuous at $\omega = \varepsilon_{qp}(k)$. When coming from the left to the quasi-particle energy, λ becomes infinity, the arctan function yields a factor $-\frac{\pi}{2}$ and Ξ_2 tends to π . When the limit is taken from the other side, Ξ_2 becomes $-\pi$. Yet, this discontinuity is exactly canceled by the step function in Ξ_1 which, above the pole, yields the needful 2π value to obtain a continuous Ξ function around $\varepsilon_{qp}(k)$. On the other hand, close to the quasi-particle pole, the Ξ_3 contribution has a node [see Eq. (3.102)]. But it is also close to this pole that λ is maximal, as seen in Fig. 3.5, and thus it is around this value that one finds the larger non-zero contributions of Ξ_3 to Ξ . As a consequence of these interplays, the total Ξ function, as seen in the full line of Fig. 3.4, is continuous around the quasi-particle energy.

Let us take a look at the regions which are far away from the quasi-particle energy. For these energies, λ tends to become very small. As a consequence, Ξ_2 and Ξ_3 are almost negligible. In addition, both contributions have opposite signs in the whole energy range and thus they cancel each other to some extent in the high (very positive) and low (very negative) energy regions. The total Ξ function is thus a continuous step-like function which yields zero for energies below $\varepsilon_{qp}(k)$ and 2π for energies far above the quasi-particle pole. When the energies are close to this value, the different contributions to Ξ become active and this increases rapidly from 0 to 2π in a continuous way.

Now that the energy dependence of the Ξ function has been explored, one

can easily infer some properties of the $\mathcal{B}(k, \omega)$ function, which is defined as its derivative with respect to the energy, Eq. (3.99). It is quite clear that, since Ξ is almost constant far away from the quasi-particle energy, the \mathcal{B} spectral function will be very small for energies which are not close to this energy. The non-zero contributions of this function will be concentrated around $\varepsilon_{qp}(k)$ where, in addition, since Ξ is a monotonously increasing function of ω , it will be positive. More interestingly, from the limiting values of the Ξ function at high and low energies, one can derive the following sum rule:

$$\int_{-\infty}^{\infty} \frac{d\omega}{2\pi} \mathcal{B}(k, \omega) = \frac{1}{2\pi} \Xi(k, \omega) \Big|_{-\infty}^{\infty} = 1, \quad (3.105)$$

which is exactly the same sum rule that the usual spectral function fulfills. Furthermore, $\mathcal{B}(k, \omega)$ is also peaked around the quasi-particle energy and they describe somehow the effects of the energy-dependent correlations in two different observables (the entropy for \mathcal{B} , the momentum distribution for \mathcal{A}). All in all, both functions share some common properties, which will be studied in more detail in Chapter 6.

In the previous section the partition function has been rewritten in terms of the convolution of a statistical factor and a B function that accounts for the correlations in the formalism [see Eq. (3.85)]. One can find an expression for the entropy of the correlated system starting from this expression. Considering once again that the temperature derivative only affects the explicit temperature factors and using the fact that:

$$\sigma(\omega) = \frac{\partial}{\partial T} T \ln [1 + e^{-\beta(\omega-\mu)}], \quad (3.106)$$

one obtains the following equation for the entropy:

$$S = \sum_k \int_{-\infty}^{\infty} \frac{d\omega}{2\pi} \sigma(\omega) B(k, \omega) - \frac{\partial}{\partial T} T \Phi. \quad (3.107)$$

In this case, the entropy should be calculated from the B spectral function and the Φ functional. The B function has been already computed by taking the energy derivative of Eq. (3.86) before the imaginary part is computed. Here, the inverse procedure will be followed and the imaginary part will be taken prior to the derivative. One obtains the following relation between Ξ and B :

$$B(k, \omega) = \frac{\partial}{\partial \omega} \Xi(k, \omega) + \frac{\partial \text{Re} \Sigma(k, \omega)}{\partial \omega} \mathcal{A}(k, \omega) + \text{Re} \Sigma(k, \omega) \frac{\partial \mathcal{A}(k, \omega)}{\partial \omega}. \quad (3.108)$$

This can be used to find a relation between B and \mathcal{B} . Note, in particular, that the B_3 contribution to B in Eq. (3.89) equals the last two terms of the previous equation. It is then clear that, since \mathcal{B} is defined as the partial derivative of Ξ with

respect to the energy, the following relation between the B and the \mathcal{B} spectral functions holds:

$$\begin{aligned}\mathcal{B}(k, \omega) &= B_1(k, \omega) + B_2(k, \omega) \\ &= \mathcal{A}(k, \omega) \left[1 - \frac{\partial \text{Re} \Sigma(k, \omega)}{\partial \omega} \right] + \frac{\partial \text{Re} \mathcal{G}(k, \omega)}{\partial \omega} \Gamma(k, \omega).\end{aligned}\quad (3.109)$$

The previous equation is also important because it gives \mathcal{B} as a function of \mathcal{A} and the real and imaginary parts of the propagator explicitly. Note, in addition, that the first term in the previous expression equals the spectral function times something that is very close to the \mathcal{Z} -factor defined in Eq. (2.136). Actually, in a no-width approximation as that of Eq. (2.142), the \mathcal{Z} -factor appearing in front of the delta function would be exactly canceled. As a consequence of this cancellation, the effects of correlations in the \mathcal{Z} -factor (such as the depletion of the population of states due to re-scattering) do not appear in the entropy of the system. In such an approximation, the third term of Eq. (3.109) would become zero and the \mathcal{B} function would become a delta function at the quasi-particle energy:

$$\mathcal{B}(k, \omega) = (2\pi)\delta[\omega - \varepsilon_{qp}(k)], \quad (3.110)$$

which would immediately imply that the entropy is given by the usual quasi-particle expression,

$$S^{QP} = \sum_k \sigma[\varepsilon_{qp}(k)]. \quad (3.111)$$

The following decomposition of the dynamical quasi-particle:

$$S^{DQ} = S_1^A + S_2^A, \quad (3.112)$$

in the two terms:

$$S_1^A = \sum_k \int_{-\infty}^{\infty} \frac{d\omega}{2\pi} \sigma(\omega) \mathcal{A}(k, \omega) \quad (3.113)$$

and

$$S_2^A = \sum_k \int_{-\infty}^{\infty} \frac{d\omega}{2\pi} \sigma(\omega) \left\{ \frac{\partial \text{Re} \mathcal{G}(k, \omega)}{\partial \omega} \Gamma(k, \omega) - \mathcal{A}(k, \omega) \frac{\partial \text{Re} \Sigma(k, \omega)}{\partial \omega} \right\}, \quad (3.114)$$

is also illustrative. This justifies somehow a naive generalization to the expression of the entropy that has been used in the literature [Coh60; Sed07] and which consists in approximating the entropy by Eq. (3.113). This is, of course, not based on basic principles, but it would be a natural extension of Eq. (2.72) to the case of the entropy. The dynamical quasi-particle entropy, however, goes beyond the naive quasi-particle approach. It introduces the corrections of Eq. (3.114) which,

as shall be seen later on, are non-negligible. Moreover, the contribution of each of the two terms can be very different depending on the density and temperature regimes considered.

The discussion, up to this point, has been limited to the S^{DQ} term of Eq. (3.94). Nothing has been said so far about the S' contribution of Eq. (3.95). This factor is supposed to account for high order correlations and, as it was shown in Ref. [Car75], it arises from the cancellation between two very similar terms, *i.e.* the temperature derivative of $T\Phi$ and the second term of Eq. (3.95). The only non-zero contributions that survive this cancellation come from terms in the perturbation expansion of Ω that have an even number of vanishing energy denominators. These were extensively analyzed in Ref. [Car75] and they were indeed identified as the terms that lead to the $T^3 \ln T$ dependence of the specific heat of He³. The diagrammatic analysis of this quantity is however quite complicated and shall not be discussed here. The most important conclusion that will be borrowed from Ref. [Car75] is that the terms with vanishing energy denominators yield δ functions in the diagrammatic contributions to the entropy. These correspond to real transitions in the system which, however, become negligible at low temperatures, due to phase space restrictions. All in all, S' is small as long as the calculations are done in the low temperature regime. For the case of nuclear matter, temperatures up to $T = 20$ MeV will be taken into account, which can be considered sufficiently small in the nuclear physics context.

The S' contribution will only be computed exactly within the Hartree-Fock theory in the following chapter. It will yield exactly zero, as expected for a quasi-particle approximation without vanishing energy denominators. For the more sophisticated computations of the SCGF method, S' will be considered to be negligible. In this way, the formalism will be simplified because there will be no need to evaluate the Φ functional. This assumption, of course, needs to be validated, and that will be done in the final part of this Thesis. Neglecting S' will lead to thermodynamical consistent results, and this will be taken as a confirmation of the fact that this contribution is small in the density and temperature range explored. The fact that S' is so small within the ladder approximation might also be taken as a justification of the idea that short-range correlations are not so important in the calculation of the Φ functional (and the S' contribution), which might be more affected by long-range correlations as well as by finite size effects. In addition, since it is precisely from the S' contribution that all the anomalous temperature dependences (of the type $T^3 \ln T$) of the entropy arise, restricting the calculations to the dynamical quasi-particle entropy S^{DQ} will only give analytical ($S \sim T, T^3$) temperature dependences.

Finally, as it has been previously noted, the Φ -functional approach can be used in the description of non-equilibrium systems. Within those approaches, it is important to find quantities that behave somehow like an entropy in equilibrium systems. These quantities must satisfy some kind of H -theorem that guarantees

that their time evolution is such that they always increase with time. In Ref. [Iva00], it was shown that, within certain Φ -derivable approaches out of equilibrium, an H -theorem could indeed be proved for a non-equilibrium kinetic entropy expressed in terms of the full Green's function and the self-energy. When considering systems in thermal equilibrium, this kinetic entropy reduces to the sum of S^{DQ} , the local or Markovian part of the kinetic entropy (S_{loc} in the language of Ref. [Iva00]), plus S' , the memory or non-Markovian part of the entropy (S_{mem}). This expression, thus, coincides with the entropy of Eq. (3.93) and justifies the different physical origin of the S^{DQ} and S' contributions.

Chapter 4

Hartree-Fock Approximation

The first approximation to the nuclear many-body problem that will be treated in this Thesis is the Hartree-Fock (HF) approach. Although the results obtained within this approximation from microscopic NN potentials are not realistic, it will be instructive to consider this method from first grounds. This will serve as an introduction to some interesting concepts (such as self-consistent renormalization) that will be used in the following chapters. In addition, this more or less easy-to-treat approximation is a testing ground for the more sophisticated many-body methods that will be used in the following chapters and allows for more transparent conclusions. Furthermore, in some fields of physics, especially in atomic physics, where correlations are not as relevant as in strongly interacting matter, the HF approximation is extensively used [Fis77]. In nuclear physics, the HF approximation is employed whenever one works with phenomenological density-dependent potentials, such as the Skyrme or the Gogny interactions, which mimic some of the many-body correlations that are lacking in the approach. In this chapter, the extension to finite temperature of the HF approach will be thoroughly described. The microscopic as well as the thermodynamical properties obtained within this approximation will provide us with a first look to the different aspects of the nuclear matter problem at finite temperatures.

4.1 Formulation in terms of Σ

In terms of the self-energy, the HF approximation arises from the two lowest order diagrams of Fig. 4.1. An analytical expression for these diagrams can be derived using the Feynman rules for the one-body propagator of Appendix B. From Eq. (B.3), the self-energy is found by eliminating the two free propagators in the extremes. This yields the following energy-independent expression:

$$\Sigma_{HF}(k) = \frac{-i}{-i\beta} \sum_{\nu_1} e^{z_{\nu_1}\eta} \int \frac{d^3k_1}{(2\pi)^3} \langle \mathbf{k}\mathbf{k}_1 | V | \mathbf{k}\mathbf{k}_1 \rangle_A \mathcal{G}_0(k_1, z_{\nu_1}). \quad (4.1)$$

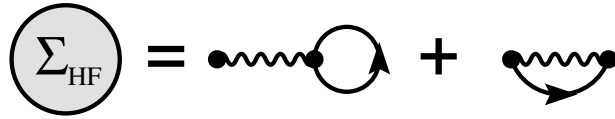


Figure 4.1: *Diagrammatic representation of the Hartree-Fock self-energy.*

The sum over Matsubara frequencies can be performed analytically with the help of the techniques discussed in Appendix C. To compute it, the sum is transformed into an integral by applying Cauchy’s theorem to a complex function formed by the propagator times $-\beta f(z)$. This last function has poles of unit residue at the Matsubara frequencies, which is the reason why one can transform the sum into an integral. The circuit C (see Fig. C.1) over which one integrates encircles the Matsubara frequencies in the positive sense. One can then deform this circuit to another one in which only the pole of the free single-particle propagator at $z = \varepsilon_0(k)$ is encircled in the negative sense. Applying the Cauchy theorem to this pole, one obtains the result:

$$\frac{1}{\beta} \sum_{\nu_1} e^{z_{\nu_1} n} \mathcal{G}_0(k_1, z_{\nu_1}) = f[\varepsilon_0(k_1)], \quad (4.2)$$

which inserted in the expression for the self-energy yields:

$$\Sigma_{HF}(k) = \int \frac{d^3 k_1}{(2\pi)^3} \langle \mathbf{k} \mathbf{k}_1 | V | \mathbf{k} \mathbf{k}_1 \rangle_A f[\varepsilon_0(k_1)]. \quad (4.3)$$

This term has a well-known intuitive explanation. The direct self-energy (which would arise from considering only the direct term of the matrix element of the two-body interaction) is the “strength” that a fermion of momentum k feels when it interacts (via the bare interaction) with the rest of occupied states of momentum k_1 (note the occupation factor $f[\varepsilon_0(k_1)]$). There is also a physical interpretation for the exchange contribution: an initial nucleon of momentum k scatters with the medium and ends up in a momentum state k_1 . In its turn, a nucleon from the medium with initial momentum k_1 scatters to a momentum k and, since both nucleons are indistinguishable, this process has to be considered in the calculation of the self-energy. This also justifies the name of the term, since the initial nucleon has been *exchanged* for the final one. In terms of the single-particle propagator, these two processes are shown in Fig. 2.3.

The HF approximation, however, goes beyond such a simple intuition. Computing the self-energy is only the first step to obtain the full HF propagator, which should be obtained from Dyson’s equation:

$$\mathcal{G}_{HF}(k, z) = \frac{1}{z - \frac{k^2}{2m} - \Sigma_{HF}(k)}. \quad (4.4)$$

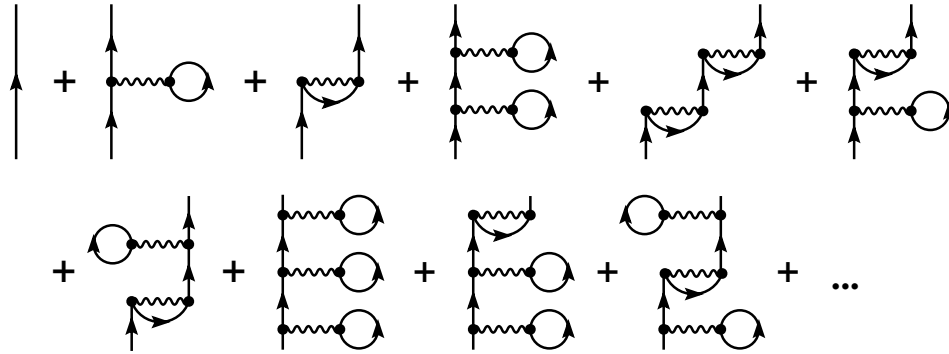


Figure 4.2: *Complete single-particle propagator in the Hartree-Fock approximation.*

Diagrammatically speaking, Dyson's equation sums the expansion of the Green's function obtained from the iteration of irreducible self-energy pieces. Thus, in the propagator of the HF approximation, not only diagrams (a) and (b) of Fig. 2.3, but also those of Fig. 4.2 are included. Note that by means of Dyson's equation a formal sum over an infinite series of diagrams, which includes terms to all orders in the perturbation expansion, has been performed. Among these diagrams one finds the iterated second order diagrams (a)-(d) of Fig. 2.4 as well as some other contributions to higher orders. Therefore, the HF propagator does not only account for the effect of a single (direct and exchange) scattering due to the bare potential, but it also includes a whole subset of infinite possible iterated scatterings (with mixed direct and exchange contributions) between the initial and the final nucleonic states.

4.2 Self-Consistent Hartree-Fock

The HF approximation sums an infinite series of diagrams when the one-body propagator is computed by means of Dyson's equation. Nevertheless, as already explained in Chapter 2, one can sum a whole new bunch of diagrams in a relatively simple way by means of the self-consistent renormalization procedure. In terms of diagrams, this amounts to replacing all the free propagators in the self-energy diagrams by dressed propagators. For the HF approach, this is shown in detail in Fig. 4.3.

As commented in Section 2.7, self-consistent renormalization is implemented formally by means of an iterative procedure. Let us consider this procedure for the HF case. In a first step, one would compute a self-energy $\Sigma^{(1)}$ according to the diagrams of Fig. 4.1. Then, using Dyson's equation, the single-particle propagator of Fig. 4.2 would be obtained. Now, if one intends to be truly self-consistent, this

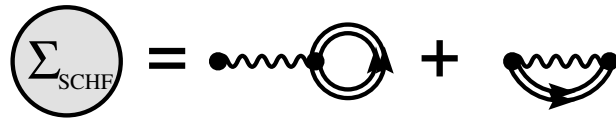


Figure 4.3: *Diagrammatic representation of the Self-Consistent Hartree-Fock self-energy.*

propagator (instead of the free one) should be used to compute the self-energy in a second iteration. The self-energy $\Sigma^{(2)}$ would then be used to compute the propagator by means of Dyson's equation. This could be inserted in the definition of the self-energy and a new $\Sigma^{(3)}$ is obtained, and so on.

In principle, as it has been already mentioned, the main difference between the SCHF and the usual HF method should come from the substitution of the bare propagator in the self-energy, Fig. 4.1, for a dressed propagator, like in Fig. 4.3. Yet, when one considers iteration by iteration the diagrams that come out in the self-consistent procedure, as it is done in Fig. 4.4, one finds new diagrams that are not contained in the original HF self-energy. Let us start with the $\Sigma^{(1)}$ contribution of Fig. 4.4, which contains the two lowest-order diagrams. A new propagator is computed from Dyson's equation and, by closing a dressed line and attaching an interaction to it, one generates the second iteration self-energy, $\Sigma^{(2)}$. It is easy to see that, in this procedure, new self-energy diagrams (with respect to the HF approach) appear. These are produced by nesting two first order diagrams, for instance. Among these, one finds diagrams (e)-(h) of Fig. 2.4. Thus, with the help of the self-consistent procedure one can generate eight of the ten second order diagrams... Already at the SCHF level! In addition to these, a whole bunch of higher order diagrams (including self-energy insertions as well as nested diagrams) are formed. When generating these contributions, however, one should always take into account that the irreducible self-energy is formed by 1PI diagrams. Any attempt to include reducible diagrams should be avoided, for all the 1PR diagrams are already generated through the iteration of Dyson's equation.

If this procedure could be carried out infinitely, the final Green's function would be a self-consistent one, in the sense that the skeleton diagrams of the self-energy would be expressed in terms of propagators which would be equivalent to the fully dressed propagator within that given approximation. In the case sketched in Fig. 4.4, for instance, if the full infinite self-consistent procedure could be carried out, the final result would be that of the diagram in Fig. 4.3 and the self-energy would be given in terms of the full propagator, instead of the bare one. The dressing of these lines involves necessarily a self-consistent procedure and this is why one calls this the *Self-Consistent Hartree-Fock* (SCHF) approach.

In addition to summing a more complete series of diagrams, the SCHF approx-

imation also solves a “conceptual” inconsistency of the HF approach. Consider once again diagram (a) of Fig. 2.3. The fermion in the propagator line interacts with another fermion from inside the system. Yet, this second particle is described in terms of a free propagator. It is clear that, to be fully consistent, one should use a full single-particle propagator instead of a bare one or, in other words, one should dress the internal propagator in all the self-energy diagrams. And this is precisely what the SCHF method achieves. Moreover, one expects this self-consistent method to be especially required at larger densities, where in-medium particles need to be necessarily dressed. The need of self-consistency can be intuitively understood from the following reasoning. The propagation of a fermion inside a many-body system is given in terms of the one-body Green’s function. Yet, this propagation modifies the properties of the surrounding fermions, which are also described by Green’s functions. Thus a determination of the full Green’s function needs of a self-consistent procedure where both the propagated particle and its effects on the surroundings are taken into account at the same level.

It has already been mentioned that to find the exact SCHF self-energy one should perform, in principle, an infinite number of iterations. In terms of the analytical equations, however, one can write down easily the final result for the self-energy in the SCHF approximation. Once convergence is reached, the only difference between the SCHF self-energy and the HF self-energy comes from the substitution, in Eq. (4.1), of the free propagator \mathcal{G}_0 for a dressed propagator \mathcal{G} . This corresponds of course to the analytical expression of the diagrams of Fig. 4.3. One can then perform the Matsubara summation to find the result:

$$\Sigma_{SCHF}(k) = \int \frac{d^3k_1}{(2\pi)^3} \langle \mathbf{k}\mathbf{k}_1 | V | \mathbf{k}\mathbf{k}_1 \rangle_A f[\varepsilon_{SCHF}(k_1)]. \quad (4.5)$$

The main difference between the previous equation and Eq. (4.1) comes from the single-particle spectrum, $\varepsilon(k)$, in the Fermi-Dirac distribution. While in the HF method the kinetic spectrum $\varepsilon_0(k) = \frac{k^2}{2m}$ is used, in the SCHF approach one uses a medium-modified spectrum, $\varepsilon_{SCHF}(k) = \frac{k^2}{2m} + \Sigma_{SCHF}(k)$. The SCHF self-energy is a part of this spectrum and thus can be thought of as a kind of interaction single-particle energy. This is the so-called mean-field, already introduced in Chapter 1, which represents the mean interaction energy that a fermion feels because of the presence of the remaining fermions in the system.

4.3 Formulation in terms of \mathcal{G}_{II}

There is an equivalent formulation of the SCHF approximation which is not based on applying diagrammatic “intuition” to the self-energy. Instead, a decoupling of the equation of motion for the one-body propagator is performed at the two-body level. Moreover, this procedure includes self-consistent effects from the beginning.

4.3. FORMULATION IN TERMS OF \mathcal{G}_{II}

First Iteration

$$\Sigma^{(1)} = \text{diagram 1} + \text{diagram 2}$$

$$\mathbb{G}^{(1)} = \frac{1}{\begin{array}{c} \uparrow \\ -1 \\ \uparrow \end{array} - \Sigma^{(1)}} = \text{diagram 1} + \text{diagram 2} + \text{diagram 3} + \text{diagram 4} + \text{diagram 5} + \text{diagram 6} + \text{diagram 7} + \text{diagram 8} + \text{diagram 9} + \text{diagram 10} + \dots$$

Second Iteration

$$\Sigma^{(2)} = \text{diagram 1} + \text{diagram 2} = \text{diagram 1} + \text{diagram 2} + \text{diagram 3} + \text{diagram 4} + \text{diagram 5} + \text{diagram 6} + \text{diagram 7} + \text{diagram 8} + \dots$$

$$\mathbb{G}^{(2)} = \frac{1}{\begin{array}{c} \uparrow \\ -1 \\ \uparrow \end{array} - \Sigma^{(2)}} = \mathbb{G}^{(1)} + \text{diagram 1} + \text{diagram 2} + \text{diagram 3} + \text{diagram 4} + \text{diagram 5} + \text{diagram 6} + \text{diagram 7} + \text{diagram 8} + \text{diagram 9} + \text{diagram 10} + \text{diagram 11} + \text{diagram 12} + \text{diagram 13} + \text{diagram 14} + \text{diagram 15} + \text{diagram 16} + \text{diagram 17} + \text{diagram 18} + \text{diagram 19} + \text{diagram 20} + \text{diagram 21} + \text{diagram 22} + \text{diagram 23} + \text{diagram 24} + \text{diagram 25} + \text{diagram 26} + \text{diagram 27} + \text{diagram 28} + \text{diagram 29} + \text{diagram 30} + \text{diagram 31} + \text{diagram 32} + \text{diagram 33} + \text{diagram 34} + \text{diagram 35} + \text{diagram 36} + \text{diagram 37} + \text{diagram 38} + \text{diagram 39} + \text{diagram 40} + \text{diagram 41} + \text{diagram 42} + \text{diagram 43} + \text{diagram 44} + \text{diagram 45} + \text{diagram 46} + \text{diagram 47} + \text{diagram 48} + \text{diagram 49} + \text{diagram 50} + \text{diagram 51} + \text{diagram 52} + \text{diagram 53} + \text{diagram 54} + \text{diagram 55} + \text{diagram 56} + \text{diagram 57} + \text{diagram 58} + \text{diagram 59} + \text{diagram 60} + \text{diagram 61} + \text{diagram 62} + \text{diagram 63} + \text{diagram 64} + \text{diagram 65} + \text{diagram 66} + \text{diagram 67} + \text{diagram 68} + \text{diagram 69} + \text{diagram 70} + \text{diagram 71} + \text{diagram 72} + \text{diagram 73} + \text{diagram 74} + \text{diagram 75} + \text{diagram 76} + \text{diagram 77} + \text{diagram 78} + \text{diagram 79} + \text{diagram 80} + \text{diagram 81} + \text{diagram 82} + \text{diagram 83} + \text{diagram 84} + \text{diagram 85} + \text{diagram 86} + \text{diagram 87} + \text{diagram 88} + \text{diagram 89} + \text{diagram 90} + \text{diagram 91} + \text{diagram 92} + \text{diagram 93} + \text{diagram 94} + \text{diagram 95} + \text{diagram 96} + \text{diagram 97} + \text{diagram 98} + \text{diagram 99} + \text{diagram 100} + \dots$$

Third Iteration

$$\Sigma^{(3)} = \text{diagram 1} + \text{diagram 2} = \text{diagram 1} + \text{diagram 2} + \text{diagram 3} + \text{diagram 4} + \text{diagram 5} + \text{diagram 6} + \text{diagram 7} + \text{diagram 8} + \text{diagram 9} + \text{diagram 10} + \text{diagram 11} + \text{diagram 12} + \text{diagram 13} + \text{diagram 14} + \text{diagram 15} + \text{diagram 16} + \text{diagram 17} + \text{diagram 18} + \text{diagram 19} + \text{diagram 20} + \text{diagram 21} + \text{diagram 22} + \text{diagram 23} + \text{diagram 24} + \text{diagram 25} + \text{diagram 26} + \text{diagram 27} + \text{diagram 28} + \text{diagram 29} + \text{diagram 30} + \text{diagram 31} + \text{diagram 32} + \text{diagram 33} + \text{diagram 34} + \text{diagram 35} + \text{diagram 36} + \text{diagram 37} + \text{diagram 38} + \text{diagram 39} + \text{diagram 40} + \text{diagram 41} + \text{diagram 42} + \text{diagram 43} + \text{diagram 44} + \text{diagram 45} + \text{diagram 46} + \text{diagram 47} + \text{diagram 48} + \text{diagram 49} + \text{diagram 50} + \text{diagram 51} + \text{diagram 52} + \text{diagram 53} + \text{diagram 54} + \text{diagram 55} + \text{diagram 56} + \text{diagram 57} + \text{diagram 58} + \text{diagram 59} + \text{diagram 60} + \text{diagram 61} + \text{diagram 62} + \text{diagram 63} + \text{diagram 64} + \text{diagram 65} + \text{diagram 66} + \text{diagram 67} + \text{diagram 68} + \text{diagram 69} + \text{diagram 70} + \text{diagram 71} + \text{diagram 72} + \text{diagram 73} + \text{diagram 74} + \text{diagram 75} + \text{diagram 76} + \text{diagram 77} + \text{diagram 78} + \text{diagram 79} + \text{diagram 80} + \text{diagram 81} + \text{diagram 82} + \text{diagram 83} + \text{diagram 84} + \text{diagram 85} + \text{diagram 86} + \text{diagram 87} + \text{diagram 88} + \text{diagram 89} + \text{diagram 90} + \text{diagram 91} + \text{diagram 92} + \text{diagram 93} + \text{diagram 94} + \text{diagram 95} + \text{diagram 96} + \text{diagram 97} + \text{diagram 98} + \text{diagram 99} + \text{diagram 100} + \dots$$

Figure 4.4: First, second and third iterations in the Self-Consistent Hartree-Fock approach. The super-indices (1), (2) and (3) denote the iteration in which the self-energy and the one-body propagator have been computed.

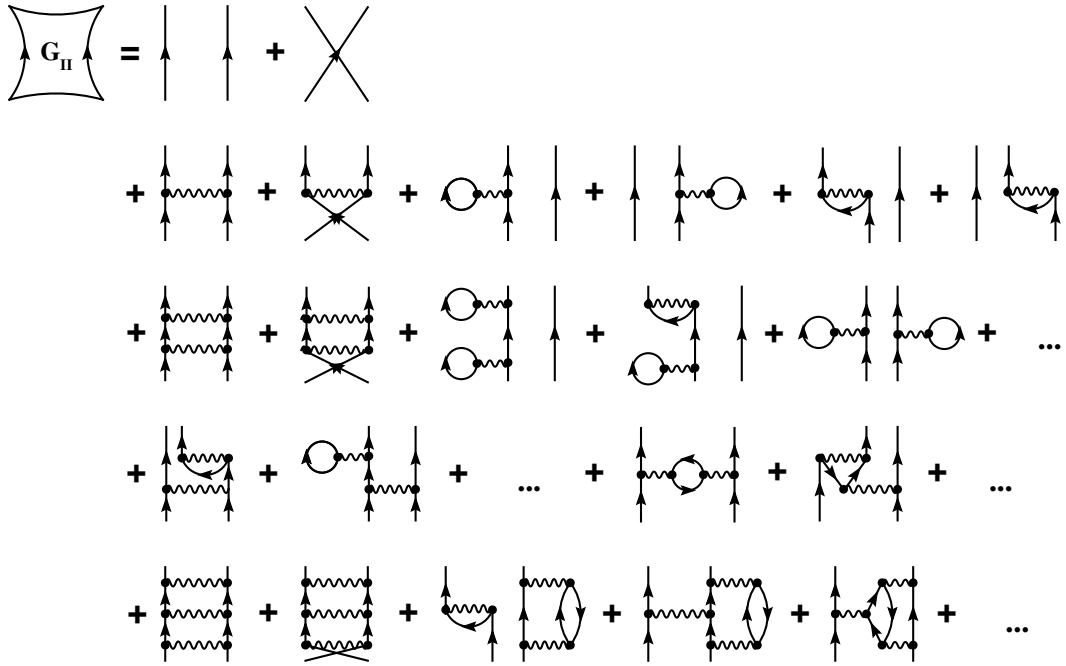


Figure 4.5: *Diagrammatic representation of the two-body propagator. All the first order and some second and third order diagrams are shown.*

One can however see that the two formulations (diagrammatic and decoupling approach) are equivalent. Indeed, for the HF approach one can draw the decoupling in terms of diagrams, which allows for an easy comparison between this and the purely diagrammatic method. As explained thoroughly in Refs. [Mat71; Mat92], some decouplings of the hierarchy of the equations of motion for the propagators can lead to equivalent diagrammatic methods, where partial sums of infinite diagrams are performed. Note, however, that not all the decouplings lead to suitable diagrammatic sums.

Consider the equation of motion for the one-body propagator, Eq. (2.99). Using the free propagator, one can recast the differential equation into an equivalent integral equation:

$$\mathcal{G}(\mathbf{1}, \mathbf{1}') = \mathcal{G}_0(\mathbf{1}, \mathbf{1}') - i \int d\bar{\mathbf{2}} \int d\bar{\mathbf{3}} \mathcal{G}_0(\mathbf{1}, \bar{\mathbf{2}}) V(\bar{\mathbf{2}} - \bar{\mathbf{3}}) \mathcal{G}_H(\bar{\mathbf{3}}\bar{\mathbf{2}}; \bar{\mathbf{3}}^+ \bar{\mathbf{1}}'). \quad (4.6)$$

To solve the equation for the one-body propagator one needs as an input the two-body Green's function. This is sometimes also called a four-point function, because it has two "input" space-time points as well as two "outputs". The two-body Green's function is shown in terms of diagrams in Fig. 4.5. In general, the two-body propagator will include all kinds of complex processes involving a couple of one-body excitations. These two individual propagators can either be disconnected or

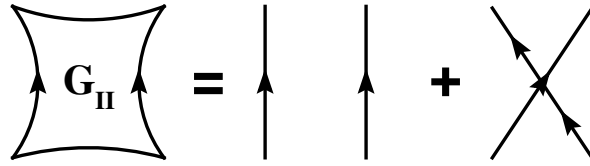


Figure 4.6: *Diagrammatic representation of the decoupling of the two-body propagator in terms of free one-body propagators in the Hartree-Fock approximation.*

connected. In the first case, the excitations propagate independently of each other but interacting with the medium. In the case of connected contributions, the two one-body propagators can either be connected by single or multiple interactions or, in more complex processes, by more complicated medium polarizations. Fig. 4.5 gives an insight on the variety of diagrams that contribute to the two-body Green's function. The multiple topologies and structures that appear already at second and third order give a hint on the difficulty of computing all the contributions to the two-body propagator in any many-body approach.

The lowest order approximation to \mathcal{G}_{II} that one can think of, is the truncation of the diagrammatic expansion in its two first terms. The two-body propagator is then given by the direct and exchange propagation of two particles that do not interact among each other neither with the medium, as depicted in Fig. 4.6. By considering these two contributions, the propagation of the two particles in the medium is taken to be independent, in the sense that the two one-body propagators are disconnected. Such an approach might be useful for physical systems where the densities are low and the interactions are relatively weak. In this case, particles will not “feel” the presence of the rest of the system and thus a pair can be treated as propagating independently. For systems at higher densities, however, it would be more sensible to decouple the two-body propagator in terms of two independent propagators which are dressed, as shown in Fig. 4.7. In this way, the equations are kept at a manageable level and the single-particle propagators include already the infinite sum carried out for the self-consistent procedure. Note that this is more sophisticated than the guess of Fig. 4.6, but is still quite simplistic because it neglects all the interaction effects between the pair of particles that propagate in the medium. This justifies somehow why this approximation does not work for nuclear matter, where the densities are relatively high and in addition the interactions are qualitatively strong.

Consider thus that one does not take into account any correlation at the two-particle level for the two-body propagator. The two-body Green's function is then simply given by the product of two (dressed) single-particle propagators:

$$\mathcal{G}_{II}(\mathbf{1}\mathbf{2}; \mathbf{1}'\mathbf{2}') = \mathcal{G}(\mathbf{1}, \mathbf{2})\mathcal{G}(\mathbf{1}', \mathbf{2}') - \mathcal{G}(\mathbf{1}, \mathbf{2}')\mathcal{G}(\mathbf{1}', \mathbf{2}), \quad (4.7)$$

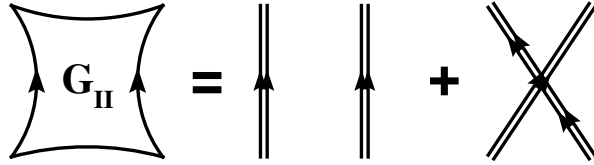


Figure 4.7: *Diagrammatic representation of the decoupling of the two-body propagator in terms of dressed one-body propagators in the Self-Consistent Hartree-Fock approximation.*

where the symmetry $\mathcal{G}_{II}(\mathbf{1}\mathbf{2}; \mathbf{1}'\mathbf{2}') = -\mathcal{G}_{II}(\mathbf{2}\mathbf{1}; \mathbf{1}'\mathbf{2}')$ has been used to find the relative sign of the exchange term. Using the definition of the self-energy, Eq. (2.115), one can find a generic expression for the HF self-energy:

$$\Sigma(\mathbf{1}, \mathbf{1}') = -i\delta(\mathbf{1} - \mathbf{1}') \int d\mathbf{2} V(\mathbf{1} - \mathbf{2}) \mathcal{G}(\mathbf{2}, \mathbf{2}^+) + iV(\mathbf{1} - \mathbf{1}') \mathcal{G}(\mathbf{1}, \mathbf{1}'). \quad (4.8)$$

The delta function signals the fact that the self-energy is an instantaneous function of time in the HF approximation. Fourier transforming the space and time variables of the previous expression, one finds precisely Eq. (4.5). Thus, the self-energy of the SCHF case can be recovered from the “lowest-order” decoupling of the hierarchy of the equations of motion (lowest in the sense that the propagation of the particles is treated as independent). Note also that, although this approach has been presented as a diagrammatic expansion for \mathcal{G}_{II} , it is indeed not of a true diagrammatic nature. Instead, one could have stated the same ideas by simply making the ansatz of Eq. (4.7). This ansatz is a truncation of the equation of motion for the one-body propagator and thus its origin is different to the diagrammatic approach of the previous section. In the following chapter, the ladder approximation will also be derived from a decoupling approximation.

4.4 Partial wave expansion

Up to this point, the discussions about many-body approaches, diagrammatic techniques and Green’s functions have been quite generic. In this section, in contrast, a first application to the nuclear matter case will be discussed. Starting from a microscopic NN interaction, which will be decomposed into partial waves, the SCHF approximation is explicitly calculated for the nuclear matter case. As explained before, this is an infinite homogeneous system of nucleons at fixed density and temperature. If not mentioned otherwise, the system is supposed to be saturated in spin (the densities of the spin up nucleons is the same as that of the spin down nucleons), as well as in isospin (the system is composed by the same number of pro-

tons and neutrons). In this case, one speaks of *symmetric* nuclear matter, whereas *asymmetric* nuclear matter contains a certain degree of isospin asymmetry.

A nucleon immersed in nuclear matter is characterized by a series of quantum numbers. Since nuclear matter is an infinite system, the single-particle momentum k is an appropriate quantum number. In addition, one has to specify a given spin s as well as its third component, that will be denoted with the Greek equivalent character, σ . For the isospin degree of freedom, one has to specify the total isospin t and the third component τ . A nucleon has a total spin $s = 1/2$ and a total isospin $t = 1/2$, and thus sometimes these will not be specified. The third component of isospin, however, describes which nucleonic component is studied: $\tau = -1/2$ corresponds to a neutron, while $\tau = 1/2$ corresponds to a proton. Thus, the third component needs to be considered explicitly in the calculations.

All of these quantum numbers are associated to single-particle nucleonic states of the system. Yet, it turns out that, in the nuclear many-body case, a coupled two-nucleon basis that takes advantage of the symmetries of the NN potential is much more convenient. The quantum numbers in this two-nucleon basis will be denoted by capital letters. For instance, the total angular momentum will be written J and its third component m_J . At some point, a change from the uncoupled (single-particle) basis, in which Feynman diagrams are formulated, to the coupled (two-particle) basis, in which the NN potential is given, will have to be introduced. Once an expression for the self-energy in terms of the NN potential in the coupled basis is available, a partial wave decomposition of the NN interaction will also be performed. In that way, one can handle easily the NN potential because, for a given partial wave, it will only depend on one diagonal relative momentum.

Consider the SCHF self-energy for a nucleon with third spin-isospin components σ and τ . It consists of a sum over all the allowed internal momenta, spin and isospin diagonal states, \mathbf{k}' , σ' and τ' :

$$\Sigma_{\sigma\tau}(k) = \sum_{\sigma'\tau'} \int \frac{d^3k'}{(2\pi)^3} \langle \mathbf{k}\sigma\tau, \mathbf{k}'\sigma'\tau' | V | \mathbf{k}\sigma\tau, \mathbf{k}'\sigma'\tau' \rangle_A n(k'). \quad (4.9)$$

Note that the label ‘‘SCHF’’ has been dropped for convenience and that in the previous expression the momentum distribution $n(k)$ is given by the Fermi-Dirac distribution computed at the quasi-particle energies, $f[\varepsilon_{SCHF}(k)]$. For symmetric nuclear matter, it is useful to take an average over the external spin-isospin quantum numbers σ and τ , with their corresponding degeneracy factors:

$$\begin{aligned} \Sigma(k) &= \frac{1}{(2s+1)(2t+1)} \sum_{\sigma\tau} \Sigma_{\sigma\tau}(k) \\ &= \frac{1}{(2s+1)(2t+1)} \sum_{\sigma\tau} \sum_{\sigma'\tau'} \int \frac{d^3k'}{(2\pi)^3} \langle \mathbf{k}\sigma\tau, \mathbf{k}'\sigma'\tau' | V | \mathbf{k}\sigma\tau, \mathbf{k}'\sigma'\tau' \rangle_A n(k'). \end{aligned} \quad (4.10)$$

Let us now transform the matrix elements, given in terms of the single-particle momenta, \mathbf{k} and \mathbf{k}' , to states expressed in terms of the relative momentum, $\mathbf{q} =$

$\frac{1}{2}(\mathbf{k} - \mathbf{k}')$:

$$|\mathbf{k}\sigma\tau, \mathbf{k}'\sigma'\tau'\rangle_A = |\mathbf{q}; \sigma\tau, \sigma'\tau'\rangle - |-\mathbf{q}; \sigma'\tau', \sigma\tau\rangle. \quad (4.11)$$

Note that the direct and exchange components of the ket have been expressed separately. Furthermore, the kets on the right-hand-side of the previous equation should include an explicit dependence on the center-of-mass momentum which, however, has been omitted because the NN potential does not depend on this quantity. This is the first step in the transformation from the single-particle to the two-nucleon coupled basis mentioned above. The next one is the introduction of the total spin, $\vec{S} = \vec{\sigma} + \vec{\sigma}'$, and total isospin, $\vec{T} = \vec{\tau} + \vec{\tau}'$, of the pair of nucleons. This is done with the help of the Clebsch-Gordan coefficients, $(jj'm_j m_{j'} | Jm_J)$, which connect the uncoupled basis, described in terms of the ‘‘single-particle’’ angular momenta j and j' , to the coupled basis, given in terms of the total angular momentum $\vec{J} = \vec{j} + \vec{j}'$:

$$\begin{aligned} |\mathbf{k}\sigma\tau, \mathbf{k}'\sigma'\tau'\rangle_A &= \sum_{S m_S} \sum_{T m_T} (s s' \sigma \sigma' | S m_S) (t t' \tau \tau' | T m_T) |\mathbf{q} S m_S T m_T\rangle \\ &\quad - \sum_{S m_S} \sum_{T m_T} (s' s \sigma' \sigma | S m_S) (t' t \tau' \tau | T m_T) |-\mathbf{q} S m_S T m_T\rangle. \end{aligned} \quad (4.12)$$

The kets in the previous equation still depend on the relative wave vector \mathbf{q} . One can decouple the ket’s dependence in the modulus q and the direction $\hat{\mathbf{e}}_q$ of this vector by means of the partial wave expansion:

$$|\mathbf{q}\rangle = \sum_{L=0}^{\infty} \sum_{m_L=-L}^L |q L m_L\rangle Y_{L m_L}^*(\hat{\mathbf{e}}_q), \quad (4.13)$$

where $Y_{L m_L}$ denotes the spherical harmonic of order L [Rin80]. The ket can then be rewritten as follows:

$$\begin{aligned} |\mathbf{k}\sigma\tau, \mathbf{k}'\sigma'\tau'\rangle_A &= \sum_{L m_L} \sum_{S m_S} \sum_{T m_T} |q L m_L S m_S T m_T\rangle \\ &\quad \times \left[(s s' \sigma \sigma' | S m_S) (t t' \tau \tau' | T m_T) Y_{L m_L}^*(\hat{\mathbf{e}}_q) \right. \\ &\quad \left. - (s' s \sigma' \sigma | S m_S) (t' t \tau' \tau | T m_T) Y_{L m_L}^*(-\hat{\mathbf{e}}_q) \right]. \end{aligned} \quad (4.14)$$

This expression can be further simplified by using the following property of the spherical harmonics:

$$Y_{L m_L}(\hat{\mathbf{e}}) = (-1)^L Y_{L m_L}(-\hat{\mathbf{e}}), \quad (4.15)$$

as well as the following relation for the Clebsch-Gordan coefficients:

$$(j j' m_j m_{j'} | J m_J) = (-1)^{J-j-j'} (j' j m_{j'} m_j | J m_J). \quad (4.16)$$

Note that when one applies this last equation to the case of the spin and isospin of the nucleon, one can profit from the fact that $s + s' = t + t' = 1$. With all this in mind, the ket can be expressed as:

$$|\mathbf{k}\sigma\tau, \mathbf{k}'\sigma'\tau'\rangle_A = \sum_{Lm_L} \sum_{Sm_S} \sum_{Tm_T} [1 - (-1)^{L+S+T}] |qLm_L Sm_S Tm_T\rangle \times (ss'\sigma\sigma'|Sm_S)(tt'\tau\tau'|Tm_T) Y_{Lm_L}^*(\hat{\mathbf{e}}_q). \quad (4.17)$$

The factor $[1 - (-1)^{L+S+T}]$ is now carrying all the restrictions imposed by the antisymmetrization of the ket state. This factor, which yields either zero or two, corresponds to a selection rule for the partial waves with

$$L + S + T = \text{odd}. \quad (4.18)$$

In other words, in the NN interaction all of those partial waves with an even $L + S + T$ sum will not need to be considered.

In Chapter 1, the properties of the NN interaction have been briefly sketched. Among these, the importance of the tensor component is remarkable. This component is characterized by the fact that it couples bras and kets with different angular momenta, L and L' . Thus the angular momentum L is not a good quantum number of the nuclear interaction. Instead, one introduces the *total angular momentum*, $\vec{J} = \vec{L} + \vec{S}$, which is indeed conserved by the NN force. A new recoupling is necessary to express the ket in terms of states with total angular momentum J :

$$|\mathbf{k}\sigma\tau, \mathbf{k}'\sigma'\tau'\rangle_A = \sum_{\substack{Jm_J \\ Lm_L}} \sum_{\substack{Sm_S \\ Tm_T}} [1 - (-1)^{L+S+T}] |qLSJm_J Tm_T\rangle (LSm_L m_S | Jm_J) \times (ss'\sigma\sigma'|Sm_S)(tt'\tau\tau'|Tm_T) Y_{Lm_L}^*(\hat{\mathbf{e}}_q). \quad (4.19)$$

The quantum numbers S , T and J as well as the third components m_J and m_T are conserved by the NN interaction. Yet the strong force can couple different partial waves, L and L' . It is thus clear that a NN matrix element can be written as:

$$\langle qLSJm_J Tm_T | V | q'L'S'J'm_J' T'm_T' \rangle = \delta_{SS'} \delta_{TT'} \delta_{JJ'} \delta_{m_T m_T'} \delta_{m_J m_J'} \langle q | V_{LL'}^{JST} | q' \rangle. \quad (4.20)$$

In the HF case, only matrix elements of the force which are diagonal in momentum are needed. Introducing the previous expressions for the bra and the ket in the coupled basis at both sides of the matrix elements of the interaction and using the delta functions to perform some trivial sums, the expression for the SCHF

self-energy reads:

$$\begin{aligned} \Sigma(k) = & \frac{1}{(2s+1)(2t+1)} \sum_{\substack{JST \\ LL'}} [1 - (-1)^{L+S+T}] \int \frac{d^3k'}{(2\pi)^3} \langle q | V_{LL'}^{JST} | q \rangle n(k') \\ & \times \sum_{m_S m_{S'}} \sum_{\sigma \sigma'} (s s' \sigma \sigma' | S m_S) (s s' \sigma \sigma' | S m_{S'}) \sum_{m_T} \sum_{\tau \tau'} (t t' \tau \tau' | T m_T) (t t' \tau \tau' | T m_T) \\ & \times \sum_{m_J} \sum_{m_L m_{L'}} (L S m_L m_S | J m_J) (L' S m_{L'} m_{S'} | J m_J) Y_{L m_L}(\hat{\mathbf{e}}_q) Y_{L' m_{L'}}^*(\hat{\mathbf{e}}_q). \end{aligned} \quad (4.21)$$

Most of the sums in the previous expressions can be easily carried out by exploiting the orthonormality condition for the Clebsch-Gordan coefficients:

$$\sum_{m_j m_{j'}} (j j' m_j m_{j'} | J m_J) (j j' m_j m_{j'} | J' m_{J'}) = \delta_{JJ'} \delta_{m_J m_{J'}}. \quad (4.22)$$

Consider, for instance, the sum over third spin components. This yields:

$$\sum_{\sigma \sigma'} (s s' \sigma \sigma' | S m_S) (s s' \sigma \sigma' | S' m_{S'}) = \delta_{SS'} \delta_{m_S m_{S'}}. \quad (4.23)$$

The same can be done for the sum over third isospin components, yielding a factor $(2T+1)$. All in all, the self-energy reads:

$$\begin{aligned} \Sigma(k) = & \frac{1}{(2s+1)(2t+1)} \sum_{\substack{JST \\ LL'}} [1 - (-1)^{L+S+T}] (2T+1) \int \frac{d^3k'}{(2\pi)^3} \langle q | V_{LL'}^{JST} | q \rangle n(k') \\ & \times \sum_{\substack{m_S m_J \\ m_L m_{L'}}} (L S m_L m_S | J m_J) (L' S m_{L'} m_{S'} | J m_J) Y_{L m_L}(\hat{\mathbf{e}}_q) Y_{L' m_{L'}}^*(\hat{\mathbf{e}}_q). \end{aligned} \quad (4.24)$$

Additionally, one can use the symmetry property of the Clebsch-Gordan coefficients:

$$(j j' m_j m_{j'} | J m_J) = (-1)^{j-J+m_{j'}} \sqrt{\frac{2J+1}{2j+1}} (J j' m_J - m_{j'} | j m_j), \quad (4.25)$$

to exchange the L and J indices in the coefficients of the previous equation and find:

$$\sum_{\substack{m_S m_J \\ m_L m_{L'}}} (L S m_L m_S | J m_J) (L' S m_{L'} m_{S'} | J m_J) = \delta_{LL'} \frac{2J+1}{2L+1} \sum_{m_L} \delta_{m_L m_{L'}}. \quad (4.26)$$

The final step comes out from the addition theorem for spherical harmonics,

$$\sum_{m_L} Y_{L m_L}(\hat{\mathbf{e}}) Y_{L m_L}^*(\hat{\mathbf{e}}') = \frac{2L+1}{4\pi} P_L(\hat{\mathbf{e}} \cdot \hat{\mathbf{e}}'), \quad (4.27)$$

as well as from the fact that the Legendre polynomials fulfill the condition $P_L(x = 1) = 1$. The sum over m_L can thus be carried out straightforwardly and the final result for the SCHF self-energy reads:

$$\begin{aligned} \Sigma_{SCHF}(k) = & \frac{1}{16\pi} \sum_{JLST} [1 - (-1)^{L+S+T}] (2T + 1)(2J + 1) \\ & \times \int \frac{d^3k'}{(2\pi)^3} \langle q[\mathbf{k}, \mathbf{k}'] | V_{LL}^{JST} | q[\mathbf{k}, \mathbf{k}'] \rangle n(k'). \end{aligned} \quad (4.28)$$

The notation $q[\mathbf{k}, \mathbf{k}']$ has been introduced to remind the reader that the relative momentum q depends on the single-particle momenta \mathbf{k} and \mathbf{k}' . From the numerical point of view, a suitable technique is needed to perform the previous integral. One usually discretizes the momenta inside the integrand in such a way that the integral can be numerically performed in an optimal way. In this case, since the potential and the momentum distributions are well-behaved functions, one can use a simple set of $N_{k'} = 50$ equally spaced internal momenta, k'_n . The external momentum k is also discretized and placed on the z -axis. Thus, for each pair of k_m and k'_n , a set of $N_\theta = 10$ values of the angle θ_{mn} of k' with respect to the z -axis is chosen. Note that the matrix elements need to be computed, for each k_m , k'_n and θ_{mn} (and for each partial wave), at the values of the relative momentum $q = \frac{1}{2} \sqrt{k_m^2 + k_n'^2 - 2k_mk_n' \cos \theta_{mn}}$. With these quantities at hand, one can then sum over partial waves and compute the remaining integral by means of, for instance, a trapezoidal rule.

4.5 Microscopic results

In this section the results for the microscopic quantities concerning symmetric nuclear matter for the HF and SCHF approaches will be given. In this way, the effects of self-consistency as well as the effects induced by interactions treated at the lowest order will be highlighted. All the results presented here have been obtained with the CDBONN potential [Mac96], with all the partial waves up to $J = 8$.

The discussion will start with the self-energy (or mean-field) of a nucleon in nuclear matter. This quantity is given in the HF approximation by Eq. (4.3), whereas in the SCHF approach it is given by Eq. (4.5). Note once again that the only difference between these two quantities comes from the momentum distribution. While in the HF case this is given by the free distribution, $n(k) = f[\frac{k^2}{2m}]$, in the SCHF case the momentum distribution is given by the self-consistent mean-field spectrum, $n(k) = f[\frac{k^2}{2m} + \Sigma_{SCHF}(k)]$. However, if one works at fixed density, this will not be the only difference between both expressions. The Fermi-Dirac distribution appearing in the two momentum distributions carries two extra parameters: the temperature T and the chemical potential μ . In principle, one should work in the

grand-canonical ensemble, *i.e.* giving the thermodynamical state of the system in terms of its temperature and chemical potential. In practice, however, it is more intuitive to work with a system at fixed temperature and density. The latter quantity is fixed by means of the following relation:

$$\rho = \nu \int \frac{d^3k}{(2\pi)^3} n(k, \tilde{\mu}), \quad (4.29)$$

where the dependence on the microscopic chemical potential has been explicitly taken into account. It is clear that if, for a given density, two different momentum distributions are used (in this case, the HF and SCHF momentum distributions), two different chemical potentials will be obtained. Thus, in the comparison of the microscopic quantities derived within the HF and the SCHF approach one should always be aware of the fact that not only the effects of self-consistency but also those coming from the differences in chemical potentials are being highlighted.

The HF and SCHF approximations are studied in the following iterative self-consistent method. In the first step, a temperature and a density are specified. One solves then Eq. (4.29) to find the chemical potential $\mu^{(0)}$, by using the free quasi-particle spectrum $\epsilon^{(0)}(k) = \frac{k^2}{2m}$. Once the chemical potential is set, the first iteration momentum distribution, $n^{(0)}(k)$ is defined. This is actually the momentum distribution in the HF approximation, which also corresponds to the free momentum distribution at that density and temperature. $n^{(0)}(k)$ can then be used to compute the first iteration of the self-energy, $\Sigma^{(0)}$, via Eq. (4.28). This first iteration of the self-energy corresponds, once again, to the HF self-energy. The self-energy $\Sigma^{(0)}$ defines the quasi-particle spectrum, $\epsilon^{(1)}(k) = \frac{k^2}{2m} + \Sigma^{(0)}(k)$, which is then used in Eq. (4.29) to find a new chemical potential, $\tilde{\mu}^{(1)}$. With the new momentum distribution, $\Sigma^{(1)}$ is computed and from it the quasi-particle spectrum can be obtained. Typically 5 iterations are enough to achieve self-consistency at an accurate level, *i.e.* the quantities $\tilde{\mu}^{(i)}$, $n^{(i)}(k)$, $\Sigma^{(i)}$ and $\epsilon^{(i)}$ do not change appreciably for $i > 5$.

Some of the results shown in this section correspond to the zero temperature case. They help us in understanding how relevant temperature effects are in the HF case. It is thus interesting to note the fact that, at zero temperature, the philosophy of the HF approximation is somewhat different to the one at finite temperature. Strictly speaking, at zero temperature no self-consistency is needed because the HF and the SCHF methods coincide. This is not difficult to understand considering the fact that, at zero temperature, there is a single momentum distribution, $n(k) = \Theta(k_F - k)$, for both cases. Thus there is no effective difference between the HF and SCHF self-energies and a single iteration is needed to achieve full convergence at zero temperature. This can also be seen in terms of diagrams. Consider the self-energy diagrams obtained in the second iteration in Fig. 4.4. The self-energy is the sum of the two first order diagrams plus higher order terms. In all these higher order diagrams, however, there is a particle and a hole in the same momentum state. At zero temperature, however, a particle and a hole cannot have equal

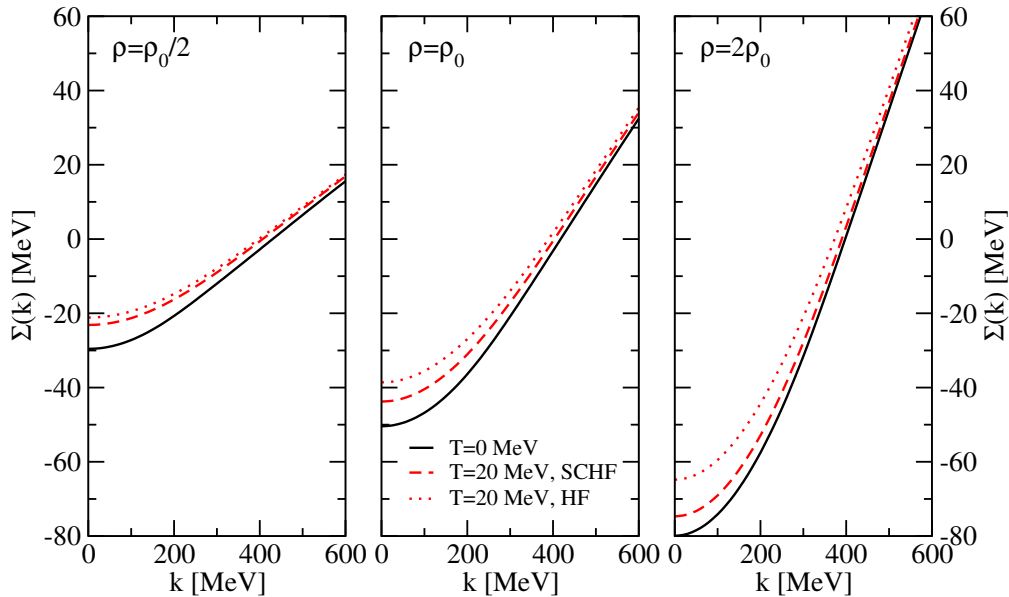


Figure 4.8: *SCHF* (dashed line) and *HF* (dotted line) results for the self-energy of a nucleon in nuclear matter at densities $\rho_0/2$, ρ_0 and $2\rho_0$ at $T = 20$ MeV. The $T = 0$ result is also shown (full line).

momenta and thus each of these diagrams vanishes exactly. An example of this is the third diagram in the second iteration of Fig. 4.4 (note that this corresponds to diagram (e) in Fig. 2.4). Since this contribution is zero, the rest of contributions involving insertions on this diagram will also be zero. At the end of the calculation, one is thus left with the HF propagator at zero temperature, which is already self-consistent.

In Fig. 4.8, the HF self-energy at zero temperature is shown at three different densities, $\rho_0/2$, ρ_0 and $2\rho_0$, with $\rho_0 = 0.16 \text{ fm}^{-3}$ the experimental saturation density of nuclear matter, in full lines. In addition, the SCHF self-energy at the corresponding densities and a temperature of $T = 20$ MeV is shown in dashed lines. The HF results at this temperature (once again these correspond to the first iteration of the SCHF procedure, in which a free momentum distribution is used) are displayed in dotted lines. In the three cases the density dependence is very similar. At higher densities, the self-energy at $k = 0$ becomes more attractive, while the momentum dependence becomes stiffer. Note that the attractive or repulsive nature of the SCHF self-energy depends on the bare NN interaction which is used [Fri04b]. In addition, there is a clear separation between the results at different temperatures. The HF results at zero temperature are the most attractive for all momenta. This might be due to the fact that, in the finite temperature self-energy, the integration over momentum is carried to higher momenta due to the thermal occupation factors. Therefore, the repulsive short-range core of the

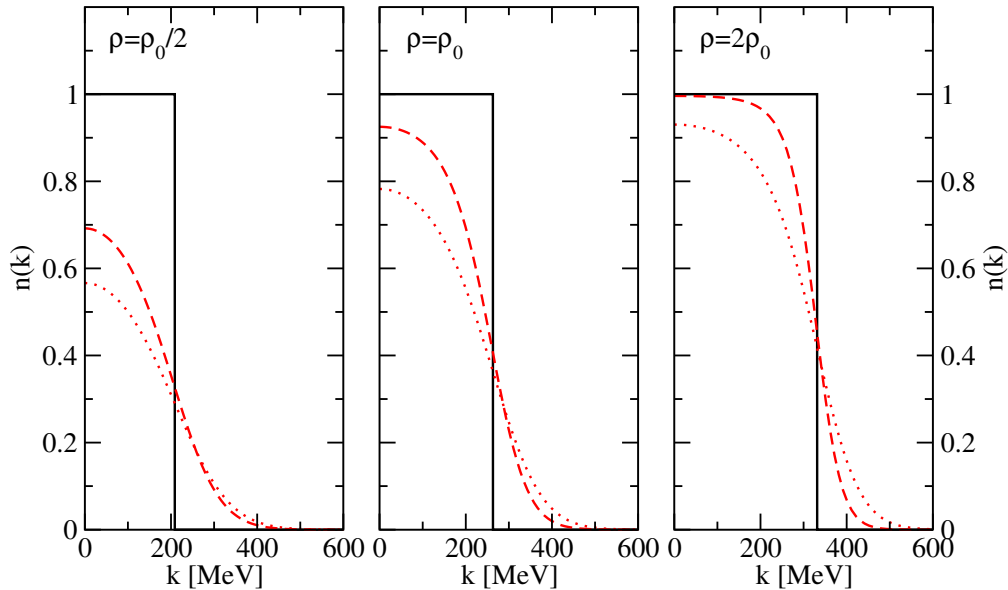


Figure 4.9: *SCHF* (dashed line) and *HF* (dotted line) results for the momentum distributions of a nucleon in nuclear matter at densities $\rho_0/2, \rho_0$ and $2\rho_0$ at $T = 20$ MeV. The $T = 0$ result is also shown (full line).

NN interaction is explored and the results at $T \neq 0$ are more repulsive than in the totally degenerate case. The differences between the two curves at finite temperature are caused by the self-consistency effects that appear through the momentum distributions. In particular, the HF self-energy is more repulsive than the SCHF one in the whole momentum range. This can be explained in the same terms as above for, as it can be seen in Fig. 4.9, the HF momentum distribution tends to populate more high-momentum states than the SCGF one. It is also interesting to note that the differences between the three approaches disappear as the momentum increases. This can be understood from the fact that high momentum states do not feel the Pauli blocking so much. Thus the modifications induced by a change in the momentum distributions are less important in the high momentum regions. Still, the effect of self-consistency is to shift the spectra to more attractive values, which yields a more realistic description. Finally, let us note that while the differences in $\Sigma(k=0)$ between the SCHF and the $T=0$ case are always similar, of about 5–6 MeV, the difference between the HF and the SCHF case at $T=20$ go from 2 MeV at $\rho = \rho_0/2$ to around 10 MeV for the highest density, $2\rho_0$. This agrees with the general idea that self-consistency effects become more important with increasing densities.

Fig. 4.9 shows in full lines the momentum distributions of the HF approach at zero temperature for the three densities, $\rho_0/2, \rho_0$ and $2\rho_0$. The momentum

distribution for the SCHF approximation at these densities and a temperature of $T = 20$ MeV are given in dashed lines. Finally, the HF momentum distribution at the same densities and temperature are displayed in dashed lines. At zero temperature the momentum distribution is given by a step function: for momenta below the Fermi momentum the states are fully occupied, while above the Fermi surface the states are completely empty. For the finite temperature case, this structure is somewhat different, and all the states above and below the Fermi surface are thermally occupied according to the Fermi-Dirac distribution at the corresponding quasi-particle energies (free spectra for HF, self-consistent spectra for SCHF).

The depletion, $d(k)$, is defined as the value $d(k) = 1 - n(k)$. For the HF case at zero temperature, it is clear that $d(k) = 0$ for $k < k_F$. When higher-order correlations are included, however, the depletion of the lowest momentum state can yield non-zero results [Dic05a]. Thus, $d(k)$ is somehow a measure of the importance of correlations that go beyond the mean-field approach. For the thermal case, the situation is again different. For $k = 0$ in the finite temperature HF approximation, for instance, it is clear from Fig. 4.9 that the momentum distribution (corresponding essentially to that of the free case) is already depleted. Note that when the correlated case is studied at finite temperature, the depletion given by thermal effects will need to be somehow disentangled from that coming from dynamical higher order correlations.

Moreover, already for correlations at the lowest order, the depletion of the HF and the SCHF cases is somewhat different. In the particular case of Fig. 4.9, for the three densities considered, the values of the HF depletion at $k = 0$ are $d(k = 0) = 0.43, 0.22$ and 0.07 respectively. Again, this depletion is purely due to the thermal distribution of the states, since the HF distribution function essentially corresponds to the free case. In the case of SCHF, however, the depletions become $d(0) = 0.31, 0.07$ and 0.004 . The difference between the two cases is related to the interplay between the chemical potential and the self-energy. Consider the expression for the zero-momentum occupation of the HF case:

$$n_{HF}(k = 0) = \frac{1}{1 + e^{-\beta\mu_{HF}}}, \quad (4.30)$$

and of the SCHF case:

$$n_{SCHF}(k = 0) = \frac{1}{1 + e^{-\beta\Delta\mu}}, \quad (4.31)$$

where $\Delta\mu = \mu_{SCHF} - \Sigma_{SCHF}(0)$. For a given temperature and density, it is easy to see that, if $n_{SCHF}(0)$ has to be higher than $n_{HF}(0)$, then the relation $\mu_{HF} < \Delta\mu$ must hold. This is indeed the case, as it can be seen in Table 4.1. It is also interesting to note that although the HF and the SCHF momentum distributions are normalized to the same density, the HF approximation yields a larger depletion than the SCHF one. Thus, if both of them have to be equally normalized, this

ρ	μ_{HF} [MeV]	μ_{SCHF} [MeV]	$\Delta\mu$ [MeV]
$\frac{\rho_0}{2}$	5.341	-6.941	16.19
ρ_0	25.60	6.569	50.34
$2\rho_0$	51.84	36.18	110.8

Table 4.1: *HF and SCHF chemical potentials at fixed temperature and three different densities. The fourth column shows the difference between μ_{SCHF} and the $k = 0$ self-energy in this approximation.*

necessarily implies that the HF momentum distribution leads to larger occupancies for high momentum states, as observed in Fig. 4.9.

The density dependence of $n(k)$ is also interesting. With increasing density, the thermal momentum distributions get closer to the zero temperature one. At constant temperature and increasing density, the ratio between the temperature and the free Fermi energy, $x = T/\varepsilon_F$, gets closer to zero. The free Fermi energy $\varepsilon_F = \frac{k_F^2}{2m}$ is the energy scale associated to the density in (free) fermionic systems. Thus, the ratio between the temperature and ε_F sets the relative importance of temperature and density effects in the system. Indeed, this dimensionless quantity defines two very different physical regimes when considered in two opposite limits. For $x \ll 1$, the system is said to be in the *degenerate limit*, characterized by low temperatures relative to the energy scale associated to the density. The properties of the degenerate system are essentially those of the zero temperature system, and any thermal effect can be studied from an expansion at low x of the finite temperature equations (see Appendix D). On the other hand, for $x \gg 1$ the system lies in the *classical limit*, at relatively large temperatures with respect to the density. In this case, the physical properties of the system are essentially those of the classical interacting gas and there is also a well-defined expansion on $1/x$ which takes into account quantal effects at lowest order (see Appendix D). This helps in understanding why the momentum distributions of the $\rho = 2\rho_0$ case in Fig. 4.9 are close to the zero temperature case. For that case $x \sim 0.35$ and thus the system lies close to the degenerate limit, where the thermal effects are to be small. For the lowest density case, on the other hand, although the system is not yet lying in its classical regime, the thermal effects are much more important, as it can be seen from the very different momentum distribution as compared to the zero temperature case.

Another important microscopic quantity is the effective mass. This is obtained from the single-particle spectrum by means of the following derivative:

$$\frac{m^*}{m} = \frac{1}{2m} \left(\frac{d\varepsilon(k)}{dk^2} \right)^{-1} = \frac{1}{1 + 2m \frac{d\Sigma(k)}{dk^2}}. \quad (4.32)$$

From a purely kinetic spectrum, one would readily obtain $m^* = m$. When interactions are introduced in the system, however, the in-medium quasi-particle

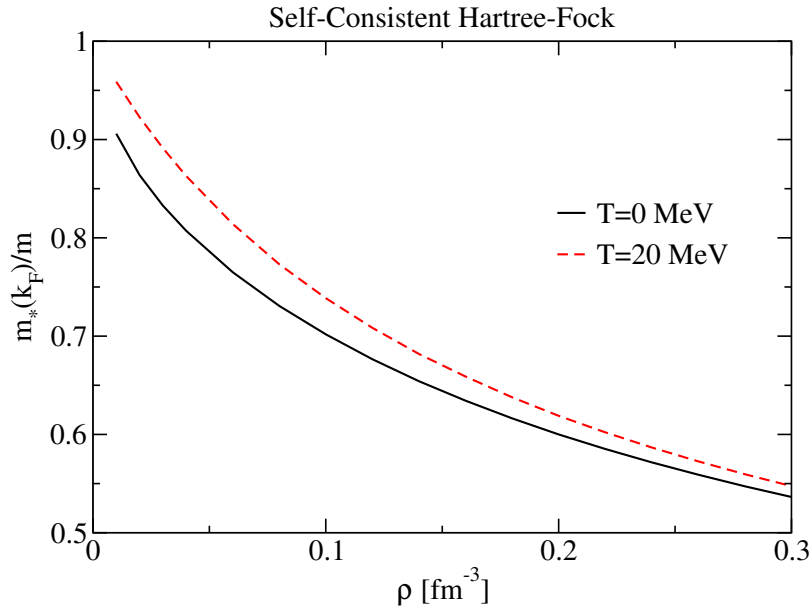


Figure 4.10: *SCHF* effective mass at the Fermi surface as a function of the density and for two different temperatures, $T = 0$ (solid line) and $T = 20$ (dashed line).

energies change and in that case the effective mass measures the stiffness of the spectrum. Usually, the effective mass is quoted at the Fermi surface (*i.e.* it is computed at $k = k_F$) and for a generic interaction it may depend on both density and temperature. For the SCHF approach, the effective mass at the Fermi surface for several densities is shown in Fig. 4.10. To pin down the temperature effects on this quantity, the zero temperature effective mass (solid line) is compared to the $T = 20$ MeV one (dashed line). The effective mass is a clearly decreasing function of the density, which corresponds to the intuitive idea that at lower densities the quasi-particles hardly interact with each other and thus their spectrum is closer to the kinetic one. This explains also why, for the lowest densities $m^*/m \rightarrow 1$. This can be understood more rigorously from Fig. 4.8, where the spectra are clearly seen to be more stiff with increasing density and therefore the effective masses become lower with increasing density. The temperature has a small influence on the effective mass and changing from 0 to 20 MeV makes the effective mass slightly higher, always within a 10% from the $T = 0$ case. Once again, the idea that the effective mass is closer to the free one when temperature increases agrees with the fact that once the thermal effects are taken into account, the spectra become less stiff. Finally, at saturation density and $T = 0$ for the SCHF approach the effective mass $m^*/m \sim 0.64$. This is a somewhat low value, that changes substantially once correlations are included in the system. These calculations do not have to be taken as realistic, but they are useful in grasping roughly the density and temperature

dependences of these quantities. This will allow us to disentangle in an easier way the thermal and density effects induced by correlations in the following chapters.

4.6 Macroscopic results

In this subsection, the thermodynamical macroscopic properties of nuclear matter studied within the SCHF method at finite temperature will be discussed. Of course, the results are not realistic because the SCHF lacks most of the correlations needed to correctly describe nuclear matter from realistic NN potentials. Yet, the density and temperature dependences of the thermodynamical quantities obtained in this method are quite generic and their understanding may allow us for a better comprehension of the results of the correlated case.

In the first place, the energy per particle will be considered. One can obtain a direct formula of the energy in terms of the temperature and density dependent SCHF self-energy from very general grounds [Fet71]. However, to keep the consistency in the presentation of the results, the energy per particle will be derived from the GMK sum rule, Eq. (2.103). From Dyson's equation, one knows that the propagator has the form of Eq. (4.4). Then, from Eq. (2.64) and the Plemejil relation, Eq. (2.61), it is easy to see that the spectral function is just a delta function (the "SCHF" subscript is dropped in the following for convenience):

$$\mathcal{A}(k, \omega) = (2\pi)\delta[\omega - \varepsilon(k)] , \quad (4.33)$$

centered at the quasi-particle energy:

$$\varepsilon(k) = \frac{k^2}{2m} + \Sigma(k) . \quad (4.34)$$

Introducing that into the GMK sum rule, the following result is obtained for the total energy per particle of an interacting gas of nucleons:

$$\frac{E}{A} = \frac{\nu}{\rho} \int \frac{d^3k}{(2\pi)^3} \frac{k^2}{2m} n(k) + \frac{\nu}{2\rho} \int \frac{d^3k}{(2\pi)^3} \Sigma(k)n(k) , \quad (4.35)$$

where the factor ν takes into account the spin-isospin degeneracy of the system. The first term is just the kinetic energy of the interacting system (note that the interaction has a certain effect on this quantity through the self-consistent spectrum $\varepsilon(k)$ as well as through the chemical potential μ inside the momentum distributions). The second term, on the other hand, yields the potential energy of the system caused by the mean-field generated by the particles in the system. Note the 1/2 factor in front of this term, which corrects the double-counting.

The results for the different terms of the previous formula are considered in Fig. 4.11. In the three panels of this figure, the total, kinetic and potential energy per particle in the SCHF approximation are given as a function of the density for

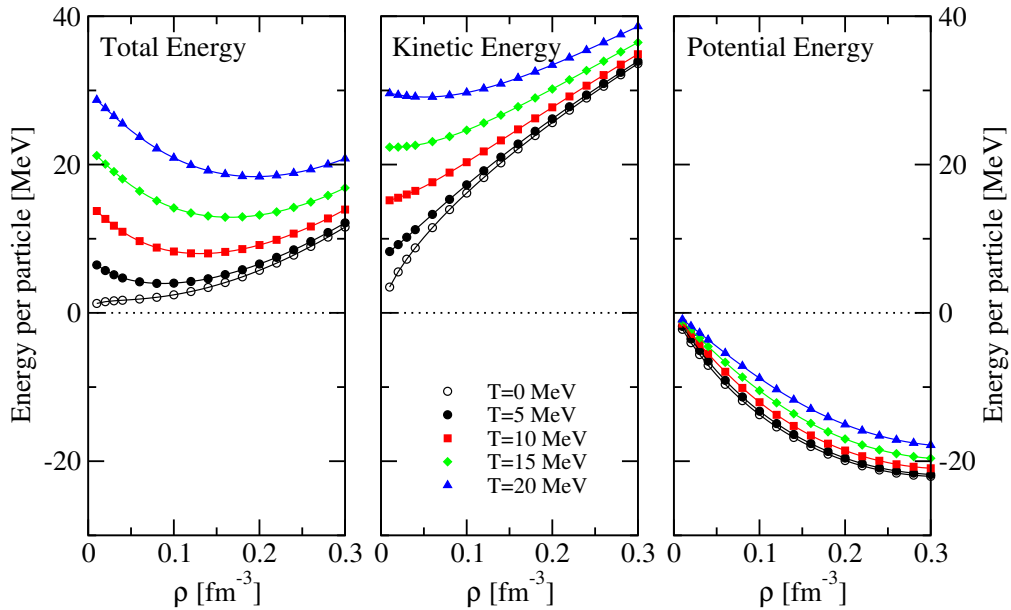


Figure 4.11: *Density dependence of the total (left panel), kinetic (central panel) and potential (right panel) energy per particle within the SCHF approach. Five temperatures are considered: 0 (empty circles), 5 (full circles), 10 (squares), 15 (diamonds) and 20 (triangles) MeV.*

five different temperatures, from 0 to 20 MeV in equidistant steps of 5 MeV. As expected, due to the lack of correlations in the HF approach, the total energy per particle yields a positive result at all densities. At zero temperature there is no sign of saturation and the total energy per particle increases steadily with density. The potential energy is indeed negative, but not negative enough as to create any binding in the total energy per particle. As it will be seen in the following chapter, the inclusion of higher order correlations is essential to obtain more attraction in the potential energy per particle.

As for thermal effects, one can say that temperature seems to have a repulsive effect on the energy per particle. At all densities and for the three panels, the energy per particle becomes more repulsive when temperature increases. This effect is more important in the kinetic energy. This is the quantity that varies the most from $T = 0$ to $T = 20$ MeV, with differences as large as 30 MeV. In particular, it is interesting to note that, for the lowest density displayed, the kinetic energy at finite temperature is always very close to the classical value, $E_{kin} = \frac{3}{2}T$. On the other hand, the repulsive effect of temperature in the potential energy is less important, not larger than 5 MeV for the largest temperature of 20 MeV in the whole density range. Indeed, the strong influence of temperature in the low density region of the total energy per particle is the cause of the kind of “saturation” behavior observed for this quantity. The high density zone, on

$$\Phi_{\text{SCHF}} = \frac{1}{2} \left(\text{Diagram 1} + \text{Diagram 2} \right)$$

Figure 4.12: *Diagrams contributing to the Φ -functional for the SCHF approach.*

the other hand, is closer to the degenerate limit and thus is less affected by the temperature increase. This yields a curve with a minimum (still too repulsive) energy per particle at finite densities.

In any case, a minimum of the energy per particle would not give the thermodynamically preferred state of the system, which is instead given by a minimum of the free energy. One should thus try to compute the free energy of the system within the SCHF approach. From thermodynamical grounds, one knows that the free energy is given in terms of the energy and the entropy by the following equality:

$$F = E - TS. \quad (4.36)$$

Therefore, one should face the problem of computing the entropy of the system (since the energy per particle is known from the GMK sum rule). The entropy of the system can be obtained from the expressions obtained in the previous chapter. First of all, since the Hartree-Fock self-energy is real and has no energy dependence, one can easily compute the \mathcal{B} spectral function from Eq. (3.109) to obtain:

$$\mathcal{B}(k, \omega) = \mathcal{A}(k, \omega) = (2\pi)\delta[\omega - \varepsilon(k)]. \quad (4.37)$$

The dynamical quasi-particle entropy per particle within the SCHF approach is readily seen to be:

$$\frac{S}{A} = \frac{\nu}{\rho} \int \frac{d^3k}{(2\pi)^3} \sigma[\varepsilon(k)]. \quad (4.38)$$

This coincides with the entropy of an interacting gas of quasi-particles and can be obtained from other methods [Fet71]. As explained in the previous chapter, this is not the only contribution to the total entropy of the system. Instead, the S' contribution of Eq. (3.95) should be considered. This involves, in particular, the calculation of the Φ -functional within the SCHF approach, which is given in terms of diagrams in Fig. 4.12. Note the factor 1/2, which takes into account the two equivalent dressed propagators in which one can cut the diagrams to obtain the SCHF self-energy of Fig. 4.3. These propagators are dressed within the approximation that one is using and thus should be computed with the self-consistent spectrum. Using a slightly modified version of the Feynman rules of

Appendix B, one obtains the following expression:

$$\Phi = \frac{\beta\nu}{2} \int \frac{d^3k}{(2\pi)^3} \int \frac{d^3k'}{(2\pi)^3} n(k)n(k') \langle kk'|V|kk'\rangle_A = \frac{\beta\nu}{2} \int \frac{d^3k}{(2\pi)^3} n(k)\Sigma(k). \quad (4.39)$$

The first contribution to S' is given by the expression [see Eq. (3.95)]:

$$\frac{\partial T\Phi}{\partial T} = \nu \int \frac{d^3k}{(2\pi)^3} \frac{\partial n(k)}{\partial T} \Sigma(k). \quad (4.40)$$

The second term in S' is an integral of the spectral function and the self-energy. Replacing the values obtained for these objects within the SCHF approximation, one finds:

$$\nu \int \frac{d^3k}{(2\pi)^3} \int_{-\infty}^{\infty} \frac{d\omega}{2\pi} \frac{\partial f(\omega)}{\partial T} \mathcal{A}(k, \omega) \text{Re} \Sigma(k, \omega) = \nu \int \frac{d^3k}{(2\pi)^3} \frac{\partial n(k)}{\partial T} \Sigma(k), \quad (4.41)$$

which is the same as the equation above. Noticing the minus sign in Eq. (3.95), one sees that within the SCHF approximation, the two terms of S' cancel each other exactly and thus their total contribution to the entropy is zero. This could have been expected from the Carneiro and Pethick statement that S' only receives contributions of diagrams with two or a larger number of even vanishing energy denominators. In the SCHF approach, no contribution has a vanishing denominator and thus $S' = 0$.

The total entropy per particle within the SCHF approach is then given by the quasi-particle expression of Eq. (4.38). The results obtained with such a formula are shown in the two panels of Fig. 4.13. The left panel displays the entropy per particle for four different temperatures (from 5 to 20 MeV in steps of 5 MeV) as a function of the density. The expected behavior is found for all temperatures: the entropy per particle decreases as density increases. The highest values are of the order of 3 – 4, while the lowest ones lie in the range 0.5 – 1.5. In addition, for all the densities the highest values correspond to the largest temperatures, as one would expect. One may wonder why the entropy has a such strong density dependence at low densities. As explained before, one can in this case compute analytical formulas for the entropy within the classical limit (see Appendix D). Note, however, that to derive this formula one must also rely on the fact that the quasi-particle spectrum is almost quadratic and that it can be well described by the effective mass, which is the case for the SCHF approach. Within these assumptions, one obtains the following expression for the entropy per particle in the classical regime:

$$\frac{S}{A} = \frac{5}{2} - \ln \frac{\rho \lambda_{dB}^3}{\nu} + \frac{3}{2} \ln \frac{m^*}{m}, \quad (4.42)$$

with λ_{dB} the de Broglie wavelength of Eq. (D.36). The results obtained with this formula are shown by the dotted lines of the left panel of Fig. 4.13. As expected,

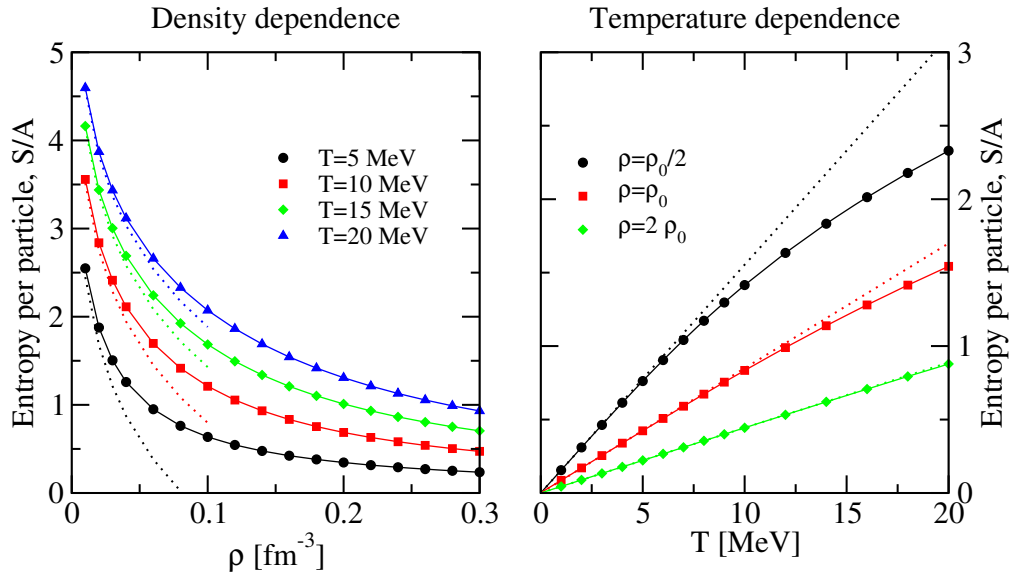


Figure 4.13: *Density dependence (left panel) and temperature dependence (right panel) of the entropy per particle within the SCHF approach. The dotted lines in the left (right) panel correspond to the classical (degenerate) approximation of Eq. (4.42) (Eq. (4.43)). Note the difference in the scale between the right and the left panel.*

they describe quite well the low density region and they are more accurate at higher temperatures. In the classical regime, the entropy depends logarithmically on the density and this accounts for the strong density dependence of the results.

The right panel of Fig. 4.13 shows the temperature dependence of the entropy at three fixed densities, $\rho = \rho_0/2, \rho_0$ and $2\rho_0$. As one would naively expect, the entropy is close to 0 for low temperatures and then increases steadily. Moreover, at all temperatures it is the lowest density which has a larger entropy. This is in accordance with the naive idea that thermal disorder is more important for systems with low densities. In the low temperature regime, the entropy depends linearly on temperature. This is what one expects from the low temperature expansion of the entropy (see Appendix D):

$$\frac{S}{A} = \frac{\pi^2}{3\rho} N(0)T, \quad (4.43)$$

where $N(0)$ is the density of states at $T = 0$ on the Fermi surface. Within a quasi-particle approximation, this quantity is essentially proportional to the effective mass (computed at $T = 0$):

$$N(0) = \frac{\nu k_F m^*(k_F)}{2\pi^2}. \quad (4.44)$$

The dotted lines shown in the right panel of Fig. 4.13 have been obtained from the previous approximation, with the results for the $T = 0$ effective mass of the previous subsection. The agreement with the data computed from the quasi-particle expression is especially good for high densities, where the system is closer to the degenerate limit. For the lowest density, the approximation only gives correct results up to about 5 – 6 MeV. At this density and for high temperatures, one cannot say that the system is in the degenerate limit anymore and thus the thermal effects become more important in a computation of the entropy.

The previous figures have shown the density and temperature dependences of the entropy of an interacting system of nucleons within the SCHF approximation. One might wonder which is the effect of the interaction in the entropy of the system. In the case of the energy per particle, for instance, the introduction of the interaction has a double influence. On the one hand, the total energy of an interacting system acquires an extra term, the potential energy, which is entirely due to interactions and which is the most important modification to the energy. On the other hand, there is also a smaller effect due to the use of self-consistent spectra in the interacting case (which modifies already the kinetic energy of an interacting system) as well as the modification introduced by the chemical potential when working at fixed densities. For the entropy, it is this combined second effect which is present. Stated differently, the difference between the entropy of the free Fermi gas, Eq. (3.62), and that of the SCHF case, Eq. (4.38), comes from the different chemical potentials and quasi-particle spectra that are used. Yet, it is not all the spectra that matters: the effective mass is what actually governs the entropy, as it is clearly seen in the classical and the degenerate approximations of Eq. (4.42) and Eq. (4.43). In the degenerate limit of high densities and low temperatures, for instance, it is easy to see that the entropy of the interacting gas can be obtained from the entropy of the non interacting gas by multiplying by a factor $\frac{m^*}{m}$ (where the effective mass is computed at the Fermi surface at zero temperature), $\frac{S}{S_0} \sim \frac{m^*}{m}$. In the classical limit, the relation is different and the entropy of the interacting system is given by the free Fermi entropy plus a factor $\frac{3}{2} \ln \frac{m^*}{m}$ which accounts for the interaction and which is computed with the corresponding effective mass of the finite temperature case. As a matter of fact, and as it is more extensively commented in Appendix D, the effective mass which is used in the degenerate limit and in the classical one have somewhat different origins. In a degenerate approximation, the expression of Eq. (4.32) appears explicitly, but it has to be computed at zero temperature and at the Fermi surface. On the other hand, the effective mass in the classical approximation just parametrizes the stiffness of the quasi-particle spectrum in the whole momentum range. Therefore, and as a general rough conclusion, one can say that the effect of the interaction in the entropy is almost exclusively caused by the effective mass.

Once the entropy is computed, one has direct access to the free energy of the system. This is shown, as a function of the density for five temperatures distributed

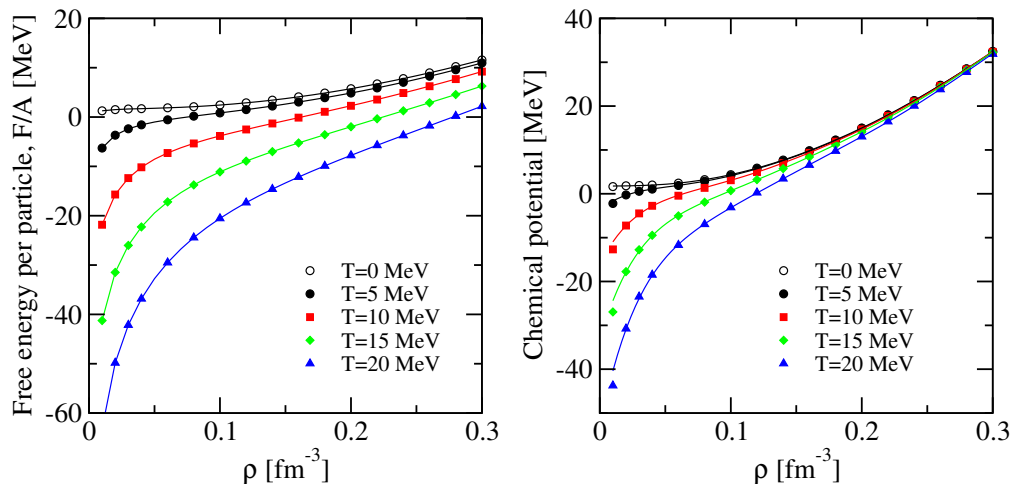


Figure 4.14: *Free energy per particle (left panel) and chemical potential (right panel) as a function of the density for five temperatures within the SCHF approach. The results for the chemical potentials correspond to the microscopic chemical potential, $\tilde{\mu}$ (symbols) and to the macroscopic μ (lines).*

in equidistant steps from 0 to 20 MeV, in the left panel of Fig. 4.14. In general terms, one can say that the free energy is an increasing function of density. At low densities, the free energy tends to very low values due to the strong density dependence of the entropy. This is thus a pure entropic effect. On the other hand, for all densities one observes that the higher the temperature, the lower the free energy. This behavior is the opposite to what was found for the energy per particle and it is a direct consequence of the $-TS$ term in the free energy. Let us also note that the free energy per particle does not have any minimum in the density and temperature regime explored, apart from that at zero densities. This in turn implies that nuclear matter within the SCHF would be unstable, because the minimum of F/A is at $\rho = 0$ and thus the system would prefer to disintegrate. However, one does observe finite nuclei in nature, which confirms that this conclusion is wrong. This incorrect behavior can be traced back to the lack of correlations in the SCHF approach.

As mentioned in Section 3.3.4, the problem of thermodynamical consistency is most suitably studied in terms of the chemical potential. On the one hand, the microscopic chemical potential, $\tilde{\mu}$, is obtained within the SCHF from the normalization condition of Eq. (4.29). On the other hand, the macroscopic chemical potential is obtained from the thermodynamical derivative,

$$\mu = \frac{\partial}{\partial \rho} \frac{\rho F(\rho, T)}{A}. \quad (4.45)$$

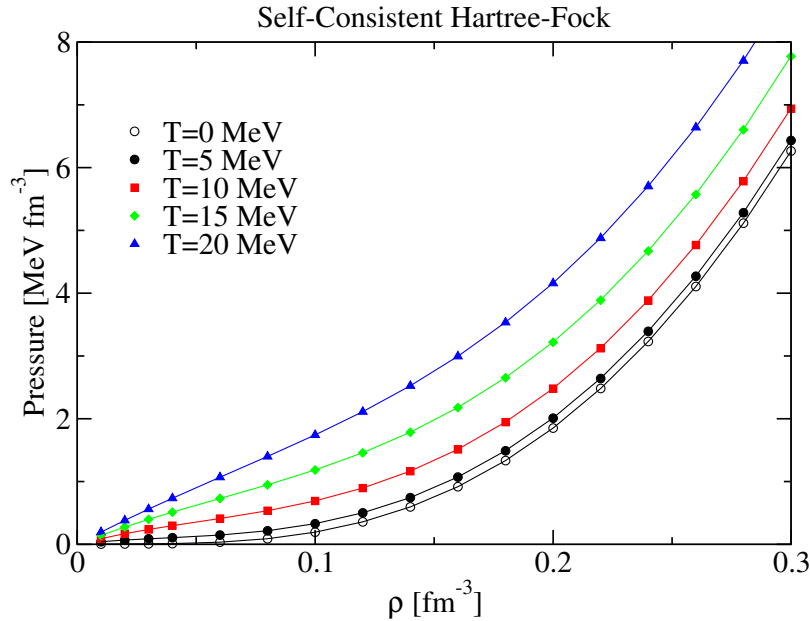


Figure 4.15: *Pressure as a function of the density for five temperatures within the SCHF approach. The symbols have been obtained with Eq. (4.46), while the lines are the results of Eq. (4.47).*

These two chemical potentials are shown in the right panel of Fig. 4.14. While the symbols represent $\tilde{\mu}$, the lines joining them have been obtained by performing the previous density derivative at each temperature. The agreement is almost perfect. This shows both the importance of the self-consistent renormalization procedure as well as the degree of accuracy that is achieved in the thermodynamical consistent results. Note that the free energy has been obtained through the sum of the GMK sum rule total energy per particle and the DQ expression for the entropy per particle. These two expressions link the micro- and the macrophysics of the system and can lead to non-consistent results if the many-body approximation under consideration is of a non-conserving nature. The Hugenholtz-van Hove theorem cannot be studied in this case because the free energy does not present any local minimum at finite density.

As for the thermal and density dependences, the chemical potential follows closely the dependence of the free energy per particle. It is an increasing function of the density, with a strong dependence at low densities, where it goes to the classical limit $\mu \rightarrow -\infty$. Moreover, for a given density it is a decreasing function of the temperature. This behavior is clear in the low and intermediate density regime, but it is less clear for high densities, where all the lines seem to converge at temperature independent values. Note that once again this is a degeneracy effect and that, for very high densities, one expects that the results do not depend

so much on temperature.

Finally, for the SCHF approach one can compute the pressure in two different but equivalent ways. On the one hand, one can take profit of the fact that, within this approach, one can compute the Φ functional explicitly, as shown in Eq. (4.39). Therefore, using Eq. (3.78) or Eq. (3.85) and taking into account the properties of the SCHF approach (zero width, energy independent self-energy), one can find an analytic expression for the grand-canonical potential within this approximation. From this expression, one can readily compute the pressure of the system by means of the thermodynamical relation $p = -\mathcal{V}\Omega$, which yields:

$$p = -\frac{\Omega}{\mathcal{V}} = \frac{\nu}{\beta} \int \frac{d^3k}{(2\pi)^3} \ln [1 + e^{-\beta(\varepsilon(k)-\mu)}] + \frac{\nu}{2} \int \frac{d^3k}{(2\pi)^3} n(k)\Sigma(k). \quad (4.46)$$

This provides the pressure of nuclear matter directly from the self-energy. It is important to remark the fact that this expression, obtained from the Luttinger-Ward approach, coincides with the expression of the mean-field pressure computed in other methods [Abr65]. The same can be said about the other thermodynamical quantities obtained from the Luttinger-Ward approach in the mean-field case, *i.e.* that they reduce to well established expressions obtained within other formalisms. On the other hand, the pressure can be computed from the thermodynamical relation $\Omega = E - TS - \mu N$. This is indeed given by the expression:

$$p = \rho\mu - \rho\frac{E}{A} + \rho T\frac{S}{A} = \rho\left(\mu - \frac{F}{A}\right). \quad (4.47)$$

If the approximation has to be consistent, the previous equation should give the same results as the pressure computed from the Φ -functional, Eq. (4.46). The consistency of our results is shown in Fig. 4.15. In this figure, the symbols have been obtained from Eq. (4.46), while the lines joining them represent Eq. (4.47). The agreement of the two results is very good and there is almost no visible difference between the two expressions. As for the temperature and density dependence, they are quite intuitive. The pressure increases with temperature for any density, as expected from the naive idea that thermal motion contributes to the pressure. In addition, the pressure is an increasing quantity with density. This is due to both the repulsive effect of the bare interaction, which is more important for high densities (where particles are in average closer to each other) and to the effect of degeneracy, which also becomes more relevant at high densities. Finally, let us note that there is no trace of saturation in the SCHF pressure, *i.e.* there is no finite density for which the pressure becomes zero. This is in contrast with the usual knowledge of nuclear physics. In the following chapter, it will be shown how, by including higher order correlations, one can obtain a more realistic description of nuclear matter at finite temperature, which reproduces qualitatively the properties of dense matter which are expected from experimental data.

Chapter 5

Ladder Approximation

The NN interaction presents a very repulsive core at short distances. Intuitively, one might think that, if it is energetically costly to put two particles together, the probability of finding them close to each other should be small. In dense nuclear systems, this mechanism would allow the particles to avoid the strong short-range repulsive core and to explore the attractive part of the interaction, so that enough binding is produced to form finite nuclei. In this sense, there is an interplay between the repulsive interaction at close relative distances, the attraction at intermediate distances and the “correlation” probability in both of these ranges. Yet, in the Hartree-Fock approximation introduced in the previous chapter, this kind of correlations have been totally neglected. The two-body Green’s function, as a matter of fact, was simply given by the propagation of two independent fermions. This lack of correlations overweights the repulsive short-range components of the interaction and it is the ultimate responsible for the poor binding in the Hartree-Fock approach. In the following, a more complete many-body approach will be studied, the so-called ladder approximation, in which two-body correlations as well as strong interactions are treated in a more consistent and sophisticated way. The numerical implementation of the approach (through the Self-Consistent Green’s Function method) as well as the results for the microscopic properties will also be discussed. In Chapter 6, the Luttinger-Ward formalism will be applied to obtain the thermodynamical properties of nuclear matter within this many-body approach.

5.1 Two-body propagator

The NN potential has a strong short-range core of a repulsive nature. Therefore, one expects that the Hartree-Fock approximation for the two-body propagator, shown in Fig. 4.6, will be quite poor. After all, if the interaction is very strong, two propagating particles will necessarily interact with each other (one or two or more times) and thus it will not be a good approximation to suppose that they

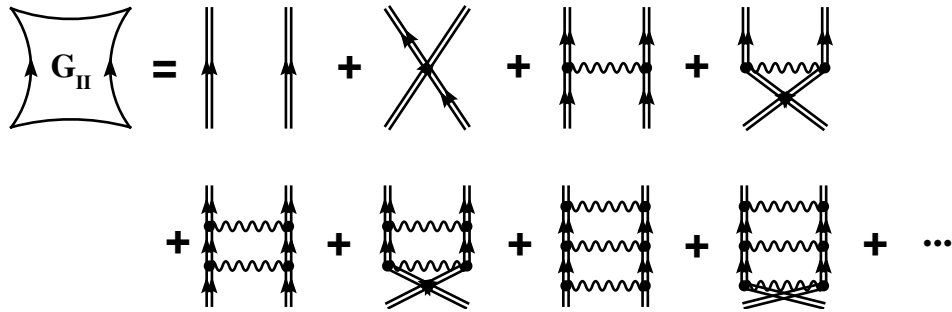


Figure 5.1: *Diagrammatic expansion of the two-body propagator in the ladder approximation.*

propagate independently. Consider, in contrast, the approximation of Fig. 5.1, in which the propagation of the two particles is given by the independent terms of the Hartree-Fock approximation plus all the possible processes in which the two particles interact successively with each other. This approximation for the two-body propagator is the so-called *ladder approximation*. In principle, this should be a reasonable approximation in systems driven by strong interactions where particles unavoidably interact with each other repeatedly. However, when the density increases particles might interact with each other via an excitation of the medium surrounding them. This kind of contributions are not treated in this approach and so the ladder approximation is suitable for low density systems with strong two-body interactions. Actually, this approximation is appropriate to compute the total energy of a system in the limit $a/r_0 \ll 1$, where a is the range of the potential and r_0 is the mean interparticle distance. This condition is fairly well fulfilled in nuclear matter: the range of the short-range component of the strong interaction is (in a boson exchange picture) given by the mass of the ω meson, $a \sim 1/m_\omega \sim 0.25$ fm, and the mean interparticle distance at saturation can be taken as $r_0 \sim \sqrt[3]{1/\rho_0} \sim 1.8$ fm, so that for nuclear matter at saturation $a/r_0 \sim 0.15$. In the original derivation of the ladder expansion by Galitskii [Gal58a], the diagrams in Fig. 5.1 did not have dressed propagators, but free single-particle Green's functions. This would of course only be valid in low density systems, in which the individual quasi-particles might behave similarly to the free ones. Whenever the densities are higher (or, in other words, if the ratio a/r_0 becomes larger, as it happens in nuclear matter), the intermediate quasi-particles should be dressed [Ram88; Dew02]. This justifies physically the inclusion of dressed propagators in Fig. 5.1, which describes more accurately the propagation of one-body disturbances in a dense system. One expects that this will also yield a better approximation to \mathcal{G}_{II} which will however necessarily involve a self-consistent approach. Furthermore, the sum of diagrams of Fig. 5.1 with dressed propagators includes a large amount of the diagrams in

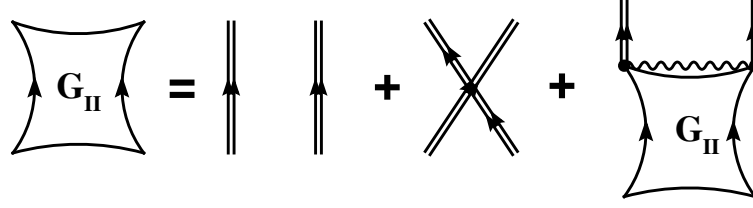


Figure 5.2: Diagrammatic representation of the two-body propagator in the ladder approximation.

Fig. 4.5 and, hopefully, it will describe more accurately the properties of strongly interacting systems. Actually, the infinite diagram series of Fig. 5.1 can be written down analytically by noticing that \mathcal{G}_{II} is already included in the right hand side of Fig. 5.1 (see Fig. 5.2). Since the intermediate space-time variables have to be integrated (the imaginary time is integrated in the whole range, from 0 to $-i\beta$), this gives rise to the following integral equation:

$$\begin{aligned} \mathcal{G}_{II}(\mathbf{1}\mathbf{2}; \mathbf{1}'\mathbf{2}') &= \mathcal{G}(\mathbf{1}, \mathbf{1}')\mathcal{G}(\mathbf{2}, \mathbf{2}') - \mathcal{G}(\mathbf{1}, \mathbf{2}')\mathcal{G}(\mathbf{2}, \mathbf{1}') \\ &+ i \int_0^{-i\beta} d\bar{\mathbf{1}} \int_0^{-i\beta} d\bar{\mathbf{2}} \mathcal{G}(\mathbf{1}, \bar{\mathbf{1}})\mathcal{G}(\mathbf{2}, \bar{\mathbf{2}})V(\bar{\mathbf{1}} - \bar{\mathbf{2}})\mathcal{G}_{II}(\bar{\mathbf{1}}\bar{\mathbf{2}}; \mathbf{1}'\mathbf{2}'). \end{aligned} \quad (5.1)$$

Note that, in a sense, the Hartree-Fock approximation is already included in the previous equation, because the two first terms in the previous expression correspond to Eq. (4.7).

It is interesting to derive the ladder approximation to \mathcal{G}_{II} , Eq. (5.1), directly from the hierarchy of the equation of motion for the two-body propagator. This gives a new insight into the physical basis of the approximation. To begin with, consider the differential equation of motion for the two-body Green's function [see Eq. (2.100)]:

$$\begin{aligned} \left\{ i \frac{\partial}{\partial t_1} + \frac{\nabla_1^2}{2m} \right\} \mathcal{G}_{II}(\mathbf{1}\mathbf{2}; \mathbf{1}'\mathbf{2}') &= \delta(\mathbf{1} - \mathbf{1}')\mathcal{G}(\mathbf{2}, \mathbf{2}') - \delta(\mathbf{1} - \mathbf{2}')\mathcal{G}(\mathbf{2}, \mathbf{1}') \\ &- i \int_0^{-i\beta} d\bar{\mathbf{3}} V(\mathbf{1} - \bar{\mathbf{3}}) \mathcal{G}_{III}(\mathbf{1}\bar{\mathbf{3}}; \mathbf{1}'\mathbf{2}'\bar{\mathbf{3}}^+). \end{aligned} \quad (5.2)$$

As expected, the previous equation couples the two-body Green's function with the dressed one-body propagator as well as with the three-body one. In order to find solvable solutions, one has to truncate this hierarchy. This is usually done by expressing the N -body Green's functions in terms of the $(N-1)$ -, $(N-2)$ -, \dots propagators and possibly some interaction among them. These are approximations in the sense that the genuine N -body (and higher order) excitations of the system are lacking and thus poorly described. The Hartree-Fock approximation, for instance, lacks any two-body correlations because the two-body Green's function is

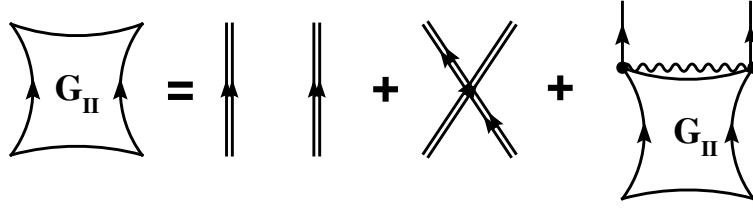


Figure 5.3: *Diagrammatic representation of the two-body propagator from the decoupling of the three-body propagator.*

defined as a product of two independent one-body propagators. Following these ideas, one can indeed approximate \mathcal{G}_{III} in different ways, which originates different decouplings. Some of these decouplings lead to well-known schemes that sum up infinite series of diagrams [Mat71]. Among the well-known many-body approximations that come out from expressing \mathcal{G}_{III} in terms of \mathcal{G} and \mathcal{G}_{II} in Eq. (5.2), one finds the random phase as well as the ladder approximations. In doing this, the full one-body and two-body correlations are taken into account. Note that genuine three-body correlations, which in the nuclear phenomenology play an important role, are only approximate in the sense that they are taken as independent excitations of couples plus individual nucleons [Day81]. The collective motion of a full indistinguishable triplet of fermions is thus not treated accurately, even though one expects these three-body correlations to be less important than those of a two-body nature for a system interacting through two-body interactions.

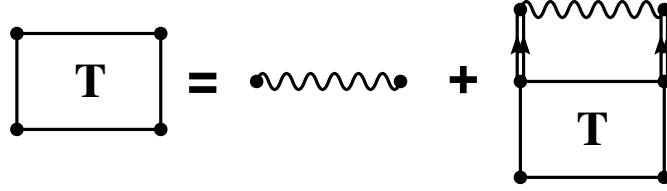
The ladder approximation is obtained from the decoupling:

$$\begin{aligned} \mathcal{G}_{III}(\mathbf{123}; \mathbf{1}'\mathbf{2}'\mathbf{3}') &\sim \mathcal{G}_{II}(\mathbf{13}; \mathbf{1}'\mathbf{3}')\mathcal{G}(\mathbf{2}, \mathbf{2}') + \mathcal{G}_{II}(\mathbf{13}; \mathbf{3}'\mathbf{2}')\mathcal{G}(\mathbf{2}, \mathbf{1}') \\ &+ \mathcal{G}_{II}(\mathbf{13}; \mathbf{2}'\mathbf{1}')\mathcal{G}(\mathbf{2}, \mathbf{3}'). \end{aligned} \quad (5.3)$$

The ordering of the time and space variables of the previous equation is very important, although it is intuitive at first sight. In fact, a different ordering might lead to an approximation that is not expressible in terms of diagrams. Plugging the previous decoupling in Eq. (5.2), one obtains the following differential equation:

$$\begin{aligned} \left\{ i \frac{\partial}{\partial t_1} + \frac{\nabla_1^2}{2m} \right\} \left\{ \mathcal{G}_{II}(\mathbf{12}; \mathbf{1}'\mathbf{2}') - \mathcal{G}(\mathbf{1}, \mathbf{1}')\mathcal{G}(\mathbf{2}, \mathbf{2}') + \mathcal{G}(\mathbf{1}, \mathbf{2}')\mathcal{G}(\mathbf{2}, \mathbf{1}') \right\} = \\ i \int_0^{-i\beta} d\bar{\mathbf{3}} V(\mathbf{1} - \bar{\mathbf{3}}) \mathcal{G}(\mathbf{2}, \bar{\mathbf{3}}^+) \mathcal{G}_{II}(\mathbf{1}\bar{\mathbf{3}}; \mathbf{1}'\mathbf{2}'). \end{aligned} \quad (5.4)$$

By means of the same technique that was used in Section 2.4 to obtain the integral form of Dyson's equation, one can write down the integral counterpart of the


 Figure 5.4: Diagrammatic expression of the T -matrix.

previous equation:

$$\begin{aligned} \mathcal{G}_{II}(\mathbf{1}\mathbf{2}; \mathbf{1}'\mathbf{2}') &= \mathcal{G}(\mathbf{1}, \mathbf{1}')\mathcal{G}(\mathbf{2}, \mathbf{2}') - \mathcal{G}(\mathbf{1}, \mathbf{2}')\mathcal{G}(\mathbf{2}, \mathbf{1}') \\ &+ i \int_0^{-i\beta} d\bar{\mathbf{1}} \int_0^{-i\beta} d\bar{\mathbf{2}} \mathcal{G}_0(\mathbf{1}, \bar{\mathbf{1}})\mathcal{G}(\mathbf{2}, \bar{\mathbf{2}})V(\bar{\mathbf{1}} - \bar{\mathbf{2}})\mathcal{G}_{II}(\bar{\mathbf{1}}\bar{\mathbf{2}}; \mathbf{1}'\mathbf{2}'). \end{aligned} \quad (5.5)$$

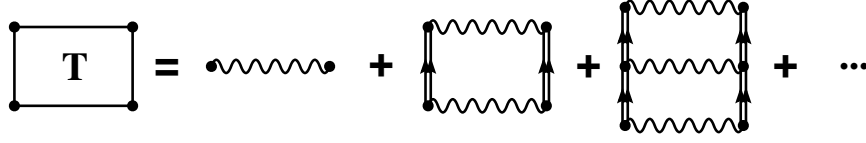
In terms of diagrams, this is shown in Fig. 5.3. This equation resembles Eq. (5.1) quite a lot. Actually, the only difference comes from the propagator in the left hand side of the integral term, which is free in the previous expression and dressed in Eq. (5.1). In terms of diagrams, this differs from Fig. 5.2 in the free single-particle propagator appearing in the top left vertex of \mathcal{G}_{II} . In the following, this free propagator will be considered to be dressed. This is a more consistent treatment, as already explained, that arises anyway when the self-consistent procedure is introduced into the approach.

5.2 In-medium interaction

Now that the fundamental equation for the two-body propagator within the ladder approximation has been obtained, one should start to devise methods to solve it. In the first place, and following Kadanoff and Baym [Kad62], the analytical properties of this scheme will be studied in detail. One usually starts by defining the so-called in-medium interaction or T -matrix:

$$\begin{aligned} T(\mathbf{1}\mathbf{2}; \mathbf{1}'\mathbf{2}') &= \delta(\mathbf{1} - \mathbf{1}')\delta(\mathbf{2} - \mathbf{2}')V(\mathbf{1} - \mathbf{2}) \\ &+ i \int_0^{-i\beta} d\bar{\mathbf{1}} \int_0^{-i\beta} d\bar{\mathbf{2}} T(\bar{\mathbf{1}}\bar{\mathbf{2}}; \mathbf{1}'\mathbf{2}') \mathcal{G}(\bar{\mathbf{1}}, \mathbf{1}') \mathcal{G}(\bar{\mathbf{2}}, \mathbf{2}')V(\mathbf{1}' - \mathbf{2}'). \end{aligned} \quad (5.6)$$

The object defined by this equation can be expressed in terms of diagrams, as in Fig. 5.4. This quantity accounts for the interaction of two dressed particles in the medium by describing their repeated scattering to all orders, as seen by iterating


 Figure 5.5: *Diagrammatic expansion of the T-matrix.*

the left hand side of the previous equation:

$$\begin{aligned}
 T(\mathbf{1}\mathbf{2}; \mathbf{1}'\mathbf{2}') &= \delta(\mathbf{1} - \mathbf{1}')\delta(\mathbf{2} - \mathbf{2}')V(\mathbf{1} - \mathbf{2}) + iV(\mathbf{1} - \mathbf{2})\mathcal{G}(\mathbf{1}, \mathbf{1}')\mathcal{G}(\mathbf{2}, \mathbf{2}')V(\mathbf{1}' - \mathbf{2}') \\
 &+ i^2 \int_0^{-i\beta} d\bar{\mathbf{1}} \int_0^{-i\beta} d\bar{\mathbf{2}} V(\mathbf{1} - \mathbf{2})\mathcal{G}(\mathbf{1}, \bar{\mathbf{1}})\mathcal{G}(\mathbf{2}, \bar{\mathbf{2}})V(\bar{\mathbf{1}} - \bar{\mathbf{2}})\mathcal{G}(\bar{\mathbf{1}}, \mathbf{1}')\mathcal{G}(\bar{\mathbf{2}}, \mathbf{2}')V(\mathbf{1}' - \mathbf{2}') \\
 &+ \dots
 \end{aligned} \tag{5.7}$$

This is sketched diagrammatically in Fig. 5.5. In this way one clearly sees that the T -matrix accounts for the repeated scattering of two nucleons in the medium. Iterating also the left hand side of Eq. (5.1), one finds the following identity between \mathcal{G}_{II} and the T -matrix:

$$\begin{aligned}
 V(\mathbf{1} - \mathbf{2})\mathcal{G}_{II}(\mathbf{1}\mathbf{2}; \mathbf{1}'\mathbf{2}') &= \\
 &\int_0^{-i\beta} d\bar{\mathbf{1}} \int_0^{-i\beta} d\bar{\mathbf{2}} \left\{ \mathcal{G}(\mathbf{1}, \bar{\mathbf{1}})\mathcal{G}(\mathbf{2}, \bar{\mathbf{2}}) - \mathcal{G}(\mathbf{1}, \bar{\mathbf{2}})\mathcal{G}(\mathbf{2}, \bar{\mathbf{1}}) \right\} T(\bar{\mathbf{1}}\bar{\mathbf{2}}; \mathbf{1}'\mathbf{2}').
 \end{aligned} \tag{5.8}$$

This equation is extremely interesting, because it relates the in-medium interaction and the two-body propagator. From this equation, for instance, one sees that even in the case where the two-body potential is a hard-core, the T -matrix might remain finite if correlations induce a vanishing \mathcal{G}_{II} at small relative distances. In other words, even if the two-body interaction is of a singular type (and thus the perturbation expansion order by order in V fails), its corresponding T -matrix remains finite and well defined.

Let us now turn to the analytical structure of the T -matrix. Consider its definition, Eq. (5.6). Because of the notation $V(\mathbf{1} - \mathbf{2}) = \delta(t_1 - t_2)V(\mathbf{r}_1 - \mathbf{r}_2)$, one can easily see that the T -matrix is instantaneous in the time difference of its initial and final states:

$$T(\mathbf{1}\mathbf{2}; \mathbf{1}'\mathbf{2}') = \delta(t_1 - t_2)\delta(t_1' - t_2')\langle \mathbf{r}_1\mathbf{r}_2 | T(t_1 - t_1') | \mathbf{r}_1'\mathbf{r}_2' \rangle, \tag{5.9}$$

and thus it only depends on a single time difference, $\tau = t_1 - t_1'$. The dependence in this variable is quite interesting. The first term of Eq. (5.7), for instance, is proportional to $\delta(\tau)$, while the second term has two single-particle propagators

that do explicitly depend on τ . In the complex time domain, thus, and following the same procedure that was used for the single-particle propagator, one splits the time dependence accordingly to the three time regions of interest:

$$\langle \mathbf{r}_1 \mathbf{r}_2 | T(\tau) | \mathbf{r}_1 \mathbf{r}_2 \rangle = \begin{cases} \langle \mathbf{r}_1 \mathbf{r}_2 | T^>(\tau) | \mathbf{r}_1 \mathbf{r}_2 \rangle, & \text{Im } \tau < 0 \\ \langle \mathbf{r}_1 \mathbf{r}_2 | T^0(\tau) | \mathbf{r}_1 \mathbf{r}_2 \rangle, & \text{Im } \tau = 0 \\ \langle \mathbf{r}_1 \mathbf{r}_2 | T^<(\tau) | \mathbf{r}_1 \mathbf{r}_2 \rangle, & \text{Im } \tau > 0, \end{cases} \quad (5.10)$$

where $T^>$ and $T^<$ are analytic functions in the time argument τ and where T^0 accounts for a possible singular term at $\tau = 0$. Actually, this corresponds to the two-body potential, $T^0 = V$.

Consider the second (and remaining) terms in the expansion of Eq. (5.7). When one takes $t_1 = 0$, the propagators depending on $\mathbf{1}$ and $\mathbf{2}$ inside the expansion will become $\mathcal{G}^<$'s. On the other hand, for $t_1 = -i\beta$ they will be equal to $\mathcal{G}^>$. At all orders in the expansion, there are only two propagators which depend on t_1 . One can thus derive the following set of identities:

$$\begin{aligned} \langle \mathbf{r}_1 \mathbf{r}_2 | T(t_1 = 0, t_{1'}) | \mathbf{r}_1 \mathbf{r}_2 \rangle &= \langle \mathbf{r}_1 \mathbf{r}_2 | T^<(t_1 = 0, t_{1'}) | \mathbf{r}_1 \mathbf{r}_2 \rangle = \\ &= \dots \mathcal{G}^<(t_1 = 0, t_{1'}) \mathcal{G}^<(t_1 = 0, t_{1'}) \dots = \\ &= \dots e^{\beta\mu} \mathcal{G}^>(t_1 = -i\beta, t_{1'}) e^{\beta\mu} \mathcal{G}^>(t_1 = -i\beta, t_{1'}) \dots = \\ &= e^{2\beta\mu} \langle \mathbf{r}_1 \mathbf{r}_2 | T^>(t_1 = -i\beta, t_{1'}) | \mathbf{r}_1 \mathbf{r}_2 \rangle = \\ &= e^{2\beta\mu} \langle \mathbf{r}_1 \mathbf{r}_2 | T(t_1 = -i\beta, t_{1'}) | \mathbf{r}_1 \mathbf{r}_2 \rangle, \end{aligned}$$

where the \dots are supposed to include the remaining quantities and integrals in the expansion of Eq. (5.7). From that chain of equations, the KMS relation for the T -matrix is found:

$$\langle \mathbf{r}_1 \mathbf{r}_2 | T(t_1 = 0, t_{1'}) | \mathbf{r}_1 \mathbf{r}_2 \rangle = e^{2\beta\mu} \langle \mathbf{r}_1 \mathbf{r}_2 | T(t_1 = -i\beta, t_{1'}) | \mathbf{r}_1 \mathbf{r}_2 \rangle. \quad (5.11)$$

This relation is again of a quasi-periodical type in the imaginary time variable but, instead of carrying a minus sign as in Eq. (2.34), it carries a plus sign. This suggests the following Fourier decomposition for T (the space variables are omitted for convenience in the following):

$$T(\tau) = \frac{1}{-i\beta} \sum_{\nu} e^{-iZ_{\nu}\tau} T(Z_{\nu}), \quad (5.12)$$

where the Matsubara frequencies are now given by $Z_{\nu} = \frac{\nu\pi}{-i\beta} + 2\mu$ and the indices ν are even integers. This is in contrast to the fermionic one-body propagator, where the ν 's are odd, but it is in agreement with the Fourier transform of the equal-time two-body Green's function, Eq. (2.80). Moreover, this is logical in a sense, because the T -matrix accounts for the coherent scattering of a couple of fermions, which

behaves like a single boson. One can also define the Fourier transforms of the $T^>$ and $T^<$ functions along the real time axis:

$$T^{\lessgtr}(\Omega) = i \int_{-\infty}^{\infty} d\tau e^{i\Omega\tau} T^{\lessgtr}(\tau). \quad (5.13)$$

The two previous functions are related by the KMS relation for the T -matrix in Fourier space:

$$T^>(\Omega) = e^{\beta(\Omega-2\mu)} T^<(\Omega). \quad (5.14)$$

This is completely equivalent to the KMS relation in frequency space for the two-body propagator, Eq. (2.87), and thus suggests the following definition of a T -matrix “spectral function”:

$$\mathbb{T}(\Omega) = T^>(\Omega) - T^<(\Omega). \quad (5.15)$$

$T^>$ and $T^<$ might be obtained from \mathbb{T} by means of the relations:

$$T^<(\Omega) = b(\Omega)\mathbb{T}(\Omega) \quad (5.16)$$

$$T^>(\Omega) = [1 + b(\Omega)]\mathbb{T}(\Omega), \quad (5.17)$$

where $b(\omega)$ is the Bose-Einstein distribution defined in Eq. (2.91). The spectral decomposition is then readily obtained:

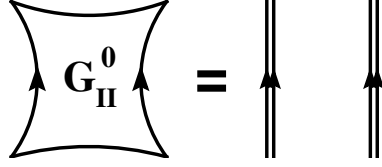
$$\begin{aligned} T(Z_\nu) &= \int_0^{-i\beta} d\tau e^{iZ_\nu\tau} T(\tau) = \int_0^{-i\beta} d\tau e^{iZ_\nu\tau} \left\{ \delta(\tau)V + T^>(\tau) \right\} \\ &= V - i \int_0^{-i\beta} d\tau \int_{-\infty}^{\infty} \frac{d\Omega'}{2\pi} e^{(iZ_\nu - i\Omega')\tau} [1 + b(\Omega')]\mathbb{T}(\Omega') \\ &= V + \int_{-\infty}^{\infty} \frac{d\Omega'}{2\pi} \frac{\mathbb{T}(\Omega')}{Z_\nu - \Omega'}. \end{aligned} \quad (5.18)$$

This function can be analytically continued to the whole complex plane with the possible exception of the real axis. Once again the procedure is unique due to the convergence properties at infinity of the previous expression. In particular, one might chose $Z = \Omega_+$. For that specific value one obtains the relation:

$$\mathbb{T}(\Omega) = -2\text{Im} T(\Omega_+). \quad (5.19)$$

All in all, the spectral decomposition of the T -matrix can be rewritten as:

$$T(Z) = V - \int_{-\infty}^{\infty} \frac{d\Omega'}{\pi} \frac{\text{Im} T(\Omega'_+)}{Z - \Omega'}. \quad (5.20)$$


 Figure 5.6: Diagrammatic representation of \mathcal{G}_{II}^0 .

Taking the previous expression slightly above the real axis, one finds the following expression for the real part of the T -matrix:

$$\text{Re } T(\Omega) = V - \mathcal{P} \int_{-\infty}^{\infty} \frac{d\Omega'}{\pi} \frac{\text{Im } T(\Omega'_+)}{\Omega - \Omega'}. \quad (5.21)$$

One thus sees that, in the limit of very high or very low energies, $\Omega \rightarrow \pm\infty$, the real part of the T -matrix reduces essentially to the bare interaction. This is also the case in the regions of momentum space where $\text{Im } T \sim 0$, independently of the energy.

To solve the equations for the \mathcal{G}_{II} propagator or the T -matrix, it is convenient to work in Fourier space. One thus needs to consider the remaining time dependences of Eq. (5.7). As already explained, this is given by the product of two (dressed) independent Green's function:

$$\langle \mathbf{r}_1 \mathbf{r}_2 | \mathcal{G}_{II}^0(t_1, t_{1'}) | \mathbf{r}'_1 \mathbf{r}'_2 \rangle = i \mathcal{G}(\mathbf{r}_1 - \mathbf{r}'_1, t_1 - t_{1'}) \mathcal{G}(\mathbf{r}_2 - \mathbf{r}'_2, t_1 - t_{1'}), \quad (5.22)$$

which is depicted in terms of diagrams in Fig. 5.6. This defines naturally the two correlation functions:

$$\mathcal{G}_{II}^0(\tau) = \begin{cases} \mathcal{G}_{II}^{0>}(\tau) = i \mathcal{G}^>(\tau) \mathcal{G}^>(\tau), \text{Im } \tau < 0 \\ \mathcal{G}_{II}^{0<}(\tau) = i \mathcal{G}^<(\tau) \mathcal{G}^<(\tau), \text{Im } \tau > 0. \end{cases} \quad (5.23)$$

The function \mathcal{G}_{II}^0 being a product of two single-particle propagators, it fulfills a KMS relation of the bosonic type:

$$\mathcal{G}_{II}^0(t_1 = 0, t_{1'}) = e^{2\beta\mu} \mathcal{G}_{II}^0(t_1 = -i\beta, t_{1'}). \quad (5.24)$$

The spectral decomposition of \mathcal{G}_{II}^0 follows the same steps as that of the two-body propagator, Eq. (2.76) to Eq. (2.88), and one finds:

$$\mathcal{G}_{II}^0(Z) = \int_{-\infty}^{\infty} \frac{d\Omega}{2\pi} \frac{\mathcal{G}_{II}^{0>}(\Omega) - \mathcal{G}_{II}^{0<}(\Omega)}{Z - \Omega}. \quad (5.25)$$

This equation can be expressed in terms of single-particle correlation functions by using the Fourier transform of Eqs. (2.41) and (2.42):

$$\mathcal{G}_{II}^{0\leq}(\Omega) = - \int_{-\infty}^{\infty} d\tau e^{i\Omega\tau} \mathcal{G}^{\leq}(\tau) \mathcal{G}^{\leq}(\tau) = \int_{-\infty}^{\infty} \frac{d\omega'}{2\pi} \mathcal{G}^{\leq}(\omega') \mathcal{G}^{\leq}(\Omega - \omega'), \quad (5.26)$$

yielding:

$$\begin{aligned} \mathcal{G}_{II}^0(Z) &= \int_{-\infty}^{\infty} \frac{d\omega}{2\pi} \int_{-\infty}^{\infty} \frac{d\omega'}{2\pi} \frac{\mathcal{G}^>(\omega) \mathcal{G}^>(\omega') - \mathcal{G}^<(\omega) \mathcal{G}^<(\omega')}{Z - \omega - \omega'} \\ &= \int_{-\infty}^{\infty} \frac{d\omega}{2\pi} \int_{-\infty}^{\infty} \frac{d\omega'}{2\pi} \mathcal{A}(\omega) \mathcal{A}(\omega') \frac{1 - f(\omega) - f(\omega')}{Z - \omega - \omega'}. \end{aligned} \quad (5.27)$$

By taking this quantity close to the real axis, $Z = \Omega_+$, it is easily to split it in an imaginary part:

$$\text{Im } \mathcal{G}_{II}^0(\Omega_+) = -\frac{1}{2} \int_{-\infty}^{\infty} \frac{d\omega}{2\pi} \mathcal{A}(\omega) \mathcal{A}(\Omega - \omega) [1 - f(\omega) - f(\Omega - \omega)], \quad (5.28)$$

and a real part:

$$\text{Re } \mathcal{G}_{II}^0(\Omega_+) = -\mathcal{P} \int_{-\infty}^{\infty} \frac{d\Omega'}{\pi} \frac{\text{Im } \mathcal{G}_{II}^0(\Omega'_+)}{\Omega - \Omega'}. \quad (5.29)$$

Note that this last dispersion relation allows to calculate the real part of \mathcal{G}_{II}^0 directly from the imaginary part. Finally, it is also interesting to note the following sum rule for the imaginary part of \mathcal{G}_{II}^0 :

$$\int_{-\infty}^{\infty} \frac{d\Omega}{\pi} \text{Im } \mathcal{G}_{II}^0(\Omega_+) = - [1 - n(k) - n(k')]. \quad (5.30)$$

This will be used further on as a test of the numerical accuracy of the many-body scheme within which the ladder approximation is solved (see Appendix E).

5.3 Lippman-Schwinger equation

All of the analytical properties for T and \mathcal{G}_{II}^0 that have just been derived are useful in the numerical resolution of the ladder approximation. An important point in this approach is to obtain the in-medium interaction by means of the integral equation Eq. (5.6). As a first step towards this solution, one should Fourier transform the equation. First of all, the time variable in Eq. (5.6) can be Fourier transformed using the previous definitions, to yield:

$$\begin{aligned} \langle \mathbf{r}_1 \mathbf{r}_2 | T(Z_\nu) | \mathbf{r}'_1 \mathbf{r}'_2 \rangle &= \delta(\mathbf{r}_1 - \mathbf{r}'_1) \delta(\mathbf{r}_2 - \mathbf{r}'_2) V(\mathbf{r}'_1 - \mathbf{r}'_2) \\ &+ \int d^3 r_{\bar{1}} \int d^3 r_{\bar{2}} V(\mathbf{r}_1 - \mathbf{r}_2) \langle \mathbf{r}_1 \mathbf{r}_2 | \mathcal{G}_{II}^0(Z_\nu) | \mathbf{r}_{\bar{1}} \mathbf{r}_{\bar{2}} \rangle \langle \mathbf{r}_{\bar{1}} \mathbf{r}_{\bar{2}} | T(Z_\nu) | \mathbf{r}'_1 \mathbf{r}'_2 \rangle. \end{aligned} \quad (5.31)$$

One can now transform the position variables in the previous equation to momentum space and find:

$$\begin{aligned} \langle \mathbf{k}_1 \mathbf{k}_2 | T(Z_\nu) | \mathbf{k}_3 \mathbf{k}_4 \rangle &= \langle \mathbf{k}_1 \mathbf{k}_2 | V | \mathbf{k}_3 \mathbf{k}_4 \rangle \\ &+ \mathcal{V} \int \frac{d^3 k_5}{(2\pi)^3} \mathcal{V} \int \frac{d^3 k_6}{(2\pi)^3} \langle \mathbf{k}_1 \mathbf{k}_2 | V | \mathbf{k}_5 \mathbf{k}_6 \rangle \mathcal{G}_{II}^0(Z_\nu; k_5 k_6) \langle \mathbf{k}_5 \mathbf{k}_6 | T(Z_\nu) | \mathbf{k}_3 \mathbf{k}_4 \rangle. \end{aligned} \quad (5.32)$$

This integral equation is a Lippman-Schwinger-type equation that defines the T -matrix in terms of the bare NN potential and the intermediate two-body propagator, \mathcal{G}_{II}^0 . The Lippman-Schwinger equation is, as a matter of fact, well-known in the field of nuclear physics, where it has been extensively used in several contexts [Day67]. In the particular case of the ladder approximation, the intermediate two-particle propagator can be rewritten as:

$$\begin{aligned} \mathcal{G}_{II}^0(Z_\nu; k, k') &= \int_{-\infty}^{\infty} \frac{d\omega}{2\pi} \int_{-\infty}^{\infty} \frac{d\omega'}{2\pi} \mathcal{A}(k, \omega) \mathcal{A}(k', \omega') \\ &\times \frac{[1 - f(\omega)][1 - f(\omega')] - f(\omega)f(\omega')}{Z_\nu - \omega - \omega'}. \end{aligned} \quad (5.33)$$

In this way, one finds that the zero-temperature limit of the previous propagator accounts, at the same time, for the propagation of a pair of particles (by means of the term proportional to $[1 - f(\omega)][1 - f(\omega')]$) and a pair of holes (through $f(\omega)f(\omega')$). In this sense, one says that \mathcal{G}_{II}^0 accounts for the in-medium particle-particle and hole-hole propagation. Note, however, that \mathcal{G}_{II}^0 is not the full two-body propagator, \mathcal{G}_{II} , but only its lowest order approximation.

In the solution of the Lippman-Schwinger equation for the T -matrix, it is important to exploit the invariance properties of the NN bare interaction. A practical solution of the equation for the T -matrix is found by means of the partial wave expansion introduced in Section 4.4. As a first step, one has to recast the Lippman-Schwinger equation in terms of the center-of-mass momentum, $\mathbf{K} = \mathbf{k} + \mathbf{k}'$, and the relative momentum, $\mathbf{k}_r = (\mathbf{k} - \mathbf{k}')/2$. Introducing the matrix element in relative space:

$$\frac{\mathcal{V}}{(2\pi)^3} \langle \mathbf{k} \mathbf{k}' | V | \mathbf{p} \mathbf{p}' \rangle = \delta(\mathbf{K} - \mathbf{P}) \langle \mathbf{k}_r | V | \mathbf{p}_r \rangle, \quad (5.34)$$

the Lippman-Schwinger equation for the scattering amplitude in the medium reads:

$$\begin{aligned} \langle \mathbf{k}_r | T(Z_\nu, \mathbf{K}) | \mathbf{p}_r \rangle &= \langle \mathbf{k}_r | V | \mathbf{p}_r \rangle \\ &+ \int d^3 q_r \langle \mathbf{k}_r | V | \mathbf{q}_r \rangle \mathcal{G}_{II}^0(Z_\nu; |\mathbf{K}/2 + \mathbf{q}_r|, |\mathbf{K}/2 - \mathbf{q}_r|) \langle \mathbf{q}_r | T(Z_\nu, \mathbf{K}) | \mathbf{p}_r \rangle. \end{aligned} \quad (5.35)$$

5.3. LIPPMAN-SCHWINGER EQUATION

An attempt to perform a partial wave expansion on the previous expansion will soon meet an additional problem. The \mathcal{G}_{II}^0 function depends explicitly on the lab frame momenta $k = |\mathbf{K}/2 + \mathbf{q}_r|$ and $k' = |\mathbf{K}/2 - \mathbf{q}_r|$. In particular, it carries a dependence on the angle θ between \mathbf{K} and \mathbf{q}_r . This leads to a coupling of the partial waves with different total angular momentum J in \mathcal{G}_{II}^0 [Sar96]. Or, in other words, the in-medium propagation of two nucleons does not conserve the total angular momentum of the pair. This coupling, of course, complicates the solution of the Lippman-Schwinger equation.

Fortunately, this problem can be circumvented by means of the so-called angle-average procedure. Within this procedure, the full \mathcal{G}_{II}^0 in Eq. (5.35) is replaced by the angle average:

$$\overline{\mathcal{G}_{II}^0}(Z_\nu; K, q_r) = \frac{1}{2} \int_{-1}^1 d(\cos \theta) \mathcal{G}_{II}^0(Z_\nu; |\mathbf{K}/2 + \mathbf{q}_r|, |\mathbf{K}/2 - \mathbf{q}_r|), \quad (5.36)$$

which does only depend on the modulus of K and q_r , and not on the angle between them. As a consequence of this replacement, the intermediate coupling between partial waves disappears and the Lippman-Schwinger equation becomes a one-dimensional integral equation. One can therefore use the partial wave expansion of Section 4.4 to expand the bras and kets in Eq. (5.35). The angular integral in θ is then easily carried out thanks to the introduction of the angle-independent $\overline{\mathcal{G}_{II}^0}$, and one finds:

$$\begin{aligned} \langle k_r | T_{LL'}^{JST}(Z_\nu, K) | p_r \rangle &= \langle k_r | V_{LL'}^{JST} | p_r \rangle \\ &+ \sum_{L''} \int dq_r q_r^2 \langle k_r | V_{LL''}^{JST} | q_r \rangle \overline{\mathcal{G}_{II}^0}(Z_\nu; K, q_r) \langle q_r | T_{L''L'}^{JST}(Z_\nu, K) | p_r \rangle. \end{aligned} \quad (5.37)$$

This gives the Lippman-Schwinger equation in terms of the partial waves in the NN interaction and in terms of an angle averaged independent two-body propagator, $\overline{\mathcal{G}_{II}^0}$. There have been estimates on the effects that the angle-averaging procedure involves in the self-energy as well as in the total energy for Brueckner-type calculations, and only small deviations from the exact results, of less than 1 MeV for both quantities around saturation, have been found [Sar96; Suz00]. To our knowledge, there are no available calculations that go beyond the quasi-particle approximation and that treat the angle-average exactly. The numerical solution of this equation is presented in Appendix E.

The in-medium interaction of Eq. (5.37) depends explicitly on the center-of-mass momentum. This is in contrast to the bare NN interaction, which only depends on the relative momenta. The explicit dependence in K of the T -matrix is a consequence of the presence of the medium, which sets a preferred frame of reference; namely, the frame in which the medium is at rest. This immediately implies the breaking of the velocity independence of the effective interaction and

sets its dependence on the total momentum of the particles interacting in the medium.

The T -matrix approximation breaks down at low temperatures for attractive interactions [Kad62; Mat92]. The ultimate reason of this breakdown is the appearance of a pole in the zero center-of-mass momentum T -matrix at an energy $\Omega = 2\mu$. This pole corresponds to a bound state of two nucleons, one with momentum k and the another one with momentum $-k$. In a BCS approach, one would say that these two nucleons, which are essentially at the Fermi surface due to the fact that their quasi-particle energies are equal to μ , form a Cooper pair. Thus the appearance of this pole signals an effect which is somehow related to superconductivity in metals. Actually, this complex pole in the effective interaction is associated to a pole in the single-particle propagator. But the fact that \mathcal{G} presents a pole goes against its analyticity conditions and thus signals the fact that, not only the T -matrix approximation, but perturbation theory itself breaks down. The appearance of such a pole is generic in fermionic systems with attractive interactions and it is known as the *pairing instability*. Actually, one can show that the problem lies in the description in terms of usual propagators of the superfluid phase. Due to the fact that paired states have different symmetry properties than single nucleons, perturbation theory cannot be described anymore within the usual Green's function approach. Instead, the theory has to be extended to include (Nambu-Gorkov) anomalous propagators [Abr65; Fet71; Mat92]. Yet, inside the normal phase one can try to quantify the critical temperature at which pairing appears by means of the Thouless criterion [Tho60]. In nuclear matter, this gives a critical temperature of about 5 MeV for the ${}^3S_1 - {}^3D_1$ pairing transition [Alm93; Alm96], although this is probably overestimated in quasi-particle approaches [Fri04a].

The T -matrix has other very interesting properties that will not be discussed here, but can be found in Refs. [Kad62] or [Kra86]. Among them, it is interesting to note that the in-medium T -matrix preserves unitarity, in the sense that it fulfills an optical theorem at finite temperature and densities. Furthermore, one can prove that, in the low-density limit, the T -matrix reduces to the usual free space scattering amplitude (which is also sometimes called the T -matrix). This of course differs from the in-medium T -matrix in the propagators (the Fermi distributions account for medium effects that are not present in free space) and in the absence of center-of-mass dependence (which is only present at finite density). One can thus fairly say that the T -matrix accounts for the scattering amplitude of two particles in the dense and hot medium.

5.4 Ladder self-energy

The ladder approximation can also be cast in terms of the self-energy. This is achieved by noticing that Eq. (5.8) gives $V \times \mathcal{G}_{II}$ in terms of the T -matrix and that the self-energy is defined in Eq. (2.115) precisely in terms of $V \times \mathcal{G}_{II}$. This

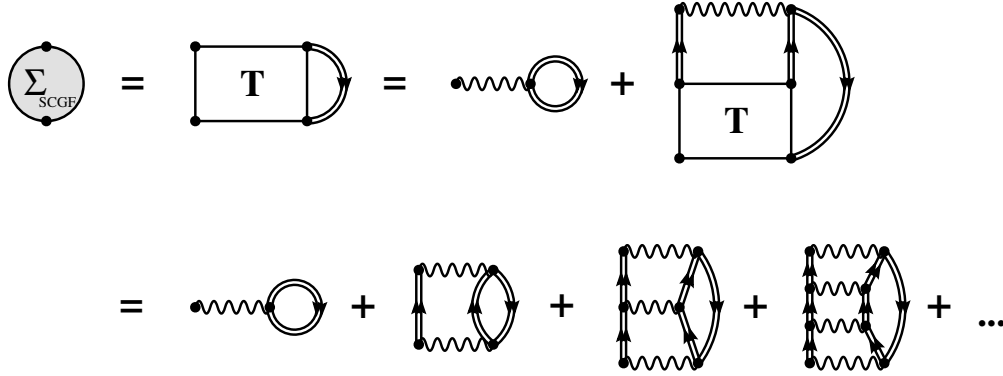


Figure 5.7: *Diagrammatic representation of the ladder self-energy.*

provides for the connection between the self-energy and the T -matrix, which is given by the equation:

$$\Sigma_L(\mathbf{1}, \mathbf{1}') = -i \int_0^{-i\beta} d\bar{\mathbf{2}} \int_0^{-i\beta} d\bar{\mathbf{3}} \langle \mathbf{1}\bar{\mathbf{2}} | T | \mathbf{1}'\bar{\mathbf{3}} \rangle_A \mathcal{G}(\bar{\mathbf{2}}, \bar{\mathbf{3}}). \quad (5.38)$$

The counterpart in terms of diagrams of this equation is given in Fig. 5.7. Note that the diagrammatic expansion of the ladder self-energy is given in terms of 2PI skeleton diagrams. The dressing of the intermediate lines is achieved by means of the iterative self-consistent procedure, as already discussed.

With this expression at hand, one can now try to study the analytical structure of the self-energy within the ladder approximation. This will follow closely the results obtained in Section 2.4. As a function of time, the ladder self-energy is decomposed in an instantaneous contribution (due to the instantaneous term in T) and two correlation functions:

$$\Sigma_L^{\lessgtr}(\mathbf{r}_1 - \mathbf{r}_1', \tau) = -i \int dr_2 \int dr_3 \langle \mathbf{r}_1 \mathbf{r}_2 | T^{\lessgtr}(\tau) | \mathbf{r}_1' \mathbf{r}_3 \rangle_A \mathcal{G}^{\lessgtr}(\mathbf{r}_2 - \mathbf{r}_3, \tau). \quad (5.39)$$

The self-energy in the imaginary time domain can be easily Fourier transformed to the Matsubara and momentum space, yielding:

$$\Sigma_L(k, z_\nu) = \frac{-i}{-i\beta} \sum_{\nu'} \int \frac{d^3 k'}{(2\pi)^3} \langle \mathbf{k} \mathbf{k}' | T(z_\nu + z_{\nu'}) | \mathbf{k} \mathbf{k}' \rangle_A \mathcal{G}(k', z_{\nu'}). \quad (5.40)$$

One can plug the spectral decomposition of the T -matrix, Eq. (5.18), into the previous equation, which then decomposes into the two contributions:

$$\Sigma_L(k, z_\nu) = \Sigma_{HF}(k) + \Sigma_C(k, z_\nu). \quad (5.41)$$

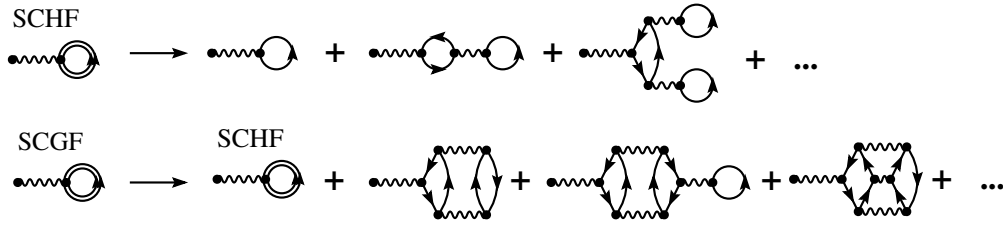


Figure 5.8: *Diagrammatic representation of the SCHF self-energy and the generalized HF contribution to the ladder self-energy.*

Note that this is the same kind of decomposition that was obtained in Section 2.4 [see Eq. (2.126)], where the properties of both terms were already discussed. The particular structure of these two contributions within the ladder approximation is explained in the following.

The first term corresponds to an instantaneous (energy-independent) contribution that comes from the bare potential:

$$\begin{aligned} \Sigma_{HF}(k) &= \frac{-i}{-i\beta} \int \frac{d^3k'}{(2\pi)^3} \langle \mathbf{k}\mathbf{k}' | V | \mathbf{k}\mathbf{k}' \rangle_A \sum_{\nu'} \mathcal{G}(k', z_{\nu'}) = \\ &= \int \frac{d^3k'}{(2\pi)^3} \langle \mathbf{k}\mathbf{k}' | V | \mathbf{k}\mathbf{k}' \rangle_A n(k'), \end{aligned} \quad (5.42)$$

where the Matsubara sum of Eq. (C.13) has been used. This has exactly the same aspect as the SCHF self-energy of Eq. (4.3). Note, however, that the previous expression is a generalized HF contribution, in the sense that the momentum distribution $n(k)$ is computed with the spectral function of the ladder approximation (which has a certain width, in contrast to the no-width spectral function of the SCHF scheme). In terms of diagrams, the difference between the SCHF self-energy and the generalized HF contribution to the SCGF self-energy come from the insertions of the internal line. While for the SCHF case these insertions are iterations of HF self-energies, in the generalized HF contribution these include all types of ladder correlations. This difference is shown schematically in Fig. 5.8. Note that, among the insertions included in the generalized HF contribution of the ladder approximation, the rearrangement term that accounts for the depletion in the Brueckner-Bethe-Goldstone theory (the second diagram in the SCGF row) is included [Jeu76; Zuo99].

The remaining term in the Fourier transform of the self-energy in Eq. (5.41) is proportional to the imaginary part of the T -matrix. Using the spectral decompo-

sition of the propagator, Eq. (2.57), this can be rewritten as:

$$\begin{aligned}\Sigma_C(k, z_\nu) &= -\frac{-i}{-i\beta} \sum_{\nu'} \int \frac{d^3k'}{(2\pi)^3} \int_{-\infty}^{\infty} \frac{d\Omega}{\pi} \frac{\langle \mathbf{k}\mathbf{k}' | \text{Im } T(\Omega_+) | \mathbf{k}\mathbf{k}' \rangle_A}{z_\nu + z_{\nu'} - \Omega} \int_{-\infty}^{\infty} \frac{d\omega'}{2\pi} \frac{\mathcal{A}(k', \omega')}{z_{\nu'} - \omega'} = \\ &= -\frac{1}{\beta} \int \frac{d^3k'}{(2\pi)^3} \int_{-\infty}^{\infty} \frac{d\Omega}{\pi} \int_{-\infty}^{\infty} \frac{d\omega'}{2\pi} \langle \mathbf{k}\mathbf{k}' | \text{Im } T(\Omega_+) | \mathbf{k}\mathbf{k}' \rangle_A \mathcal{A}(k', \omega') F(z_\nu, \Omega, \omega'),\end{aligned}\quad (5.43)$$

where $F(z_\nu, \Omega, \omega')$ is given by the Matsubara sum:

$$F(z_\nu, \Omega, \omega') = \sum_{\nu'} \frac{1}{z_{\nu'} + z_\nu - \Omega} \frac{1}{z_{\nu'} - \omega'}.\quad (5.44)$$

This sum involves a function with two poles. The procedure to compute it is sketched in Appendix C. First of all, the sum is converted into an integral of the summed function times $-\beta f(z)$, which is a function with unit poles at the Matsubara frequencies. One can deform the original contour C , which encircled each of the Matsubara frequencies in the positive sense, to a contour C' that only includes the poles of the integrand at $z_1 = \Omega - z_\nu$ and $z_2 = \omega'$ in the negative sense. Applying Cauchy's theorem to those poles (and noting that the contributions of the arcs at infinity vanish), one gets:

$$F(z_\nu, \Omega, \omega') = \beta \frac{f(\omega') - f(\Omega - z_\nu)}{z_\nu + \omega' - \Omega}.\quad (5.45)$$

One can now use the relation $f(\Omega - z_\nu) = -b(\Omega)$, valid for odd integers ν , to rewrite the Σ_C term as follows:

$$\Sigma_C(k, z_\nu) = - \int \frac{d^3k'}{(2\pi)^3} \int_{-\infty}^{\infty} \frac{d\Omega}{\pi} \int_{-\infty}^{\infty} \frac{d\omega'}{2\pi} \langle \mathbf{k}\mathbf{k}' | \text{Im } T(\Omega_+) | \mathbf{k}\mathbf{k}' \rangle_A \mathcal{A}(k', \omega') \frac{f(\omega') + b(\Omega)}{z_\nu + \omega' - \Omega}.\quad (5.46)$$

All the dependence in z_ν is now in the denominator of the last term in the previous expression. This allows to find the imaginary part of the self-energy within the ladder approximation:

$$\begin{aligned}\text{Im } \Sigma_L(k, \omega_+) &= \int \frac{d^3k'}{(2\pi)^3} \int_{-\infty}^{\infty} \frac{d\omega'}{2\pi} \langle \mathbf{k}\mathbf{k}' | \text{Im } T(\omega + \omega'_+) | \mathbf{k}\mathbf{k}' \rangle_A \mathcal{A}(k', \omega') \\ &\quad \times [f(\omega') + b(\omega + \omega')].\end{aligned}\quad (5.47)$$

It has already been shown (see Section 2.4) that the real part of the self-energy can be obtained from this imaginary part by means of the dispersion relation:

$$\text{Re } \Sigma_L(k, \omega) = \Sigma_{HF}(k) - \mathcal{P} \int_{-\infty}^{\infty} \frac{d\lambda}{\pi} \frac{\text{Im } \Sigma_L(k, \lambda_+)}{\omega - \lambda}.\quad (5.48)$$

The (purely real) generalized HF contribution within the ladder approximation has to be included in this expression. The remaining term is a principal value integral of the width, Γ , and involves a dispersive contribution that vanishes for large ω 's.

Several interesting properties arise from the previous expressions. In the first place, the correlated part of the self-energy in Eq. (5.47) has a surprising bosonic term. This appears due to the symmetric treatment of particle-particle and hole-hole propagation in the T -matrix. It is, for instance, absent in a BHF-type calculation, where only particle-particle correlations are taken into account. Furthermore, it is very important to note that the self-energy is the result of a very subtle cancellation. On the one hand, the bosonic function $b(\Omega)$ has a pole at $\Omega = 2\mu$. On the other hand, the imaginary part of the T -matrix has a node at this precise energy. This is easily seen from the fact that the imaginary part of the in-medium interaction is essentially proportional to $\text{Im} \mathcal{G}_{II}^0$. Rewriting the phase space factor of Eq. (5.28) as:

$$1 - f(\omega) - f(\Omega - \mu) = b^{-1}(\Omega)f(\omega)f(\Omega - \mu), \quad (5.49)$$

one finds that $\text{Im} \mathcal{G}_{II}^0(\Omega = 2\mu) = 0$ and thus $\text{Im} T(\Omega = 2\mu) = 0$. As long as this is true, the integrand in Eq. (5.47) will be a smooth function of ω' and the integral will yield finite results.

To complete this section, let us note that, in any calculation in nuclear matter, the T -matrix will be given in partial waves. It is thus reasonable to give an expression of the self-energy in terms of the partial wave decomposed T -matrix. This can be done following the same steps that were used for the SCHF self-energy in Section 4.4. The final result yields:

$$\begin{aligned} \text{Im} \Sigma_L(k, \omega_+) &= \frac{1}{16\pi} \sum_{JLST} [1 - (-1)^{L+S+T}] (2T + 1)(2J + 1) \\ &\int \frac{d^3 k'}{(2\pi)^3} \int_{-\infty}^{\infty} \frac{d\omega'}{2\pi} \langle q[\mathbf{k}, \mathbf{k}'] | \text{Im} T_{LL}^{JST}(P[\mathbf{k}, \mathbf{k}'], \omega + \omega'_+) | q[\mathbf{k}, \mathbf{k}'] \rangle \\ &\times \mathcal{A}(k', \omega') [f(\omega') + b(\omega + \omega')]. \end{aligned} \quad (5.50)$$

The notation $q[\mathbf{k}, \mathbf{k}']$ and $P[\mathbf{k}, \mathbf{k}']$ once again denotes that both the relative and the total momentum depend on the single-particle momenta, \mathbf{k} and \mathbf{k}' .

5.5 Self-Consistent Green's Functions scheme

The SCGF method is a particular scheme devised to obtain the spectral function within the ladder approximation in an iterative way. The equations involved in this process are sketched in Table 5.1. The self-consistency of the method refers, in this case, to the fact that the three relevant quantities (the T -matrix, the self-energy and the spectral function) are computed from each other at each step of

5.5. SELF-CONSISTENT GREEN'S FUNCTIONS SCHEME

Step	Eq.	SELF-CONSISTENT GREEN'S FUNCTION SCHEME
1	(3.47)	$\rho = \nu \int \frac{d^3k}{(2\pi)^3} \int_{-\infty}^{\infty} \frac{d\omega}{2\pi} \mathcal{A}(k, \omega) f(\omega, \tilde{\mu})$
2	(5.28)	$\text{Im } \mathcal{G}_{II}^0(\Omega_+; k, k') = -\frac{1}{2} \int_{-\infty}^{\infty} \frac{d\omega}{2\pi} \mathcal{A}(k, \omega) \mathcal{A}(k', \Omega - \omega) \times [1 - f(\omega) - f(\Omega - \omega)]$
3	(5.29)	$\text{Re } \mathcal{G}_{II}^0(\Omega; k, k') = -\mathcal{P} \int_{-\infty}^{\infty} \frac{d\Omega'}{\pi} \frac{\text{Im } \mathcal{G}_{II}^0(\Omega'_+; k, k')}{\Omega - \Omega'}$
4	(5.36)	$\overline{\mathcal{G}_{II}^0}(\Omega; K, q_r) = \frac{1}{2} \int_{-1}^1 d(\cos \theta) \mathcal{G}_{II}^0(\Omega; \mathbf{K}/2 + \mathbf{q}_r , \mathbf{K}/2 - \mathbf{q}_r)$
5	(5.35)	$\langle \mathbf{k}_r T(\Omega_+, K) \mathbf{p}_r \rangle = \langle \mathbf{k}_r V \mathbf{p}_r \rangle + \int d^3q_r \langle \mathbf{k}_r V \mathbf{q}_r \rangle \overline{\mathcal{G}_{II}^0}(\Omega; K, q_r) \langle \mathbf{q}_r T(\Omega_+, K) \mathbf{p}_r \rangle$
6	(5.47)	$\text{Im } \Sigma_L(k, \omega_+) = \int \frac{d^3k'}{(2\pi)^3} \int_{-\infty}^{\infty} \frac{d\omega'}{2\pi} \langle \mathbf{k}\mathbf{k}' \text{Im } T(\omega + \omega'_+, K) \mathbf{k}\mathbf{k}' \rangle_A \times \mathcal{A}(k', \omega') [f(\omega') + b(\omega + \omega')]$
7	(5.42)	$\Sigma_{HF}(k) = \int \frac{d^3k'}{(2\pi)^3} \langle \mathbf{k}\mathbf{k}' V \mathbf{k}\mathbf{k}' \rangle_A n(k')$
8	(2.131)	$\text{Re } \Sigma_L(k, \omega_+) = \Sigma_{HF}(k) - \mathcal{P} \int_{-\infty}^{\infty} \frac{d\lambda}{\pi} \frac{\text{Im } \Sigma_L(k, \lambda_+)}{\omega - \lambda}$
9	(2.130)	$\mathcal{A}(k, \omega) = \frac{-2\text{Im } \Sigma_L(k, \omega_+)}{\left[\omega - \frac{k^2}{2m} - \text{Re } \Sigma_L(k, \omega)\right]^2 + \left[\text{Im } \Sigma_L(k, \omega_+)\right]^2}$

Table 5.1: Set of equations iterated in the SCGF method.

the iterative process. Note that for every iteration these are calculated in both its energy and momentum dependence, *i.e.* they are off-shell. In this sense, when the results are converged, the spectral function that enters in, say, Eq. (5.47) to determine Σ_L , is the same one that is obtained from this self-energy through Eq. (2.130) in the whole energy-momentum range.

The iterative process starts usually with a given approximation to the spectral function. For a fixed temperature and density, one can then invert Eq. (3.47) to find the chemical potential $\tilde{\mu}$, which is used in the remaining thermal distribution functions that appear in this iteration. With \mathcal{A} and $\tilde{\mu}$, one can readily compute the imaginary part of the non-correlated two-body propagator, $\text{Im } \mathcal{G}_{II}^0$. By means of the dispersion relation of Eq. (5.29), the real part of this quantity can be determined. The dependence of \mathcal{G}_{II}^0 on the angle between the center-of-mass momentum and the relative momentum is then averaged out. With this result, one now solves the Lippman-Schwinger integral equation, Eq. (5.35), with the help of standard matrix inversion techniques. Once this is achieved, one has access to the imaginary part of the in-medium scattering amplitude which, via Eq. (5.47), yields the width Γ in the ladder approximation. At this point one can compute the real part of the self-energy. To this end, one needs both the generalized HF contribution of Eq. (5.42) and the dispersive contribution of Eq. (2.131). With the real and the imaginary parts of the self-energy, the spectral function is readily computed from Eq. (2.130). This spectral function can now be used to obtain a new chemical potential by means of Eq. (3.47), which starts a new iteration in the scheme.

It is also interesting to note that, in each iteration of the SCGF scheme, the spectral function is computed from the corresponding self-energy. The one-body propagator for an iteration is thus obtained from the self-energy of the previous iteration via Dyson's equation, which corresponds to a self-consistent renormalization procedure, as explained in Section 2.7. The renormalization process is however slightly different than the one introduced in the Hartree-Fock case (see Section 4.2), because in this case the initial guess is not the free one-body propagator, but a dressed propagator at a different temperature and density (see Appendix E). The analysis in terms of diagrams of this process is thus not as clean as in the SCHF case, where each iteration step could be seen to correspond to a given set of self-energy insertions (see Fig. 4.4). The convergence in the iterative process, however, guarantees that the final result corresponds to the self-consistent one-body propagator (self-consistent in the sense that it has gone through a self-consistent renormalization process).

About 5 to 10 iterations are enough to achieve full numerical consistency. The starting point for this iterative process (for a given density and temperature) is the spectral function of a different density and temperature. The exact number of iterations however depends strongly on how close the initial guess is from the final result and also on the level of degeneracy. At very high densities or low temperatures, for instance, where the system is very degenerate and thus close to

the $T = 0$ result, one needs a large number of mesh points in both momentum and energy to sample the sharp structures that arise in most of the quantities, especially close to the Fermi surface. This complicates the calculations and makes them very time-consuming. Note that this is also one of the reasons why the finite temperature calculations are more suitable than the zero-temperature ones. The softening of the peak-like structures in the spectral functions with temperature, for instance, is extremely useful in the numerical treatment. Still, the SCGF scheme at finite temperature, starting from a realistic NN interaction, is a very demanding task. The main difficulty lies precisely in correctly sampling these momentum and energy dependences for all the quantities, which usually implies the construction of accurate meshes which have to consider at the same time sharp structures at the Fermi surface as well as very wide tails in the low and high energy regions.

The full numerical resolution of the SCGF approach in nuclear matter was achieved in Refs. [Fri03; Fri04a]. Part of the results presented in this Thesis are based on this original work of the Tübingen group. The SCGF method is implemented numerically with the help of the MATLAB software, which is especially suited for the treatment of the large multi-dimensional arrays that appear in these calculations. A full iteration takes about 3 hours on a desktop computer and thus a full calculation takes about a day of computing time to achieve consistency. In Appendix E the numerical details entering the resolution of the SCGF scheme are presented. The reader might also find detailed explanations in Tobias Frick's Thesis [Fri04a].

5.6 Connection to other approaches

The SCGF scheme results from the requirement that the single-particle propagator, the self-energy and the in-medium interaction in the ladder approximation are obtained from one another at each iteration in a self-consistent manner. Both the energy and the momentum dependences are iterated self-consistently. Other many-body approximations soften these self-consistency requirements to a certain extent. Two of these approximations, which are close in spirit to the SCGF but which lack its full off-shell self-consistency, will now be discussed.

A somewhat intuitive approach that can be derived from the SCGF equations appears, for instance, from a no-width quasi-particle approximation to the spectral function, Eq. (2.137). Using this approximation, one can solve the equation for the T -matrix with the following non-correlated two-body propagator:

$$\overline{\mathcal{G}}_{IIQP}^0(\Omega_+; k, k') = \left\langle \mathcal{Z}(k)\mathcal{Z}(k') \frac{1 - f[\varepsilon_{QP}(k)] - f[\varepsilon_{QP}(k')]}{\Omega_+ - \varepsilon_{QP}(k) - \varepsilon_{QP}(k')} \right\rangle_{\theta}, \quad (5.51)$$

where the notation $\langle \cdot \rangle_{\theta}$ is meant to represent the angle average procedure. In this approximation, a pole in the denominator shows up and thus needs to be extracted

with a suitable technique [Haf70]. From the in-medium interaction, one computes the self-energy from the equation:

$$\begin{aligned} \text{Im } \Sigma_{QP}(k, \omega_+) = & \int \frac{d^3k'}{(2\pi)^3} \mathcal{Z}(k') \langle \mathbf{k}\mathbf{k}' | T(\omega_+ + \varepsilon_{QP}(k'), K) | \mathbf{k}\mathbf{k}' \rangle_A \\ & \times [f[\varepsilon_{QP}(k')] + b[\omega + \varepsilon_{QP}(k')]]. \end{aligned} \quad (5.52)$$

This can be computed for different energies ω and then, by means of the dispersion relation of Eq. (5.48), one obtains an energy-dependent $\text{Re } \Sigma$. For each momentum, this can be used to find a new quasi-particle spectrum:

$$\varepsilon_{QP}(k) = \frac{k^2}{2m} + \text{Re } \Sigma_{QP}(k, \varepsilon_{QP}(k)), \quad (5.53)$$

which is then introduced in Eq. (5.51) to compute a new T -matrix and a new self-energy. The procedure can be iterated, until consistency in the quasi-particle spectrum, $\varepsilon_{QP}(k)$, is reached. The real and imaginary parts of the self-energy thus obtained can be used to build a spectral function \mathcal{A} , which contains a non-trivial energy dependence. These equations (usually defined with $\mathcal{Z} = 1$) form the so-called *Quasi-Particle Green's Function* (QPGF) approach [Ram88; Ram89]. Note that the main difference between this and the SCGF approach is the self-consistency in the off-shell behavior of $\mathcal{A}(k, \omega)$. While in the SCGF method the spectral function is treated at every step in both its momentum and energy variables, the QPGF works with a no-width spectral function until the last iteration. In this sense, the QPGF method does not treat off-shell effects consistently.

The QPGF method describes the intermediate particle-particle and hole-hole propagation at the quasi-particle level. This is already one step beyond the usual BHF approach, in which only particle-particle correlations are considered. Both methods, however, differ in their foundations. While the QPGF approach is derived from the diagrammatic expansion of the Green's function, the BHF approach relies on the Goldstone expansion for the total energy of a many-body system [Gol57]. This is somewhat equivalent to the linked cluster expansion for Ω , but at zero temperature and expressed in terms of the so-called Goldstone diagrams. One can sum up an infinite series of these diagrams by introducing the G -matrix, an in-medium interaction that is corrected with the Pauli blocking effects that act on the scattering process of two intermediate particles. This is related to the T -matrix introduced above and also fulfills a Lippman-Schwinger equation. The total energy of the system can then be expanded in terms of diagrams containing G -matrices and a given number of hole lines. Actually, Bethe showed that the correct expansion parameter is given by the number of hole lines which, roughly speaking, is proportional to the density [Bet65]. This is the so-called Brueckner-Bethe-Goldstone (or hole-line) expansion for the total energy of an interacting many-body system. Taking the lowest order term in this expansion gives the BHF approximation, which was the first successful theory in describing qualitatively the properties of nuclear matter from microscopical interactions [Day67].

One can derive a certain extension of the BHF theory at finite temperatures from the SCGF approach. This is achieved by keeping in the \mathcal{G}_{II}^0 of Eq. (5.27) only the contribution of the $\mathcal{G}^>$ correlation functions which correspond, in the zero-temperature limit, to the particle propagators. With this prescription, \mathcal{G}_{II}^0 becomes the particle-particle propagator:

$$\begin{aligned}\mathcal{G}_{II,BHF}^0(\Omega_+; k, k') &= \int_{-\infty}^{\infty} \frac{d\omega}{2\pi} \int_{-\infty}^{\infty} \frac{d\omega'}{2\pi} \frac{\mathcal{G}^>(k, \omega)\mathcal{G}^>(k', \omega')}{\Omega_+ - \omega - \omega'} \\ &= \int_{-\infty}^{\infty} \frac{d\omega}{2\pi} \int_{-\infty}^{\infty} \frac{d\omega'}{2\pi} \mathcal{A}(k, \omega)\mathcal{A}(k', \omega') \frac{[1 - f(\omega)][1 - f(\omega')]}{\Omega_+ - \omega - \omega'}.\end{aligned}\quad (5.54)$$

Now one might take also the no-width quasi-particle approximation with $\mathcal{Z} = 1$ and angle-average this quantity to get:

$$\overline{\mathcal{G}_{II,BHF}^0}(\Omega_+; k, k') = \left\langle \frac{[1 - f[\varepsilon_{BHF}(k)]] [1 - f[\varepsilon_{BHF}(k')]]}{\Omega_+ - \varepsilon_{BHF}(k) - \varepsilon_{BHF}(k')} \right\rangle_{\theta}. \quad (5.55)$$

This reduces to the in-medium propagator of two-particles in the zero temperature limit, where the phase space factors of the numerator become the Pauli blocking factors $\Theta[k - k_F]\Theta[k' - k_F]$. The denominator in the previous expression is given by the quasi-particle spectrum $\varepsilon_{BHF}(k)$, both below and above the Fermi surface. Within a zero temperature BHF framework, the quasi-particle energies are determined from:

$$\varepsilon_{BHF}(k) = \frac{k^2}{2m} + \Sigma_{BHF}(k, \varepsilon_{BHF}(k)), \quad (5.56)$$

only for hole ($k < k_F$) states, according to the Bethe-Brandow-Petschek theorem [Bet63]. Above the Fermi surface, one is free to chose the particle spectrum. The traditional choice is to use a free spectrum, which introduces an energy gap in the spectrum at the Fermi surface and is accordingly called the gap choice. Yet, the continuous choice arises more naturally in Green's function theory and it has been proposed as an alternative [Jeu76]. In addition, the continuous choice at the two-hole line level yields results which are closer to the full three-hole line expansion, which is a sign of its better convergence properties in the hole-line expansion [Son98]. The in-medium interaction associated to this BHF approach at finite temperature reads:

$$\begin{aligned}\langle k_r | G(\Omega_+, K) | p_r \rangle &= \langle k_r | V | p_r \rangle \\ &+ \int d^3q_r \langle k_r | V | q_r \rangle \overline{\mathcal{G}_{II,BHF}^0}(\Omega_+; K, q_r) \langle q_r | G(\Omega_+, K) | p_r \rangle,\end{aligned}\quad (5.57)$$

which defines the so-called G -matrix. Now one can determine the corresponding BHF self-energy from this interaction. Nevertheless, an extra approximation has

to be carried out before one can strictly say that the BHF approach is derived from the SCGF method. It has already been commented that the bosonic factor appearing in Eq. (5.47) is due to the consistent propagation of both particle-particle and hole-hole pairs. Within the BHF approximation at zero temperature, only particle-particle pairs propagate and thus no bosonic factor should appear. Indeed, both the real and imaginary part of the on-shell self-energy are obtained from the following expression:

$$\Sigma_{BHF}(k) = \int \frac{d^3k'}{(2\pi)^3} \langle \mathbf{k}\mathbf{k}' | G([\varepsilon_{BHF}(k) + \varepsilon_{BHF}(k')]_+, K) | \mathbf{k}\mathbf{k}' \rangle f[\varepsilon_{BHF}(k')]. \quad (5.58)$$

The set of equations Eq. (5.56), Eq. (5.57) and Eq. (5.58) are to be solved self-consistently. Note that, in contrast to the SCGF method, in the BHF approach one only needs to compute the on-shell self-energy at each step of the iterative process.

The equations presented above give, in the zero temperature limit, the corresponding expressions of the G -matrix and the self-energy of the usual zero-temperature BHF approach. Yet, this does not necessarily mean that this is the correct generalization of the BHF method at finite temperature. As a matter of fact, there is no such direct generalization and one cannot associate the scheme presented above to a partial summation of diagrams for the energy per particle at finite temperature. Instead, a partial sum can be achieved for the grand-canonical potential in the so-called Bloch-de Dominicis (BdD) approach [Blo58a; Blo58b; Blo59a; Blo59b]. This correspond to a different many-body method than the one presented in this Thesis. Its diagrammatic expansion, for instance, is written in terms of cylindrical diagrams (see [Nic05], for a complete discussion about this scheme). Within this theory, a similar expression to Eq. (5.57) for the in-medium temperature-dependent interaction can be obtained, but in principle there is not a straightforward expression for the energy per particle of the finite temperature system. The grand-potential, on the other hand, can be expressed in terms of the in-medium interaction and, from it, the remaining thermodynamical properties of the system can be derived. Traditionally, however, the BHF approach has been extended to finite temperatures in a more naive way, closer to the scheme introduced above. One simply replaces the zero temperature momentum distribution, $n(k) = \Theta(k_F - k)$, with the Fermi-Dirac distribution $f[\varepsilon_{BHF}(k)]$ in all the equations of the zero temperature BHF approximation. In this way, Eq. (5.57) for the G -matrix is reproduced and the total energy of the system is given by:

$$\begin{aligned} \frac{E^{BHF}}{A} &= \frac{\nu}{\rho} \int \frac{d^3k}{(2\pi)^3} f[\varepsilon_{BHF}(k)] \frac{k^2}{2m} \\ &+ \frac{\nu}{2\rho} \int \frac{d^3k}{(2\pi)^3} \int \frac{d^3k'}{(2\pi)^3} f[\varepsilon_{BHF}(k)] f[\varepsilon_{BHF}(k')] \\ &\times \langle \mathbf{k}\mathbf{k}' | G([\varepsilon_{BHF}(k) + \varepsilon_{BHF}(k')]_+, K) | \mathbf{k}\mathbf{k}' \rangle. \end{aligned} \quad (5.59)$$

The free energy is then computed from this generalization of the energy per particle plus a mean-field expression for the entropy of the system [Lej86; Bom94; Zuo03; Rio05a]. The BHF calculations presented in this Thesis have been obtained within this scheme. Even though this approximation is not based on first principles, it yields reasonable results, because the dominant diagrams of the BdD expansion reduce to this naive finite temperature BHF approach for low temperatures [Bal99]. The BdD approach has been applied to hot nuclear matter from realistic NN potentials by the Catania group [Bal99; Bal04; Nic05]. To our knowledge, there is no detailed study in which the BdD theory and the Green's function approach at finite temperatures are thoroughly compared.

5.7 Microscopic results

All the results quoted in this and the following sections have been obtained with the finite temperature SCGF scheme described in detail in Appendix E using the CDBONN potential [Mac96]. In the numerical treatment, partial waves up to $J = 8$ have been included in the generalized Hartree-Fock term and up to $J = 2$ in the inversion procedure for the T -matrix. On the other hand, the quoted BHF results have been computed with the same NN potential with partial waves up to $J = 4$. None of these calculations include three-body forces. The saturation point of nuclear matter is thus not reproduced and, in this sense, the results presented in this Thesis should be taken as a first study of the properties of nuclear matter within SCGF theory.

5.7.1 In-medium interaction

Once the sum over partial waves of Eq. (5.37) is performed, the resulting diagonal T -matrix depends on three quantities: the total energy of the two scattering particles, Ω ; the center-of-mass momentum, P , and the relative momentum, q . In the figures here presented, the relative momentum has been set to zero, $q = 0$, and thus the single-particle momenta of the two scattering particles are equal. In the left panel of Fig. 5.9, a density plot of the imaginary part of the T -matrix is shown at ρ_0 and $T = 10$ MeV. On top of the density plot, the dashed line corresponds to the relation $\Omega = 2\varepsilon_{qp}(P)$. This curve defines two very different regions for the imaginary part of the in-medium interaction at this momentum. The region of the $P - \Omega$ plane where $\text{Im } T$ is different from zero corresponds roughly to $\Omega > 2\varepsilon_{qp}(P)$. Actually, in a quasi-particle picture at zero temperature one can show that, below this value, the imaginary part of the in-medium interaction cancels exactly [Ram88; Dew02]. As seen in the figure, this is also approximately true in the SCGF scheme at finite temperature.

Moreover, the Fermi momentum also defines two different regions of interest for the T -matrix. Above $P = k_F$, for instance, $\text{Im } T$ is restricted to the region $\Omega > 2\mu$,

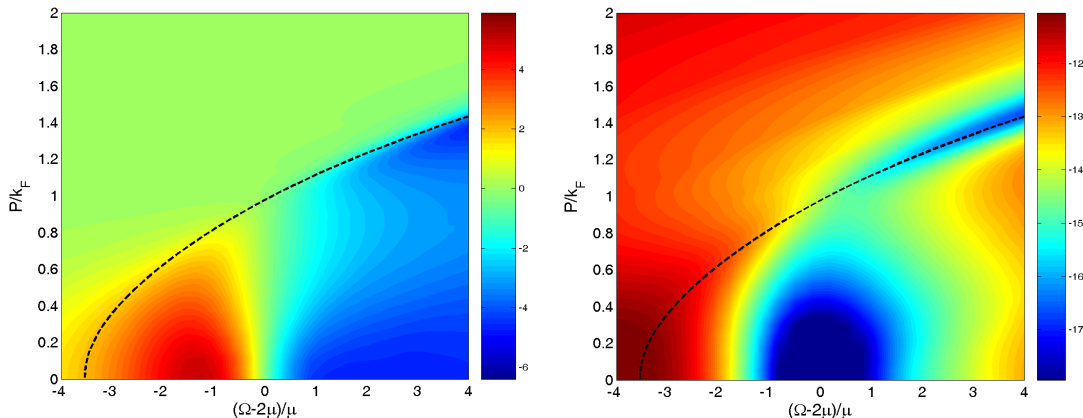


Figure 5.9: *Left panel: Density plot of the imaginary part of the T -matrix (the units are MeV fm^3) as a function of the total energy $\Omega - 2\mu$ (in units of the chemical potential, $\mu = -24.8 \text{ MeV}$) and the center-of-mass momentum P (in units of the Fermi momentum, $k_F = 263 \text{ MeV}$) for a relative momentum of $q = 0$. The black dashed line is given by the relation $\Omega = 2\varepsilon_{qp}(P)$. The density is $\rho = \rho_0$ and the temperature is 10 MeV . Right panel: real part of the T -matrix in the same conditions.*

it is negative and it presents a valley-like structure that follows closely $\Omega = 2\varepsilon_{qp}(P)$ relation energies (see also Fig. 5.10). Below the Fermi surface, on the other hand, the structure of the imaginary part is quite different. While for energies below 2μ it is basically positive, at energies above the chemical potential the imaginary part of the in-medium interaction becomes negative. This corresponds to the wiggly-like structure that is most easily seen in Fig. 5.10. Note that, both above and below the Fermi momentum, the imaginary part of the T -matrix has a node at $\Omega = 2\mu$. As commented previously, this condition is necessary in order to cancel the pole of the bosonic contribution in Eq. (5.47).

The imaginary part of the T -matrix is shown in a three-dimensional plot in Fig. 5.10. This allows for a clear overall view of its properties as a function of the two-particle energy, Ω , and the center-of-mass momentum, P , at $q = 0$. The two effective interactions of the figure have been computed for the same density, but the left and right panels correspond to two different temperatures, chosen to illustrate its temperature dependence. While the left panel is obtained from a low temperature, $T = 5 \text{ MeV}$, the right one is computed for a high temperature of $T = 20 \text{ MeV}$. In the first place, let us note that from the figure it is clear that the region with finite contributions of $\text{Im } T$ is mostly independent of temperature. This region is given by the condition $\Omega > 2\varepsilon_{qp}(P)$ and its temperature independence signals the fact that the quasi-particle energies are almost independent of temperature. This will be seen more clearly in the following (see Fig. 5.16). In addition, in both

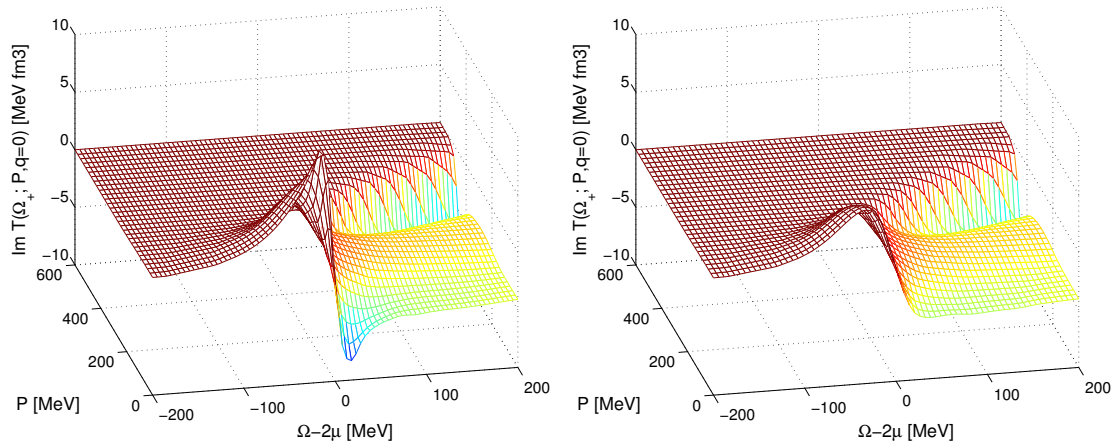


Figure 5.10: *Imaginary part of the T -matrix as a function of the total energy $\Omega - 2\mu$ and the center-of-mass momentum P for $q = 0$. The density is $\rho = \rho_0$ and the temperature is 5 MeV for the left panel and 20 MeV for the right panel.*

panels one can see the valley-like structure above $P = k_F$, which corresponds to the energies set by the quasi-particle relation $\Omega = 2\varepsilon_{qp}(P)$. The figures in both panels, however, display a relevant difference: the wiggly structure close to $P = 0$ and $\Omega = 2\mu$ is much more pronounced in the low temperature T -matrix than in the high-temperature one. As explained above, this is the region where pairing is mostly favored and the appearance of this strength can be related to this low-temperature phenomenon. This also explains why at higher temperatures, where pairing is less important, the structure is softened.

The precursor effects of the pairing transition are most clearly seen in the real part of the T -matrix, shown in Fig. 5.11 for the same conditions. The real and the imaginary part of the T -matrix are related by the dispersion relation of Eq. (5.21). In general terms, one expects that, whenever the imaginary part presents a structure, this is translated into the real part by means of this dispersive integral. This explains the fact that the pairing structure is seen in Fig. 5.11 in the same region as commented above. For the low temperature, however, the structure is particularly strong. As mentioned previously, at very low temperatures the presence of a pole at $q = 0, \Omega = 2\mu$ signals the onset of a phase in which nucleons tend to form Cooper pairs. Actually, the dip in $\text{Re} T$ is related to the strong attraction that nucleons feel in this kinematical conditions and thus can be taken as a precursor effect of the pairing instability. For a temperature lower than $T = 5$ MeV, this structure will eventually become a pole, signaling the breakdown of the T -matrix approximation. Apart from this low momentum structure, the general aspect of the two panels in Fig. 5.11 is quite similar. At very low energies and high momenta, for instance, the real part of the T -matrix becomes constant

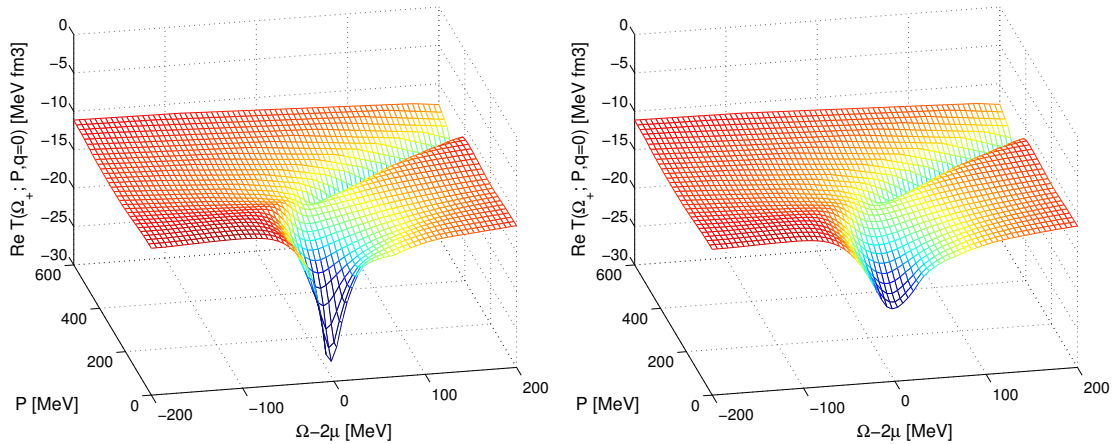


Figure 5.11: *Real part of the T -matrix as a function of the total energy $\Omega - 2\mu$ and the center-of-mass momentum P for $q = 0$. The density is $\rho = \rho_0$ and the temperature is 5 MeV for the left panel and 20 MeV for the right panel.*

at the two temperatures. From Eq. (5.21), it is easy to see that this energy and momentum independent contribution comes from the bare NN interaction. In fact, the zones where $\text{Re}T$ becomes a constant are essentially those where the dispersive contribution of Eq. (5.21) gives no contribution to the in-medium interaction. Moreover, the real part of the effective interaction presents a valley-like structure above $P = k_F$ which follows closely the relation $\Omega = 2\varepsilon_{qp}(P)$. This is clearly seen in the right panel of Fig. 5.9, where the dashed line coincides, above k_F and 2μ , with the minima of $\text{Re}T$. Finally, it is interesting to note that, in the region $P \sim k_F$ and $\Omega \sim 2\mu$, the real part of the in-medium interaction presents a neck, where its total contribution is smaller in absolute value than both the low momentum and low energy pairing region and the high momentum and high energy valley structure.

5.7.2 Self-energy

As explained above, once the in-medium interaction is known, the self-energy can be readily computed. In particular, the imaginary part of the ladder self-energy is given by the integral of Eq. (5.47), in which the spectral function, the imaginary part of the in-medium interaction and the phase space factor play an important role. In the numerical evaluation of $\text{Im}\Sigma$ there is an interplay between the signs of these functions above and below 2μ , so that the final convolution yields a negative $\text{Im}\Sigma$ in the whole energy and momentum domain, as it should be according to Eq. (2.129). Once this is known, the dispersion relation of Eq. (2.131) can be used to obtain the real part of the ladder self-energy.

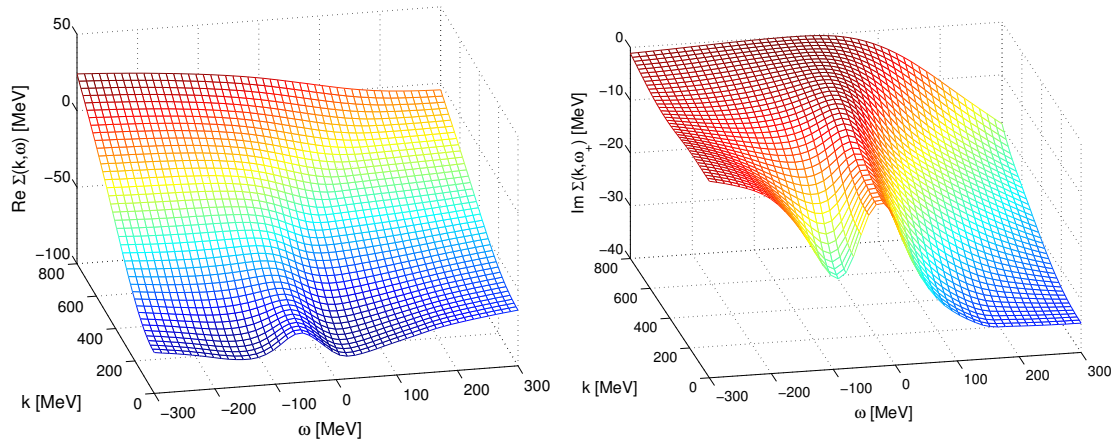


Figure 5.12: *Real (left panel) and imaginary (right panel) part of the self-energy as a function of the momentum k and energy ω . This has been computed at ρ_0 and $T = 10$ MeV.*

The real part of the self-energy is shown in the left panel of Fig. 5.12 for nuclear matter at ρ_0 and $T = 10$ MeV as a function of the single-particle momentum k and the energy ω . In the zone close to $k \sim 0$ and $\omega = \mu$, a wiggle is neatly seen. Apart from that small structure at intermediate energies, the real part of the self-energy appears to be almost energy independent. This is a consequence of the fact that the generalized HF contribution yields large values that easily overcome the dispersive contribution of Eq. (5.48). The important momentum dependence is also essentially given by the HF contribution, which becomes very repulsive at large momenta. At low momentum, the presence of the (overall) attractive dispersive contribution helps in getting a more attractive real self-energy.

The right panel of Fig. 5.12 displays the imaginary part of the self-energy for the same density and temperatures. Around $\omega \sim \mu$ and for low momenta, the imaginary part of Σ presents a cusp. This can be understood from a careful analysis of the convolution of the different factors in Eq. (5.47) [Fri04a]. At energies close to the chemical potential, the available phase space is reduced and $\text{Im } \Sigma$ tends to be negligible. Actually, for a zero temperature calculation, Luttinger [Lut60] showed that, due to phase space restrictions, the imaginary part of the self-energy must have a parabolic shape:

$$\text{Im } \Sigma(k, \omega) \sim a(\omega - \mu)^2. \quad (5.60)$$

One can see that this parabolic shape is kept at finite temperature, although the width does not vanish anymore once thermal effects are included in the system. As a matter of fact, for low temperatures the previous relation is modified to:

$$\text{Im } \Sigma(k, \omega) \sim a[(\omega - \mu)^2 + \pi^2 T^2], \quad (5.61)$$

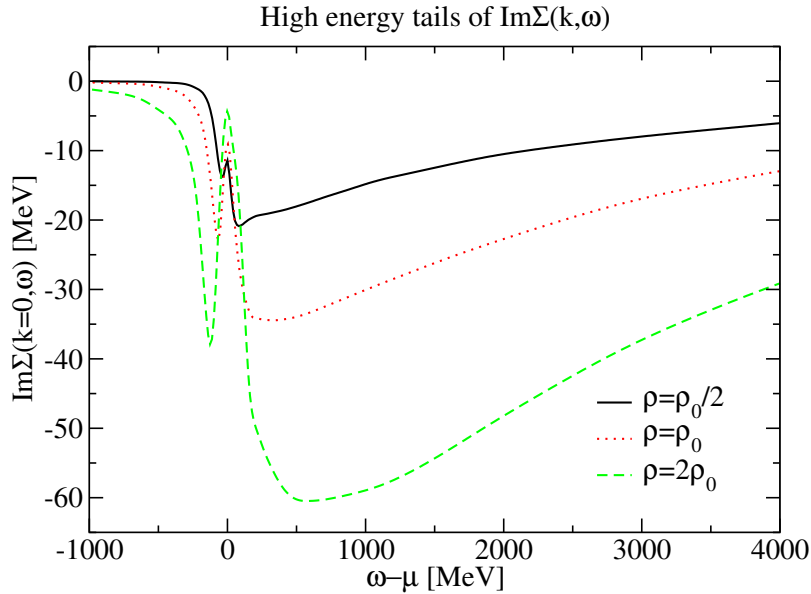


Figure 5.13: *High energy tails of $\text{Im}\Sigma(k=0, \omega)$. The three curves are given at three different densities: $\rho_0/2$ (full line), ρ_0 (dotted line) and $2\rho_0$ (dashed line).*

which yields a width that, for $\omega = \mu$, increases quadratically with temperature [Abr65]. For energies slightly below μ , the phase space is still small, but the convolution of the bosonic and fermionic term with the spectral function of particle ($k > k_F$) states is relevant and gives large results. For energies above (but close to) μ , the hole states of the spectral function convolute with the phase space factors to give a non-zero $\text{Im}\Sigma$ [Fri04a]. This explains the large values for energies somewhat lower and larger than μ , which are translated into a strong cusp in the imaginary part of Σ . This cusp is softened at high momentum, where the imaginary part of the self-energy becomes essentially flat and close to zero below $\omega = \mu$. For zero momentum states, there is an intermediate minimum between the $\omega \sim \mu$ cusp and the zero at very negative energies. This dip disappears with increasing momentum. There is also a minimum between $\omega = \mu$ and the high energy region where $\text{Im}\Sigma \rightarrow 0$. This is however not resolved in the figure due to the small energy range shown. Let us note that this minimum, in contrast to the one appearing in the hole ($\omega < \mu$) region, does not disappear at large momenta.

The tails for very negative (low) and very positive (high) energies of the imaginary part of the self-energy at $k = 0$ are shown in a large range of energies in Fig. 5.13. The density dependence of these tails is explored by showing the results obtained at $\rho_0/2$, ρ_0 and $2\rho_0$. The first thing to note is the strong asymmetry in the energy regions. While, at negative energies of around $\omega \sim \mu - 1000$ MeV the imaginary part of the self-energy is already negligible at all densities, for positive

energies at $\omega \sim \mu + 4000$ MeV it still yields large values. This strength of the self-energy at very high energies is closely related to the short-range core of the NN interaction. When iterated in the formalism, this short-range core excites low-energy and low-momentum states to higher energy and momentum states. The exact details of this excitation depend on the short-range behavior of the bare potential, which nonetheless might not be well resolved by experimental NN scattering data. One can however analyze the density dependence of these queues. The low energy damping of the imaginary-part, on the one hand, is strongly density dependent and is mainly due to the attenuation of the $\text{Im}T$ matrix elements at very negative energies. On the other hand, the high energy queues decrease almost linearly with density. This behavior can be traced back to the density independence of the T -matrix at high energies. Since this factor is independent of ρ , the density dependence must come from the remaining integral of the phase space factors, which indeed gives a contribution almost proportional to the density [Fri04a].

The density and temperature dependences of the imaginary part of the self-energy are studied, for energies close to μ , in Fig. 5.14. The left column of panels displays the energy dependence for five different densities, distributed in equidistant steps from 0.1 to 0.5 fm^{-3} , while the right column shows $\text{Im}\Sigma$ at four temperatures, from $T = 5$ to 20 MeV. The momentum dependence is explored by showing three panels corresponding to the momenta $k = 0$ (upper), k_F (middle) and $2k_F$ (lower panels). A striking difference can be observed when comparing the two columns. While the imaginary part of the self-energy is strongly density dependent (with changes of up to 60 MeV for all momenta in the high energy region), this quantity does not change appreciably with temperature. For the panel on the right column corresponding to $k = 2k_F$, for instance, there is no appreciable difference among the $\text{Im}\Sigma$'s at the four displayed temperatures. At the Fermi surface ($k = k_F$), differences start to appear, mainly in the region close to $\omega = \mu$, where the absolute value of $\text{Im}\Sigma$ increases with temperature. As explained before, in the zero temperature limit, $\text{Im}\Sigma(k, \omega = \mu)$ should cancel exactly. At low temperatures, one is close to this cancellation, but with a quadratic temperature dependence [Boz02]. The same behavior is obtained for the zero momentum self-energy, where the effect of temperature is however larger. Moreover, for this momentum some appreciable differences appear both above and below the chemical potential. In these regions, one finds that the imaginary part decreases in absolute value with temperature. These variations with temperature are easily smeared out with energy, and for $\omega < \mu - 200$ MeV or $\omega > \mu + 400$ MeV they are not anymore observable.

Concerning the momentum dependence of the results, it is interesting to note that in all cases one observes a local minimum below $\omega = \mu$, although this dip becomes shallower and wider with higher momenta. It is hardly appreciated at $k = 2k_F$, for instance. Furthermore, the position of this low-energy dip is strongly

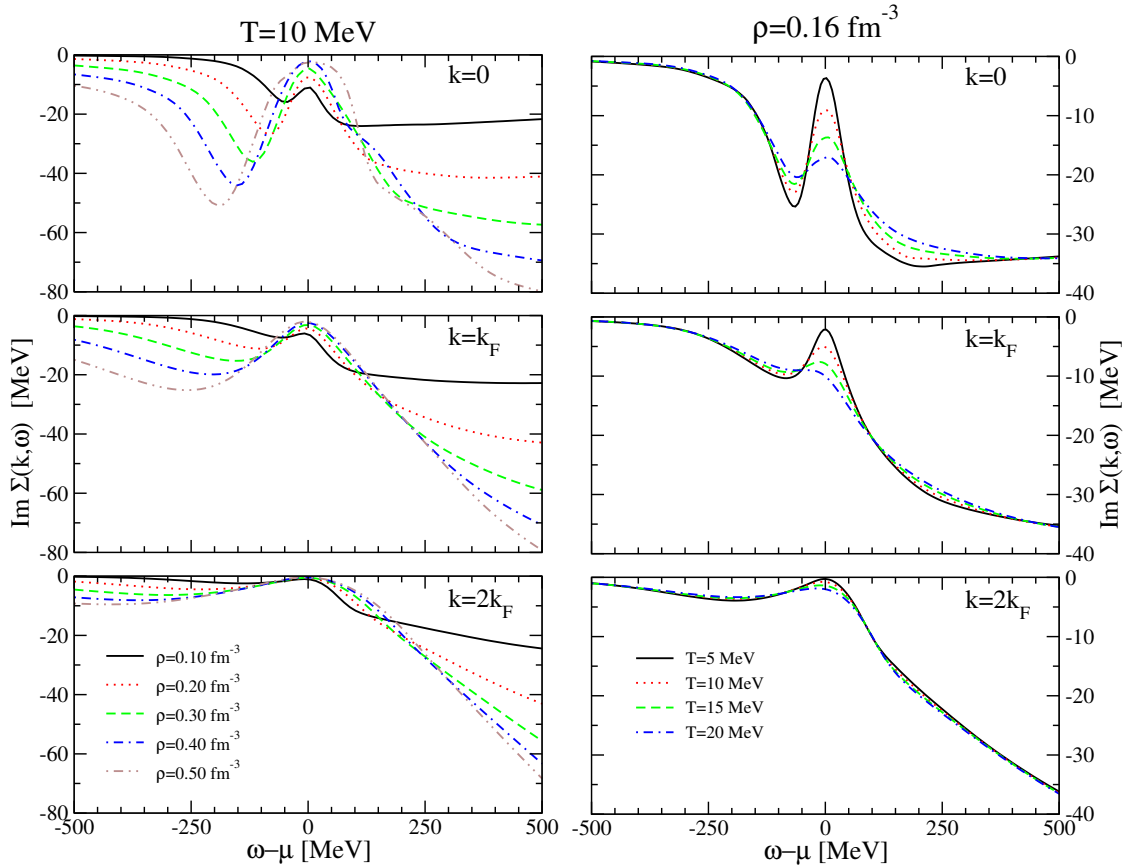


Figure 5.14: $\text{Im } \Sigma(k, \omega)$ as a function of the energy $\omega - \mu$ for three momenta: $k = 0$ (upper panel), k_F (middle panel) and $2k_F$ (lower panel). In the left panels, the different lines correspond to five different densities (from 0.1 to 0.5 fm^{-3} in equidistant steps). In the right panels, the different lines correspond to four different temperatures (from 5 to 20 MeV in equidistant steps).

density dependent. For $k = 0$ and $\rho = 0.1 \text{ fm}^{-3}$, it lies at $\omega \sim \mu - 50 \text{ MeV}$, while for $\rho = 0.5 \text{ fm}^{-3}$ it is located at $\omega \sim \mu - 250 \text{ MeV}$. Both at $k = k_F$ and at $k = 2k_F$, the dip becomes shallower and the structure in the imaginary part of the self-energy below μ is wider. Thus the minimum becomes less pronounced. It is also interesting to note that, far below μ , the higher the density, the higher in absolute value the imaginary part of the self-energy becomes. The same behavior is observed, in a much more enhanced scale, at energies far above μ where, as already commented, the imaginary part of the self-energy increases linearly with density. For energies close to the chemical potential, the opposite behavior is found and with higher densities the imaginary part of the self-energy becomes closer to zero. This result can be attributed to the increasing degeneracy of the system. At a fixed temperature and increasing the density, the system is closer to the degenerate limit and thus to the $T = 0$ result which, as already commented, yields

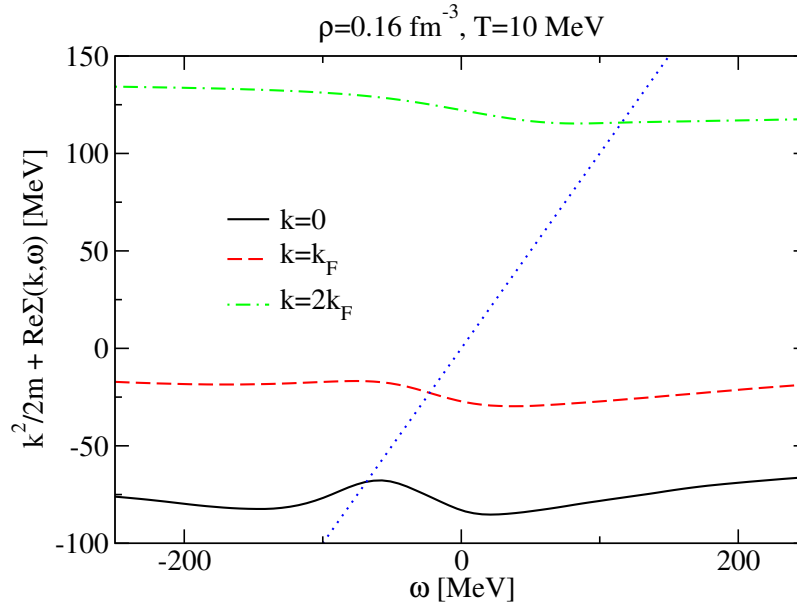


Figure 5.15: Graphical solution of Eq. (5.62) for the real part of the SCGF self-energy at ρ_0 and $T = 10$ MeV for three different momenta: $k = 0$ (full line), k_F (dashed line) and $2k_F$ (dot-dashed line). The dotted line corresponds to $\omega = \omega$.

a vanishing width at $\omega = \mu$.

A useful quantity which is of interest in the comparison with other many-body approaches as well as in the treatment of dynamical quasi-particles in the entropy is the quasi-particle energy (or single-particle spectrum). This is obtained from the self-consistent equation:

$$\varepsilon_{qp}(k) = \frac{k^2}{2m} + \text{Re} \Sigma(k, \varepsilon_{qp}(k)). \quad (5.62)$$

The solution of this equation, which corresponds to a vanishing real part of the inverse propagator, describes, whenever the width Γ is small enough, the quasi-particle peak of the spectral function. In highly correlated systems, the self-consistent spectrum might be hard to find due to the strong energy dependence of $\text{Re} \Sigma(k, \omega)$. This is not the case for nuclear matter within the ladder approximated, as shown by Fig. 5.15. The graphical solution of the previous equation is shown for the empirical saturation density at $T = 10$ MeV for three different momenta, $k = 0, k_F$ and $2k_F$. The point where the dotted $\omega = \omega$ function crosses the lines corresponding to the $\frac{k^2}{2m} + \text{Re} \Sigma(k, \omega)$ function gives the solution of Eq. (5.62) and therefore yields the corresponding quasi-particle energy at a fixed momentum. Note that the wiggle of the real self-energy close to the quasi-particle energy does not affect the final result, in the sense that the solution of Eq. (5.62) for a given

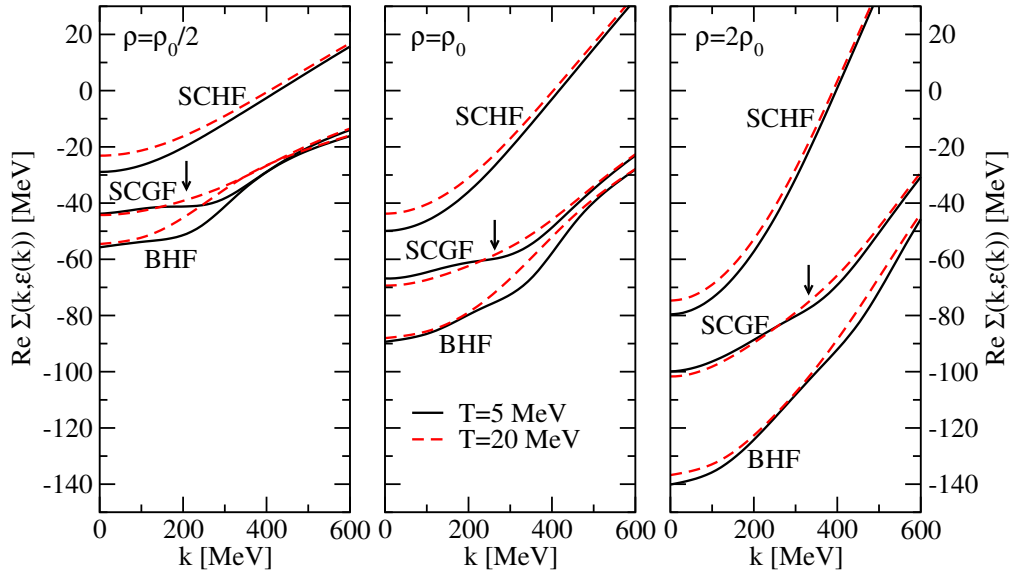


Figure 5.16: *SCHF* (upper), *SCGF* (middle) and *BHF* (lower) results for the real on-shell self-energy of a nucleon in nuclear matter at densities $\rho_0/2$, ρ_0 and $2\rho_0$. The full lines correspond to $T = 5$ MeV and the dashed lines to $T = 20$ MeV. The arrows signal the position of the corresponding Fermi momentum.

momentum is unique. This allows for a clean definition of quasi-particle states in the ladder approximation.

A brief sketch of the momentum, density and temperature dependence of these self-consistent quasi-particle energies is given in Fig. 5.16. The three panels display $\text{Re}\Sigma(k, \epsilon_{qp}(k))$ as a function of momenta for two different temperatures ($T = 5$ MeV and $T = 20$ MeV). The three panels correspond to three different densities ($\rho_0/2$, ρ_0 and $2\rho_0$). Moreover, the corresponding *SCHF* [see Fig. 4.8] and *BHF* results are also shown for comparison. Let us start by discussing the differences between the *SCHF* and the *SCGF* spectra. The $T = 20$ MeV results at $k = 0$ for the *SCGF* approximation are about 25 MeV more attractive than the *SCHF* results at the three densities. The binding of the lowest momentum state in the *SCGF* scheme increases considerably from half saturation, where it gives about -45 MeV, to twice saturation density, where it is almost -100 MeV. Although the magnitude of this increase is close to that of the *SCHF* scheme, the *SCGF* spectra are much more attractive than the mean-field ones at large momenta. Therefore, the effect of correlations (which keeps nucleons from penetrating the repulsive core of the interaction) is essential to obtain attractive spectra at all momenta. As a result of this fact, the *SCGF* spectra are less stiff than the *SCHF* ones. Moreover, the inclusion of correlations induces a flattening close to the Fermi momentum for $T = 5$ MeV. This flattening, which is also characteristic of the *BHF* spectra, is

related to the deuteron structure in the 3S_1 partial wave of the T -matrix elements. The temperature dependence of the SCGF spectra is also different than the one of the SCHF approach. While in the latter temperature makes the spectra more repulsive at all momenta, in the SCGF the increase of temperature results in a more attractive spectrum below the Fermi surface and a more repulsive one at higher momenta. Note also that the temperature effects become less important for very high momenta, due to the softening of phase space blocking effects.

The single-particle spectra of the BHF approach yield more attractive results at low momenta than the SCGF spectra. Thus, in general, one can say that intermediate hole-hole scattering produces a repulsive effect in the spectra that, in consequence, become shallower. This may affect in turn other quantities, such as the internal energy which, in the BHF approach, is computed directly from $\text{Re} \Sigma_{BHF}$. The size of these differences is however density dependent. At half saturation, the zero-momentum spectra of the BHF approach are about 10 MeV more attractive, while at twice saturation the BHF spectra are 40 MeV more bound than the SCGF ones. These differences are smeared out for higher momentum, where the effects of dressing hole states are less important. It is also interesting to take into account the different temperature dependence of the single-particle spectra in the BHF scheme and in the SCGF method. In the finite-temperature calculations within a BHF approach, the single-particle potential becomes more repulsive with temperature at all momenta [Zuo03; Rio05a]. This is intuitively expected from the fact that the thermal factors affecting the self-energy allow for an exploration of larger relative momenta with increasing temperature. The high relative momentum states of the effective interaction are repulsive and thus give rise to an overall repulsive contribution in the spectrum. This picture changes, however, when hole-hole correlations are taken into account. In an extended BHF calculation, one can introduce a certain amount of these correlations by means of the so-called M_2 contribution to the self-energy, which corresponds to the lowest-order rearrangement term in the single-particle spectrum. When this term is included in the approach, it gives a repulsive contribution to the spectrum at momenta below k_F for low temperatures [Zuo06]. With increasing temperature, however, this rearrangement potential loses importance and the spectra become more attractive below the Fermi surface. This is exactly what happens when hole-hole correlations are included at all orders, as seen in Fig. 5.16. Intuitively, one can associate this repulsive effect at low momenta and low temperatures to the idea that hole-hole correlations renormalize the long-range part of the interaction, which is of an attractive nature. Thus, their effect (which is limited to the hole part of the spectrum, $k < k_F$) is to soften the attractive contributions to the single-particle spectra, which is translated into a repulsive effect for momenta below the Fermi surface. Once temperature is introduced, this repulsive contribution disappears due to the softening of Pauli blocking factors, thus explaining the temperature dependence of the self-consistent spectra at low momenta.

5.7.3 Spectral function

In Chapter 2 the main properties of fermionic systems at finite temperature were derived from the one-body Green's function and, in particular, from the spectral function associated to its spectral decomposition. Once the self-energy is computed within the SCGF method, the spectral function is easily computed from the following formula [see Eq. (2.130)]:

$$\mathcal{A}(k, \omega) = \frac{\Gamma(k, \omega)}{\left[\omega - \frac{k^2}{2m} - \text{Re} \Sigma(k, \omega)\right]^2 + \left[\frac{\Gamma(k, \omega)}{2}\right]^2}. \quad (5.63)$$

The general properties of this function can be grasped in a simple way. In the first place, since the width is positive definite, it is clear that this function cannot present a pole. Secondly, for a fixed momentum, the spectral function usually has a maximum close to the quasi-particle energy, $\omega \sim \varepsilon_{qp}(k)$, because at this value the first term of the denominator vanishes. In addition, and since Γ goes to zero with decreasing temperatures for $\omega \sim \mu$, the spectral function is small at this value. When the momentum is such that $\varepsilon_{qp}(k) \sim \mu$ (for low temperatures this condition is fulfilled at $k = k_F$) the two terms in the denominator as well as the numerator will become simultaneously small. The numerical solution of the SCGF scheme will show that this competition is resolved in favor of a narrow and high quasi-particle peak at $k = k_F$.

The study of the energy, momentum, density and temperature dependences of the spectral function $\mathcal{A}(k, \omega)$ is carried out in Fig. 5.17. This is equivalent to Fig. 5.14 and the left (right) column shows the calculations at a fixed temperature (density) for different densities (temperatures). The three panels (upper, central, lower) show the spectral function at three different momenta ($k = 0, k_F$ and $2k_F$, respectively) as a function of the energy $\omega - \mu$. Note that in all the figures a logarithmic scale is used, which allows for a more careful study of the low (very negative) and high (very positive) energy tails of the spectral function. In addition, the dotted line that is depicted on top of the spectral functions in the left panels represents the Fermi-Dirac distribution, whose convolution in energies with the spectral function gives the momentum distribution. This will be useful in the analysis of the momentum distribution, in the following subsection.

The top left panel of Fig. 5.17 shows the evolution of $\mathcal{A}(k = 0, \omega)$ with density. The spectral function presents a clear peak, whose position is dictated by the quasi-particle energy. This quasi-particle peak moves to lower (more attractive) energies with higher densities, reflecting the fact that zero momentum states get more bound with density (see the discussion in the previous subsection). Moreover, the width associated to the quasi-particle peak becomes larger when the density is increased. This matches with the naive intuition that higher densities correspond to larger correlations and thus to broader quasi-particle peaks. In this sense, the quasi-particle picture (which is associated to narrow quasi-particle peaks) becomes worse with increasing densities at this momentum. It is also interesting

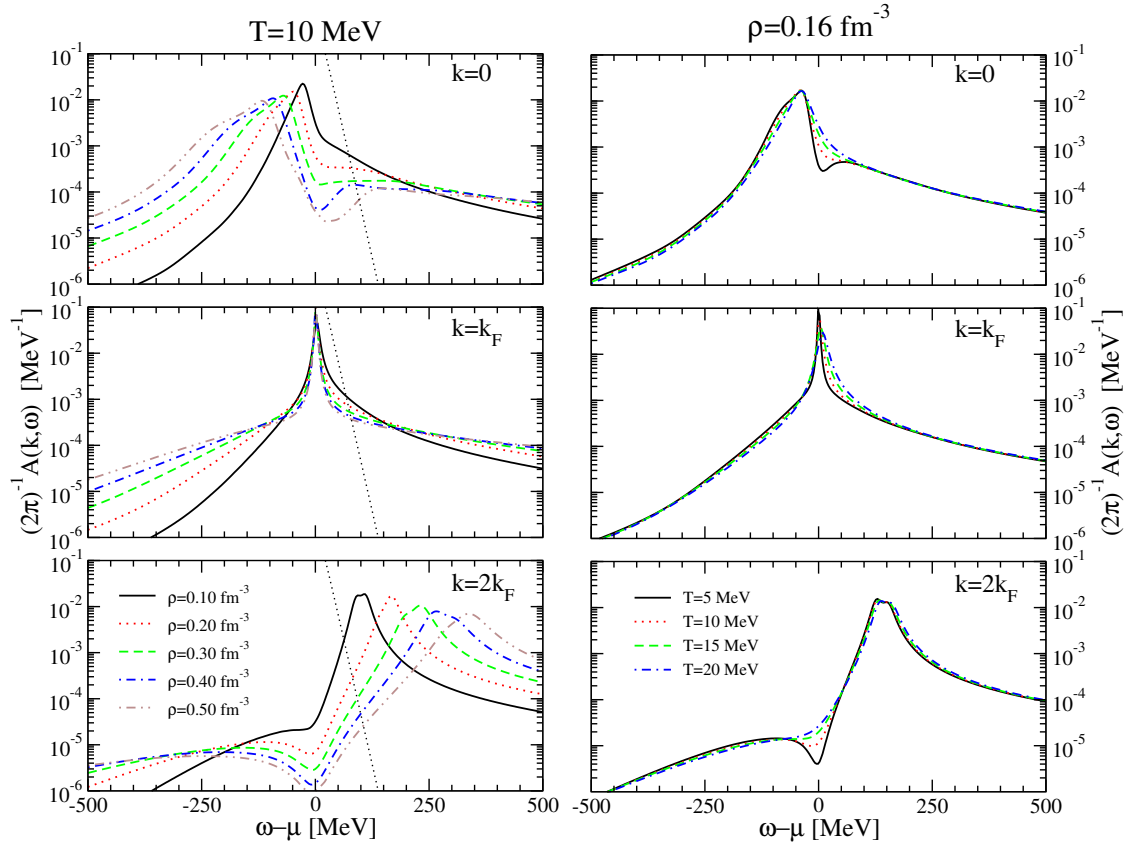


Figure 5.17: Spectral function as a function of the energy $\omega - \mu$ for three momenta: $k = 0$ (upper panel), k_F (middle panel) and $2k_F$ (lower panel). In the left panels, the different lines correspond to five different densities (from 0.1 to 0.5 fm^{-3} in equidistant steps). The dotted line shows the thermal distribution $f(\omega)$ for this temperature. In the right panels, the different lines correspond to four different temperatures (from 5 to 20 MeV in equidistant steps).

to analyze the low and high energy tails of the spectral function, which are quite different. While at high energies the spectral function becomes almost flat and its value is more or less independent of the density (in contrast to what happened to the imaginary part of the self-energy, see Fig. 5.14), in the low energy zone the spectral function yields density dependent results. In this region, the higher densities correspond to higher spectral functions. The high and low energy tails of \mathcal{A} are caused by short-range and tensor correlations, which are responsible for the fragmentation of the quasi-particle peak. These correspond to non-vanishing probabilities of finding a nucleon at energies which are far above or far below the quasi-particle peak. Thus, the increase in the strength of the low energy tails with density is in agreement with the idea that higher densities involve higher correlations. At this momentum, since the low and high energy tails are larger at high densities and since the spectral functions at all densities fulfill the same sum rule

[see Eq. (2.48)], it is natural to find that the height of the quasi-particle peak decreases with density. Note that this could also have been expected from Fig. 5.14, where the minimum of the self-energy at the quasi-particle peak becomes deeper with density. This enters the denominator of the spectral function quadratically and thus reduces its value at the peak. It is also clear that the small absolute value of $\text{Im}\Sigma$ at $\omega \sim \mu$ is translated into low values of \mathcal{A} close to these energies. Indeed, the spectral function presents a dip at this energy that is more pronounced with higher densities, as expected from the increasing degeneracy of the system.

The spectral function at $k = 2k_F$ has a somewhat similar structure. The quasi-particle peak is however above the chemical potential and thus should be associated to “particle” states. This peak is shifted to higher energy values with increasing density, in agreement with the fact that the quasi-particle energies become stiffer with increasing densities. The width associated to the quasi-particle peak also increases with density, as expected from the behavior of $\text{Im}\Sigma$ (see Fig. 5.14 at this momentum) and consequently the height of the peak decreases with increasing density. The dip of the spectral function at $\omega = \mu$ is very well resolved at this momentum, especially at high densities. The presence of this dip allows for a clean separation between a quasi-particle peak at “particle” energies ($\omega > \mu$) and a background “hole” ($\omega < \mu$) contribution.

At the Fermi surface, $k = k_F$, the spectral function behaves differently to what has been described until now. The quasi-particle peak at this momentum is located very close to $\omega = \mu$. At low temperatures, this is the expected behavior for, at that momentum, the quasi-particle energy at the Fermi surface defines the chemical potential, $\mu = \varepsilon_{qp}(k_F)$. Although with increasing temperatures this is not necessarily true anymore, the relation holds approximately and the quasi-particle peak is still very close to the chemical potential. In contrast to what is observed for other momenta, the quasi-particle peak becomes increasingly narrow with increasing density. Once again, this can be explained in terms of the degeneracy of the system. At a constant temperature and with higher densities the system is closer to its degenerate limit. Now, at zero temperature the correlated spectral function becomes a delta-peak for $\omega = \varepsilon_{qp}(k_F)$ and thus the increase of degeneracy leads to a decrease of the width at the Fermi surface. The quasi-particle peak becomes higher with increasing density. Yet, this effect is softer than the narrowing of the peak and, to keep the sum rule constant, the spectral function develops larger high energy tails with increasing density. Therefore, the height of these tails can be taken as a measure of the increasing correlations acting on the system with increasing densities at all momenta.

In accordance to what was observed for the imaginary part of Σ in Fig. 5.14, the effect of temperature in the spectral function is much weaker than that of density. For all momenta, for instance, the quasi-particle peak hardly changes its position with temperature. For the three momenta shown in the figure, the effects of temperature are concentrated in a region of energies close to the chemical

potential. The spectral function becomes smaller with decreasing temperature and its dip at $\omega = \mu$ becomes deeper at $k = 0$ and $k = 2k_F$ (once again due to phase space restrictions). On the other hand, the effect of temperature at $k = k_F$ is essentially that of a widening and lowering of the quasi-particle peak with temperature, in accordance with the reasoning in terms of degeneracy introduced in the previous paragraph. Let us finally remark the fact that, since the spectral function is weakly temperature dependent, any strong temperature dependence in the quantities derived from it should be attributed to its convolution with the remaining thermal factors.

An accurate description of the properties of asymmetric nuclear matter is beyond the scope of this Thesis. The dependence of some microscopical properties of matter in the isospin asymmetry has been studied in Ref. [Fri05], where it has been found that the spectral functions depend strongly on the asymmetry due to the fact that, for high asymmetries, the tensor correlations (which act mainly in isospin zero states) decrease considerably. In addition, the fact that the Fermi momentum of the less abundant species goes to zero with increasing asymmetry has an important effect on the structure of the spectral function at low momenta. Furthermore, it is interesting to note that the spectral function fulfills, apart from the m_0 sum rule of Eq. (2.48), higher order energy weighted sum rules, such as the m_1 sum rule:

$$\int_{-\infty}^{\infty} \frac{d\omega}{2\pi} \mathcal{A}(k, \omega) \omega = \frac{k^2}{2m} + \Sigma_{HF}(k), \quad (5.64)$$

where the self-energy on the right hand side of the previous equation corresponds to the generalized Hartree-Fock term of Eq. (5.42). These sum rules are automatically preserved by any self-consistent calculation, but they might serve as a numerical check for the different momentum and energy integration meshes in the numerical computations of spectral functions. Moreover, the running integrals of these spectral functions provide information on the detailed structure of the quasi-particle peak [Pol94]. They can thus be used in outlining differences arising from the use of different bare interactions [Fri04b] or from the changes in the isospin asymmetry of the system [Rio06a].

5.7.4 Momentum distribution and depletion

A relevant quantity that can be derived from the spectral function is the momentum distribution. This quantity is important because it can be extracted experimentally from $(e, e'p)$ experiments on finite nuclei [Kel96; Dic04; Roh04]. As explained in Chapter 1, $n(k)$ is given, for each momentum, by the convolution in energies of the spectral function and the Fermi-Dirac distribution:

$$n(k) = \int_{-\infty}^{\infty} \frac{d\omega}{2\pi} \mathcal{A}(k, \omega) f(\omega). \quad (5.65)$$

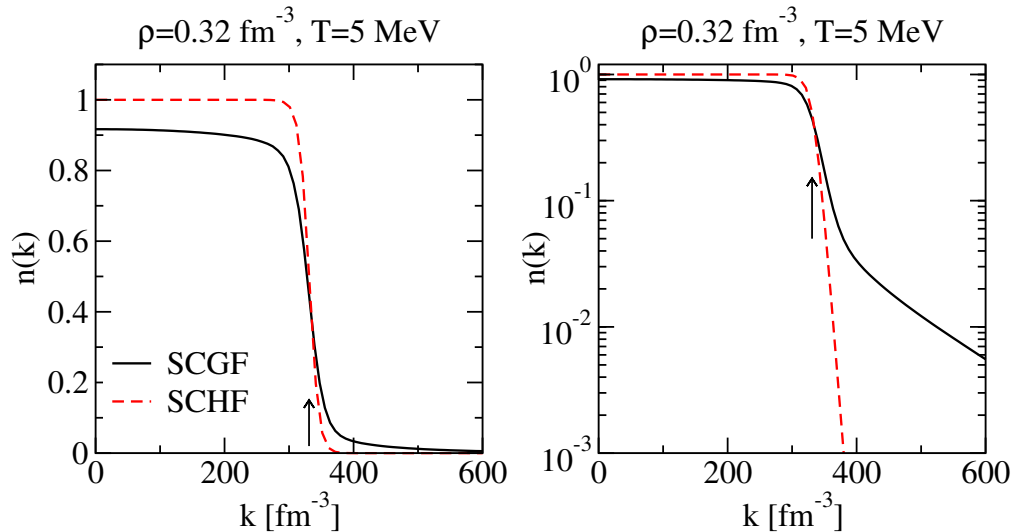


Figure 5.18: *Momentum distribution for the SCGF (full line) and the SCHF (dashed line) approaches at $2\rho_0$ and $T = 5$ MeV. The arrow denotes the Fermi momentum.*

The difference between a correlated and a mean-field quasi-particle momentum distribution can be seen in Fig. 5.18. For the same density ($2\rho_0$) and temperature ($T = 5$ MeV), the momentum distribution in the SCGF (full line) and in the SCHF (dashed line) are shown. The left and the right panel only differ in the use of a linear and a logarithmic scale, respectively. Let us start with the left panel. The hole states of the correlated case (that is, the states with $k < k_F$) have a lower occupancy than those of the mean-field case. Physically, this depletion is due to the short-range correlations that scatter off low momentum states to higher momenta. The tensor component of the force has also an important role for the depletion, which is substantially larger for bare interactions with large tensor components [Fan84]. Correspondingly, this leads to a higher occupancy of the states above the Fermi surface, which is more clearly seen in the right panel of Fig. 5.18. The population of the high momentum states in the correlated case decreases much slower than that of the mean-field distribution, as a consequence of the non-vanishing spectral function for low energies at high momenta. Another important feature of both the SCGF and the SCHF momentum distributions is the presence of a strong fall-off close to $k \sim k_F$. At zero temperature, this strong fall-off is actually a discontinuity. Within a quasi-particle approach, the momentum distribution becomes a step function at zero temperature, $n(k) = \Theta(k_F - k)$, and thus the height of this discontinuity is 1, which can be reexpressed in terms of the condition:

$$\lim_{\delta \rightarrow 0} \{n(k_F - \delta) - n(k_F + \delta)\} = 1. \quad (5.66)$$

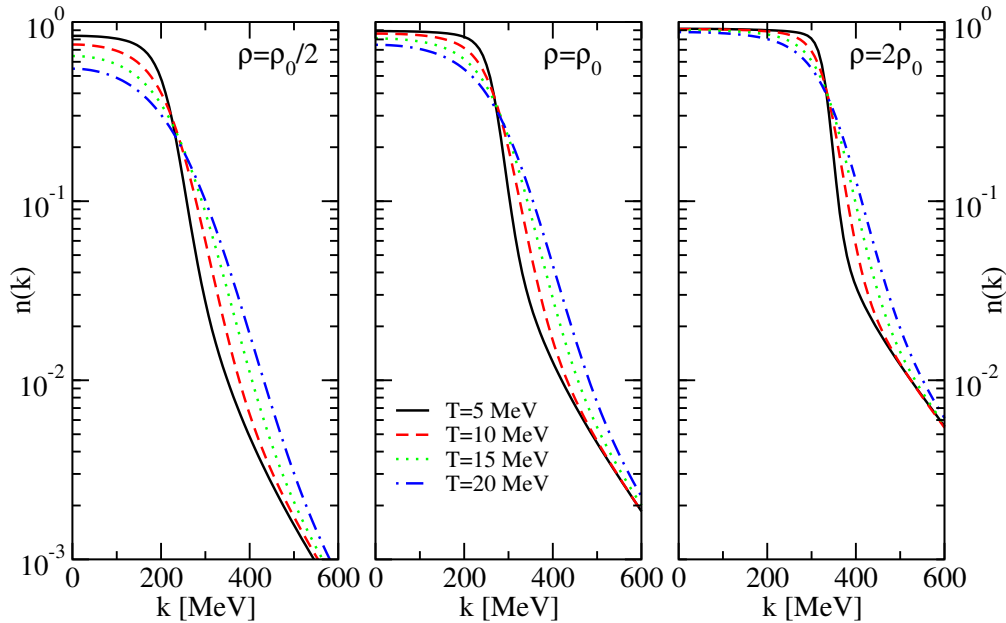


Figure 5.19: *Momentum distribution within the SCGF approach. The three panels correspond to the densities $\rho_0/2$ (left panel), ρ_0 (central panel) and $2\rho_0$ (right panel). Four different temperatures have been chosen, from $T = 5$ MeV to $T = 20$ MeV in equidistant steps.*

In a correlated approach, however, the hole states are depleted and the particle states have large occupancies. One can indeed show that the zero-temperature discontinuity is given by the \mathcal{Z} -factor:

$$\lim_{\delta \rightarrow 0} \{n(k_F - \delta) - n(k_F + \delta)\} = \mathcal{Z}(k_F). \quad (5.67)$$

For the temperature and density of Fig. 5.18, $\mathcal{Z}(k_F)$ can be computed from the real part of the self-energy using Eq. (2.136), which yields the value $\mathcal{Z}_F \sim 0.75$. This is, for instance, in accordance with the discontinuity in the momentum distribution at k_F found in Ref. [Boz02]. Note that this is also close to the experimental values [Kel96; Dic04].

A detailed analysis of the temperature and density dependence of the momentum distribution can be extracted from Fig. 5.19. The three panels show the momentum distribution for four different temperatures (from 5 to 20 in equidistant steps) at three densities: $\rho_0/2$ for the left panel; ρ_0 for the central panel and $2\rho_0$ for the right panel. The overall picture is quite similar for the three cases. The momentum distribution are depleted at $k < k_F$, although the magnitude of this depletion depends considerably on the density and the temperature under consideration (see Fig. 5.21). Close to the Fermi momentum (for the three densities displayed, this corresponds to $k_F \sim 208, 260$ and 330 MeV respectively), the

momentum distribution has a strong decrease and for higher momenta it bends to some extent. The occupancies at large momenta depend on the temperature under consideration. The higher temperatures, which have lower zero momentum populations, have a large population for high momentum states. Due to these differences, there is an intermediate momentum, close to k_F , at which the momentum distributions of the different temperatures (for a fixed density) meet.

Each of the three different regimes (flat behavior at low momenta, fall off close to k_F and bending at large momenta) can be explained in terms of the convolution of the spectral function and the Fermi-Dirac distribution. Consider, for instance, the case of $k = 0$. The corresponding spectral function are those of the upper panels of Fig. 5.17 and the Fermi-Dirac distribution is given by the dotted line in the figure. For a fixed temperature and increasing the density, the occupation is larger due to the fact that, although the quasi-particle peak is lower in height, it is much more wide in the region $\omega - \mu < 0$, where the Fermi-Dirac factor is maximal. This behavior is surprising, because one would naively expect the depletion to increase with the amount of correlations and thus with density. A full explanation of this phenomenon is still lacking, although it is clear that it is caused by the increasing low-energy tails of the zero-momentum spectral function with density. The fall-off of the momentum distribution close to $k = k_F$ is intuitively explained by the fact that, with increasing momentum, the quasi-particle peak moves to higher energies. At the Fermi surface, as commented above, it leaves the “hole” region ($\omega < \mu$) and enters the “particle” region ($\omega > \mu$). At the same time, the Fermi-Dirac distribution decreases close to $\omega \sim \mu$ (note that it gives 1/2 for $\omega = \mu$). Therefore, the importance of the quasi-particle peak in the convolution integral is lower once the peak enters the particle region. For higher momenta, the quasi-particle peak becomes more and more repulsive and thus its contribution dies out due to the convolution with $f(\omega)$. Still, the spectral function at high momentum shows a non-negligible hole background in the region where the thermal distribution is maximal. This gives rise to a visible amount of population at high momenta, which accounts for the bending of $n(k)$ at large momenta.

As for the temperature dependence at a fixed density, it has already been mentioned that the spectral function is almost temperature independent. Thus, the sizeable differences observed for different temperatures in Fig. 5.19 can be attributed to the corresponding Fermi-Dirac distributions. To understand this thermal behavior, in Fig. 5.20 the spectral functions at the empirical saturation density for two momenta ($k = 0$ and $k = 2k_F$) and different temperatures are shown. On top of these, the corresponding thermal factor $f(\omega)$ are also displayed. Consider the lowest temperature, $T = 5$ MeV. On the one hand, the spectral function at $k = 0$ corresponds to the full line, and has most of its strength concentrated around the quasi-particle peak. On the other hand, the thermal factor at this temperature is very sharp close to $\omega = \mu$ and thus its convolution with $\mathcal{A}(k, \omega)$ includes the full contribution of the quasi-particle peak. At the largest

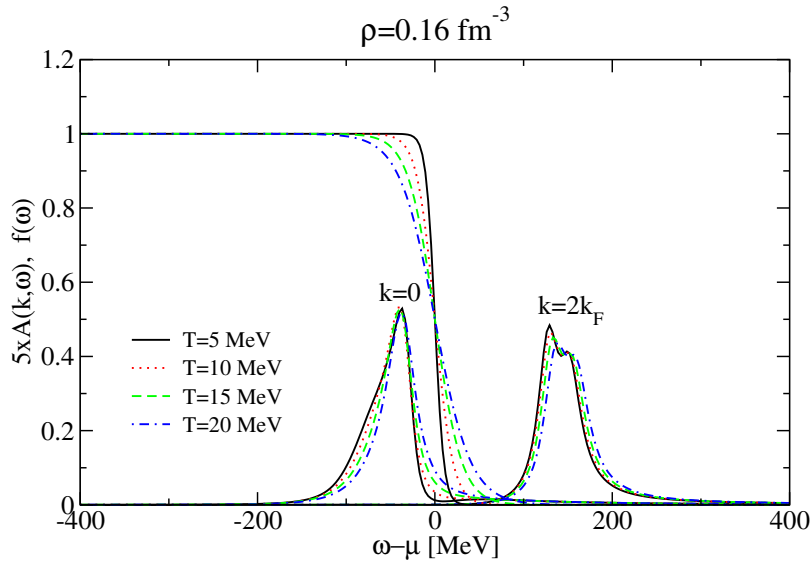


Figure 5.20: Convolution of $\mathcal{A}(k, \omega)$ and $f(\omega)$ at four different temperatures, from 5 to 20 MeV in equidistant steps at ρ_0 . The lines below are proportional to the spectral functions of the $k = 0$ and $k = 2k_F$ momentum states.

temperature of $T = 20$ MeV, however, the thermal factor is softer and indeed it has already decreased a 10% factor at the quasi-particle peak. As a consequence of this lowering, the convolution of the Fermi-Dirac factor with the spectral function decreases in magnitude with temperature, in agreement with the increase of the depletion with temperature. This is however a pure thermal effect, because the small differences in the spectral functions at the different temperatures cannot explain the large differences observed in the momentum distribution. At large momenta, a similar reasoning can be applied, although the results are precisely the opposite. Once again, neither the position nor the structure of the quasi-particle peak change substantially with temperature, but the thermal factor at high temperatures is larger in the quasi-particle peak region, and thus its convolution with $\mathcal{A}(k, \omega)$ yields larger values. This is in accordance to the findings of Fig. 5.19, where, for a given density, the larger population in the high momentum region corresponds to the larger temperature. Nevertheless, it is also interesting to note that, already at ρ_0 , the $T = 10$ and the $T = 5$ MeV depletions are very close to each other, up to the point that the change in temperature is almost not appreciable for the highest density. One can thus say that, to a certain extent, in the low temperature and high density regime, the depletion caused by correlations overcomes the depletion caused by thermal effects, which is the result of a subtle interplay between the structure of \mathcal{A} and the temperature and density dependences of $f(\omega)$.

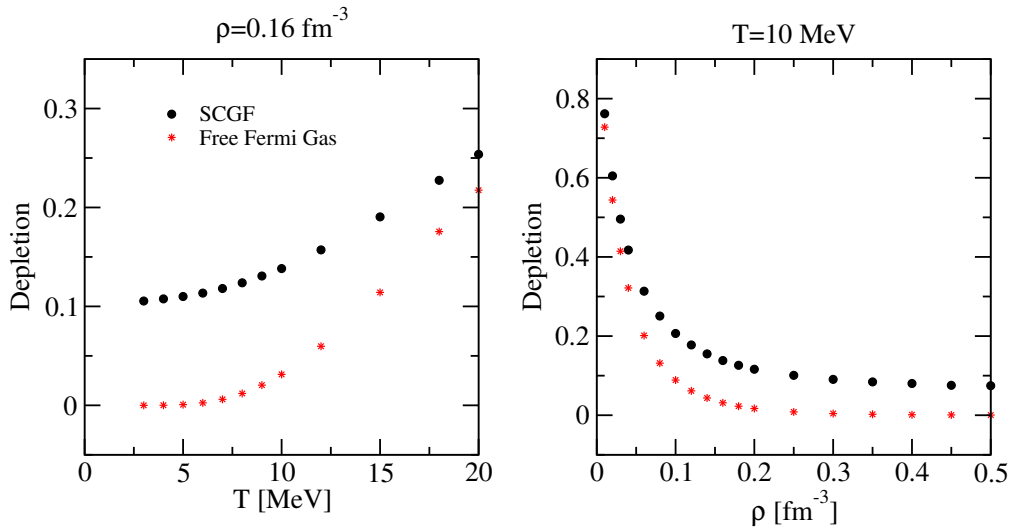


Figure 5.21: *Temperature (left) and density (right) dependence of the depletion of the lowest momentum state (circles). The depletion of the corresponding free Fermi gas is shown in stars.*

To explore in a more effective way these interplays, the left (right) panel of Fig. 5.21 shows the depletion of the lowest momentum state, $d(k=0) = 1 - n(k=0)$, as a function of the temperature (density) at saturation (at a temperature of $T = 10$ MeV). The corresponding depletion of the free Fermi sea in the same conditions is also shown. This is simply given by:

$$d(0) = 1 - f(0) = [1 + e^{\beta\mu}]^{-1}. \quad (5.68)$$

At a fixed density and for decreasing temperatures (which corresponds to the left panel of Fig. 5.21), the chemical potential in the free case tends to a constant, $\mu \rightarrow k_F^2/2m$, and the decrease of the depletion is due to the decrease in temperature inside the thermal factor. In the correlated case, on the other hand, and by virtue of the sum rule of Eq. (2.48), the depletion can be rewritten as:

$$d(0) = \int_{-\infty}^{\infty} \frac{d\omega}{2\pi} \mathcal{A}(0, \omega) [1 - f(\omega)]. \quad (5.69)$$

As temperature decreases, the spectral function does not change considerably (see the top right panel of Fig. 5.17). The thermal factor gets closer to a sharp step function, which yields zero below μ and one above this value. The non-zero depletion for very low temperatures is thus explained by the fact that the spectral function presents high energy tails (the “particle” background) which yield a non-zero convolution with the thermal factor¹. The increase of the depletion with temperature

¹In this reasoning, one assumes that the description in terms of Green’s function is still valid

(from 0.1 at low temperatures to 0.25 at $T = 20$ MeV) can be understood in terms of the convolution of spectral function with the thermal factor $[1 - f(\omega)]$. When temperature increases, this factor is softer close to $\omega = \mu$, and thus the convolution with the quasi-particle peak of $\mathcal{A}(k, \omega)$ becomes more important. Since the detailed structure of this peak hardly changes with temperature, the temperature dependence of the depletion can be attributed to the thermal factor and thus it is similar to the dependence of the free Fermi gas. In other words, the fact that the depletion increases with temperatures does not mean that dynamical correlations become more important at large temperatures.

The increase of depletion at low densities observed in the right panel of Fig. 5.21 has a somewhat different origin. Since the temperature in this case is fixed, the chemical potential of the thermal factor has a more important role in this case. For a fixed temperature, the free Fermi gas depletion increases due to the fact that $\mu \rightarrow -\infty$ (the classical limit) when the density decreases. In the correlated case, the factor $[1 - f(\omega)]$ for a fixed temperature is only a function of $\omega - \mu$. In the top left panel of Fig. 5.17, the dotted line represents the factor $f(\omega)$. The $[1 - f(\omega)]$ factor would be given by a line with the opposite slope, increasing from 0 to 1 with increasing energy. Thus, at large densities, where the quasi-particle peak is far below the chemical potential, the depletion is essentially due to the particle background which, for large energies, is qualitatively density independent. The increase of depletion with lower densities can be explained in terms of the relative position of the quasi-particle peak with respect to the chemical potential. With decreasing density, this peak concentrates more strength and it approaches from below the region of $\omega \sim \mu$. The convolution of this peak with the thermal factor is thus larger, which leads to higher depletions for lower densities. Note that this explanation relies on both the presence of the high energy tails and the position of the quasi-particle peak relative to μ and thus it depends to a certain extent on the details of the dynamical correlations. Note also that at very low densities (say, below 0.05 fm^{-3}), the spectral function is very close to a free quasi-particle peak, which explains why the correlated depletion is very close to the free one. In contrast to this low density behavior, for densities above $2\rho_0$ the depletion is almost density independent and yields a value of $d(0) = 0.1$. In this region, one can say that the depletion is caused entirely by the high energy tails of the spectral function and thus it is essentially caused by dynamical correlation effects.

Assuming that an extrapolation to zero temperature is safe at saturation density, one could say that the depletion in the degenerate limit is close to the value $d(0) = 0.1$. One can compare this to the value obtained in other approaches which, in general terms, is about $d(0) \sim 0.15$ [Ben89; Bal90; Von93; Dew02; Dic04]. Although this is 0.05 units larger than our value (which supposes a large relative correction), one has to say that the depletion depends strongly on the many-body

at low temperatures, which is only true in the density and temperature regime where no pairing transition is present.

approach as well as on the bare interaction which is used in its computation. As a matter of fact, using the Argonne V18 potential within the SCGF one obtains a somewhat larger depletion (due mainly to the differences in the tensor component) [Fri04a]. Note also that all these values for the depletion are still below the experimental values [Kel96].

5.8 Beyond the ladder approximation

So far the microscopic properties of the ladder approximation obtained by means of the SCGF method have been described. In the following chapter, the thermodynamical properties of nuclear matter within this approach will be presented. There are however a lot of questions that arise before applying this formalism to realistic calculations. Among them, maybe the most important one is the assessment of the error which is being made. In any theoretical prediction (especially in the many-body field), several approximations have to be introduced in order to obtain sensible results. Therefore, one should be aware of the reliability of the approximations that are being made and hopefully have a certain control on these errors, trying to minimize them within a given computational scheme.

This question is however difficult to answer for the SCGF case. This scheme is not based in a perturbative expansion and one is not expanding, say, the Green's function in terms of some parameter. One cannot therefore improve its accuracy by taking into account higher order terms. Instead, a full resummation of certain classes of diagrams is carried out in the SCGF scheme. The choice of the diagrams is not arbitrary, however, and one usually chooses those which are more important for the physical problem under consideration. In the ladder approximation, as already explained, one takes the diagrams which are relevant for low density and strongly interacting systems. The renormalization process induced by self-consistency accounts for the extension of the formalism to higher densities. Due to the fact that one is dealing with strongly repulsive hard-cores that are softened by the renormalization process, one also says that the ladder approximation accounts for the short-range correlations induced by the NN potential. An error estimate of the ladder approximation would thus require the calculation of some of the diagrams not included in the formalism. This could help in having a flavor of the magnitude of the terms that are disregarded by the ladder approximation. Note that this is an important difference with respect to the BHF approach, in which the energy per particle is expanded systematically in terms of the number of hole lines. In this scheme, by taking into account two, three and more hole lines one can in principle find better estimates for the total binding energy of the system.

To be more specific, let us consider the two different derivations of the ladder approximation introduced previously in this chapter (see Section 5.1). On the one hand, the ladder approximation arises from assuming that the two-body Green's

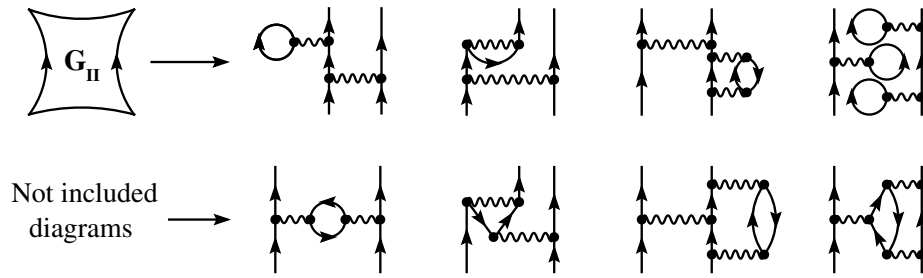


Figure 5.22: *Diagrams appearing and lacking in the ladder approximation.*

function is formed by the iterated scattering of two particles in the medium due to the bare interaction (see Fig. 5.1). This approximation neglects to a certain extent the medium-mediated interactions (through polarization effects, for instance) which involve correlations that go beyond the two-body level. These would include processes like the first diagram on the second row of Fig. 5.22. The intermediate bubble represents a particle-hole excitation of the medium that interacts with the external couple of particles. This is a kind of three-body process that does not appear explicitly in the approximation. On the other hand, the decoupling of the two-body propagator given by Eq. (5.3) corresponds to the propagation of two particles that interact strongly with each other, but not with any other third particle in the medium. The self-consistency of the approach, however, is helpful and allows for the inclusion of many-particle (three-, four-, five-body...) processes, like those appearing on the top right section of Fig. 5.22. However, the ladder approximation does not include genuine three-body processes and thus one expects it to fail whenever the densities are high enough for the overlapping of three nucleons to be non-negligible.

This fact points towards one of the main disadvantages of the SCGF scheme, namely the lack of this kind of three-body correlations as well as of three-body forces. It is a very well-known issue that, already at the BHF level, the inclusion of three-body forces is necessary to reproduce the saturation properties of nuclear matter [Day81]. The inclusion of three-body effects within a Green's function approach presents however quite a lot of complications. On the one hand, one can try to describe better the three-body correlations that arise from two-body NN interactions. This would probably need for a decoupling of \mathcal{G}_{III} different from the one presented here, including explicitly the effect of three-body correlations. On the other hand, one could try to work with three-body forces from the very beginning, already at the level of the Hamiltonian. Unfortunately, this would also complicate the formalism. The GMK sum rule, for instance, would not be valid anymore, because its derivation relies on the two-body nature of the force. New means of deriving the total energy of the system should thus be devised [Som06].

Moreover, the inclusion of a three-body force would also lead to a modification of the equation of motion for the propagator. In the case of the one-body Green's function, this would imply a coupling not only to the two-body propagator, \mathcal{G}_{II} , but also to the three-body propagator, \mathcal{G}_{III} .

Furthermore, it is also interesting to note that, already at the two-body level there is some room for improvement. As explained previously, the ladder approximation accounts for the short-range correlations of the system. These are not, however, the only relevant correlations in nuclear systems. Modifications due to the long-range effects, for instance, play an important role in the study of the response properties of infinite systems. Their treatment needs of different tools than the ones exploited here, like the random phase approximation or the Fermi liquid theory. Both of these approaches can be translated into a Green's function language [Mat92; Pin89] and, as a matter of fact, a method has been devised that allows to sum diagrams which include both short and long-range correlations (*i.e.* a self-consistent sum of both the ladder and bubble diagrams at all orders). This is the so-called parquet diagram technique, that leads to a set of self-consistent equations which so far has not been applied to realistic nuclear matter calculations [Jac82].

Yet, even if the SCGF lacks some specific kind of correlations and does not include three-body forces, it still does a good job in the treatment of the microscopic and bulk properties of infinite nuclear matter at low and intermediate densities. The results obtained in the following chapter shall show that the SCGF has the same degree of "accuracy" than the BHF approach for nuclear matter described with two-body forces. In other words, neither one nor the other approach are capable of reproducing the empirical saturation point of nuclear matter (which in the case of the CDBONN potential lies at too high densities), but still they give a qualitatively correct and similar description of the properties of nuclear matter from a microscopic many-body approach. In addition, the SCGF is thermodynamically consistent, which is a great advantage in the application of this method to finite temperature systems. Furthermore, the ladder approximation includes hole-hole correlations and thus it takes into account a larger amount of correlations than the BHF scheme. At least in this sense, it should be taken as a more reliable description of infinite matter at finite temperatures.

Chapter 6

Thermodynamical properties of nuclear matter

In Chapter 3, the Luttinger-Ward approach has been introduced. Within this formalism, the entropy of a correlated many-fermion system can be computed directly from the one-body propagator. In the previous chapter, the ladder approximation to nuclear matter and the numerical results obtained from the SCGF scheme have been discussed. It is thus natural to use these results as the starting point for the Luttinger-Ward calculations. In this manner, the thermodynamical properties of nuclear matter will be obtained from a fully correlated approach. The quantities obtained within this scheme will be compared with those arising from other approaches. Special attention will be paid to the comparison with the BHF result. The importance of thermodynamical consistency will be revealed in this way. Finally, the perspectives which this approach opens in the many-body nuclear field will be briefly outlined.

6.1 Microscopic results

Within the Luttinger-Ward approach, the entropy of a system of interacting fermions is split in a dynamical quasi-particle contribution, the S^{DQ} of Eq. (3.94), and a contribution which includes higher order correlations, the S' of Eq. (3.95). This second term can be neglected safely at low temperatures, while still keeping the thermodynamical consistency of the approach [Car75]. In Chapter 3, the dynamical quasi-particle contribution to the entropy was shown to arise from the \mathcal{B} spectral function. The properties of this function are very close to those of the usual spectral function, $\mathcal{A}(k, \omega)$. It fulfills, for instance, the same sum rule [see Eqs. (2.48) and (3.105)] and it also accounts for the effect of correlations in the width of quasi-particles. It is thus natural to compare the two functions. Before that, however, one can get a rough idea of the differences between both functions following an argument first proposed by Carneiro and Pethick [Car75]. On the one

hand, let us express the spectral function \mathcal{A} as a function of the real and imaginary parts of the self-energy. One obtains the well-known Lorentzian-like function of Eq. (2.130). For a given momentum, the spectral function has a peak around the quasi-particle energy, $\omega \sim \varepsilon_{qp}(k)$, of height $\mathcal{A} \sim 4/\Gamma(k, \varepsilon_{qp}(k))$. On the other hand, the \mathcal{B} spectral function can also be rewritten in terms of the self-energy. Starting from Eq. (3.96) and taking the derivative with respect to the energy according to Eq. (3.99), one gets:

$$\begin{aligned} \mathcal{B}(k, \omega) = & \frac{1}{2} \frac{\Gamma^3(k, \omega)}{\left[\left[\omega - \frac{k^2}{2m} - \text{Re} \Sigma(k, \omega) \right]^2 + \left[\frac{\Gamma(k, \omega)}{2} \right]^2 \right]^2} \left\{ 1 - \frac{\partial \text{Re} \Sigma(k, \omega)}{\partial \omega} \right\} \\ & - \frac{1}{2} \frac{\Gamma^2(k, \omega)}{\left[\left[\omega - \frac{k^2}{2m} - \text{Re} \Sigma(k, \omega) \right]^2 + \left[\frac{\Gamma(k, \omega)}{2} \right]^2 \right]^2} \left\{ \omega - \frac{k^2}{2m} - \text{Re} \Sigma(k, \omega) \right\} \frac{\partial \Gamma(k, \omega)}{\partial \omega}. \end{aligned} \quad (6.1)$$

If one assumes that the frequency dependence of Γ and $\text{Re} \Sigma$ are smooth close to the quasi-particle energy, one finds:

$$\mathcal{B}(k, \omega) \sim \frac{1}{2} \frac{\Gamma^3(k, \omega)}{\left[\left[\omega - \frac{k^2}{2m} - \text{Re} \Sigma(k, \omega) \right]^2 + \left[\frac{\Gamma(k, \omega)}{2} \right]^2 \right]^2}, \quad (6.2)$$

which corresponds to a function which decays faster than a Lorentzian close to $\varepsilon_{qp}(k)$, but which has a stronger peak at the quasi-particle energy, $\mathcal{B} \sim 8/\Gamma(k, \varepsilon_{qp}(k))$.

One can check that this schematic scenario is indeed true in Fig. 6.1, where the \mathcal{B} (full lines) and the \mathcal{A} (dashed lines) spectral functions are shown as a function of the energy for three different momenta: $k = 0$, $k = k_F$ and $k = 2k_F$. The two functions have been computed at the empirical saturation density ρ_0 and at a temperature of $T = 10$ MeV. In the three panels, corresponding to the three different momenta, one observes that both functions are peaked around the quasi-particle energies. The peak shifts from negative values of the energy with respect to the chemical potential (“hole” states) to positive values (“particle” states) when going from zero-momentum to higher momentum states, just following the position of the quasi-particle peak. However, while the \mathcal{A} spectral function has high-energy tails that contribute in a non-negligible way to the total strength of the nucleon, the tails of the \mathcal{B} spectral function are lower and less extended in energy. This is easily understood if one considers that both functions fulfill the same sum rule. Since the \mathcal{B} function has a higher quasi-particle peak, the strength of the peak is contributing substantially to the total sum rule and there is no need to generate high-energy tails. The presence of these high-energy tails in the \mathcal{A} function is an indication of the importance of the correlations that go beyond the mean-field approach [Fri03]. Thus, the lack of such tails in the \mathcal{B} function is signaling

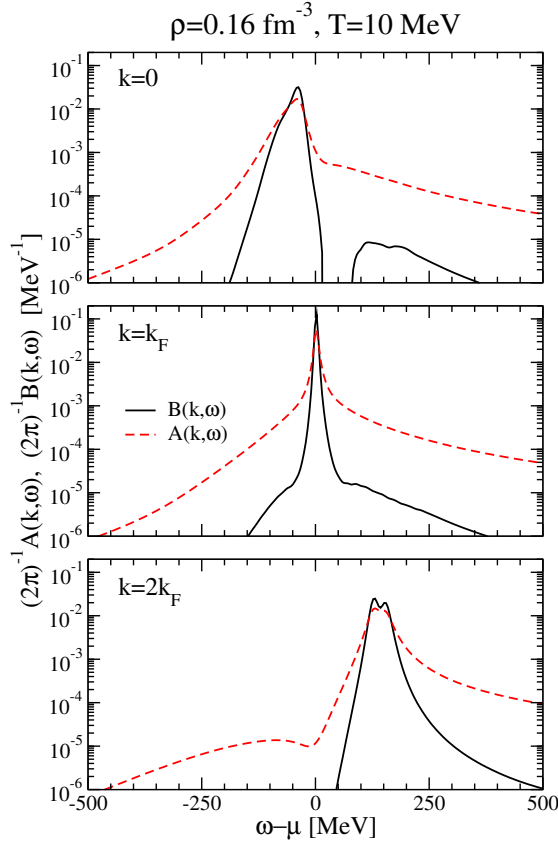


Figure 6.1: \mathcal{B} (solid lines) and \mathcal{A} (dashed lines) spectral functions at ρ_0 and $T = 10 \text{ MeV}$ for three different momenta: $k = 0, k_F$ and $2k_F$.

somehow that these correlations will have a small influence in the total entropy of the system.

This idea is also in accordance with the behavior of the width of both spectral functions. Far away from the Fermi momenta, the two functions are relatively broad around the peak. Again, in the case of the \mathcal{A} function this is a consequence of the correlations that redistribute the nucleon single-particle strength within a wide range of energies. The \mathcal{B} function has a smaller width, which indicates that it is less affected by correlations. Close to the Fermi momentum, however, both functions approach a delta-peak behavior, reminiscent of the fact that at zero temperature, even when correlations are included, the spectral function has a delta-like contribution. At this momentum and for the temperature considered, the \mathcal{B} function is narrower and much more peaked than the usual spectral function \mathcal{A} . Thus, at all momenta, \mathcal{B} seems to be less affected by dynamical correlations or, in other words, the width of the quasi-particles associated to \mathcal{B} appears to be smaller. It is also interesting to note that the values for the \mathcal{B} function are positive

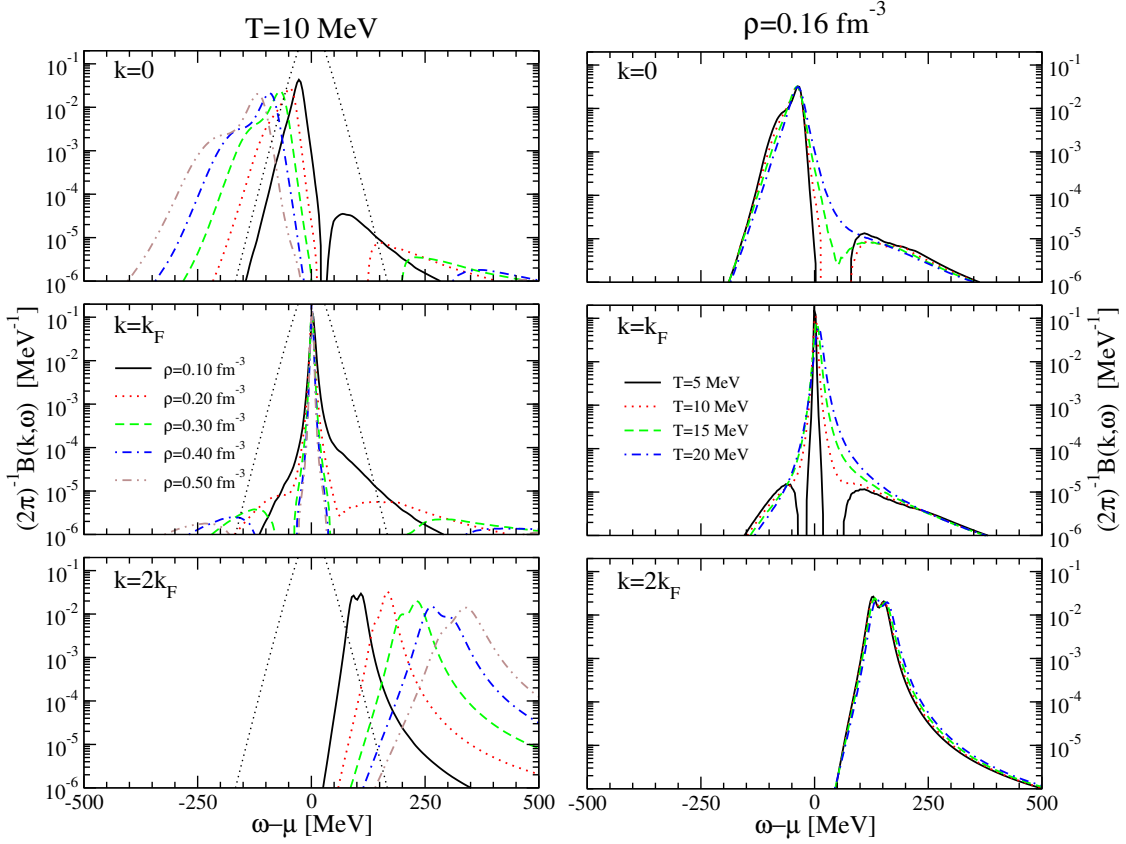


Figure 6.2: \mathcal{B} spectral function as a function of the energy $\omega - \mu$ for three momenta: $k = 0$ (upper panel), k_F (middle panel) and $2k_F$ (lower panel). In the left panels, the different lines correspond to five different densities (from 0.1 to 0.5 fm^{-3} in equidistant steps). The dotted line shows the statistical factor $\sigma(\omega)$ for this temperature. In the right panels, the different lines correspond to four different temperatures (from 5 to 20 MeV in equidistant steps).

(except for a very small region at $k = 0$) for all the energies and momenta here considered. This is in contrast to the weighting function B , which is defined in Eq. (3.90) and is used in Ref. [Som06]. The fact that the evaluation of the entropy using the weighting function B exhibits strong cancellation effects (see Fig. 4 of Ref. [Som06]) may be taken as an indication that the splitting of the entropy into the two contributions according to Eq. (3.107) is not optimal.

In order to understand the density dependence of the dynamical quasi-particle entropy, in the left panels of Fig. 6.2 the \mathcal{B} spectral function is shown as a function of the energy for different densities ($\rho = 0.1, 0.2, 0.3, 0.4, 0.5 \text{ fm}^{-3}$) at the same three momenta previously introduced and at a fixed temperature of $T = 10 \text{ MeV}$. In addition, the dotted line represents the statistical weighting function $\sigma(\omega)$. It is precisely the product of these two functions (\mathcal{B} and σ), integrated over energies and momenta, that gives rise to the dynamical quasi-particle entropy, and thus it will be

interesting to study their overlap. The general features of the \mathcal{B} spectral function as a function of density are very close to those of the usual spectral function \mathcal{A} (see Fig. 5.17). In the case of $k = 0$, the quasi-particle peak moves to more and more attractive energies as density increases, reflecting the fact that the binding energy of a zero-momentum nucleon increases with density. Above the Fermi surface (at $k = 2k_F$), the situation is the opposite and the peak of the \mathcal{B} function moves to higher energies with increasing density. The width of these peaks, both at zero momentum and at twice the Fermi momentum, is broadened with density. This is in accordance with the naive idea that correlation effects increase with density. In addition, as a consequence of this broadening, the strength of the high energy tails (visible at high positive energies for the $k = 0$ state) decreases with density, allowing the sum rule Eq. (3.105) to be fulfilled. Note that this behavior does not coincide with the one observed for the \mathcal{A} spectral function, in which the same lowering and widening of the quasi-particle peak is found, but the strength of the tails grows with density.

The situation is different at the Fermi surface: when the density is increased, the peak remains at $\omega = \mu$, while its width becomes narrower and concentrates more strength. This can be understood if one takes into account that, as already commented, at zero temperature, *i.e.* for the fully degenerate system, the correlated \mathcal{A} spectral function shows a delta peak which would also be present in the \mathcal{B} spectral function. At a fixed non-zero temperature, however, the system moves towards the degenerate limit (the ratio T/ϵ_F decreases) with increasing density and thus the \mathcal{B} spectral function becomes closer to the delta-like behavior. This is actually what can be seen in the central panel of Fig. 6.2. At high densities ($\rho \geq 0.2 \text{ fm}^{-3}$), a clear separation between the quasi-particle peak and the background contribution to the \mathcal{B} spectral function is observed. This separation is enhanced in the logarithmic scale due to the (very small) negative values of the \mathcal{B} spectral function between these two regions. Since a positive-definiteness condition for \mathcal{B} seems difficult to prove, one cannot say whether these negative values are physical or caused by small inaccuracies in the numerical derivatives of the spectral function [see Eq. (3.109)].

From the left panels of Fig. 6.2, it is clear that the quasi-particle peak and the peak of the σ function only coincide for momenta close to k_F and energies around $\omega = \mu$. Therefore, the more important contributions to the dynamical quasi-particle entropy of the system will be those of momenta close to the Fermi surface and energies close to the chemical potential. It is precisely the interplay between σ and \mathcal{B} that gives rise to the density dependence of the entropy. Since the value of \mathcal{B} at $k = k_F$ and $\omega = \mu$ increases with density, one may expect that the entropy would increase with density. However, it is also true that, for lower densities, the quasi-particle peak is closer to μ at all momenta and thus there are contributions of the quasi-particle peak for momenta not necessarily close to k_F . In fact, when these contributions are summed, one finds that the entropy density

increases with density, but the entropy per particle is a decreasing function of density.

To gain insight into the temperature dependence of the dynamical quasi-particle entropy, the \mathcal{B} spectral function as a function of energy for the same three different momenta considered previously at a fixed density $\rho = 0.16 \text{ fm}^{-3}$ and at four different temperatures $T = 5, 10, 15$ and 20 MeV is shown in the right panels of Fig. 6.2. It is clear that, for all momenta, the variations of temperature mainly result in changes of the width of the quasi-particle peak, while the position in energy of this peak relative to the chemical potential is nearly unchanged. In addition, the momentum states far above the Fermi surface are not affected by temperature, as it is seen in the lowest panel, corresponding to $k = 2k_F$. Note that the same behavior was found for $\text{Im} \Sigma(k, \omega)$ in Fig. 5.14 and for $\mathcal{A}(k, \omega)$ in Fig. 5.17. At the Fermi surface, on the other hand, the effects are more important. As temperature increases, the height of the quasi-particle peak decreases, while its width increases. Moreover, at the lowest temperature ($T = 5 \text{ MeV}$) a clean separation is observed between a quasi-particle peak and a “particle” ($\omega > \mu$) and “hole” ($\omega < \mu$) background. This is again enhanced by the fact that the \mathcal{B} spectral function acquires negative (but very small) values in this region. This separation is softened at $T = 10 \text{ MeV}$ and disappears completely above this temperature. Such a behavior is again understood in terms of the degeneracy of the system. The lower the temperature, the higher the degeneracy and the smaller the width of the \mathcal{B} spectral function at the Fermi surface. For the $k = 0$ state, a similar situation is found. The peak lies below the chemical potential, and it is clearly split from the particle background at $T = 5 \text{ MeV}$. For temperatures above $T = 10 \text{ MeV}$ this separation disappears and a smooth transition from “particle” to “hole” states is found in the \mathcal{B} function. It is also interesting to notice that the width of the peak remains more or less constant, thus indicating that temperature-induced effects on the width of the quasi-particle peak are only relevant around $k = k_F$.

As for the total contribution to the dynamical quasi-particle entropy, the convolution between $\sigma(\omega)$ and $\mathcal{B}(k, \omega)$ is again crucial. At low temperatures, $\sigma(\omega)$ is very peaked around $\omega \sim \mu$. The convolution will thus only be different from zero whenever the quasi-particle peak is close to μ , *i.e.*, at $k \sim k_F$. On the other hand, at higher temperatures $\sigma(\omega)$ is different from zero in a wider region of energies, which results in a non-zero convolution at all momenta. When one integrates over momenta, the final dynamical quasi-particle entropy is higher for the higher temperature. Thus, in accordance with intuition, the entropy of this correlated system grows with temperature.

6.2 Comparison among different approximations

When presenting the different ways of computing the entropy of a correlated system of fermions in Chapter 3, various approximations and expressions for this

quantity have been deduced. These will now be studied separately in order to establish more clearly the differences and similarities among them. In addition, some examples will be given of the temperature and density dependences of the different approaches presented.

Dynamical quasi-particle entropy

The full dynamical quasi-particle entropy S^{DQ} can be computed either from Eq. (3.94) or from Eq. (3.98):

$$\frac{S^{DQ}}{\mathcal{V}} = \nu \int \frac{d^3k}{(2\pi)^3} \int_{-\infty}^{\infty} \frac{d\omega}{2\pi} \sigma(\omega) \mathcal{B}(k, \omega) = \nu \int \frac{d^3k}{(2\pi)^3} \int_{-\infty}^{\infty} \frac{d\omega}{2\pi} \frac{\partial f(\omega)}{\partial T} \Xi(k, \omega). \quad (6.3)$$

While the first of the previous expressions is more intuitive, because it gives the entropy in terms of the convolution of a \mathcal{B} spectral function and a statistical factor, it is less convenient from the numerical point of view. Consider the expression of the \mathcal{B} spectral function [see Eq. (3.109)]:

$$\mathcal{B}(k, \omega) = \mathcal{A}(k, \omega) \left[1 - \frac{\partial \text{Re} \Sigma(k, \omega)}{\partial \omega} \right] + \frac{\partial \text{Re} \mathcal{G}(k, \omega)}{\partial \omega} \Gamma(k, \omega). \quad (6.4)$$

The spectral function, the real part of the self-energy and the width are all outputs of the SCGF scheme. The real part of the propagator can also be computed from these quantities:

$$\text{Re} \mathcal{G}(k, \omega) = \frac{\omega - \frac{k^2}{2m} - \text{Re} \Sigma(k, \omega)}{\left[\omega - \frac{k^2}{2m} - \text{Re} \Sigma(k, \omega) \right]^2 + \left[\frac{\Gamma(k, \omega)}{2} \right]^2}. \quad (6.5)$$

Thus, within the SCGF method, one has access to all the functions forming the \mathcal{B} spectral function. However, there are numerical derivatives which have to be performed on $\text{Re} \Sigma$ and on $\text{Re} \mathcal{G}$. These derivatives require an accurate sampling of the quasi-particle region, where both functions have strong energy dependences, and thus should be done with extreme care.

Instead of this approach, our results will rely on Eq. (3.94) [the second term in Eq. (6.3)]. The only derivative appearing in this expression is the temperature derivative of the Fermi-Dirac distribution, which can be computed analytically. The remaining term is formed by the $\Xi(k, \omega)$ function:

$$\Xi(k, \omega) = 2\pi\Theta[\text{Re} \mathcal{G}^{-1}(k, \omega)] - 2 \arctan \lambda(k, \omega) + \frac{2\lambda(k, \omega)}{1 + \lambda^2(k, \omega)}, \quad (6.6)$$

which was already analyzed in Chapter 3. This is formed by a step-like (quasi-particle) contribution plus two terms which depend on $\lambda(k, \omega)$ [see Eq. (3.72)]. The

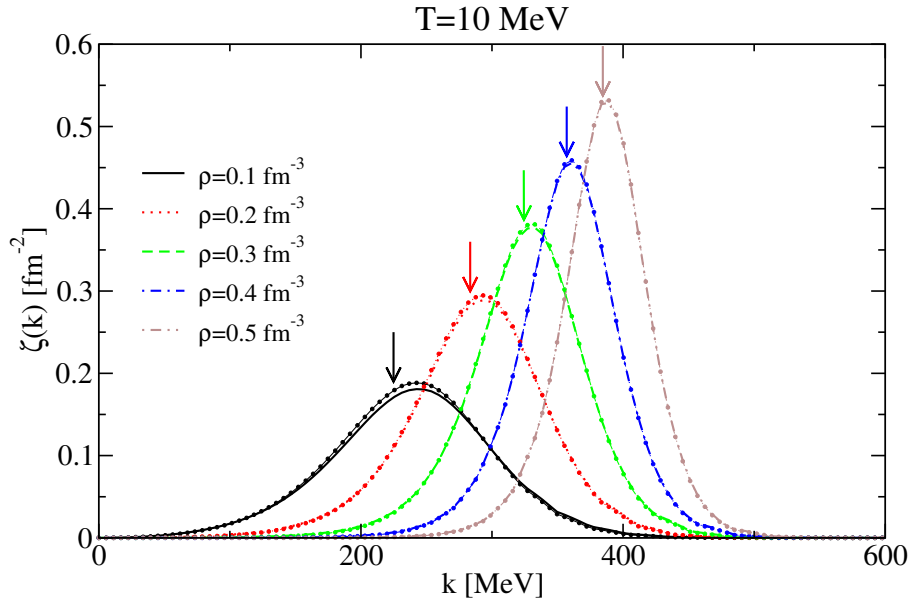


Figure 6.3: Momentum dependence of the ζ function [see Eq. (6.7)] for five different densities (from $\rho = 0.1$ to 0.5 fm^{-3} in equidistant steps) at a fixed temperature of $T = 10 \text{ MeV}$. The lines with dots correspond to the quasi-particle approximation ζ^{QP} for the same conditions. The arrows signal the position of the Fermi momentum at each density.

final Ξ function is smooth in energies, but has a strong variation close to the quasi-particle pole (see Fig. 3.4). On the other hand, the $\frac{\partial f}{\partial T}$ function is negative below μ and positive above it, which might induce large cancellations in the integral. Therefore, one has to sample both energy regions (the quasi-particle peak and the regions above and below μ) accurately in order to obtain S^{DQ} .

To illustrate the importance and the structure of these convolutions, let us consider the first expression for the dynamical quasi-particle entropy density of Eq. (6.3). From it, one finds that the contribution of each momentum state to the dynamical quasi-particle entropy density is given by:

$$\zeta(k) = \frac{\nu}{2\pi^2} k^2 \int_{-\infty}^{\infty} \frac{d\omega}{2\pi} \sigma(\omega) \mathcal{B}(k, \omega). \quad (6.7)$$

The momentum dependence of this function is shown in Fig. 6.3. As the density increases, this integrand becomes larger at the Fermi surface, but less extended in momenta. This is in agreement with the previously discussed ideas, *i.e.*, that for less degenerate systems the contributions at all momenta are relevant, while for degenerate systems the contribution of the $k = k_F$ state is the most important one. It is also interesting to note that at all densities, ζ peaks slightly above the Fermi momentum.

Quasi-particle approximation

The quasi-particle approximation to the dynamical quasi-particle entropy is obtained from the no-width approximation for the \mathcal{B} spectral function. When this is included into the expression of the entropy density, one finds [see Eq. (3.111)]:

$$\frac{S^{QP}}{\mathcal{V}} = \nu \int \frac{d^3k}{(2\pi)^3} \sigma[\varepsilon_{qp}(k)]. \quad (6.8)$$

In other words, the quasi-particle entropy is obtained by evaluating the statistical factor $\sigma(\omega)$ at the quasi-particle energies given by the SCGF approach. The difference between S^{DQ} and S^{QP} is given by the term S_2^{DQ} of Eq. (3.103), which is computed from an integral of functions of the λ variable. Whenever Γ is small, λ will become negligible and the S_2^{DQ} contribution will also be small in front of S^{QP} . Actually, the magnitude of λ is given by the ratio of Γ and $\text{Re}\mathcal{G}^{-1}$, and it can happen that even when Γ is relatively large, the denominator cancels the contribution of λ . In these cases, S_2^{DQ} can keep on being small even though the dynamical correlations become large.

It is also instructive to consider the entropy density of each momentum state in the quasi-particle approximation. This is given by:

$$\zeta^{QP}(k) = \frac{\nu}{2\pi^2} k^2 \sigma[\varepsilon_{qp}(k)], \quad (6.9)$$

and it is shown in Fig. 6.3 in circles. The differences between this approximation and the full $\zeta(k)$ of Eq. (6.7) are only relevant for the lowest densities and in a range of momenta close to the Fermi momentum. This is again a signature of the small role played by the correlations that fragment the quasi-particle states on the entropy. Therefore, one expects that the quasi-particle approximation to the entropy, Eq. (3.111), will describe correctly the full dynamical quasi-particle entropy, S^{DQ} .

Brueckner-Hartree-Fock entropy

The equivalent to the zero temperature BHF theory for finite temperatures is the BdD approach. This involves the calculation of a grand-canonical potential, whose temperature derivative would essentially yield an entropy which embeds the particle-particle correlations inherent of the BHF approach. Still, in the finite temperature BHF calculations performed in this Thesis, the entropy has been computed from the mean-field-like expression:

$$\frac{S^{BHF}}{\mathcal{V}} = \nu \int \frac{d^3k}{(2\pi)^3} \sigma[\varepsilon_{BHF}(k)], \quad (6.10)$$

where the quasi-particle energies are computed from the BHF self-energy [see Eqs. (5.56) and (5.58)]. This differs from the quasi-particle entropy introduced

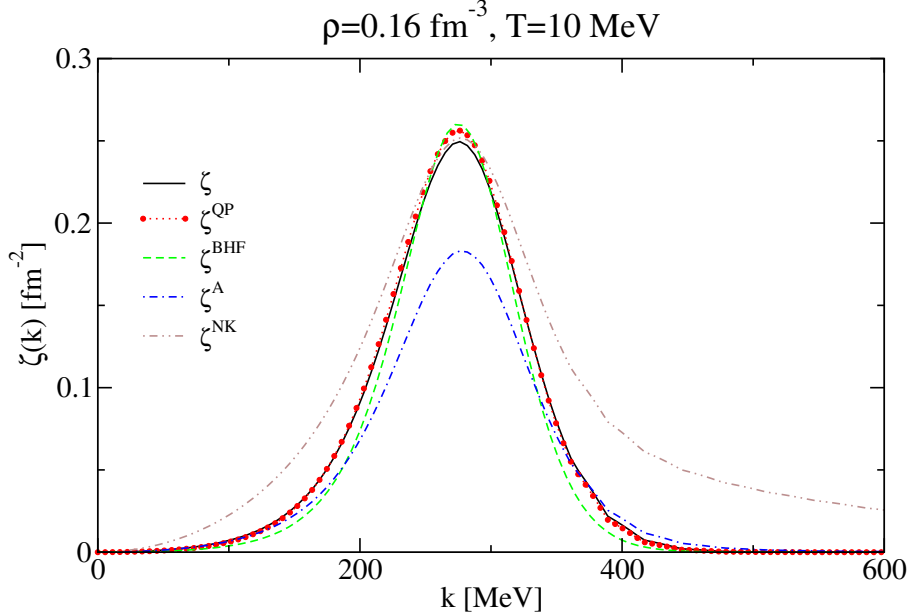


Figure 6.4: *Momentum dependence of the ζ function for five different approximations at a fixed density ρ_0 and a temperature of $T = 10$ MeV.*

above in both the position of the single-particle peaks (given by $\varepsilon_{qp}(k)$ in the first case and by $\varepsilon_{BHF}(k)$ in the second) and in the different values of the chemical potentials in the statistical factor, $\sigma(\omega)$, within each approximation. In our BHF calculations, this chemical potential is obtained by means of the normalization condition:

$$\rho = \nu \int \frac{d^3k}{(2\pi)^3} f(\varepsilon_{BHF}(k), \tilde{\mu}^{BHF}). \quad (6.11)$$

The quasi-particle spectra from the BHF and the SCGF differ especially in the hole region, where the BHF approximation leads to more attractive values (about 20 MeV more attractive at saturation, see Fig. 5.16). This difference can be compensated by the difference in microscopic chemical potentials, which in the BHF is also around 20 MeV more attractive at saturation than for the SCGF approach (see Fig. 6.7). All in all, the correction to the final entropy can be small due to the cancellation of these differences in the argument of σ , where $\varepsilon(k)$ and μ are subtracted.

The size of these effects is explored by means of Fig. 6.4, where the different approximations to $\zeta(k)$ are shown as a function of momentum at the empirical saturation density at $T = 10$ MeV. As already explained, it is hard to distinguish the full dynamical quasi-particle entropy from the quasi-particle approximation to the entropy, except for the momenta close to k_F . The BHF approximation is, on the other hand, less extended in momentum, but it has a slightly stronger peak.

The first effect is actually more important and the entropy per particle obtained in the BHF yields smaller entropies.

Spectral function entropy

The spectral function entropy is given by the following “intuitive” expression:

$$\frac{S_1^A}{\mathcal{V}} = \nu \int \frac{d^3k}{(2\pi)^3} \int_{-\infty}^{\infty} \frac{d\omega}{2\pi} \sigma(\omega) \mathcal{A}(k, \omega), \quad (6.12)$$

which is however not justified from thermodynamical grounds. This expression is actually the first term of the dynamical quasi-particle entropy [see Eq. (3.113)]. Therefore, it should be taken as another contribution to the total value and not as any kind of approximation to it. One can also guess easily its magnitude: the \mathcal{A} spectral function is lower than the \mathcal{B} spectral function at the quasi-particle peak, where it has its more relevant contribution. Consequently, and even though it might have a larger width in energies, the \mathcal{A} spectral function contribution to the entropy is always lower than the dynamical quasi-particle entropy. This can also be seen in Fig. 6.4, where the corresponding ζ function:

$$\zeta^{\mathcal{A}}(k) = \frac{\nu}{2\pi^2} k^2 \int_{-\infty}^{\infty} \frac{d\omega}{2\pi} \sigma(\omega) \mathcal{A}(k, \omega), \quad (6.13)$$

is plotted as a function of momentum. One can indeed see that the peak of this function is much lower than that of the other ζ functions.

Momentum distribution entropy

In addition to the previous approximations, a quantity which is computed from the correlated momentum distribution of the system, $n(k)$ [see Eq. (2.72)], will also be displayed in Fig. 6.6. This is the entropy of the momentum distribution, obtained from the expression:

$$\frac{S^{NK}}{\mathcal{V}} = -\nu \int \frac{d^3k}{(2\pi)^3} \left\{ n(k) \ln n(k) + [1 - n(k)] \ln [1 - n(k)] \right\}. \quad (6.14)$$

Note that the depleted momentum distribution is used here. Although this might seem a reasonable guess at first sight, one should be careful with this expression in two aspects. On the one hand, it is not derived from thermodynamical grounds and thus one cannot guarantee that it reproduces the entropy of a correlated fermionic system. On the other hand, one should take into account that the dynamical correlations induced by interaction effects are included in the momentum distribution, $n(k)$. This carries also some thermal correlations, as seen by the fact that it has a temperature dependence. Still, the entropy is a purely thermodynamical quantity which (in the microcanonical ensemble) simply accounts for the number

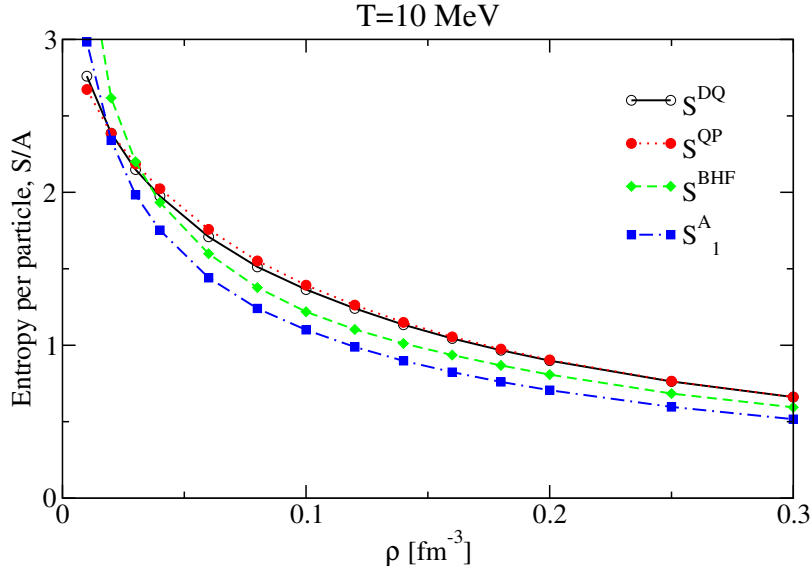


Figure 6.5: *Different approximations to the entropy as a function of density for a $T = 10$ MeV temperature. The full lines correspond to S^{DQ} ; the dotted lines to S^{QP} ; the dashed lines to S^{BHF} and the dot-dashed lines to S_1^A .*

of thermally accessible states of the system. Therefore, it should not care so much about the interaction or the dynamical correlations induced by it. Note that if dynamical effects are present (as it is the case of S^{NK}), one might be overcounting correlations in the entropy.

This is also reflected in Fig. 6.4. The contribution of each momentum state to the momentum distribution entropy density is given by:

$$\zeta^{NK}(k) = -\frac{\nu}{2\pi^2} k^2 \left\{ n(k) \ln n(k) + [1 - n(k)] \ln [1 - n(k)] \right\}. \quad (6.15)$$

Since the momentum distribution is depleted, ζ^{NK} gives large contributions in the low momentum region, much larger than any other approximation. The peak region is similar in height to the other ζ functions, but at high momenta S^{NK} yields again large contributions, due to the fact that momentum states are more populated than in the thermal case. The fact that ζ^{NK} is larger in the low and high momentum regions implies that S^{NK} will be larger in the whole density and temperature range here considered.

Density dependence

One can now try to quantify the effects introduced by each of the previous approximations by directly comparing the density and temperature dependences of

the entropy computed from the different schemes. To begin with, in Fig. 6.5 the density dependence of the different approximations to the entropy per particle is shown for a fixed temperature of $T = 10$ MeV. As a general feature, one can say that all of these entropies decrease substantially with density, from values of around 2.5 at densities around 0.02 fm^{-3} , down to values of around 0.5 for the highest density here considered, $\rho = 0.3 \text{ fm}^{-3}$. An important result that arises from Fig. 6.5 is the fact that, at all densities, S^{DQ} and S^{QP} are very close. This is somehow in agreement with the idea that the inclusion of the width of quasi-particles has a small effect in the entropy. As discussed in relation with Fig. 6.3, the effect is larger at lower densities, where both approximations differ more, but it is never higher than a 5%. At high densities, the difference is so small that cannot be appreciated in the figure. This result is not at all intuitive. It indicates that S_2^{DQ} , which is nothing but the difference between S^{DQ} and S^{QP} , decreases with density. But, since it has been argued that S_2^{DQ} represents somehow the finite width effects on the entropy and since correlations grow with density, one would also expect it to grow with density. However, the higher the density, the smaller the width of the \mathcal{B} spectral function at $k = k_F$ (which is the more relevant contribution at high densities) and thus the lower the effects of correlations. This is why at higher densities both approximations to the entropy tend to be similar. The fact that S_2^{DQ} is negative at intermediate densities (say from $\rho = 0.05 \text{ fm}^{-3}$ to 0.20 fm^{-3}) is quite interesting: in addition to stressing the fact that finite lifetime effects to the entropy are small, one can say that it looks like correlations (*i.e.* the width of the quasi-particle) tend to order the system.

The self-consistent propagation of holes is the cause of the difference between S^{DQ} and S^{BHF} . Since the effect of the width on S^{DQ} is small at this temperature, the difference between both entropies arises from the different quasi-particle energies and chemical potentials of the two approaches. In the intermediate density region, the BHF entropy has values that are about 10 % below the dynamical quasi-particle one. The presence of hole-hole correlations, thus, increases the entropy, *i.e.* the thermal disorder. This is related to the fact that hole-hole correlations tend to increase the density of single-particle states close to the Fermi energy. If one tries to parameterize the quasi-particle spectrum close to μ in terms of an effective mass m^* , for instance, one obtains larger values for the parameterization of the SCGF spectrum than for the BHF energies [Fri03].

Finally, the contribution of S_1^A to the dynamical quasi-particle entropy is also shown. As already mentioned, this expression comes from a naive generalization to incorporate width effects which, nevertheless, gives a reasonable first guess to the entropy per particle. Intuitively, one would expect that, since the \mathcal{A} spectral function is wider than the \mathcal{B} one, the overlap between $\mathcal{A}(k, \omega)$ and $\sigma(\omega)$ at a given momentum should be higher and thus the final S_1^A entropy could overestimate S^{DQ} . However, this is not the case, except for the lowest densities. This can be understood from the height of the quasi-particle peak for \mathcal{A} being, roughly

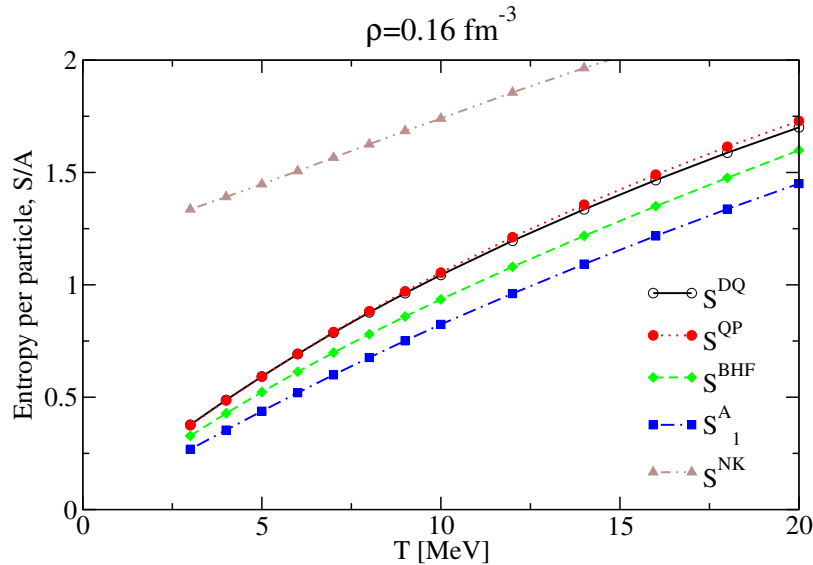


Figure 6.6: *Different approximations to the entropy as a function of temperature at a density of $\rho = 0.16 \text{ fm}^{-3}$. The full lines correspond to S^{DQ} ; the dotted lines to S^{QP} ; the dashed lines to S^{BHF} ; the dot-dashed lines to S_1^A and the double dot-dashed lines to S^{NK} .*

speaking, a factor of 2 lower than that for \mathcal{B} . Thus, although more extended in momentum, the $\zeta(k)$ function for the \mathcal{A} spectral function is smaller and gives rise to a lower entropy (see Fig. 6.4). The difference of both entropies is between 20 – 30% for the intermediate density region. The origin of such differences is the S_2^A contribution of Eq. (3.114), which is the integral of two terms. Both terms are of the same order at $\rho \sim 0.1 \text{ fm}^{-3}$ but, while the contribution proportional to \mathcal{A} decreases with density, the one proportional to Γ increases, and above $\rho = 0.3 \text{ fm}^{-3}$ it carries more than 80% of the total correction.

Temperature dependence

In Fig. 6.6, the temperature dependence of the entropy at the empirical saturation density computed within different approximations is shown. As a general trend, one observes the same features previously discussed concerning the density dependence. The quasi-particle approximation S^{QP} using SCGF energies reproduces the dynamical quasi-particle entropies at all temperatures very well, especially below $T = 10 \text{ MeV}$. The BHF entropy describes the entropy of the system with an error of about 15 %. This difference is quite small, which is again a sign that both the fragmentation of single-particle strength and the exact position of the quasi-particle peak are not that crucial in the final result of the entropy per particle. Since the quasi-particle approximation to the entropy is always larger than the

BHF one, one can generally say that the inclusion of hole-hole propagation tends to increase the entropy. The \mathcal{A} spectral function contribution to the entropy is again correct respect to its temperature behavior, but it still gives a too small value for the entropy per particle of the system, with errors as large as a 30 %. As previously discussed, this is due to the lower quasi-particle peak of the \mathcal{A} spectral function, which makes the S_1^A contribution to the entropy lower than the S^{DQ} entropy. The difference between these two functions is given by the S_2^A contribution. This is composed of the two terms in Eq. (3.114), which have different relative weights as temperature changes. While the term proportional to the \mathcal{A} spectral function amounts to 90 % of the total correction at $T = 4$ MeV, its relative importance decreases linearly to a 30 % contribution for the $T = 20$ MeV case. Finally, the entropy of Eq. (6.14) is given in terms of the fully correlated momentum distributions. This momentum distribution includes both thermal and correlation effects. In fact, in S^{NK} both effects are taken on the same footing and consequently dynamical correlations mimic extra thermal effects. This is why this is the only approximation which tends to give a non-zero entropy at $T = 0$. In the fully degenerate limit, the momentum distributions given by Eq. (2.72) are not Fermi step functions and they are corrected by correlation effects. These correlations are the responsible for a certain amount of entropy, when this is computed with Eq. (6.14) at $T = 0$. Thus, at finite temperatures thermal effects are overestimated in S^{NK} due to the presence of correlations, and S^{NK} produces a far too large entropy (almost a factor of three too large at $T = 5$ MeV).

One can say that all the approximations to the entropy in the figure increase with temperature (as expected) and approach a linear dependence at low T . It is a well-known feature of Fermi liquids that the slope coefficient for such a linear behavior is proportional to the zero temperature density of states computed at the Fermi surface, $N(T = 0)$:

$$\frac{S_{low}}{A} = \frac{\pi^2}{3\rho} N(0) T. \quad (6.16)$$

Each approximation goes to the $T = 0$ limit with different slopes, and one can thus obtain different densities of states from a fit of the different slopes. As a matter of fact, one can find analytical expressions for the density of states at zero temperature for the S^{DQ} (S^A) approximation in terms of the \mathcal{B} (\mathcal{A}) spectral function [see Appendix D]. To calculate $N(0)$ for these approximations, however, one needs the spectral functions at zero temperature and one should thus extrapolate the results to the $T = 0$ limit, which cannot be done within our approach reliably. Instead of that, the expression of $N(0)$ in terms of the \mathcal{B} and \mathcal{A} spectral functions is extended to finite temperatures. In doing this, one gets the “density of states” related to the \mathcal{B} spectral function:

$$N_{\mathcal{B}}(T) = \nu \int \frac{d^3k}{(2\pi)^4} \mathcal{B}(k, \omega = \mu), \quad (6.17)$$

and the usual one, related to the \mathcal{A} spectral function:

$$N_{\mathcal{A}}(T) = \nu \int \frac{d^3k}{(2\pi)^4} \mathcal{A}(k, \omega = \mu), \quad (6.18)$$

where T denotes the fact that these have been calculated at the finite temperature at which the spectral functions have been computed. Note that at low T and $\omega = \mu$ the functions \mathcal{A} and \mathcal{B} differ basically by a factor \mathcal{Z} (where \mathcal{Z} denotes the renormalization of the quasi-particle pole):

$$\mathcal{A}(k, \omega = \mu) \sim \mathcal{Z}(k, \omega = \mu) \mathcal{B}(k, \omega = \mu) \quad (6.19)$$

and thus the two densities of states differ approximately by such a factor. Note, however, that the density of states that gives the correct linear fit to the dynamical quasi-particle entropy is that of Eq. (6.17). In fact, one can numerically check that it is this quantity that reduces to the well-known quasi-particle expression (see Appendix D):

$$N_{QP}(0) = \frac{\nu k_F m^*(k_F)}{2\pi^2} \quad (6.20)$$

at low enough temperatures, where the effective mass is obtained through the derivative of Eq. (4.32) evaluated at the Fermi surface using the finite temperature SCGF quasi-particle spectrum, $\varepsilon_{qp}(k)$. This can be seen in Table 6.1, where the densities of states computed with the \mathcal{A} and the \mathcal{B} spectral functions together with that obtained from the QP expression, Eq. (6.20), at $\rho = 0.16 \text{ fm}^{-3}$ are given for a set of low temperatures. The effective mass at k_F is given in the fifth column of Table 6.1 for completeness. The numerical values confirm that, at low temperatures, the density of states from the \mathcal{B} spectral function reduces to the quasi-particle one, hence indicating that from a thermodynamical point of view this is the correct density of states. In contrast, from a microscopic point of view, the \mathcal{A} density of states is the one which has been commonly used [Kel96; Müt95; Che01]. One should keep in mind that in a no-width approximation with $\mathcal{Z} = 1$ both of them would reduce to the same expression, Eq. (6.20). The linear approximation of the entropy of Eq. (6.16) with the density of states coming from the \mathcal{B} spectral function at the lowest temperature ($T = 4 \text{ MeV}$) reproduces the total entropy per particle with a 20% accuracy up to $T = 10 \text{ MeV}$. Yet, the density of states has a certain temperature dependence, which is almost linear in the case of the \mathcal{B} “density of states”. If one takes into account this temperature dependence and computes the entropy per particle with the \mathcal{B} density of states evaluated at the corresponding finite temperatures, the dynamical quasi-particle expression of the entropy can be reproduced with less than a 10 % discrepancy for temperatures up to $T = 10 \text{ MeV}$.

In the context of nucleus-nucleus collisions at intermediate energies, there exists a growing amount of experimental data [Poc95; Nat02] which should be useful to

T [MeV]	$N_{\mathcal{A}}(T)$ [$\text{MeV}^{-1}\text{fm}^{-3}$]	$N_{\mathcal{B}}(T)$ [$\text{MeV}^{-1}\text{fm}^{-3}$]	$N_{QP}(T)$ [$\text{MeV}^{-1}\text{fm}^{-3}$]	$\frac{m^*}{m}$
4	0.00435	0.00608	0.00608	0.935
6	0.00430	0.00585	0.00586	0.901
8	0.00424	0.00566	0.00570	0.875
10	0.00416	0.00548	0.00557	0.855

Table 6.1: *Densities of states related to the \mathcal{A} (first column) and \mathcal{B} (second column) spectral functions at $\rho = \rho_0$ for different temperatures. The quasi-particle approximation to the density of states, Eq. (6.20), is displayed in the fourth column, together with the effective mass at the Fermi surface in the fifth column.*

constrain the thermal properties of nuclei and nuclear matter. In particular, the liquid-gas phase transition and the caloric curve give a hint on the properties of nuclei at low temperatures. In the study of the caloric curve, it is customary to parameterize the excitation energy at low temperatures in terms of the so-called inverse level density parameter K (see [De98] for a theoretical description), which is inversely proportional to the density of states introduced here. The values obtained here for K [defined as $K^{-1} = \frac{\pi^2}{6\rho} N_{\mathcal{B}}(0)$] are close to the Fermi gas value $K \sim 14.6$ MeV at the empirical saturation density. This can be understood from the fact that $N_{\mathcal{B}}$ reduces to the quasi-particle value of Eq. (6.20) which, in addition, is similar to the free Fermi gas value because, in the case of the CDBONN potential at these densities, the effective mass is almost equal to the bare nucleon mass at low temperatures. A word of caution must be raised, however. The value for K is obtained here from a calculation in infinite isospin symmetric matter in which only short-range correlations are treated. Nevertheless, it is clear that a study of the inverse level parameter should include both the effects of finite size and long-range correlations, which are very important in determining the low energy excitations of nuclei.

6.3 Thermodynamical consistency

From first principles, the ladder approximation is known to be Φ -derivable [Bay62] and thus if the dynamical quasi-particle approximation to the entropy is correct, one would expect thermodynamical consistency to be fulfilled. In other words, the preservation of thermodynamical consistency can be taken as a confirmation that S' is negligible in our approach. The left panel of Fig. 6.7 shows the accuracy that is reached with the SCGF results. For the sake of comparison, the corresponding BHF results are shown in the right panel. The solid lines with full circles in the left panel correspond to the free energies per particle computed within the SCGF

approach:

$$F^{SCGF} = E^{GMK} - TS^{DQ}, \quad (6.21)$$

with the energy computed with the GMK sum rule, Eq. (2.103) (shown with the solid line with squares in the figure) and the entropy with the dynamical quasi-particle expression, Eq. (3.94). The BHF free energy is displayed by a solid line with circles in the right panel and it is given by:

$$F^{BHF} = E^{BHF} - TS^{BHF}, \quad (6.22)$$

with the energy computed from the generalization of the $T = 0$ BHF approach, Eq. (5.59) and the entropy from Eq. (6.10). Note that the BHF energy is also shown with a solid line with squares in the right panel of Fig. 6.7. Moreover, the dotted lines with empty circles correspond to the microscopic chemical potentials, $\tilde{\mu}$, obtained from inverting Eq. (3.47) for the SCGF scheme and from inverting Eq. (6.11) in the BHF approach, respectively. Both chemical potentials are compared with the macroscopic chemical potentials, μ , obtained from the derivatives of the free energy density with respect to density:

$$\mu = \frac{\partial F(\rho, T)}{\partial \rho \mathcal{V}}, \quad (6.23)$$

shown with dashed lines in both panels. These derivatives have been performed numerically after adjusting F to a third-order polynomial. Although the low density region is not well reproduced in this rough approximation, the results of the intermediate density region can be fully trusted and in addition they will be smooth with density.

The fulfillment of thermodynamical consistency for the SCGF approach is thus nicely illustrated in Fig. 6.7. The agreement between $\tilde{\mu}$ and μ is very good above 0.05 fm^{-3} , with discrepancies of less than 1 MeV up to $\rho = 0.5 \text{ fm}^{-3}$. As a consequence, the Hugenholtz-van Hove theorem is also very well fulfilled, and the minimum of F/A and $\tilde{\mu}$ do nicely coincide at about $\rho \sim 0.27 \text{ fm}^{-3}$. The situation for the BHF approach, on the other hand, is much worse, as it is well-known [Cze02]. The chemical potentials $\tilde{\mu}$ and μ differ by about 10 MeV at $\rho = 0.16 \text{ fm}^{-3}$ and by almost 30 MeV at the highest density here considered. In addition, the Hugenholtz-van Hove theorem is badly violated, and the value of F/A at saturation differs from $\tilde{\mu}$ by about 20 MeV.

Both panels of Fig. 6.7 also display the corresponding energies per particle of the SCGF and the BHF approaches. It is well-known that the propagation of holes has a repulsive effect on the total energy per particle [Fri03; Fri04a]. As a matter of fact, the difference in both energies is quite density dependent. Below 0.03 fm^{-3} , for instance, the BHF method yields more repulsive energies per particle. Above this density, the BHF results are more repulsive than those of the SCGF approach,

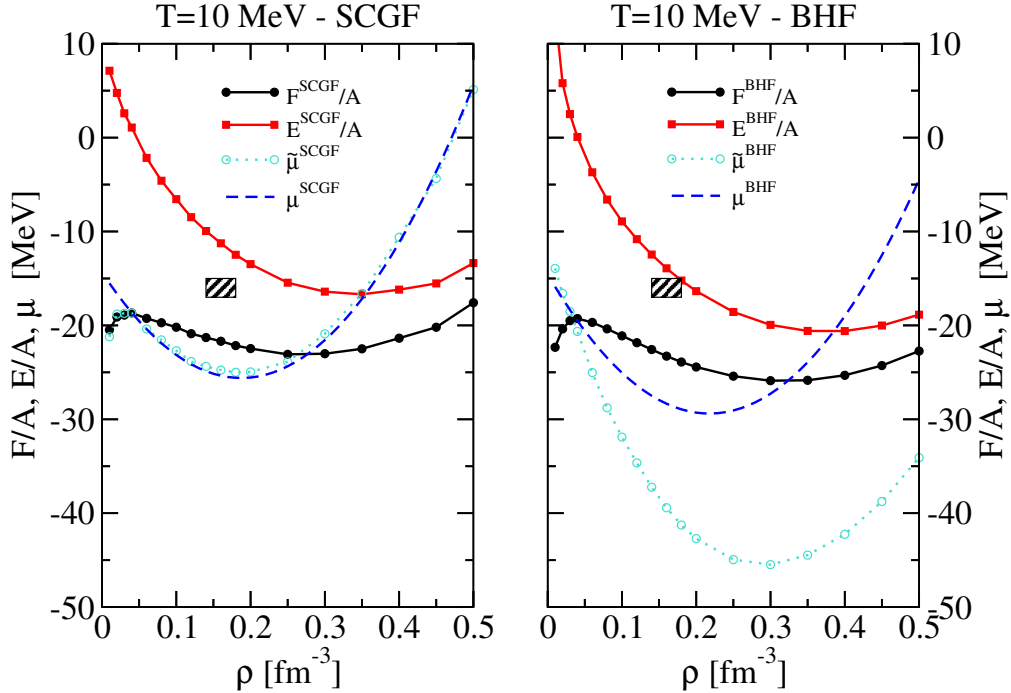


Figure 6.7: Free energies per particle (solid circles), total energies per particle (solid squares) and $\tilde{\mu}$ chemical potentials (dotted lines with empty circles) for the SCGF (left panel) and BHF (right panel) approaches as a function of density for a temperature of $T = 10$ MeV. The μ chemical potential obtained through a numerical derivative are displayed with dashed lines. The hatched areas represent the empirical saturation point of symmetric nuclear matter.

about 3 MeV more repulsive at ρ_0 . The repulsive effect of hole-hole propagation increases with density, and for $\rho = 0.5 \text{ fm}^{-3}$ it is already of the order of 5 MeV. The same repulsive effect is observed in the free-energy per particle, which is less attractive for the SCGF scheme in the whole density range. Once again this is a density dependent effect, which involves about half an MeV difference at low densities and about 5 MeV in the largest ones. It is interesting to note that the differences in free energies between the BHF and the SCGF approaches are smaller than the differences in energies, due to their different entropy contributions.

An important empirical quantity concerning infinite nuclear matter is the saturation density and the binding energy at this density. It is a well-known feature of zero temperature BHF calculations with two-body forces that this quantities are not reproduced. Instead, the BHF results yield either a correct saturation density with too little attraction or a correct binding energy at a too high saturation density. The saturation points for different bare interactions form a band in the binding energy-saturation density plane, known as the Coester band [Coe70]. The

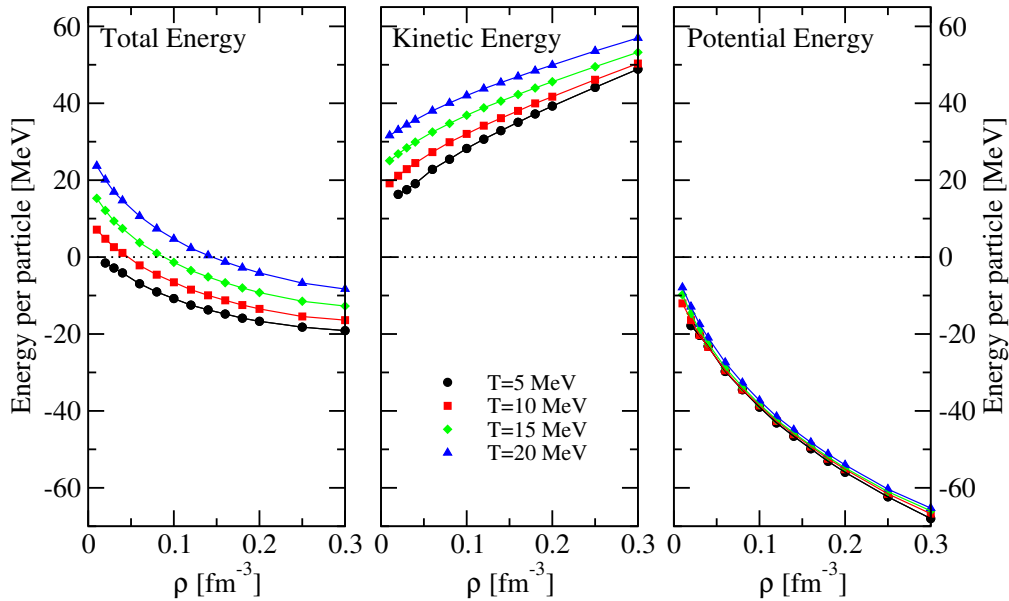


Figure 6.8: Density dependence of the total (left panel), kinetic (central panel) and potential (right panel) energy per particle within the SCGF approach. Four temperatures are considered: 5 (full circles), 10 (squares), 15 (diamonds) and 20 (triangles) MeV.

inclusion of hole-hole propagation has a repulsive effect in the saturation energy, which leads to more realistic results for this quantity, while the saturation densities obtained from the SCGF scheme are still too large [Dew03]. The hatched region in Fig. 6.7 represents the empirical saturation point of nuclear matter. At finite temperature one should probably study the saturation properties of the corresponding thermodynamical potential, *i.e.* the free energy per particle. This can be compared to the saturation properties of the total internal energy per particle. Both quantities saturate at far too large densities (at almost twice the experimental value of saturation density), but while the free-energy gives about -21 MeV, the energy per particle saturates at about -16 MeV. The fact that this value coincides with the empirical saturation energy is however just a coincidence, caused by thermal effects. A calculation for lower temperatures shows that the saturation at zero temperature leads to more attractive energies per particle (see Fig. 6.8).

6.4 Macroscopic results

Now that the thermodynamical consistency of our approach has been exposed, it is time to study the density and temperature dependence of the thermodynamical properties of nuclear matter. The energy per particle will be studied in the first

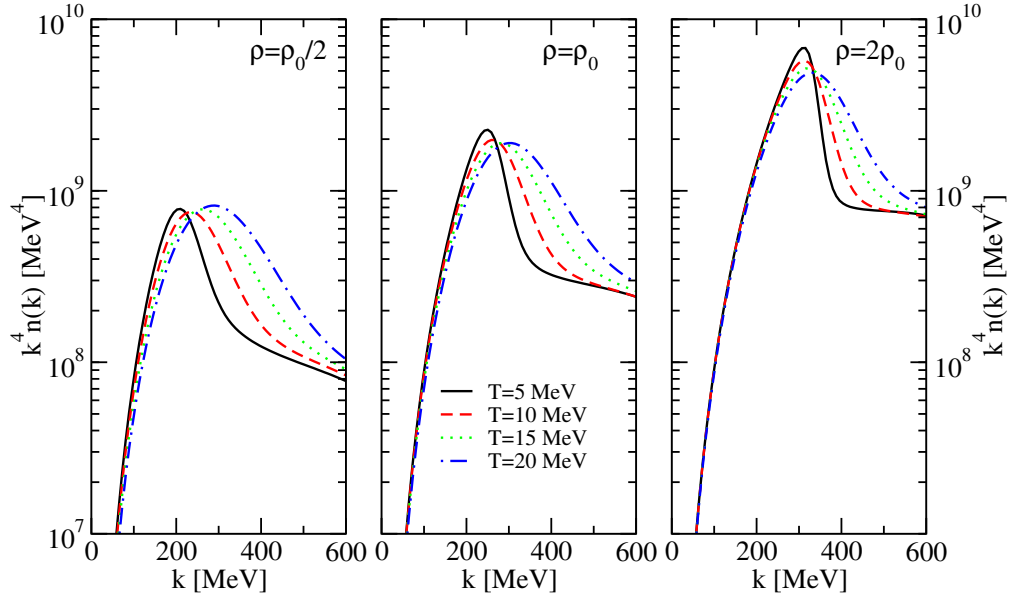


Figure 6.9: *Contribution of the momentum distribution to the kinetic energy within the SCGF approach. The three panels correspond to the densities $\rho_0/2$ (left panel), ρ_0 (central panel) and $2\rho_0$ (right panel). Four different temperatures have been chosen, from $T = 5$ MeV to $T = 20$ MeV in equidistant steps.*

place. To this end, the three different contributions to the energy per particle are shown in the three panels of Fig. 6.8: total (left panel), kinetic (central panel) and potential energy per particle (right panel). Within the SCGF method, the kinetic energy is given by the expression [see Eq. (3.22)]:

$$\frac{\mathcal{K}}{A} = \frac{\nu}{\rho} \int \frac{d^3k}{(2\pi)^3} \frac{k^2}{2m} n(k), \quad (6.24)$$

which is computed with the correlated momentum distribution of Eq. (2.72). At first sight, the results show the naively expected dependence and the kinetic energy increases with density. This is due to the fact that the momentum distributions give sizeable contributions up to the Fermi momentum, which increases with density. Moreover, the integrand in Eq. (6.24) is proportional to $k^4 n(k)$. Due to this k^4 factor, the high momentum components are enhanced, which also favors an increasing density dependence of the kinetic energy per particle (see Fig. 5.19). The increase with temperature at fixed densities can also be understood from the $k^4 n(k)$ factor. This is displayed in Fig. 6.9 for the same conditions at which the momentum distribution of Fig. 5.19 where computed. In that figure, one could already see that the high momentum states were more populated with higher temperatures (for a fixed density). If these large momentum states are weighted with

a k^4 factor, their contribution will be larger, as seen in Fig. 6.9. It is interesting to note that, although in Fig. 6.9 momenta as high as 600 MeV are shown, no sign of attenuation of the $k^4 n(k)$ factor is observed. Actually, one needs to go to momenta of the order of $5 - 6k_F$ to find that the integral for the kinetic energy saturates to a constant value [Fri04a]. For a non-correlated momentum distribution, in contrast, the exponential decay of the momentum distribution cuts out the k^4 dependence and, for small temperatures (far away from the classical limit), no sizeable contributions are found above the Fermi surface. Note, on the other hand, that an analysis in terms of momenta is somehow limited in perspective. Since the spectral functions are a result of the SCGF scheme, one could study the contributions of each momentum and energy state to the total kinetic energy per particle. In this kind of studies, which are outside the scope of this Thesis, one usually finds that about 50% of the total kinetic energy comes from the quasi-particle region (*i.e.* from states with energies and momenta described by the relation $\omega = \varepsilon_{qp}(k)$). The very negative excitation energy and high-momentum regions, which are populated due to the fragmentation of the quasi-particle peak, are responsible for the remaining contribution [Ben89; Fri04a].

It is also instructive to compare the values of the kinetic energy from the SCHF and the SCGF approaches. Since it is difficult to do this at naked eye, in the left panel of Fig. 6.10 the ratio of the correlated to the mean-field kinetic energies are plotted, for various temperatures, as a function of the density. At low densities the SCGF results for the high temperatures are quite close to the SCHF results. Actually, in Fig. 6.8 one can see that the kinetic energy per particle tends to the classical limit, $\frac{3}{2}T$, for the higher temperatures. Moreover, except for the $T = 5$ MeV case, the ratio grows with density at low densities. This is not anymore true for higher densities, where the results tend to become constant and the correlated results become about 1.5 times larger than the non-correlated ones. Indeed, for densities above ρ_0 , the ratio becomes also independent of temperature, which reflects the fact that the temperature dependence of both approaches is very similar. Therefore, although the density and temperature dependences of the mean-field and the correlated kinetic energies can be quite different in the low density region, they become very similar for larger densities. It is important to note that the correlated kinetic energy is a direct outcome of the Green's function treatment. In contrast, a BHF calculation does not give direct access to this quantity, which has to be evaluated by means of the Hellman-Feynman theorem [Müt00]. At zero temperature, the ratio of the correlated kinetic energy to the free kinetic energy depends strongly on the NN interaction which is used [Müt99]. One would thus expect the results presented here to be potential-dependent to a large extent.

The main effect of two-body correlations in the internal energy is reflected into

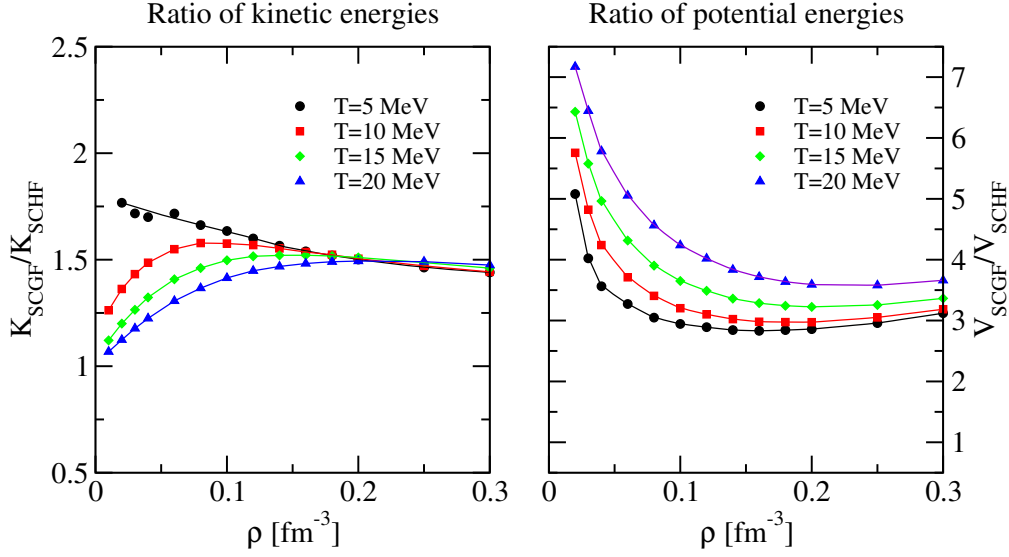


Figure 6.10: *Ratio of the SCGF to the SCHF kinetic (left panel) and potential (right panel) energies as a function of density for four different temperatures (distributed in equidistant steps from $T = 5$ to 20 MeV).*

the potential energy. This is defined as the integral [see Eq. (3.23)]:

$$\frac{\langle V \rangle}{\rho} = \frac{\nu}{\rho} \int \frac{d^3k}{(2\pi)^3} \int_{-\infty}^{\infty} \frac{d\omega}{2\pi} \frac{1}{2} \left\{ \omega - \frac{k^2}{2m} \right\} f(\omega) \mathcal{A}(k, \omega). \quad (6.25)$$

As already commented in the previous chapter, the modifications induced by the renormalization of short-range correlations allow the nucleons to avoid the strongly repulsive core of the bare NN interaction and thus lead to much more attractive results. As seen by a direct comparison of the right panels of Fig. 4.11 and Fig. 6.8, the effect is very large at high densities, where one goes from a value of about -20 MeV for the potential energy per particle in the SCHF approach to about -65 MeV in the SCGF scheme. This makes more than a factor three of difference and thus stresses once again the importance of the inclusion of short-range correlations in this quantity. The size of these differences is explored in the right panel of Fig. 6.10, where the ratio of the correlated to the mean-field potential energies is shown. The strong effect of correlations can be seen from the fact that this ratio is, for all the densities and temperatures explored, above 3. Except for the strong decrease with density below $\rho = 0.1 \text{ fm}^{-3}$, which is a consequence of the low values that the mean-field potential energy acquires in this region, the ratio is quite density independent for each temperature. The density dependence of both potential energies is thus comparable in the high density region, although the correlated case leads to much more attractive results. In contrast to the case of the kinetic energy, however, the correlated potential energy has a different temperature dependence than the mean-

field approach. As a consequence, the ratios computed at different temperatures do not fall on top of each other and the ratios become increasingly large with growing temperature. Note that the temperature dependence of the ratio is caused by the temperature dependence of the non-correlated case, as it is deduced from the fact that the correlated potential energy has a very soft temperature dependence.

Compared to the SCHF results, the correlated kinetic energy is (for intermediate densities) about 1.5 times more repulsive, while the correlated potential energy yields about 3 – 3.5 times more attractive results. All in all, the large potential energy overcomes easily the repulsive contributions in the kinetic energy and the total correlated energy per particle, for any temperature and density, is more attractive than its mean-field counterpart. More specifically, the internal energy per particle is attractive in the whole density range for the lowest temperature ($T = 5$ MeV), as seen in Fig. 6.8. For this particular temperature, the attraction increases with density, until it saturates at about 0.3 fm^{-3} with a value of -20 MeV. This situation changes with temperature, mainly because of the temperature dependence of the kinetic energy. Actually, the effect of temperature in the total energy per particle is fairly density independent. The repulsive effect of temperature on \mathcal{K}/A induces a positive internal energy per particle at low densities. In particular, while the saturation density associated to the total energy per particle remains almost constant for the whole temperature range and stays close to a value of 0.3 fm^{-3} , the corresponding binding energy depends on temperature, and goes from about -19 MeV at 5 MeV to about -8 MeV at 20 MeV. Assuming a quadratical temperature dependence (which would be approximately correct for mean-field approaches and which is also quite approximate in the correlated case), one can extrapolate these results to zero temperature. The binding energy at saturation would then be of about -21 MeV. This is a too large value, if compared to the empirical saturation binding energy, but it is however quite close to the corresponding BHF result for zero temperature [Müt00]. Note however that this extrapolation should be taken with extreme care for, as already explained before, pairing effects might affect the zero temperature results.

The results for the entropy per particle have already been sketched in a previous section. Here the SCGF results for S^{DQ} in the Luttinger-Ward approach will be presented for a wider range of densities and temperatures. The left panel of Fig. 6.11 shows the density dependence of the entropy per particle for four different temperatures. The results are quite similar to those obtained in the mean field approach, where the entropy was found to be a decreasing function of density and an increasing function of temperature. In general terms, however, one finds that the entropies of the correlated approach are larger than those of the SCHF scheme. This is in accordance with the idea that the correlations that go beyond the mean-field tend to increase the entropy. This effect is less notorious at low densities, where the correlated approach yields entropies which are actually smaller than the mean-field approach by about half a unit. One can observe this in Fig. 6.12,

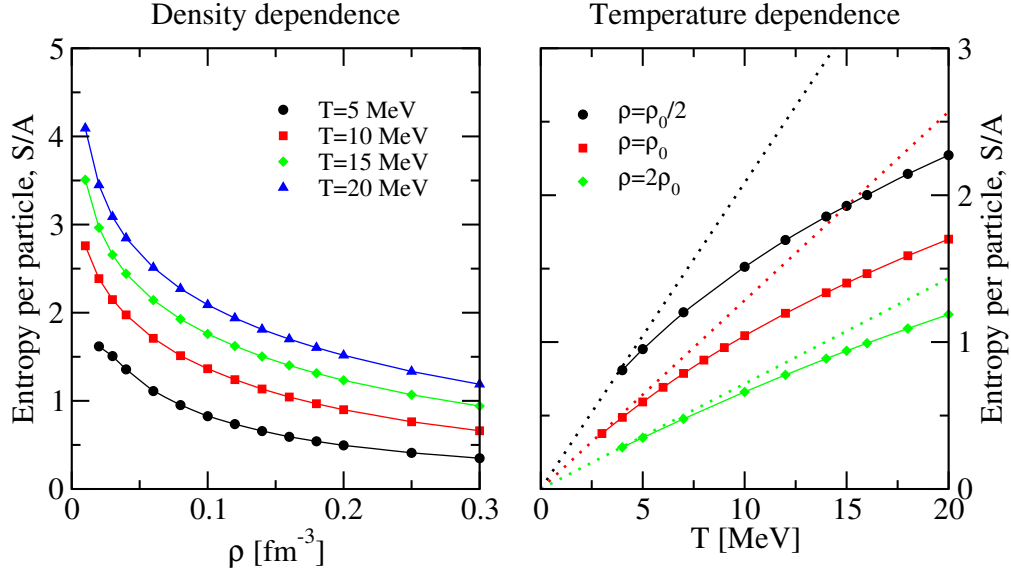


Figure 6.11: *Density dependence (left panel) and temperature dependence (right panel) of the entropy per particle within the DQ approximation. The dotted lines in the right panel correspond to the degenerate approximation of Eq. (D.30). Note the difference in the scale between the right and the left panel.*

where the density and temperature dependence of the ratio of the dynamical quasi-particle to the mean-field entropy is shown. Below $\rho = 0.05 \text{ fm}^{-3}$, the dynamical quasi-particle entropy is somewhat lower than the SCHF one, although this effect is quite density and temperature dependent. For high densities and for the lowest temperature, the dynamical quasi-particle entropy is about 1.5 times higher than the mean field one. The influence of correlations in the entropy is however quite temperature dependent, and the difference between the correlated and the non-correlated entropy decreases when the temperature increases (for densities above 0.05 fm^{-3}). The same effect is observed in the right panel of Fig. 6.12, where the ratio is explored at three constant densities as a function of temperature. For each temperature, the ratio decreases slightly with temperature. The fact that the effect of correlations in S decreases with temperature is in accordance with the intuitive idea that correlations have a smaller influence in systems at larger temperatures, where thermal correlations may overcome the effects of dynamical correlations.

The decrease in the ratio of S^{DQ} to S^{MF} shows that the dynamical quasi-particle entropy does not exactly have the same temperature dependence as S^{MF} . In the right panel of Fig. 6.11 one actually sees that the behavior is qualitatively linear only for the highest density. It has already been mentioned that, within the low temperature limit of the DQ entropy, the coefficient in front of the linear

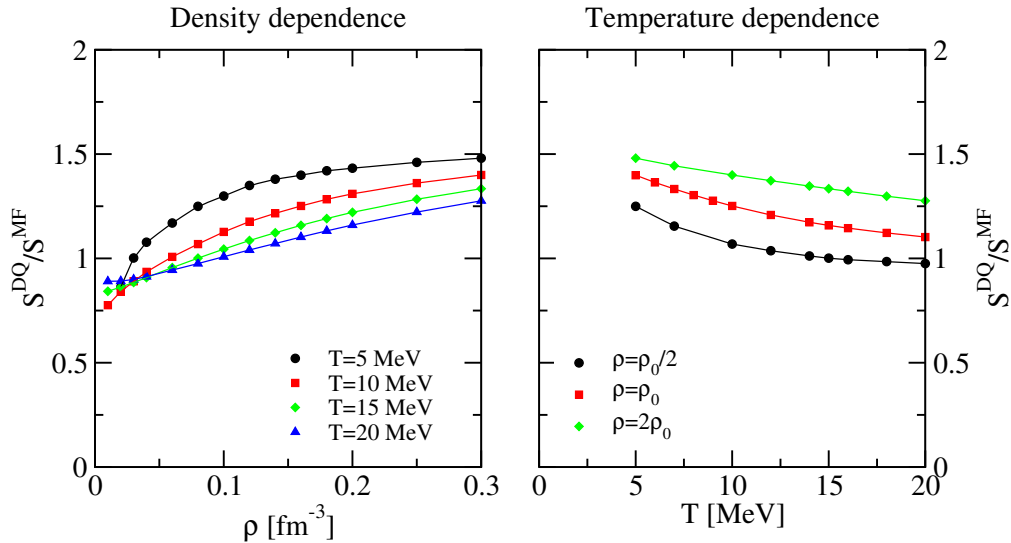


Figure 6.12: *Density dependence (left panel) and temperature dependence (right panel) of the ratio of the DQ to the SCHF entropy.*

temperature dependence should be essentially proportional to the density of states associated to the \mathcal{B} -spectral function. This quantity is also very close to the quasi-particle density of states, Eq. (6.20), which has to be computed from the zero temperature effective mass. Since this is not possible in our approach, the effective mass at the lowest temperature ($T = 4$ MeV for $\rho_0/2$ and $2\rho_0$; $T = 3$ MeV for ρ_0) is used in order to compute the quasi-particle density of states. The linear approximation to the entropy arising from this density of states is shown in dotted lines in Fig. 6.11. Although the entropy decreases with temperature for a constant density, it is also clear that the linear approximation only holds for the higher density and at the lowest temperatures. Even though this is the expected behavior (the linear behavior should only hold in very degenerate systems), it is interesting to note that the linear approximation in the correlated case works much worse than in the mean-field one. For the case of twice saturation density, for instance, the points at high temperature were perfectly reproduced by the linear law in Fig. 4.13, while they deviate by about 0.3 units in the largest temperature of Fig. 6.11. At half saturation, the results are much worse and, while in the SCHF entropy of Fig. 4.13 the linear behavior held up to temperatures of 6 – 8 MeV, in the correlated case it already deviates from the linear behavior at 5 MeV. All in all, it looks like the correlated system has more difficulties in achieving the degenerate limit. The cause of this difficulty can be attributed to the temperature dependence of the \mathcal{B} spectral function close to the Fermi surface. This introduces an additional source of temperature dependence in the treatment of the degenerate limit, which may account for the deviation of our results from the linear law of Eq. (6.16).

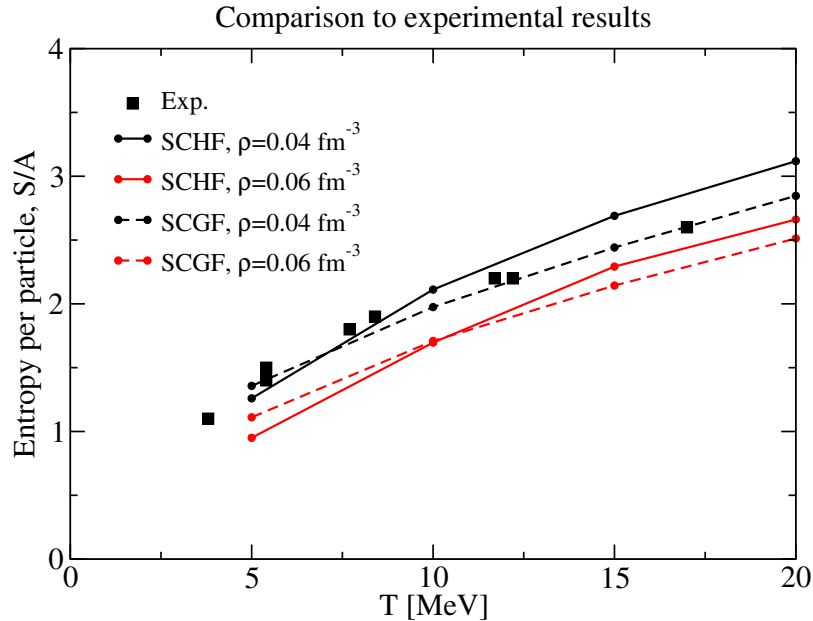


Figure 6.13: *Temperature dependence of the experimental values (squares) taken from [Dze95] to the dynamical quasi-particle and mean field results at two densities, $\rho = 0.04$ and $\rho = 0.06$ fm $^{-3}$.*

A similar lack of agreement is found if one tries to describe the low density dependence of the entropy at constant temperature in terms of the classical approximation to the entropy, Eq. (4.42). The quasi-particle spectra in the SCGF have a richer momentum dependence than the mean-field ones, due to the structures that appear in the in-medium interaction (see Fig. 5.16). Therefore, it becomes difficult to parametrize correctly the spectrum with a constant effective mass for all momenta. Consequently, from the theoretical point of view, it is difficult to derive a closed expression for the classical approximation of the dynamical quasi-particle entropy, at least within the scheme adopted in Appendix D. This can be taken as an indication that the classical approximation may not be valid for correlated systems.

One of the final aims of the study of heavy ion collisions at intermediate energies is the study of the properties of hot and dense hadronic matter. One can, for instance, extract conclusions about the properties of the equation of state in a given density range [Dan02]. Moreover, the matter created in the interior of these collisions forms a dense fireball which might eventually reach thermal equilibrium for very short times. One can then study the fragments that remain after the collision and, assuming that they were emitted from a source in thermal equilibrium, deduce some properties of the initial fireball. Within these assumptions, the isotopic yields of fragments can give information on the entropy per particle

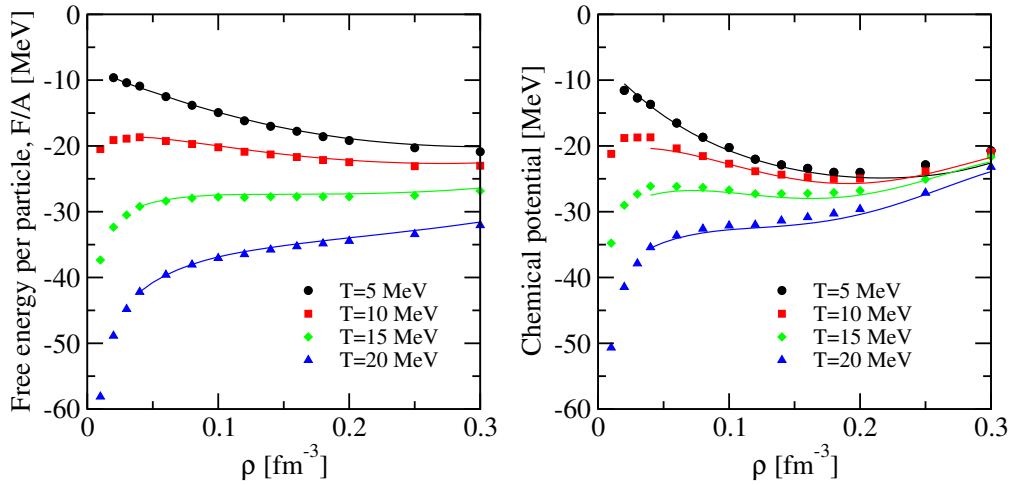


Figure 6.14: *Free energy per particle (left panel) and chemical potential (right panel) as a function of the density for five temperatures within the SCGF approach.*

of the initial fireball [Jac83; Cse86; Wad87; Kuh93; Dze95]. There are a lot of uncertainties in this analysis, however, mostly due to the statistical models used in the extraction of data, which rely on the hypothesis that the initial fireball is in thermal equilibrium. Even though an extensive comparison of our results with those found in these experiments has to be taken with extreme care (because, for instance, there are no finite size or fragmentation effects on our entropy), the temperature dependence of the SCHF and the DQ approaches to the entropy per particle for two low densities (0.04 and 0.06 fm^{-3}) is compared in Fig. 6.13 to the experimental points of Ref. [Dze95]. These correspond to the baryonic entropies extracted from the total charge bound in fragments with Z between 2 and 15 for Au+Au collisions at energies between $100A$ and $400A$ MeV assuming that the freeze out density of the fireball is $0.3\rho_0 = 0.05 \text{ fm}^{-3}$. If the progenitor dense system should be at this density and at the measured temperatures, its entropy should correspond to the one plotted in the figure. The two theoretical curves for each approach account for possible small deviations of this central density. It is interesting to note that the results are in qualitative agreement, although the higher mean-field entropy seems to account better for the experimental points. The fact that both the non-correlated and the correlated entropy are so similar for this temperature and density range does not allow for a clear disentanglement of both approximations from the experimental data.

Once the total energy and the total entropy per particle of the system are known, one can readily compute the free energy per particle. At finite temperatures this is the relevant thermodynamical potential, whose minimization gives the equilibrium state of the system. This quantity is shown as a function of density for

several temperatures in the left panel of Fig. 6.14. In contrast to the free energy per particle of the SCHF case, the correlated free energy has a local minimum at low temperatures in the high density region. This is the equivalent to the saturation point of nuclear matter, but in the finite temperature regime. The fact that this minimum disappears with increasing temperature is associated to a phase transition of the liquid-gas type [Sur98; Poc97]. Above a certain temperature (the so called flashing temperature, T_{fl}) the preferred state of this system would appear to be in the very low density region. The pressure of the low density gas, however, is still sizeable at this temperature, which prevents the system from decaying to the low density phase. Instead, it keeps itself in the liquid-gas coexistence zone as long as the critical temperature T_c of the phase transition is not reached. Above this temperature, the thermodynamically preferred state of the system is at very low densities and nuclear matter would tend to form a gas of dilute nucleons, most plausibly formed by clusters or droplets of finite sizes.

Independently of the position of the minimum in F/A , it is interesting to study the temperature and density dependence of the correlated free energy. As expected, this is more attractive in the whole density-temperature range than the mean field case. Moreover, it is a decreasing function of temperature. Once again this is a pure entropic effect, because the energy per particle tends to be more repulsive with temperature (see Fig. 6.8). The strong density dependence of the entropy for low densities is also responsible for the bending and the large attractive values of the free energy per particle in this region. Note, however, that this effect is reduced with respect to the non-correlated case. For the $T = 10$ MeV case, for instance, there is almost no bending at the lowest density, in contrast to the strong density dependence in the mean-field case of Fig. 4.14.

The corresponding microscopic chemical potentials, $\tilde{\mu}$, are shown by the symbols in the right panel of Fig. 6.14. The lines that join these symbols at fixed temperatures correspond to the chemical potentials obtained as the derivatives of a polynomial fit to F/\mathcal{V} . The agreement with the points is very good, with discrepancies of less than 3 MeV for all temperatures and densities higher than 0.04 fm^{-3} . The strong density dependence of $\tilde{\mu}$ at low densities is hard to handle with a polynomial fit and this is the reason why it has been skipped in this figure. Note however that this is mainly a numerical problem and that one should not take it as a failure of the thermodynamical consistency of the approach. A cross check of this consistency is actually shown by the lines joining the symbols of the free energies in the left panel of Fig. 6.14. These have been obtained from the following integral:

$$\frac{F(\rho, T)}{\mathcal{V}} = \frac{F(\rho_i, T)}{\mathcal{V}} + \int_{\rho_i}^{\rho} d\rho \tilde{\mu}(\rho, T), \quad (6.26)$$

with $\rho_i = 0.04 \text{ fm}^{-3}$. The previous calculation needs of an initial baseline, $F(\rho_i, T)$, which in this case has been set to be equal to the free energy density of our results

at ρ_i . This is a somewhat arbitrary criterion, of course. Yet, here one should not compare the absolute values of the two curves, but its density dependence. The dependence of the free energy per particle is indeed very well reproduced by the integral of the microscopic chemical potential, $\tilde{\mu}$. If one tried to follow this procedure with the microscopic chemical potential of the BHF approach, the differences between the integrated free energy and the microscopic free energy would increase with density, and at ρ_0 they could be as large as 5 MeV. This stresses once again the importance of the thermodynamical consistency of the approach.

The density and temperature dependence of the chemical potential follows that of the free energy per particle. The low density region of the chemical potential shows some bending at high temperatures, which shifts to lower densities with lower temperatures (this is the reason why it is not observed in the $T = 5$ MeV case). Furthermore, for the intermediate density range the chemical potential has a local minimum and then increases with density. As a matter of fact, the chemical potential for $T = 10$ and 15 MeV, reaches a minimum at about 0.15 fm^{-3} and then increases steadily with density. At 20 MeV, in contrast, the chemical potential does not show any local minimum. This small change makes an important difference in the thermodynamical properties of the system. The existence of this local minimum is associated to the possibility of having two phases (a gas and a liquid phase) with different densities but the same chemical potential. Therefore, the temperature at which this local minimum disappears signals the critical temperature for the liquid-gas phase coexistence. From the two panels of Fig. 6.14, one can already deduce that the critical temperature is somewhere between $T = 15$ and $T = 20$ MeV.

With all the previous information, one is now ready to compute the pressure of nuclear matter within a correlated approach. This is obtained from the thermodynamical relation [see Eq. (4.47)]:

$$p = \rho \left(\tilde{\mu} - \frac{F}{A} \right). \quad (6.27)$$

The results are shown in Fig. 6.15. Let us in the first place compare these results with the mean-field ones shown in Fig. 4.15. The pressure in the correlated case is in general lower than the mean-field one. As a matter of fact, these pressures are not only lower, but they also become negative in a certain range of densities. The point of zero pressure actually corresponds to $\tilde{\mu} = \frac{F}{A}$ and thus sets the saturation density for a given temperature. Actually, one can also see that this corresponds to a minimum of the free energy per particle:

$$p = \rho^2 \frac{\partial}{\partial \rho} \frac{F(\rho, T)}{A}. \quad (6.28)$$

As discussed previously, these minima correspond to around 0.3 fm^{-3} for $T = 5$ MeV and around 0.26 fm^{-3} for $T = 10$ MeV. At $T = 15$ MeV there is no point of

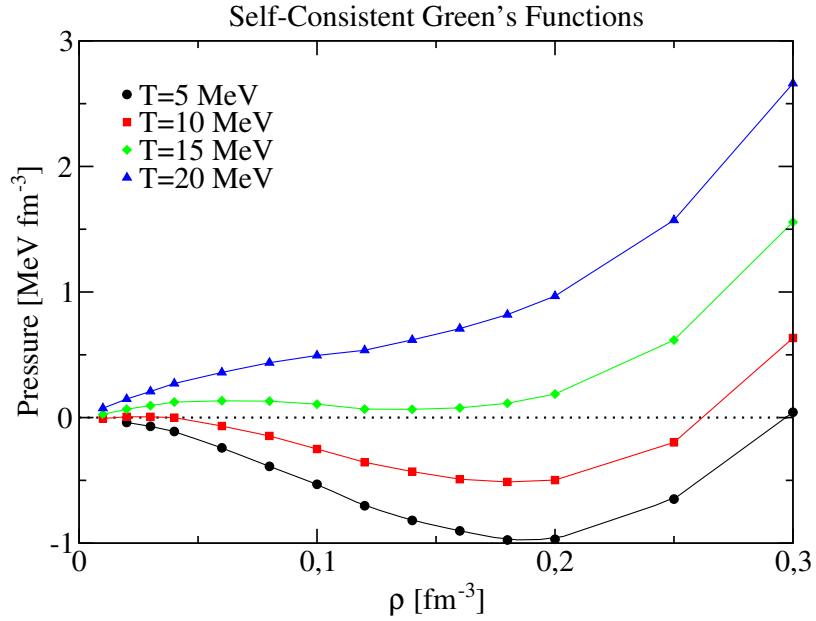


Figure 6.15: *Pressure as a function of the density for five temperatures within the SCGF approach.*

zero pressure and thus this is an upper bound to the flashing temperature of the system. It is also interesting to take into account the following thermodynamical relation:

$$\frac{\partial p}{\partial \rho} = \rho \frac{\partial \mu}{\partial \rho}, \quad (6.29)$$

which shows that the stability points of the chemical potential and the pressure coincide. This can also be checked visually by looking at the minima and maxima of $\tilde{\mu}$ in Fig. 6.14 and of p in Fig. 6.15.

In between the local maximum of the pressure at low density and its local minimum at a somewhat higher density, there is a region where the pressure decreases with density:

$$\frac{\partial p}{\partial \rho} < 0. \quad (6.30)$$

This is a thermodynamically forbidden zone: a system in this region would be unstable against small density fluctuations and will thus suffer of a mechanical instability. Such a zone is in correspondence with the region of chemical instability:

$$\frac{\partial \mu}{\partial \rho} < 0, \quad (6.31)$$

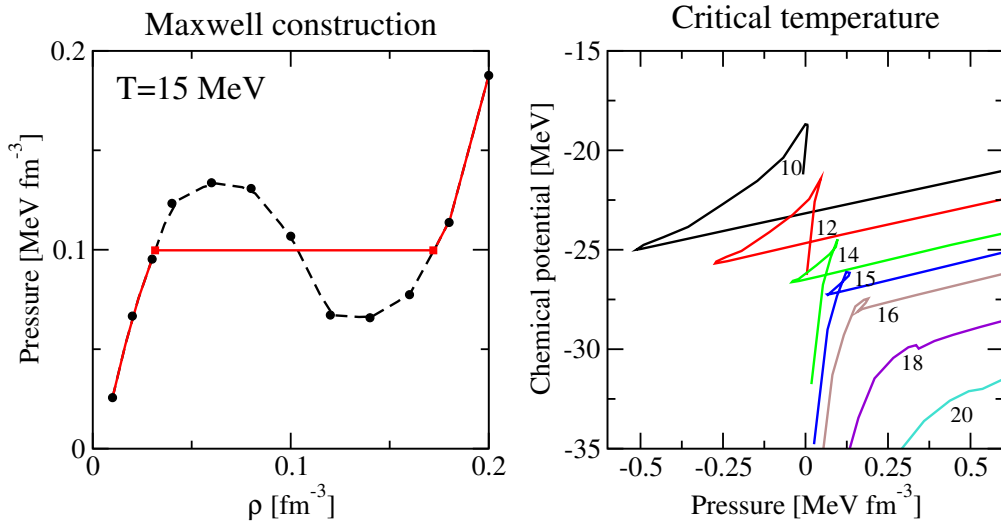


Figure 6.16: *Left panel: Maxwell construction for the pressure at $T = 15$ MeV. Right panel: Approximate determination of the critical temperature with $\mu - p$ curves.*

where the system might suffer of a chemical decomposition. The region of temperature and densities in which the two previous equations are fulfilled is the so-called spinodal region. In order to avoid this unphysical region, one usually introduces the Maxwell construction for the coexistence of phases. In this construction, one defines, for each fixed temperature, a low density, ρ_G , associated to the gas phase and a large density, ρ_L , associated to the liquid phase, which fulfill the following two equations simultaneously :

$$p(\rho_G, T) = p(\rho_L, T) \quad (6.32)$$

$$\mu(\rho_G, T) = \mu(\rho_L, T). \quad (6.33)$$

In between these two densities, one supposes that the pressure and the chemical potential are constant due to the equilibration of the two phases. The Maxwell construction for the pressure at $T = 15$ MeV case is shown in the left panel of Fig. 6.16. If one could have access to nuclear matter at that temperature and one could slowly increase the density, the system would follow the continuous line. At first, a pure gas of nucleons at low densities would be found. With increasing densities, the gas would condensate from ρ_G to ρ_L at constant pressure, until the liquid phase would be reached. Above ρ_L , the pressure would increase slowly. Note that the spinodal region is enclosed by the liquid-gas coexistence zone.

In a one component system, there is a simple way to estimate the critical temperature of the phase transition. Consider the plot in the right panel of Fig. 6.16, where the chemical potential is displayed versus the pressure at each temperature. Below the critical temperature, there are two different densities in which the chem-

ical potential and the pressure coincide. In the $\mu - p$ plot, this is translated into the point in which the branch which comes from the far right meets the descending branch of the chemical potential at each temperature. Since above T_c there is only one pressure and chemical potential which are stable, this crossing point disappears. The right panel of Fig. 6.16 offers the possibility to grasp the temperature at which the liquid-gas coexistence disappears, which for this potential and within the SCGF approach seems to be around $T_c \sim 17$ MeV. The effect of the lacking three-body forces in this quantity should be small, because the liquid-gas phase transition takes place at relatively low densities. Thus one can take this a fairly reliable value for the critical temperature of the liquid-gas phase transition in infinite matter. This is in qualitative agreement with the critical temperature obtained within other approaches [Bal99], but it is far too high to match the experimental value of around 5 – 10 MeV [Poc97; Nat02]. This discrepancy is caused by finite size and Coulomb effects which, for finite systems, induce a broadening of the phase transition and a reduction of the critical temperature.

The relation between the pressure and the density is mostly important for astrophysical environments, where it defines the equation of state of the dense hadronic matter forming the interiors of compact objects such as neutron stars. At present, however, our calculations cannot be applied realistically to astrophysical calculations. In the first place, to describe the dense interiors of neutron stars, it is absolutely necessary to include some kind of three-body force in the approach. Otherwise, the equation of state is too soft and the obtained final mass of the neutron star, below the observable bounds. In the second place, in astrophysical environments one deals with very neutron rich systems and thus one should unavoidably deal with isospin asymmetry. A first step towards this direction was taken in [Fri05], where the SCGF for nuclear matter was extended to isospin asymmetric systems. The isospin asymmetry of the system is governed by the β -stability conditions, which result in a series of equations for the chemical potential that have to be solved numerically. Note that since the microscopic chemical potentials of the SCGF approach correspond directly to those obtained macroscopically, one can use them directly in the solution of these equations. On a BHF type calculation in dense matter, on the other hand, the macroscopic chemical potential has to be derived numerically from the free energy density before it can be applied in the calculation of the β -stability conditions, introducing a certain amount of numerical errors in the results.

6.5 Future perspectives

The results presented here should be taken as a first step towards a full treatment of the thermal properties of infinite nuclear matter within a formalism that includes short-range correlations in a thermodynamical consistent way. From our point of view, this formalism can find several applications within the many-body and

nuclear physics community. At the thermodynamical level, a first outcome could be the detailed study of the liquid-gas phase transition of symmetric nuclear matter from a realistic NN potential. Since the formalism here presented is especially suitable for low density and low temperature systems, the results are expected to be fairly reliable. A critical study of the usually assumed low-temperature dependences for the relevant thermodynamical properties of hot dense matter (of the type T^2) could also be assessed. As mentioned previously, the correlated system seems to have difficulties in achieving the classical and the degenerate regimes and one should try to analyze more carefully why this is the case as well as the magnitude of the observed deviations.

Other applications, such as the study of the finite temperature equation of state, will probably demand for the inclusion of three-body forces in the formalism, in order to reproduce the empirical saturation properties of nuclear matter. It has already been commented that this complicates the formalism to a large extent. The first attempts might however not include directly the effect of microscopic three-body forces. Instead of that, one could try to use a phenomenological ρ^α term. Another possibility could be the use of a reduced two-body version of a more realistic three-body interaction. In this approach, one accounts for the repulsive effect at high densities by means of an average of the coordinates of one of the particles [Gra89]. This method has been used for BHF calculation with successful results for the saturation properties of nuclear matter [Bal99].

The introduction of a realistic description of nuclear matter in astrophysical environments can also be relevant for the dynamical properties of compact objects. There is a growing amount of information on the properties of both isolated and compound compact objects [Pag06]. A consistent treatment of these objects should try to describe at once as many of these properties as possible, from, say, the mass-radius relation to the cooling times at its surface [Kla06]. Even though our approach might not be applicable to the whole density range achieved in neutron stars, at least in the low density phase it might provide very valuable information. A full treatment of the response of this density and temperature region which includes the effects of the fragmentation of the quasi-particle peak is, to our knowledge, lacking. This could have an effect in the neutrino propagation through the dense matter [Sed07]. Moreover, the ladder approximation is devised to correctly describe the properties of low-density homogeneous systems and thus the SCGF results might shed some light into the properties of the outer crust of neutron stars.

Furthermore, dense astrophysical systems are not formed only by nucleons and leptons. In the high density interiors of neutron stars, the β -stability conditions favor the presence of other species of hadrons. Among these, hyperons are likely to appear at about twice saturation density [Vid00]. Their presence will naturally affect the static and dynamical properties of the neutron star in several ways. Thus, it would be interesting to have a many-body approach in which their in-

medium properties could be treated in a consistent way. The off-shell propagation of hyperons in dense matter is a difficult numerical task that, nonetheless, could lead to interesting conclusions on the medium-induced effects on the properties of baryons. These results could at the same time be tested in hypernuclear systems [Rob03; Rob04].

As for the possible consequences of our results in the study of intermediate energy heavy ion collisions [Dan02], there are also several aspects which could be addressed within our formalism. On the one hand, as previously mentioned, the thermal behavior of dense matter is explored with these experiments and one should try to pin down whether correlations might have an important effect on the experimentally measured properties. In addition, the use of spectral functions in the description of correlated nucleons goes beyond the quasi-particle picture customarily used in transport codes. Although some results point out the fact that off-shell effects in the propagation of nucleons are small [Cas00], a treatment of a kinetic equation including full spectral functions obtained from realistic NN potentials (following, for instance, [Bot90] or [Köh95]) is, to our knowledge, still lacking. Moreover, even within the usual quasi-particle description, some of the in-medium modifications of nucleons (such as effective masses or NN cross-sections) are usually taken as simple parameterizations [Dan00]. Our model permits the calculation of these quantities from realistic NN potentials in a fully microscopic and thermodynamical consistent basis which, properly parameterized, could be used in this kind of studies.

In the description of both the micro- and the macroscopic properties of nuclear matter, one should always try to analyze the model-dependence of the approach which is being used. It would thus be very interesting to find the dependence of the bulk properties of matter on the different microscopic approaches. In this Thesis, a comparison has been established among the results of the SCHF, the BHF and the SCGF approaches. A comparison with other many-body microscopic models at finite temperature (such as the variational approach) would have a high theoretical interest. Since hot nuclear matter is often studied with phenomenological mean-field approaches, it could also be interesting to study the similarities and differences between these and the correlated schemes.

Following this spirit, one should also try to find which are the allowed model-dependences within a given formalism. In the SCGF approach, for instance, the use of different bare interactions might yield very different results. Even though they might reproduce the NN phase shift at the same level of accuracy, the different microscopic interactions have different short-range cores and tensor components. In the first case, this is due to the lack of experimental knowledge of these phase-shifts above a certain collision energy. The difference in tensor components is caused by the particular structure of each NN interaction as well as by the assumptions that are made in the building process of these microscopic force. Since the fragmentation of the quasi-particle peak is, to a great extent, a consequence of

the short-range and tensor components of the interaction, one expects the structure of the spectral function to change with the NN force. Even though there have been studies in which the results arising from several potentials have been discussed [Dew02] as well as some partial comparisons [Fri04b], there is not, to our knowledge, a detailed discussion of the NN interaction dependence of the spectral functions in infinite nuclear matter. As a consequence of this study, one could also tackle the effects of using different bare forces in the macroscopic properties of the system. Within a given approximation, this could be a useful way of measuring the error that our lack of knowledge on NN interactions is introducing.

In this Thesis, the problems associated to pairing correlations have only been briefly discussed in Chapter 5. The fact that pairing effects are important in the low-density and low-temperature region of the nuclear matter phase diagram has been particularly stressed. Yet, the introduction of short-range correlations has an important effect on pairing properties and one should try to acknowledge the importance of this effect. A full many-body treatment of pairing correlations is not yet available, although there have been attempts to study the influence of self-consistent off-shell propagation in the pairing gap in approximate treatments [Dic05b]. One could also carry out a study in the normal phase, where the influence of the dressing effects of nucleons in the critical density and critical temperature could be analyzed and compared to the mean-field or BCS predictions. The use of the Thouless criterion for this kind of studies has already been discussed in Refs. [Alm93; Alm96; Dew02].

Finally, let us mention once again that many-body quantum mechanics has a wide range of applications, apart from the nuclear physics field. This is the reason why an effort has been devoted to write the formal developments of this Thesis in a very general form. In doing so, the application of the formalism to the study of other many-body quantum systems at finite temperature will be, hopefully, carried out more easily. The SCGF method for the description of the dynamical properties together with the Luttinger-Ward approach for the treatment of the thermodynamical properties offers a very useful theoretical tool in the description of dilute and strongly interacting quantum many-body systems. This approach unifies the Green's function description for the microscopic and thermodynamical properties of a system in a consistent framework. It is our wish that it becomes a more widespread tool in the many-body community, where it will for sure find a lot of applications.

Summary and conclusions

There is a large amount of data confirming the fragmentation of single-particle states in finite nuclei. This fact claims for formal developments in the nuclear many-body problem which go beyond the quasi-particle as well as the mean-field pictures. Such approaches should also include the short-range and tensor correlations which characterize microscopic NN interactions and which give rise to strong deviations from a mean-field many-body wave function. In a first step, long-range correlations can be skipped in the study of nuclear matter because their effects concern mainly its dynamical response and do not modify substantially its bulk properties.

The first chapter of this Thesis has been devoted to a general review of the nuclear many-body problem. In the first place, the main characteristics of the free-space NN interaction have been described. Since the final aim of the nuclear many-body problem is to reproduce the properties of nuclear matter, these have been introduced in the usual way, *i.e.* from an extrapolation to infinite matter of some experimental data on heavy nuclei, which define essentially the saturation point of nuclear matter. In this Thesis, the treatment of nuclear matter follows an *ab initio* approach. In other words, one chooses the constituents of the system, which in this case are the nucleons, and a realistic interaction among them. One applies then a sophisticated many-body machinery, hoping to reproduce the saturation point of nuclear matter. Several *ab initio* many-body approaches have been devised to treat this problem, and a short description of them is given in Chapter 1.

Among these, the many-body Green's functions formalism offers an interesting framework for the study of nuclear matter. In this approach one has the possibility of performing a diagrammatic analysis of the many-body propagators in terms of free one-body Green's functions and two-body interactions. This is the outcome of a perturbative expansion which results in an infinite series of diagrams, among which one has to choose those which are physically suitable for the description of the problem under consideration. Depending on the approximation, one can either choose a given number of diagrams or sum an infinite series of them, which usually results in a more realistic description. In this Thesis, two of these diagrammatic approaches have been studied, the Hartree-Fock and the ladder approximations. While the first one results from the lowest-order approximation to the two-body propagator, the second one is obtained from an infinite sum of diagrams which

account for the effects of the repeated scattering of two nucleons in matter. In diagrammatic approaches one can have an intuitive idea of the processes that are included in the approximation. Within the Green's function formalism, however, one can also introduce the approximations by means of a truncation in the hierarchy of the equations of motion, decoupling the N -body propagator from the $N - 1$ - and the $N + 1$ -body Green's functions. One can actually show that the diagrammatic approaches which are widely used in the nuclear many-body problem arise from these decouplings. This is actually the case of the Hartree-Fock and the ladder approximations, and the way to perform this truncation has been briefly discussed in this Thesis.

The description of nuclear matter at zero temperature within the ladder approximation encompasses at once particle-particle and hole-hole propagation and also includes a full off-shell treatment of the in-medium propagation of nucleons. In this sense, this approach goes both beyond the mean-field and the quasi-particle pictures. The extension of this formalism to finite temperature is useful in the description of dense matter in extreme conditions, which is found in the latest stages of the evolution of supernovae or in the fireballs formed in intermediate energy heavy ion collisions. In addition to these very interesting applications, the finite temperature formalism presents an important advantage with respect to the zero temperature one. In a certain regime of low densities and very low temperatures, the strong correlations induced by the microscopic force favor the creation of nucleonic Cooper pairs, which give rise to a superfluid behavior in nuclear matter. The application of a finite temperature treatment above the critical temperature for this pairing transition avoids the difficulties of having to treat the pairing phenomenon explicitly from a microscopical point of view.

In order to treat hot nuclear matter from a Green's function point of view, one has to deal with many-body Green's functions theory at finite temperature. In Chapter 2, this theory has been introduced and extensively discussed. This formalism is among the few which can provide a consistent treatment of the microscopic properties of dense matter from very first principles. The foundations of this theory rely on the imaginary time formalism, which exploits the formal similarity between the time evolution factor in quantum mechanics and the Boltzmann factor appearing in statistical mechanics. The introduction of complex times, although difficult to grasp in an intuitive way, is helpful in the analytical treatments of the theory and provides a unified description of equilibrium quantum statistical mechanics at finite temperatures. Therefore, the second chapter of this Thesis has been mainly devoted to discuss in depth this well-known approach, trying to clarify some of the misconceptions which often appear in its treatment. Among the results found, it is interesting to mention that:

- The analytical properties of the one-body propagator are very general and can be obtained from the Lehmann representation without any particular assumption on the characteristics of fermionic systems.

- The spectral decomposition of the propagator allows to obtain all of its properties from the spectral function, which in addition can be associated to a probability distribution in the momentum and energy space.
- The effects of the interaction in the one-body propagator can be accounted for by means of the self-energy operator, whose analytical properties are also very general. This is achieved by means of Dyson's equation, whose diagrammatic counterpart expresses the one-body propagator in terms of the iteration of irreducible self-energy pieces.
- The self-energy, in its turn, is usually expressed in terms of the one-body propagator. Since the propagator is determined from Dyson's equation, the procedure of finding a self-energy and a propagator in dense matter should be self-consistent. In terms of diagrams, the requirement of self-consistency is equivalent to replacing all the free propagators in the perturbation expansion by dressed propagators. This accounts for an infinite sum of diagrams in the intermediate propagators of the self-energy diagrams, which become dressed by self-energy insertions.

The many-body Green's function formalism is devoted to the description of the microscopic excitations of many-body systems and therefore gives an insight on their microscopic properties. Yet, physical systems in equilibrium are driven by thermodynamics, which concerns their macroscopical properties. Although quantum statistical mechanics is the bridge between the micro- and the macrophysics of many-body systems, it is difficult to derive expressions that relate both scales directly. A connection between them can be achieved by means of the Luttinger-Ward formalism, which gives the partition function of the system as a functional of the dressed one-body Green's function. These ideas have been explored in the third chapter of this Thesis, and one can conclude that:

- The Luttinger-Ward formalism is a non-perturbative approach which sums infinite sets of diagrams for the partition function of interacting many-body systems. Its starting point is the dressed one-body propagator and thus the Luttinger-Ward functional includes the correlations embedded in the approximations to the one-body Green's function.
- The partition function within this formalism is essentially the same that is obtained from the more widespread coupling constant method. This second method is also exact within the approximations to the one-body propagator, but it is however not practical for nuclear matter due to the need of performing calculations for different coupling constants.
- The thermodynamical consistency of the approach, which establishes the equivalence of the microscopically derived results to the macroscopically obtained ones, is automatically preserved within the Luttinger-Ward formalism.

This presents an advantage with respect to the BHF approach, which does not preserve thermodynamical consistency.

- Analytical expressions can be derived for the partition function and the entropy of interacting many-body systems in terms of the spectral function and the self-energy. In particular, the Luttinger-Ward approach leads to an entropy which can be decomposed in a dominant term, the dynamical quasi-particle entropy, which includes the effects of the fragmentation of the quasi-particle peak, plus a correction which is negligible at low temperatures and which accounts for higher order correlations.

Before studying nuclear matter with a sophisticated many-body approximation, it is always useful to set some ideas by using simple models. The fourth chapter of this Thesis is devoted to the Hartree-Fock approximation and its application in nuclear matter with realistic NN potentials. Even though the results obtained within this mean-field quasi-particle approach are not realistic, in the sense that they cannot reproduce the empirical saturation point of nuclear matter, the Hartree-Fock approximation offers an easy-to-treat scheme that provides an excellent testing ground for some of the concepts which are needed in more sophisticated approaches. Some ideas of this chapter that deserve to be outlined are the following:

- The Hartree-Fock approximation at finite temperature can be derived either from a diagrammatic approach or from the lowest-order decoupling of the hierarchy of the equations of motion for the two-body propagator. The self-consistent renormalization procedure arises however more naturally in the second approach, and accounts for a larger sum of diagrams which allows for the inclusion of nested second order self-energy insertions in the one-body propagator.
- The effects of the self-consistent renormalization procedure can be studied by comparing the SCHF approximation, which includes self-energy insertions to all orders, and the HF approximation, which is computed from a self-energy with a bare propagator. The numerical results differ both because of this difference and because of the chemical potentials used in the two approaches. In general terms, the effects of self-consistency are more important for larger densities, where the differences in the SCHF and the HF single-particle potentials can be as large as some tenths of MeV.
- The application of the Luttinger-Ward formalism to the SCHF approximation yields expressions for the thermodynamical properties which coincide with those of other formalisms. The energy and the entropy, in particular, are those of a gas of interacting quasi-particles.

- In general terms, the SCHF results for the macroscopic properties are not realistic. The total energy per particle is repulsive in the whole density-temperature range explored, despite the fact that the potential energy with the CDBONN potential yields attractive results. The free energy does not show any minimum at intermediate densities and therefore the pressure of the system is positive.
- The degenerate and the classical approximations describe correctly the temperature and density dependences of the different thermodynamical quantities in the relevant regimes. This is particularly true for the entropy per particle, which is described by a linear temperature dependence at low temperatures and high densities and by a logarithmic density dependence in the high temperature-low density regime.

Chapter 5 is devoted to the application of the ladder approximation to nuclear matter at finite temperature. The ladder approximation can be derived either diagrammatically, expressing the two-body propagator as an infinite sum of iterated two-particle scattering processes, or by means of a suitable truncation of the equation of motion of the three-body propagator. In both cases, one obtains an integral equation for the two-body propagator which can be reexpressed in terms of the T -matrix. This effective in-medium interaction fulfills a Lippman-Schwinger equation, which is easier to solve in the momentum-frequency space. This requires the knowledge of the analytical properties of the T -matrix, which are closely related to those of the ladder self-energy. This last quantity defines the one-body propagator, which in turn is needed to determine the intermediate particle-particle and hole-hole propagator in the Lippman-Schwinger equation. The ladder approximation thus defines a self-consistent approach and one needs to devise tools to solve it numerically. One can point out the following set of conclusions for this chapter:

- The ladder approximation for nuclear matter at finite temperatures can be solved by means of the SCGF scheme, in which the full off-shell dependence of the spectral function, the self-energy and the T -matrix are iterated self-consistently. Once the numerical solution of this scheme is achieved, one has access to the temperature and density dependences of different microscopic quantities.
- Although a description of pairing phenomena is not possible in the ladder approximation, a precursor effect can be observed in the in-medium effective interaction in the form of a strong structure for the kinematical conditions $\Omega = 2\mu$, $P = k_F$ and $q = 0$ at low temperatures.
- While the real part of the self-energy is essentially dominated by a generalized Hartree-Fock contribution (which includes ladder self-energy insertions), the

imaginary part has a strong energy dependence, with non-vanishing tails in both the large positive and negative energy limits. The effect of temperature on this quantity is rather small, but these tails exhibit a strong density dependence.

- Within the ladder approximation for nuclear matter, one can introduce well-defined quasi-particle energies. When compared to the corresponding SCHF spectra, the SCGF quasi-particle energies are more attractive and less stiff. The BHF single-particle spectra are however more attractive at low momenta, and yield similar results for $k > k_F$. The spectra become more repulsive with increasing temperature within the SCHF and the BHF approaches, in contrast to the SCGF spectrum, which loose repulsion in the hole region.
- The spectral function has a strong quasi-particle peak at all momenta, whose properties are only mildly changed with temperature and strongly modified with density. The variations induced with increasing density depend on momentum. At $k = k_F$ the quasi-particle peak becomes narrower, a behavior that can be understood in terms of the increasing degeneracy. At $k = 0$, the peak becomes much wider and shifts to lower energies. The low and high energy tails, on the other hand, have a common behavior and their strength increases with density, which shows that one can take them as a reliable measure of the importance of the correlations that fragment the quasi-particle peak.
- At low momenta, the correlated momentum distributions are depleted with respect to the mean-field ones, while at large momenta they yield larger populations. The depletion of the lowest momentum state increases with temperature, although this effect is similar to the one observed in the free Fermi gas and is therefore caused by thermal correlations. Dynamical correlations, on the other hand, are responsible for the almost constant $k = 0$ depletion at high densities. A steady decrease of this quantity with increasing density is observed, which goes against intuition and thus deserves further investigation.

Once the microscopic properties of nuclear matter have been determined from the implementation of the SCGF scheme, the Luttinger-Ward approach described in Chapter 3 can be applied to obtain the thermodynamical properties of the system. This is actually done in Chapter 6 of this Thesis. The energy per particle can be obtained directly from the GMK sum rule. Thus, to obtain the free energy of the system one needs to compute the entropy of the correlated system of nucleons. This has been one of the main objectives of this Thesis and, to our knowledge, it is the first time that the effects that the correlations which go beyond the quasi-particle and the mean-field pictures have on the entropy are thoroughly discussed

for nuclear systems. The more important results obtained with the Luttinger-Ward formalism can be summarized as follows:

- The \mathcal{B} spectral function, which introduces the effect of dynamical correlations into the dynamical quasi-particle entropy, has a strong quasi-particle peak, which is narrower than the one of the usual spectral function. This fact points towards the small influence of the correlations that fragment the quasi-particle states into the entropy of the system. Moreover, the \mathcal{B} spectral function has a similar density and temperature dependence than the usual \mathcal{A} spectral function.
- One can use different approximations to compute the entropy per particle of nuclear matter. Even though the dynamical quasi-particle entropy includes the effect of correlations by means of the \mathcal{B} spectral function, a no-width quasi-particle approximation to this quantity reproduces the entropy extremely well. If one uses a BHF approximation, the differences in chemical potentials and in the position of the quasi-particle peak yield an entropy which is about 10% lower than the dynamical quasi-particle entropy. The contribution of the \mathcal{A} spectral function to the entropy is in general about 20 – 30% lower than the dynamical quasi-particle one.
- The temperature and density dependence of the dynamical quasi-particle entropy is qualitatively similar to the mean-field one, although it yields somewhat larger results, up to 1.5 times larger. The low temperature behavior of the entropy is quite linear and the corresponding density of states is the one associated to a momentum integration of the \mathcal{B} spectral function. This is very close to the quasi-particle density of states at low temperatures. Still, the linear behavior is worse than the one obtained in the mean-field case and one can say that the degenerate limit is more difficult to achieve in the correlated case. The same holds for the classical regime.
- The approximations introduced in the BHF scheme lead to a violation of thermodynamical consistency which, in the case of the chemical potential, can yield differences of up to 20 MeV. This is not the case for the SCGF scheme that, together with the Luttinger-Ward formalism, yields thermodynamically consistent results in the whole density and temperature range, with a 2 MeV accuracy. The Hugenholtz-van Hove theorem is thus very well fulfilled, although the detailed saturation properties do strongly depend on temperature.
- The total energy per particle results to be attractive in a defined range of densities and temperatures. While the kinetic energy is about 1.5 times larger than the mean-field one, the effect of correlations is much larger for the potential energy, which in a wide range of densities is about 3 – 4 times more attractive than the mean field one.

- The results for the chemical potential and the free energy are consistent with the presence of a phase transition of the liquid-gas type for nuclear matter. A first guess for the critical temperature of this transition is about $T_c = 17$ MeV, while the flashing temperature is below $T = 15$ MeV.

The results presented in this Thesis are still far from being realistic. The saturation point of nuclear matter, if extrapolated at zero temperature, corresponds to a too large saturation density and a too attractive saturation energy. Still, the Green's function approach in the ladder approximation together with the Luttinger-Ward formalism give rise to thermodynamical consistent results which account, at the microscopic level, for correlations both beyond the mean-field and the quasi-particle pictures. These can therefore be taken as the first qualitative results of the approach, which should be further extended to include three-body correlations. This would improve the description of nuclear matter and could yield more accurate results for the equation of state. The treatment of isospin asymmetry in the formalism should also be devised at some point, especially if the results have to be applied either to finite nuclei or to the extremely asymmetric matter found in the interior of astrophysical compact objects. Furthermore, the formalism introduced in this Thesis could be applied to other hot, dilute and strongly interacting many-body systems in order to understand the effect that microscopic dynamical correlations produce on their macroscopical thermodynamical properties.

Appendix A

Perturbation Expansion of the Green's Function

In complete analogy to the zero temperature case, the single-particle Green's function of a finite temperature many-body system can be expanded in terms of free single-particle Green's functions. This expansion is most suitably depicted in terms of Feynman diagrams, which allow for a more physical interpretation of the many-body problem. In addition, diagrams are an optimal tool for understanding the approximations in the many-body problem. In this appendix, the main steps that lead to expressing the full propagator in terms of free Green's functions and two-body interactions will be reviewed. The connection of this expansion with Feynman diagrams will be sketched in the following Appendix. Most of the discussions will be rather qualitative, but further details can be found in Refs. [Abr65; Fet71].

For a system of interacting fermions, the full Hamiltonian \hat{H} is given by a kinetic term:

$$\hat{H}_0(t) = \int d^3r \hat{a}^\dagger(\mathbf{r}t) \hat{T}(\mathbf{r}) \hat{a}(\mathbf{r}t), \quad (\text{A.1})$$

plus a term due to the two-body interaction:

$$\hat{H}_1(t) = \frac{1}{2} \int d^3r \int d^3r' \hat{a}^\dagger(\mathbf{r}t) \hat{a}^\dagger(\mathbf{r}'t) V(\mathbf{r}, \mathbf{r}') \hat{a}(\mathbf{r}'t) \hat{a}(\mathbf{r}t). \quad (\text{A.2})$$

In the previous expressions the field operators $\hat{a}(\mathbf{r}t)$ are expressed in the Heisenberg picture. The time evolution of any of these Heisenberg operators is given by the full Hamiltonian:

$$\hat{O}_H(\mathbf{r}t) = e^{i\hat{H}t} \hat{O}_S(\mathbf{r}) e^{-i\hat{H}t}, \quad (\text{A.3})$$

where, for the initial time $t = 0$, the operator is of the Schrödinger type. This is the basic relation that links the Heisenberg and Schrödinger pictures in usual quantum mechanics. Formally, this relation can be extended to complex times (although

in practice, only purely imaginary times are needed). The same imaginary-time extension can be carried out for the interaction picture, in which operators evolve in time with the kinetic hamiltonian \hat{H}_0 :

$$\hat{O}_I(\mathbf{r}t) = e^{i\hat{H}_0 t} \hat{O}_S(\mathbf{r}) e^{-i\hat{H}_0 t}. \quad (\text{A.4})$$

From the two previous expressions one finds that the operators in the Heisenberg and in the interaction pictures are related by the transformation:

$$\hat{O}_H(\mathbf{r}t) = \mathbb{U}(0, t) \hat{O}_I(\mathbf{r}t) \mathbb{U}(t, 0), \quad (\text{A.5})$$

where $\mathbb{U}(t, t')$ is the so-called time evolution operator:

$$\mathbb{U}(t, t') = e^{i\hat{H}_0 t} e^{-i\hat{H}(t-t')} e^{-i\hat{H}_0 t'}. \quad (\text{A.6})$$

For imaginary times, in contrast to what happens with real times, \mathbb{U} is not anymore unitary. However, it still obeys the group property:

$$\mathbb{U}(t, t') \mathbb{U}(t', t'') = \mathbb{U}(t, t''), \quad (\text{A.7})$$

and fulfills the boundary condition:

$$\mathbb{U}(t, t) = \mathbb{I}. \quad (\text{A.8})$$

In addition, by taking a derivative with respect to a time variable, one finds that its time dependence is governed by the differential equation:

$$i \frac{\partial}{\partial t} \mathbb{U}(t, t') = H_1(t) \mathbb{U}(t, t'). \quad (\text{A.9})$$

Note that \hat{H}_1 evolves in time as an interaction picture operator, *i.e.* with Eq. (A.4). The well-known formal solution of this equation is given in terms of time-ordered products [Fet71]:

$$\mathbb{U}(t, t') = \sum_{n=0}^{\infty} \frac{(-i)^n}{n!} \int_t^{t'} dt_1 \cdots \int_t^{t'} dt_n \mathbb{T} \left[\hat{H}_1(t_1) \cdots \hat{H}_1(t_n) \right], \quad (\text{A.10})$$

in which the time ordering operator \mathbb{T} orders the operators in such a way that the time arguments decrease from left to right. This time ordering is slightly different from the one appearing, for instance, in the Green's function, Eq. (2.15), because it does not include any change of permutation sign when the operators are ordered. Ultimately, this difference is irrelevant because the \hat{H}_1 operators are of a bosonic nature and no phase needs to be added when the times are ordered with either prescription.

The grand-partition function Ω is related to the statistical operator $e^{-\beta(\hat{H}-\mu\hat{N})}$ via the equation:

$$e^{-\beta\Omega} = \text{Tr} e^{-\beta(\hat{H}-\mu\hat{N})}. \quad (\text{A.11})$$

If one expresses the statistical operator in terms of the time evolution operator at complex times:

$$e^{-\beta(\hat{H}-\mu\hat{N})} = e^{-\beta(\hat{H}_0-\mu\hat{N})}\mathbb{U}(t = -i\beta, 0), \quad (\text{A.12})$$

the following expansion for the grand-partition function is found:

$$e^{-\beta\Omega} = e^{-\beta\Omega_0} \sum_{n=0}^{\infty} \frac{(-i)^n}{n!} \int_0^{-i\beta} dt_1 \cdots \int_0^{-i\beta} dt_n \text{Tr} \left\{ \hat{\rho}_0 \mathbb{T} \left[\hat{H}_1(t_1) \cdots \hat{H}_1(t_n) \right] \right\}. \quad (\text{A.13})$$

Inside the trace, the density matrix of the non-interacting system has been introduced:

$$\hat{\rho}_0 = \frac{e^{-\beta(\hat{H}_0-\mu\hat{N})}}{\text{Tr} e^{-\beta(\hat{H}_0-\mu\hat{N})}} = \frac{e^{-\beta(\hat{H}_0-\mu\hat{N})}}{e^{-\beta\Omega_0}}. \quad (\text{A.14})$$

Note, in addition, that in the previous expressions the quantities are all evaluated with the chemical potential μ , corresponding to that of the fully interacting system which is in principle an external fixed parameter in the grand-canonical picture. Let us now turn our attention to the single-particle Green's function:

$$i\mathcal{G}(\mathbf{r}t, \mathbf{r}'t') = \frac{\text{Tr} \left\{ e^{-\beta(\hat{H}-\mu\hat{N})} \mathcal{T} \left[\hat{a}(\mathbf{r}t) \hat{a}^\dagger(\mathbf{r}'t') \right] \right\}}{e^{-\beta\Omega}}, \quad (\text{A.15})$$

which can be rewritten in terms of the time evolution operators:

$$i\mathcal{G}(\mathbf{r}t, \mathbf{r}'t') = e^{\beta(\Omega-\Omega_0)} \text{Tr} \left\{ \hat{\rho}_0 \mathcal{T} \left[\mathbb{U}(-i\beta, t) \hat{a}_I(\mathbf{r}t) \mathbb{U}(t, t') \hat{a}_I^\dagger(\mathbf{r}'t') \mathbb{U}(t', 0) \right] \right\}, \quad (\text{A.16})$$

where \hat{a}_I (\hat{a}_I^\dagger) denotes a destruction (creation) operator in the interaction picture. One can now expand the time evolution operators inside the trace. This will lead to three different infinite sums of integrals of time-ordered terms. Making use of the relation:

$$\begin{aligned} \sum_{\nu=0}^{\infty} \frac{(-i)^\nu}{\nu!} \int_{t_a}^{t_c} dt_1 \cdots \int_{t_a}^{t_c} dt_\nu \mathcal{T} \left[\hat{H}_1(t_1) \cdots \hat{H}_1(t_\nu) \hat{O}(t_b) \right] = \\ \sum_{n=0}^{\infty} \frac{(-i)^n}{n!} \int_{t_a}^{t_b} dt_1 \cdots \int_{t_a}^{t_b} dt_n \mathcal{T} \left[\hat{H}_1(t_1) \cdots \hat{H}_1(t_n) \right] \times \hat{O}(t_b) \\ \times \sum_{m=0}^{\infty} \frac{(-i)^m}{m!} \int_{t_b}^{t_c} dt_1 \cdots \int_{t_b}^{t_c} dt_m \mathcal{T} \left[\hat{H}_1(t_1) \cdots \hat{H}_1(t_m) \right], \end{aligned} \quad (\text{A.17})$$

which is valid for $t_a < t_b < t_c$, the three sums are converted into a single sum where the integrated time variable runs from 0 to $-i\beta$. The single-particle propagator

can then be cast in the following form:

$$i\mathcal{G}(\mathbf{r}t, \mathbf{r}'t') = e^{\beta(\Omega - \Omega_0)} \sum_{n=0}^{\infty} \frac{(-i)^n}{n!} \quad (\text{A.18})$$

$$\times \int_0^{-i\beta} dt_1 \cdots \int_0^{-i\beta} dt_n \text{Tr} \left\{ \hat{\rho}_0 \mathcal{T} \left[\hat{H}_1(t_1) \cdots \hat{H}_1(t_n) \hat{a}_I(\mathbf{r}t) \hat{a}_I^\dagger(\mathbf{r}'t') \right] \right\}.$$

The interacting part of the hamiltonian, \hat{H}_1 , can be rewritten in terms of interaction picture creation and destruction operators:

$$\hat{H}_1(t_1) = \frac{1}{2} \int d^3r_1 \int d^3r'_1 \int_0^{-i\beta} dt'_1 \hat{a}_I^\dagger(\mathbf{r}_1 t_1) \hat{a}_I^\dagger(\mathbf{r}'_1 t'_1) V(\mathbf{r}_1 t_1, \mathbf{r}'_1 t'_1) \hat{a}_I(\mathbf{r}'_1 t'_1) \hat{a}_I(\mathbf{r}_1 t_1), \quad (\text{A.19})$$

where the notation:

$$V(\mathbf{r}_1 t_1, \mathbf{r}_2 t_2) = \delta(t_1 - t_2) V(\mathbf{r}_1, \mathbf{r}_2) \quad (\text{A.20})$$

has been used in order to write expressions in a more symmetric way. If one introduces the expansion of \hat{H}_1 in Eq. (A.19), the corresponding expansion of the full Green's function in terms of creation and destruction operators (in the interaction picture) is obtained. Each term of order n in this expansion will have $4n$ operators coming from \hat{H}_1 plus 2 operators coming from the definition of the Green's function. Each contribution will thus contain $4n + 2$ creation and destruction operators. The first term in the expansion is of zero-th order and has the following form:

$$i\mathcal{G}^{(0)}(\mathbf{r}t, \mathbf{r}'t') = e^{\beta(\Omega - \Omega_0)} \left[\text{Tr} \left\{ \hat{\rho}_0 \mathcal{T} \left[\hat{a}_I(\mathbf{r}t) \hat{a}_I^\dagger(\mathbf{r}'t') \right] \right\} \right]. \quad (\text{A.21})$$

The first order term is already quite involved, but its appearance can be simplified with the help of the notation:

$$\int d^3r_1 \int_0^{-i\beta} dt_1 \rightarrow \int d\mathbf{1} \quad \text{and} \quad \text{Tr} \left\{ \hat{\rho}_0 \hat{X} \right\} = \langle \hat{X} \rangle_0. \quad (\text{A.22})$$

Note that the statistical average $\langle \cdots \rangle_0$ is taken over the non-interacting states of the system. With the help of these changes, the first order term is written:

$$i\mathcal{G}^{(1)}(\mathbf{r}t, \mathbf{r}'t') = e^{\beta(\Omega - \Omega_0)} \left[\frac{(-i)}{2} \int d\mathbf{1} \int d\mathbf{1}' V(\mathbf{1}, \mathbf{1}') \times \quad (\text{A.23}) \right.$$

$$\left. \left\langle \mathcal{T} \left[\hat{a}_I^\dagger(\mathbf{1}) \hat{a}_I^\dagger(\mathbf{1}') \hat{a}_I(\mathbf{1}') \hat{a}_I(\mathbf{1}) \hat{a}_I(\mathbf{r}t) \hat{a}_I^\dagger(\mathbf{r}'t') \right] \right\rangle_0 \right].$$

One can also write down an expression for the n th-order term:

$$\begin{aligned}
 i\mathcal{G}^{(n)}(\mathbf{r}t, \mathbf{r}'t') &= e^{\beta(\Omega - \Omega_0)} \left[\frac{(-i)^n}{n!2^n} \int d\mathbf{1} \int d\mathbf{1}' \cdots \int d\mathbf{n} \int d\mathbf{n}' V(\mathbf{1}, \mathbf{1}') \cdots V(\mathbf{n}, \mathbf{n}') \right. \\
 &\quad \left. \times \left\langle \mathcal{T} \left[\hat{a}_I^\dagger(\mathbf{1}) \hat{a}_I^\dagger(\mathbf{1}') \hat{a}_I(\mathbf{1}) \hat{a}_I(\mathbf{1}') \cdots \hat{a}_I^\dagger(\mathbf{n}) \hat{a}_I^\dagger(\mathbf{n}') \hat{a}_I(\mathbf{n}) \hat{a}_I(\mathbf{n}') \hat{a}_I(\mathbf{r}t) \hat{a}_I^\dagger(\mathbf{r}'t') \right] \right\rangle_0 \right].
 \end{aligned}
 \tag{A.24}$$

It is clear that, at any order in the expansion, one has to evaluate an ensemble average over non-interacting states of a time-ordered product of creation and destruction operators. In the same way as it is done for the zero temperature case, one can prove a Wick theorem that relates these averages with contractions of operators. These contractions, which are C -numbers with well-known properties, are essential for the calculation of the traces and are the final step before one can have a completed perturbation expansion of the propagator. Note, however, that there is a fundamental difference with respect to the zero temperature case. While the Wick theorem in that case is an *exact* operator identity, the finite temperature Wick theorem is only valid for thermally *averaged* operators.

In a generic term in the perturbation expansion, one always finds a statistical average of the type:

$$\left\langle \mathcal{T} [AB \cdots F] \right\rangle_0,
 \tag{A.25}$$

where A, B, \dots denote creation and destruction operators in the interaction picture. A contraction between two of these operators is defined as:

$$\overline{AB} = \left\langle \mathcal{T} [AB] \right\rangle_0.
 \tag{A.26}$$

In particular, the contraction of a destruction and a creation operator in the interaction picture simply yields the Green's function of the non-interacting system:

$$\overline{a_I(\mathbf{r}t) a_I^\dagger(\mathbf{r}'t')} = \left\langle \mathcal{T} [a_I(\mathbf{r}t) a_I^\dagger(\mathbf{r}'t')] \right\rangle_0 = i\mathcal{G}_0(\mathbf{r}t, \mathbf{r}'t').
 \tag{A.27}$$

The generalized Wick theorem then states that:

The ensemble average of any time-ordered product of operators equals the sum over all possible fully contracted terms.

Provided that this theorem holds and knowing that, in addition, the contraction of two creation or annihilation operators vanishes, one can decompose the time-ordered averages in terms of contractions. Let us do this for the product in the first order term (for simplicity the creation operators are named C and the annihilation

ones, A):

$$\begin{aligned}
 \left\langle \mathcal{T} [C_1 C_{1'} A_1 A_1 A C'] \right\rangle_0 &= \overbrace{C_1 C_{1'} A_1 A_1 A C'} + \overbrace{C_1 C_{1'} A_1 A_1 A C'} \\
 &+ \overbrace{C_1 C_{1'} A_1 A_1 A C'} + \overbrace{C_1 C_{1'} A_1 A_1 A C'} \\
 &+ \overbrace{C_1 C_{1'} A_1 A_1 A C'} + \overbrace{C_1 C_{1'} A_1 A_1 A C'} . \quad (\text{A.28})
 \end{aligned}$$

The previous six terms can be divided in two groups. The first one would be formed by the first and the third contributions. They involve a contraction between the operators which carry the explicit external dependence on time and space, $\hat{a}_I(\mathbf{r}t)$ and $\hat{a}_I^\dagger(\mathbf{r}'t')$ (A and C' in the previous notation), and contractions among the remaining operators whose variables are integrated. The latter contraction is thus independent from the other and can be factored out. This kind of contributions are called *disconnected*, because they can be decomposed in an *external* (which includes the dependence on the external time and space variables) and an *internal* (with no explicit dependence) contribution. In the previous case, the disconnected terms yield the result:

$$\overline{AC'} \times \left[\overline{A_1 C_1 A_{1'} C_{1'}} - \overline{A_1 C_{1'} A_1 C_1} \right], \quad (\text{A.29})$$

with $\overline{AC'}$ the external contribution.

The remaining four terms in the first order expansion are formed by contractions which join external as well as internal variables. They are called *connected* contributions. It is not by chance that the *external* term in Eq. (A.29) corresponds to the connected contribution of the zeroth order term. As a matter of fact, one can show that the whole expansion series for the propagator factorizes in a term composed of an infinite number of connected contributions, \mathbb{S}^{con} , times a sum that includes all the internal contributions, \mathbb{S}^{int} :

$$i\mathcal{G}(\mathbf{r}t, \mathbf{r}'t') = e^{\beta(\Omega - \Omega_0)} \left[\mathbb{S}^{con}(\mathbf{r}t, \mathbf{r}'t') \times \mathbb{S}^{int} \right]. \quad (\text{A.30})$$

To obtain this result, one can consider an ν -th order term in the expansion of the propagator. In general, this term will be formed by n connected contributions and m internal ones. There are $\frac{\nu!}{n!m!}$ different ways to carry out this factorization that yield the same result. Summing over all these possibilities with the restriction that $\nu = m + n$, one gets the ν -th order contribution. As a consequence of this

factorization, the full propagator is given by the following sum to all orders in ν :

$$\begin{aligned}
 i\mathcal{G}(\mathbf{r}t, \mathbf{r}'t') &= e^{\beta(\Omega-\Omega_0)} \sum_{\nu=0}^{\infty} \frac{(-i)^\nu}{\nu!} \left\{ \sum_{n=0}^{\infty} \sum_{m=0}^{\infty} \delta_{\nu, n+m} \frac{\nu!}{n!m!} \right. \\
 &\quad \int_0^{-i\beta} dt_1 \cdots \int_0^{-i\beta} dt_n \left\langle \mathcal{T} \left[\hat{H}_1(t_1) \cdots \hat{H}_1(t_n) a_I(\mathbf{r}t) a_I^\dagger(\mathbf{r}'t') \right] \right\rangle_0^{con} \\
 &\quad \times \left. \int_0^{-i\beta} dt_1 \cdots \int_0^{-i\beta} dt_m \left\langle \mathcal{T} \left[\hat{H}_1(t_1) \cdots \hat{H}_1(t_m) \right] \right\rangle_0^{int} \right\}, \quad (\text{A.31})
 \end{aligned}$$

where the $\langle \cdots \rangle_0^{con}$ subscript denotes the fact that in the Wick decomposition only connected terms have to be considered and where the $\langle \cdots \rangle_0^{int}$ subscript denotes a contribution formed only by internal lines. Using the δ -function to carry out the sum over ν , the following factorization is obtained:

$$\begin{aligned}
 i\mathcal{G}(\mathbf{r}t, \mathbf{r}'t') &= e^{\beta(\Omega-\Omega_0)} \\
 &\times \left\{ \sum_{n=0}^{\infty} \frac{(-i)^n}{n!} \int_0^{-i\beta} dt_1 \cdots \int_0^{-i\beta} dt_n \left\langle \mathcal{T} \left[\hat{H}_1(t_1) \cdots \hat{H}_1(t_n) a_I(\mathbf{r}t) a_I^\dagger(\mathbf{r}'t') \right] \right\rangle_0^{con} \right\} \\
 &\times \left\{ \sum_{m=0}^{\infty} \frac{(-i)^m}{m!} \int_0^{-i\beta} dt_1 \cdots \int_0^{-i\beta} dt_m \left\langle \mathcal{T} \left[\hat{H}_1(t_1) \cdots \hat{H}_1(t_m) \right] \right\rangle_0^{int} \right\}. \quad (\text{A.32})
 \end{aligned}$$

One can carry out a similar analysis for the expansion of the function $e^{\beta(\Omega-\Omega_0)}$, Eq. (A.13). It is clear that, since it does not contain any external dependence, the terms that contribute to this function are all of the internal type. Indeed, by comparing the previous equation and Eq. (A.13) one finds that:

$$e^{-\beta(\Omega-\Omega_0)} = \mathbb{S}^{int}. \quad (\text{A.33})$$

Using this and Eq. (A.30), one can see that the propagator is formed by the sum of all connected diagrams:

$$i\mathcal{G}(\mathbf{r}t, \mathbf{r}'t') = \mathbb{S}^{con}(\mathbf{r}t, \mathbf{r}'t'), \quad (\text{A.34})$$

which leads to the expansion:

$$\begin{aligned}
 i\mathcal{G}(\mathbf{r}t, \mathbf{r}'t') &= \sum_{n=0}^{\infty} \frac{(-i)^n}{n!2^n} \int d\mathbf{1} \int d\mathbf{1}' \cdots \int d\mathbf{n} \int d\mathbf{n}' V(\mathbf{1}, \mathbf{1}') \cdots V(\mathbf{n}, \mathbf{n}') \times \\
 &\quad \left\langle \mathcal{T} \left[\hat{a}_I^\dagger(\mathbf{1}) \hat{a}_I^\dagger(\mathbf{1}') \hat{a}_I(\mathbf{1}') \hat{a}_I(\mathbf{1}) \cdots \hat{a}_I^\dagger(\mathbf{n}) \hat{a}_I^\dagger(\mathbf{n}') \hat{a}_I(\mathbf{n}') \hat{a}_I(\mathbf{n}) \hat{a}_I(\mathbf{r}t) \hat{a}_I^\dagger(\mathbf{r}'t') \right] \right\rangle_0^{con}. \quad (\text{A.35})
 \end{aligned}$$

Still, a further important simplification can be achieved by taking a closer look to the contribution of the connected contributions at first order, Eq. (A.28). The

fourth and the sixth (and also the second and the fifth) terms yield the same result, since they just differ in a permutation of the integration variables. At a given order n , one can make $n!$ different permutations of integration variables (without taking into account any additional phase, because inside the time-ordered product one always has to do an even number of permutations). In addition, since $V(\mathbf{1}, \mathbf{1}') = V(\mathbf{1}', \mathbf{1})$, at each order one can perform 2^n permutations of the type $\mathbf{1} \leftrightarrow \mathbf{1}'$ which leave the result unchanged. Therefore, each contribution to the sum of contractions has $n!2^n$ terms which give the same result (these are *topologically equivalent* contractions, because they lead to equivalent Feynman diagrams). Such repeated contributions cancel the $\frac{1}{n!2^n}$ factor in Eq. (A.35).

After all these considerations, one is left out with an expansion of the single-particle Green's function, \mathcal{G} , in terms of the non-interacting Green's function, \mathcal{G}_0 , and the interaction strength, V . Up to first order this expansion reads:

$$\begin{aligned}
 i\mathcal{G}(\mathbf{r}t, \mathbf{r}'t') &= i\mathcal{G}_0(\mathbf{r}t, \mathbf{r}'t') \\
 &+ i^2 \int d^3r_1 \int_0^{-i\beta} dt_1 \int d^3r'_1 \int_0^{-i\beta} dt'_1 V(\mathbf{r}_1t_1, \mathbf{r}'_1t'_1) \\
 &\times \left[-\mathcal{G}_0(\mathbf{r}t, \mathbf{r}_1t_1)\mathcal{G}_0(\mathbf{r}'_1t'_1, \mathbf{r}'_1t'^+_1)\mathcal{G}_0(\mathbf{r}_1t_1, \mathbf{r}'t') \right. \\
 &\quad \left. + \mathcal{G}_0(\mathbf{r}_1t, \mathbf{r}'_1t'_1)\mathcal{G}_0(\mathbf{r}'_1t'_1, \mathbf{r}_1t_1)\mathcal{G}_0(\mathbf{r}_1t_1, \mathbf{r}'_1t') \right] + \dots \quad (\text{A.36})
 \end{aligned}$$

Note that, in the third line, a prescription is needed to evaluate \mathcal{G}_0 at equal times. This contribution arises from the contraction between two operators that come from the same interaction hamiltonian, \hat{H}_1 . Since in \hat{H}_1 the creation operators are always to the left of the destruction ones, one takes this as a prescription and the time argument of the creation operator is always slightly larger than the time in the destruction operator:

$$\mathcal{G}_0(\mathbf{r}t, \mathbf{r}'t^+) = \lim_{t' \rightarrow t^+} \left\langle \mathcal{T} \left[a_I(\mathbf{r}t) a_I^\dagger(\mathbf{r}'t') \right] \right\rangle_0. \quad (\text{A.37})$$

By considering the previous expressions, one can see that a general contribution of order n in the expansion of the single-particle propagator contains n interaction terms convoluted with $2n + 1$ non-interacting propagators. In addition, at a given order, each topological distinct contribution should only be taken into account once. However, for each of these contributions one needs to compute $2n$ spatial integrals plus $2n$ imaginary time integrals, *i.e.* $4n$ integrals. In a uniform and isotropic system, it is very useful to Fourier transform these expressions to momentum space, because the momentum conservation can be applied at each vertex (each point in k -space where a propagator coincides with an interaction). This allows to carry out many integrals in a straightforward way. Furthermore, the quasi-periodicity of the Green's function in the imaginary time variable (see Chapter 2) allows for a discrete Fourier transform from imaginary time to the so-called Matsubara frequencies, which are also conserved at the vertices. The final

expression for the Fourier transformed propagator is:

$$\mathcal{G}(\mathbf{r}t, \mathbf{r}'t') = \int \frac{d^3k}{(2\pi)^3} e^{i\mathbf{k}(\mathbf{r}-\mathbf{r}')} \frac{1}{-i\beta} \sum_{\nu} e^{-iz_{\nu}(t-t')} \mathcal{G}(k, z_{\nu}). \quad (\text{A.38})$$

The conservation of momentum and energy is actually implemented in terms of the integral representations of the Dirac delta function in three-momentum:

$$\int d^3x e^{i\mathbf{k}\mathbf{x}} = (2\pi)^3 \delta(\mathbf{k}), \quad (\text{A.39})$$

and the relation of Matsubara frequencies:

$$\int_0^{-i\beta} dt e^{-i(z_{\nu}-z_{\nu'})t} = -i\beta \delta_{\nu,\nu'}. \quad (\text{A.40})$$

The expansion that has just been derived for the propagator, although very useful for theoretical considerations, is very hard to use in practice. Already at second order one needs to carry out the contractions between several operators, distinguish among those who are topologically equivalent, perform a lot of integrals and Fourier transform complicated expressions. This is clearly a tedious task. Fortunately, this task can be enormously simplified with the introduction of Feynman diagrams. The diagrammatic interpretation of the propagator is based on a one-to-one correspondence between each term in the perturbative expansion of the propagator and a diagram. A set of rules (the so-called Feynman rules) relate in a systematic way each term of a given order in the expansion of the Green's function to a diagram. With the help of those rules, the value of an n -th order contribution can be determined more easily. The Feynman rules for the momentum-frequency space representation of the one-body Green's Function are given in the following appendix.

Appendix B

Feynman rules and diagrams

The Feynman rules provide a dictionary that translates each term in the perturbation expansion of the Green's function into diagrams. A term of order n in the expansion of \mathcal{G} is given by the Feynman rules for an homogeneous system of identical particles interacting through a time independent two-body potential. In the momentum-frequency representation, these are the following:

1. At a given n -th order in the interaction, draw all the topologically distinct connected diagram with n interaction (wavy) lines and $2n + 1$ (straight) fermion lines. In these lines, an arrow indicates the direction of the momentum flow.
2. Associate a momentum \mathbf{k}_i and a Matsubara frequency z_{ν_i} with each fermion line ($i = 1, 2, \dots, n$). The external lines in the diagram carry a momentum \mathbf{k} and a frequency z_ν .
3. For each line write down a factor:

$$\mathcal{G}_0(k_i, z_{\nu_i}) = \frac{1}{z_{\nu_i} - k_i^2/2m},$$

coming from the non-interacting propagator.

4. Each interaction line involves a factor:

$$i\langle \mathbf{k}_1 \mathbf{k}_2 | V | \mathbf{k}_3 \mathbf{k}_4 \rangle.$$

The labels of the propagator lines associated to the interaction vertices are shown in Fig. B.1.

5. At each interaction vertex the total momentum and the total Matsubara frequencies are conserved. The Dirac and Kronecker delta functions that guarantee these conservation laws are given by:

$$(2\pi)^3 \delta^{(3)}(\mathbf{k}_1 + \mathbf{k}_2 - \mathbf{k}_3 \mathbf{k}_4) (-i\beta) \delta_{\nu_1 + \nu_2, \nu_3 + \nu_4},$$

at each vertex.

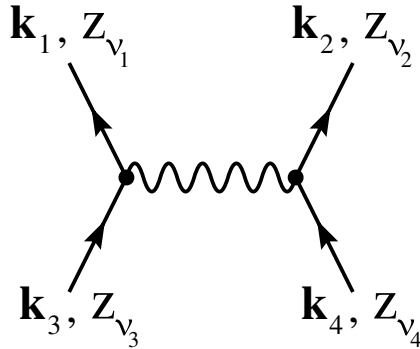


Figure B.1: *Prescription for the in- and out-going fermion lines in the interaction vertices.*

6. Integrate over all the momenta associated with fermion lines, except for the external one, labeled \mathbf{k} . Sum over the Matsubara frequencies of all the fermion lines, except for the external one, labeled z_ν . Associate a factor $(2\pi)^{-3}$ to each integration and a factor $(-i\beta)^{-1}$ to each Matsubara sum.
7. Sum over the spin and isospin quantum numbers of all the internal fermionic lines.
8. Add a factor $(-1)^F$ to the final result, with F the number of closed fermion loops in the diagram. This factor comes from the odd number of permutations that one has to perform in order to bring the external operators to the left of all the internal operators.
9. The prescription for equal-time Green's functions is acknowledged by adding a factor $e^{z\nu\eta}$ to the expression whenever a propagator line closes on itself or it is joined by the same interaction line. The factor η is small and positive, such that:

$$\lim_{\text{Re } z \rightarrow \infty} \eta \text{Re } z = \infty,$$

and is needed to prevent the divergent contributions from the arches in contour integrations.

As an example of the application of these rules, the contributions of the diagrams (a), (b) and (c) of Fig. B.2 will be computed. Diagram (a), for instance,

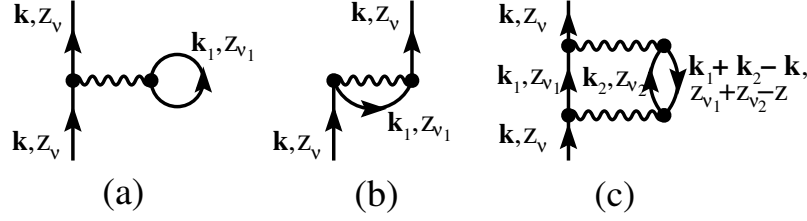


Figure B.2: *Examples of the application of Feynman rules to Feynman diagrams for the one-body propagator. Diagrams (a) and (b) are the two first order contributions, while diagram (c) corresponds to the first non-trivial second order contribution.*

yields:

$$\begin{aligned}
 \mathcal{G}^{(a)}(k, z_\nu) &= (-1) \frac{1}{-i\beta} \sum_{\nu_1} e^{z_{\nu_1} \eta} \int \frac{d^3 k_1}{(2\pi)^3} \mathcal{G}_0(k, z_\nu) i \langle \mathbf{k} \mathbf{k}_1 | V | \mathbf{k} \mathbf{k}_1 \rangle \\
 &\times \mathcal{G}_0(k_1, z_{\nu_1}) \mathcal{G}_0(k, z_\nu) = \\
 &= \mathcal{G}_0(k, z_\nu) \left[\frac{-i}{-i\beta} \sum_{\nu_1} e^{z_{\nu_1} \eta} \int \frac{d^3 k_1}{(2\pi)^3} \langle \mathbf{k} \mathbf{k}_1 | V | \mathbf{k} \mathbf{k}_1 \rangle \mathcal{G}_0(k_1, z_{\nu_1}) \right] \mathcal{G}_0(k, z_\nu).
 \end{aligned} \tag{B.1}$$

Diagram (b) is basically the exchange counterpart of diagram (a), in the sense that, apart for a sign, the only difference is found in the permutation of the ket vectors in the potential:

$$\mathcal{G}^{(b)}(k, z_\nu) = \mathcal{G}_0(k, z_\nu) \left[\frac{i}{-i\beta} \sum_{\nu_1} e^{z_{\nu_1} \eta} \int \frac{d^3 k_1}{(2\pi)^3} \langle \mathbf{k} \mathbf{k}_1 | V | \mathbf{k}_1 \mathbf{k} \rangle \mathcal{G}_0(k_1, z_{\nu_1}) \right] \mathcal{G}_0(k, z_\nu). \tag{B.2}$$

Indeed, both of them can be written together by means of the antisymmetric matrix element, $|\mathbf{k} \mathbf{k}' \rangle_A = |\mathbf{k} \mathbf{k}' \rangle - |\mathbf{k}' \mathbf{k} \rangle$:

$$\mathcal{G}^{(a+b)}(k, z_\nu) = \mathcal{G}_0(k, z_\nu) \left[\frac{-i}{-i\beta} \sum_{\nu_1} e^{z_{\nu_1} \eta} \int \frac{d^3 k_1}{(2\pi)^3} \langle \mathbf{k} \mathbf{k}_1 | V | \mathbf{k} \mathbf{k}_1 \rangle_A \mathcal{G}_0(k_1, z_{\nu_1}) \right] \mathcal{G}_0(k, z_\nu). \tag{B.3}$$

The contribution of Diagram (c) is already more involved, since it is a second order diagram. The momentum labels, once the total momentum and Matsubara frequency conservation at the vertex has been applied, are shown in Fig. B.2. This conservation cancels one of the momentum integrations (with its corresponding

$(2\pi)^{-3}$ factor) and a Matsubara sum (and its $(-i\beta)^{-1}$ factor), thus yielding:

$$\begin{aligned} \mathcal{G}^{(c)}(k, z_\nu) = & \mathcal{G}_0(k, z_\nu) \left[\frac{-i^2}{(-i\beta)^2} \sum_{\nu_1, \nu_2} \int \frac{d^3 k_1}{(2\pi)^3} \int \frac{d^3 k_2}{(2\pi)^3} \mathcal{G}_0(k_1, z_{\nu_1}) \right. \\ & \times \langle \mathbf{k}_1, \mathbf{k}_2 | V | \mathbf{k}, \mathbf{k}_1 + \mathbf{k}_2 - \mathbf{k} \rangle \mathcal{G}_0(k_2, z_{\nu_2}) \langle \mathbf{k}, \mathbf{k}_1 + \mathbf{k}_2 - \mathbf{k} | V | \mathbf{k}_1, \mathbf{k}_2 \rangle \\ & \left. \times \mathcal{G}_0(|\mathbf{k}_1 + \mathbf{k}_2 - \mathbf{k}|, z_{\nu_1} + z_{\nu_2} - z_\nu) \right] \mathcal{G}_0(k, z_\nu). \end{aligned} \quad (\text{B.4})$$

Appendix C

Sums over Matsubara frequencies

In the finite temperature formalism used throughout this Thesis, a few infinite sums of Matsubara frequencies had to be performed. These sums are carried out by means of complex variable calculus techniques, mainly Cauchy's theorem and integrations over closed contours in the complex plane. In this Appendix, three examples of Matsubara sums that appear in this Thesis will be explicitly performed. In all these three cases, the main ideas and mathematical tools are the same and only minor mathematical considerations change from one to the other. In the first place, one evaluates the sum of a function computed at an infinite set of Matsubara frequencies as the result of a Cauchy integral of the original function times a function which has poles of unit residue at these frequencies. The original contour of this integral is then deformed to another contour that involves poles or cuts for real frequencies (thus switching from imaginary to physical frequencies). Finally, applying Cauchy's theorem to these poles, one finds a final result in terms of the poles (or cuts) of the original function in the real axis.

C.1 Functions with a single pole

As a first example, let us consider the sum over Matsubara frequencies appearing in the Hartree-Fock contribution, Eq. (4.1). Consider the following function of a complex variable:

$$-\beta f(z) = \frac{-\beta}{1 + e^{\beta(z-\mu)}}. \quad (\text{C.1})$$

It has poles of order one and unit residue at the Matsubara frequencies. Thus the infinite sum over the free propagator can be transformed to an integral by virtue of Cauchy's theorem:

$$\sum_{\nu} e^{z\nu\eta} \mathcal{G}_0(k, z_{\nu}) = -\beta \int_C \frac{dz}{2\pi i} e^{z\eta} f(z) \mathcal{G}_0(k, z), \quad (\text{C.2})$$

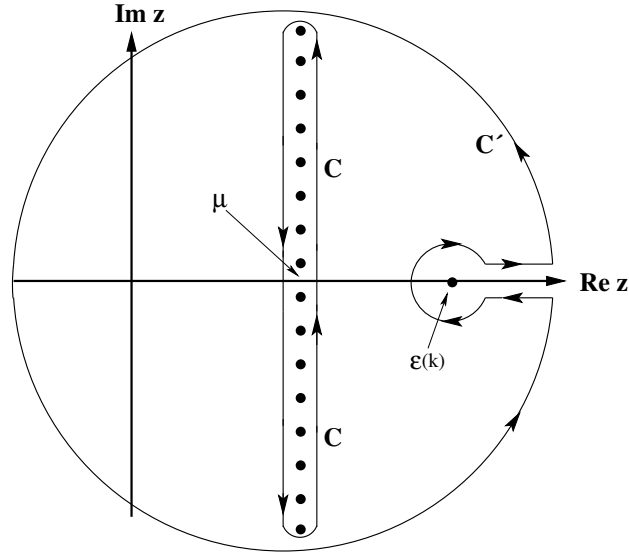


Figure C.1: *Integration contours C and C' in the complex plane. Note the negative sense in C' around the pole at $z = \varepsilon(k)$.*

where C is a contour that surrounds the poles at the Matsubara frequencies in the positive sense (see Fig. C.1). Since the integrated function is analytical in the remaining regions of the complex plane, one can deform the contour C to a contour C' , as shown in Fig. C.1. This contour can be split in three different regions. Firstly, the region of the arches at infinity. The integral in this region vanishes with the help of the convergence factor $e^{z\eta}$. Secondly, the contributions of the two parallel paths above and below the real axis cancel because the integrand is analytical above and below the real axis. Finally, one is left with the contribution of the pole of the free propagator at $z = \varepsilon(k)$. This is computed with the help of Cauchy's theorem:

$$\sum_{\nu} e^{z\nu\eta} \mathcal{G}_0(k, \omega) = -\beta \int_{C'} \frac{dz}{2\pi i} e^{z\eta} f(z) \frac{1}{z - \varepsilon(k)} = \beta f[\varepsilon(k)]. \quad (\text{C.3})$$

Note the minus sign due to the clockwise orientation around the pole. This result is independent of the relative position of $\varepsilon(k)$ with respect to μ , as can be easily shown by drawing a contour C' with $\varepsilon(k)$ below μ . Let us also mention that the previous sum over Matsubara frequencies involves the free one-body propagator. The same sum over the dressed propagator can be performed with the help of the spectral decomposition of \mathcal{G} , Eq. (2.57).

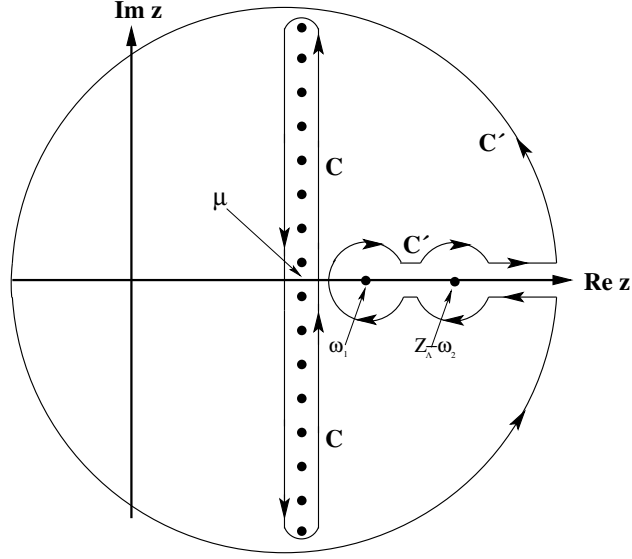


Figure C.2: *Integration contours C and C' in the complex plane. Note the negative sense in C' around the poles at $z = \omega_1$ and $z = Z_\Lambda - \omega_2$.*

C.2 Functions with double poles

The second example consists of a sum of a function of Matsubara functions which has to poles on the real axis. This is not technically more involved than the previous result. Consider the non-correlated two-body propagator:

$$\mathcal{G}_{II}^0(k_1, k_2, Z_\Lambda) = -\frac{1}{\beta} \sum_{\nu} \mathcal{G}(k_1, z_{\nu}) \mathcal{G}(k_2, Z_\Lambda - z_{\nu}), \quad (\text{C.4})$$

where Z_Λ is a Matsubara frequency of a bosonic nature. Inserting the spectral decomposition of the one-particle propagator, Eq. (2.57), one obtains:

$$\begin{aligned} \mathcal{G}_{II}^0(k_1, k_2, Z_\Lambda) &= \int_{-\infty}^{\infty} \frac{d\omega_1}{2\pi} \int_{-\infty}^{\infty} \frac{d\omega_2}{2\pi} \mathcal{A}(k_1, \omega_1) \mathcal{A}(k_2, \omega_2) \\ &\quad \times \frac{-1}{\beta} \sum_{\nu} \frac{1}{z_{\nu} - \omega_1} \frac{1}{Z_\Lambda - z_{\nu} - \omega_2}. \end{aligned} \quad (\text{C.5})$$

Once again, the sum can be converted into an integral over the contour C with the help of the Fermi-Dirac function:

$$\frac{-1}{\beta} \sum_{\nu} \frac{1}{z_{\nu} - \omega_1} \frac{1}{Z_\Lambda - z_{\nu} - \omega_2} = \int_C \frac{dz}{2\pi i} e^{z\eta} f(z) \frac{1}{z - \omega_1} \frac{1}{Z_\Lambda - z - \omega_2}. \quad (\text{C.6})$$

The contour C is now deformed to the contour C' as depicted in Fig. C.2. The contributions of the arches as well as those coming from the parallel paths above

and below the real axis vanish. The only contribution thus left is that of the poles at $z = \omega_1$ and $z = Z_\Lambda - \omega_2$. The result of the integral is thus simply the sum of residues of the integrated function at these poles:

$$\begin{aligned} \frac{-1}{\beta} \sum_{\nu} \frac{1}{z_{\nu} - \omega_1} \frac{1}{Z_\Lambda - z_{\nu} - \omega_2} &= \int_{C'} \frac{dz}{2\pi i} e^{z\eta} f(z) \frac{1}{z - \omega_1} \frac{1}{Z_\Lambda - z - \omega_2} \\ &= -\frac{f(\omega_1)}{Z_\Lambda - \omega_1 - \omega_2} + \frac{f(Z_\Lambda - \omega_2)}{Z_\Lambda - \omega_1 - \omega_2}. \end{aligned} \quad (\text{C.7})$$

As explained above, Z_Λ is a Matsubara frequency of the bosonic type and thus Λ is an even number. Note that the picture in Fig. C.2 is only valid for $\Lambda = 0$, where Z_Λ is real. For a generic complex Z_Λ , the position of the second pole would be somewhere above or below the real axis, but the ideas exposed above would still be valid as long as the contribution of the parallel paths coming from and going to the pole at $Z_\Lambda - \omega_2$ vanish. All in all, one finds the following expression:

$$\mathcal{G}_{II}^0(k_1, k_2, Z_\Lambda) = \int_{-\infty}^{\infty} \frac{d\omega_1}{2\pi} \int_{-\infty}^{\infty} \frac{d\omega_2}{2\pi} \mathcal{A}(k_1, \omega_1) \mathcal{A}(k_2, \omega_2) \frac{f(Z_\Lambda - \omega_2) - f(\omega_1)}{Z_\Lambda - \omega_1 - \omega_2}. \quad (\text{C.8})$$

In the numerator of the previous integrand, the function $f(Z_\Lambda - \omega_2)$ appears. When trying to perform the analytical continuation of $\mathcal{G}_{II}^0(Z_\Lambda)$ to the whole complex plane Z , one finds that the previous function does not go to zero as $|Z| \rightarrow \infty$ in all directions. Actually, for $\text{Re } Z < 0$ one finds $\lim_{|Z| \rightarrow \infty} f(Z - \omega) \rightarrow 1$. Yet, the condition $\lim_{|Z| \rightarrow \infty} \mathcal{G}_{II}^0(Z) \rightarrow 0$ needs to be fulfilled for the analytical continuation to be uniquely defined (see Section 2.2.4). Therefore, before performing the analytical continuation it is convenient to use the relation $f(Z_\Lambda - \omega) = 1 - f(\omega)$, which holds for even Λ , in the numerator. With this replacement in the numerator, the uncorrelated two-body propagator becomes:

$$\mathcal{G}_{II}^0(k_1, k_2, Z_\Lambda) = \int_{-\infty}^{\infty} \frac{d\omega_1}{2\pi} \int_{-\infty}^{\infty} \frac{d\omega_2}{2\pi} \mathcal{A}(k_1, \omega_1) \mathcal{A}(k_2, \omega_2) \frac{1 - f(\omega_1) - f(\omega_2)}{Z_\Lambda - \omega_1 - \omega_2}, \quad (\text{C.9})$$

which vanishes for $|Z_\Lambda| \rightarrow \infty$.

C.3 Functions with cuts in the real axis

The last section of this Appendix is devoted to the computation of the somewhat more tricky case of a sum over a function of Matsubara frequencies which has a cut in the real axis, as it is the case of the logarithm. Let us consider the case of the free partition function, Eq. (4.1), which involves the sum:

$$\ln Z_0 = \sum_{k, \nu} e^{z\nu\eta} \ln [\varepsilon_0(k) - z_\nu]. \quad (\text{C.10})$$

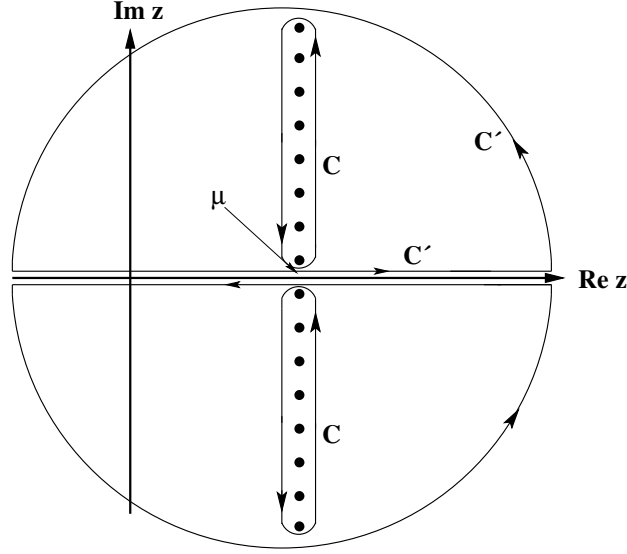


Figure C.3: *Integration contours C and C' in the complex plane. Note that the contributions above and below the real axis can get as close as needed to it.*

The Matsubara sum is, as seen before, transformed to a Cauchy integral over the contour C which, however, for this case, avoids the real axis in which the logarithm has a cut:

$$\sum_{\nu} e^{z_{\nu}\eta} \ln [\varepsilon_0(k) - z_{\nu}] = -\beta \int_C \frac{dz}{2\pi i} e^{z\eta} f(z) \ln [\varepsilon_0(k) - z]. \quad (\text{C.11})$$

The contour C is now deformed to C' . The contributions of the arches vanish thanks to the convergence factor and the only contribution left is that of the circuit slightly above and below the real axis. Thus:

$$\begin{aligned} \sum_{\nu} e^{z_{\nu}\eta} \ln [\varepsilon_0(k) - z_{\nu}] &= -\beta \int_{C'} \frac{dz}{2\pi i} f(z) \ln [\varepsilon_0(k) - z] = \\ &= -\beta \int_{-\infty}^{\infty} \frac{d\omega}{2\pi i} f(\omega) \ln [\varepsilon_0(k) - \omega - i\eta] \\ &\quad - \beta \int_{\infty}^{-\infty} \frac{d\omega}{2\pi i} f(\omega) \ln [\varepsilon_0(k) - \omega + i\eta] = \\ &= -\beta \int_{-\infty}^{\infty} \frac{d\omega}{2\pi i} f(\omega) \{ \ln [\varepsilon_0(k) - \omega_+] - \ln [\varepsilon_0(k) - \omega_-] \}. \end{aligned} \quad (\text{C.12})$$

Up to here the result is completely general. However, one can profit from the property $\ln(z^*) = \ln(z)^*$ and of the definition of the imaginary part of a complex

number, $\text{Im } z = \frac{1}{2i} [z - z^*]$, to get:

$$\sum_{\nu} e^{z_{\nu}\eta} \ln [\varepsilon_0(k) - z_{\nu}] = -\beta \int_{-\infty}^{\infty} \frac{d\omega}{\pi} f(\omega) \text{Im} \{ \ln [\varepsilon_0(k) - \omega_+] \}. \quad (\text{C.13})$$

As a matter of fact, this result turns out to be quite general and is used thoroughly in the developments of this Thesis. Take any function of a complex variable with the property:

$$F(z^*) = [F(z)]^*. \quad (\text{C.14})$$

Even if F does not have a cut in the real axis, one can take the sum over Matsubara frequencies and deform the contour C to C' as long as F decays at infinity and has no poles in the complex plane. Then, the previous results hold and the sum over Matsubara frequencies equals an integral of the imaginary part of the function slightly above the real axis:

$$\sum_{\nu} e^{z_{\nu}\eta} F(z_{\nu}) = -\beta \int_{-\infty}^{\infty} \frac{d\omega}{2\pi} f(\omega) 2\text{Im} \{ F(\omega_+) \}. \quad (\text{C.15})$$

Since both the propagator and the self-energy are analytical everywhere in the complex plane (with the possible exception of the real axis), decay at infinity and satisfy Eq. (C.14) [see Eqs. (2.63) and (2.125)], this result can be directly applied to the sums which involve \mathcal{G} and Σ . As a consequence, Eq. (C.15) turns out to be extremely useful in the field of finite temperature many-body quantum mechanics, where it is extensively used.

Appendix D

Degenerate and classical limits

In the field of many-body physics at finite temperature, the presence of Fermi-Dirac (or Bose-Einstein) distribution functions makes it hard to obtain analytical expressions for the density or temperature dependences of the thermodynamical quantities. This is in contrast to the zero temperature mean-field case, where the step-like momentum distribution allows to obtain analytical results in simple cases. Yet, in a certain range of densities and temperatures, one can use approximations which allow to handle these dependences in a more or less straightforward way. These density-temperature regimes are defined by the ratio $x = \frac{T}{\varepsilon_F}$. While the temperature T defines a natural energy scale for thermal effects, the free Fermi energy $\varepsilon_F = \frac{k_F^2}{2m}$ sets the energy scale associated to finite density effects in fermionic systems. The limit $x \ll 1$ defines the degenerate limit, in which the degeneracy of the system dominates its physics, while its opposite, $x \gg 1$, corresponds to the classical limit. In the following, the approximations that these two limits introduce in the observables of many-body physics will be discussed. Note that the usual derivation of these approximations relies often in a quasi-particle-like description.

D.1 Degenerate limit

The degenerate limit is achieved when the condition $T/\varepsilon_F \ll 1$ holds, *i.e.* when temperature effects are small relative to the density ones. This limit holds when the system is either at very low temperatures or very high densities. In both cases, the system behaves essentially like in the zero temperature case and thus one can obtain the temperature dependences for very degenerate systems by taking profit of the step-like behavior of the momentum distribution close to the Fermi surface. This is achieved in terms of the Sommerfeld expansion, which is introduced below.

Chemical potential

At finite temperature, the microscopic chemical potential of an interacting system of fermions is found from inverting:

$$\rho = \nu \int \frac{d^3k}{(2\pi)^3} \int_{-\infty}^{\infty} \frac{d\omega}{2\pi} \mathcal{A}(k, \omega) f(\omega). \quad (\text{D.1})$$

Let us assume a no-width approximation for the spectral function. The quasi-particle spectrum is defined by:

$$\varepsilon(k) = \frac{k^2}{2m} + \Sigma(k), \quad (\text{D.2})$$

where $\Sigma(k)$ is a real energy-independent self-energy. In a Hartree-Fock approximation, this is given by the self-consistent self-energy of Eq. (4.5). When the mean-field is derived from a realistic potential and contains many-body effects, it is generally quite difficult (if not impossible) to find an analytic approximation for the momentum dependence of the mean-field Σ . Still, in order to find manageable expressions, one commonly assumes that the self-energy (or single-particle potential, in a quasi-particle language) has a quadratic dependence in k . This corresponds to the following spectrum:

$$\varepsilon(k) \simeq \frac{k^2}{2m} + ak^2 + \bar{U} = \frac{k^2}{2m^*} + \bar{U}. \quad (\text{D.3})$$

The effective mass m^* introduced above, which is given by:

$$\frac{m^*}{m} = \frac{1}{1 + 2ma}, \quad (\text{D.4})$$

accounts for the (approximate) quadratic momentum dependence of the potential, while the term \bar{U} is just a constant that sets the value at $k = 0$ of the quasi-particle spectrum. Within this quadratic approximation, the effective mass is momentum independent. This is of course not true for a realistic case (see the self-energies of Fig. 5.16), in which the parameter a would either be momentum-dependent or should try to fit the momentum dependence for a given momentum regime. It is important to note that, in general, the a and \bar{U} parameters that describe the spectrum can be density dependent.

Within the previous assumptions, one can find an analytical expression for the chemical potential, because Eq. (D.1) reduces to the expression:

$$\rho = \nu \int \frac{d^3k}{(2\pi)^3} \frac{1}{1 + e^{\beta[\varepsilon(k) - \mu]}} = \frac{\nu}{2\pi^2} \int_0^{\infty} dk \frac{k^2}{1 + e^{\beta\left[\frac{k^2}{2m^*} + \bar{U} - \mu\right]}}. \quad (\text{D.5})$$

Let us now define $\bar{\mu} = \mu - \bar{U}$ and perform the change of variables $x = \beta \left[\frac{k^2}{2m^*} - \bar{\mu} \right]$. The integral is now adimensional and becomes:

$$\rho = \frac{\nu}{4\pi^2} (2m^*)^{3/2} T \int_{-\frac{\bar{\mu}}{T}}^{\infty} dx \frac{1}{1 + e^x} \sqrt{\bar{\mu} + xT}, \quad (\text{D.6})$$

which, after an integration by parts, becomes:

$$\rho = \frac{\nu}{6\pi^2} (2m^* \bar{\mu})^{3/2} \int_{-\frac{\bar{\mu}}{T}}^{\infty} dx \frac{e^x}{(1 + e^x)^2} \left(1 + x \frac{T}{\bar{\mu}} \right)^{3/2}. \quad (\text{D.7})$$

The Fermi-Dirac distribution, $f(x) = \frac{1}{1+e^x}$, changes rapidly close to $x \sim 0$, while it is almost constant for $x \ll 0$ and $x \gg 0$. Its derivative, $f'(x) = -\frac{e^x}{(1+e^x)^2}$, is thus peaked for $x \sim 0$, and close to zero elsewhere (see Fig. D.1). As a consequence of this peak-like behavior, for low enough temperatures (with respect to $\bar{\mu}$), one can safely expand the second term in the previous integrand. The exponential decay of the first term kills the contributions to the integral for large x . This is exactly the Sommerfeld expansion, in which one expands the integrand for very degenerate systems. Moreover, as T goes to zero (or $\bar{\mu}$ increases), the lower limit goes to $-\infty$, which allows to perform the x -integral analytically.

Let us first consider the expansion to zero-th order:

$$\rho = \frac{\nu}{6\pi^2} (2m^* \bar{\mu})^{3/2}, \quad (\text{D.8})$$

which can be inverted to obtain the well-known zero temperature result:

$$\mu = \frac{k_F^2}{2m^*} + \bar{U}, \quad (\text{D.9})$$

so that the chemical potential is simply given by the quasi-particle energy at the Fermi surface. Note that, to find the previous result, the integral:

$$\int_{-\infty}^{\infty} dx \frac{e^x}{(1 + e^x)^2} = 1 \quad (\text{D.10})$$

has been used.

To obtain the first temperature correction, one has to expand Eq. (D.7) to second order (the first order result cancels exactly due to the symmetry properties of the integrand):

$$\rho = (2m^* \bar{\mu})^{3/2} \frac{\nu}{6\pi^2} \left\{ 1 + \frac{\pi^2 T^2}{8 \bar{\mu}^2} \right\}, \quad (\text{D.11})$$

which is obtained with the help of the result:

$$\int_{-\infty}^{\infty} dx \frac{e^x}{(1 + e^x)^2} x^2 = \frac{\pi^2}{3}. \quad (\text{D.12})$$

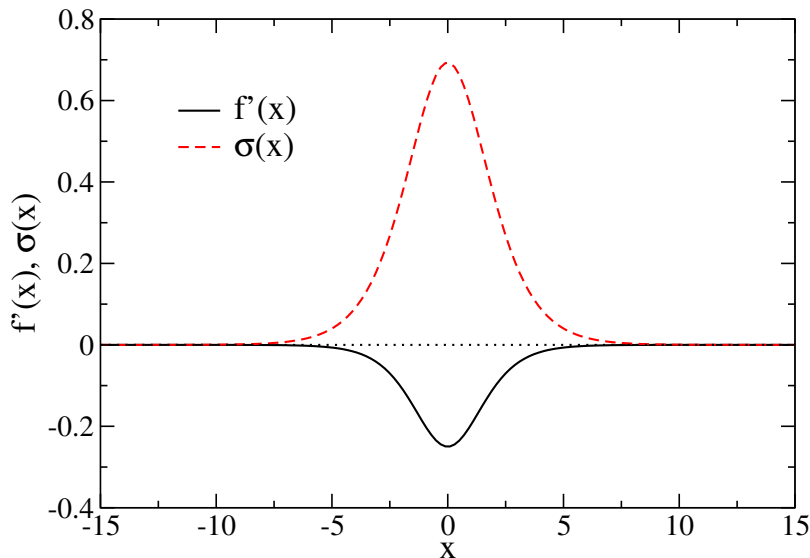


Figure D.1: Peak structure of the $f'(x)$ and $\sigma(x)$ functions close to $x = 0$.

Up to T^2 , one can take $\left(\frac{T}{\bar{\mu}}\right)^2 = \left(\frac{T}{\varepsilon_F^*}\right)^2$, with $\varepsilon_F^* = \frac{k_F^2}{2m^*}$. With this result at hand, one finds:

$$\mu = \varepsilon_F^* \left\{ 1 - \frac{\pi^2}{12} \left(\frac{T}{\varepsilon_F^*} \right)^2 \right\} + \bar{U}, \quad (\text{D.13})$$

which shows that the first temperature correction to the chemical potential is proportional to T^2 and tends to make it slightly more attractive. Note that the expansion is performed in terms of the parameter T/ε_F^* , which is modified from the non-interacting case by the effective mass.

Expanding the right term in Eq. (D.7) to a higher order, one would find the thermal corrections to the chemical potential at higher orders. Since the derivative of the Fermi-Dirac function is a symmetric function, this expansion is given in terms of even powers of the temperature. Let us finally note that in a fully correlated approach, the explicit temperature dependence of the spectral function does not allow to obtain an analytical expansion for $\mu(T)$ beyond the zeroth order.

Energy

The energy per particle, when treated within a (no-width) quasi-particle approach, has a similar Sommerfeld expansion. Let us first consider the kinetic energy:

$$\frac{\mathcal{K}}{A} = \frac{\nu}{\rho} \int \frac{d^3k}{(2\pi)^3} \frac{k^2}{2m} \frac{1}{1 + e^{\beta[\varepsilon(k) - \mu]}} = \frac{\nu}{2\pi^2 \rho} \frac{1}{2m} \int_0^\infty dk \frac{k^4}{1 + e^{\beta\left[\frac{k^2}{2m^*} - \bar{\mu}\right]}}. \quad (\text{D.14})$$

After performing the change to the adimensional x variable defined above and integrating by parts, one obtains the following expression:

$$\frac{\mathcal{K}}{A} = \frac{\nu}{10\pi^2\rho} \frac{(2m^*\bar{\mu})^{5/2}}{2m} \int_{-\frac{\bar{\mu}}{T}}^{\infty} dx \frac{e^x}{(1+e^x)^2} \left(1 + x\frac{T}{\bar{\mu}}\right)^{5/2}. \quad (\text{D.15})$$

Expanding it to zeroth order and using the results obtained previously for $\bar{\mu}$ at this order, one finds the usual expression for the zero temperature kinetic energy per particle:

$$\frac{\mathcal{K}}{A} = \frac{3}{5} \frac{k_F^2}{2m}. \quad (\text{D.16})$$

The calculation to second order is also carried straightforwardly and yields:

$$\frac{\mathcal{K}}{A} = \frac{3}{5} \frac{k_F^2}{2m} \left\{ 1 + \frac{\pi^2}{12} \left(\frac{T}{\varepsilon_F^*} \right)^2 \right\}. \quad (\text{D.17})$$

Note that, as expected, thermal correlations are translated into a quadratic increase of the kinetic energy with temperature. Once again, higher order terms in the Sommerfeld expansion would involve even powers of the temperature. On the other hand, the potential energy is obtained from the expression:

$$\frac{\langle V \rangle}{A} = \frac{\nu}{2\rho} \int \frac{d^3k}{(2\pi)^3} \Sigma(k) \frac{1}{1 + e^{\beta[\varepsilon(k) - \bar{\mu}]}} = \frac{1}{2} \bar{U} + \frac{\nu}{4\pi^2\rho} a \int_0^{\infty} dk \frac{k^4}{1 + e^{\beta\left[\frac{k^2}{2m^*} - \bar{\mu}\right]}}. \quad (\text{D.18})$$

The integral over momenta is essentially the same one that is computed for the kinetic energy. Thus, it is easy to see that the expansion for low temperatures of the potential energy of quasi-particles yields:

$$\frac{\langle V \rangle}{A} = \frac{1}{2} \bar{U} + \frac{3}{5} k_F^2 a \left\{ 1 + \frac{\pi^2}{12} \left(\frac{T}{\varepsilon_F^*} \right)^2 \right\}, \quad (\text{D.19})$$

which is once again a quadratic temperature correction with respect to the zero temperature result. Finally, summing both contributions, one finds that the total energy per particle reads:

$$\frac{E}{A} = \frac{3}{5} \frac{\varepsilon_F^*}{\varepsilon_F^*} \frac{1 + ma}{1 + 2ma} \left\{ 1 + \frac{\pi^2}{12} \left(\frac{T}{\varepsilon_F^*} \right)^2 \right\} + \frac{1}{2} \bar{U}. \quad (\text{D.20})$$

The Sommerfeld expansion for the correlated energy per particle should be derived from the GMK sum rule, Eq. (2.103). There are two difficulties which prevent us for performing it. On the one hand, the integration by parts involves

the knowledge of the m_0 and m_1 running integrals of the spectral function, which are not known analytically. On the other hand, the temperature dependence of the self-energy, Eq. (5.61), is non-negligible already at the first order in the Sommerfeld expansion $O(T^2)$. This automatically involves that the spectral function has a non-trivial temperature dependence (see Fig. 5.17), which also spoils the Sommerfeld expansion at the first non-trivial order.

Entropy

The expansion at low temperatures of the entropy, however, can be performed in an approximation which considers the finite width of the quasi-particle peak. Consider the expression for the dynamical quasi-particle Eq. (3.98):

$$\frac{S}{A} = \frac{\nu}{\rho} \int \frac{d^3k}{(2\pi)^3} \int_{-\infty}^{\infty} \frac{d\omega}{2\pi} \mathcal{B}(k, \omega) \sigma[\beta(\omega - \mu)], \quad (\text{D.21})$$

and perform the change of variables $x = \beta(\omega - \mu)$. The entropy becomes:

$$\frac{S}{A} = T \frac{\nu}{\rho} \int \frac{d^3k}{(2\pi)^3} \int_{-\infty}^{\infty} \frac{dx}{2\pi} \mathcal{B}(k, \mu + xT) \sigma(x), \quad (\text{D.22})$$

where $\sigma(x)$ is peaked around $x \sim 0$ (see Fig. D.1). Therefore, it is safe to perform a Sommerfeld expansion on the previous expression for low T 's (high μ 's). To lowest order, in which the temperature dependence of the \mathcal{B} spectral function can be neglected:

$$\frac{S}{A} = \frac{\pi^2}{3\rho} T \nu \int \frac{d^3k}{(2\pi)^4} \mathcal{B}(k, \mu). \quad (\text{D.23})$$

The integral:

$$\int_{-\infty}^{\infty} dx \sigma(x) = \frac{\pi^2}{3} \quad (\text{D.24})$$

has been used to obtain the previous result. Note that, in contrast to the chemical potential or the energy per particle, one can use an expression that goes beyond the quasi-particle picture in the Sommerfeld expansion of the entropy. It is however important to stress that this value is valid at lowest order in the expansion of T/μ and thus the \mathcal{B} spectral function of Eq. (D.23) should be computed at zero temperature.

To find the no-width counterpart of the previous expression, let us introduce the no-width \mathcal{B} -spectral function:

$$\mathcal{B}(k, \omega) = (2\pi) \delta[\omega - \varepsilon_{qp}(k)], \quad (\text{D.25})$$

so that the integral over momenta reads:

$$\int \frac{d^3k}{(2\pi)^3} \delta[\mu - \varepsilon_{qp}(k)] = \frac{1}{2\pi^2} \int_0^\infty dk k^2 \delta\left[\mu - \frac{k^2}{2m} - \Sigma(k)\right]. \quad (\text{D.26})$$

To perform the integration over the delta function, the relation:

$$\delta[f(x)] = \sum_{x_0} \frac{\delta(x - x_0)}{|f'(x_0)|} \quad (\text{D.27})$$

has to be used, where x_0 denotes any zero of $f(x)$ in the integration region. In the quasi-particle case, this corresponds to:

$$\mu = \frac{k^2}{2m} + \Sigma(k), \quad (\text{D.28})$$

which, for $T = 0$ and in a thermodynamically consistent approach, defines the Fermi momentum. The integral thus reads:

$$\begin{aligned} & \frac{1}{2\pi^2} \int_0^\infty dk k^2 \delta(k - k_F) \frac{1}{\left|\frac{k}{m} + \frac{d}{dk}\Sigma(k)\right|} = \\ & = \frac{1}{2\pi^2} \int_0^\infty dk k^2 \delta(k - k_F) \left|\frac{m^*(k)}{k}\right| = \frac{k_F m^*(k_F)}{2\pi^2}, \end{aligned} \quad (\text{D.29})$$

where the effective mass in this case is obtained from Eq. (4.32). Note that this effective mass does not correspond to any generic parameterization of the spectrum, but to its derivative with respect to the momentum at $k = k_F$. Once again, since this corresponds to the lowest order expansion, the effective mass $m^*(k_F)$ should be computed at zero temperature. All in all, the low temperature entropy depends linearly on the temperature and reads:

$$\frac{S}{A} = \frac{\pi^2}{3\rho} N(0)T, \quad (\text{D.30})$$

where the quasi-particle density of states $N(0)$ is computed at zero temperature and equals:

$$N(0) = \frac{\nu k_F m^*(k_F)}{2\pi^2}. \quad (\text{D.31})$$

The previous linear law for the entropy per particle can also be derived within Fermi liquid theory [Abr65; Fet71]. As a matter of fact, Eq. (D.30) can be easily translated into physical terms. The entropy is a measure of the total number of states that a system can occupy due to thermal agitation. Since small thermal fluctuations only modify the vicinity of the Fermi surface, the entropy of low temperature systems must be related to the available states close to this surface.

Actually, the density of states, $N(0)$, gives the number of available states close to the Fermi surface per energy unit. It is thus natural that the entropy of the system is given by the number of available states times the temperature, which is the available energy that one has to use in order to populate them.

In analogy with the previous subsections, one would be tempted to carry out the previous expansion in terms of the temperature to higher orders. Nevertheless, in the expansion of $\mathcal{B}(k, \mu + xT)$ for low temperatures, one should keep track of the temperature dependence of \mathcal{B} which, due to its implicit temperature dependence on the functions $\text{Im } \Sigma$, $\text{Re } \Sigma$, etc. cannot be performed analytically.

D.2 Classical limit

When a system is at very low density, quantum effects tend to be less relevant, up to a point that one cannot say that it is degenerate anymore. A similar behavior is achieved if one increases the temperature to very high values. Therefore, quantum effects tend to become irrelevant in the regime $T/\varepsilon_F \gg 1$ and in this limit one recovers the properties of a classical system. One can find analytical density and temperature dependences by means of an expansion in terms of the fugacity parameter, $e^{\beta\bar{\mu}}$. This is a very small quantity in the classical limit, because the chemical potential μ becomes very negative.

Chemical potential

Following the same steps introduced above, let us consider the normalization condition for the density in a no-width quasi-particle approach, Eq. (D.5). Since $\mu \rightarrow -\infty$ in the classical regime, the fugacity $\gamma = e^{-\beta\bar{\mu}}$ is very large and one can approximate the Fermi-Dirac distribution by the expression:

$$\frac{1}{1 + e^{\beta\left[\frac{k^2}{2m^*} + \bar{U} - \mu\right]}} = \frac{1}{1 + \gamma e^{\beta\frac{k^2}{2m^*}}} \sim \gamma^{-1} e^{-\beta\frac{k^2}{2m^*}}. \quad (\text{D.32})$$

Within this approximation, the density is given by the expression:

$$\rho = \frac{\nu}{2\pi^2} \gamma^{-1} \int_0^\infty dk k^2 e^{-\beta\frac{k^2}{2m^*}}, \quad (\text{D.33})$$

which, introducing the adimensional variable $y = \beta\frac{k^2}{2m^*}$, can be computed analytically:

$$\rho = \frac{\nu}{4\pi^2} \gamma^{-1} \left(\frac{2m^*}{\beta}\right)^{3/2} \underbrace{\int_0^\infty dy \sqrt{y} e^{-y}}_{\Gamma\left(\frac{3}{2}\right) = \frac{\sqrt{\pi}}{2}}. \quad (\text{D.34})$$

The previous density-chemical potential relation can be easily inverted and one finds:

$$\mu = T \ln \frac{\rho \lambda_{dB}^3}{\nu} - \frac{3}{2} T \ln \frac{m^*}{m} + \bar{U}, \quad (\text{D.35})$$

which yields the chemical potential in terms of the density, the effective mass, the potential \bar{U} and the de Broglie wavelength:

$$\lambda_{dB} = \sqrt{\frac{2\pi}{Tm}}. \quad (\text{D.36})$$

The density and temperature dependences of the chemical potential in the classical limit are thus logarithmic. Note that the interaction affects the chemical potential via the logarithmic dependence on the effective mass and the linear dependence of the momentum-independent term, \bar{U} . In the low density limit, where particles hardly interact with each other, \bar{U} will be negligible and $m^* = m$. The following term in the fugacity expansion of the Fermi-Dirac distribution, Eq. (D.32), would give the first quantal correction to the chemical potential.

Energy

The kinetic energy can also be expressed in terms of the fugacity expansion. Using Eq. (D.32), one can show that the kinetic energy is given by:

$$\begin{aligned} \frac{\mathcal{K}}{A} &= \frac{\nu}{\rho} \int \frac{d^3k}{(2\pi)^3} \frac{k^2}{2m} \frac{1}{1 + e^{\beta[\varepsilon(k) - \mu]}} \sim \frac{\nu}{2\pi^2 \rho} \frac{1}{2m} \gamma^{-1} \int_0^\infty dk k^4 e^{-\beta \frac{k^2}{2m^*}} = \\ &= \frac{\nu}{4\pi^2 \rho} \frac{1}{2m} \gamma^{-1} \left(\frac{2m^*}{\beta} \right)^{5/2} \underbrace{\int_0^\infty dy y^{3/2} e^{-y}}_{\Gamma(\frac{5}{2}) = \frac{3\sqrt{\pi}}{4}} = \frac{3}{2} \frac{m^*}{m} T. \end{aligned} \quad (\text{D.37})$$

Note that, except for the effective mass factor, this is just the expected result from the equipartition theorem of classical statistical mechanics for a gas in three dimensions. As a matter of fact, in the low density limit, where $\frac{m^*}{m} \rightarrow 1$ the kinetic energy per particle is essentially given by the temperature. Note that the kinetic energy should be almost density independent and in fact the only density dependence that enters the expression is the one coming from the effective mass.

The potential energy is once again given by a term proportional to \bar{U} and the contribution of the momentum dependent term, which is actually given by the same integral over k^4 of the previous result:

$$\frac{\langle V \rangle}{A} = \frac{3}{2} \frac{m^*}{m} T m a + \frac{1}{2} \bar{U}. \quad (\text{D.38})$$

The total energy per particle is thus given by the a term proportional to the temperature and the momentum dependence of the mean field and a term proportional to \bar{U} :

$$\frac{E}{A} = \frac{3}{2} \frac{1+ma}{1+2ma} T + \frac{1}{2} \bar{U}. \quad (\text{D.39})$$

Once again, in the low density limit where both a and \bar{U} tend to zero, the equipartition theorem will be valid for the total energy per particle. Note, however, that in an intermediate density regime (close to the classical limit, but not close to the free gas) the energy per particle is modified and is given in terms of a virial expansion in which the phase shifts determine in a model-independent way the energy per particle [Hor06].

Entropy

Let us now consider the fugacity expansion to first order for the statistical weighting function $\sigma(\omega)$:

$$\begin{aligned} \sigma(\omega) &= -\{f(\omega) \ln f(\omega) + [1 - f(\omega)] \ln[1 - f(\omega)]\} \\ &\sim -\{\beta(\omega - \mu)\gamma^{-1}e^{-\beta\omega} + \gamma^{-1}e^{-\beta\omega}\}. \end{aligned} \quad (\text{D.40})$$

Introducing this expansion into the quasi-particle expression for the entropy, one finds:

$$\frac{S}{A} \sim -\frac{\nu\gamma^{-1}}{\rho} \int \frac{d^3k}{(2\pi)^3} \{\beta[\varepsilon(k) - \mu]e^{-\beta\varepsilon(k)} + e^{-\beta\varepsilon(k)}\}, \quad (\text{D.41})$$

which, using Eqs. (D.34) and (D.37), is given by:

$$\frac{S}{A} = \frac{5}{2} - \ln \frac{\rho\lambda_{dB}^3}{\nu} + \frac{3}{2} \ln \frac{m^*}{m}. \quad (\text{D.42})$$

The entropy per particle depends logarithmically on the density and the temperature of the system. In addition, the interaction affects the entropy only via the effective mass, m^* , which in this case has to be taken as a momentum independent effective mass that parameterizes the quadratic dependence of the spectrum in k . In the degenerate regime, on the other hand, the entropy is given by the derivative of the quasi-particle spectrum close to the Fermi surface and, formally, there is no need for this spectrum to be quadratic. In contrast, in this case the quadratic dependence is necessary to obtain these analytical results.

Appendix E

Numerical implementation of the SCGF scheme

The implementation of the SCGF scheme is quite demanding from the numerical point of view. In this Appendix, the details associated to the numerical calculations which have been used in this Thesis will be explained. Following the scheme presented in Table 5.1, each of the different steps involved in the calculation will be reviewed. Complementary information on this numerical treatment can be found in Ref. [Fri04a].

Step 1

The starting point of the SCGF method is the initial guess of a spectral function. The very first calculation in the SCGF involved a spectral function obtained from a quasi-particle approach, which was extended to treat off-shell dependences [Fri04a]. Yet, once this first calculation was done, it was found that the results converged faster if one used as an initial guess the converged spectral function of a different density and temperature. With the knowledge of this spectral function, one can compute a chemical potential that matches the density at which the calculation is performed. To achieve this, one performs the momentum and energy integration of Eq. (3.47) for Fermi-Dirac distributions with different chemical potentials, $\tilde{\mu}$. Note that this is approximate, in the sense that one should also consistently change the chemical potential inside the spectral function. Since one does not a priori know the chemical potential dependence of \mathcal{A} , this is kept fixed. The iterative process will lead to a converged result in which the chemical potential of the spectral function matches the $\tilde{\mu}$ in $f(\omega)$.

Steps 2-5

Steps 2-5 are devoted to compute the angle averaged non-correlated two-body propagator, $\overline{\mathcal{G}}_{II}^0$. This function has an imaginary and a real part. The optimal

starting point to compute this object is Eq. (5.28). This gives $\text{Im } \mathcal{G}_{II}^0$ from a single ω -integral over two spectral functions. For a given momentum, these two spectral functions have very sharp peaks around their respective quasi-particle energies and thus the numerical integral can be hard to handle. In order to evaluate Eq. (5.28) conveniently, one can consider a change of variables in the integration variable, $\tilde{\omega} = \omega - \varepsilon_{qp}(k)$:

$$\text{Im } \mathcal{G}_{II}^0(\Omega; k, k') = -\frac{1}{2} \int_{-\infty}^{\infty} \frac{d\tilde{\omega}}{2\pi} \mathcal{A}(k, \tilde{\omega} + \varepsilon_{qp}(k)) \mathcal{A}(k', \Omega - \tilde{\omega} - \varepsilon_{qp}(k)) \times [1 - f(\tilde{\omega} + \varepsilon_{qp}(k)) - f(\Omega - \tilde{\omega} - \varepsilon_{qp}(k))]. \quad (\text{E.1})$$

Note that, with the help of this change of variables, the integrand is always peaked around $\tilde{\omega} = 0$ independently of the external momentum k . This is very useful in the construction of the integration meshes, which are easier to build thanks to the fact that they are independent of k . Instead of sampling the quasi-particle peak for each k , for instance, it is enough to sample in detail the region of $\tilde{\omega} \sim 0$. The same effect can indeed be obtained for the k' variable if one considers the change $\tilde{\Omega} = \Omega - \varepsilon_{qp}(k) - \varepsilon_{qp}(k')$. The integral then becomes:

$$\text{Im } \mathcal{G}_{II}^0(\tilde{\Omega}; k, k') = -\frac{1}{2} \int_{-\infty}^{\infty} \frac{d\tilde{\omega}}{2\pi} \mathcal{A}(k, \tilde{\omega} + \varepsilon_{qp}(k)) \mathcal{A}(k', \tilde{\Omega} - \tilde{\omega} + \varepsilon_{qp}(k')) \times [1 - f(\tilde{\omega} + \varepsilon_{qp}(k)) - f(\tilde{\Omega} + \varepsilon_{qp}(k') - \tilde{\omega})], \quad (\text{E.2})$$

and the integrand is peaked around $\tilde{\omega} = 0$ and $\tilde{\omega} = \tilde{\Omega}$, independently of k and k' . The region of $\tilde{\Omega} = 0$ corresponds to the energies in which there is a maximum overlap between the two spectral functions and thus yields the larger results for the integral. To see this clearly, consider the quasi-particle approximation to $\text{Im } \mathcal{G}_{II}$:

$$\text{Im } \mathcal{G}_{II}^0(\Omega; k, k') = -\pi \mathcal{Z}(k) \mathcal{Z}(k') [1 - f(\varepsilon_{qp}(k)) - f(\varepsilon_{qp}(k'))] \times \delta[\Omega - \varepsilon_{qp}(k) - \varepsilon_{qp}(k')], \quad (\text{E.3})$$

which is obtained by taking the no-width quasi-particle limit of Eq. (2.142) in the spectral functions of Eq. (5.28). In terms of the $\tilde{\Omega}$ variable, this function simplifies to the expression:

$$\text{Im } \mathcal{G}_{II}^0(\tilde{\Omega}; k, k') = -\pi \mathcal{Z}(k) \mathcal{Z}(k') [1 - f(\varepsilon_{qp}(k)) - f(\varepsilon_{qp}(k'))] \times \delta[\tilde{\Omega}], \quad (\text{E.4})$$

which is different from zero only at the value $\tilde{\Omega} = 0$, independently of the momenta. Thus, if one is able to build the function $\text{Im } \mathcal{G}_{II}^0(\tilde{\Omega}; k, k')$ by means of Eq. (E.2), it will be peaked around $\tilde{\Omega} = 0$. This is a useful property that can be used later on in the angle average procedure.

The procedure to obtain numerically \mathcal{G}_{II}^0 follows three steps. In the first one, for each of the external k and k' , one interpolates the integrand from the ω, Ω to the $\tilde{\omega}, \tilde{\Omega}$ variables, as already explained. The integrand being peaked around two

very concrete regions ($\tilde{\omega} \sim 0$ and $\tilde{\omega} \sim \tilde{\Omega}$), an accurately distributed mesh around those values is enough to perform the integral. In order to check the numerical accuracy, the sum rule of Eq. (5.30) can be used, since the right hand side is easily computed from the single-particle propagator. The meshes are adjusted to reproduce the sum rule within a 1% accuracy with k and k' up to 2000 MeV. As a final result, $\text{Im} \mathcal{G}_{II}^0$ is computed for a given distribution of $\tilde{\Omega}$'s and stored. The stored data is then used to perform the dispersion integral of Eq. (5.29), which allows one to obtain $\text{Re} \mathcal{G}_{II}^0$. This is a principal value integral and thus care must be taken in the integration procedure in order to treat properly the possible large cancellations. To this end, $N_{\tilde{\Omega}} = 120$ mesh points are distributed symmetrically around the pole $\Omega' = \Omega$. Note that since the momentum mesh has 70 points, this involves the calculation of $N_{\tilde{\Omega}} \times N_k \times N_{k'} \sim 6 \times 10^5$ integrals.

Once the real and the imaginary parts of \mathcal{G}_{II}^0 are obtained, one can proceed to perform, for every energy Ω , the angle average procedure in the angle between $\mathbf{K} = \mathbf{k} + \mathbf{k}'$ and $\mathbf{k}_r = (\mathbf{k} - \mathbf{k}')/2$. \mathcal{G}_{II}^0 is indeed easily reexpressed in terms of this angle:

$$\begin{aligned} \mathcal{G}_{II}^0(\tilde{\Omega}; k, k') &= \mathcal{G}_{II}^0(\tilde{\Omega}; |\mathbf{K}/2 + \mathbf{k}_r|, |\mathbf{K}/2 - \mathbf{k}_r|) \\ &= \mathcal{G}_{II}^0(\tilde{\Omega}; \sqrt{K^2/4 + k_r^2} + Kk_r \cos \theta, \sqrt{K^2/4 + k_r^2} - Kk_r \cos \theta). \end{aligned} \quad (\text{E.5})$$

Interpolating the initial \mathcal{G}_{II}^0 to the values given by the square roots above, one obtains a set of values for $\mathcal{G}_{II}^0(\tilde{\Omega}; K, k_r, \theta)$. The angle average is then performed for every K and k_r by means of a simple trapezoidal rule in the θ variable. This is the third and last step to obtain numerically the angle-averaged propagator of two dressed independent particles, $\overline{\mathcal{G}_{II}^0}$. This will now be a basic ingredient in the solution of the Lippman-Schwinger equation.

Step 5

The Lippman-Schwinger equation for the T -matrix is a one dimensional integral equation for each allowed combination of $\alpha = (J, S, T)$. For a given α , there can be at most $N_c = 2$ coupled L partial waves, due to the tensor component of the NN interaction. To begin with, let us discretize the momentum q_r in the integral of Eq. (5.37), which then becomes the sum:

$$\int_0^\infty dq_r h(q_r) \rightarrow \sum_{n=1}^{N_I} u_n h(q_n). \quad (\text{E.6})$$

The N_I momenta q_n at which the integrand of Eq. (5.37) is computed as well as their corresponding integration weights u_n , are chosen to optimize the accuracy in the integral. In addition, one usually discretizes the external momenta, $k_r \rightarrow k_m$.

All in all, the Lippman-Schwinger equation in its discretized form reads:

$$\begin{aligned} \langle k_m | T_{LL'}^\alpha(\Omega_+, K) | p_r \rangle &= \langle k_m | V_{LL'}^\alpha | p_r \rangle \\ &+ \sum_{L''} \sum_{n=1}^{N_I} q_n^2 u_n \langle k_m | V_{LL''}^\alpha | q_n \rangle \overline{\mathcal{G}_{II}^0}(\Omega_+; K, q_n) \langle q_n | T_{L''L'}^\alpha(\Omega_+, K) | p_r \rangle. \end{aligned} \quad (\text{E.7})$$

If the discrete momenta k_m and q_n are chosen to be the same, the previous discretized equation can be rewritten as:

$$\begin{aligned} \langle k_m | V_{LL'}^\alpha | p_r \rangle &= \sum_{L''} \sum_{n=1}^{N_I} \left[\delta_{mn} \delta_{LL''} - u_n q_n^2 \langle k_m | V_{LL''}^\alpha | q_n \rangle \overline{\mathcal{G}_{II}^0}(\Omega_+; K, q_n) \right] \\ &\times \langle q_n | T_{L''L'}^\alpha(\Omega_+, K) | p_r \rangle. \end{aligned} \quad (\text{E.8})$$

To understand better the structure of this expression, let us consider a channel α such that there is no transition between different angular momenta, $L = L'$. Discretizing the remaining momentum p_r in a mesh, p_s , of N_p points, one obtains the following equation:

$$\mathbb{V}_{mL, sL}^\alpha = \sum_{n=1}^{N_I} \mathbb{M}_{mL, nL}^\alpha(\Omega_+, K) \mathbb{T}_{nL, sL}^\alpha(\Omega_+, K), \quad (\text{E.9})$$

where the $N_I \times N_p$ matrices

$$\mathbb{V}_{mL, sL}^\alpha = \langle k_m | V_{LL}^\alpha | p_s \rangle, \quad (\text{E.10})$$

$$\mathbb{T}_{nL, sL}^\alpha(\Omega_+, K) = \langle q_n | T_{LL}^\alpha(\Omega_+, K) | p_s \rangle, \quad (\text{E.11})$$

as well as the $N_I \times N_I$ matrix

$$\mathbb{M}_{mL, nL}^\alpha(\Omega_+, K) = \delta_{mn} - \langle k_m | V_{LL}^\alpha | q_n \rangle \overline{\mathcal{G}_{II}^0}(\Omega_+; K, q_n) u_n q_n^2, \quad (\text{E.12})$$

have been introduced. It is clear that Eq. (E.9) defines the product of the \mathbb{M} and \mathbb{T} matrices. Thus, by means of the discretization procedure, the one dimensional Lippman-Schwinger equation for the T -matrix has been converted into a complex matrix equation. This can be solved by means of standard numerical techniques, simply inverting the \mathbb{M} -matrix to yield:

$$\mathbb{T}^\alpha(\Omega_+, K) = [\mathbb{M}^\alpha(\Omega_+, K)]^{-1} \cdot \mathbb{V}^\alpha. \quad (\text{E.13})$$

Up to here only diagonal terms in L have been treated. When the coupling between different partial waves acts, the philosophy is essentially the same and the T -matrix equation can also be treated in a matricial form:

$$\begin{pmatrix} \mathbb{V}_{mL, sL}^\alpha & \mathbb{V}_{mL, sL'}^\alpha \\ \mathbb{V}_{mL', sL}^\alpha & \mathbb{V}_{mL', sL'}^\alpha \end{pmatrix} = \sum_n \begin{pmatrix} \mathbb{M}_{mL, nL}^\alpha & \mathbb{M}_{mL, nL'}^\alpha \\ \mathbb{V}_{mL', nL}^\alpha & \mathbb{M}_{mL', nL'}^\alpha \end{pmatrix} \cdot \begin{pmatrix} \mathbb{T}_{nL, sL}^\alpha & \mathbb{T}_{nL, sL'}^\alpha \\ \mathbb{T}_{nL', sL}^\alpha & \mathbb{T}_{nL', sL'}^\alpha \end{pmatrix}$$

This suggests the introduction of the multi-indices $M = (m, L)$, $N = (n, L)$ and $S = (s, L)$, which characterize the $N_c N_I \times N_c N_p$ matrices:

$$\mathbb{V}_{MS}^\alpha = \langle k_m | V_{LL'}^\alpha | p_s \rangle, \quad (\text{E.14})$$

$$\mathbb{T}_{NS}^\alpha(\Omega_+, K) = \langle q_n | T_{LL'}^\alpha(\Omega_+, K) | p_s \rangle, \quad (\text{E.15})$$

as well as the square $N_c N_I \times N_c N_I$ matrix:

$$\mathbb{M}_{MN}^\alpha(\Omega_+, K) = \delta_{MN} - \langle k_m | V_{LL'}^\alpha | q_n \rangle \overline{\mathcal{G}_{II}^0}(\Omega_+; K, q_n) u_n q_n^2. \quad (\text{E.16})$$

With these matrices in hand, Eq. (E.8) is easily rewritten as:

$$\mathbb{V}_{MS}^\alpha = \sum_{N=1}^{N_c \times N_I} \mathbb{M}_{MN}^\alpha(\Omega_+, K) \mathbb{T}_{NS}^\alpha(\Omega_+, K), \quad (\text{E.17})$$

and the final solution for the T -matrix is again given by the inversion:

$$\mathbb{T}^\alpha(\Omega_+, K) = [\mathbb{M}^\alpha(\Omega_+, K)]^{-1} \cdot \mathbb{V}^\alpha. \quad (\text{E.18})$$

Note, however, that the matrices are in this case N_c times larger than in the non-coupled case.

The inversion of the complex square \mathbb{M} matrix can be a time-consuming task if its number of columns is very large. Therefore one should try to minimize the number of integration mesh points, N_I , without losing physical information. In the case of the non-correlated two-particle propagator, for a fixed external total energy and center-of-mass momentum, one has to sample correctly both the region around q_0 , where \mathcal{G}_{II}^0 is maximal due to the overlap of spectral functions, as well as the high (relative) momentum region, where \mathcal{G}_{II}^0 might not be negligible due to correlation effects. This is achieved by defining an intermediate momentum q_X , below which one always finds q_0 and above which one has the high-momentum region. In the interval $[0, q_X]$, different sets of Gauss-Legendre mesh points and weights are defined to correctly sample the structures in \mathcal{G}_{II}^0 . Around the quasi-particle peak q_0 , the integrand varies rapidly. In this zone, a especially dense mesh of points is applied, in a symmetric way above and below q_0 in order to favor any possible cancellation of contributions with opposite sign. For the interval $[q_X, \infty]$, a tangential map is used. In this way, the interval $[q_X, \infty]$ is mapped into a finite interval by means of the transformation:

$$q_j = q_X + c \tan\left(\frac{\pi}{2} x_j\right), \quad (\text{E.19})$$

where x_j are Gauss-Legendre mesh points in the $[0, 1]$ interval and where c is chosen to give an adequate sampling of the high momentum region, up to where the potential is suppressed by its natural cut-off. The integration weights w_j

J	S	T	Channel	N_c
0	0	1	1S_0	1
0	1	1	3P_0	1
1	0	0	1P_1	1
1	1	0	$^3S_1 - ^3D_1$	2
1	1	1	3P_1	1
2	0	1	1D_2	1
2	1	0	3D_2	1
2	1	1	$^3P_2 - ^3F_2$	2

Table E.1: *Quantum numbers of the NN interaction channels up to $J = 2$. Only the values that fulfill the antisymmetry constrain $L + S + T = \text{odd}$ are considered.*

of the original Gauss-Legendre mesh have to be transformed, accordingly to the tangential map:

$$u_j = c \frac{\frac{\pi}{2} w_j}{\cos^2\left(\frac{\pi}{2} x_j\right)}. \quad (\text{E.20})$$

With this transform, the $[q_X, \infty]$ region is well sampled and the integral yields faithful results. The actual calculations are performed with $N_I = 50$ mesh points, 14 of which are in the $[q_X, \infty]$ region. The T -matrix is computed on an external three-dimensional mesh formed by the total pair energies Ω (sampled with $N_\Omega = 80$ points), the center-of-mass momenta P ($N_P = 30$) and the relative momenta p_r ($N_p = 30$). Since \mathbb{M} does not depend explicitly on p_r , this $N_c N_I \times N_c N_I$ matrix is inverted $N_{MI} = N_\Omega \times N_P \times N_\alpha$ times, with N_α the number of (JST) partial waves that are chosen in the calculation. In this case, waves up to $J = 2$ have been chosen for the inversion procedure, which yields a total of $N_\alpha = 10$ (see Table E.1). Thus, in the program, the complex 50×50 (or 100×100 , depending on whether $N_c = 1$ or 2) \mathbb{M} -matrix is inverted $N_{MI} = 12000$ times. Not surprisingly, this is the more time-consuming task in the SCGF program.

A nice property of the SCGF scheme is that there is no need to worry about poles in the inversion of the T -matrix. In other descriptions of nuclear matter, the equivalent equations for the in-medium interaction have integrands which may contain poles. These have to be treated somehow, generally by means of the pole subtraction technique introduced in Ref. [Haf70]. In the SCGF scheme this is not necessary, because the integrand remains finite for all energies and momenta in the normal phase. There is however a pole in the bosonic function that is canceled by a node of the T -matrix. The accurate treatment of this cancellation requires a careful construction of the N_Ω mesh points for the Ω variable in the inversion procedure, especially around the values $\Omega \sim 2\mu$.

Moreover, it has already been mentioned that for low temperatures the T -matrix acquires a pole in the $P = 0$ and $\Omega = 2\mu$ region, where the pairing instability appears. In terms of the equations here presented, the pole in the T -matrix would be directly reflected into the \mathbb{M} -matrix [Alm93; Dew02]. The Thouless criterion for the onset of superconductivity states that, for a given density and decreasing the temperature, the critical temperature T_C for the onset of pairing is the one at which, for any channel α , the following condition is fulfilled:

$$\det [\mathbb{M}^\alpha(\Omega = 2\mu, P = 0)] = 0. \quad (\text{E.21})$$

In symmetric nuclear matter around saturation density, the largest gaps are usually found for neutron-proton pairing in the channel ${}^3S_1 - {}^3D_1$ [Dea03]. Within a quasiparticle approach, the corresponding critical temperatures depend strongly on the many-body approach which is used to describe pairing correlations. It is however believed that the critical temperature lies in the range $T_c \sim 5$ MeV.

Steps 6-8

The remaining steps in SCGF approach have to do with the computation of the self-energy from the T -matrix. The more difficult step from the numerical point of view is the computation of the imaginary part of Σ_L from Eq. (5.50). For a fixed external momentum k and energy ω , one has to integrate over k' , thus defining several center-of-mass, P , and relative momenta, q . The energy integral is also somewhat tricky, because of the pole in the Bose function. Even though this is canceled by the node in $\text{Im} T$, one has to take care of it numerically. Once again, a symmetric mesh is defined around the pole to evaluate correctly the possible cancellations. This mesh of $N_\omega = 1000$ points is used for the energy integral, while the integration over momenta is performed with $N_{k'} = 80$ points linearly distributed between 0 and $4k_F$, as well as with $N_\theta = 40$ points for the angle integration over the internal momentum k' . With these meshes one can carry out accurately the integration of Eq. (5.50) for a wide range of densities and temperatures. The relative importance of each of the contributions to the integrand (\mathcal{A} , $\text{Im} T$ and the phase space factor $[f + b]$) is discussed in length in [Fri04a].

The real part of the self-energy is easily computed from this imaginary part via Eq. (5.29). The generalized Hartree-Fock contribution can be directly calculated by means of Eq. (5.42). The momentum distribution entering this equation, however, is computed from the spectral function by means of the energy integral of Eq. (2.72). The remaining momentum integral is easily performed by means of, for instance, a trapezoidal rule. The principal part integral of Eq. (5.29) is performed as already explained above, with a symmetric mesh around the pole at $\lambda = \omega$. Note that the high energy region, where $\text{Im} \Sigma$ is non-negligible, must also be treated. This is achieved by splitting the integration variable in two different

regions, one of them sampling the quasi-particle structures and the remaining one covering the high and low energy structures in $\text{Re}\Sigma$.

Once the self-consistent self-energy is obtained, it can be interpolated to the momentum and energy meshes which are needed in order to build the corresponding spectral function by means of Eq. (2.130). It is very important to interpolate the smooth $\text{Im}\Sigma$ and $\text{Re}\Sigma$ functions. If the interpolation was performed on the spectral function, one could sample incorrectly the strong peaks and structures of the spectral function and thus introduce an important source of numerical inaccuracies. Note that, once again, the energy mesh has to be accurate enough to reproduce correctly at the same time the intermediate energy region, where the quasi-particle peak lies, as well as the high and low-energy tails of \mathcal{A} . This simultaneous sampling is vital for the resolution of the SCGF procedure and it is probably the largest source of difficulties in its numerical implementation.

Resum en català

El problema nuclear de molts cossos

La mecànica quàntica de molts cossos intenta descriure les propietats dels sistemes quàntics formats per un gran nombre de partícules. Des dels propis àtoms (que són sistemes formats per molts electrons) fins als nuclis atòmics, molts dels sistemes que ens envolten són sistemes de molts cossos que podem descriure mitjançant aquesta teoria. El rang d'aplicacions de la mecànica quàntica de molts cossos és, doncs, molt ampli. D'entre els problemes que la disciplina s'ha plantejat en la seva història, el problema nuclear de molts cossos destaca tant per la seva dificultat com pel seu interès pràctic. La descripció dels nuclis atòmics en termes dels seus constituents bàsics (neutrons i protons) i de la interacció fonamental que els lliga és clarament un problema interessant des del punt de vista teòric que, a més, gràcies a l'ampli nombre d'aplicacions de la física nuclear, podria tenir un cert ressò en el camp de la física aplicada. Malauradament, hi ha factors que dificulten la resolució d'aquest problema. Entre ells, potser les complicacions que sorgeixen en estudiar les correlacions induïdes per la interacció en sistemes finits són les més importants. És per això que el problema nuclear de molts cossos s'acostuma a formular en termes de la matèria nuclear, un sistema infinit compost per nucleons en què es negligeix la interacció electromagnètica entre els protons. Gràcies a aquesta simplificació, podem estalviar-nos el tràngol d'haver de trobar les funcions d'ona mono-particulars (que per un sistema infinit són simples ones planes) i estudiar directament l'efecte de les correlacions que la interacció nucleó-nucleó (NN) indueix sobre la funció d'ona de molts cossos d'un sistema infinit.

A diferència d'altres sistemes, en què la força que actua entre les partícules és coneguda *a priori*, la informació que es té sobre la interacció NN és relativament limitada. L'estudi experimental de reaccions de dos nucleons (dispersió protó-protó o neutró-protó) ens permet conèixer els desfasaments per un cert rang d'energies (és a dir, per un cert rang de distàncies relatives) en diferents ones parcials. Gràcies a aquestes dades, per exemple, podem arribar a deduir que la interacció NN a curtes distàncies és fortament repulsiva. Els desfasaments també ens informen de l'atracció a distàncies intermèdies que, en última instància, és la responsable del lligam dels nuclis finits [Rin80]. D'altra banda, les propietats del deuteró, l'únic estat lligat de dos nucleons, permeten obtenir informació sobre

les característiques d'aquesta interacció. El seu moment quadrupolar no nul, per exemple, només pot explicar-se en termes d'una component tensorial, que acobla funcions d'ona amb diferents moment angulars [Eis72]. Hom pot aconseguir una descripció molt acurada d'aquestes propietats mitjançant els anomenats potencials NN microscòpics. De forces microscòpiques de caràcter teòric n'hi ha de diferents tipus, des d'ajustos que intenten contenir tot el caràcter operatorial de la força en l'espai d'espín-isospín fins a models basats en teories efectives. En aquesta tesi s'ha emprat el potencial de CDBONN, que descriu la interacció NN mitjançant un model de bescanvi de mesons. Aquests actuen com a portadors de la interacció forta i, segons llurs propietats físiques, descriuen una característica o altra del potencial (el mesó ω és responsable de la repulsió a curtes distàncies, el pió de les components de llarg abast, etc.). Les propietats d'aquests mesons així com els seus acoblaments amb els nucleons s'ajusten generalment a les dades experimentals (desfasaments, energia de lligam del deuteró, etc.) i d'aquesta manera s'aconsegueixen interaccions que reproduïxen amb molta exactitud les propietats físiques dels sistemes de dos nucleons.

Un cop aconseguida aquesta descripció quantitativa, els potencials NN microscòpics es poden emprar com a punt de partida per a càlculs de molts cossos. En particular, el problema nuclear de molts cossos permet posar a prova tant les propietats d'aquestes interaccions com la qualitat de les aproximacions que necessàriament cal introduir en el tractament de les correlacions a molts cossos. Però, quines són exactament les propietats que volem reproduir si, com hem dit, la matèria nuclear és un sistema fictici? Doncs bé, les propietats de la matèria nuclear les podem deduir gràcies a l'extrapolació de les propietats dels nuclis finits a la matèria infinita. La fórmula semiempírica de masses, per exemple, reproduïx qualitativament l'energia de lligam d'un nucli amb N neutrons i Z protons prop de la vall d'estabilitat [Rin80]:

$$B(N, Z) = a_V A + a_S A^{2/3} + a_C \frac{Z^2}{A^{1/3}} + a_I \frac{(N - Z)^2}{A} - \delta(A). \quad (1)$$

Aquesta fórmula permet trobar l'energia per partícula d'un sistema nuclear infinit amb el mateix nombre de neutrons i protons (el que anomenem matèria nuclear *simètrica*, per distingir-la de la matèria *asimètrica*, que pot tenir $N \neq Z$) en el límit:

$$\lim_{A \rightarrow \infty} \frac{B(N, Z)}{A} = a_V \sim 16 \text{ MeV}. \quad (2)$$

A més d'aquesta energia de lligam, podem extrapolar altres propietats de nuclis finits a la matèria nuclear. La densitat central dels nuclis pesats, per exemple, és relativament constant i és fàcil extrapolar-la a $A \rightarrow \infty$, on s'obté el valor $\rho_0 = 0.16 \text{ fm}^{-3}$. D'aquesta manera, qualsevol càlcul *ab initio* que vulgui descriure les propietats de la matèria nuclear hauria de reproduir aquest punt empíric de saturació o, en altres paraules, hauria de presentar un mínim de l'energia per

partícula amb una energia de lligam per partícula de -16 MeV a una densitat de 0.16 fm^{-3} .

Tot i que la formulació del problema nuclear de molts cossos és relativament simple (emprar un potencial NN a dos cossos, aplicar-lo a un sistema infinit, trobar la funció d'ona de molts cossos corresponent i reproduir el punt empíric de saturació), podem dir que encara som lluny de resoldre'l. El problema és essencialment degut al caràcter de la interacció NN, que té una estructura operatorial molt rica i una forta repulsió a curtes distància. Ambdues propietats modifiquen substancialment la funció d'ona de molts cossos, que ha de reflexar tant les diferències entre les diferents components en ones parcials com el fet que és energèticament improbable trobar dos nucleons prop l'un de l'altre [Müt00]. El tractament del problema és necessàriament molt sofisticat i és per això que, en la llarga evolució de la física nuclear de molts cossos, s'han fet servir nombroses aproximacions, sovint molt diferents entre elles, per intentar resoldre'l.

D'aquestes aproximacions, n'hi ha de relativament simples, com les de camp mig, que tenen un caràcter fenomenològic i intenten reproduir les propietats de la matèria nuclear en un ampli rang de densitats i isospins mitjançant un ajust de les seves propietats a prop de la saturació. Tot i l'èxit de què gaudeixen, gràcies sobretot a la seva simplicitat i a l'aplicabilitat en càlculs de nuclis finits, les aproximacions de camp mig no són una solució al problema nuclear de molts cossos perquè no poden considerar-se càlculs *ab initio*. Tanmateix, existeixen una gran quantitat de mètodes i tècniques que intenten resoldre el problema nuclear des de la seva base. Alguns d'ells proven de reproduir la funció d'ona de molts cossos de la matèria nuclear, generalment mitjançant els anomenats factors de Jastrow que codifiquen l'efecte de les correlacions. En general, aquests factors tenen una certa dependència funcional que s'intenta ajustar mitjançant una minimització de l'energia per partícula del sistema i, en aquest sentit, es pot dir que són càlculs variacionals. Per calcular l'energia de l'estat fonamental, cal desenvolupar tècniques especials, com ara les de Fermi hypernetted chain [Fan75] o càlculs Monte-Carlo en què es mostreja tot l'espai d'espín-isospín.

D'altra banda, es poden formular aproximacions que no busquen reproduir la funció d'ona, sinó altres quantitats microscòpiques del sistema. En una aproximació diagramàtica, per exemple, s'expandeix l'energia per partícula o el propagador en termes de diagrames de Feynman [Mat92]. Generalment es necessiten infinits diagrames per obtenir resultat físicament correctes. Així doncs, s'han de trobar maneres per sumar sèries infinites dels diagrames físicament més rellevants. En general, aquestes sumes infinites poden calcular-se mitjançant la introducció d'interaccions efectives, que tenen en compte la renormalització que el medi nuclear genera en la interacció NN de l'espai lliure. Entre aquestes aproximacions diagramàtiques, potser la més important pel problema nuclear és l'anomenada aproximació de Brueckner-Hartree-Fock (BHF) [Bru54; Day67], que es basa en l'expansió de Goldstone de l'energia per partícula d'un sistema de molts cossos

en termes de diagrames de Feynman [Gol57]. Si en aquesta expansió es tenen en compte un cert tipus de diagrames, es pot definir una interacció efectiva, la matriu G , que inclou els efectes del medi nuclear. Un cop obtinguda, podem calcular l'energia per partícula en una expansió ben definida que té en compte el nombre de forats (estats per sota del moment de Fermi) que apareixen en cada diagrama. L'aproximació a ordre més baix d'aquesta expansió en el nombre de forats és precisament el que es coneix com a aproximació BHF. Tot i que a partir d'interaccions NN microscòpiques l'aproximació de BHF no dona resultats quantitativament correctes pel punt de saturació empíric de la matèria nuclear, el comportament que se n'obté és qualitativament correcte [Müt00].

L'aproximació diagramàtica utilitzada en aquesta tesi, però, no es basa en una expansió de l'energia per partícula, sinó en l'expansió pertorbativa del propagador (o funció de Green) a un cos. Mitjançant aquesta expansió, es pot representar el propagador a un cos d'un sistema interactuant en termes de diagrames que només inclouen propagadors lliures a un cos i interaccions a dos cossos (veieu Apèndix A). En el mètode de les funcions de Green, doncs, s'aproxima el propagador mitjançant una suma infinita de diagrames que inclouen les correlacions més adequades pel sistema que s'estudia. Com que totes les partícules del sistema vénen descrites en termes de funcions de Green i la propagació d'una d'aquestes partícules es veu afectada i alhora afecta el medi circumdant, el mètode de les funcions de Green és necessàriament autoconsistent. És precisament per això que s'anomena mètode de les Funcions de Green Autoconsistentes (Self-Consistent Green's Function o SCGF en el seu acrònim anglès). Una aproximació que reproduïx correctament les correlacions a dos cossos del sistema nuclear és l'aproximació d'escala, que suma una sèrie infinita de diagrames amb aspecte d'"escala" (d'aquí el seu nom), en què es té en compte la interacció successiva de dos nucleons dins del sistema [Dic05a]. Aquesta interacció successiva es pot tenir en compte mitjançant la definició d'una interacció efectiva, la matriu T , que va una mica més enllà que la matriu G del mètode de BHF perquè inclou, a més de les correlacions partícula-partícula, les correlacions de tipus forat-forat.

Malauradament, la descripció de la matèria nuclear mitjançant el mètode de les SCGF a temperatura nul·la comporta una complicació addicional. En qualsevol sistema fermiònic amb una interacció atractiva es generen, a prou baixes temperatures, parells de Cooper que estan fortament lligats. La descripció d'aquests parells no es pot dur a terme en el marc l'expansió pertorbativa del propagador i l'aproximació de SCGF, doncs, no pot descriure el sistema en el rang de densitats en què l'aparellament és present. El fenomen d'aparellament depèn fortament de la temperatura, de manera que per sobre d'una certa temperatura crítica els fermions deixen d'aparellar-se. Independentment d'aquest fet, hi ha sistemes formats per nucleons a la natura en què les temperatures són prou altes com per ser comparables amb les escales d'energia associades a la interacció forta. Els protoestels de neutrons, per exemple, es poden trobar a les fases finals d'una supernova de

tipus II i, en els seus primers instants de vida, tenen temperatures prou altes, que poden arribar a la desena de MeV [Pra97]. De la mateixa manera, a l'interior de les col·lisions d'ions pesats a energies intermèdies s'hi formen fragments de matèria hadrònica a alta densitat i temperatura [Cse86]. Tant per descriure aquests sistemes com per evitar el problema de l'aparellament en matèria nuclear, la teoria de les Funcions de Green Autoconsistents s'ha estès a temperatura finita [Kra86] i s'ha aplicat amb èxit a l'estudi de la matèria nuclear [Fri04a].

La teoria de les funcions de Green té com a objectiu descriure les propietats microscòpiques del sistema. En termes de propagadors podem estudiar, per exemple, les excitacions del sistema nuclear, tant de natura mono-particular com de natura col·lectiva, la seva distribució de moments o l'autoenergia (l'energia potencial d'interacció associada a la presència de la resta de partícules del sistema). De fet, a partir de la funció de Green a un cos podem calcular qualsevol quantitat de caràcter mono-particular del sistema [Fet71]. La regla de suma de Galitskii-Migdal-Koltun (GMK), a més, ens permet conèixer l'energia per partícula del sistema a partir del propagador a un cos. Ara bé, un sistema a temperatura finita es regeix per les lleis de la termodinàmica i el seu estat d'equilibri ve dictat per la minimització del potencial termodinàmic corresponent. En el cas d'un sistema a temperatura i densitat fixat, aquest potencial és l'energia lliure i és aquesta quantitat macroscòpica que caldria calcular per trobar l'estat d'equilibri del sistema. Un dels objectius principals d'aquesta tesi ha estat precisament construir un pont entre les propietats microscòpiques del sistema, descrites en termes de funcions de Green, i les seves propietats termodinàmiques. L'enllaç entre les dues escales és possible gràcies al formalisme de Luttinger-Ward. Abans d'introduir aquest formalisme, tanmateix, val la pena descriure succintament algunes de les propietats de les funcions de Green a temperatura finita.

Funcions de Green de molts cossos a temperatura finita

En la mecànica estadística quàntica, els observables són el resultat d'un promig sobre estats propis amb diferents energies i nombre de partícules, pesats pel seu factor de Boltzmann corresponent, $e^{-\beta(E_i - \mu N_i)}$, on β representa l'invers de la temperatura i μ el potencial químic. La funció de Green a un cos a temperatura finita ve donada precisament pel promig estadístic d'una operació de creació $\hat{a}^\dagger(\mathbf{r}, t)$ i una operació de destrucció $\hat{a}(\mathbf{r}, t)$ ordenats temporalment mitjançant l'operador de Wick \mathcal{T} (que introdueix un signe menys si la permutació que representa és senar):

$$i\mathcal{G}(\mathbf{r}t, \mathbf{r}'t') = \text{Tr} \left\{ \hat{\rho} \mathcal{T} [\hat{a}(\mathbf{r}t) \hat{a}^\dagger(\mathbf{r}'t')] \right\}. \quad (3)$$

De la mateixa manera, es poden definir les anomenades funcions de correlació, que representen promitjos estadístics d'operadors de creació i destrucció sense cap

ordenació temporal específica:

$$i\mathcal{G}^>(\mathbf{r}t, \mathbf{r}'t') = \text{Tr} \left\{ \hat{\rho} \hat{a}(\mathbf{r}t) \hat{a}^\dagger(\mathbf{r}'t') \right\} \quad (4)$$

$$i\mathcal{G}^<(\mathbf{r}t, \mathbf{r}'t') = -\text{Tr} \left\{ \hat{\rho} \hat{a}^\dagger(\mathbf{r}'t') \hat{a}(\mathbf{r}t) \right\}. \quad (5)$$

Cadascuna d'aquestes funcions és igual al propagador en l'interval $t > t'$ o $t < t'$, segons el seu respectiu super-índex, $>$ o $<$. L'evolució temporal dels operadors de creació i destrucció ve donada, en imatge de Heisenberg, per la següent equació:

$$\hat{a}(\mathbf{r}t) = e^{i\hat{H}t} \hat{a}(\mathbf{r}0) e^{-i\hat{H}t}. \quad (6)$$

L'operador d'evolució temporal s'assembla precisament al factor de Boltzmann, a què es redueix (excepte el terme amb potencial químic) en el temps imaginari $t = -i\beta$. La generalització a temps complexos, tot i que pugui semblar artificial a primera vista, és especialment útil en el camp de la física de molts cossos a temperatura finita, ja que permet obtenir una colla de resultats interessants de manera relativament simple. D'entre aquests resultats, cal destacar la relació de Kubo-Martin-Schwinger, que relaciona les funcions de correlació en espai de freqüències d'un sistema en equilibri tèrmic:

$$\mathcal{G}^<(k, \omega) = e^{-\beta(\omega - \mu)} \mathcal{G}^>(k, \omega). \quad (7)$$

Aquesta relació ve donada per freqüències físiques (és a dir, freqüències reals), però la introducció de temps complexos comporta igualment un tractament en termes de freqüències complexes. En termes d'aquesta variable complexa, la descomposició espectral del propagador s'expressa:

$$\mathcal{G}(k, z_\nu) = \int_{-\infty}^{\infty} \frac{d\omega}{2\pi} \frac{\mathcal{A}(k, \omega)}{z_\nu - \omega}, \quad (8)$$

on z_ν correspon a un conjunt infinit però discret de freqüències de Matsubara i on $\mathcal{A}(k, \omega)$ és la funció espectral associada al propagador a un cos. La continuació analítica d'aquesta quantitat és ben definida i el propagador retardat s'obté, per exemple, en el límit $z_\nu \rightarrow \omega' + i\eta$. D'aquesta manera, es pot demostrar que un cop determinada la funció espectral, totes les propietats del propagador a un cos queden fixades a través de l'Eq. (8). La funció espectral és important, doncs, perquè determina el propagador i, per tant, totes les propietats a un cos del sistema [Fet71]. Una altra propietat interessant d'aquesta funció sorgeix de la representació de Lehmann del propagador, que ens permet escriure-la de la següent manera:

$$\mathcal{A}(k, \omega) = 2\pi \sum_{n,m} \frac{e^{-\beta(E_n - \mu N_n)} + e^{-\beta(E_m - \mu N_m)}}{Z} |\langle m | \hat{a}_{\mathbf{k}}^\dagger | n \rangle|^2 \delta[\omega - (E_m - E_n)]. \quad (9)$$

Escrita d'aquesta manera, veiem que la funció $\frac{\mathcal{A}(k, \omega)}{2\pi} d\omega$ dona la probabilitat d'afegir o extreure una partícula de moment k del sistema a través de l'extracció o de

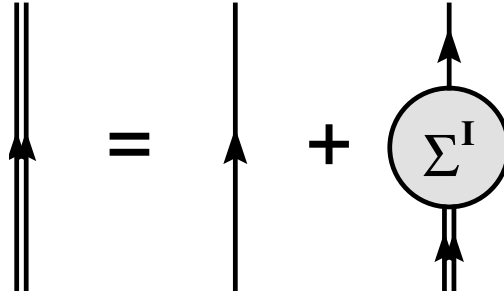


Figura 1: Representació diagramàtica de l'equació de Dyson.

l'aportació d'una energia entre ω i $\omega + d\omega$. El fet que la funció espectral compleix una regla de suma, que en defineix la normalització, recolza aquesta visió probabilística.

Els resultats que hem obtingut fins aquí no depenen de detalls particulars del sistema. No hem considerat en cap moment, per exemple, els efectes de la interacció. A nivell del propagador, tota la informació sobre la interacció del sistema queda reduïda a l'operador d'autoenergia, Σ , que està relacionat amb la funció de Green a un cos mitjançant l'equació de Dyson en espai de moments i de freqüències:

$$\mathcal{G}(k, z) = \frac{1}{z - \frac{k^2}{2m} - \Sigma(k, \omega)}. \quad (10)$$

La representació diagramàtica d'aquesta expressió es reproduïx a la Fig. 1, on la línia doble representa un propagador vestit (interactuant) i la línia simple en representa un de simple. La iteració d'aquesta equació permet obtenir el propagador vestit com una suma infinita de peces d'autoenergia i de propagadors lliures intermedis. L'autoenergia que s'ha d'incloure en aquesta suma té, però, la particularitat de ser irreduïble a un cos, *i.e.* els diagrames que la representen no s'han de poder dividir en dues parts quan es talla alguna de llurs línies fermiòniques. D'aquesta manera, podem trobar totes les propietats del propagador a un cos d'un sistema interactuant a partir de l'autoenergia Σ , en particular, la funció espectral s'obté de l'equació següent:

$$\mathcal{A}(k, \omega) = \frac{-2\text{Im } \Sigma(k, \omega)}{[\omega - \frac{k^2}{2m} - \text{Re } \Sigma(k, \omega)]^2 + [\text{Im } \Sigma(k, \omega)]^2}. \quad (11)$$

En general, les aproximacions en mecànica quàntica de molts cossos es defineixen a partir d'aproximacions a l'autoenergia, que s'expressa en termes de la interacció i del propagador vestit. En conseqüència, les equacions que defineixen una aproximació de molts cossos han de ser autoconsistents, ja que el propagador i l'autoenergia es defineixen l'un a partir de l'altre. L'exigència d'autoconsistència

en l'aproximació té, a més, certa importància a nivell diagramàtic, ja que permet sumar una nova sèrie de diagrames en què els propagadors intermedis de l'aproximació queden vestits per insercions d'autoenergia. Aquesta suma addicional de diagrames permet, a més, obtenir resultats més realistes i justifica d'alguna manera l'extensió del formalisme a densitats més altes.

Formalisme de Luttinger-Ward

Ja hem comentat que, a partir del propagador a un cos, podem obtenir totes les propietats mono-particulars d'un sistema de fermions interactuants [Fet71]. Aquest teorema ben conegut és vàlid també a temperatura finita, però no ens ajuda, per exemple, a entendre les propietats termodinàmiques del sistema. Per un sistema a temperatura i potencial químic fix, el potencial termodinàmic corresponent és el gran-potencial. S'han formulat diferents tècniques destinades a calcular el gran-potencial a partir de les propietats microscòpiques del sistema [Abr65; Fet71; Neg88]. Potser la més coneguda d'elles és el mètode de la constant d'acoblament, en què el hamiltonià es divideix en un terme senzill de tractar, \hat{H}_0 , més un terme, $\lambda\hat{H}_1$, que generalment inclou la contribució de la interacció. Per $\lambda = 1$, doncs, recuperem el hamiltonià complet del sistema. El gran-potencial associat al sistema interactuant, Ω , es pot calcular a partir del gran-potencial del sistema simple, Ω_0 , més una integral del propagador i l'autoenergia de sistemes amb constants d'acoblament variables:

$$\Omega = \Omega_0 + \frac{1}{2\beta} \int_0^1 \frac{d\lambda}{\lambda} \widetilde{\text{Tr}} \Sigma_\lambda \mathcal{G}_\lambda, \quad (12)$$

on la traça $\widetilde{\text{Tr}}$ representa una suma sobre tots els moments i energies de l'autoenergia i el propagador. Aquesta aproximació és essencialment exacta, en el sentit que totes les correlacions incloses en el propagador a un cos queden automàticament incorporades al gran-potencial a través de la integral d'acoblament. Tanmateix, aquesta fórmula no és útil per aquelles aproximacions en què calcular el propagador (o equivalentment l'autoenergia) requereixin temps de càlcul llargs. Per calcular la integral sobre la constant d'acoblament, cal trobar Σ i \mathcal{G} per diferents valors de λ i això pot allargar excessivament el temps de càlcul. La situació encara empitjora més si els càlculs s'han de fer a densitat finita.

A diferència del mètode de la constant d'acoblament, el formalisme de Luttinger-Ward permet obtenir la funció de partició d'un sistema de fermions interactuants a partir del propagador vestit a un cos. És a dir, si mitjançant alguna aproximació de molts cossos (com el mètode de les SCGF) podem calcular la funció de Green mono-particular vestida, el formalisme de Luttinger-Ward ens dona accés directe a la funció de partició del sistema. L'equació central d'aquest formalisme és l'expressió de Luttinger-Ward per la funció de partició del sistema:

$$\ln Z\{\mathcal{G}\} = \widetilde{\text{Tr}} \ln [-\mathcal{G}^{-1}] + \widetilde{\text{Tr}} \Sigma\{\mathcal{G}\} \mathcal{G} - \Phi\{\mathcal{G}\}, \quad (13)$$

en què totes les quantitats són funcionals del propagador a un cos, \mathcal{G} . La dependència funcional de l'autoenergia ve donada per l'equació de Dyson, mentre que el funcional Φ queda fixat a través del principi variacional que garanteix que el propagador vestit correspon a un estat estacionari de la funció de partició:

$$\left. \frac{\delta \Phi\{\mathcal{G}\}}{\delta \mathcal{G}} \right|_{\mathcal{G}_0} = \Sigma\{\mathcal{G}\} . \quad (14)$$

L'autoenergia defineix, mitjançant l'equació de Dyson, el propagador a un cos que, alhora, es pot fer servir per calcular la funció de partició i, en conseqüència, un nou Φ . Aquesta aproximació autoconsistent no s'ha emprat en aquesta tesi (en què es determina el propagador vestit a banda, mitjançant l'aproximació diagramàtica de les SCGF), però ha trobat nombroses aplicacions en el camp de la física hadrònica [Rap96; Wei98a], en la teoria quàntica de camps fora de l'equilibri [Iva99; Bla04] i en matèria condensada [Dup05; Pot06]. És difícil dur a terme una anàlisi diagramàtica de la funció de partició en termes de propagadors vestits ja que, en diagrames tancats i connectats com els que defineixen el gran-potencial, no s'hi poden identificar les parts que corresponen a una inserció diagramàtica i les que provenen del diagrama mare. Ara bé, el formalisme de Luttinger-Ward es pot derivar diagramàticament [dD64b] i cada terme del funcional es pot identificar amb una suma infinita de termes amb propietats topològiques pròpies. En particular, el funcional Φ correspon a la suma de a tots els diagrames tancats, connectats, irreduïbles a dues partícules i amb les línies fermiòniques vestides [Bla86].

L'expressió de Luttinger-Ward per la funció de partició és completament equivalent a l'expressió obtinguda en termes de la integral de la constant d'acoblament, Eq. (12) [Bay62]. A més, les propietats variacionals del funcional permeten demostrar que els resultats obtinguts en les aproximacions de molts cossos que respectin l'equació generadora del funcional Φ , Eq. (14), són termodinàmicament consistents. En altres paraules, si una certa aproximació de molts cossos a l'autoenergia té associat un funcional Φ a través de l'Eq. (14) i es pot calcular una quantitat microscòpicament en termes dels propagadors i macroscòpicament en termes de la funció de partició, els resultats obtinguts seran equivalents. Cal fer notar que certes aproximacions de molts cossos (com la de BHF) no respecten aquesta propietat perquè les aproximacions diagramàtiques a nivell microscòpic són, en certa manera, inconsistents amb les introduïdes a nivell macroscòpic.

A un nivell més pràctic, és útil tenir expressions que relacionin directament les propietats termodinàmiques del sistema amb la funció espectral i l'autoenergia, ja que en última instància són aquestes quantitats les que s'empren en l'estudi de les propietats microscòpiques del sistema. Per trobar aquestes relacions, cal calcular explícitament les traces de l'Eq. (13) mitjançant la tècnica de les sumes de freqüències de Matsubara (veieu Apèndix C). D'aquesta manera, per exemple,

es troba la següent expressió per la funció de partició:

$$\ln Z = \beta \sum_k \int_{-\infty}^{\infty} \frac{d\omega}{2\pi} f(\omega) \left[2\pi\Theta[\operatorname{Re} \mathcal{G}^{-1}(k, \omega)] - 2 \arctan [\lambda(k, \omega)] \right. \\ \left. + \mathcal{A}(k, \omega) \operatorname{Re} \Sigma(k, \omega) + \Gamma(k, \omega) \operatorname{Re} \mathcal{G}(k, \omega) \right] - \Phi, \quad (15)$$

en termes de la funció espectral, la part real del propagador invers $\operatorname{Re} \mathcal{G}^{-1}(k, \omega) = \omega - \frac{k^2}{2m} - \operatorname{Re} \Sigma(k, \omega)$, el funcional Φ , l'amplada $\Gamma(k, \omega) = -2\operatorname{Im} \Sigma(k, \omega_+)$ i la funció $\lambda(k, \omega)$, que correspon al quocient entre la part imaginària i la part real del propagador invers. Integrant per parts l'equació anterior, es pot arribar a una expressió potser més intuïtiva per la funció de partició:

$$\ln Z = \sum_k \int_{-\infty}^{\infty} \frac{d\omega}{2\pi} \ln [1 + e^{-\beta(\omega-\mu)}] B(k, \omega) - \Phi, \quad (16)$$

en què el factor tèrmic associat al logaritme és el mateix que es troba en el cas lliure. En aquesta fórmula, els efectes de la interacció queden reduïts al funcional Φ i a una espècie de funció espectral:

$$B(k, \omega) = \mathcal{A}(k, \omega) + \frac{\partial \mathcal{A}(k, \omega)}{\partial \omega} \operatorname{Re} \Sigma(k, \omega) + \frac{\partial \operatorname{Re} \mathcal{G}(k, \omega)}{\partial \omega} \Gamma(k, \omega), \quad (17)$$

que inclou els efectes de la fragmentació del pic de la quasi-partícula en la seva dependència en energies i que es pot calcular a partir de magnituds conegudes, com la funció espectral $\mathcal{A}(k, \omega)$ o l'amplada $\Gamma(k, \omega)$.

Una característica atractiva del formalisme de Luttinger-Ward és que, gràcies a les propietats variacionals del funcional, les derivades respecte a diferents quantitats termodinàmiques només afecten els factors tèrmics, mentre que no cal tenir en compte les (en general complicades) dependències en temperatura dels factors dinàmics, com el propagador o l'autoenergia. D'aquesta manera, el formalisme de Luttinger-Ward permet trobar expressions analítiques per l'entropia del sistema:

$$S = - \left. \frac{\partial \Omega}{\partial T} \right|_{\mu}. \quad (18)$$

A partir de les expressions Eqs. (15) i (16) per la funció de partició, per exemple, veiem que l'entropia d'un sistema correlacionat es divideix en dos termes:

$$S = S^{DQ} + S', \quad (19)$$

l'entropia de quasi-partícula dinàmica, S^{DQ} , i un terme, S' , que té en compte correlacions d'ordre més alt en el formalisme i que es pot negligir a temperatures prou baixes [Car75]. En el formalisme de Luttinger-Ward, es poden trobar diferents

expressions per l'entropia de quasi-partícula dinàmica. D'entre totes elles, potser la més interessant és la següent:

$$S^{DQ} = \sum_k \int_{-\infty}^{\infty} \frac{d\omega}{2\pi} \sigma(\omega) \mathcal{B}(k, \omega), \quad (20)$$

que ve donada per la convolució en energies de la funció espectral $\mathcal{B}(k, \omega)$:

$$\mathcal{B}(k, \omega) = \mathcal{A}(k, \omega) \left[1 - \frac{\partial \text{Re} \Sigma(k, \omega)}{\partial \omega} \right] + \frac{\partial \text{Re} \mathcal{G}(k, \omega)}{\partial \omega} \Gamma(k, \omega), \quad (21)$$

i un factor estadístic associat a l'entropia:

$$\sigma(\omega) = - \left\{ f(\omega) \ln [f(\omega)] + [1 - f(\omega)] \ln [1 - f(\omega)] \right\}. \quad (22)$$

Aquesta expressió és particularment important perquè els efectes tèrmics, que estan representats bàsicament per aquest factor $\sigma(\omega)$, han quedat desacoblats dels efectes de correlacions dinàmiques, que vénen descrits per la funció espectral $\mathcal{B}(k, \omega)$. Aquesta funció comparteix algunes propietats amb la funció espectral usual, $\mathcal{A}(k, \omega)$, entre elles la regla de suma que en garanteix la normalització.

És interessant fer notar que el terme S' :

$$S' = - \frac{\partial}{\partial T} T \Phi[G] + \sum_k \int_{-\infty}^{\infty} \frac{d\omega}{2\pi} \frac{\partial f(\omega)}{\partial T} \mathcal{A}(k, \omega) \text{Re} \Sigma(k, \omega), \quad (23)$$

inclou la derivada del funcional Φ . D'ara endavant negligirem aquest terme i, per tant, no es necessari calcular el funcional Φ per obtenir l'entropia del sistema correlacionat. La contribució S' a l'entropia és fruit d'una cancel·lació entre la derivada de Φ i la convolució de \mathcal{A} i $\text{Re} \Sigma$. Aquestes cancel·lacions són tals que, a baixes temperatures, les restriccions d'espai fàsic fan que S' sigui negligible. A nivell diagramàtic, les úniques contribucions a S' sorgeixen de diagrames en què com a mínim dos denominadors d'energia s'anul·len. En altres paraules, S' inclou termes deguts a correlacions que van més enllà del camp mig. És important destacar, tanmateix, que aquest terme és important en sistemes molt correlacionats, com ho demostra el fet que és el responsable de la dependència de tipus $T^3 \ln T$ en el calor específic de ${}^3\text{He}$ [Car75; Gre83].

L'aproximació de Hartree-Fock

L'aproximació de Hartree-Fock (HF) sorgeix de considerar l'aproximació diagramàtica a ordre més baix per l'autoenergia d'un sistema interactuant. En aquesta aproximació, l'autoenergia ve donada per la suma dels diagrames directes i de bescanvi de la primera línia de la Fig. 2. Els propagadors interns d'aquesta figura

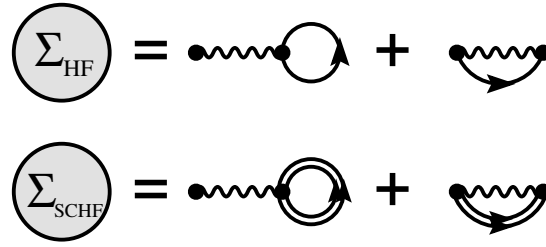


Figura 2: Representació diagramàtica de l'autoenergia en les aproximacions de Hartree-Fock (a) i de Hartree-Fock autoconsistent (a) baix).

estan representats per línies simples i, en conseqüència, l'autoenergia s'ha calculat a partir de propagadors a un cos lliures. Ara bé, ja hem dit que, mitjançant l'equació de Dyson, els efectes de la interacció vesteixen el propagador. Així doncs, si utilitzem l'autoenergia per generar un nou propagador de HF a un cos mitjançant l'equació de Dyson de la Fig. 1, generarem un propagador vestit que podríem incloure de nou en el càlcul de l'autoenergia. Iterant aquest procés podríem arribar a un resultat autoconsistent, en què el propagador vestit i el que hi hagués a les línies fermiòniques en l'aproximació de l'autoenergia fossin equivalents. En tal cas, sumariem una sèrie infinita de diagrames indirectament. Aquesta suma va més enllà de la suma introduïda per l'equació de Dyson, en què es consideren tan sols les iteracions de peces d'autoenergia irreduïbles. Aquest procediment defineix l'aproximació de Hartree-Fock autoconsistent (Self-Consistent Hartree-Fock o SCHF, en el seu acrònim anglès).

Una aproximació simple, com la de SCHF, ens permet tractar certs aspectes, com ara l'autoconsistència, de manera relativament senzilla. L'autoenergia en aquesta aproximació, per exemple, és purament real, no depèn de l'energia i per tant n'hi ha prou amb representar-la en funció del moment, com a la Fig. 3. Per calcular aquesta quantitat en un esquema autoconsistent cal seguir un procediment iteratiu. La primera iteració de l'autoenergia s'obté de normalitzar la distribució de moments a la densitat, tot ajustant el potencial químic corresponent:

$$\rho = \nu \int \frac{d^3k}{(2\pi)^3} n(k, \tilde{\mu}), \quad (24)$$

on la distribució de moments que s'ha fet servir correspon a la del sistema no interactuant. El potencial químic fixa la distribució de moments a aquesta densitat, amb què podem calcular la primera iteració de l'autoenergia:

$$\Sigma(k) = \int \frac{d^3k_1}{(2\pi)^3} \langle \mathbf{k}\mathbf{k}_1 | V | \mathbf{k}\mathbf{k}_1 \rangle_A n(k). \quad (25)$$

En aquesta iteració, la distribució de moments correspon a la distribució lliure i l'autoenergia que se n'obté és precisament la de HF (representada per la primera

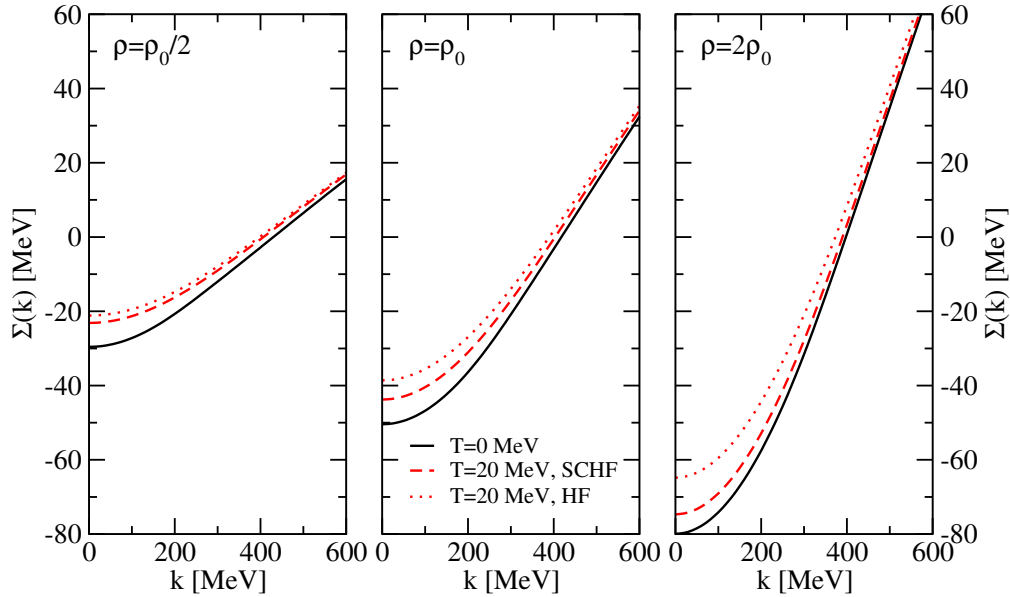


Figura 3: Resultats per l'autoenergia SCHF (línia discontinua) i HF (línia puntejada) a les densitats $\rho_0/2$, ρ_0 i $2\rho_0$ per una temperatura de $T = 20$ MeV. Els resultats de temperatura $T = 0$ corresponents a la línia contínua.

línia de la Fig. 2). Per implementar numèricament l'equació anterior cal dur a terme una expansió en ones parcials. Ara bé, si un cop calculada aquesta autoenergia, definim un nou espectre mono-particular a partir de l'equació $\varepsilon(k) = \frac{k^2}{2m} + \Sigma(k)$, podem introduir aquest espectre en la distribució de moments i obtenir un nou potencial químic mitjançant la normalització de l'Eq. (24). Iterant aquest procés successivament, obtindrem l'autoenergia en l'aproximació SCHF. A la Fig. 3 representem l'autoenergia de SCHF a $T = 0$ (línia contínua) i a $T = 20$ MeV (línia discontinua), fet que ens permet entendre els efectes que la temperatura té sobre aquesta quantitat. Els resultats de cadascun dels tres panells s'han calculat per tres densitats diferents: $\rho_0/2$ (panell esquerre), ρ_0 (panell central) i $2\rho_0$ (panell dret), i ens informen dels efectes de la densitat en l'autoenergia. Finalment, els efectes d'autoconsistència són els responsables de les diferències entre la línia puntejada, que dona l'autoenergia en l'aproximació de HF (sense autoconsistència) a $T = 20$ MeV, i la línia discontinua, que correspon a l'autoenergia SCHF en les mateixes condicions. El fet que aquestes energies potencials mono-particulars siguin atractives és un efecte particular del potencial de CDBONN; altres potencials realistes donen autoenergies repulsives en les mateixes condicions. En general, la temperatura té un efecte repulsiu per tots els moments, ja que els factors tèrmics permeten explorar un rang de moments més ampli en la interacció lliure, que van associats a elements de matriu generalment repulsius. A més, l'efecte tèrmic és menor com major és la densitat, fet que es correspon amb la intuïció que un sis-

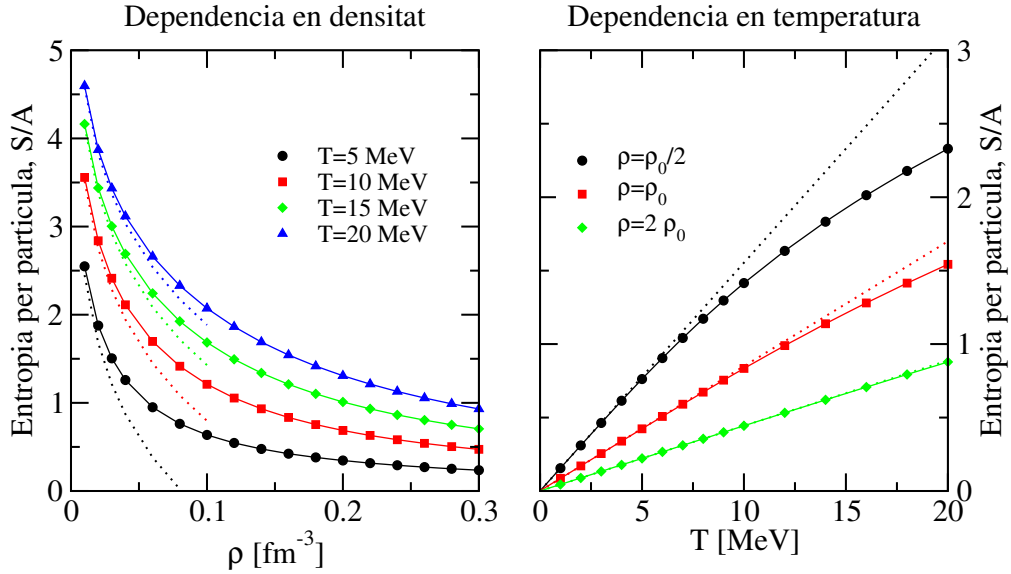


Figura 4: Dependència en densitat i temperatura de l'entropia per partícula en l'aproximació de SCHF.

tema a alta densitat es veu menys afectat per les correlacions tèrmiques perquè es troba en un estat més degenerat. Finalment, la diferència entre les autoenergies de HF i de SCHF és una barreja de l'efecte d'autoconsistència i de la diferència en els potencials químics de les dues aproximacions. Tot i això, els resultats són els esperats. D'una banda, les diferències són majors com major és la densitat i, de l'altra, els resultats autoconsistents són més atractius en tot el rang de moments, en coincidència amb la idea que la influència dels propagadors vestits permet una descripció més realista a altes densitats.

Quant a les propietats termodinàmiques del sistema, presentem aquí els resultats per l'entropia per partícula en l'aproximació de SCHF. En aquesta aproximació de quasi-partícula, la funció espectral és una delta de Dirac centrada a l'energia de quasi-partícula. A més, l'autoenergia en l'aproximació de SCHF és real. Amb aquesta informació podem utilitzar les Eqs. (20) i (21), corresponents a l'entropia de quasi-partícula dinàmica, i obtenir l'expressió:

$$\frac{S}{A} = \frac{\nu}{\rho} \int \frac{d^3k}{(2\pi)^3} \sigma[\varepsilon(k)]. \quad (26)$$

És interessant destacar que aquesta equació, obtinguda a partir del formalisme de Luttinger-Ward, es pot obtenir a través d'altres derivacions de l'entropia en l'aproximació de camp mig [Fet71]. En aquesta aproximació, a més, és fàcil demostrar que $S' = 0$. El panell esquerre (dret) de la Fig. 4 mostra l'entropia per partícula en funció de la densitat (temperatura) a temperatura (densitat) fixa. Els resultats són força intuïtius i s'acosten al que esperaríem trobar. D'una banda,

l'entropia per partícula a temperatura fixa decreix amb la densitat. Aquest decreixement és particularment important a baixes densitats. D'altra banda, l'entropia per partícula a densitat fixa augmenta amb la temperatura. A temperatures prou baixes, però, l'entropia tendeix cap a zero i ho fa de manera lineal. Ambdós comportaments (dependència logarítmica amb la densitat, dependència lineal amb la temperatura) es corresponen als esperats en els règims clàssic i degenerat, en què es poden obtenir expressions analítiques per l'entropia del sistema. Els dos règims corresponen a un límit diferent del quocient $x = \frac{T}{\varepsilon_F}$ (amb $\varepsilon_F = \frac{k_F^2}{2m}$). D'una banda, el règim clàssic correspon a densitats baixes o altes temperatures, *i.e.* $k_F \ll 1$ o $T \gg 1$ i, per tant, $x \gg 1$. L'entropia per partícula en aquest règim es pot obtenir de la fórmula:

$$\frac{S}{A} = \frac{5}{2} - \ln \frac{\rho \lambda_{dB}^3}{\nu} + \frac{3}{2} \ln \frac{m^*}{m}, \quad (27)$$

on λ correspon a la longitud de de Broglie, $\lambda_{dB} = \sqrt{2\pi/(Tm)}$, i la massa efectiva s'obté d'un ajust de la dependència quadràtica del potencial mono-particular (veieu Apèndix D). El bon funcionament d'aquesta aproximació s'observa en les línies puntejades del panell dret, que representen el límit clàssic de l'entropia a les densitats i temperatures corresponents. És clar que en la zona de baixes densitats reproduïxen de forma quantitativa els resultats de l'entropia per partícula. El límit degenerat, d'altra banda, correspon a temperatures baixes i densitats altes, això és $x \ll 1$. L'expressió analítica per l'entropia en aquest règim és la següent:

$$\frac{S}{A} = \frac{\pi^2}{3\rho} N(0)T, \quad (28)$$

on $N(0)$ és la densitat d'estats a la superfície de Fermi a temperatura zero. Aquesta quantitat és essencialment proporcional a la massa efectiva:

$$N(0) = \frac{\nu k_F m^*(k_F)}{2\pi^2}, \quad (29)$$

que en aquest cas ve donada per la següent derivada del potencial mono-particular:

$$\frac{m^*}{m} = \frac{1}{2m} \left(\frac{d\varepsilon(k)}{dk^2} \right)^{-1} = \frac{1}{1 + 2m \frac{d\Sigma(k)}{dk^2}} \quad (30)$$

(veieu Apèndix D). Les línies puntejades del panell dret s'han obtingut amb aquesta aproximació lineal que, com era d'esperar, funciona millor en el rang de baixes temperatures i densitats altes.

La resta de propietats termodinàmiques obtingudes en l'aproximació de SCHF no donen resultats realistes. L'energia lliure per partícula, per exemple, no té cap mínim i, en conseqüència, la pressió és positiva per totes les densitats i temperatures. No hi ha, doncs, cap punt de saturació. El mateix podem dir de l'energia

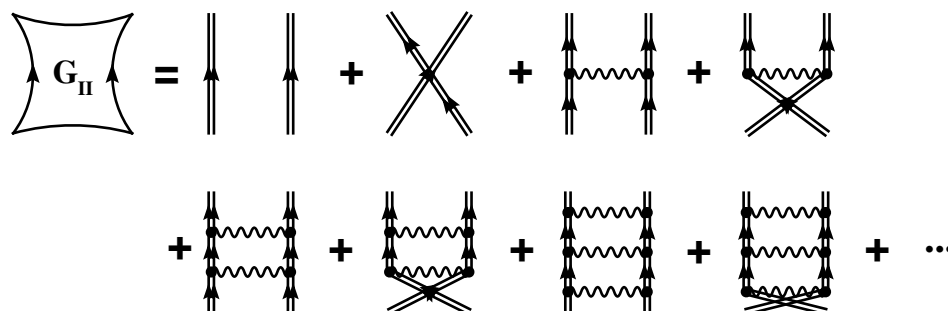
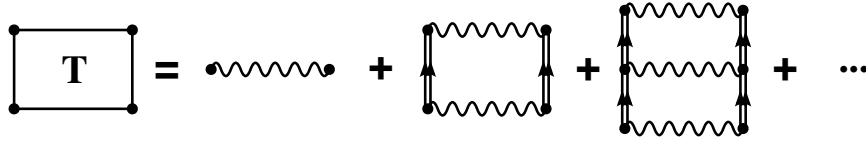


Figura 5: *Expansió diagramàtica del propagador a dos cossos en l'aproximació d'escala.*

per partícula que, tot i la component atractiva de l'energia potencial, també és repulsiva. L'utilitat que té calcular aquestes quantitats en una aproximació poc realista com la de SCHF és doble. D'una banda, es pot comprovar que les expressions que el formalisme de Luttinger-Ward dona per les diferents quantitats termodinàmiques es redueixen a les obtingudes mitjançant altres formalismes en l'aproximació de camp mig. De l'altra, els efectes tèrmics són particularment transparents en aquesta aproximació i és doncs fàcil estudiar les dependències en densitat i temperatura en els règims clàssic i degenerat dels diferents potencials termodinàmics del sistema.

L'aproximació d'escala

L'energia total que s'obté a l'aproximació de SCHF és, com acabem de dir, positiva en un rang molt ampli de densitats i temperatures. És clar, doncs, que en aquesta aproximació no podem reproduir el punt de saturació empíric de la matèria nuclear. La causa d'aquest comportament incorrecte rau en la pròpia base de l'aproximació, que només és apropiada per sistemes diluïts amb interaccions relativament febles. Per una interacció fortament repulsiva a curtes distàncies (com és el cas de la força NN), tanmateix, hauria de ser energèticament poc probable trobar dos nucleons relativament a prop els uns dels altres. Gràcies a això, els nucleons, en terme mig, exploren una regió de distàncies intermèdies en què la interacció és atractiva i l'energia total pot esdevenir atractiva en un cert rang de densitats. És clar, però, que aquest és un efecte causat per les correlacions a dos cossos. Com que l'aproximació de HF no inclou aquest tipus de correlacions, els resultats que s'obtenen per l'energia per partícula són repulsius. En termes diagramàtics, el propagador a dos cossos de l'aproximació de HF ve donat per la suma dels dos primers diagrames de la Fig. 5. Ara bé, per un sistema relativament poc dens amb una interacció forta, és clar que l'aproximació donada per la


 Figura 6: *Expansió diagramàtica de la matriu T.*

suma infinita dels diagrames representats a la Fig. 5 donarà lloc a resultats més realistes. Aquests diagrames tenen en compte la propagació de dues partícules que interaccionen successivament una, dues, tres, etc. vegades i, per la seva estructura, s'anomenen diagrames d'escala. És per això que aquesta aproximació és coneguda com l'aproximació d'escala al propagador de dos cossos. Naturalment, el fet que representi una suma infinita de diagrames té com a conseqüència un tractament més acurat de les propietats microscòpiques i macroscòpiques del sistema.

L'estructura diagramàtica en termes d'"escales" es pot absorbir de manera natural en l'anomenada matriu T o interacció efectiva en el medi, la representació diagramàtica de la qual presentem a la Fig. 6. Aquesta interacció efectiva està formada per una suma infinita de diagrames. A ordre més baix, la matriu T equival al potencial nuu. A ordres superiors, la suma inclou termes en què un parell de partícules es difon mitjançant interaccions successives. En el límit a temperatura zero d'aquestes expressions, es pot veure que, de fet, els dos estats intermedis que es propaguen són estats de tipus partícula-partícula i forat-forat. En aquest sentit, aquesta interacció és més rica que la matriu G de l'aproximació de BHF, en què només es té en compte la propagació intermèdia de parells de partícules. Tant la matriu G com la matriu T satisfan una equació del tipus Lippman-Schwinger:

$$\begin{aligned} \langle \mathbf{k}_1 \mathbf{k}_2 | T(Z_\nu) | \mathbf{k}_3 \mathbf{k}_4 \rangle &= \langle \mathbf{k}_1 \mathbf{k}_2 | V | \mathbf{k}_3 \mathbf{k}_4 \rangle \\ &+ \mathcal{V} \int \frac{d^3 k_5}{(2\pi)^3} \mathcal{V} \int \frac{d^3 k_6}{(2\pi)^3} \langle \mathbf{k}_1 \mathbf{k}_2 | V | \mathbf{k}_5 \mathbf{k}_6 \rangle \mathcal{G}_{II}^0(Z_\nu; k_5 k_6) \langle \mathbf{k}_5 \mathbf{k}_6 | T(Z_\nu) | \mathbf{k}_3 \mathbf{k}_4 \rangle. \end{aligned} \quad (31)$$

\mathcal{G}_{II}^0 és un propagador intermedi, que difereix segons l'aproximació emprada. En l'aproximació d'escala a temperatura finit, correspon a un propagador d'estats partícula-partícula i forat-forat, que es pot calcular íntegrament a partir de la funció espectral:

$$\mathcal{G}_{II}^0(Z_\nu; k, k') = \int_{-\infty}^{\infty} \frac{d\omega}{2\pi} \int_{-\infty}^{\infty} \frac{d\omega'}{2\pi} \mathcal{A}(k, \omega) \mathcal{A}(k', \omega') \frac{1 - f(\omega) - f(\omega')}{Z_\nu - \omega - \omega'}. \quad (32)$$

La dependència en k i k' d'aquesta equació és particularment molesta a l'hora de dur a terme l'expansió en ones parcials de l'Eq. (31), ja que comporta una

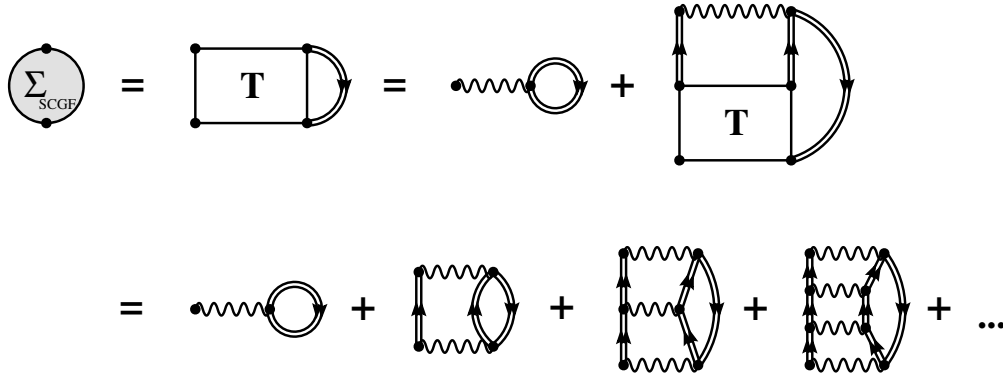


Figura 7: Representació diagramàtica de l'autoenergia en l'aproximació d'escala.

dependència angular que duu a un acoblament de diferents ones parcials. La solució d'aquesta inconveniència passa per promitjar la dependència angular de \mathcal{G}_{II}^0 . En l'aproximació de BHF, aquest promig angular té un efecte de menys d'un MeV a l'energia per partícula [Sar96]. No hi ha raons per creure que l'error introduït en l'aproximació d'escala sigui major.

Tota aproximació del propagador a dos cossos té una traducció directa en termes de l'autoenergia. L'aproximació d'escala no és una excepció i l'autoenergia d'escala queda completament determinada per la matriu T . La relació diagramàtica entre la interacció efectiva i l'autoenergia correspon al segon diagrama de la Fig. 7. A través de les propietats analítiques del propagador i de la matriu T , a més, es pot demostrar que l'autoenergia d'escala es descomposa en dos termes:

$$\Sigma_L(k, z_\nu) = \Sigma_{HF}(k) + \Sigma_C(k, z_\nu). \quad (33)$$

La primera contribució correspon a una autoenergia del tipus HF, però és lleugerament diferent a l'autoenergia de SCHF ja que inclou insercions de peces d'autoenergia més riques. Ara bé, es calcula també a partir de la interacció NN nua. El terme correlacionat, en canvi, correspon al diagrama superior de la Fig. 7 i conté els efectes de la matriu T . Com que el terme de HF generalitzat de l'autoenergia és purament real, la part imaginària de l'autoenergia d'escala correspon a la part imaginària de Σ_C i ve donada per l'expressió:

$$\begin{aligned} \text{Im } \Sigma_L(k, \omega_+) = \int \frac{d^3 k'}{(2\pi)^3} \int_{-\infty}^{\infty} \frac{d\omega'}{2\pi} \langle \mathbf{k}\mathbf{k}' | \text{Im } T(\omega + \omega'_+) | \mathbf{k}\mathbf{k}' \rangle_A \mathcal{A}(k', \omega') \\ \times [f(\omega') + b(\omega + \omega')], \end{aligned} \quad (34)$$

on la funció $b(\omega + \omega')$ és una distribució de Bose-Einstein que sorgeix en tractar de forma simètrica la propagació de parells partícula-partícula i forat-forat. És

important fer notar que, de la mateixa manera que la part real de la matriu T es pot obtenir a partir de la seva part imaginària mitjançant una relació de dispersió, la part real i imaginària de l'autoenergia estan relacionades a través d'una integral de dispersió.

Les Eqs. (11), (24), (31) i (34), juntament amb les corresponents relacions de dispersió, defineixen un conjunt d'equacions que, a una densitat i temperatura, es poden resoldre de manera autoconsistent, tot i donant lloc a l'esquema de les Funcions de Green Autoconsistentes (SCGF). La resolució numèrica d'aquest esquema ve dificultada pel fet que s'iteren autoconsistentment les dependències en moment i energia tant de la funció espectral com de l'autoenergia i de la matriu T . A més, les correlacions de curt abast indueixen una població no negligible als estats d'altres energies, de manera que a nivell numèric cal controlar tant les regions d'energies molt positives i molt negatives com les estructures abruptes que sorgeixen al voltant del pic de quasi-partícula. Sortosament, aquestes estructures són més senzilles de mostrear numèricament a temperatura finita. De fet, és gràcies a l'extensió d'aquest formalisme a sistemes de temperatura no nul·la que s'ha pogut obtenir una solució numèrica completa del problema [Fri03].

La funció espectral $\mathcal{A}(k, \omega)$ obtinguda en aquesta aproximació conté totes les correlacions de l'aproximació d'escala, i està representada en un ampli rang de densitats i temperatures als diferents panells de la Fig. 8. Mentre que la columna dreta representa l'evolució d'aquesta quantitat amb la densitat, l'esquerra en dona l'evolució tèrmica. Els tres panells (superior, central i inferior) corresponen a diferents moments ($k = 0, k_F$ i $2k_F$ respectivament) i ens informen de la dependència en moment d'aquesta quantitat. Una de les conclusions més interessants que podem extreure d'aquesta figura és que, mentre els efectes tèrmics són relativament poc importants i estan concentrats al voltant de la regió $\omega = \mu$, els efectes de densitat afecten la funció espectral en tot el rang d'energies i moments. Una característica comú de tots els panells és, a més, la presència d'un pic prominent en la funció espectral, que és una reminiscència de l'estructura mono-particular dels sistemes nuclears. Si ens fixem en l'evolució en densitat de l'estat amb $k = 0$, s'observa que aquest pic es desplaça cap a energies cada cop més negatives respecte μ . Aquest fet es correspon amb la idea que l'energia de quasi-partícula de l'estat $k = 0$ és més lligada quan augmenta la densitat. L'amplada d'aquest pic i les cues a energies molt positives i molt negatives augmenten a mida que s'incrementa la densitat. La funció espectral a $k = 2k_F$ presenta unes característiques semblants i, tot i que el pic de quasi-partícula tendeix a energies més repulsives a mida que la densitat augmenta, tant la seva amplada com les cues a altes energies esdevenen més importants amb la densitat. D'altra banda, el comportament de la funció espectral a k_F és qualitativament diferent. Així, la posició del pic de quasi-partícula amb prou feines varia, mentre que la seva amplada disminueix amb la densitat. Aquest comportament és remissiu del fet que, a temperatura zero *i.e.* pel sistema totalment degenerat, la funció espectral té una estructura de delta de Dirac a $k = k_F$ i

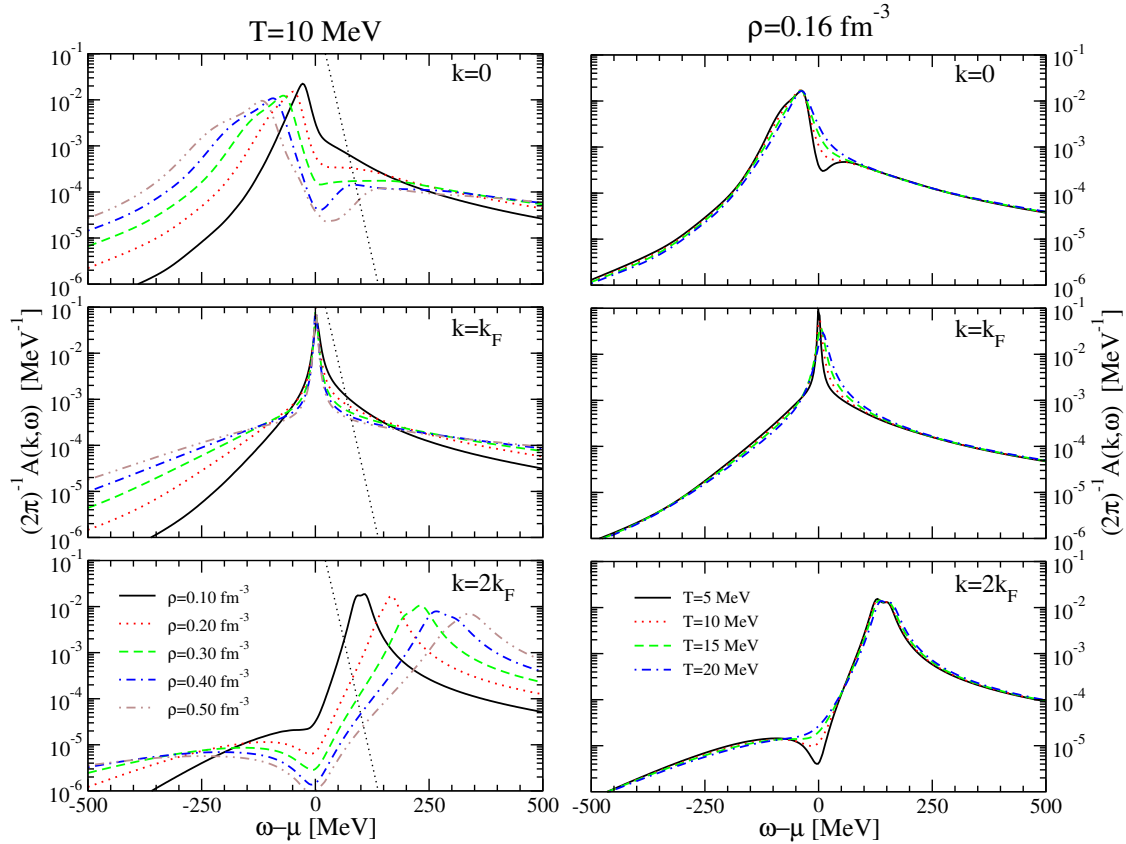


Figura 8: *Funció espectral en funció de l'energia $\omega - \mu$ per tres moments: $k = 0$ (panell superior), k_F (panell central) i $2k_F$ (panell inferior). A la columna esquerra, les diferents línies corresponen a cinc densitats diferents (de 0.1 a 0.5 fm^{-3} en passos equidistants). La línia puntejada correspon a la distribució tèrmica $f(\omega)$ a aquesta temperatura. A la columna dreta, les diferents línies corresponen a quatre temperatures diferents (de 5 a 20 MeV en passos equidistants).*

$\omega = \mu$. La funció espectral, doncs, tendeix a tenir una estructura de tipus delta per sistemes més degenerats, *i.e.* per sistemes a altes densitats i temperatures baixes. La dependència de les cues d'altres energies en densitat és, tanmateix, comú per tots els moments i a $k = k_F$ també s'observa l'augment de la seva importància amb la densitat. Aquest fet es correspon amb la idea intuïtiva que les correlacions que fragmenten el pic de quasi-partícula augmenten amb la densitat.

Acabem de comentar que la funció espectral presenta un pic de quasi-partícula per tots els moments i energies. La prominència d'aquest pic permet descriure el sistema, com a mínim a nivell qualitatiu, en termes de quasi-partícules. En particular, a cada moment li podem associar una sola energia de quasi-partícula mitjançant la relació recurrent:

$$\varepsilon(k) = \frac{k^2}{2m} + \text{Re} \Sigma(k, \varepsilon(k)), \quad (35)$$

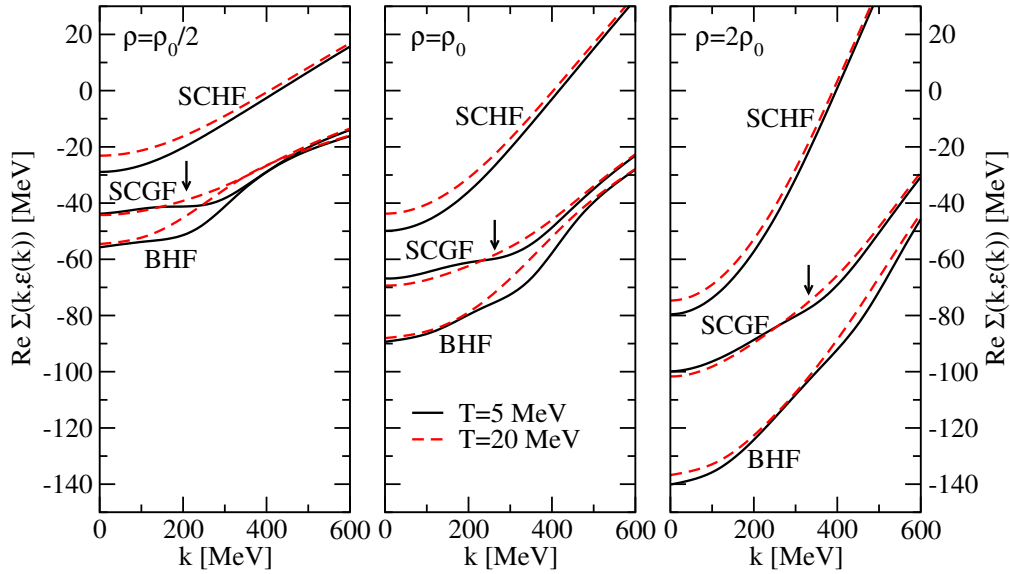


Figura 9: Resultats per l'autoenergia on-shell de les aproximacions de SCHF, SCGF i BHF a les densitats $\rho_0/2$, ρ_0 i $2\rho_0$. Les línies contínues corresponen a una temperatura de $T = 5$ MeV i les línies discontinües a $T = 20$ MeV. Les fletxes assenyalen la posició del moment de Fermi corresponent.

que defineix precisament l'energia a què es troba el pic de la quasi-partícula en la funció espectral. La relació de dispersió definida per aquesta relació es pot comparar amb els espectres mono-particulars de les aproximacions de SCHF o de BHF, com fem a la Fig. 9, on es mostren els espectres per tres densitats diferents: $\rho_0/2$ (panell esquerre), ρ_0 (panell central) i $2\rho_0$ (panell dret). Dins de cada panell, les línies contínues representen una temperatura baixa ($T = 5$ MeV) i les discontinües una de relativament alta ($T = 20$ MeV). Els efectes de la densitat són qualitativament semblants pels espectres en les tres aproximacions. La densitat fa que les energies de quasi-partícula esdevinguin més atractives i la seva dependència en moment, més acusada. Quant a les diferències entre les aproximacions, els espectres realistes de SCGF són en general uns 15 MeV més atractius que els de SCHF a $k = 0$, però a mida que augmenta el moment aquestes diferències es fan més significatives. Aquest efecte és diferent quan comparem les aproximacions de BHF i de SCGF i, mentre que a baix moment la diferència entre ambdós espectres depèn de la densitat, a moments per sobre de k_F les variacions tendeixen a ser menors. D'altra banda, l'efecte de la temperatura és diferent segons l'aproximació que considerem. En les aproximacions de SCHF i de BHF, els espectres són més repulsius a mida que augmenta T a tots els moments. Per l'aproximació de SCGF, en canvi, l'espectre dels forats (estats amb $k < k_F$) esdevé més atractiu i el de les partícules més repulsiu. Aquest mateix efecte s'ha observat en càlculs BHF estesos

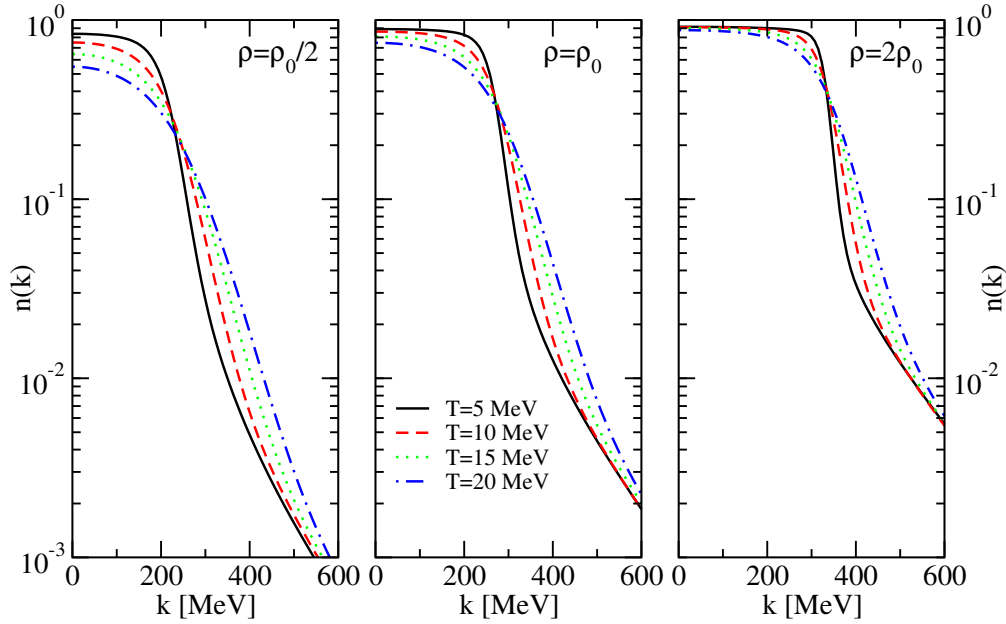


Figura 10: *Distribució de moments en l'aproximació de SCGF. Els tres panells corresponen a les densitats $\rho_0/2$ (panell esquerre), ρ_0 (panell central) i $2\rho_0$ (panell dret). S'hi mostren quatre temperatures diferents, de $T = 5$ MeV a $T = 20$ MeV en passos equidistants.*

que tracten de manera aproximada les correlacions de forats [Zuo06].

Pocs observables a nivell microscòpic reflexen tant bé la influència de les correlacions com la distribució de moments. Mentre que en una aproximació de quasi-partícula, aquesta quantitat ve donada per la distribució de Fermi-Dirac calculada a les corresponents energies de quasi-partícula, $n(k) = f[\varepsilon(k)]$, en una aproximació de molts cossos correlacionada la distribució de moments té en compte la fragmentació del pic de quasi-partícula mitjançant la funció espectral:

$$n(k) = \int_{-\infty}^{\infty} \frac{d\omega}{2\pi} \mathcal{A}(k, \omega) f(\omega). \quad (36)$$

La convolució en energies d' $\mathcal{A}(k, \omega)$ i $f(\omega)$ dona lloc a una distribució de moments que per sota de la superfície de Fermi està relativament despoblada respecte al cas de quasi-partícula (diem que presenta una certa depleció), mentre que per sobre de k_F presenta estats més poblats que la distribució de Fermi. La distribució de moments es pot determinar empíricament a partir dels experiments de difusió ($e, e'p$), en què un electró expulsa un protó d'un nucli pesat [Kel96; Dic04; Roh04]. Aquests resultats experimentals són la millor eina per discernir els efectes de les correlacions de curt abast en nuclis finits. Els nostres càlculs, malauradament, s'han fet a temperatura finita, mentre que els experiments tenen lloc a temperatura zero. Això impedeix, és clar, una comparació directa amb els resultats experimentals.

La distribució de moments correlacionada en un cert rang de moments es presenta a la Fig. 10. Els tres panells representen les mateixes densitats que la Fig. 9, però en cadascun d'ells hi apareixen els resultats per temperatures de $T = 5$ fins a $T = 20$ MeV en passos de 5 MeV. En general, l'efecte tèrmic es limita a fer disminuir la població per sota de $k = k_F$ i a fer-la augmentar per sobre d'aquest moment. Hem vist que els efectes de la temperatura sobre la funció espectral són relativament petits i, per tant, aquesta dependència en temperatura la podem atribuir bàsicament a les correlacions tèrmiques o, en altres paraules, a les modificacions que la temperatura indueix sobre $f(\omega)$. A mida que la temperatura augmenta, la dependència en energia d'aquesta funció es fa més suau i els estats d'energia per sota (per sobre) de μ tendeixen a estar menys (més) poblats. La importància relativa de la convolució amb el pic de quasi-partícula, que per $k < k_F$ es troba per sota de μ , disminueix a mida que augmenta la temperatura. Aquesta disminució explica la dependència en temperatura de la depleció. D'altra banda, per $k > k_F$ el pic de quasi-partícula es troba per sobre de $\omega = \mu$ i la seva convolució amb $f(\omega)$ es fa més important a mida que la temperatura creix. La densitat té diversos efectes sobre la distribució de moments. D'una banda, el moment de Fermi augmenta amb la densitat i per tant el moment en què la població comença a disminuir augmenta. D'altra banda, la depleció de la distribució de moments per estats de forat ($k < k_F$) es fa menys important i els efectes de temperatura sobre ella són cada cop menors. Aquest segon comportament és relativament intuïtiu, ja que en augmentar la densitat el sistema és més degenerat i els efectes tèrmics es fan menys importants. La disminució de la depleció amb la densitat, en canvi, va en contra del comportament que esperariem trobar. La depleció dels estats de forat és una conseqüència de les correlacions de curt abast, que difonen estats de moment baix cap a estats d'alt moment i, com a efecte de molts cossos, caldria esperar que augmentés amb la densitat. La raó d'aquest comportament anti-intuïtiu encara no està del tot compresa.

Propietats termodinàmiques de la matèria nuclear

Un cop coneguda la funció espectral a partir de la resolució numèrica del mètode de les SCGF, podem calcular les propietats microscòpiques mono-particulars del sistema així com algunes propietats macroscòpiques, com ara l'energia per partícula a través de la regla de suma de GMK. Per determinar les propietats termodinàmiques del sistema, que en regiran l'evolució a nivell macroscòpic, podem fer servir el formalisme de Luttinger-Ward. Els punts d'equilibri d'un sistema a temperatura i densitat fixes vénen determinats pels mínims de l'energia lliure:

$$F = E - TS. \quad (37)$$

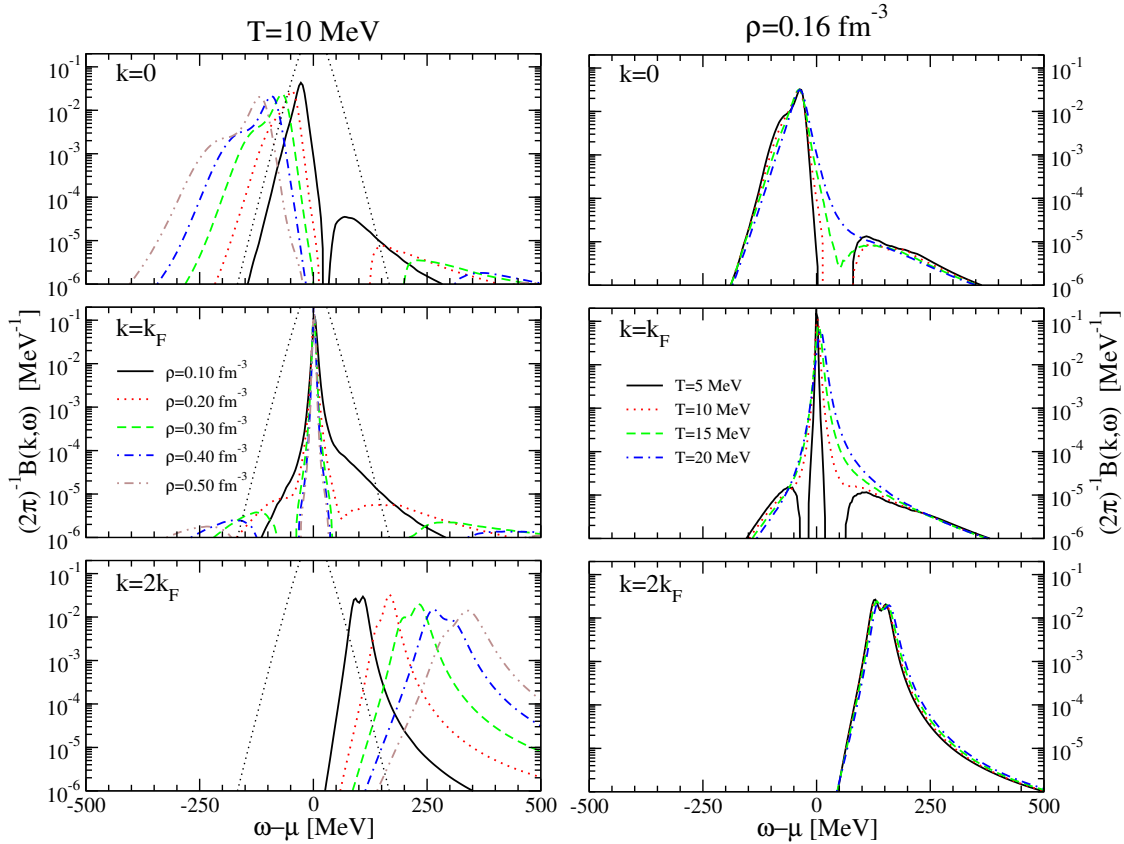


Figura 11: *Funció espectral \mathcal{B} en funció de l'energia $\omega - \mu$ per tres moments: $k = 0$ (panell superior), k_F (panell central) i $2k_F$ (panell inferior). A la columna esquerra, les diferents línies corresponen a cinc densitats diferents (de 0.1 a 0.5 fm^{-3} en passos equidistants). La línia puntejada correspon al factor estadístic $\sigma(\omega)$ a aquesta temperatura. A la columna dreta, les diferents línies corresponen a quatre temperatures diferents (de 5 a 20 MeV en passos equidistants).*

Com que l'energia per partícula ve determinada per la regla de suma de GMK, és clar que necessitem determinar l'entropia del sistema correlacionat. Aquesta entropia és ben descrita per l'aproximació de quasi-partícula dinàmica, Eq. (20). El càlcul d'aquesta quantitat ha estat un dels objectius fonamentals d'aquesta tesi.

Els efectes que la interacció i les correlacions dinàmiques generen en l'entropia de quasi-partícula dinàmica van essencialment associats a la funció espectral \mathcal{B} , definida a l'Eq. (21) i que es mostra en la Fig. 11 en les mateixes condicions en què s'ha calculat la funció espectral a la Fig. 8. A nivell qualitatiu, la funció espectral \mathcal{B} presenta unes característiques força semblants a les de la funció espectral \mathcal{A} . D'una banda, en tot el rang de moments, densitats i temperatures explorat, presenta un pic de quasi-partícula molt pronunciat (noteu l'escala logarítmica), encara més marcat que el de la funció espectral \mathcal{A} . A l'estat de moment zero, aquest pic tendeix a desplaçar-se a energies més negatives a mida que augmenta la densitat,

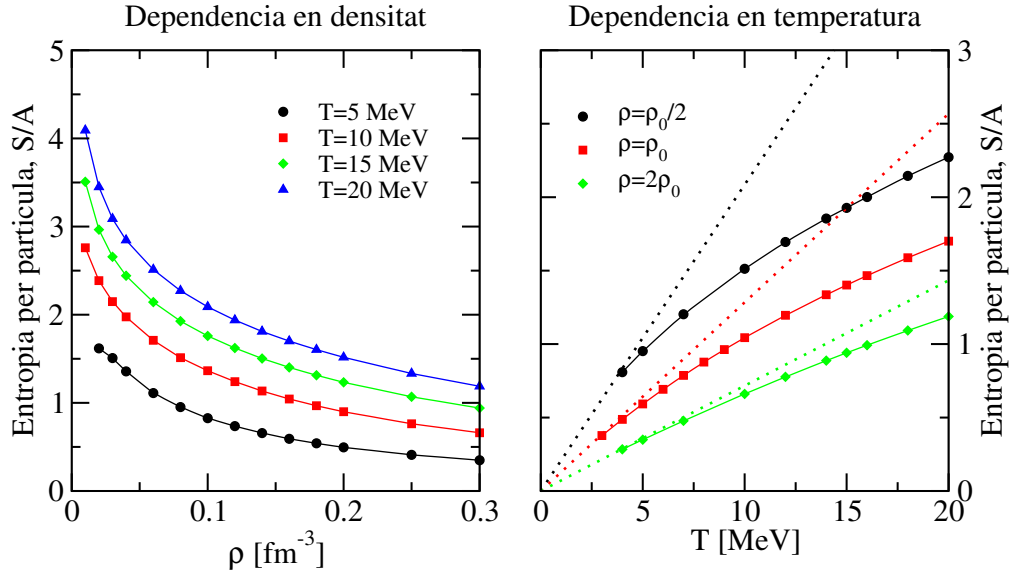


Figura 12: Dependència en densitat (panell esquerre) i en temperatura (panell dret) de l'entropia per partícula en l'aproximació de quasi-partícula dinàmica. Les línies puntejades del panell dret corresponen a l'aproximació degenerada de l'Eq. (28). Noteu la diferència en les escales del panell esquerre i del panell dret.

mentre que per $2k_F$ el pic es fa cada cop més repulsiu. Altra vegada, aquests pics es fan més amples i més baixos a mida que augmenta la densitat. A diferència de la funció espectral \mathcal{A} , les cues a energies molt positives i molt negatives decreixen amb la densitat. A la superfície de Fermi ($k = k_F$), la importància d'aquestes cues decreix igualment amb la densitat, però el pic de quasi-partícula esdevé més estret i més alt amb la densitat, d'acord amb l'augment de la degeneració. Els efectes tèrmics sobre \mathcal{B} són, en canvi, molt limitats i es concentren al voltant de la regió $\omega \sim \mu$ per moments baixos ($k \leq k_F$). És important fer notar que l'estretesa del pic de quasi-partícula en la funció espectral \mathcal{B} assenyala el fet que les correlacions que fragmenten el pic de quasi-partícula són poc importants en el càlcul de l'entropia. De fet, una aproximació de quasi-partícula sense amplada reproduïx l'entropia de quasi-partícula dinàmica amb menys d'un 5% de diferència en tot el rang de densitats i temperatures estudiat.

A la Fig. 12 hi mostrem l'entropia de quasi-partícula dinàmica, en funció de la densitat (a temperatura fixa) al panell esquerre i de la temperatura (a densitat fixa) al panell dret. A primera vista no s'observen grans diferències respecte l'entropia de camp mig de la Fig. 4 i, de fet, el quocient d'ambdues quantitats no és mai superior a un factor 1.5. L'entropia de quasi-partícula dinàmica és generalment superior a la de camp mig, especialment a les densitats més altes. En certa manera, doncs, sembla que les correlacions que van més enllà del camp mig tendeixen

a augmentar l'entropia. Quant a la dependència en densitat, s'observa novament un decreixement acusat a baixes densitats. Aquest decreixement és, però, menys important que en el cas no correlacionat. De fet, l'aproximació clàssica no reproduceix bé la dependència en densitat de l'entropia per partícula. En canvi, la dependència en temperatura a densitat fixa és més o menys lineal a baixes temperatures, d'acord amb el límit degenerat. Hi ha, però, diverses diferències respecte al límit degenerat del cas no correlacionat. En aquell cas, l'aproximació lineal s'obtenia a partir de la densitat d'estats a temperatura zero. Malauradament, l'aproximació SCGF no es pot extrapolar de manera fiable a aquesta temperatura (on els efectes d'aparellament són necessàriament importants) i s'ha de fer servir la densitat d'estats de la temperatura més baixa per calcular l'aproximació lineal. A partir del límit degenerat de l'entropia correlacionada de l'Eq. (20), es pot obtenir una expressió per la densitat d'estats:

$$N_{\mathcal{B}}(T) = \nu \int \frac{d^3k}{(2\pi)^4} \mathcal{B}(k, \omega = \mu), \quad (38)$$

on T denota el fet que aquesta densitat d'estats ha estat calculada a una temperatura T concreta no nul·la. L'estretesa de la funció espectral \mathcal{B} fa que, a baixes temperatures, aquesta quantitat sigui molt semblant a la densitat d'estats en l'aproximació de quasi-partícula, Eq. (29). En tot cas, l'entropia per partícula no presenta un comportament tan lineal com l'entropia a temperatures baixes en el cas no correlacionat. Per exemple, l'entropia en l'aproximació de SCHF a $\rho = 2\rho_0$ es reproduceix amb l'aproximació lineal fins a $T = 20$ MeV, mentre que en el cas correlacionat comencen a apreciar-se desviacions del comportament lineal a partir de $T = 10$ MeV. En certa manera, doncs, sembla que al sistema correlacionat li costa més arribar als límits clàssic i degenerat.

Per arribar al potencial termodinàmic, encara ens cal calcular l'energia per partícula. Aquesta quantitat s'ha de calcular, com hem repetit anteriorment, a partir de la regla de suma de GMK i la presentem a la Fig. 13. Els tres panells mostren l'energia total (panell esquerre), l'energia cinètica (panell central) i l'energia potencial (panell dret) per partícula en un cert rang de densitats per cinc temperatures diferents. A la temperatura més baixa ($T = 5$ MeV) els resultats per l'energia total són atractius per totes les densitats explorades, en contra del que passa al cas no correlacionat. Aquesta és una conseqüència clara de la introducció de correlacions a dos cossos en el formalisme, que permeten assolir resultats més realistes. A mida que la temperatura augmenta, l'energia total augmenta de manera uniforme a totes les densitats. Aquest efecte es deu essencialment a l'augment en energia cinètica, ja que l'energia potencial amb prou feines canvia amb la temperatura. El creixement de l'energia per partícula és bàsicament quadràtic amb la temperatura a totes les densitats, com s'espera en el límit degenerat d'un sistema fermiònic. Tanmateix, s'ha de fer notar que en el cas correlacionat és difícil trobar una expressió analítica pel coeficient que acompanya aquesta dependència

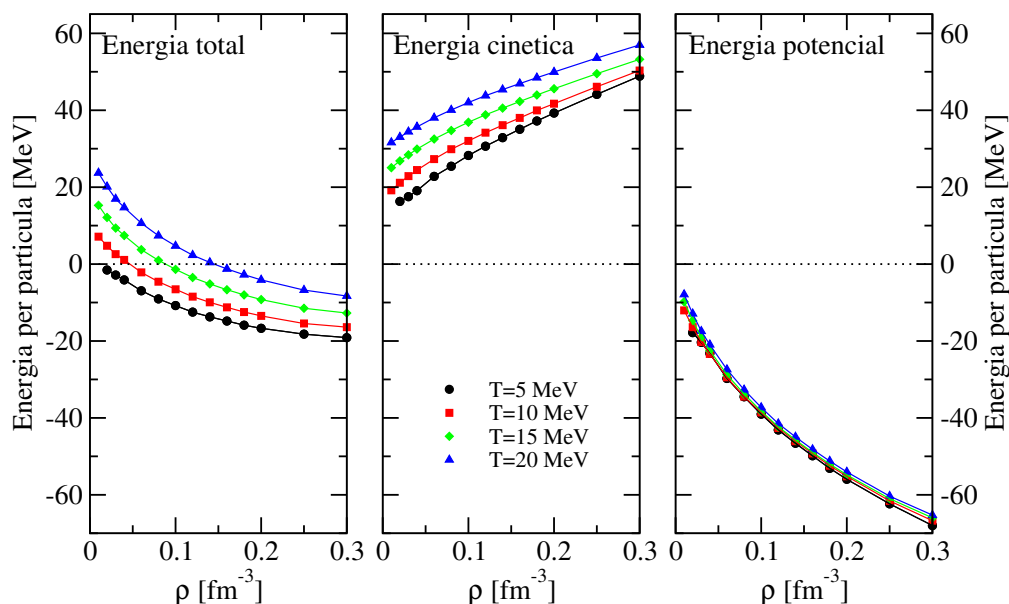


Figura 13: Dependència en densitat de l'energia per partícula total (panell esquerre), l'energia cinètica (panell central) i l'energia potencial (panell dret) en l'aproximació de SCGF. S'hi mostren quatre temperatures: 5 (cercles), 10 (quadrats), 15 (diamants) i 20 (triangles) MeV.

quadràtica (veieu Apèndix D). És important esmentar que l'energia cinètica presenta una dependència en densitat i temperatura relativament semblant a la del cas no correlacionat, però és 1.5 vegades superior. Aquest increment es deu a la introducció de les correlacions, que modifiquen la distribució de moments i fan augmentar la població a alts moments. D'altra banda, l'energia potencial és entre 3 i 4 vegades més atractiva que en el cas de l'aproximació de SCHF, gràcies a la inclusió de les correlacions a dos cossos. Tot plegat es tradueix en l'existència d'un punt de saturació per l'energia total, que ocorre a un densitat força alta, $\rho = 0.3 \text{ fm}^{-3}$, pràcticament constant per totes les temperatures explorades. L'energia de saturació associada a aquesta densitat, tanmateix, depèn substancialment de la temperatura i va des dels -19 MeV a $T = 5 \text{ MeV}$ fins als -8 MeV a $T = 20 \text{ MeV}$.

Un cop calculades l'energia i l'entropia del sistema correlacionat, podem utilitzar els resultats per obtenir l'energia lliure del sistema. La línia contínua amb cercles del panell esquerre de la Fig. 14 representa precisament l'energia lliure per partícula de la matèria nuclear en funció de la densitat a una temperatura de $T = 10 \text{ MeV}$. La línia contínua amb quadres dona l'energia per partícula en el mateix rang de densitats i temperatures. Al panell dret hi mostrem les mateixes quantitats obtingudes amb l'aproximació de BHF. A nivell qualitatiu, podem dir que a densitats altes i intermèdies ambdues quantitats són més repulsives en l'aproximació de SCGF que en la de BHF. A aquesta temperatura en

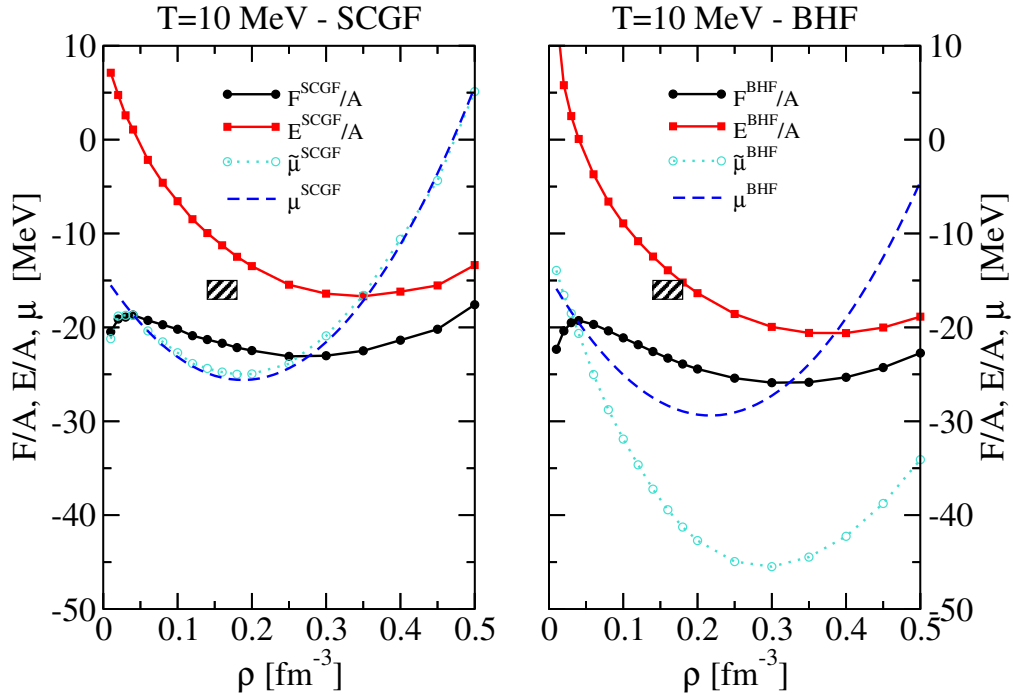


Figura 14: *Energia lliure per partícula (línia contínua), energia total per partícula (línia contínua amb cercles) i potencial químic $\tilde{\mu}$ (línia puntejada amb cercles) per les aproximacions de SCGF (panell esquerre) i BHF (panell dret) en funció de la densitat per una temperatura de $T = 10$ MeV. El potencial químic μ obtingut mitjançant una derivada numèrica de F/A es mostra en línies discontinües. L'àrea ressaltada representa el punt empíric de saturació de la matèria nuclear simètrica.*

particular, l'efecte és tal que situa l'energia de saturació de SCGF a uns -16 MeV, en coincidència amb l'energia de saturació empírica. Ara bé, com ja hem comentat, aquesta quantitat depèn substancialment de la temperatura i una extrapolació a $T = 0$ dona una energia de saturació de -21 MeV.

Ja hem esmentat que la consistència termodinàmica en una aproximació de molts cossos es tradueix en una equivalència entre els valors obtinguts per una quantitat determinada, ja sigui de forma microscòpica o de manera termodinàmica. Hi ha maneres de demostrar que una aproximació respecta la consistència termodinàmica i és ben sabut que tant l'aproximació d'escala com la de HF són consistents [Bay62]. Un observable que sovint s'utilitza per estudiar aquesta consistència és el potencial químic. D'una banda, el potencial químic es pot determinar mitjançant la normalització de la distribució de moments, Eq. (24). Aquest és el potencial químic microscòpic, $\tilde{\mu}$. D'altra banda, a nivell termodinàmic el potencial

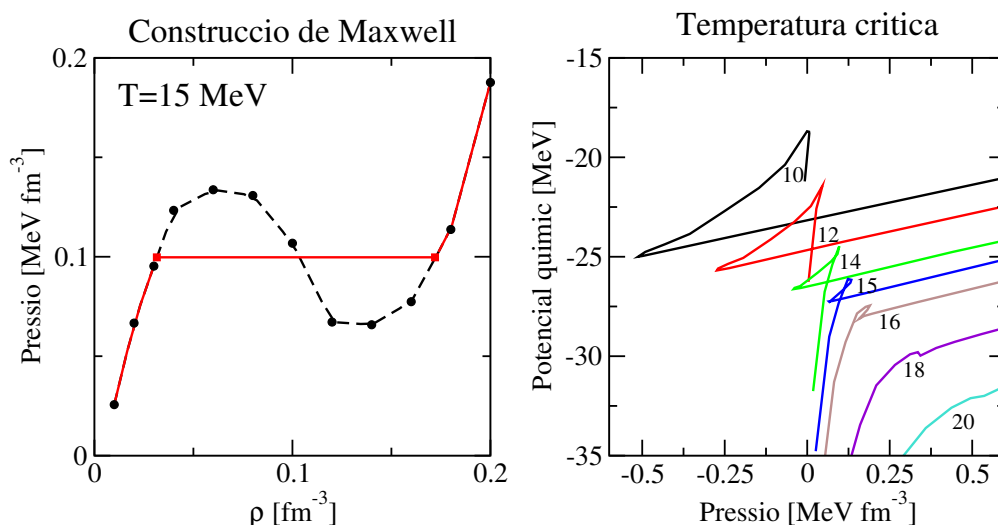


Figura 15: *Panell esquerre: construcció de Maxwell per la pressió a $T = 15$ MeV. Panell dret: determinació aproximada de la temperatura crítica amb corbes $\mu - p$.*

químic s'obté de derivar la densitat d'energia lliure respecte de la densitat:

$$\mu(\rho, T) = \frac{\partial F(\rho, T)}{\partial \rho} \frac{1}{\mathcal{V}}. \quad (39)$$

Als panells esquerre i dret de la Fig. 14 hi presentem $\tilde{\mu}$ amb una línia puntejada amb cercles buits i μ amb una línia discontinua. S'observa que, per sobre de 0.03 fm^{-3} , els potencials químics pràcticament coincideixen en l'aproximació de SCGF. Els resultats de l'aproximació de BHF, en canvi, difereixen pràcticament en una vintena de MeV a ρ_0 . L'absència de consistència termodinàmica és un dels principals desavantatges de l'aproximació de BHF, i obliga, en gairebé totes les aplicacions pràctiques, a obtenir el potencial químic a partir de derivades numèriques de l'energia lliure. L'aproximació de SCGF complementada amb el formalisme de Luttinger-Ward permet, en canvi, obtenir resultats consistents a nivell microscòpic. Noteu que aquesta consistència es pot prendre com a la confirmació que l'aproximació de l'entropia correlacionada en termes de l'entropia de quasi-partícula dinàmica és raonable.

Com a primera aplicació d'aquesta metodologia a la matèria nuclear, presentem a la Fig. 15 dos panells associats a la transició de fase de tipus líquid-gas que té lloc a densitats baixes per aquest sistema. L'existència d'aquesta transició es pot deduir de la dependència en densitat tant del potencial químic com de la pressió. Aquesta última s'obté de la igualtat:

$$p = \rho \left(\tilde{\mu} - \frac{F}{A} \right), \quad (40)$$

i mostra un màxim a densitats intermèdies (veieu línia discontinua en el panell esquerre de la Fig. 15). La zona de pressions decreixents amb la densitat, que es correspon també amb la zona de potencials químics decreixents, és inestable mecànicament i determinada l'anomenada zona espinodal. La presència d'aquesta zona és un signe de la descomposició de fases del sistema, ja que, a una temperatura fixa, implica la presència de dues densitats amb pressions iguals. De fet, les dues densitats que satisfan simultàniament les següents igualtats per una temperatura donada:

$$p(\rho_G, T) = p(\rho_L, T) \quad (41)$$

$$\mu(\rho_G, T) = \mu(\rho_L, T) \quad (42)$$

defineixen la densitat de dues fases qualitativament diferents: la fase de gas, a una densitat baixa ρ_G , i la fase de líquid, a una densitat $\rho_L > \rho_G$. Entre ambdues densitats hi ha, a cada temperatura, una zona de coexistència de fases en què, segons la construcció de Maxwell de les transicions de fase, tant el potencial químic com la pressió haurien de constants. Al panell esquerre de la Fig. 15 mostrem aquesta construcció per la pressió del cas correlacionat a $T = 15$ MeV. A l'interior de la zona de pressió constant hi coexisteixen un fase gasosa i una de líquida. A partir d'una certa temperatura, però, tant la pressió com el potencial químic passen a ser funcions monòtones de la densitat i ja no s'hi observa cap coexistència de fases. Una manera relativament senzilla de trobar aquesta temperatura crítica, T_c , ens la dona el panell de la dreta de la Fig. 15. En efecte, la coexistència de fases implica que, en la gràfica de la pressió en funció del potencial químic, hi ha d'haver un creuament de dues branques de la mateixa funció. Per sobre de la temperatura crítica, en canvi, el potencial químic és una funció monòtona de la pressió. El canvi d'un comportament a l'altre s'observa, a la Fig. 15, entre $T = 16$ i $T = 18$ MeV i per tant la temperatura crítica rau al voltant dels $T_c \sim 17$ MeV. És important fer notar que per dur a terme el mateix càlcul en una aproximació que no fos termodinàmicament consistent, caldria obtenir el potencial químic a cada densitat mitjançant una derivada numèrica.

Resum i conclusions

El principal objectiu d'aquesta tesi ha estat l'estudi del problema nuclear de molts cossos a temperatura finita a partir d'un càlcul *ab initio*. Més concretament, en aquesta tesi hem volgut descriure la connexió entre les propietats termodinàmiques del sistema i les seves excitacions microscòpiques descrites en termes de funcions de Green. La teoria de les funcions de Green és un dels pocs tractaments de molts cossos que es pot generalitzar sense ambigüitats a temperatura finita. L'ús d'aquest formalisme ens permet trobar les propietats espectrals de la funció de Green a un cos i, a partir d'elles, tenim accés a totes les propietats mono-particulars del sistema de molts cossos, a més de l'energia per partícula.

Ara bé, la connexió entre aquestes propietats microscòpiques i les propietats termodinàmiques del sistema s'ha d'establir de manera consistent. Això és precisament el que fa el formalisme de Luttinger-Ward. En aquest formalisme, la funció de partició s'expressa en termes de la funció de Green vestida i és en aquest sentit que hom diu que es tracta d'una aproximació no pertorbativa. D'entre les propietats termodinàmiques que podem estudiar, l'entropia és particularment senzilla d'obtenir i permet, juntament amb l'energia per partícula derivada a partir de la regla de suma de GMK, trobar el potencial termodinàmic relevant del sistema, *i. e.* l'energia lliure. En aquest formalisme l'entropia correlacionada es pot calcular en l'aproximació de quasi-partícula dinàmica, en què l'entropia ve donada per una convolució en energies d'un factor estadístic, $\sigma(\omega)$, i una funció espectral que conté els efectes deguts a les correlacions dinàmiques.

Com a primer càlcul dins del mètode de les funcions de Green i del formalisme de Luttinger-Ward, hem analitzat la matèria nuclear en l'aproximació de HF a partir d'una interacció realista. Els efectes de l'autoconsistència, que poden ser importants a densitats prou elevades, es poden estudiar a través de l'autoenergia. La manca de correlacions a dos cossos en aquesta aproximació duu, però, a resultats positius per l'energia per partícula. L'aproximació de HF és, per tant, molt lluny de ser realista. Tot i això, aquesta aproximació de camp mig ens permet entendre qualitativament les propietats termodinàmiques del sistema, especialment les seves dependències en densitat i temperatura, que es poden descriure en certs règims de densitats i temperatures mitjançant els límits clàssic i degenerat.

Un mètode més realista per tractar el problema de la matèria nuclear és l'aproximació d'escala, que suma diagrames d'interaccions successives entre dues partícules a nivell del propagador a dos cossos. La resolució numèrica d'aquesta aproximació tot i considerant tant la dependència en moment com en energies de totes les quantitats es pot dur a terme mitjançant l'esquema de les Funcions de Green Autoconsistents (SCGF). D'aquesta manera, podem tenir accés a la funció espectral d'un nucleó en la matèria nuclear, que presenta alhora un pic de quasi-partícula molt accentuat i cues no negligibles a altes energies. Aquestes cues són causades, en última instància, per les correlacions de curt abast i diem que el pic de quasi-partícula s'ha fragmentat com a conseqüència d'aquestes correlacions.

L'aplicació d'aquests resultats microscòpics a l'estudi de les propietats termodinàmiques del sistema es pot dur a terme mitjançant el formalisme de Luttinger-Ward. Aquest formalisme suggereix l'ús de l'entropia de quasi-partícula dinàmica, en què els efectes de les correlacions queden inclosos en una funció espectral \mathcal{B} més estreta i més alta que la funció espectral habitual. En aquesta aproximació, els resultats obtinguts pel potencial químic són termodinàmicament consistents. Tant l'energia per partícula com l'energia lliure per partícula que se n'obtenen són més repulsives en l'aproximació d'escala que en la de BHF. Això permet obtenir resultats més realistes per l'energia de saturació, tot i que la densitat de saturació corresponent és encara massa alta. Una primera aplicació d'aquests resultats ha

estat la determinació de la temperatura crítica de la matèria nuclear simètrica, que en el cas correlacionat es troba al voltant de $T_c \sim 17$ MeV. La combinació de la teoria de funcions de Green i el formalisme de Luttinger-Ward estableix un marc comú, consistent i basat en primers principis en què es poden obtenir qualitativament les propietats termodinàmiques de la matèria nuclear. Aquest mètode obre la porta a futures aplicacions de càlculs realistes en el camp de la matèria densa, que ens poden permetre entendre millor des de l'estructura i característiques d'objectes astrofísics compactes fins les propietats més genèriques de les col·lisions d'ions pesats.

Bibliography

- [Abr65] A. A. ABRIKOSOV, L. P. GORK'OV AND I. Y. DZIALOSHINSKII, *Quantum Field Theoretical Methods in Statistical Physics* (Pergamon Press, 1965), Second Edition.
- [Alm93] T. ALM, B. L. FRIMAN, G. RÖPKE AND H. SCHULZ, *Pairing instability in hot asymmetric nuclear matter*, Nuclear Physics A **551**, 45 (1993).
- [Alm96] T. ALM, G. RÖPKE, A. SCHNELL, N. H. KWONG AND H. S. KÖHLER, *Nucleon spectral function at finite temperature and the onset of superfluidity in nuclear matter*, Physical Review C **53**, 2181 (1996).
- [Ami68a] D. J. AMIT, J. W. KANE AND H. WAGNER, *Coupling of density and spin fluctuations to quasiparticles in a Fermi liquid*, Physical Review **75**, 313 (1968).
- [Ami68b] D. J. AMIT, J. W. KANE AND H. WAGNER, *Logarithmic terms in specific heat of a normal Fermi liquid*, Physical Review **75**, 326 (1968).
- [Bal90] M. BALDO, I. BOMBACI, G. GIANSIRACUSA, U. LOMBARDO, C. MAHAUX AND R. SARTOR, *Nuclear matter properties from a separable representation of the Paris potential*, Physical Review C **41**, 1748 (1990).
- [Bal99] M. BALDO AND L. S. FERREIRA, *Nuclear liquid-gas phase transition*, Physical Review C **59**, 682 (1999).
- [Bal04] M. BALDO, L. S. FERREIRA AND O. E. NICOTRA, *The limiting temperature of hot nuclei from microscopic equation of state*, Physical Review C **69**, 034321 (2004).
- [Bay61] G. BAYM AND N. D. MERMIN, *Determination of thermodynamic Green's Function*, Journal of Mathematical Physics **2**, 232 (1961).
- [Bay62] G. BAYM, *Self-consistent approximations in many-body systems*, Physical Review **127**, 1391 (1962).

-
- [Ben89] O. BENHAR, A. FABROCINI AND S. FANTONI, *The nucleon spectral function in nuclear matter*, Nuclear Physics A **505**, 267 (1989).
- [Ben92] O. BENHAR, A. FABROCINI AND S. FANTONI, *Nuclear matter Green's functions in correlated-basis theory*, Nuclear Physics A **550**, 201 (1992).
- [Ben03] M. BENDER, P.-H. HEENEN AND P.-G. REINHARD, *Self-consistent mean-field models for nuclear structure*, Reviews of Modern Physics **75**, 121 (2003).
- [Ber66] N. F. BERK AND J. R. SCHRIEFFER, *Effect of ferromagnetic spin correlations on superconductivity*, Physical Review Letters **17**, 433 (1966).
- [Ber04] J. BERGES, *Introduction to nonequilibrium quantum field theory*, arXiv:hep-ph/0409233 (2004).
- [Bet63] H. A. BETHE, B. H. BRANDOW AND A. G. PETSCHKE, *Reference spectrum method for nuclear matter*, Physical Review **129**, 225 (1963).
- [Bet65] H. A. BETHE, *Three-body correlations in nuclear matter*, Physical Review **138**, B804 (1965).
- [Bet90] H. A. BETHE, *Supernova mechanisms*, Reviews of Modern Physics **62**, 801 (1990).
- [Bis91] R. F. BISHOP, *An overview of coupled cluster theory and its applications in physics*, Theoretica Chimica Acta **80**, 95 (1991).
- [Bla86] J.-P. BLAIZOT AND G. RIPKA, *Quantum Theory of Finite Systems* (MIT Press, Cambridge, Massachusetts, 1986), First Edition.
- [Bla95] J.-P. BLAIZOT, J. F. BERGER, J. DECHARGÉ AND M. GIROD, *Microscopic and macroscopic determinations of nuclear compressibility*, Nuclear Physics A **591**, 435 (1995).
- [Bla04] J.-P. BLAIZOT, E. IANCU AND U. REINOSA, *Renormalization of Φ -derivable approximations in scalar field theories*, Nuclear Physics A **736**, 149 (2004).
- [Blo58a] C. BLOCH, *Sur la détermination de l'état fondamental d'un système de particules*, Nuclear Physics **7**, 451 (1958).
- [Blo58b] C. BLOCH AND C. DE DOMINICIS, *Un développement du potentiel de Gibbs d'un système quantique composé d'un grand nombre de particules*, Nuclear Physics **7**, 459 (1958).

-
- [Blo59a] C. BLOCH AND C. DE DOMINICIS, *Un développement du potentiel de Gibbs d'un système quantique composé d'un grand nombre de particules (II)*, Nuclear Physics **10**, 181 (1959).
- [Blo59b] C. BLOCH AND C. DE DOMINICIS, *Un développement du potentiel de Gibbs d'un système quantique composé d'un grand nombre de particules. III. La contribution des collisions binaires*, Nuclear Physics **10**, 509 (1959).
- [Bog03] S. K. BOGNER, T. T. S. KUO AND A. SCHWENK, *Model-independent low momentum nucleon interaction from phase shift equivalence*, Physics Reports **386**, 1 (2003).
- [Bog05] S. K. BOGNER, A. SCHWENK, R. J. FURNSTAHL AND A. NOGGA, *Is nuclear matter perturbative with low-momentum interactions?*, Nuclear Physics A **763**, 59 (2005).
- [Bom94] I. BOMBACI, T. T. S. KUO AND U. LOMBARDO, *Temperature and asymmetry dependence of nuclear incompressibility and supernova explosions*, Physics Reports **242**, 165 (1994).
- [Bot90] W. BOTERMANS AND R. MALFLIET, *Quantum transport theory of nuclear matter*, Physics Reports **198**, 115 (1990).
- [Boz99] P. BOZEK, *Superfluid nuclear matter calculations*, Nuclear Physics A **657**, 187 (1999).
- [Boz01] P. BOZEK AND P. CZERSKI, *Thermodynamic consistency for nuclear matter calculations*, European Physical Journal A **11**, 271 (2001).
- [Boz02] P. BOZEK, *One-body properties of nuclear matter with off-shell propagation*, Physical Review C **65**, 054306 (2002).
- [Boz03a] P. BOZEK, *Superfluidity with dressed nucleons*, Physics Letters B **551**, 93 (2003).
- [Boz03b] P. BOZEK AND P. CZERSKI, *In medium T -matrix with realistic nuclear interactions*, Acta Physica Polonica **B 34**, 2759 (2003).
- [Bre67] W. BRENIG, H. J. MIKESKA AND E. RIEDEL, *On specific heat of Fermi liquids*, Zeitschrift für Physik **206**, 439 (1967).
- [Bro71] G. E. BROWN, *Landau, Brueckner-Bethe, and Migdal theories of Fermi systems*, Reviews of Modern Physics **43**, 1 (1971).
- [Bro90] R. BROCKMANN AND R. MACHLEIDT, *Relativistic nuclear structure. I. Nuclear matter*, Physical Review C **42**, 1965 (1990).
-

-
- [Bru54] K. A. BRUECKNER, C. A. LEVISON AND H. M. MAHMOUD, *Two-body forces and nuclear saturation. I. Central forces*, Physical Review **95**, 217 (1954).
- [Bru60] K. A. BRUECKNER AND D. T. GOLDMAN, *Single particle energies in the theory of nuclear matter*, Physical Review **117**, 207 (1960).
- [Car75] G. M. CARNEIRO AND C. J. PETHICK, *Specific-heat of a normal Fermi-Liquid. 2. Microscopic approach*, Physical Review B **11**, 1106 (1975).
- [Cas00] W. CASSING AND S. JUCHEM, *Semiclassical transport of particles with dynamical spectral functions*, Nuclear Physics A **665**, 377 (2000).
- [Che01] Q. CHEN, K. LEVIN AND I. KOSZTIN, *Superconducting phase coherence in the presence of a pseudogap: Relation to specific heat, tunneling, and vortex core spectroscopies*, Physical Review B **63**, 184519 (2001).
- [Cho04] P. CHOMAZ, M. COLONNA AND J. RANDRUP, *Nuclear spinodal fragmentation*, Physics Reports **389**, 263 (2004).
- [Chu06] A. V. CHUBUKOV, D. L. MASLOV AND A. J. MILLIS, *Nonanalytic corrections to the specific heat of a three-dimensional Fermi liquid*, Physical Review B **73** (2006).
- [Cla66] J. W. CLARK AND P. WESTHAUS, *Method of correlated basis functions*, Physical Review **141**, 833 (1966).
- [Cla79] J. W. CLARK, *Variational theory of nuclear matter*, Progress in Particle and Nuclear Physics **2**, 89 (1979).
- [Coe70] F. COESTER, S. COHEN, B. D. DAY AND C. M. VINCENT, *Variation in nuclear-matter binding energies with phase-shift-equivalent two-body potentials*, Physical Review C **1**, 769 (1970).
- [Coh60] M. COHEN, *Relation between inelastic neutron scattering and thermodynamic functions of liquid helium*, Physical Review **118**, 27 (1960).
- [Cor74] J. M. CORNWALL, R. JACKIW AND E. TOMBOULI, *Effective action for composite operators*, Physical Review D **10**, 2428 (1974).
- [Cse86] L. P. CSERNAI AND J. I. KAPUSTA, *Entropy and cluster production in nuclear collisions*, Physics Reports **131**, 223 (1986).
- [Cze02] P. CZERSKI, A. DE PACE AND A. MOLINARI, *Revisiting the Hugenholtz-van Hove theorem in nuclear matter*, Physical Review C **65**, 044317 (2002).

-
- [Dan00] P. DANIELEWICZ, *Determination of the mean-field momentum-dependence using elliptic flow*, Nuclear Physics A **673**, 375 (2000).
- [Dan02] P. DANIELEWICZ, R. LACEY AND W. G. LYNCH, *Determination of the Equation of State of Dense Matter*, Science **298**, 1592 (2002).
- [Day67] B. D. DAY, *Elements of the Brueckner-Goldstone theory of nuclear matter*, Reviews of Modern Physics **39**, 719 (1967).
- [Day81] B. D. DAY, *Three-body correlations in nuclear matter*, Physical Review C **24**, 1203 (1981).
- [dD64a] C. DE DOMINICIS AND P. C. MARTIN, *Stationary entropy principle and renormalization in normal and superfluid systems. I. Algebraic formulation*, Journal of Mathematical Physics **5**, 14 (1964).
- [dD64b] C. DE DOMINICIS AND P. C. MARTIN, *Stationary entropy principle and renormalization in normal and superfluid systems. II. Diagrammatic formulation*, Journal of Mathematical Physics **5**, 31 (1964).
- [De98] J. N. DE, S. SHLOMO AND S. K. SAMADDAR, *Level density parameter in a refined Thomas-Fermi theory*, Physical Review C **57**, 1398 (1998).
- [Dea03] D. J. DEAN AND M. HJORTH-JENSEN, *Pairing in nuclear systems: from neutron stars to finite nuclei*, Reviews of Modern Physics **75**, 607 (2003).
- [Dec80] J. DECHARGÉ AND D. GOGNY, *Hartree-Fock-Bogolyubov calculations with the D1 effective interaction on spherical nuclei*, Physical Review C **21**, 1568 (1980).
- [Dew02] Y. DEWULF, D. V. NECK AND M. WAROQUIER, *Effects of self-consistency in a Green's function description of saturation in nuclear matter*, Physical Review C **65**, 054316 (2002).
- [Dew03] Y. DEWULF, W. H. DICKHOFF, D. V. NECK, E. R. STODDARD AND M. WAROQUIER, *Saturation of nuclear matter and short-range correlations*, Physical Review Letters **90**, 152501 (2003).
- [Dic99] W. H. DICKHOFF, C. C. GEARHART, E. P. ROTH, A. POLLS AND A. RAMOS, *Phase shifts and in-medium cross sections for dressed nucleons in nuclear matter*, Physical Review C **60**, 064319 (1999).
- [Dic04] W. H. DICKHOFF AND C. BARBIERI, *Self-consistent Green's function method for nuclei and nuclear matter*, Progress in Particle and Nuclear Physics **52**, 377 (2004).
-

-
- [Dic05a] W. DICKHOFF AND D. V. NECK, *Many-Body Theory Exposed!* (World Scientific Publishing, London, 2005), First Edition.
- [Dic05b] W. H. DICKHOFF AND H. MÜTHER, *Pairing properties of nucleonic matter employing dressed nucleons*, Physical Review C **72**, 054313 (2005).
- [Don66] S. DONIACH AND S. ENGELBERG, *Low-temperature properties of nearly ferromagnetic Fermi liquids*, Physical Review Letters **17**, 750 (1966).
- [Dup05] N. DUPUIS, *Renormalization group approach to fermion systems in the two-particle-irreducible formalism*, European Physical Journal B **48**, 319 (2005).
- [Dze95] M. DZELALIJA *et al.*, *Entropy in central Au+Au reactions between 100 and 400A MeV*, Physical Review C **52**, 346 (1995).
- [Eis72] J. M. EISENBERG AND W. GREINER, *Microscopic Theory of the Nucleus* (North-Holland Publishing, Amsterdam, 1972), First Edition.
- [Ent03] D. R. ENTEM AND R. MACHLEIDT, *Accurate charge-dependent nucleon-nucleon potential at fourth order of chiral perturbation theory*, Physical Review C **68**, 041001 (2003).
- [Fan75] S. FANTONI AND S. ROSATI, *Hypernetted-chain approximation for a fermion system*, Nuovo Cimento della Società Italiana di Fisica A **25**, 593 (1975).
- [Fan84] S. FANTONI AND V. J. PANDHARIPANDE, *Momentum distribution of nucleons in nuclear matter*, Nuclear Physics A **427**, 473 (1984).
- [Fan97] S. FANTONI AND A. FABROCINI, *Correlated basis function theory for fermion systems*, in *Microscopic quantum many-body theories and their applications* (Eds. J. Navarro and A. Polls), Lecture Notes in Physics **510** (1997).
- [Far99] M. FARINE, D. VON-EIFF, P. SCHUCK, J. F. BERGER, J. DECHARGÉ AND M. GIROD, *Towards a new effective interaction of the Gogny type*, Journal of Physics G **25**, 863 (1999).
- [Fel98] H. FELDMEIER, T. NEFF, R. ROTH AND J. SCHNACK, *A unitary correlation operator method*, Nuclear Physics A **632**, 61 (1998).
- [Fet71] A. L. FETTER AND J. D. WALECKA, *Quantum Theory of Many-Particle Systems* (McGraw-Hill, New York, 1971), Second Edition.

-
- [Fey65] R. P. FEYNMAN AND A. R. HIBBS, *Quantum Mechanics and Path Integrals* (McGraw-Hill, New York, 1965), First Edition.
- [Fis77] C. F. FISCHER, *The Hartree-Fock method for atoms: a numerical approach* (Wiley, New York, 1977).
- [Fri02] S. FRITSCH, N. KAISER AND W. WEISE, *Chiral dynamics of nuclear matter at finite temperature*, Physics Letters B **545**, 73 (2002).
- [Fri03] T. FRICK AND H. MÜTHER, *Self-consistent solution to the nuclear many-body problem at finite temperature*, Physical Review C **68**, 034310 (2003).
- [Fri04a] T. FRICK, *Self-Consistent Green's Functions in Nuclear Matter at Finite Temperature*, Ph.D. thesis, University of Tübingen (2004), advisor: Prof. H. Müther.
- [Fri04b] T. FRICK, H. MÜTHER AND A. POLLS, *Sum rules and short-range correlations in nuclear matter at finite temperature*, Physical Review C **69**, 054305 (2004).
- [Fri05] T. FRICK, H. MÜTHER, A. RIOS, A. POLLS AND A. RAMOS, *Correlations in hot asymmetric nuclear matter*, Physical Review C **71**, 014313 (2005).
- [Fur97] R. J. FURNSTAHL, B. D. SEROT AND H. B. TANG, *A chiral effective Lagrangian for nuclei*, Nuclear Physics A **615**, 441 (1997).
- [Gal58a] V. M. GALISTKII, *The energy spectrum of a non-ideal Fermi gas*, Soviet Physics–JETP **7**, 104 (1958).
- [Gal58b] V. M. GALITSKII AND A. B. MIGDAL, *Application of quantum field theory methods to the many body problem*, Soviet Physics–JETP **7**, 96 (1958).
- [Gol57] J. GOLDSTONE, *Derivation of the Brueckner many-body theory*, Proceedings of the Royal Society of London, Series A **293**, 267 (1957).
- [Gra89] P. GRANGÉ, A. LEJEUNE, M. MARTZOLFF AND J.-F. MATHIOT, *Consistent three-nucleon forces in the nuclear many-body problem*, Physical Review C **40**, 1040 (1989).
- [Gre83] D. S. GREYWALL, *Specific heat of normal liquid ^3He* , Physical Review B **27**, 2747 (1983).
- [Haf70] M. I. HAFTEL AND F. TABAKIN, *Nuclear saturation and the smoothness of nucleon-nucleon potentials*, Nuclear Physics A **158**, 1 (1970).
-

-
- [Hey88] J. HEYER, T. T. S. KUO, J. P. SHEN AND S. S. WU, *Finite-temperature density-dependent HF calculation of nuclear matter with Gogny interaction*, Physics Letters B **202**, 465 (1988).
- [Hor06] C. J. HOROWITZ AND A. SCHWENK, *Cluster formation and the virial equation of state of low-density nuclear matter*, Nuclear Physics A **776**, 55 (2006).
- [Hub98] H. HUBER, F. WEBER AND M. K. WEIGEL, *Symmetric and asymmetric nuclear matter in the relativistic approach at finite temperatures*, Physical Review C **57**, 3484 (1998).
- [Hug58] N. M. HUGENHOLTZ AND L. V. HOVE, *A theorem on the single particle energy in a Fermi gas with interaction*, Physica **24**, 363 (1958).
- [Iva99] Y. B. IVANOV, J. KNOLL AND D. N. VOSKRESENSKY, *Self-consistent approximations to non-equilibrium many-body systems*, Nuclear Physics A **657**, 413 (1999).
- [Iva00] Y. B. IVANOV, J. KNOLL AND D. N. VOSKRESENSKY, *Resonance transport and kinetic entropy*, Nuclear Physics A **672**, 313 (2000).
- [Jac82] A. D. JACKSON, A. LANDÉ AND R. A. SMITH, *Variational and perturbation theories made planar*, Physics Reports **25**, 55 (1982).
- [Jac83] B. V. JACAK *et al.*, *Measurement of complex fragments and clues to the entropy production from 42-137-MeV/nucleon Ar+Au*, Physical Review Letters **51**, 1846 (1983).
- [Jeu76] J. P. JEUKENNE, A. LEJEUNE AND C. MAHAUX, *Many-body theory of nuclear matter*, Physics Reports **25**, 83 (1976).
- [Kad62] L. P. KADANOFF AND G. BAYM, *Quantum Statistical Mechanics* (Benjamin, New York, 1962), First Edition.
- [Kai02] N. KAISER, S. FRITSCH AND W. WEISE, *Chiral dynamics and nuclear matter*, Nuclear Physics A **697**, 255 (2002).
- [Kel96] J. J. KELLY, *Nucleon knockout by intermediate energy electrons*, Advances in Nuclear Physics **23**, (Eds. J. W. Negele and E. W. Vogt, Plenum Press, NY), (1996).
- [Kla06] T. KLAHN *et al.*, *Constraints on the high-density nuclear equation of state from the phenomenology of compact stars and heavy-ion collisions*, Physical Review C **74**, 035802 (2006).

-
- [Koh60] W. KOHN AND J. M. LUTTINGER, *Ground-State Energy of a Many-Fermion System. I*, Physical Review **118**, 41 (1960).
- [Köh95] H. S. KÖHLER, *Memory and correlation effects in nuclear collisions*, Physical Review C **51**, 3232 (1995).
- [Kol74] D. S. KOLTUN, *Theory of mean removal energies for single particles in nuclei*, Physical Review **9**, 484 (1974).
- [Kra86] W. D. KRAEFT, D. KREMP, W. EBELING AND G. RÖPKE, *Quantum Statistics of Charged Particle Systems* (Akademie-Verlag, Berlin, 1986).
- [Kuh93] C. KUHN *et al.*, *Entropy production in the Au+Au reaction between 150A and 800A MeV*, Physical Review C **48**, 1232 (1993).
- [lal04] *Extended density functionals in nuclear structure physics*, (Eds. G. A. Lalazissis, P. Ring and D. Vretenar), Lecture Notes in Physics **641** (Springer, Berlin Heidelberg) (2004).
- [Lee75] T. D. LEE AND M. MARGULIES, *Interaction of a dense fermion medium with a scalar-meson field*, Physical Review D **11**, 1591 (1975).
- [Lej86] A. LEJEUNE, P. GRANGÉ, M. MARTZOLFF AND J. CUGNON, *Hot nuclear matter in an extended Brueckner approach*, Nuclear Physics A **453**, 189 (1986).
- [Lut60] J. M. LUTTINGER AND J. C. WARD, *Ground-State Energy of a Many-Fermion System. II*, Physical Review **118**, 1417 (1960).
- [Lut61] J. M. LUTTINGER, *Analytic properties of single-particle propagators for many-fermion systems*, Physical Review **121**, 942 (1961).
- [Lut00] M. LUTZ, B. FRIMAN AND C. APPEL, *Saturation from nuclear pion dynamics*, Physics Letters B **474**, 7 (2000).
- [LV06] D. LÓPEZ-VAL, A. RIOS, A. POLLS AND I. VIDANA, *Ferromagnetic instabilities in neutron matter at finite temperature with the Gogny interaction*, Physical Review C **74**, 068801 (2006).
- [Mac96] R. MACHLEIDT, *Nonlocal nature of the nuclear force and its impact on nuclear structure*, Physical Review C **53**, R1483 (1996).
- [Mac01] R. MACHLEIDT, *High-precision, charge-dependent Bonn nucleon-nucleon potential*, Physical Review C **63**, 024001 (2001).
- [Mah90] G. D. MAHAN, *Many-particle Physics* (Plenum Press, NY, 1990), Second Edition.
-

-
- [Mar59] P. C. MARTIN AND J. SCHWINGER, *Theory of Many-Particle Systems. I*, Physical Review **115**, 1342 (1959).
- [Mat71] R. D. MATTUCK AND A. THEUMANN, *Expressing the decoupled equations of motion for the Green's function as a partial sum of Feynman diagrams*, Advances in Physics **20**, 721 (1971).
- [Mat92] R. D. MATTUCK, *A Guide to Feynman Diagrams in the Many-Body Problem* (Dover, NY, 1992), Second Edition.
- [Mül95] H. MÜLLER AND B. D. SEROT, *Phase transitions in warm, asymmetric nuclear matter*, Physical Review C **52**, 2072 (1995).
- [Mül00] H.-M. MÜLLER, S. E. KOONIN, R. SEKI AND U. VAN KOLCK, *Nuclear matter on a lattice*, Physical Review C **61**, 044320 (2000).
- [Müt95] H. MÜTHER, A. POLLS AND W. H. DICKHOFF, *Momentum and energy distributions of nucleons in finite nuclei due to short-range correlations*, Physical Review C **51**, 3040 (1995).
- [Müt99] H. MÜTHER AND A. POLLS, *Correlations derived from modern nucleon-nucleon potentials*, Physical Review C **61**, 014304 (1999).
- [Müt00] H. MÜTHER AND A. POLLS, *Two-body correlations in nuclear systems*, Progress in Particle and Nuclear Physics **45**, 243 (2000).
- [Nat02] J. B. NATOWITZ *et al.*, *Caloric curves and critical behavior in nuclei*, Physical Review C **65**, 034610 (2002).
- [Nef02] T. NEFF, *Short-ranged central and tensor correlations in nuclear many-body systems*, Ph.D. thesis, Technische Universität Darmstadt (2002), advisor: Prof. H. Feldmeier.
- [Neg88] J. W. NEGELE AND H. ORLAND, *Quantum Many-Particle Systems* (Addison-Wesley Publishing, 1988), First Edition.
- [Nic05] O. E. NICOTRA, *Nuclear matter equation of state, from nuclei to compact stellar objects*, Ph.D. thesis, University of Catania (2005), advisor: Prof. M. Baldo.
- [nnoa] <http://nn-online.org>, a service created and maintained by the Theoretical High Energy Physics Group, Radboud University Nijmegen, the Netherlands.
- [nnob] <http://gwdac.phys.gwu.edu>, a service created and maintained by the Center for Nuclear Studies, Department of Physics, The George Washington University, Virginia, USA.

-
- [Nor75] R. E. NORTON AND J. M. CORNWALL, *On the formalism of relativistic many body theory*, Annals of Physics **91**, 106 (1975).
- [Pag06] D. PAGE AND S. REDDY, *Dense matter in compact stars: Theoretical developments and observational constraints*, Annual Review of Nuclear and Particle Science **56**, 327 (2006).
- [Pet73] C. J. PETHICK AND G. M. CARNEIRO, *Specific-heat of a normal Fermi-Liquid. 1. Landau-theory approach*, Physical Review A **7**, 304 (1973).
- [Pie01] S. C. PIEPER, V. R. PANDHARIPANDE, R. B. WIRINGA AND J. CARLSON, *Realistic models of pion-exchange three-nucleon interactions*, Physical Review C **64**, 014001 (2001).
- [Pin89] D. PINES AND P. NOZIÈRES, *The Theory of Quantum Liquids* (Addison-Wesley, Redwood City, CA, 1989).
- [Poc95] J. POCHODZALLA *et al.*, *Probing the nuclear liquid-gas phase transition*, Physical Review Letters **75**, 1040 (1995).
- [Poc97] J. POCHODZALLA, *The search for the liquid-gas phase transition in nuclei*, Progress in Particle and Nuclear Physics **39**, 443 (1997).
- [Pol94] A. POLLS, A. RAMOS, J. VENTURA, S. AMARI AND W. H. DICKHOFF, *Energy weighted sum rules for spectral functions in nuclear matter*, Physical Review C **49**, 3050 (1994).
- [Pot06] M. POTTHOFF, *Non-perturbative construction of the Luttinger-Ward functional*, Condensed matter physics **9**, 557 (2006).
- [Pra97] M. PRAKASH, I. BOMBACI, M. PRAKASH, P. ELLIS, J. LATTIMER AND R. KNORREN, *Composition and structure of protoneutron stars*, Physics Reports **280**, 1 (1997).
- [Pud97] B. S. PUDLINER, V. R. PANDHARIPANDE, J. CARLSON, S. C. PIEPER AND R. B. WIRINGA, *Quantum Monte Carlo calculations of nuclei with $A < \sim 7$* , Physical Review C **56**, 1720 (1997).
- [Puf61] R. D. PUFF, *Ground-state properties of nuclear matter*, Annals of Physics **13**, 317 (1961).
- [Ram88] A. RAMOS, *Beyond a mean field description of nuclear systems within Self-Consistent Green's Function theory*, Ph.D. thesis, Universitat de Barcelona (1988), advisor: Profs. W. H. Dickhoff and A. Polls.

-
- [Ram89] A. RAMOS, A. POLLS AND W. DICKHOFF, *Single-particle properties and short-range correlations in nuclear matter*, Nuclear Physics A **503**, 1 (1989).
- [Rap96] R. RAPP AND J. WAMBACH, *Equation of state of an interacting pion gas with realistic $\pi - \pi$ interactions*, Physical Review C **53**, 3057 (1996).
- [Rey63] J. C. REYNOLDS AND R. D. PUFF, *Volume properties of ground-state nuclear matter*, Physical Review **130**, 1877 (1963).
- [Rin80] P. RING AND P. SCHUCK, *The Nuclear Many-Body Problem* (Springer-Verlag, New York, 1980), First Edition.
- [Rio05a] A. RIOS, A. POLLS, A. RAMOS AND I. VIDANA, *Bulk and single-particle properties of hyperonic matter at finite temperature*, Physical Review C **72**, 024316 (2005).
- [Rio05b] A. RIOS, A. POLLS AND I. VIDANA, *Ferromagnetic instabilities in neutron matter at finite temperature with the Skyrme interaction*, Physical Review C **71**, 055802 (2005).
- [Rio06a] A. RIOS, A. POLLS AND H. MÜTHER, *Sum rules and correlations in asymmetric nuclear matter*, Physical Review C **73**, 024305 (2006).
- [Rio06b] A. RIOS, A. POLLS, A. RAMOS AND H. MÜTHER, *Entropy of a correlated system of fermions*, Physical Review C **74**, 054317 (2006).
- [Rob03] N. J. ROBERTSON, *Effects of short-range correlations on Λ decay in nuclear matter*, Ph.D. thesis, Washington University, St. Louis, Missouri (2003), advisor: Prof. W. H. Dickhoff.
- [Rob04] N. J. ROBERTSON AND W. H. DICKHOFF, *Correlation effects on Λ propagation in nuclear matter*, Physical Review C **70**, 044301 (2004).
- [Roh04] D. ROHE *et al.*, *Correlated strength in the nuclear spectral function*, Physical Review Letters **93**, 182501 (2004).
- [Sar96] R. SARTOR, *Solution of the Bethe-Goldstone equation with an exact propagator*, Physical Review C **54**, 809 (1996).
- [Sch96] A. SCHNELL, T. ALM AND G. RÖPKE, *Nucleon self-energies and spectral functions in nuclear matter at finite temperature with a realistic potential*, Physics Letters B **387**, 443 (1996).
- [Sed07] A. SEDRAKIAN, *The physics of dense hadronic matter and compact stars*, Progress in Particle and Nuclear Physics **58**, 168 (2007).

-
- [Ser86] B. D. SEROT AND J. D. WALECKA, *The relativistic nuclear many-body problem*, Advances in Nuclear Physics **16**, (Eds. J. W. Negele and E. W. Vogt, Plenum Press, NY), (1986).
- [Sil04] T. SIL, S. K. SAMADDAR, J. N. DE AND S. SHLOMO, *Liquid-gas phase transition in infinite and finite nuclear systems*, Physical Review C **69**, 014602 (2004).
- [Som06] V. SOMA AND P. BOZEK, *Diagrammatic calculation of thermodynamical quantities in nuclear matter*, Physical Review C **74**, 045809 (2006).
- [Son98] H. Q. SONG, M. BALDO, G. GIANIRACUSA AND U. LOMBARDO, *Bethe-Brueckner-Goldstone expansion in nuclear matter*, Physical Review Letters **81**, 1584 (1998).
- [Ste05] A. STEINER, M. PRAKASH, J. LATTIMER AND P. ELLIS, *Isospin asymmetry in nuclei and neutron stars*, Physics Reports **411**, 325 (2005).
- [Sto03] J. R. STONE, J. C. MILLER, R. KONCEWICZ, P. D. STEVENSON AND M. R. STRAYER, *Nuclear matter and neutron-star properties calculated with the Skyrme interaction*, Physical Review C **68**, 034324 (2003).
- [Sur98] E. SURAUD, *La matière nucléaire: des étoiles aux noyaux* (Hermann, Paris, 1998).
- [Suz00] K. SUZUKI, R. OKAMOTO, M. KOHNO AND S. NAGATA, *Exact treatment of the Pauli exclusion operator in nuclear matter calculation*, Nuclear Physics A **665**, 92 (2000).
- [tH86] B. TER HAAR AND R. MALFLIET, *Equation of state of nuclear matter in the relativistic Dirac-Brueckner approach*, Physical Review Letters **56**, 1237 (1986).
- [Tho60] D. J. THOULESS, *Perturbation theory in statistical mechanics and the theory of superconductivity*, Annals of Physics **10**, 553 (1960).
- [Van98] B. VANDERHEYDEN AND G. BAYM, *Self-consistent approximations in relativistic plasmas: Quasiparticle analysis of the thermodynamic properties*, Journal of Statistical Physics **93**, 843 (1998).
- [Vau72] D. VAUTHERIN AND D. M. BRINK, *Hartree-Fock calculations with Skyrme's interaction. I. Spherical nuclei*, Physical Review C **5**, 626 (1972).
- [vD04] E. N. E. VAN DALEN, C. FUCHS AND A. FAESSLER, *The relativistic Dirac-Brueckner approach to asymmetric nuclear matter*, Nuclear Physics A **744**, 227 (2004).
-

-
- [Vid00] I. VIDAÑA, A. POLLS, A. RAMOS, L. ENGVIK AND M. HJORTH-JENSEN, *Hyperon-hyperon interactions and properties of neutron star matter*, Physical Review C **62**, 035801 (2000).
- [Von93] B. E. VONDERFECHT, W. H. DICKHOFF, A. POLLS AND A. RAMOS, *Influence of tensor and short-range correlations on nucleon properties in the nuclear medium*, Nuclear Physics A **555**, 1 (1993).
- [Wad87] R. WADA *et al.*, *Isotopic-yield ratios for complex fragments from intermediate-energy heavy-ions reactions*, Physical Review Letters **58**, 1829 (1987).
- [Web85] F. WEBER AND M. K. WEIGEL, *Ground-state properties of nuclear matter using the Λ approximations of the Green's function theory*, Physical Review C **32**, 2141 (1985).
- [Wei98a] W. WEINHOLD, *Thermodynamik mit Resonanzzuständen*, Ph.D. thesis, Technische Hochschule Darmstadt (1998), advisor: Prof. W. Nörenberg.
- [Wei98b] W. WEINHOLD, B. FRIMAN AND W. NÖRENBERG, *Thermodynamics of Δ resonances*, Physics Letters B **433**, 236 (1998).
- [Wir95] R. B. WIRINGA, V. G. J. STOKS AND R. SCHIAVILLA, *Accurate nucleon-nucleon potential with charge-independence breaking*, Physical Review C **51**, 38 (1995).
- [Yao06] W.-M. YAO AND OTHERS (PARTICLE DATA GROUP), *Review of Particle Physics*, Journal of Physics G **33**, 1 (2006).
- [Yuk35] H. YUKAWA, *On the interaction of elementary particles*, Proceedings of the Physical and Mathematical Society of Japan **17**, 48 (1935).
- [Zuo99] W. ZUO, I. BOMBACI AND U. LOMBARDO, *Asymmetric nuclear matter from an extended Brueckner-Hartree-Fock approach*, Physical Review C **60**, 024605 (1999).
- [Zuo03] W. ZUO, Z. H. LI AND G. C. LU, *Hot nuclear matter equation of state with a three-body force*, Physical Review C **69**, 064001 (2003).
- [Zuo06] W. ZUO, Z. H. LI, U. LOMBARDO, G. C. LU AND H.-J. SCHULZE, *Temperature dependence of single-particle properties in nuclear matter*, Physical Review C **73**, 035208 (2006).

List of publications

1. T. Frick, H. Mütter, A. Rios, A. Polls and A. Ramos,
Correlations in hot asymmetric nuclear matter,
Physical Review C **71**, 014313 (2005).
2. A. Rios, A. Polls and I. Vidaña,
Ferromagnetic instabilities in neutron matter at finite temperature with the Skyrme interaction,
Physical Review C **71**, 055802 (2005).
3. A. Rios, A. Polls, A. Ramos and I. Vidaña,
Bulk and single-particle properties of hyperonic matter at finite temperature,
Physical Review C **72**, 024316 (2005).
4. I. Bombaci, A. Polls, A. Ramos, A. Rios and I. Vidaña,
Microscopic calculations of spin polarized neutron matter at finite temperature,
Physics Letters B **632**, 638 (2006).
5. A. Rios, A. Polls and H. Mütter,
Sum rules of single-particle spectral functions in hot asymmetric nuclear matter,
Physical Review C **73**, 024305 (2006).
6. A. Rios,
El pentaquark Θ^+ i les tècniques d'unitarització quirals,
Revista de Física **3**, (10), 34 (2006).
7. A. Rios, A. Polls and J. Margueron,
Neutrino propagation in dense hadronic matter,
Acta Physica Polonica B **37**, 2403 (2006).
8. A. Rios, A. Polls, A. Ramos and H. Mütter,
Entropy of a correlated system of nucleons,
Physical Review C **74**, 054317 (2006).
9. D. López-Val, A. Rios, A. Polls and I. Vidaña,
Ferromagnetic instabilities in neutron matter at finite temperature with the Gogny interaction,
Physical Review C **74**, 068801 (2006).